Ningsu Luo
Yolanda Vidal
Leonardo Acho   *Editors*

Wind Turbine Control and Monitoring

AIC

Springer

Advances in Industrial Control

Series editors

Michael J. Grimble, Glasgow, UK
Michael A. Johnson, Kidlington, UK

Ningsu Luo · Yolanda Vidal
Leonardo Acho
Editors

Wind Turbine Control and Monitoring

 Springer

Editors
Ningsu Luo
University of Girona
Girona
Spain

Yolanda Vidal
Leonardo Acho
Polytechnic University of Catalonia
Barcelona
Spain

Preface

The development of environmentally compatible energy technologies has been accelerated in response to the growing concern of the impacts from climate change. Wind energy is rapidly emerging as a low carbon, resource efficient, cost-effective sustainable technology in the world. Due to the demand of higher power production installations with less environmental impacts, the continuous increase of the size of wind turbines and the recently developed offshore (floating) technologies have led to new challenges in the wind turbine systems.

Wind turbines are complex systems with large flexible structures that work under very turbulent and unpredictable environmental conditions for a variable electrical grid. The maximization of wind energy conversion systems, load reduction strategies, mechanical fatigue minimization problems, costs per kilowatt hour reduction strategies, reliability matters, stability problems, and availability (sustainability) aspects demand the use of advanced (multivariable and multi-objective) cooperative control systems to regulate variables such as pitch, torque, power, rotor speed, power factors of every wind turbine, etc. Meanwhile, the purpose of wind turbine monitoring and fault diagnosis systems is to detect and locate degradations and failures in the operation of wind turbine components as early as possible, so that maintenance operations can be performed in due time (e.g., during time periods with low wind speed). Therefore, the number of costly corrective maintenance actions can be reduced and consequently the loss of wind power production due to maintenance operations is minimized.

This book is mainly research-oriented, covers, and advances the current state-of-the-art of aforementioned subjects. It provides new understanding, methodologies, and algorithms of control and monitoring, and computer tools for modeling and simulation, along with several illustrative examples and practical case studies, and therefore includes extensive application features not found in solely academic textbooks. This book is primarily intended for researchers and postgraduates in the field of wind turbines, wind energy, and various disciplines ranging from electrical, mechanical to control engineering, and graduate and senior undergraduate students in engineering wishing to expand their knowledge of wind energy systems. The practicing engineers of wind technology will also benefit from the

comprehensive coverage of all topics of this book for acquiring new knowledge on wind turbine systems.

This book is divided into five main parts: Power Converter Systems (Chaps. 1–3); Control (Chaps. 4–7); Monitoring and Fault Diagnosis (Chaps. 8–11); Vibration Mitigation (Chaps. 12–13); and Test-Bench for Research/Education (Chaps. 14–15).

Chapter 1 studies the variable speed permanent-magnetic synchronous generator with power electronic converters. The proposed supervisory reactive power control scheme can be applied to larger wind farms and network configurations. Chapter 2 proposes a higher-order sliding mode control strategy for the doubly-fed induction generators-based wind turbines. Simulations using the NREL FAST code have shown its effectiveness and attractiveness in terms of robustness (fault ride-through capability enhancement) and sensorless control. Chapter 3 deals with the problem of grid integration of the wind energy conversion systems by optimizing the power delivered to the grid in order to provide the voltage support ancillary service at the point of common coupling. Maximum power point tracking control algorithms are proposed for the variable speed wind energy conversion systems. Chapter 4 presents a robust pitch control design for variable speed wind turbines operating along the entire wind speed range. H_∞ and advanced antiwindup techniques are used to provide a high performance control solution for both low wind and high wind operating modes with optimum performance in the transition zone. Chapter 5 proposes a unified design procedure for different multivariable robust controllers. The designed feedback control strategies can reduce the wind effect in structural modes and consequently mitigate the fatigue loads in the wind turbine. Chapter 6 presents an individual pitch static output feedback controller for an offshore floating wind turbine system. By properly designing a constrained control gain matrix, the proposed control strategy is robust and fault tolerant to the pitch sensor failure. Chapter 7 focuses on investigations of different aspects related to a fault tolerant control approach to sustainable wind turbine systems. Fault tolerant control strategies based on the Takagi-Sugeno fuzzy framework are presented for offshore wind turbines. Chapter 8 studies the problem of the ice accumulation monitoring and active de-icing control of wind turbine blades. An optical ice sensing method is proposed for the direct detection of ice on the blade. An aero/thermodynamic model is developed to predict the heat flux locally needed for de-icing under variable atmospheric conditions. Chapter 9 provides a structural health monitoring solution for wind turbine blades. A fatigue damage detection system is developed by using high-spatial-resolution differential pulse-width pair Brillouin optical time-domain analysis sensing system. Chapter 10 presents new methods of single sensor based monitoring, and redundant sensors based fault detection/isolation, in which the analytical redundancy for sensor fault detection/isolation is considered and a decision system based on a recursive statistical change detection/isolation algorithm is used. Chapter 11 studies the structural loading effects of various pitch system faults in an offshore floating wind turbine. The considered faults include the bias and gain errors in pitch sensor measurements, the performance degradation of the pitch actuator, in addition to the

actuator stuck and actuator runaway faults. Chapter 12 deals with the problem of vibration mitigation of wind turbine towers. Tuned mass damper and tuned liquid column damper are used to reduce the resonant tower vibrations induced by the soil-structure interaction and eventual seismic excitation, and thus to improve the fatigue life of wind turbines. Chapter 13 proposes the use of magnetorheological dampers to control the structural response of wind turbines. Based on the smart base restraint (a combination of the smooth hinge, elastic springs and magneto-rheological dampers), a semiactive control algorithm commands instantaneously the magnetorheological dampers during the motion, making them modulating the reactive force as needed to achieve the performance goals. Chapter 14 presents a new low-cost, flexible test-bench wind farm for advanced research and education in optimum wind turbine, which is useful for making experimental validation of wind farm design, modeling, estimation and multiloop cooperative control. Chapter 15 illustrates how to set up an inexpensive but effective hard-ware-in-the-loop platform for the test of wind turbine controllers.

Finally, we would like to express our deep gratitude to all authors for their high-quality contributions, and to all reviewers and managing personal of Springer for their interest and enthusiasm throughout the editing process of this book.

Girona, Spain   Ningsu Luo
Barcelona, Spain   Yolanda Vidal
                                                                                                                   Leonardo Acho

Contents

Part III   Monitoring and Fault Diagnosis

Part IV   Vibration Mitigation

Part V   Test-Bench for Research/Education

Part I
Power Converter Systems

Chapter 1
Modeling and Control of PMSG-Based Variable-Speed Wind Turbine

Hee-Sang Ko

Abstract This chapter presents a control scheme of a variable-speed wind turbine with a permanent-magnet synchronous-generator (PMSG) and full-scale back-to-back voltage source converter. A comprehensive dynamical model of the PMSG wind turbine and its control scheme is presented. The control scheme comprises both the wind-turbine control itself and the power-converter control. In addition, since the PMSG wind turbine is able to support actively the grid due to its capability to control independently active and reactive power production to the imposed set-values with taking into account its operating state and limits, this chapter presents the supervisory reactive-power control scheme in order to regulate/contribute the voltage at a remote location. The ability of the control scheme is assessed and discussed by means of simulations, based on a candidate site of the offshore wind farm in Jeju, Korea.

Keywords Permanent-magnetic synchronous generator · Wind turbine · Wind farm · Variable speed · Voltage control · Point- of-common coupling

Nomenclature

PMSG	Permanent magnetic synchronous generator
TR	Transformer
TL	Transmission line
Ca	Cable
IB	Infinite bus
VSC	Voltage source converter
PCC	Point-of-common coupling
WT	Wind turbine
Sub-script: 1–5	Bus number
v, i	Voltage, current

H.-S. Ko (✉)
Wind Energy Laboratory, Korea Institute of Energy Research, Daejeon, Korea
e-mail: heesangko@kier.re.kr

Sub-scripts: d, q	Direct, quadratic axis in synchronous reference frame
R, L, C	Resistance, inductance, capacitance
ω_e	Stator electrical angular speed of PMSG
ω_b	Base angular speed in rad/sec
ω_r	Generator rotational speed of PMSG
L_s	Stator leakage inductance of PMSG
ψ_m	Exciter flux of PMSG
ψ	Flux leakage of PMSG
P_g^{set}	Set-value for active power of grid-side controller of VSC
Q_g^{set}	Set-value for reactive power of grid-side controller of VSC
Q_s^{set}	Set-value for reactive power of generator-side controller of VSC
Sub-script: s	Stator quantity of PMSG and/or generator-side quantity of generator-side controller of VSC
Sub-script: g	Grid-side quantity of grid-side controller of VSC
Sub-script: b	Base quantity for per-unit
Sub-script: $filt$	Filter quantity of RL-filter
Sub-script: dc	Dc-link quantity of VSC
k_p, k_i	Proportional and integral gain of PI controller

1.1 Introduction

Variable-speed power generation enables the operation of the turbine at its maximum power coefficient over a wide range of wind speeds, obtaining a larger energy capture from the wind with a power converter which allows variable-speed operation. One of the problems associated with variable-speed wind systems today is the presence of the gearbox coupling the wind turbine (WT) to the generator. This mechanical element suffers from considerable faults and increases maintenance expenses. To improve reliability of the WT and reduce maintenance expenses the gearbox should be eliminated.

Megawatt (MW) class wind turbines equipped with a permanent-magnetic synchronous generator (PMSG) have been announced by Siemens Power Generation and GE Energy. In this concept, the PMSG can be directly driven or can have smaller gearboxes or even gearless and is connected to the ac power grid through the power converter. Use of the power converter is essential because it allows the linkage of the generator operating at variable speed to the ac power grid at a fixed electrical frequency. The converter rating must be similar to or even larger than the rated power of the generator. Permanent-magnet excitation allows to use a smaller pole pitch than do conventional generators, so these machines can be designed to rotate at rated speeds of 20–200 rpm, depending on the generator rated power [1].

However, the electromagnetic construction of the PMSG is more complex than in the case of conventional WT concepts such as fixed-speed with squirrel induction generators and variable-speed with doubly-fed induction generators, etc. Also, the reduced gear ratio may require an increase in the number of generator pole pairs, which complicates the generator construction [1–8].

MW class WTs have been commissioned in large (offshore) wind farms connected directly to transmission networks. However, increased wind power generation has influenced the overall power system operation and planning in terms of power quality, security, stability, and voltage control [9–14]. The local power flow pattern and the system's dynamic characteristics change when large WTs are connected to the utility grid [15]. Thus, compliance with the grid codes of national Transmission System Operators (TSOs) becomes an important issue [16].

Therefore, the interaction between WFs and power systems is a research topic that needs more attention. To get a better understanding of how the control systems of the individual WTs and WFs influence each other, modeling and simulation are essential. To investigate the interaction between controllers of WTs or WFs and the controllers of the grid is considered a challenge. With more advanced control algorithms, WTs and WFs can provide ancillary services to the grid, e.g., by providing reactive power or participate in voltage/frequency control. To study the impacts of these advanced control strategies on a system level, more modeling efforts are required.

Therefore, this chapter presents the detail system modeling and the control design of a PMSG-based-WT. Also, alternative design and/or control solutions are proposed to improve the voltage control at a required location such as a point-of-common coupling (PCC).

This chapter is organized as follows: The detail dynamic model including voltage source converter (VSC) control design is presented in Sect. 1.2; in Sect. 1.3, the supervisory reactive-power control scheme is proposed; case studies are carried out in Sect. 1.4; and conclusions are drawn in Sect. 1.5.

1.2 Dynamic Model of PMSG-WT-Based Power Systems

The system considered in this chapter is shown in Fig. 1.1. The WF consists of 5 units of WT. Each WT is equipped with a 0.69/22.9 kV step-up transformer (TR). The WF is connected to the grid using a 2 km submarine cable (Ca) and a 14 km overhead transmission line (TL). The considered operating condition is as follows: the WF supplies 7 MW of active power and 0.3 MVar of reactive power to the local load, which consumes 8 MW and 1.9 MVar. The remaining active power comes through the 154 kV utility grid, which is represented by an infinite bus.

Although the fundamental principle of a WT is straightforward, modern WTs are complex systems. The design and optimization of the WT's blades, drive train,
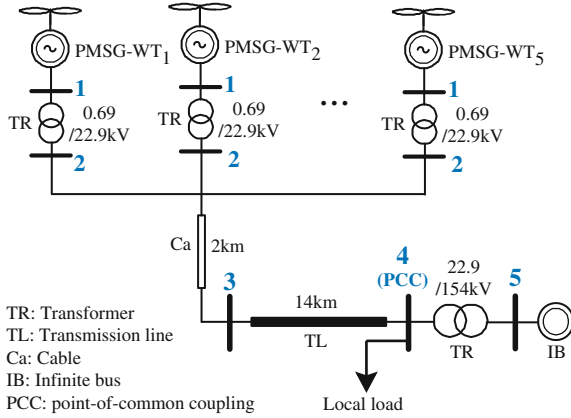
Fig. 1.1 Grid-connected wind turbine system
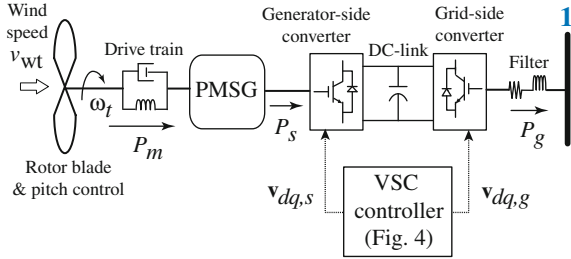
Fig. 1.2 Permanent-magnetic synchronous generator wind turbine (PMSG-WT)

and tower require extensive knowledge of aerodynamics, mechanical and structural engineering, control and protection of electrical subsystems, etc.

The details of the WT considered in the model are shown in Fig. 1.2. The WT consists of the following components: a three-bladed rotor with the corresponding pitch controller [17]; a PMSG with two converters, a dc-link capacitor, a grid filter; and converter controllers.

The generator parameters of a 2 MW PMSG-WT can be found in [1]. The electrical part of the overall system is modeled using the dq-synchronous reference frame [18, 19] representation of the individual components. Wherein, the d-axis is assumed to be aligned to the stator flux, and the current coming out of the machine is considered positive. The PMSG controllers utilize the concept of disconnection of the active and reactive power controls by transformation of the machine parameters into the dq-reference frame and by separating forming of the stator voltages. Then, the active power can be controlled by influencing the d-axis component of the stator current while the reactive power can be controlled by influencing the q-axis components of the stator current. The system parameters and control gains, etc., are summarized in the Appendix.

1.2.1 Permanent-Magnetic Synchronous-Generator

The PMSG was represented by the following equations [1] :

$$\frac{1}{\omega_b}\frac{d\psi_{ds}}{dt} = v_{ds1} + R_s i_{ds} + \omega_e \psi_{qs}$$

$$\frac{1}{\omega_b}\frac{d\psi_{qs}}{dt} = v_{qs1} + R_s i_{qs} - \omega_e \psi_{ds}$$

(1.1)

with

$$\psi_{ds} = -L_{ds}i_{ds} - \psi_m, \qquad \psi_{qs} = -L_{qs}i_{qs} \tag{1.2}$$

where v is the voltage, R is the resistance, i is the current, ω_e is the stator electrical angular speed, ω_b is the base angular speed in rad/sec, L_s is the stator leakage inductance, ψ_m is the exciter flux of the PMSG, and ψ is the flux linkage. The subscripts d and q indicate the direct and quadrature axis components, respectively. The subscripts s and 1 indicate stator quantities and bus 1 shown in Fig. 1.1, respectively. The electrical active and reactive power delivered by the stator are given by

$$P_s = v_{ds1}i_{ds} + v_{qs1}i_{qs}, \quad Q_s = v_{ds1}i_{qs} - v_{qs1}i_{ds} \tag{1.3}$$

The mathematical model of a TL, a TR, a cable, and a load can be obtained from the description of the R, L, C segment [20] into the dq-synchronous reference frame. The equations of the TL, the TR, the cable, and the RL load are given in Eqs. 1.4–1.7 based on Fig. 1.3 where superscripts s and e stand for the sending-end and the receiving-end.
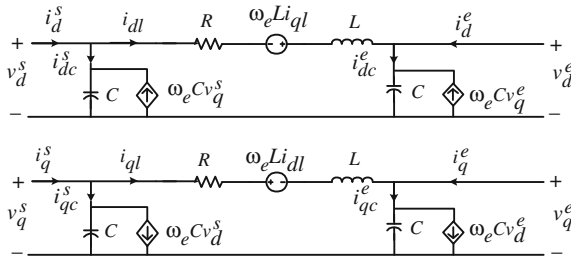
Fig. 1.3 Lumped-parameter π equivalent-circuit description in the dq-domain

1.2.2 Transmission Line

$$\frac{L_{TL}}{\omega_b}\frac{\mathrm{d}i_{dl}}{\mathrm{d}t} = v_{d4} - v_{d3} - R_{TL}i_{dl} + \omega_e L_{TL}i_{ql}$$

$$\frac{L_{TL}}{\omega_b}\frac{\mathrm{d}i_{ql}}{\mathrm{d}t} = v_{q4} - v_{q3} - R_{TL}i_{ql} - \omega_e L_{TL}i_{dl}$$

$$\frac{C_{TL}}{\omega_b}\frac{\mathrm{d}v_{d3}}{\mathrm{d}t} = i_{dc}^s + \omega_e C_{TL}v_{q1}, \quad \frac{C_{TL}}{\omega_b}\frac{\mathrm{d}v_{q3}}{\mathrm{d}t} = i_{qc}^s - \omega_e C_{TL}v_{d3} \quad (1.4)$$

$$\frac{C_{TL}}{\omega_b}\frac{\mathrm{d}v_{d4}}{\mathrm{d}t} = i_{dc}^e + \omega_e C_{TL}v_{q4}, \quad \frac{C_{TL}}{\omega_b}\frac{\mathrm{d}v_{q4}}{\mathrm{d}t} = i_{qc}^e - \omega_e C_{TL}v_{d4}$$

1.2.3 Transformer

$$\frac{L_{tr}}{\omega_b}\frac{\mathrm{d}i_{dl}}{\mathrm{d}t} = v_{d2} - v_{d1} - R_{tr}i_{dl} + \omega_e L_{tr}i_{ql}$$

$$\frac{L_{tr}}{\omega_b}\frac{\mathrm{d}i_{ql}}{\mathrm{d}t} = v_{q2} - v_{q1} - R_{tr}i_{ql} - \omega_e L_{tr}i_{dl} \quad (1.5)$$

$$\frac{C_o}{\omega_b}\frac{\mathrm{d}v_{d1}}{\mathrm{d}t} = i_{dl} + \omega_e C_o v_{q1}, \quad \frac{C_o}{\omega_b}\frac{\mathrm{d}v_{q1}}{\mathrm{d}t} = i_{ql} - \omega_e C_o v_{d1}$$

1.2.4 Cable

$$\frac{L_{ca}}{\omega_b}\frac{\mathrm{d}i_{dl}}{\mathrm{d}t} = v_{d3} - v_{d2} - R_{ca}i_{dl} + \omega_e L_{ca}i_{ql}$$

$$\frac{L_{ca}}{\omega_b}\frac{\mathrm{d}i_{ql}}{\mathrm{d}t} = v_{q3} - v_{q2} - R_{ca}i_{ql} - \omega_e L_{ca}i_{dl} \quad (1.6)$$

$$\frac{C_{ca}}{\omega_b}\frac{\mathrm{d}v_{d2}}{\mathrm{d}t} = i_{dc}^s + \omega_e C_{ca}v_{q2}, \quad \frac{C_{ca}}{\omega_b}\frac{\mathrm{d}v_{q2}}{\mathrm{d}t} = i_{qc}^s - \omega_e C_{ca}v_{d2}$$

1.2.5 RL Load

The RL load in the dq-domain can be described as

$$\frac{L_{\mathrm{load}}}{\omega_b}\frac{\mathrm{d}i_{dL}}{\mathrm{d}t} = v_{d4} - R_{\mathrm{load}}i_{dL} + \omega_e L_{\mathrm{load}}i_{qL}$$

$$\frac{L_{\mathrm{load}}}{\omega_b}\frac{\mathrm{d}i_{qL}}{\mathrm{d}t} = v_{q4} - R_{\mathrm{load}}i_{qL} - \omega_e L_{\mathrm{load}}i_{dL} \quad (1.7)$$

$$\frac{C_o}{\omega_b}\frac{\mathrm{d}v_{d4}}{\mathrm{d}t} = i_{dL} + \omega_e C_o v_{q4}, \quad \frac{C_o}{\omega_b}\frac{\mathrm{d}v_{q4}}{\mathrm{d}t} = i_{qL} - \omega_e C_o v_{d4}$$

As shown in Fig. 1.2, the grid-side converter is connected to the grid through the filter. The voltage equations for the *RL*-filter in the dq–synchronous reference frame can be derived as shown in Sect. 2.6.

1.2.6 RL-Filter on the Grid-Side Converter

$$\frac{L_{\text{filt}}}{\omega_b}\frac{\mathrm{d}i_{\text{dg}}}{\mathrm{d}t} = v_{\text{d}1} - R_{\text{filt}}i_{\text{dg}} + \omega_e L_{\text{filt}}i_{qg}$$
$$\frac{L_{\text{filt}}}{\omega_b}\frac{\mathrm{d}i_{qg}}{\mathrm{d}t} = v_{q1} - R_{\text{filt}}i_{qg} - \omega_e L_{\text{filt}}i_{\text{dg}} \tag{1.8}$$

where subscript filt stands for filter.

1.2.7 Voltage Source Converter Controller

Figure 1.4 presents the detailed block diagram of the VSC controller depicting the respective input and output variables. Here, P_g^{set} is the set-value for the active power for the WT terminal. The value of P_g^{set} is determined from the WT energy-harvesting characteristic as shown in Fig. 1.5, which is represented here as a lookup table $P_g^{\text{set}}(\omega_r)$ determined in terms of generator rotational-speed ω_r. Since variable-speed WTs are traditionally operated in PFC mode to achieve the unity power factor at the terminal of the WT, the reactive power set-point Q_g^{set} is set to zero.

The VSC control module consists of the generator-side, the dc-link, and the grid-side converter controller. These controllers utilize proportional-integral (PI) controllers. These PI controllers are tuned using the Nyquist constraint technique to deal with model uncertainties [21, 22]. Each of the controllers is briefly described below.
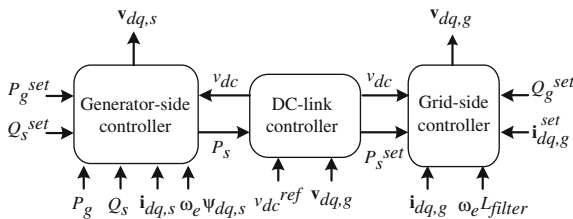
Fig. 1.4 Block diagram of the VSC controller showing the input/output variables

Fig. 1.5 WT maximum
energy-harvesting curve
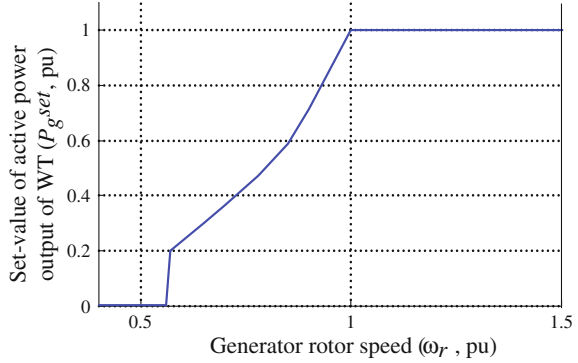
Fig. 1.6 Block diagram of
the generator-side converter
controller
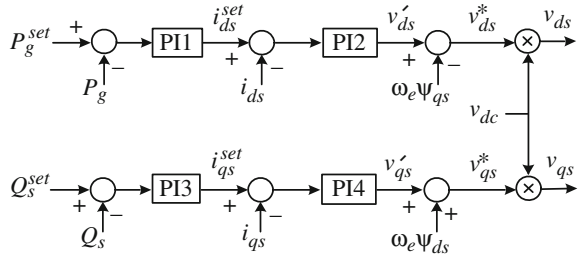
A. *Generator-side converter controller*: Fig. 1.6 shows a block diagram of the
generator-side converter controller module, which includes four internal PI
controllers, PI1 through PI4. The controller is implemented as two branches,
one for the active power (PI1 and PI2) and one for the reactive power (PI3 and
PI4) with the corresponding de-coupling terms between the d and q axes,
respectively.

The transfer function from the stator voltage to the stator current is approximated as

$$\begin{bmatrix} \dfrac{I_{ds}(s)}{V'_{ds}(s)} & \dfrac{I_{qs}(s)}{V'_{qs}(s)} \end{bmatrix}^{T} = \begin{bmatrix} \dfrac{1}{R_s + s(L_{ds}/\omega_b)} & \dfrac{1}{R_s + s(L_{qs}/\omega_b)} \end{bmatrix}^{T} \qquad (1.9)$$

Similarly, the transfer function from the stator current to reactive and active
power is approximated as

$$\begin{bmatrix} \dfrac{P_s(s)}{I_{ds}(s)} & \dfrac{Q_g(s)}{I_{qs}(s)} \end{bmatrix}^{T} = \begin{bmatrix} R_s + s\dfrac{L_{ds}}{\omega_b} & R_s + s\dfrac{L_{qs}}{\omega_b} \end{bmatrix}^{T} \qquad (1.10)$$

Then, Eq. 1.9 is used to tune PI2 and PI4, and Eq. 1.10 is used to tune PI1 and
PI3.

Fig. 1.7 Block diagram of
the grid-side converter
controller
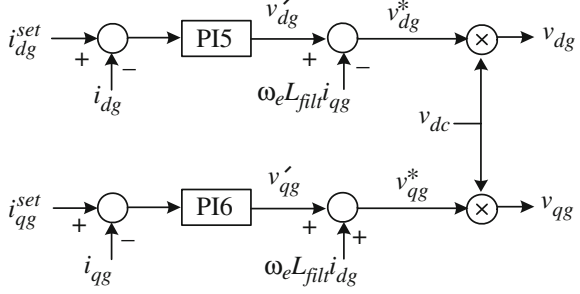
B. *Grid-side converter controller*: Fig. 1.7 shows a block diagram of the grid-side
converter controller module, which also includes two internal PI controllers PI5
and PI6, with corresponding de-coupling terms between the d and q axes.

The voltage equation for the grid-side converter RL-filter can be expressed as

$$
\begin{aligned}
\left(\frac{L_{\text{filt}}}{\omega_b}\right)\frac{di_{dg}}{dt} &= v_{d1} - R_{\text{filt}}i_{dg} + \omega_e L_{\text{filt}}i_{dg} \\
\left(\frac{L_{\text{filt}}}{\omega_b}\right)\frac{di_{qg}}{dt} &= v_{q1} - R_{\text{filt}}i_{qg} - \omega_e L_{\text{filt}}i_{dg}
\end{aligned}
\tag{1.11}
$$

from which the transfer function from the filter voltage to current is

$$
\begin{aligned}
&\left[\frac{I_{dg}(s)}{V_{d1}(s)} \quad \frac{I_{qg}(s)}{V_{q1}(s)}\right]^T = \\
&\left[\frac{1}{R_{\text{filt}} + s(L_{\text{filt}}/\omega_b)} \quad \frac{1}{R_{\text{filt}} + s(L_{\text{filt}}/\omega_b)}\right]^T
\end{aligned}
\tag{1.12}
$$

The inputs to the grid-side controller are the set-values for the currents, which
flows to the grid through the VSC. The set-values of the input currents are cal-
culated by the active and reactive power commands P_s^{set} and Q_g^{set} as follows:

$$
\begin{bmatrix} i_{qg}^{\text{set}} \\ i_{dg}^{\text{set}} \end{bmatrix} = \begin{bmatrix} v_{q1} & v_{d1} \\ -v_{d1} & v_{q1} \end{bmatrix}^{-1} \begin{bmatrix} P_s^{\text{set}} \\ Q_g^{\text{set}} \end{bmatrix}
\tag{1.13}
$$

where P_s^{set} and Q_g^{set} are the set-points of the active and reactive power commands.
The value for P_s^{set} is provided by the dc-link controller, which determines the flow
of active power and regulates the dc-link voltage by driving it to a constant
reference value.

C. *DC-link dynamic model and its controller*: The capacitor in the dc-link is an
energy storage device. Neglecting losses, the time derivative of the energy in
this capacitor depends on the difference in the power delivered to the grid filter,
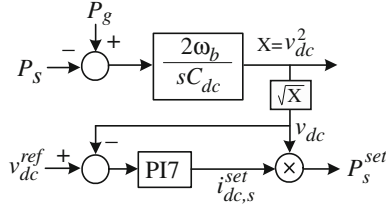
Fig. 1.8 DC-link model and its controller

P_g, and the power provided by the stator circuit of the PMSG, P_s, which can be expressed as

$$\frac{1}{2}\frac{C_{dc}}{\omega_b}\frac{dv_{dc}^2}{dt} = P_g - P_s \tag{1.14}$$

The dc-link controller regulates the capacitor voltage by driving it to the reference value v_{dc}^{ref}, and outputs the set point for the active power P_s^{set} needed in Eq. 1.13. Figure 1.8 shows the dc-link model with its controller PI7. The set point for the output active power by $P_s^{set} = v_{dc}i_{dc,s}^{set}$.

1.3 The Supervisory Reactive Power Control

The purpose of the proposed supervisory reactive power control is to regulate the voltage at the specified remote PCC (see Fig. 1.1) by adjusting the reactive power produced by the grid-side converter, taking into account its operating state and limits. As shown in Fig. 1.9, the control objective is to utilize Q_j from the grid-side VSC to control the voltage at the PCC to the predefined value by the reactive power set-point control signal Q_j^{set}.
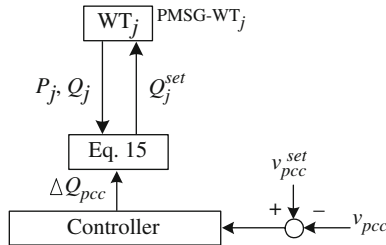
Fig. 1.9 Schematic diagram of the supervisory reactive power control

Fig. 1.10 VSC active and reactive power operating limits
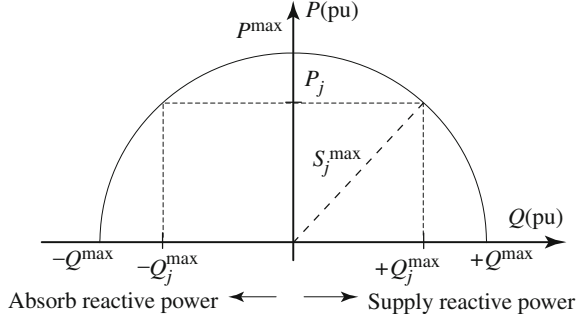
When controlling WT, it is important that the operating limit of WT is not exceeded. The reactive power required from an individual grid-side converter of the VSC can be computed as

$$Q_j^{\text{set}} = \min\left\{ Q_j^{\text{max}}, \quad \frac{Q_j^{\text{max}}}{Q_1^{\text{max}} + \cdots + Q_5^{\text{max}}} \Delta Q_{pcc} \right\} \tag{1.15}$$

where $j = 1, \cdots, 5$, Q_j^{max} is the maximum reactive power (limit) that the jth grid-side converter can provide, and ΔQ_{pcc} is the total reactive power required to support the voltage at the PCC.

Figure 1.10 shows the active- and the reactive-power operating limits, wherein it is assumed that the grid-side converter should not exceed its apparent power limit S_j^{max} depicted by the half-circle. Suppose that at a given time each grid-side converter is delivering the active power denoted herein by P_j. Then, in addition to the active power, the converter can supply or absorb a maximum of Q_j^{max} of the reactive power. Therefore, the reactive power available from the grid-side converter lies within the limits $\left[-Q_j^{\text{max}}; \quad +Q_j^{\text{max}} \right]$, which are operating-condition dependent.

Thus, the maximum available reactive power from the each grid-side converter can be expressed as

$$Q_j^{\text{max}} = \sqrt{\left(S_j^{\text{max}} \right)^2 - P_j^2} \tag{1.16}$$

where it is assumed that the nominal apparent power of the each converter is S_j^{max}, defined here as the WT rating. Based on Fig. 1.10, it also follows that $-S_j^{\text{max}} \leq P_j \leq S_j^{\text{max}}$. Thus, the maximum reactive power set-point of Q_j^{set} (see Fig. 1.4) can be determined by Eqs. 1.15–1.16.

Finally, a PI controller is designed for a controller shown in Fig. 1.9. The PI gains are summarized in the Appendix. Since limiting control action should be implemented together with the integrator-anti-windup scheme that would stop integrating the error when the limit is being reached, a PI controller with the

Fig. 1.11 Implementation of PI controller with the distributed anti-windup
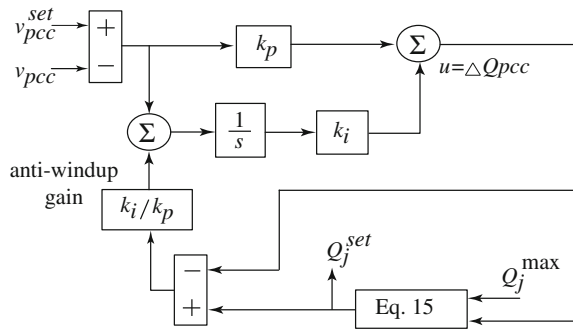
proposed distributed anti-windup is implemented in Matlab/Simulink [18] as shown in Fig. 1.11 for case studies.

The attractive features of the supervisory reactive-power control scheme can be summarized as follows: it does not require installation of additional compensating devices, voltage regulation is achieved by controlling the available reactive power that can be produced by each WT, dynamically changing operating state and limits of each WT are taken into account, the supervisory control action stops automatically for each individual WT whenever its limits have been reached, and the scheme is very general and is readily extendible to multiple variable-speed WTs.

1.4 Case Studies

The system depicted in Fig. 1.1 was implemented in detail using the Matlab/Simulink [23]. Computer studies considering the wind-speed variations, the local-load variations, and the voltage sag due to the fault were conducted to compare the dynamic responses of the system with different controls. In comparison, Mode 1 indicates the PFC-mode operation of the WT, which Q_g^{set} is set to zero. As the proposed operation, Mode 2 actively utilizes Q_g^{set} for voltage control at the PCC.

1.4.1 Wind-Speed Variation

In this study, the wind speeds shown in Fig. 1.12 were considered for the WT. Figure 1.13 shows the voltage at the PCC, predicted by the model with different controls, respectively. As shown in Fig. 1.13, Mode 1 operation caused the voltage deviation about 3 %, which is much higher than the permissible voltage range of HV power system network $\pm$ 2 %, while Mode 2 operation achieved the voltage regulation at the PCC. Figure 1.14 shows the measured data of the active power

Fig. 1.12 Wind speed (m/s)
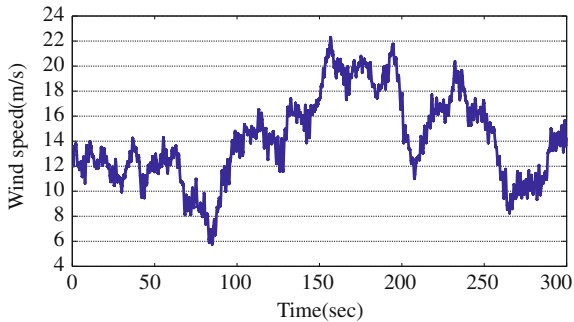
Fig. 1.13 Voltage observed at the PCC due to the wind speed variation
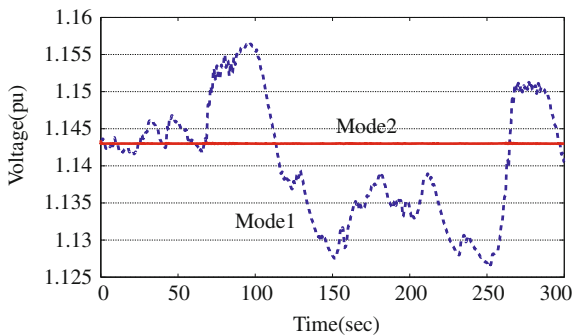
Fig. 1.14 Active and reactive power from WF to PCC for wind speed variation
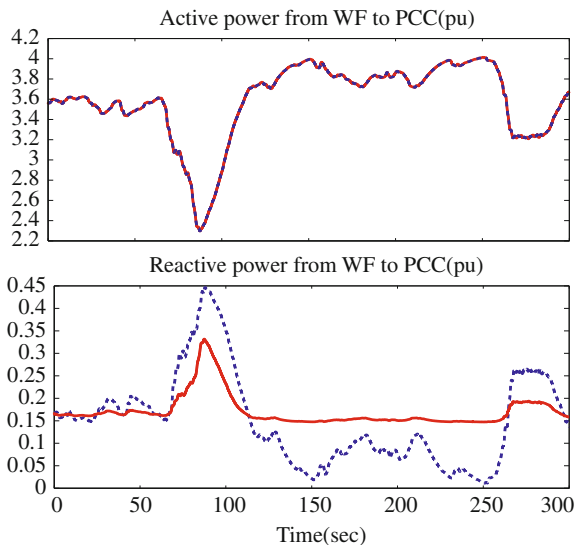
Fig. 1.15 Voltage observed
at the PCC due to the 20 %
impedance decrease
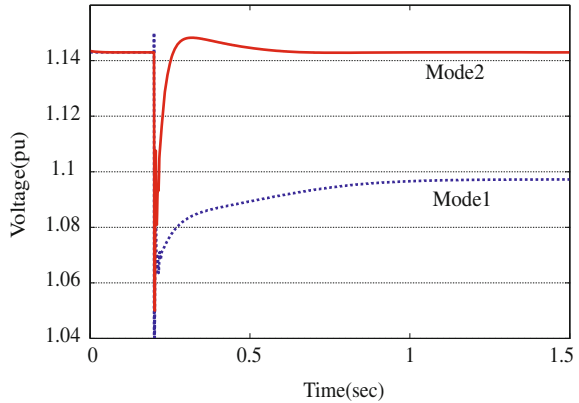
and reactive power from the WF to the PCC (see Fig. 1.1). The reactive power
contribution from the WTs is the difference between Mode 1 and Mode 2.

1.4.2 Local-Load Variation

For this study, the local-load impedance is decreased by 20 % with wind speed
12 m/s. The comparison of the voltage transients observed at the PCC is shown in
Fig. 1.15. As can be noticed, when Mode 1 was in operation, the load impedance
changes resulted in a noticeable drop in the bus voltage by 4.5 % which does not
satisfy the permissible voltage range ± 2 %. When the WT operated in Mode 2, the
voltage recovery to its predefined value was achieved. Thus, the performance in
Mode 2 operation has been significantly improved at the PCC from Mode 1
operation. Figure 1.16 shows the measured data of the active power and the
reactive power from the WF to the PCC. The reactive power contribution from the
WTs is the difference between Mode 2 and Mode 1.

1.4.3 Voltage Sag in the Infinite Bus

To emulate this scenario, it is assumed that there was a fault at $t = 0.5s$ in the
network that caused a 10 % voltage drop at the infinite bus. The wind speed is also
12 m/s. As can be noted in Fig. 1.17, Mode 1 operation showed the significant
voltage drop by 14.5 %, while Mode 2 operation resulted in the voltage recovery
to its predefined voltage at the PCC. Figure 1.18 shows the measured data of the
active and reactive power from WF to the PCC.

Fig. 1.16 Active and reactive power from WF to PCC for load variation
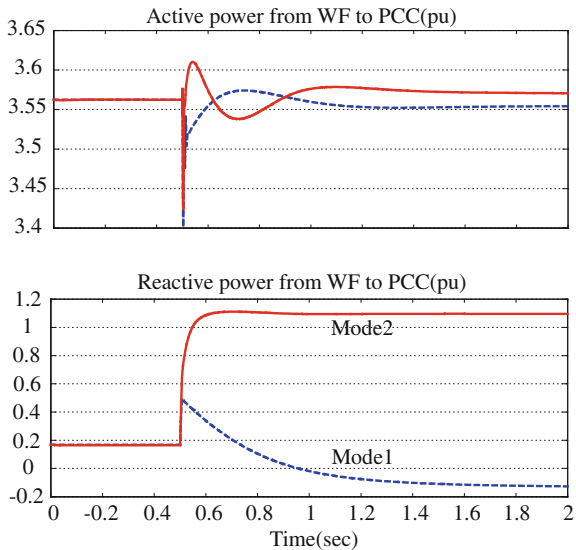
Fig. 1.17 Voltage observed at the PCC for voltage sag in the infinite bus
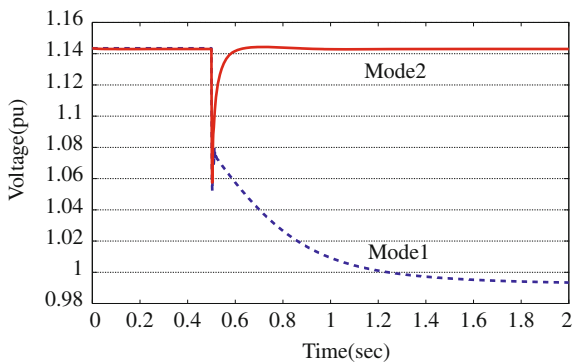
1.4.4 Fault-Ride Through Study

A three-phase symmetrical fault was assumed in the middle of TL with wind speed 12 m/s. To emulate this fault scenario, the fault was assumed at $t = 0.2$ s and was subsequently cleared at $t = 0.36$ s by restoring the initial TL impedance. As can be noted in Fig. 1.19, the fault resulted in significant voltage swings that can undesirably interfere with the protection circuitry and possibly trip the WT. From this point of view, it is desirable to minimize and/or suppress the voltage swings. During the fault, the voltage drop has been slightly improved in Mode 2. After the fault was cleared, faster voltage recovery to reach to its predefined voltage at the

Fig. 1.18 Active and
reactive power from WF to
PCC for voltage sag in the
infinite bus
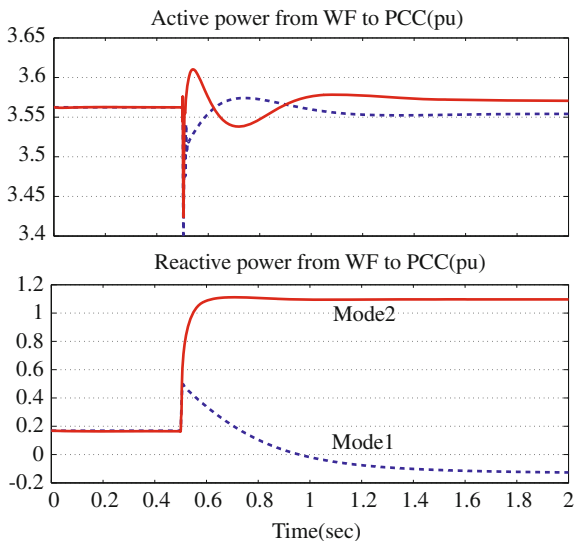
Fig. 1.19 Voltage observed
at the PCC for three-phase
fault
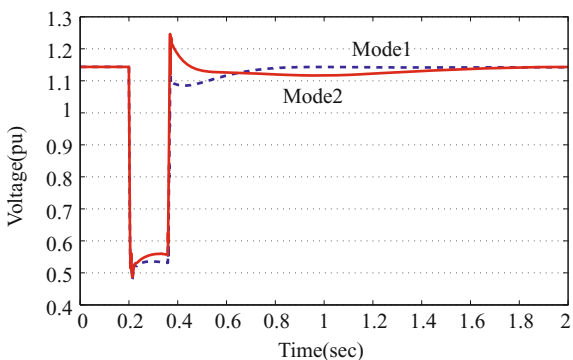
PCC was noticed in Mode 2. Figure 1.20 shows the measured data of the active
power and the reactive power from the WF to the PCC. The reactive power
contribution from the WTs is the difference between Mode 2 and Mode 1.

Fig. 1.20 Active and reactive power from WF to PCC for three-phase fault
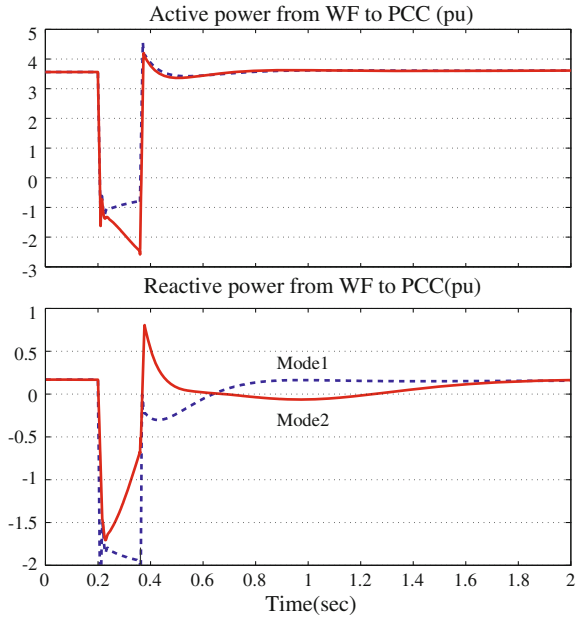
1.5 Conclusion

The chapter presented the modeling and the control design of the variable-speed WT with a permanent-magnet synchronous generator. A comprehensive dynamic simulation model was presented and implemented in Matlab/Simulink. The control scheme facilitates independent control of the active and reactive power to the imposed set values at variable speed. Moreover, the supervisory reactive-power control scheme, developed for voltage control at a remote location, takes into account the power generated by the wind turbine and ensures that the local operating limits are not exceeded. The information passed to the supervisory control module is used to calculate the reactive power required from the grid-side converter to achieve the voltage control objective at the PCC. The supervisory reactive-power control scheme can be general and is readily extendible to multiple variable-speed wind turbines, and is also beneficial and cost-effective, compared to installation of auxiliary devices, which are required when the voltage control scheme such as power factor control is applied for voltage regulation at the PCC.

Appendix

Base values

$$S_b = 2\text{MVA}, _{,b} = 690\text{V}, \quad \omega_b = 2\pi f(rad/\sec), = 60\text{Hz},$$

$$\text{V}_{\text{dc}} = 800\text{V}, \quad Z_b = \left(V_b / \sqrt{3}\right) / i_{b,b} = Z_b / \omega_b, \quad C_b = 1/(Z_b \omega_b),$$

$$T_b = S_b / \omega_b, \quad J_b = S_b / \left(\omega_b^2\right), \quad i_{\text{dc}} = S_b / \text{V}_{\text{dc}},$$

$$Z_{\text{dc}} = \text{V}_{\text{dc}} / i_{\text{dc}}, \quad L_{\text{dc}} = Z_{\text{dc}} / \omega_b, \quad C_{\text{dc}} = 1/(Z_{\text{dc}} \omega_b)$$

Infinite bus voltage and maximum operating limit of VSC (pu)

$$\mathbf{v}_{\text{dq,IB}} = \begin{bmatrix} 1.15 & 0.5 \end{bmatrix}, S_{\max} = 1$$

Line parameter (pu)

$$R_{TL} = 0.0059, \quad L_{TL} = 0.1132, \quad C_{TL} = 0.025, \quad R_{ca} = 0.006,$$

$$L_{ca} = 0.003, \quad C_{ca} = 0.042, \quad R_{\text{filt}} = 0.014, \quad L_{\text{filt}} = 0.175,$$

$$R_{tr1} = 0.0003, \quad L_{tr1} = 0.001, \quad R_{tr2} = 0.0005, \quad L_{tr2} = 0.004$$

PMSG (pu)

$$R_s = 0.042, \quad L_{ds} = 1.05, \quad L_{qs} = 0.75, \quad \psi_m = 1.16$$

Controller gains (pu)

A. *Generator-side converter:*
   Controllers PI1 and PI3: $k_p = 0.2952, \quad k_i = 12.4832$
   Controllers PI2 and PI4: $k_p = 21.5, \quad k_i = 11.5$
B. *Grid-side converter:*
   Controllers PI5 and PI6: $k_p = 0.7147, \quad k_i = 7.1515$
   DC link module: $v_{\text{dc}}^{ref} = 1.16, \quad C_{\text{dc}} = 0.1, \quad k_p = 0.9544, \quad k_i = 7.8175$
C. *Reactive power controllers:* $k_p = 0.001, \quad k_i = 120$

Future Work

This work provides a feasibility study for dynamic modeling and voltage control for wind farm based on simulation. This work will be applied to a demonstration project in order to validate the dynamic modeling and also voltage control and expand its application.

References

1. Ackermann T (2005) Wind power in power systems. Wiley, New York
2. Lampola P, Perho J, Saari J (1995) Electromagnetic and thermal design of a low speed permanent magnet wind generator. In: Proceeding of the international symposium on electric power engineering, 211–216
3. Grauers A (1996) Design of direct-driven permanent magnet generators for wind turbines. Technical Report 292, Chalmers University of Technology, Goteborg
4. Akhmatov V (2003) Variable-speed wind turbines with multi-pole synchronous permanent magnet generators. Part 1. modeling in dynamic simulation tools. J Wind Eng 27:531–548
5. Gonzales-Longatt FM (2005) Dynamic model of variable speed WECS: attend of simplification. In: Proceeding of the 5th international workshop on large-scale integration of wind power and transmission networks for offshore wind farms
6. Hansen LH, Helle L, Blaabjerg F, Ritchie E, Munk-Nielsen S, Binder H, Sørensen P, Bak-Jensen B (2001) In: Conceptual survey of generators and power electronics for wind turbines. Risø National Laboratory, Denmark
7. Cavagnino A, Lazzari M, Profumo F, Tenconi A (2000) A comparison between the axial and the radial flux structures for PM synchronous motors. IEEE Ind Appl Conf Proc 3:1611–1618
8. Spooner E, Williamson AC (1996) Direct coupled, permanent magnet generators for wind turbine applications. IEEE Electric Power Appl Proc 143:1–8
9. Doherty R, Denny E, O'Malley M (2004) System operation with a significant wind power penetration. IEEE Power Eng Summer Meeting Proc 1:1002–1007
10. Salman SK, Teo ALJ (2003) Windmill modeling consideration and factors influencing the stability of a grid-connected wind power-based embedded generator. IEEE Trans Power Syst Proc 18:793–802
11. Litipu Z, Nagasaka K (2004) Improve the reliability and environment of power system based on optimal allocation of WPG. IEEE Power Syst Conf Exposition Proc 1:913–918
12. Dizdarevic N, Dizdarevic N, Majstrovic M, Zutobradic S (2004) Power quality in a distribution network after wind power plant connection. IEEE Power Syst Conf Exposition Proc 2:913–918
13. ON Netz E (2005) Wind power report. http://www.nowhinashwindfarm.co.uk/EON_Netz_Windreport_e_eng.pdf. Accessed 22 Apr 2005
14. Protter N, Garnett G, Pai S (2004) BC Wind Integration System Expansion Study. Elsam Eng 1:1002–1007
15. Gjengedal T (2004) Large scale wind power farms as power plants. In: Proceeding of the nordic wind power conference
16. Matevosyan J, Ackermann T, Bolik SM (2005) Technical regulations for the interconnection of wind farms to the power system. Wind Power Power Syst Proc 25(3):115–142
17. Ko HS (2006) Supervisory voltage control scheme for grid-connected wind farms, PhD Dissertation, Department of Electrical and Computer Engineering at the University of British Columbia, Vancouver, BC, Canada
18. Ong CH (1998) Dynamic simulation of electric machinery. Prentice Hall, New Jersey
19. Morren J, de Haan SWH, Bauer P, Pierik JTG (2003) Comparison of complete and reduced models of a wind turbine using doubly-fed induction generator. In: Proceedings of the 10th European conference on power electronics and applications
20. Krause PC, Wasynczuk O, Sudhoff SD (2002) Analysis of electric machinery and drive systems. Wiley, New York
21. Astrom K, Hagglung T (2004) PID Controllers. Lund Institute of Technology, Sweden
22. Ko HS, Bruey S, Dumont G, Jatskevich J, Ali A (2007) A PI control of DFIG-based wind farm for voltage regulation at remote location. IEEE Power Eng Soc Gen Meet Proc 1–6:35
23. MATLAB® and Simulink®, MathWorks, January 2000

Chapter 2
High-Order Sliding Mode Control of DFIG-Based Wind Turbines

Mohamed Benbouzid

Abstract Actually, variable speed wind turbines are continuously increasing their market share, since it is possible to track the changes in wind speed by adapting shaft speed, and thus maintaining optimal power generation. The more variable speed wind turbines are investigated, the more it becomes obvious that their behavior is significantly affected by the used control strategy. Typically, they use aerodynamic controls in combination with power electronics to regulate torque, speed, and power. The aerodynamic control systems, usually variable-pitch blades or trailing-edge devices, are expensive and complex, especially for larger turbines. This situation provides a motivation to consider alternative control approaches. This chapter deals, therefore, with high-order sliding mode control of doubly-fed induction generator-based wind turbines. This kind of control strategy presents attractive features such as chattering-free behavior (no extra mechanical stress), finite reaching time, and robustness with respect to external disturbances (grid faults) and unmodeled dynamics (generator and turbine). High-sliding mode control appropriateness will be highlighted in terms of sensorless control and enhanced fault-ride through capabilities. Simulations using the NREL FAST code will be shown for validation purposes.

Nomenclature

WT	Wind turbine
DFIG	Doubly-fed induction generator
HOSM	High-order sliding mode
MPPT	Maximum power point tracking
FRT	Fault ride-through

M. Benbouzid (✉)
EA 4325 LBMS, University of Brest, Rue de Kergoat, CS 93837, 29238 Brest Cedex 03, France
e-mail: Mohamed.Benbouzid@univ-brest.fr

LVRT   Low-voltage ride-through
v Wind speed (m/sec)
ρ Air density (kg/m^3)
R Rotor radius (m)
P_a Aerodynamic power (W)
T_a Aerodynamic torque (Nm)
λ Tip speed ratio (TSR)
$C_p(\lambda)$ Power coefficient
β Pitch angle
ω_{mr} WT rotor speed (rad/sec)
ω_{mg} Generator speed (rad/sec)
T_g Generator electromagnetic torque (Nm)
J_t Turbine total inertia (kg m^2)
K_t Turbine total external damping (Nm/rad sec)
d, q Synchronous reference frame index
s, (r) Stator (rotor) index
V (I) Voltage (Current)
P (Q) Active (Reactive) power
ϕ Flux
T_{em} Electromagnetic torque
R Resistance
L (M) Inductance (Mutual inductance)
σ Leakage coefficient
ω_r (ω_s) Angular speed (Synchronous speed)
s Slip
p Pole pair number

2.1 Introduction

Actually, variable speed wind turbines are continuously increasing their market
share, since it is possible to track the changes in wind speed by adapting shaft
speed, and thus maintaining optimal power generation. The more variable speed
wind turbines are investigated, the more it becomes obvious that their behavior is
significantly affected by the used control strategy. Typically, they use aerodynamic
controls in combination with power electronics to regulate torque, speed, and
power. The aerodynamic control systems, usually variable-pitch blades or trailing-
edge devices, are expensive and complex, especially for larger turbines [1]. This
situation provides a motivation to consider alternative control approaches [2].

   The main control objective of variable speed wind turbines is power extraction
maximization. To reach this goal the turbine tip speed ratio should be maintained at its
optimum value despite wind variations. Nevertheless, control is not always aimed at
capturing as much energy as possible. In fact, in above-rated wind speed, the captured

power needs to be limited. Although there are both mechanical and electrical constraints, the more severe ones are commonly on the generator and the converter. Hence, regulation of the power produced by the generator is usually intended, and this is the main objective of this chapter for a DFIG (Doubly-Fed Induction Generator)-based WT (Wind Turbine) using a second order sliding mode controller [3]. In particular, three control aspects will be presented: (1) A high-gain observer to estimate the aerodynamic torque [4]; (2) A high-order sliding mode speed observer [5]; (3) Fault-ride trough performance using high-order sliding mode control [6].

Simulations using the NREL FAST code will be shown for validation purposes.

2.2 The Wind Turbine Modeling

The global scheme for a grid-connected wind turbine is given in Fig. 2.1.

2.2.1 Turbine Model

The turbine modeling is inspired from [7]. In this case, the aerodynamic power P_a captured by the wind turbine is given by

$$P_a = \frac{1}{2}\pi\rho R^2 C_p(\lambda)v^3 \tag{2.1}$$

where the tip speed ratio is given by

$$\lambda = \frac{R\omega_{mr}}{v} \tag{2.2}$$

and where ω_{mr} is the wind turbine rotor speed, ρ is the air density, R is the rotor radius, C_p is the power coefficient, and v is the wind speed.

The $C_p - \lambda$ characteristics, for different values of the pitch angle β, are illustrated in Fig. 2.2. This figure indicates that there is one specific λ at which the turbine is most efficient. Normally, a variable speed wind turbine follows the C_{pmax} to capture the maximum power up to the rated speed by varying the rotor speed to keep the system at λ_{opt}. Then it operates at the rated power with power regulation during high wind periods by active control of the blade pitch angle or passive regulation based on aerodynamic stall.

The rotor power (aerodynamic power) is also defined by

$$P_a = \omega_{mr}T_a \tag{2.3}$$

where T_a is the aerodynamic torque.
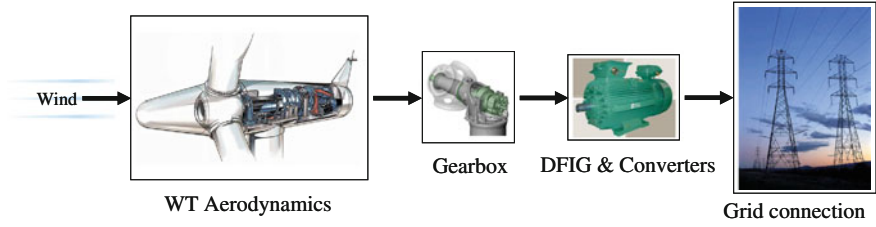
Fig. 2.1 Wind turbine global scheme

Fig. 2.2 Wind turbine power coefficient
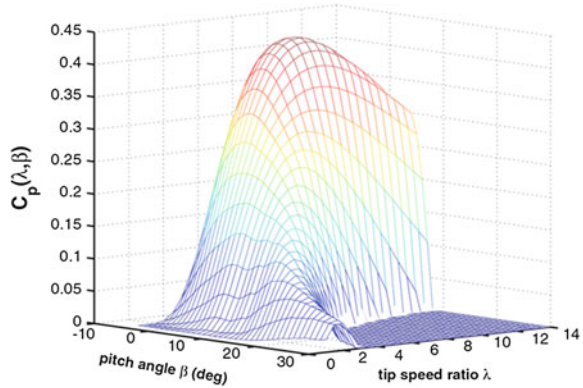
As is in [7], the following simplified model is adopted for the turbine (drive train) for control purposes.

$$J_t\dot{\omega}_{mr} = T_a - K_t\omega_{mr} - T_g \tag{2.4}$$

Where J_t is the turbine total inertia, K_t is the turbine total external damping, and T_g is the generator electromagnetic torque.

2.2.2 Generator Model

The WT adopted generator is the DFIG (Fig. 2.3). DFIG-based WT will offer several advantages including variable speed operation (± 33 % around the synchronous speed), and four-quadrant active and reactive power capabilities. Such system also results in lower converter costs (typically 25 % of total system power) and lower power losses compared to a system based on a fully fed synchronous generator with full-rated converter. Moreover, the generator is robust and requires little maintenance [8].
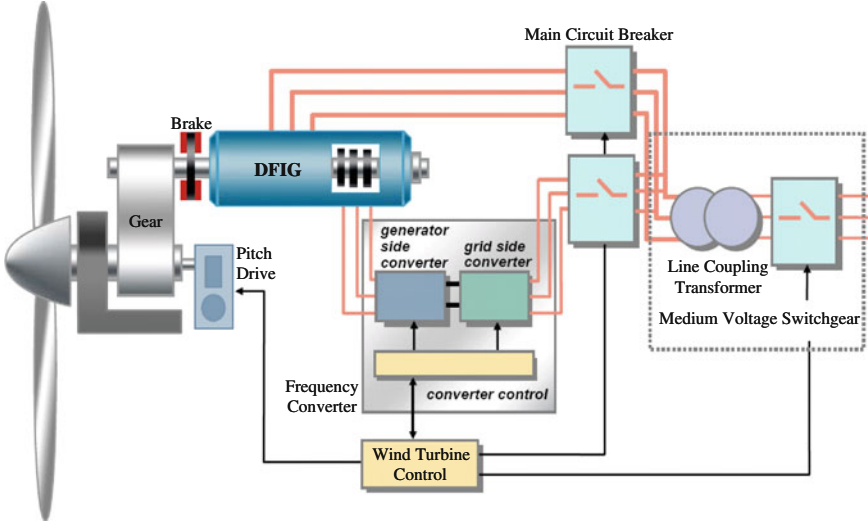
Fig. 2.3 Schematic diagram of a DFIG-based wind turbine

The control system is usually defined in the synchronous $d - q$ frame fixed to either the stator voltage or the stator flux. For the proposed control strategy, the generator dynamic model written in a synchronously rotating frame $d - q$ is given by Eq. (2.5).

$$
\begin{cases}
V_{sd} = R_s I_{sd} + \frac{d\phi_{sd}}{dt} - \omega_s \phi_{sq} \\
V_{sq} = R_s I_{sq} + \frac{d\phi_{sq}}{dt} + \omega_s \phi_{sd} \\
V_{rd} = R_r I_{rd} + \frac{d\phi_{rd}}{dt} - \omega_r \phi_{rq} \\
V_{rq} = R_r I_{rq} + \frac{d\phi_{rq}}{dt} + \omega_r \phi_{rd} \\
\phi_{sd} = L_s I_{sd} + M I_{rd} \\
\phi_{sq} = L_s I_{sq} + M I_{rq} \\
\phi_{rd} = L_r I_{rd} + M I_{sd} \\
\phi_{rq} = L_r I_{rq} + M I_{sq} \\
T_{em} = pM \left(I_{rd} I_{sq} - I_{rq} I_{sd} \right)
\end{cases}
\tag{2.5}
$$

where V is the voltage, I is the current, ϕ is the flux, ω_s is the synchronous, ω_r is the angular speed, R is the resistance, L is the inductance, M is the mutual inductance, T_{em} is the electromagnetic torque, and p is the pole pair number.

For simplification purposes, the q-axis is aligned with the stator voltage and the stator resistance is neglected. These will lead to Eq. (2.6).

$$\begin{cases} \frac{dI_{\text{rd}}}{dt} = \frac{1}{\sigma L_r}\left(V_{\text{rd}} - R_r I_{\text{rd}} + s\omega_s \sigma L_r I_{\text{rq}} - \frac{M}{L_s}\frac{d\phi_{\text{sd}}}{dt}\right) \\ \frac{dI_{\text{rq}}}{dt} = \frac{1}{\sigma L_r}\left(V_{\text{rq}} - R_r I_{\text{rq}} - s\omega_s \sigma L_r I_{\text{rd}} - s\omega_s \frac{M}{L_s}\phi_{\text{sd}}\right) \\ T_{\text{em}} = -p\frac{M}{L_s}\phi_{\text{sd}}I_{\text{rq}} \end{cases} \tag{2.6}$$

where σ is the leakage coefficient ($\sigma = 1 - M^2/L_s L_r$).

2.3 Control of the DFIG-Based Wind Turbine

2.3.1 Problem Formulation

Wind turbines are designed to produce electrical energy as cheaply as possible. Therefore, they are generally designed so that they yield maximum output at wind speeds around 15 m/sec. In case of stronger winds, it is necessary to waste part of the excess energy of the wind in order to avoid damaging the wind turbine. All wind turbines are therefore designed with some sort of power control. This standard control law keeps the turbine operating at the peak of its C_p curve.

$$T_{\text{ref}} = k\omega^2, \text{ with } k = \frac{1}{2}\pi\rho R^5 \frac{C_{\text{pmax}}}{\lambda_{\text{opt}}^3} \tag{2.7}$$

There is a significant problem with this standard control. Indeed, wind speed fluctuations force the turbine to operate off the peak of its C_p curve much of the time. Tight tracking C_{pmax} would lead to high mechanical stress and transfer aerodynamic fluctuations into the power system. This, however, will result in less energy capture.

To effectively extract wind power while at the same time maintaining safe operation, the wind turbine should be driven according to the following three fundamental operating regions associated with wind speed, maximum allowable rotor speed, and rated power. The three distinct regions are shown by Fig. 2.4, where v_{rmax} is the wind speed at which the maximum allowable rotor speed is reached, while $v_{\text{cut-off}}$ is the furling wind speed at which the turbine needs to be shut down for protection. In practice, there are three possible regions of turbine operation, namely, the high-, constant- and low-speed regions. High speed operation (III) is frequently bounded by the power limit of the machine while speed constraints apply in the constant-speed region. Conversely, regulation in the low-speed region (I) is usually not restricted by speed constraints. However, the system has nonlinear non-minimum phase dynamics in this region. This adverse behavior is an obstacle to perform the regulation task [9].

A common practice in addressing DFIG control problem is to use a linearization approach [10–12]. However, due to the stochastic operating conditions and the inevitable uncertainties inherent in DFIG-based wind turbines, much of these control
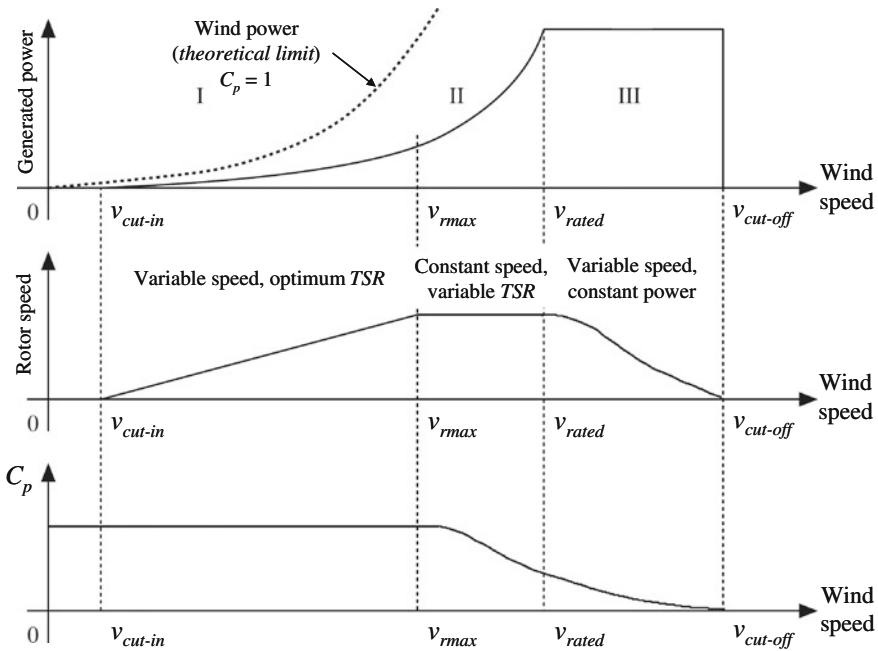
Fig. 2.4 Wind turbine control regions

methods come at the price of poor system performance and low reliability. Hence, the need for nonlinear and robust control to take into account these control problems. Although many modern techniques can be used for this purpose [13], sliding mode control has proved to be especially appropriate for nonlinear systems, presenting robust features with respect to system parameter uncertainties and external disturbances. For wind turbine control, sliding mode should provide a suitable compromise between conversion efficiency and torque oscillation smoothing [7, 14, 15].

Sliding mode control copes with system uncertainty keeping a properly chosen constraint by means of high-frequency control switching. Featuring robustness and high accuracy, the standard (first-order) sliding mode usage is, however, restricted due to the chattering effect caused by the control switching, and the equality of the constraint relative degree to 1. High-order sliding mode approach suggests treating the chattering effect using a time derivative of control as a new control, thus integrating the switching [16].

2.3.2 High-Order Sliding Modes Control Design

As the chattering phenomenon is the major drawback of practical implementation of sliding mode control, the most efficient ways to cope with this problem is higher

order sliding mode. This technique generalizes the basic sliding mode idea by acting on the higher order time derivatives of the sliding manifold, instead of influencing the first time derivative as it is the case in the standard (first order) sliding mode. This operational feature allows mitigating the chattering effect, keeping the main properties of the original approach [16].

The DFIG stator-side reactive power is given by

$$Q_s = \frac{3}{2}\left(V_{sq}I_{sd} - V_{sd}I_{sq}\right) \tag{2.8}$$

For a decoupled control, a $d - q$ reference frame attached to the stator flux was used. Therefore, setting the stator flux vector aligned with the d-axis, the reactive power can be expressed as

$$Q_s = \frac{3}{2}\frac{V_s}{L_s}\left(\phi_s - MI_{rd}\right) \tag{2.9}$$

Setting the reactive power to zero will, therefore, lead to the rotor reference current.

$$I_{rd\_ref} = \frac{V_s}{\omega_s M} \tag{2.10}$$

The DFIG-based WT control objective is to optimize the wind energy capture by tracking the optimal torque T_{ref} (Eq. 2.7). This control objective can be formulated by the following tracking errors.

$$\begin{cases} e_{I_{rd}} = I_{rd} - I_{rd\_ref} \\ e_{T_{em}} = T_{em} - T_{ref} \end{cases} \tag{2.11}$$

Then we will have

$$\begin{cases} \dot{e}_{I_{rd}} = \frac{1}{\sigma L_r}\left(V_{rd} - R_r I_{rd} + s\omega_s L_r \sigma I_{rq} - \frac{M}{L_s}\frac{d\phi_{sd}}{dt}\right) - \dot{I}_{rd\_ref} \\ \dot{e}_{T_{em}} = -p\frac{M}{\sigma L_s L_r}\phi_s\left(V_{rq} - R_r I_{rq} - s\omega_s L_r \sigma I_{rd} - s\omega_s \frac{M}{L_s}\phi_{sd}\right) - \dot{T}_{ref} \end{cases} \tag{2.12}$$

If we define the functions G_1 and G_2 as follows

$$\begin{cases} G_1 = \frac{1}{\sigma L_r}\left(s\omega_s\sigma L_r I_{rq} - \frac{M}{L_s}\frac{d\phi_{sd}}{dt} - R_r I_{rd}\right) - \dot{I}_{rd\_ref} \\ G_2 = -p\frac{M}{\sigma L_s L_r}\phi_s\left(-R_r I_{rq} - s\omega_s\sigma L_r I_{rd} - s\omega_s \frac{M}{L_s}\phi_{sd}\right) - \dot{T}_{ref} \end{cases} \tag{2.13}$$

Thus, we have

$$
\begin{cases}
\ddot{e}_{I_{rd}} = \frac{1}{\sigma L_r}\dot{V}_{rd} + \dot{G}_1 \\
\ddot{e}_{\Gamma_{em}} = -p\frac{M}{\sigma L_s L_r}\phi_s \dot{V}_{rq} + \dot{G}_2
\end{cases}
\tag{2.14}
$$

To overcome standard sliding mode control chattering, a natural modification is to replace the discontinuous function in the vicinity of the discontinuity by a smooth approximation. Nevertheless, such a smooth approximation is not easy to carry-out. This is why common approaches use current references. Therefore, a high-order sliding mode seems to be a good alternative.

The main problem with high-order sliding mode algorithm implementations is the increased required information. Indeed, the implementation of an nth-order controller requires the knowledge of $\dot{S}, \ddot{S}, \dddot{S}, \ldots, S^{(n-1)}$. The exception is the *supertwisting* algorithm, which only needs information about the sliding surface S [16]. Therefore, the proposed control approach has been designed using this algorithm.

Now, lets us consider the following second-order sliding mode controller based on the supertwisting algorithm [16]. In the considered case, the control could be approached by two independent High-Order Sliding Mode (HOSM) controllers. Indeed, the control matrix is approximated by a diagonal one. Hence, V_{rd} controls I_{rd} (reactive power) and V_{rq} controls the torque (MPPT strategy).

$$
\begin{cases}
V_{rd} = y_1 - B_1|e_{I_{rd}}|^{\frac{1}{2}}\mathrm{sgn}(e_{I_{rd}}), \ \dot{y}_1 = -B_2\mathrm{sgn}(e_{I_{rd}}) \\
V_{rq} = y_2 + B_3|e_{T_{em}}|^{\frac{1}{2}}\mathrm{sgn}(e_{T_{em}}), \ \dot{y}_2 = +B_4\mathrm{sgn}(e_{T_{em}})
\end{cases}
\tag{2.15}
$$

where the constants B_1, B_2, B_3, and B_4 are defined as

$$
\begin{cases}
B_1^2 > \frac{2\sigma^2 L_r^2\left(\frac{B_2}{\sigma L_r}+\Phi_1\right)}{\left(\frac{B_2}{\sigma L_r}-\Phi_1\right)}, \ B_2 > \sigma L_r\Phi_1, \ |\dot{G}_1| < \Phi_1 \\
B_3^2 > 2\left(\frac{\sigma L_s L_r}{pM}\right)^2\frac{\left(p\frac{M}{\sigma L_s L_r}B_4+\Phi_2\right)}{\left(p\frac{M}{\sigma L_s L_r}B_4-\Phi_2\right)}, \ B_4 > \frac{\sigma L_s L_r}{pM}\Phi_2 \\
|\dot{G}_2| < \Phi_2
\end{cases}
\tag{2.16}
$$

In practice the parameters are never assigned according to inequalities. Usually, the real system is not exactly known, the model itself is not really adequate, and the parameters estimations are much larger than the actual values. The larger the controller parameters are the more sensitive will be the controller to any switching measurement noises. The right way is to adjust the controller parameters during computer simulations.

The above-described high-order sliding mode control strategy for a DFIG-based WT is illustrated by the block diagram in Fig. 2.5 [17].
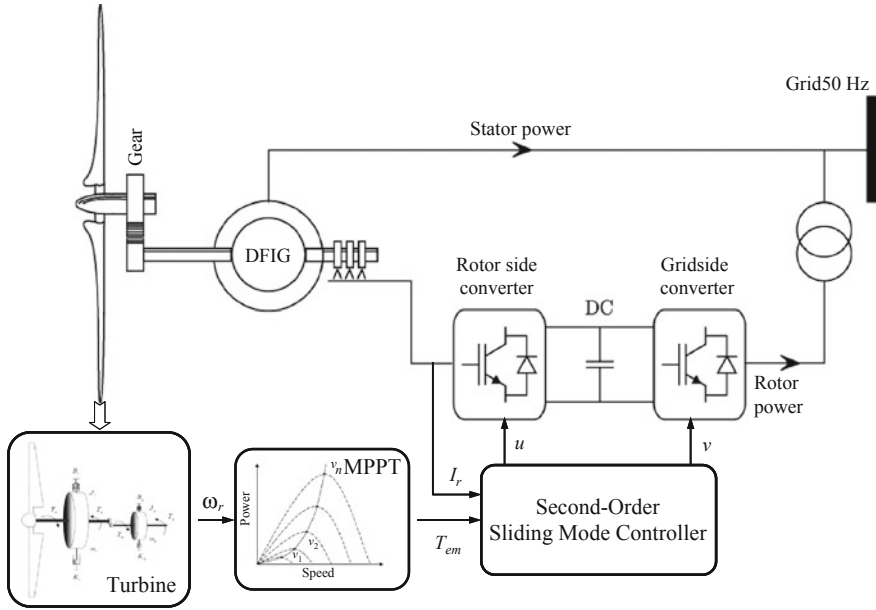
Fig. 2.5 The high-order sliding mode control structure

2.3.3 High-Gain Observer

A high-gain observer can be used to estimate the aerodynamic torque. A key feature of a high-gain observer is that it will reduce the chattering induced by a sliding mode observer [18].

From Eq. (2.4), we have

$$\dot{\omega} = \frac{T_a}{J} - \frac{K_t \omega}{J} - \frac{T_{em}}{J} \tag{2.17}$$

The following notations are introduced.

$$\begin{cases} x_1 = \omega \\ x_2 = \frac{T_a}{J} \end{cases} \tag{2.18}$$

Thus, we have

$$x = \begin{cases} \dot{x}_1 = x_2 - \frac{K}{J} x_1 - \frac{T_{em}}{J} \\ \dot{x}_2 = f(t) \end{cases} \tag{2.19}$$

or in matrix form

$$\begin{cases} \dot{x} = Ax + \varphi(x,u) + \varepsilon(t) \\ y = Cx \end{cases}$$

where

$$\begin{cases} A = \begin{bmatrix} 0 & 1 \\ 0 & 0 \end{bmatrix} \\ C = \begin{bmatrix} 1 & 0 \end{bmatrix} \\ \varphi(x,u) = \begin{bmatrix} \frac{-Kx_1-u}{J} \\ 0 \end{bmatrix} \\ \varepsilon(t) = \begin{bmatrix} 0 \\ f(t) \end{bmatrix} \end{cases}.$$

A candidate observer could be [18]

$$\dot{\hat{x}} = A\hat{x} + \varphi(\hat{x},u) - \theta\Delta_\theta^{-1}S^{-1}C^TC(\hat{x}-x) \tag{2.20}$$

where $\Delta_\theta = \begin{bmatrix} 1 & 0 \\ 0 & \frac{1}{\theta} \end{bmatrix}$, $S = \begin{bmatrix} 1 & -1 \\ -1 & 2 \end{bmatrix}$

Let S be the unique solution of the algebraic Lyapunov equation

$$S + A^TS + SA - C^TC = 0 \tag{2.21}$$

Let us define $\bar{x} = \Delta_\theta(\hat{x}-x)$ then

$$\dot{\bar{x}} = \theta(A - S^{-1}C^TC)\bar{x} + \Delta_\theta(\varphi(\hat{x}) - \varphi(x)) - \Delta_\theta\varepsilon(t) \tag{2.22}$$

Consider the quadratic function

$$V = \bar{x}^T S \bar{x} \tag{2.23}$$

then

$$\begin{cases} \dot{V} = 2\bar{x}^T S \dot{\bar{x}} \\ \dot{V} = -\theta V - \bar{x}^T C^T C \bar{x} + 2\bar{x}^T S \Delta_\theta(\varphi(\hat{x}) - \varphi(x)) \\ \quad\quad - 2\bar{x}^T S \Delta_\theta \bar{\varepsilon}(t) \end{cases}$$

Therefore,

$$\dot{V} \leq -\theta V + 2\|\bar{x}\|\lambda_{\max}(S)\begin{pmatrix} \|\Delta_\theta(\varphi(\hat{x}) - \varphi(x))\| \\ +\|\Delta_\theta\bar{\varepsilon}(t)\| \end{pmatrix} \tag{2.24}$$

We can assume that (triangular structure and the Lipschitz assumption on φ)

$$\begin{cases} \|\Delta_\theta(\varphi(\hat{x}) - \varphi(x))\| \le \xi\|\bar{x}\| \\ \|f(t)\| \le \delta \end{cases} \text{ with } \xi = \frac{K}{J}$$

It comes that

$$\dot{V} \le -\theta V + 2\|\bar{x}\|^2 \lambda_{\max}(S)\xi + 2\|\bar{x}\|\lambda_{\max}(S)\frac{\delta}{\theta}$$

then,

$$\dot{V} \le -\theta V + c_1 V + c_2 \frac{\delta}{\theta}\sqrt{V}$$

with

$$\begin{cases} c_1 = 2\frac{\lambda_{\max}(S)}{\lambda_{\min}(S)}\xi \\ c_2 = 2\frac{\lambda_{\max}(S)}{\sqrt{\lambda_{\min}(S)}} \end{cases}$$

Now taking

$$\begin{cases} \theta_0 = \max\{1, c_1\} \\ \lambda = \sqrt{\frac{\lambda_{\max}(S)}{\lambda_{\min}(S)}} \\ \mu_\theta = \frac{\theta - c_1}{2} \\ M_\theta = 2\frac{\lambda_{\max}(S)}{\lambda_{\min}(S)(\theta - c_1)} \end{cases}$$

and $\theta > \theta_0$, we obtain

$$\|e(t)\| \le \theta\lambda\exp(-\mu_\theta t)\|e(0)\| + M_\theta\delta \tag{2.25}$$

With $\hat{T}_a = J\hat{x}_2$, it comes that

$$\tilde{T}_a = \hat{T}_a - T_a \le J[\theta\lambda\exp(-\mu_\theta t)\|e(0)\| + M_\theta\delta] \tag{2.26}$$

A practical estimate of the aerodynamic torque is then obtained as M_θ decreases when θ increases. The asymptotic estimation error can be made as small as desired by choosing high enough values of θ. However, very large values of θ are to be avoided in practice since the estimator may become noise sensitive.

Now, the control objective can be formulated by the following tracking errors

$$e_T = T_{\text{opt}} - T_a \tag{2.27}$$

where T_a is observed. Then we will have

$$\dot{e}_T = 2k_{\text{opt}}\omega\left(T_a - K_t\omega - T_g\right) - \dot{T}_a \tag{2.28}$$

If we define the following functions

$$\begin{cases} F = 2k_{\text{opt}}\omega \\ G = 2k_{\text{opt}}\omega(T_a - K_t\omega) - \dot{T}_a \end{cases} \tag{2.29}$$

then

$$\ddot{e}_T = -F\dot{T}_g + \dot{G} \tag{2.30}$$

Let us consider the following observer based on the supertwisting algorithm [16, 19].

$$\begin{cases} T_g = y + B_1|e_T|^{\frac{1}{2}}\text{sgn}(e_T) \\ \dot{y} = +B_2\text{sgn}(e_T) \end{cases} \tag{2.31}$$

The gains B_1 and B_2 are chosen as

$$\begin{cases} B_1 > \frac{\Phi_2}{\Gamma_m} \\ B_2^2 \geq \frac{4\Phi_2\Gamma_M(A_1 + \Phi_1)}{\Gamma_m^2(A_1 - \Phi_1)} \\ \left|\dot{G}\right| < \Phi_2 \\ 0 < \Gamma_m \leq F < \Gamma_M \end{cases} \tag{2.32}$$

Thus, we will guaranty the convergence of e_T to 0 in a finite time t_c. The aerodynamic torque estimation is then deduced.

$$T_a = T_{\text{opt}}, \ t > t_c. \tag{2.33}$$

The above-proposed high-gain observer principal is illustrated by the block diagram in Fig. 2.6.

2.3.4 High-Order Sliding Mode Speed Observer

Figure 2.7 illustrates the main reference frames on which is based the proposed speed observer development.

In this case, θ_s can be easily determined using stator voltage measurements and a PLL.

If the stator flux is assumed to be aligned with the d-axis,
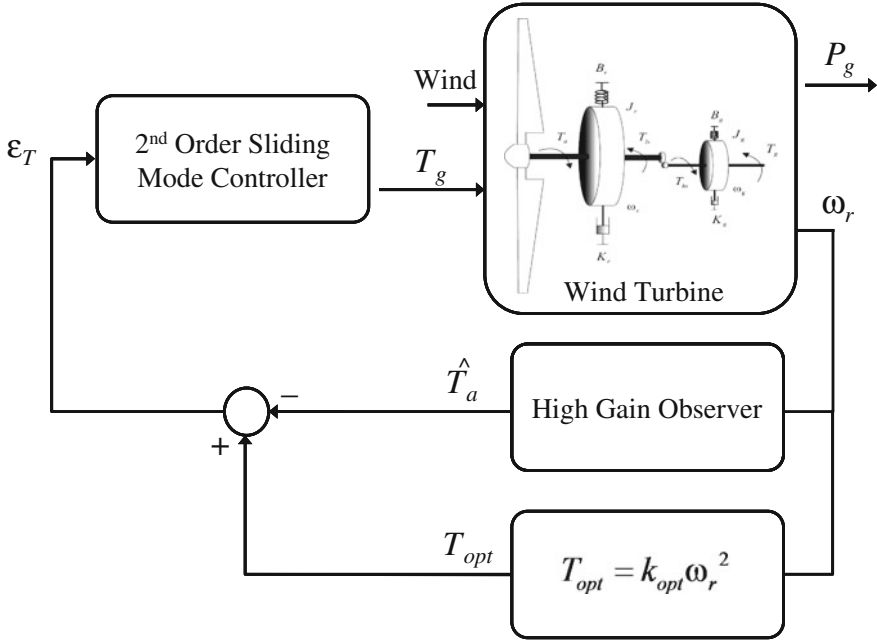
Fig. 2.6 High gain observer principle

Fig. 2.7 Stator S_α _ S_β, rotor R_α _ R_β, and $d - q$ reference frames
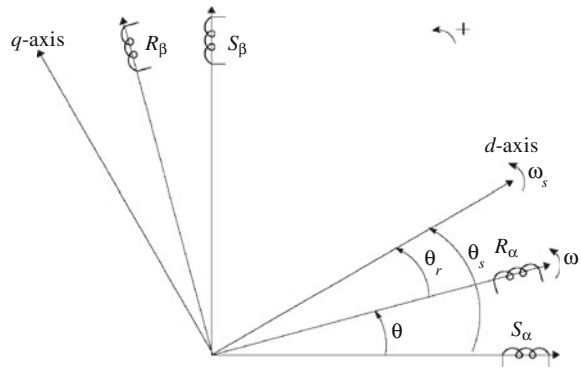
$$\begin{cases} \phi_{sd} = \phi_s \\ \phi_{sq} = 0 \end{cases} \tag{2.34}$$

then, the $d - q$ rotor current can be estimated as

$$\begin{cases} \hat{I}_{rd} = \frac{\phi_s}{M} - \frac{L_s}{M} I_{sd} \\ \hat{I}_{rq} = -\frac{L_s}{M} I_{sq} \end{cases}$$

Let us now define θ_r such as

$$\hat{I}_{rq} = \sqrt{\frac{2}{3}} \begin{pmatrix} -I_{ra} \sin \theta_r + \frac{1}{2} I_{rb} \sin \theta_r \\ +\frac{\sqrt{3}}{2} I_{rb} \cos \theta_r + \frac{1}{2} I_{rc} \sin \theta_r \\ -\frac{\sqrt{3}}{2} I_{rc} \cos \theta_r \end{pmatrix} \qquad (2.35)$$

Using $x = \tan\left(\frac{\theta_r}{2}\right)$, I_{rq} can be rewritten as

$$\hat{I}_{rq} = \sqrt{\frac{2}{3}} \begin{pmatrix} -I_{ra} \frac{2x}{1+x^2} + \frac{1}{2} I_{rb} \frac{2x}{1+x^2} \\ +\frac{\sqrt{3}}{2} I_{rb} \frac{1-x^2}{1+x^2} + \frac{1}{2} I_{rc} \frac{2x}{1+x^2} \\ -\frac{\sqrt{3}}{2} I_{rc} \frac{1-x^2}{1+x^2} \end{pmatrix} \qquad (2.36)$$

After some algebraic manipulations, it comes that

$$\hat{I}_{rq} = \frac{1}{1+x^2} \sqrt{\frac{2}{3}} \begin{bmatrix} x^2 \left(\frac{\sqrt{3}}{2} I_{rc} - \frac{\sqrt{3}}{2} I_{rb} \right) \\ +x \left(-2I_{ra} + I_{rb} + I_{rc} \right) \\ +\left(-\frac{\sqrt{3}}{2} I_{rc} + \frac{\sqrt{3}}{2} I_{rb} \right) \end{bmatrix} \qquad (2.37)$$

This equation can further be rewritten in a compact form

$$\hat{I}_{rq} = \frac{x^2 a + xb + c}{1+x^2} \qquad (2.38)$$

$$at^2 + bt + c = 0 \quad \text{with} \quad \begin{cases} a = \sqrt{\frac{3}{2}} \hat{I}_{rq} + \frac{\sqrt{3}}{2} (I_{rb} - I_{rc}) \\ b = 2I_{ra} - I_{rc} - I_{rc} \\ c = \sqrt{\frac{3}{2}} \hat{I}_{rq} - \frac{\sqrt{3}}{2} (I_{rb} - I_{rc}) \end{cases}$$

The solutions of this equation are the following.

$$\begin{cases} x_1 = \frac{-b + \sqrt{b^2 - 4ac}}{2a} \\ x_2 = \frac{-b - \sqrt{b^2 - 4ac}}{2a} \end{cases} \qquad (2.39)$$

Now we will estimate the derivative of the following value $z = 2 \arctan x_1$ using a second-order sliding mode. The same result is obtained with $\arctan x_2$.

As for the above-discussed problem, the proposed speed observer is designed using the *supertwisting* algorithm [19].

Let us therefore consider the following observer

$$\begin{cases} \dot{y} = -B_2 \text{sgn}(e) \\ \dot{W} = y - B_1|e|^{\frac{1}{2}}\text{sgn}(e) \end{cases} \tag{2.40}$$

where the constants B_1 and B_2 are defined as

$$\begin{cases} B_2 > \phi \\ B_1^2 > \frac{4(B_2+\phi)^2}{2(B_2-\phi)} \end{cases} \tag{2.41}$$

Lets us consider the following tracking error.

$$\begin{cases} e = W - z \\ \dot{e} = y - B_1|e|^{\frac{1}{2}}\text{sgn}(e) - \dot{z} \\ \ddot{e} = -B_2\text{sgn}(e) - B_1\frac{\dot{e}}{2|e|^{\frac{1}{2}}} - \ddot{z} \end{cases} \tag{2.42}$$

Assume now, for simplicity, that the initial values are $e = 0$ and $\dot{e} = \dot{e}_0 > 0$ at $t = 0$. Let e_M be the intersection of the curve $\ddot{e} = -(B_2 - \phi)$ with $\dot{e} = 0$, $|\ddot{z}| < \phi$. We have then

$$2e_M(B_2 - \phi) = \dot{e}_0^2 \tag{2.43}$$

$$e > 0,\ \dot{e} < -(B_2 + \phi)\frac{2e_M^{1/2}}{B_1} \Rightarrow \ddot{e} > 0$$

Thus, the majorant curve with $e > 0$ may be taken as

$$\begin{cases} \dot{e}_0^2 = 2(B_2 - \phi)(e_M - e) \quad \text{with } \dot{e} > 0 \\ e = e_M \quad \text{with } 0 \geq \dot{e} > -(B_2 + \phi)\frac{2e^{\frac{1}{2}}}{B_1} \\ \dot{e} = \dot{e}_M = -(B_2 + \phi)\frac{2e_M^{\frac{1}{2}}}{B_1} \quad \text{with } \dot{e} < -(B_2 + \phi)\frac{2e^{\frac{1}{2}}}{B_1} \end{cases} \tag{2.44}$$

Let the trajectory next intersection with $e = 0$ axis be e_1. Then, obviously

$$|\dot{e}_1/\dot{e}_0| \leq q \quad \text{with } q = |\dot{e}_M/\dot{e}_0| = \sqrt{\frac{\left(\frac{2}{B_1}\right)^2(B_2 + \phi)^2}{2(B_2 - \phi)}} \tag{2.45}$$

Extending the trajectory into the half plane $e < 0$ and carrying-out a similar reasoning show that successive crossings of the $e = 0$ axis satisfy the inequality

$$\left|\frac{\dot{e}_{i+1}}{\dot{e}_i}\right| \leq q$$

The $q < 1$ condition is sufficient for the algorithm convergence. Indeed, the real trajectory consists of an infinite number of segments. The total variance is given by

$$Var(\dot{e}) = \sum |\dot{e}_i| \leq |\dot{e}_0|\left(1 + q + q^2 + \cdots\right) = \frac{|\dot{e}_0|}{1 - q} \tag{2.46}$$

Therefore, the algorithm obviously converges.

The convergence time is to be estimated now. Consider an auxiliary variable

$$\eta = y - \dot{z} \tag{2.47}$$

$\eta = \dot{e}$ when $e = 0$. Thus, η tends to zero. Its derivative

$$\ddot{e} = -B_2\text{sgn}(e) - G \tag{2.48}$$

satisfies the inequalities

$$0 < B_2 - \phi \leq -\dot{\eta}\text{sgn}(e_{I_{rd}}) \leq B_2 + \phi \tag{2.49}$$

The real trajectory consists of an infinite number of segments between $\eta_i = \dot{e}_i$ and $\eta_{i+1} = \dot{e}_{i+1}$ associated to the time t_i and t_{i+1}, respectively. Consider t_c, the total convergence time.

$$\begin{cases} t_c = \sum (t_{i+1} - t_i) \leq \sum \frac{|\eta_i|}{B_2 - \phi} \\ t_c \leq \frac{1}{B_2 - \phi} \sum |\dot{e}_i| \\ t_c \leq \frac{|\dot{e}_0|}{(B_2 - \phi)(1 - q)} \end{cases} \tag{2.50}$$

This means that the observer objective is achieved. It exist t_c such as $\omega_r = \dot{W}$.

The above-presented sensorless HOSM control strategy using a HOSM speed observer is illustrated by the block diagram in Fig. 2.8.

2.4 Simulation Using the FAST Code

The proposed HOSM control strategy, the high-gain, and the HOSM speed observers have been tested for validation using the NREL FAST code [20]. The FAST (Fatigue, Aerodynamics, Structures, and Turbulence) code is a comprehensive aeroelastic simulator capable of predicting both the extreme and fatigue loads of two- and three-bladed horizontal-axis wind turbines. This simulator has been chosen for validation because it is proven that the structural model of FAST
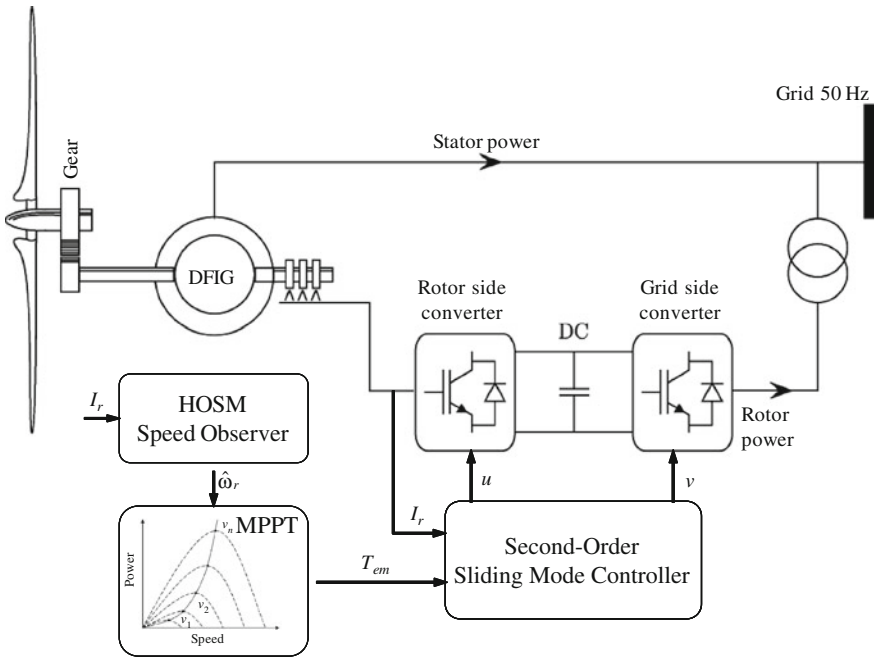
Fig. 2.8 The high-order sliding mode sensorless control s structure
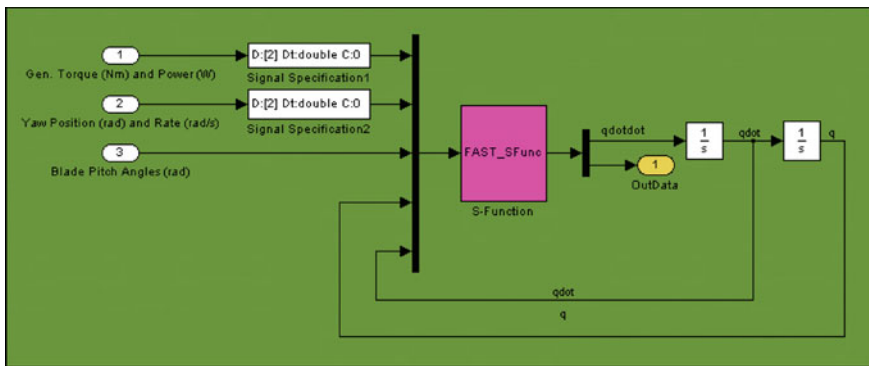
Fig. 2.9 FAST wind turbine block

is of higher fidelity than other codes [21]. An interface has been developed between FAST and Matlab-Simulink® enabling users to implement advanced turbine controls in Simulink convenient block diagram form (Fig. 2.9). Hence, electrical model (DFIG, grid, control system, etc.) designed in the Simulink environment is simulated while making use of the complete nonlinear

Fig. 2.10 Simulink model
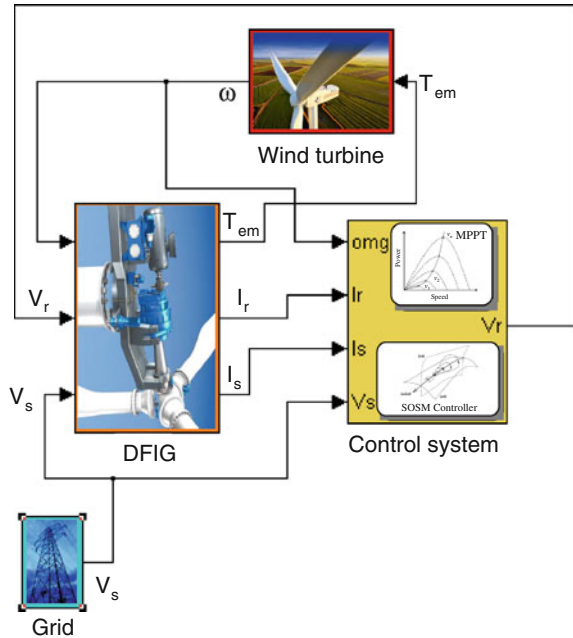
aerodynamic wind turbine motion equations available in FAST (Fig. 2.10). This introduces tremendous flexibility in wind turbine controls implementation during simulation.

2.4.1 Test Conditions

Numerical validations, using FAST with Matlab-Simulink® have been carried-out on the NREL WP 1.5-MW wind turbine. The wind turbine and the DFIG ratings are given in the Appendix.

2.4.2 HOSM Control Performances

Validation tests were performed using turbulent FAST wind data with 7 and 14 m/sec minimum and maximum wind speeds, respectively (Fig. 2.11). As clearly shown in Figs. 2.12 and 2.13, very good tracking performances are achieved in terms of DFIG rotor current and WT torque with respect to wind fluctuations. The HOMS control strategy does not induce increased mechanical stress as there are no strong torque variations. Indeed and as expected, the aerodynamic torque remains smooth (Fig. 2.13).
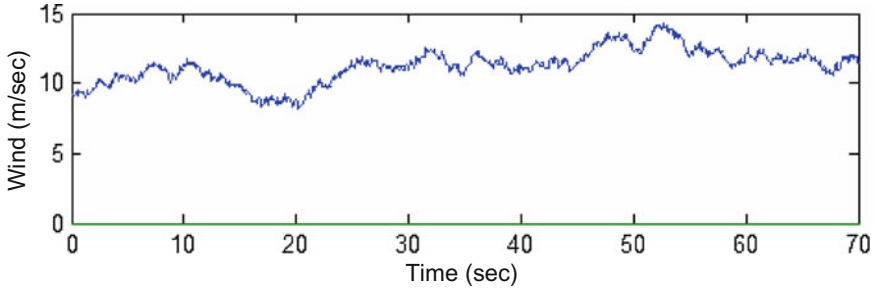
Fig. 2.11 Wind speed profile
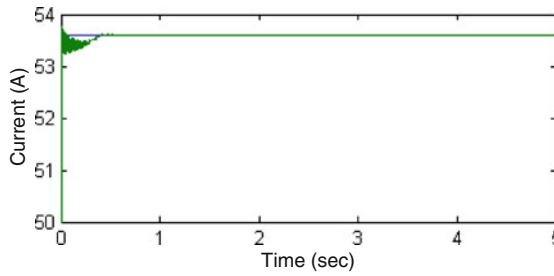
Fig. 2.12 Current I_{rd} tracking performance: Reference (*blue*) and real (*green*)

Fig. 2.13 Torque tracking performance: Reference (*blue*) and real (*green*)
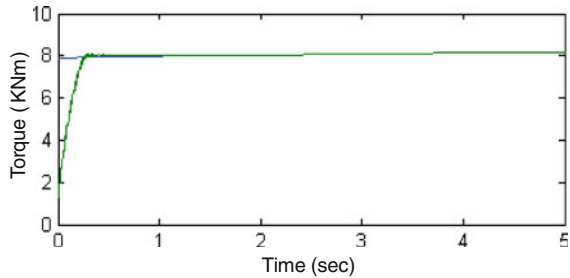
2.4.3 HOSM Control Performances with High-Gain Observer

The observer validation is clearly illustrated by Fig. 2.14.

Indeed, the aerodynamic torque tracks efficiently the optimal torque. As shown in Figs. 2.15 and 2.16, very good tracking performances are achieved in terms of DFIG rotor current and WT torque with respect to wind fluctuations. The control strategy does not induce increased mechanical stress as again there are no strong torque variations.
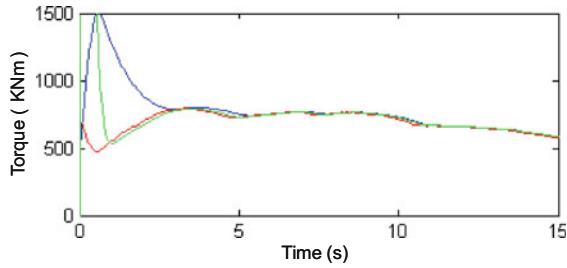
Fig. 2.14 Aerodynamic torque: T_{opt} (*blue*), T_a real (*red*), T_a observed (*green*)
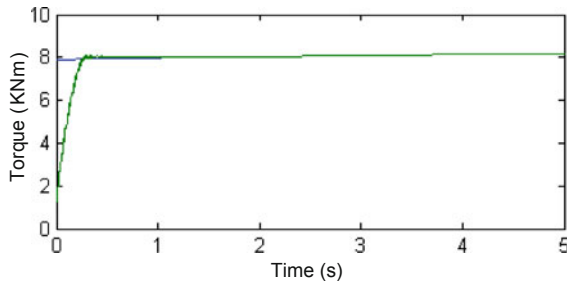
Fig. 2.15 Torque tracking performance: Reference (*blue*) and real (*green*)
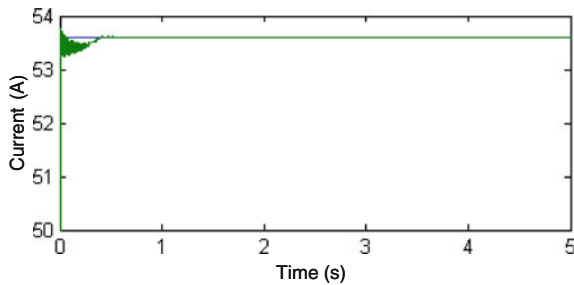
Fig. 2.16 Current I_{rd} tracking performance: Reference (*blue*) and real (*green*)

2.4.4 Sensorless HOSM Control Performances

The performances of the proposed HOSM speed observer are illustrated by Fig. 2.17. The achieved results show quiet good tracking chattering free performances.

Figures 2.18 and 2.19 illustrate the HOSM sensorless control performances in terms of DFIG rotor current and wind turbine torque. In this case, quiet good tracking performances are achieved according to the wind fluctuations. As mentioned above,
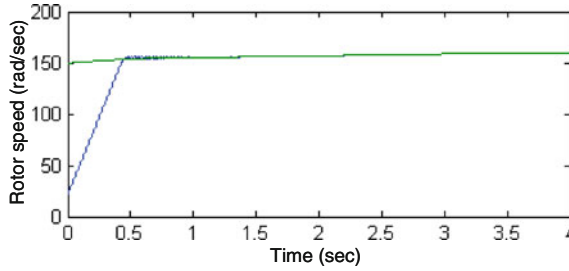
Fig. 2.17 Rotor speed: Observer (*blue*) and real (*green*)

the sensorless control strategy does not induce mechanical stress as there is no chattering in the wind turbine torque (Fig. 2.19).

2.4.5 HOSM Control FRT Performances

This subsection deals with the fault ride-through capability assessment of a DFIG-based WT using a HOSM control. Indeed, it has been recently suggested that sliding mode control is a solution of choice to the fault ride-through problem [22, 23].

LVRT capability is considered to be the biggest challenge in wind turbines design and manufacturing technology. LVRT requires wind turbines to remain
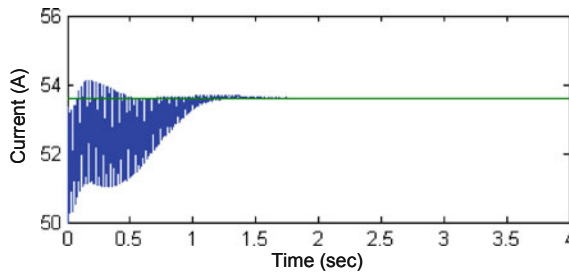
Fig. 2.18 Current I_{rd} tracking performance: Reference (*green*) and real (*blue*)

Fig. 2.19 Torque tracking performance: Reference (*green*) and real (*blue*)
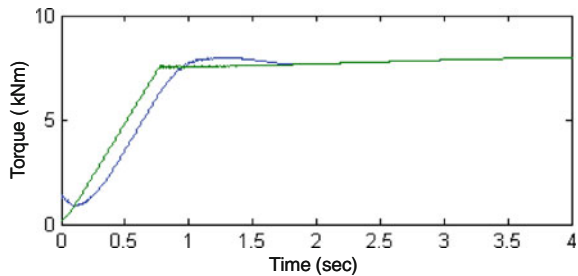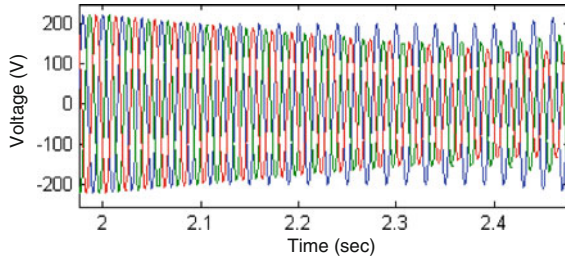
Fig. 2.20 Grid voltage
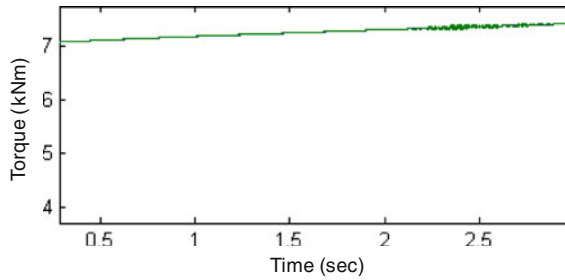
Fig. 2.21 Torque tracking performance during unbalanced voltage sags: Reference (*blue*) and real (*green*)

connected to the grid in the presence of grid voltage sags. The HOSM control performances are, therefore, assessed against this grid fault. In this context, when unbalanced sags occur (Fig. 2.20), very high current, torque, and power oscillations appear at double the electrical frequency, forcing a disconnection.

The LVRT performances are illustrated by Fig. 2.21 where an almost constant torque is achieved. Good tracking performances are also achieved in terms of DFIG rotor current (Fig. 2.22). Fault-tolerance performances are also confirmed by the quadratic error shown by Fig. 2.23.
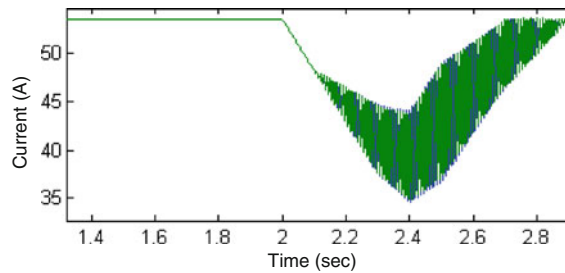
Fig. 2.22 Current I_{rd} tracking performance during unbalanced voltage sags: Reference (*blue*) and real (*green*)

Fig. 2.23 Quadratic error between the reference torque and the SOSM control-based one (voltage sags)
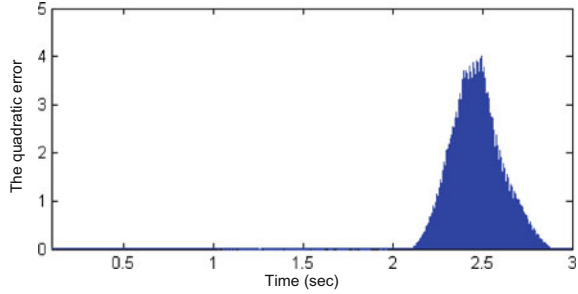
2.5 Conclusions

This chapter dealt with high-order sliding mode control of doubly-fed induction generator-based wind turbines. Simulations using the NREL FAST code clearly show the HOSM control approach effectiveness and attractiveness in terms of robustness (FRT capability enhancement) and of sensorless control. Moreover, it has been confirmed that there is no mechanical extra stress induced on the wind turbine drive train as there are no strong torque variations.

2.6 Future Work

Future works should be oriented toward the evaluation of high-order sliding modes control for the following key investigations:

- Power control according to grid active and reactive power references.
- Wind turbine grid synchronization.

Appendix

Characteristics of the simulated wind turbine

Number of blades	3
Rotor diameter	70 m
Hub height	84.3 m
Rated power	1.5 MW
Turbine total Inertia	4.4532×10^5 kg m^2

Parameters of the simulated DFIG

$R_s = 0.005~\Omega,~L_s = 0.407$ mH, $R_r = 0.0089~\Omega,~L_r = 0.299$ mH, $M = 0.016$ mH, $p = 2$

(continued)

Control parameters
$B_1 = 10$, $B_2 = 20000$, $B_3 = 7$, $B_4 = 500$

Parameters of the emulated wind turbine
$R = 1.5$ m, $J_t = 0.1$ kg m^2, $C_{pmax} = 0.4760$, $\lambda = 7$

Parameters of the DC motor
6.5 kW, 3850 rpm, 310 V, 24.8 A
$R_s = 78$ Ω, $R_r = 0.78$ Ω, $L_r = 3.6$ H, $J = 0.02$ kg.m^2

Parameters of the tested DFIG
$R_s = 0.325$ Ω, $L_s = 4.75$ mH, $R_r = 0.13$ Ω, $L_r = 1.03$ mH,
$M = 57.3$ mH, $p = 2$

References

1. Liserre M, Cardenas R, Molinas M, Rodriguez J (2011) Overview of multi-MW wind turbines and wind parks. IEEE Trans Ind Electron 58(4):1081–1095
2. Bianchi, FD, de Battista H, Mantz RJ (2007) Wind turbine control systems: principles, modelling and gain scheduling design. Springer, London
3. Beltran, B, Benbouzid MEH, Ahmed-Ali T (2009) High-order sliding mode control of a DFIG-based wind turbine for power maximization and grid fault tolerance. In: Proceedings of the IEEE IEMDC'09, Miami, USA, pp 183–189, May 2009
4. Beltran B, Benbouzid MEH, Ahmed-Ali T, Mangel H (2011) DFIG-based wind turbine robust control using high-order sliding modes and a high gain observer. Int Rev Model Simul 4(3):1148–1155
5. Benbouzid MEH, Beltran B, Mangel H, Mamoune A (2012) A high-order sliding mode observer for sensorless control of DFIG-based wind turbines. In: Proceedings of the 2012 IEEE IECON, Montreal, Canada, pp 4288–4292, October 2012
6. Benbouzid MEH, Beltran B, Amirat Y, Yao G, Han J, Mangel H (2013) High-order sliding mode control for DFIG-based wind turbine fault ride-through. In: Proceedings of the 2013 IEEE IECON, Vienna, Austria, pp 7670–7674, Nov 2013
7. Beltran B, Ahmed-Ali T, Benbouzid MEH (2008) Sliding mode power control of variable speed wind energy conversion systems. IEEE Trans Energy Convers 23(22):551–558
8. Tazil M, Kumar V, Bansal RC, Kong S, Dong ZY, Freitas W, Mathur HD (2010) Three-phase doubly fed induction generators: an overview. IET Power Appl 4(2):75–89
9. Senjyu T, Sakamoto R, Urasaki N, Funabashi T, Fujita H, Sekine H (2006) Output power leveling of wind turbine generator for all operating regions by pitch angle control. IEEE Trans Energy Convers 21(2):467–475
10. Pena R, Cardenas R, Proboste J, Asher G, Clare J (2008) Sensorless control of doubly-fed induction generators using a rotor-current-based MRAS observer. IEEE Trans Ind Electron 55(1):330–339
11. Xu L, Cartwright P (2006) Direct active and reactive power control of DFIG for wind energy generation. IEEE Trans Energy Convers 21(3):750–758
12. Cardenas R, Pena R, Proboste J, Asher G, Clare J (2005) MRAS observer for sensorless control of standalone doubly fed induction generators. IEEE Trans Energy Convers 20(4):710–718
13. Vepa R (2011) Nonlinear, optimal control of a wind turbine generator. IEEE Trans Energy Convers 26(2):468–478

14. Munteanu I, Bacha S, Bratcu AI, Guiraud J, Roye D (2008) Energy-reliability optimization of wind energy conversion systems by sliding mode control. IEEE Trans Energy Convers 23(3):975–985
15. Valenciaga F, Puleston PF (2008) Variable structure control of a wind energy conversion system based on a brushless doubly fed reluctance generator. IEEE Trans Energy Convers 22(2):499–506
16. Beltran B, Ahmed-Ali T, Benbouzid MEH (2009) High-order sliding mode control of variable speed wind turbines. IEEE Trans Ind Electron 56(9):3314–3321
17. Beltran B, Benbouzid MEH, Ahmed-Ali T (2012) Second-order sliding mode control of a doubly fed induction generator driven wind turbine. IEEE Trans Energy Convers 27(2):261–269
18. Farza M, M'Saad M, Rossignol L (2004) Observer design for a class of MIMO nonlinear systems. Automatica 40(1):135–143
19. Levant A, Alelishvili L (2007) Integral high-order sliding modes. IEEE Trans Autom Control 52(7):1278–1282
20. http://wind.nrel.gov/designcodes/simulators/fast/
21. Manjock A (2005) Design codes FAST and ADAMS® for load calculations of onshore wind turbines. Report No.72042, Germanischer Lloyd WindEnergie *GmbH*, Hamburg, Germany, May 26, 2005
22. Cardenas R, Pena R, Alepuz S, Asher G (2013) Overview of control systems for the operation of DFIGs in wind energy applications. IEEE Trans Ind Electron 60(7):2776–2798
23. Benbouzid MEH, Beltran B, Ezzat M, Breton S (2013) DFIG driven wind turbine grid fault-tolerance using high-order sliding mode control. Int Rev Model Simul 6(1):29–32

Chapter 3
Maximum Power Point Tracking Control of Wind Energy Conversion Systems

Yong Feng and Xinghuo Yu

Abstract This chapter studies the control problems in grid integration of wind energy conversion systems. Sliding-mode control technique will be used to optimize the control of wind energy conversion systems. The maximum power point tracking control algorithms for variable-speed wind energy conversion systems are presented. The grid integration of wind energy conversion systems can be optimized in terms of power delivered to the grid and providing the voltage support ancillary service at the point of common coupling. The control objective for the grid integration of wind energy conversion systems is to keep the DC-link voltage in a desirable value and the input or output power factors staying unitary. The high-order terminal sliding-mode voltage and current regulators are designed, respectively, to control the DC-link voltage and the current rapidly and exactly. The numerical simulations will be carried out to evaluate the control schemes.

Keywords DFIG-based wind power system · Voltage-oriented control (VOC) · Grid-side PWM converter · Sliding-mode control · Terminal sliding mode

Nomenclature

P_w	Input power to the wind turbine
r	Wind turbine radius
v_w	Wind speed
ρ	Air density
P_m	Mechanical power
C_p	Power coefficient

Y. Feng (✉)
Department of Electrical Engineering, Harbin Institute of Technology,
Harbin 150001, China
e-mail: yfeng@hit.edu.cn

Y. Feng · X. Yu
School of Electrical and Computer Engineering, RMIT University, Melbourne,
VIC 3001, Australia
e-mail: x.yu@rmit.edu.au

β	Pitch angle
λ	Tip speed ratio
ω_w	Turbine angular speed
P, Q	Active and reactive power for the induction generator
i_{ds}, i_{qs}	Stator currents in d-q axes
u_{ds}, u_{qs}	Stator voltages in d-q axes
L	Inductor of the grid side filter
R	Resistance of the grid side filter
C	DC-link capacitor
i_d, i_q	d- and q-axis current components of the converter
s_d, s_q	d- and q-axis switching control signals
e_d, e_q	d- and q-axis voltage component of the three-phase supply
ω	Angular frequency of the power source
P_{ac}, P_{dc}	Active power of AC and DC sides

3.1 Introduction

Renewable energy is an important sustainable energy in the world. It comes from natural resources, such as wind, solar, rain, tides, biomass, and geothermal heat. Up to now, as an essential part of low emissions energy in a lot of countries, renewable energy has been an important to the national energy security, and played a significant role in reducing carbon emissions.

Wind energy is a large and important renewable energy source, and widely used in the world and has become a reliable and competitive means for electric power generation. Total global wind power capacity is near 198 gigawatts (GW) in 2010 [1].

Wind energy conversion system (WECS) is an apparatus for converting the kinetic energy available in the wind to mechanical energy that can be used to operate an electrical generator for producing electricity. A typical WECS includes a wind turbine, a generator, interconnection apparatus, and control systems. Generators for wind turbines generally include the following types: synchronous, permanent magnet synchronous, doubly-fed induction, and induction generators. For small-to-medium power wind turbines, permanent-magnet and squirrel-cage induction generators are often used because of their reliability and low cost. Induction, permanent magnet synchronous, and wound field synchronous generators are currently used in various high-power wind turbines [2].

A lot of control methods for WECS have been proposed in literatures. A wind speed sensorless neural network (NN) based maximum power point tracking (MPPT) control algorithm for variable-speed WECS is proposed in [3]. The power regulation of variable-speed WECS was studied in [4]. A sliding-mode control (SMC) strategy was proposed to assure the system stability and impose the ideally designed feedback control solution in spite of model uncertainties. A second-order sliding-mode control (2-SMC) scheme for a wind turbine-driven doubly-fed

induction generator (DFIG) was proposed in [5]. The tasks of grid synchronization and power control were undertaken by two different algorithms, designed to command the rotor-side converter (RSC) at fixed switching frequency. Despite conventional synchronous generators, permanent magnet synchronous generators, and doubly- fed induction generators, the switched reluctance generator (SRG) can also be considered as a wind generator. In [6], a novel speed control of SRG by using adaptive neural network (ANN) controller was presented. The SRG is driven by variable-speed wind turbine and it is connected to the grid through an asymmetric half bridge converter, DC-link, and DC-AC inverter system. Among a lot of control methods, SMC offers some superior properties including fast and finite-time convergence, and high steady-state precision [7] and has been used in WECS.

This chapter describes a control strategy for wind energy integration into power network. A typical WECS and its mathematical model are analyzed. For a wind turbine to have the maximum active power extraction from the wind at any given instant, the electrical load on the generator is regulated using the MPPT method. For wind energy integration into power network, the structure of dual PWM inverter is utilized. Both the voltage and currents in the WECS are measured and control signals for both two PWM inverters are generated based on the control algorithms. An improved outer-loop control strategy is designed to control the square of the DC-link voltage.

Compared to other control methods, sliding-mode control (SMC) has many important features, such as simplicity for implementation, high robustness to external disturbances and low sensitivity to the system parameter variations [8–11]. SMC includes conventional linear sliding-mode (LSM) control and nonlinear terminal sliding-mode (TSM) control. The former are asymptotically stable, and the latter are finite-time stable. Compared to traditional LSM control, TSM control exhibits various superior properties such as fast and finite-time convergence, and smaller steady-state tracking errors [12, 13]. In the chapter TSM is used to make the error of the current and DC-link voltage reach zero in finite time. Meanwhile, high-order sliding-mode technique is utilized to eliminate the chattering phenomenon existing in sliding-mode control. The actual control signal is soften to be continuous and smooth. The TSM control strategy described in the chapter can improve the performance of the grid-side PWM converter of the wind power system.

3.2 Model of Wind Turbine

A typical WECS is shown in Fig. 3.1. It consists of a wind turbine, a gearbox, a generator, a machine-side PWM inverter, an intermediate DC circuit, a grid side PWM inverter, a transformer, and a control system. The generator may be a synchronous, permanent magnet synchronous, doubly-fed induction, or induction generator.
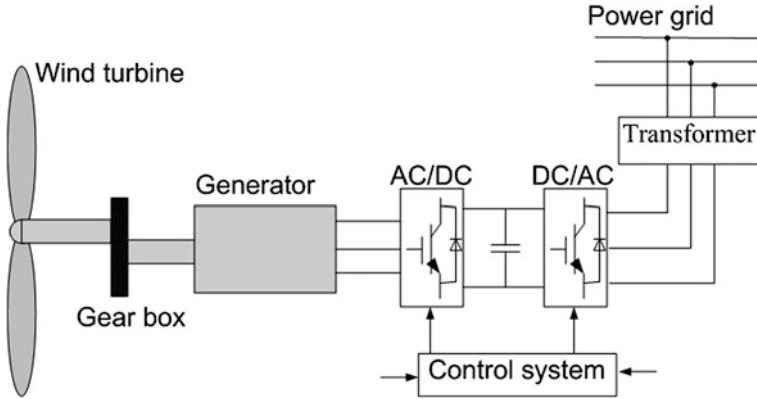
Fig. 3.1 Structure of a typical wind energy conversion system

The wind turbine absorbs the energy from an air stream and drives the generator to produce electricity. The control system is used to control both the machine side and the grid-side PWM inverters. The former controls the speed of the generator to rotate at the optimal speed and have the maximum active power extraction from the wind at different environment conditions. The latter transforms the DC voltage in the DC link to AC voltage, and further to the distribution power grid.

The input power to a wind turbine can be described as follows [3]:

$$P_w = \frac{1}{2}\rho\pi r^2 v_w^3 \tag{3.1}$$

where r is the turbine radius (m), v_w the wind speed (m/s), ρ the air density (generally it is 1.25 kg/m^3).

The mechanical power generated by the wind turbine can be expressed as follows:

$$P_m = C_p(\lambda, \beta)P_w = \frac{1}{2}C_p(\lambda, \beta)\rho\pi r^2 v_w^3 \tag{3.2}$$

where C_p is the power coefficient of the turbine representing the efficiency of the wind turbine, β the pitch angle, and λ the tip speed ratio representing the status of the turbine in different wind speeds and defined by

$$\lambda = \frac{\omega_w r}{v_w} \tag{3.3}$$

where ω_w is the turbine angular speed, as shown in Fig. 3.1.

Assume the pitch angle β is zero, the power coefficient of the turbine can be approximately expressed as follows [14, 15]:

$$C_p(\lambda, \beta) = 0.5176\left(\frac{116}{\lambda_i} - 0.4\beta - 5\right)e^{-\frac{21}{\lambda_i}} + 0.0068\lambda \tag{3.4}$$

where

$$\lambda_i = \frac{1}{\lambda + 0.08\beta} - \frac{0.035}{\beta^3 + 1}$$

To obtain the maximum active power extraction from the wind, the power coefficient Eq. (3.4) should be kept the optimal value, i.e.,

$$\left.\frac{d}{d\lambda}C_p(\lambda, \beta)\right|_{\lambda=\lambda_{opt}} = 0 \tag{3.5}$$

which can lead to $C_{pmax}(\lambda_{opt}, \beta) = \max\{C_{pmax}(\lambda, \beta)\}$ for $\lambda = \lambda_{opt}$.

The optimal maximum output power and torque of a turbine can be obtained, respectively, as follows from Eqs. (3.2), (3.3) and (3.5):

$$P_{m\max} = K_{opt}\omega_{wopt}^3 \tag{3.6}$$

$$T_{m\max} = K_{opt}\omega_{wopt}^2 \tag{3.7}$$

where K_{opt} is a constant determined by the characteristics of the wind turbine and given by the following equation:

$$K_{opt} = \frac{1}{2}C_p(\lambda, \beta)\rho\pi r^5 \tag{3.8}$$

3.3 Maximum Power Point Tracking

The electrical load of the generator in Fig. 3.1 should be regulated suitably for maximizing the active power extraction of a wind turbine at any given instant. It can be neither too large nor too small for a particular wind speed, otherwise the operating point of the wind turbine will deviate from the optimal power point and the efficiency of the wind turbine will be lower [16]. The wind turbine can only generate a maximum power for a particular wind speed and can acquire more power from the wind by decreasing or increasing the load on the generator via regulating the speed of the generator.

A lot of methods on the MPPT have been proposed. The simplest method is based on the tip speed of the wind turbine. Assume that the optimal value of the tip speed ratio can be obtained from Eq. (3.5), the optimal speed of the wind turbine can be calculated from Eq. (3.14) by:
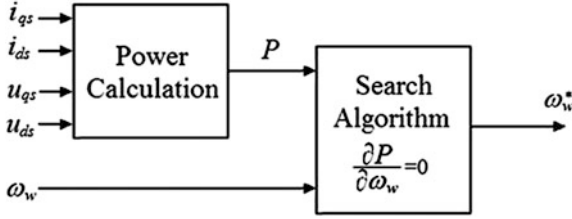
Fig. 3.2 the block diagram of the MPPT control system

$$\omega_{wopt} = \frac{\lambda_{opt}}{r} v_w \qquad (3.9)$$

Although this method is simple, it needs an additional anemometer for measuring the wind speed in the tip of the wind turbine, which is much difficult.

Another more popular method for MPPT is based on the active power of the generator. Suppose that the generator in the wind turbine is an induction generator. The block diagram of the MPPT control system for the wind turbine is shown in Fig. 3.2.

For the induction generator, the active and reactive power can be expressed as follows, respectively:

$$P = i_{qs}u_{qs} + i_{ds}u_{ds} \qquad (3.10)$$

$$Q = i_{qs}u_{qs} - i_{ds}u_{ds} \qquad (3.11)$$

where i_{ds} and i_{qs} are the stator currents in d-q axes, u_{ds} and u_{qs} the stator voltages in d-q axes.

In Fig. 3.2, the search algorithm is basically based on the calculation of the power gradient to the speed of the wind turbine. Since the curve of the power versus the turbine speed is convex, there is no local maximum among the whole turbine speed. Hence based on the power gradient, the search algorithm can find the maximum point corresponding to the maximum power point of the wind turbine and finally produce the reference speed of the generator. To obtain maximum power from the wind, the speed of the wind turbine should be always controlled to rotate at the optimal speed $\omega_{\omega opt}$ by controlling the speed of the generator.

3.4 Model of Wind Energy Conversion System

The block diagram of the WECS is shown in Fig. 3.3. The back-to-back PWM converters are utilized in the WECS, and consist of the generator-side PWM converter, the intermediate DC circuit and the grid-side PWM converter. As shown in Fig. 3.3, the left is the distribution power networks, the right the generator,
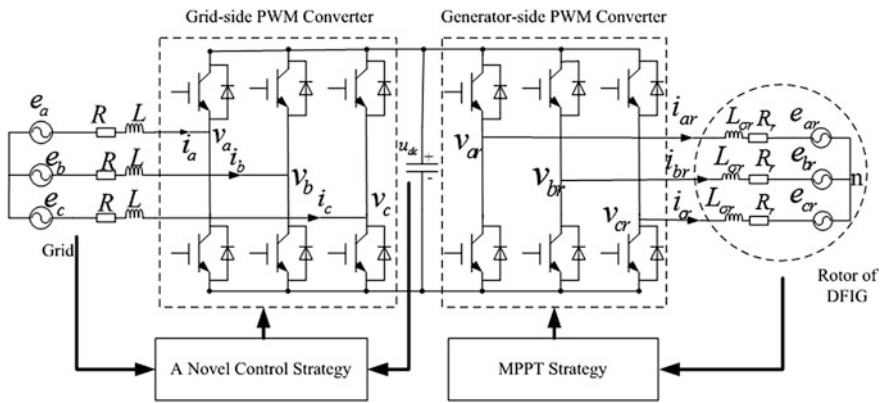
Fig. 3.3 Back-to-back PWM converter topology

which may be an induction generator, a permanent magnet synchronous generator, or a DFIG. The intermediate DC circuit makes it possible for the two sides to be controlled independently.

Back-to-back PWM converters have many significant advantages, such as unity power factor, bidirectional power flow, and controllable DC-link voltage [17], which makes it widely used in many industrial applications. To achieve these performances simultaneously, the design of controllers is important. At present, there are many researches on the design of the controllers. With the development of the design method, it can be roughly classified into two categories: linear and nonlinear control. In [18] and [19], proportional-integral (PI) controllers have been proposed, which are for achieving unity power factor, meanwhile a cascaded PI controller is used to regulate the DC-link voltage indirectly by controlling the input currents. However, the design of these controllers depends on the accurate parameters of the system to provide a linear model, so they are sensitive to parameter disturbances. Since the grid-side PWM converter is a multiple variables, strong coupling nonlinear system, the nonlinear control strategy without ignoring nonlinearities of the system can achieve better both static and dynamic performances. Nonlinear control methods, such as fuzzy control methods, are applied to improve the system performance [20, 21], which are lack of theoretical analysis and cannot ensure stability and damping characteristics of the closed-loop system.

Fig. 3.4 The Grid-side
PWM Converter Model
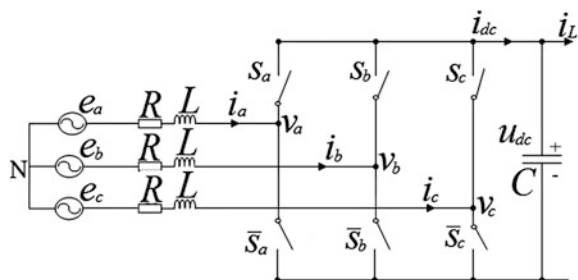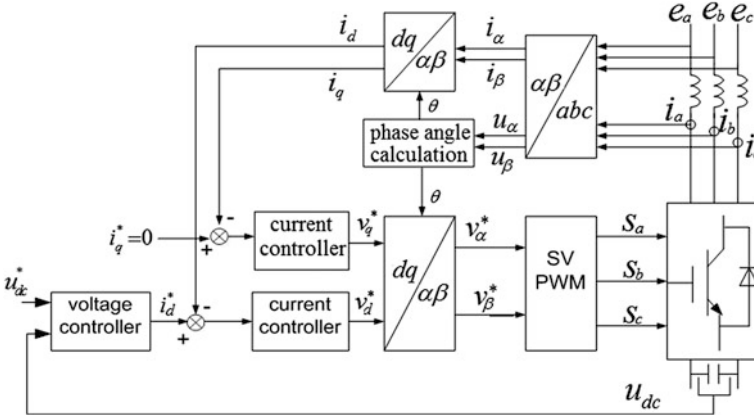
Fig. 3.5 Diagram of VOC scheme

Feedback linearization techniques [22, 23], which show an enhanced performance in simulation, however, are sensitive to model uncertainties. Hence sliding-mode control will be applied in the chapter.

The grid-side PWM converter model is shown in Fig. 3.4, where L is the inductor of the grid side filter, R the resistance, C the DC-link capacitor. The input line voltages and currents are expressed by the notations v_k and $i_k, k = a, b, c$.

In this chapter, the voltage-oriented control (VOC) scheme is used. It is a dual-loop structure including DC-link voltage outer loop and dq-axes current inner loop. A reference frame is chosen to rotate synchronously with the grid voltage space vector and the d-axis is made to orient to the grid voltage space vector. The block diagram of VOC is shown in Fig. 3.5. For converter, VOC can achieve decoupling between active and reactive currents as the d-axis of the synchronously rotating d-q frame is aligned with the grid voltage vector. The mathematical model in d-q synchronous rotating reference frame can be expressed by [16]

$$\begin{cases} L\dot{i}_d = -Ri_d + \omega Li_q + e_d - s_d u_{dc} \\ L\dot{i}_q = -Ri_q - \omega Li_d + e_q - s_q u_{dc} \\ C\dot{u}_{dc} = (s_d i_d + s_q i_q) - i_L \end{cases} \qquad (3.12)$$

where i_d, i_q are the d- and q-axis current components of the converter; s_d, s_q the d- and q-axis switching control signals in d-q reference frame; e_d and e_q the d- and q-axis voltage component of the three-phase supply; ω the angular frequency of the power source.

It can be seen from Eq. (3.12) that it is difficult to design the regulators due to the multiplication of the state variables by the control inputs. To design the controllers, the dynamical Eq. (3.12) should be simplified based on the power balance between AC and DC sides of the system. The active power of AC and DC sides are expressed by the notations P_{ac} and P_{dc} respectively. Neglecting the

converter loss, the active power of the AC side is equal to the active power of the DC side, i.e.,

$$P_{ac} = P_{dc} \tag{3.13}$$

The active power of AC and DC sides can be calculated by:

$$P_{ac} = e_d i_d + e_q i_q \tag{3.14}$$

$$P_{dc} = u_{dc} i_{dc} = u_{dc}(C\dot{u}_{dc} + i_L) \tag{3.15}$$

Based on Eqs. (3.13)–(3.15), it can be obtained:

$$u_{dc}(C\dot{u}_{dc} + i_L) = e_d i_d + e_q i_q \tag{3.16}$$

Define a new variable $u = u_{dc}^2$. Equation (3.16) can be simplified as:

$$\dot{u} = \frac{2}{C}(e_d i_d + e_q i_q) - \frac{2}{C}\sqrt{u} i_L \tag{3.17}$$

Now from Eqs. (3.12) and (3.17), new dynamic model of the converter in d-q synchronous rotating reference frame can be expressed as:

$$\begin{cases} L\dot{i}_d = -Ri_d + \omega Li_q + e_d - u_d \\ L\dot{i}_q = -Ri_q - \omega Li_d + e_q - u_q \\ \dot{u} = \frac{2}{C}(e_d i_d + e_q i_q) - \frac{2}{C}\sqrt{u} i_L \end{cases} \tag{3.18}$$

where $u_d = s_d \cdot u_{dc}$, $u_q = s_q \cdot u_{dc}$.

As the d-axis of the synchronously rotating d-q frame is aligned with the grid voltage vector, d- and q-axis components of grid voltage can be obtained as follows:

$$\begin{cases} e_d = E_s \\ e_q = 0 \end{cases} \tag{3.19}$$

where E_s is equal to the grid voltage vector. So Eq. (3.18) can be further simplified as:

$$\begin{cases} L\dot{i}_d = -Ri_d + \omega Li_q + E_s - u_d \\ L\dot{i}_q = -Ri_q - \omega Li_d - u_q \\ \dot{u} = \frac{2}{C}E_s i_d - \frac{2}{C}\sqrt{u} i_L \end{cases} \tag{3.20}$$

It can be seen from Eq. (3.20) that the DC-link voltage, $u_{dc} = \sqrt{u}$, can be controlled using the q-axis current, i_d.

3.5 Control Strategy for Wind Energy Integration into Power Network

In the WECS, as shown in Fig. 3.3, the energy generated by a generator is firstly transformed to a DC voltage by the machine side PWM inverter connecting the machine to the DC link. Then, the grid side PWM inverter connecting the DC link to the power grid transforms the DC to AC voltages, which is delivered to the power grid. We can use the dual PWM inverters to transform the renewable energy to the grid without any additional circuit. The machine side PWM inverter and the grid side PWM inverter are independent. Both of them can be controlled separately. A unit power ratio for the WECS can be realized using some control strategy.

It can be seen in Fig. 3.3 that the output of the DC-link voltage controller is the d-axis reference current i_d^*. For achieving the rectification or the inversion with unity power factor, the component of the reactive current i_q^* should be set to zero [24].

3.5.1 DC-Link Voltage Controller Design

Define the given DC-link voltage as u_{dc}^* and its square as $u^* = u_{dc}^{*2}$, then the error between the square of the DC-link and the square of the given DC-link voltage e_1 is:

$$e_1 = u^* - u \tag{3.21}$$

Based on Eq. (3.20), the error e_1 can be expressed as:

$$\dot{e}_1 = \dot{u}^* - \dot{u} = -\frac{2}{C} E_s i_d + \frac{2}{C} \sqrt{u} i_L \tag{3.22}$$

To achieve fast error convergence and better tracking precision, a TSM manifold was designed as follows [12, 13]:

$$s_1 = \dot{e}_1 + \gamma_1 e_1^{q_1/p_1} \tag{3.23}$$

where $\gamma_1 > 0$, $p_1 > 0$, $q_1 > 0$, p_1 and q_1 are odd.

After the system states reach the TSM manifold $s_1 = 0$ in finite time, both e_1 and $\dot{e}_1$ will converge to the original points along $s_1 = 0$ in finite time, i.e.,

$$e_1 = \dot{e}_1 = 0 \tag{3.24}$$

Theorem 1 *If the TSM manifold is chosen as Eq.* (3.23), *and the TSM control is designed as follows, e_1 can converge to zero in finite time* [25]:

$$i_d^* = i_{deq}^* + i_{dn}^* \tag{3.25}$$

$$i_{deq}^* = \frac{\sqrt{u}}{E_s} i_L + \frac{C}{2E_s} \gamma_1 e_1^{q_1/p_1} \tag{3.26}$$

$$\dot{i}_{dn}^* + T_1 i_{dn}^* = v \tag{3.27}$$

$$v = (k_1 + \eta_1)\text{sgn}(s_1) \tag{3.28}$$

where $\eta_1 = \max(|T_1 i_{dn}^*|)$, $T_1 > 0$, $k_1 > 0$.

Proof Consider the following Lyapunov function:

$$V = \frac{1}{2} s_1^2 \tag{3.29}$$

Differentiating V with respect to time gives:

$$\dot{V} = s_1 \dot{s}_1 \tag{3.30}$$

Based on Eqs. (3.22) and (3.23), it can be obtained:

$$s_1 = -\frac{2}{C} E_s i_d + \frac{2}{C} \sqrt{u} i_L + \gamma_1 e_1^{q_1/p_1}$$

Substituting Eqs. (3.25) and (3.26) into the above equation gives:

$$s_1 = -\frac{2}{C} E_s i_{dn}^*$$

Differentiating s_1 with respect to time, it can be obtained:

$$\dot{s}_1 = -\frac{2}{C} E_s \dot{i}_{dn}^*$$

Substituting the above equation into Eq. (3.30) gives:

$$s_1 \dot{s}_1 = -\frac{2}{C} E_s s_1 \dot{i}_{dn}^*$$

Substituting Eqs. (3.27) and (3.28) into the above equation gives:

$$\begin{aligned}
s_1\dot{s}_1 &= -\frac{2}{C}E_s s_1 \dot{i}^*_{dn} \\
&= -\frac{2}{C}E_s s_1 (\dot{i}^*_{dn} + T_1 i^*_{dn} - T_1 i^*_{dn}) \\
&= -\frac{2}{C}E_s s_1 ((k_1 + \eta_1)\mathrm{sgn}(s_1) - T_1 i^*_{dn}) \\
&= -\frac{2}{C}E_s ((k_1 + \eta_1)|s_1| - T_1 s_1 i^*_{dn}) \\
&\leq -\frac{2}{C}E_s k_1 |s_1|
\end{aligned}$$

i.e.,

$$\dot{V}_1 \leq -\frac{2}{C}E_s k_1 |s_1| < 0 \text{ for } |s_1| \neq 0$$

The system (3.22) satisfies the sufficient condition of the existence of the sliding mode. Therefore, the states of the system (3.22) can reach the TSM manifold $s_1 = 0$ within finite time.

3.5.2 d-*Axis Current Controller Design*

Define an error variable between the required and actual *d*-axis current:

$$e_2 = i^*_d - i_d \tag{3.31}$$

Based on Eq. (3.20), the *d*-axis current error dynamics can be expressed by:

$$\dot{e}_2 = \dot{i}^*_d + \frac{R}{L}i_d - \omega i_q - \frac{E_s}{L} + \frac{u_d}{L} \tag{3.32}$$

A TSM manifold is designed as follows [12, 13]:

$$s_2 = \dot{e}_2 + \gamma_2 e_2^{q_2/p_2} \tag{3.33}$$

where $\gamma_2 > 0$, $p_2 > 0$, $q_2 > 0$, p_{22} and q are odd.

Theorem 2 *If the TSM manifold is chosen as Eq. (3.33), and the control is designed as follows, e_2 can converge to zero in finite time* [25]:

$$u_d = u_{deq} + u_{dn} \tag{3.34}$$

$$u_{deq} = -L\dot{i}^*_d - Ri_d + \omega Li_q + E_s - L\gamma_2 e_2^{q_2/p_2} \tag{3.35}$$

$$\dot{u}_{dn} + T_2 u_{dn} = v \tag{3.36}$$

$$v = -(k_2 + \eta_2)\mathrm{sgn}(s_2) \tag{3.37}$$

where $\eta_2 = \max(|T_2 u_{dn}|)$, $T_2 > 0$, $k_2 > 0$.

3.5.3 q-*Axis Current Controller Design*

Define an error variable between the required and actual q-axis current:

$$e_3 = i_q^* - i_q \tag{3.38}$$

Based on Eq. (3.20), the q-axis current error dynamics can be expressed by:

$$\dot{e}_3 = \frac{R}{L}i_q + \omega i_d + \frac{u_q}{L} \tag{3.39}$$

A TSM manifold is designed as follows [12, 13]:

$$s_3 = \dot{e}_3 + \gamma_3 e_3^{q_3/p_3} \tag{3.40}$$

where $\gamma_3 > 0$, $p_3 > 0$, $q_3 > 0$, p_3 and q_3 are odd.

Theorem 3 *If the TSM manifold is chosen as Eq. (3.40), and the control is designed as follows, e_3 can converge to zero in finite time* [25]:

$$u_q = u_{qeq} + u_{qn} \tag{3.41}$$

$$u_{qeq} = -Ri_q - \omega L i_d - L\gamma_3 e_3^{q_3/p_3} \tag{3.42}$$

$$\dot{u}_{qn} + T_3 u_{qn} = v \tag{3.43}$$

$$v = -(k_3 + \eta_3)\mathrm{sgn}(s_3) \tag{3.44}$$

where $\eta_3 = \max(|T_3 u_{qn}|)$, $T_3 > 0$, $k_3 > 0$.

The proof of Theorems 2 and 3 is similar to that of Theorem 1 and hence is omitted here.

In Theorem 2 and 3, the control signals, u_d and u_q, can be transformed to the control signals s_d and s_q in Eq. (3.12) by using the following equations:

Fig. 3.6 u_{dc} in load current change
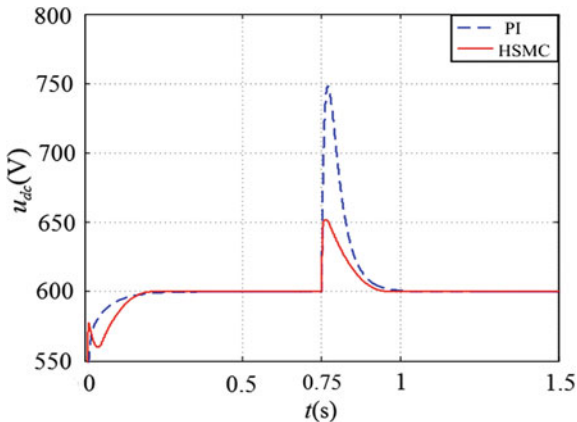
Fig. 3.7 e_a and i_a in load current change
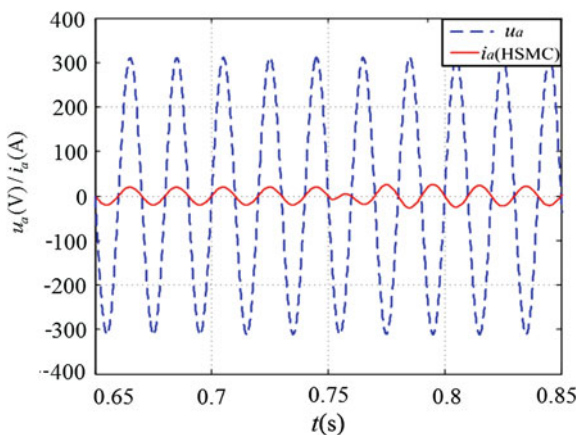
$$s_d = u_d/u_{dc} \tag{3.45a}$$

$$s_q = u_q/u_{dc} \tag{3.45b}$$

3.6 Simulations

The parameters of the gird-side PWM converter are given as follows [25]:

$E_m = 220\sqrt{2}$(V), $L = 0.006$(H), $R = 0.5$(Ω), $C = 0.00136$(F), $u_{dc}^* = 600$(V), $f = 50$ (HZ).

To prove the validity and advantages of the new control strategy, the results are compared between the high-order TSM control strategy and the traditional PI control strategy. In order to illustrate the fast error convergence and strong robustness of the new control strategy, the results under different cases are given, such as step changes in the load currents and step changes in the source voltages.

Fig. 3.8 i_q in load current change
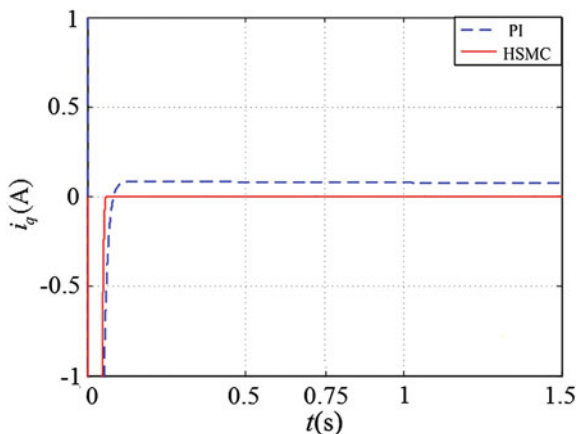
Fig. 3.9 i_d in load current change
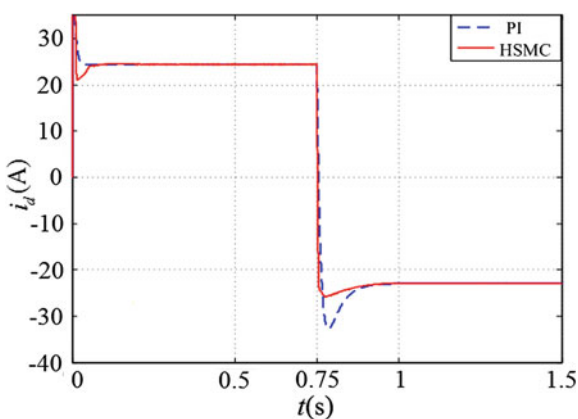
3.6.1 Step Changes in the Load Current

In this test, the load current is changed from 15A to -15A at the time $t = 0.75$ s. It can be seen from Fig. 3.6 that the DC-link voltage with the TSM control can track the given voltage and have lower ripple and faster convergence than that using PI control. From Fig. 3.7, it can be seen that the grid-side PWM converter works as a rectifier with unity power factor and absorbs the energy from the power grid before $t = 0.75$ s and works as an inverter with unity power factor and transfer the energy to the power grid after $t = 0.75$ s. Figure 3.8 shows that the current in q-axis converges to zero, and the TSM control has higher tracking accuracy. Figure 3.9 presents that the error of the current in d-axis with the TSM control strategy can achieve lower ripples and faster convergence. The control signals for SMC and TSMC control are shown in Figs. 3.10 and 3.11. It can be seen that traditional SMC signals exist chattering, but high-order TSM control signals are smooth.
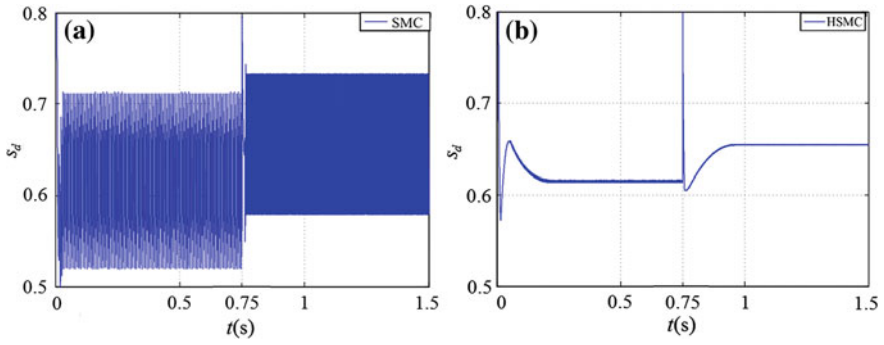
Fig. 3.10 Control signals in *d*-axis. **a** traditional SMC; **b** high-order TSMC
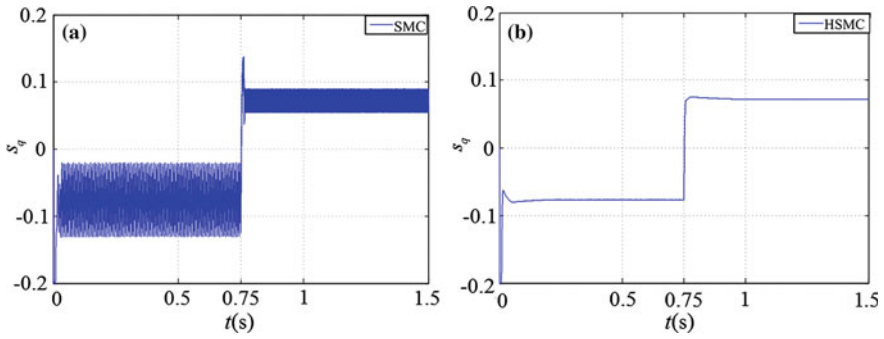
Fig. 3.11 Control signals in *q*-axis. **a** traditional SMC; **b** high-order TSMC

Fig. 3.12 u_{dc} in the source voltage change
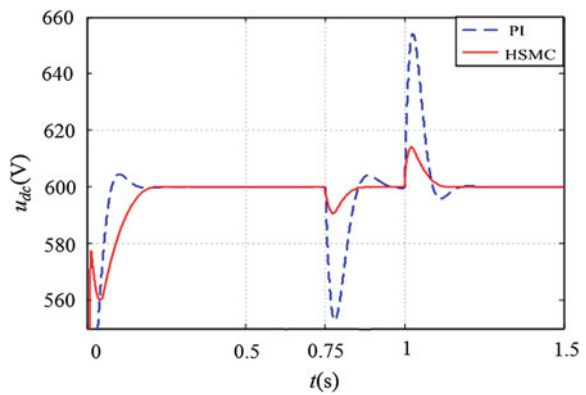
Fig. 3.13 i_q in the source voltage change
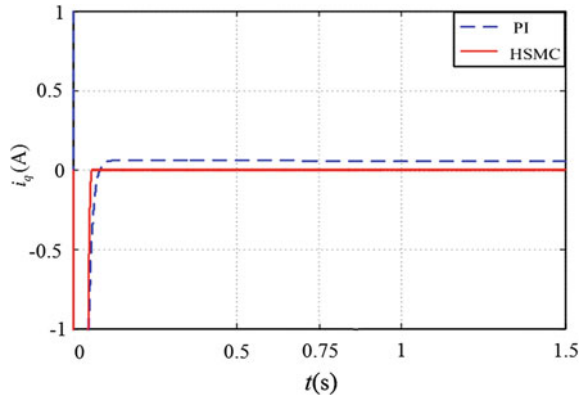
Fig. 3.14 i_d in the source voltage change
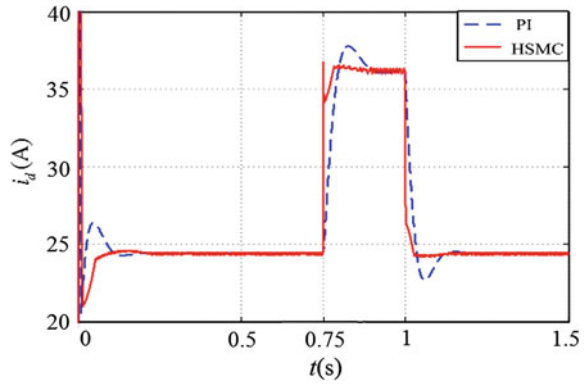
Fig. 3.15 Control signals of the inverter
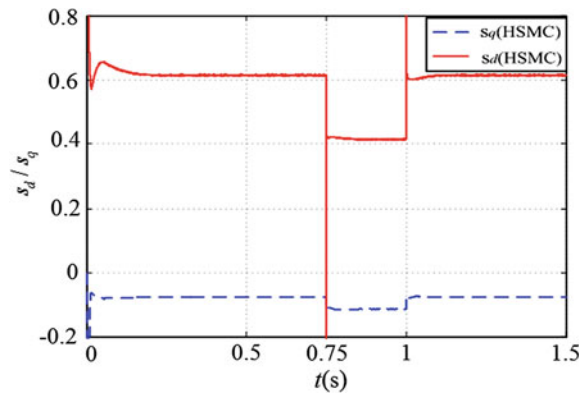
3.6.2 Step Changes in the Source Voltage

The amplitude of source voltage reduces by 20 % at 0.75 s and restores to initial value at 0.85 s. The load current is 15 A. The DC-link voltage responses to step changes of the voltage in the power grid in Fig. 3.12. It can be seen that the DC-link voltage almost has no fluctuations when the system is controlled by high-order TSM control. The q- and d-axis current responses to step changes in source voltage are depicted in Figs. 3.13 and 3.14. The control signals of the inverter are displayed in Fig. 3.15.

3.7 Conclusions

This chapter has described the control issues in grid integration of WECS. A structure of dual PWM inverter is presented in the wind energy integration into power network. Both of two PWM inverters are controlled separately using one control system. A control strategy for the grid-side PWM inverter has been designed to guarantee that the WECS has a unit power ratio. Sliding-mode control theory and technique have been used to optimize the control of WECS. A control strategy for the grid-side PWM converter of DFIG-based wind power system has been developed. The high-order TSM control technique provides the fast convergence, strong robustness, and high tracking accuracy. A smooth control signal of the controller can be generated by utilizing the second-order sliding-mode technique. The effect of the equivalent low pass filter in the high-order sliding-mode mechanism can be regulated optionally. The simulation results have shown the correctness of the proposed method.

Although a lot of theoretical research work on the control of WECS has been done, the future work will involve providing more efficient and robust control algorithms, and trying to do experiments in practical application environments.

References

1. REN21 (2011) Renewables 2011: Global Status Report. http://www.ren21.net/Portals/97/documents/GSR/GSR2011_Master18.pdf
2. The Encyclopedia (2011) wind energy conversion system. http://www.daviddarling.info/encyclopedia/W/AE_wind_energy_conversion_system.html
3. Thongam JS, Bouchard P, Beguenane R, Fofana I (2010) Neural network based wind speed sensorless MPPT controller for variable-speed wind energy conversion systems. In: Proceedings of IEEE electric power energy conference: "sustainable energy intelligent grid", Halifax, NS, USA, 25–27 Aug 2010
4. De Battista H, Mantz RJ, Christiansen CF (2000) Dynamical sliding mode power control of wind driven induction generators. IEEE Trans Energy Convers 15(4):451–457

5. Susperregui A, Tapia G, Martinez MI, Blanco A (2011) Second-order sliding-mode controller design and tuning for grid synchronization and power control of a wind turbine-driven DFIG. In: Proceedings of the IET conference on renewable power generation (RPG 2011), Edinburgh, UK, 6–8 Sept 2011

6. Hasanien HM, Muyeen SM (2012) Speed control of grid-connected switched reluctance generator driven by variable speed wind turbine using adaptive neural network controller. Electr Power Syst Res 84(1):206–213

7. Yu X, Man Z (1996) Model reference adaptive control systems with terminal sliding modes. Int J Control 64(6):1165–1176

8. Feng Y, Zheng J, Yu X, Truong NV (2009) Hybrid terminal sliding-mode observer design method for a permanent-magnet synchronous motor control system. IEEE Trans Ind Electron 56(9):3424–3431

9. Feng Y, Yu X, Han F (2013) On nonsingular terminal sliding-mode control of nonlinear systems. Automatica 49(6):1715–1722

10. Feng Y, Han X, Wang Y, Yu X (2007) Second-order terminal sliding mode control of uncertain multivariable systems. Int J Control 80(6):856–862

11. Feng Y, Bao S, Yu X (2004) Inverse dynamics nonsingular terminal sliding mode control of two-link flexible manipulators. Int J Robot Autom 19(2):91–102

12. Feng Y, Yu XH, Man ZH (2002) Nonsingular adaptive terminal sliding mode control of rigid manipulators. Automatica 38(12):2167–2179

13. Feng Y, Yu X, Han F (2013) High-order terminal sliding-mode observer for parameter estimation of a permanent magnet synchronous motor. IEEE Trans Ind Electron 60(10):4272–4280

14. Anderson PM, Bose A (1983) Stability simulation of wind turbine systems. IEEE Power Appar Syst PAS-102(12):3791–3795

15. Ghanes M, Zheng G (2009) On sensorless induction motor drives: sliding-mode observer and output feedback controller. IEEE Trans Ind Electron 56(9): 3404–3413

16. Feng Y, Zhou M, Wang Y, Yang Y (2013) High-order terminal sliding-mode control strategy for wind energy Integration into power network. In: Proceedings of the 32nd chinese control conference (CCC), Xi'an, China, 26–28 Jul 2013, pp 3186–3189

17. Malesani L, Rossetto L, Tomasin P (1993) AC/DC/AC PWM Converter with Minimum Energy Storage in the DC Link. In: Proceedings of IEEE applied power electronics conference APEC'93, San Diego, CA, USA, 7–11 Mar 1993, pp 306–311

18. Blasko V, Kaura V (1997) A new mathematical model and control of three-phase AC-DC voltage source converter. IEEE Trans Power Electron 12(1):116–123

19. Green AW, Boys JT (1989) Hysteresis current-forced three-phase voltage-sourced reversible rectifier. IEEE Trans Power Electron 136(3):113–120

20. Kazmierkowski MP, Cichowlas M, Jasinski M (2003) Artificial intelligence based controllers for industrial PWM power converters. In: Proceedings of the IEEE international conference industrial informatics, Banff, Alta., Canada, 21–24 Aug 2003, pp 187–191

21. Konstantopoulos GC (2012) "Novel dynamic nonlinear control scheme for three-phase AC/DC voltage source converters. In: Proceedings of 2012 IEEE international conference industrial technology, ICIT 2012, Athens, Greece, 19–21 Mar 2012, pp 638–643

22. Lee TS (2003) Input-output linearization and zero-dynamics control of three-phase AC/DC voltage-source converters. IEEE Trans Power Electron 18:11–22

23. Deng WH, Hu ZB (2005) "The research of decoupled state variable feedback linearization control method of three-phase voltage source PWM rectifier. Proc CSEE (China) 25(7):97–103

24. Komurcugil H, Kukrer O (2005) A novel current-control method for three-phase PWM AC/DC voltage-source converters. IEEE Trans Ind Electron 46(3):544–553

25. Chen B, Feng Y, Zhou M (2013) Terminal sliding-mode control scheme for grid-side PWM converter of DFIG-based wind power system. In: Proceedings of 39th annual conference of the IEEE industrial electronics society (IECON 2013), Vienna, Austria, 10-13 Nov 2013, pp 8014–8018

Part II
Control

Chapter 4
Gain Scheduled H_∞ Control of Wind Turbines for the Entire Operating Range

Fernando A. Inthamoussou, Fernando D. Bianchi, Hernán De Battista and Ricardo J. Mantz

Abstract Two different operating modes can be clearly identified in wind turbine control systems. In low wind speeds, the main control objective is the energy capture maximization, whereas in high wind speeds it is desired to regulate turbine power and speed at their rated values. The fulfillment of these different control objectives implies the transition through low controllability operating conditions that impose severe constraints on the achievable performance. The control task is usually tackled using two separate controllers, one for each operating mode, and a switching logic. Although satisfactory control solutions have been developed for low and high wind speeds, controller design needs refinement in order to improve performance in the transition zone. This chapter overviews a control scheme covering the entire operating range with focus on the transition zone. H_∞ and advanced anti-windup techniques are exploited to design a high performance control solution for both operating modes with optimum performance in the transition zone.

F.A. Inthamoussou · H. De Battista
CONICET and Instituto LEICI, Facultad de Ingeniería, Universidad Nacional de La Plata, CC 91 (1900), La Plata, Argentina
e-mail: intha@ing.unlp.edu.ar

H. De Battista
e-mail: deba@ing.unlp.edu.ar

F.D. Bianchi (✉)
Catalonia Institute for Energy Research, IREC, Jardins de Les Dones de Negre 1, 08930 Sant Adrià de Besòs, Barcelona, Spain
e-mail: fbianchi@irec.cat

R.J. Mantz
CIC and Instituto LEICI, Facultad de Ingeniería, Universidad Nacional de La Plata, CC 91 (1900), La Plata, Argentina
e-mail: mantz@ing.unlp.edu.ar

Nomenclature

β	Pitch angle
β_r	Pitch angle command
β_o	Optimum pitch angle
Θ	Torsion angle
λ	Tip-speed-ratio
λ_o	Optimum tip-speed-ratio
ρ	Air density
τ	Time constant of the pitch actuator
Ω_g	Generator speed
Ω_N	Rated rotational speed
Ω_r	Rotor speed
B_r	Intrinsic rotor damping
B_s	Drive-train damping
C_P	Power coefficient
$C_{P_{\max}}$	Maximum power coefficient
J_g	Generator inertia
J_t	Rotor inertia
K_s	Drive-train stiffness
k_β	Torque-pitch gain
k_{gs}	Gain-scheduling gain
k_V	Torque-wind speed gain
N_g	Gear-box ratio
P_r	Rotor power
P_N	Rated power
R	Rotor radius
T_g	Generator torque
T_N	Rated torque
T_r	Aerodynamic torque
T_{sh}	Shaft torque
V	Wind speed
V_N	Rated wind speed
$\|G(s)\|_\infty$	Denotes the ∞-norm of the stable system with transfer function $G(s)$
$\bar{x}$	Denotes steady-state value of x
$\hat{x}$	Denotes variation with respect to the steady-state value of x
$\dot{x}$	Denotes dx/dt

4.1 Introduction

Wind turbines are highly complex dynamical systems. They are flexible, mechanical structures subjected to spatially and temporally distributed disturbances, with interconnected dynamics, poorly damped, with physical constraints, etc. Additionally, they are operated and controlled in different modes depending on the wind speed. The operational region of wind turbines can be divided into three regions. On the one side, at low wind speeds one finds the partial-load region, also called region 1, where the main control objective is energy capture maximization. A complementary objective in this region is to reduce, or at least not to amplify, the aerodynamic loads [1]. At the opposite side of the operational wind speed range there is region 3, the full-load region. The objective there is to keep the turbine at its rated operating point. In this region, mitigation of aerodynamic and mechanical losses is crucial for the useful life of the wind turbine. In between, there exists a transition region (region 2) where the objective is to achieve a smooth transition between power tracking and regulation. Therefore, controller performance is mainly assessed in terms of loads alleviation.

Wind turbine control has been traditionally addressed in two ways. In one way, a multivariable controller is designed to guarantee satisfactory performance along the whole wind speed envelope. Some problems like low controllability and poorly damped oscillations make this task very complicated, leading to solutions that are too conservative. In the other approach, two different controllers are designed to fulfill the control objectives for partial- and full-load, whereas a bumpless or anti-windup compensation avoids undesirable responses after controller switching. This is the control structure implemented in commercial wind turbines.

For many years, the focus has been on improving controller performance in low and high wind speeds. Less attention has been given to the transition region where there was not a clear control objective (see for instance [2–5]). However, the detrimental effects of loading is increasing as wind turbine size grows exponentially, thus moving the attention to load mitigation. That is why operation and controller performance in the transition zone, where the low controllability problems appear, is now receiving special interest in the wind industry and academy.

In this chapter, the two-controller approach with anti-windup compensation is revisited. A robust, gain-scheduling control scheme designed in the H_∞ optimal control framework is discussed in detail, with special focus on the performance in the transition zone. The turbine is controlled through the generator torque in the partial-load region, and through the pitch angle in the full-load one. An optimal anti-windup strategy is also included to achieve smooth operation in the transition region.

4.2 Wind Turbine Modeling

The energy captured by a wind turbine is a function of the rotor radius R, the wind speed V, the rotor speed Ω_r and the pitch angle β. More precisely, the rotor power can be expressed as

$$P_r(V, \beta, \Omega_r) = \frac{\pi \rho R^2}{2} C_P(\lambda, \beta) V^3, \tag{4.1}$$

where ρ is the air density and $\lambda = \Omega_r R / V$ is the tip-speed ratio. The efficiency of the energy capture is characterized by the power coefficient $C_P(\cdot)$. Figure 4.1 shows the power coefficient of the 5 MW NREL wind turbine benchmark reported in [6].

The rotor torque results from dividing the captured power by the rotational speed:

$$T_r(V, \beta, \Omega_r) = P_r(V, \beta, \Omega_r)/\Omega_r. \tag{4.2}$$

Modern wind turbines are complex mechanical systems exhibiting coupled translational and rotational movements. This complex dynamic behavior is in general well-captured by aeroelastic simulation codes such as the FAST (Fatigue, Aerodynamics, Structures, and Turbulence) code developed by the National Renewable Energy Laboratory (NREL) [7]. However, these models are not suitable for control design purposes. Simpler models including only a few oscillation modes are enough to design a control law. Here, for the sake of clarity, a two-mass model capturing just the first drive-train mode is used, whereas the unmodeled dynamics will be covered by additive uncertainty. The dynamical equations describing this model are

$$\dot{\Theta} = \Omega_r - \Omega_g/N_g,$$
$$J_t \dot{\Omega}_r = T_r - T_{\text{sh}}, \tag{4.3}$$
$$J_g \dot{\Omega}_g = T_{\text{sh}}/N_g - T_g,$$

where the state variables are the torsion angle Θ, the rotor speed Ω_r and the generator speed Ω_g. The model variables T_g and $T_{\text{sh}} = K_s \Theta + B_s(\Omega_r - \Omega_g)$ are the generator and shaft torques, respectively. The model parameters are the inertia J_t combining the hub and the blades, the generator inertia J_g, the gear box ratio N_g, and the shaft stiffness K_s and friction B_s coefficients. A representation of this two-mass model can be observed in Fig. 4.2.

In variable-speed wind turbines, the electrical generator is interfaced by a full or partial power converter that controls the generator torque T_g and decouples the rotational speed from the electrical grid. Since the power converter and generator dynamics are much faster than the mechanical subsystem, it can be assumed for

Fig. 4.1 Power coefficient C_P for a 5 MW variable-speed variable-pitch wind turbine [6]
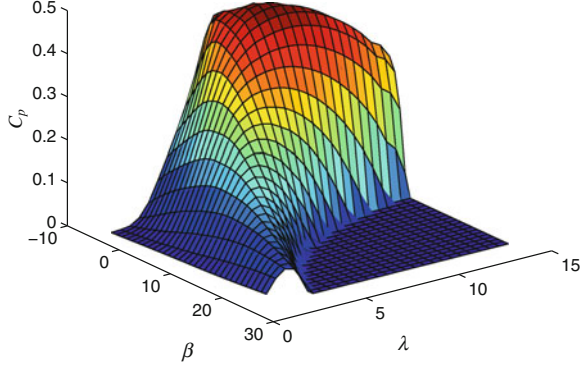
Fig. 4.2 Two-mass model describing the first drive-train mode
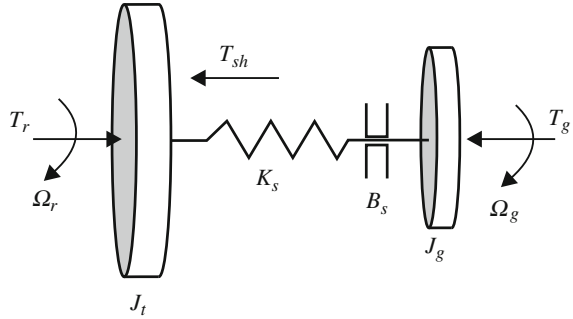
the purpose of this work that the torque reference of the power converter coincides with the electrical torque T_g imposed to the wind rotor. That is, it can be assumed that T_g is a control input.

The pitch actuator is a highly nonlinear mechanic and hydraulic system [5]. For control-oriented purposes, it is usually modeled as a first-order low-pass filter with saturation in the amplitude β and rate of change $\dot{\beta}$. The pitch system is showed in Fig. 4.3. In the linear zone, the pitch actuator dynamics can be described by

$$\dot{\beta} = -\frac{1}{\tau}\beta + \frac{1}{\tau}\beta_r, \tag{4.4}$$

where τ is the time constant and β_r the pitch angle command.

The drive-train dynamics (Eq. 4.3) is highly nonlinear. This nonlinearity comes mainly from the aerodynamic torque (Eq. 4.2). For optimal control design, a linear representation of the system dynamics is necessary. With this aim, the aerodynamic torque is linearized around the operating point:

$$\hat{T}_r(\bar{V}, \bar{\beta}, \bar{\Omega}_r) = B_r(\bar{V}, \bar{\beta}, \bar{\Omega}_r)\hat{\Omega}_r + k_V(\bar{V}, \bar{\beta}, \bar{\Omega}_r)\hat{V} + k_\beta(\bar{V}, \bar{\beta}, \bar{\Omega}_r)\hat{\beta}, \tag{4.5}$$
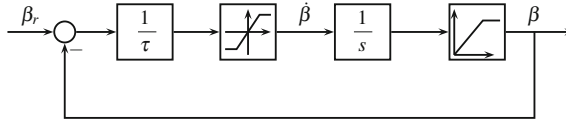
Fig. 4.3 Pitch actuator model

where

$$B_r(\bar{V}, \bar{\beta}, \bar{\Omega}_r) = \left.\frac{\partial T_r}{\partial \Omega_r}\right|_{(\bar{V}, \bar{\beta}, \bar{\Omega}_r)}, \quad k_V(\bar{V}, \bar{\beta}, \bar{\Omega}_r) = \left.\frac{\partial T_r}{\partial V}\right|_{(\bar{V}, \bar{\beta}, \bar{\Omega}_r)},$$

$$k_\beta(\bar{V}, \bar{\beta}, \bar{\Omega}_r) = \left.\frac{\partial T_r}{\partial \beta}\right|_{(\bar{V}, \bar{\beta}, \bar{\Omega}_r)},$$

The bar over the variables denotes the corresponding values at the operating point, whereas the hat denotes deviations with respect to the operating point.

Substituting the linearized expression of the aerodynamic torque (Eq. 4.5) in the two-mass model (Eq. 4.3) and adding the linear model of the pitch system, the wind turbine becomes described, locally around a given operating point, by

$$
\dot{x} = \begin{bmatrix}
0 & 1 & -1/N_g & 0 \\
-K_s/J_r & (B_r(\bar{V}, \bar{\beta}, \bar{\Omega}_r) - B_s)/J_r & B_s/J_r N_g & k_\beta(\bar{V}, \bar{\beta}, \bar{\Omega}_r)/J_r \\
K_s/J_g N_g & B_s/J_g N_g & -B_s/J_g N_g^2 & 0 \\
0 & 0 & 0 & -1/\tau
\end{bmatrix} x
$$

$$
+ \begin{bmatrix}
0 & 0 & 0 \\
k_V(\bar{V}, \bar{\beta}, \bar{\Omega}_r)/J_r & 0 & 0 \\
0 & -1/J_g & 0 \\
0 & 0 & 1/\tau
\end{bmatrix} \begin{bmatrix} \hat{V} \\ T_g \\ \beta_r \end{bmatrix},
$$

(4.6)

where $x = [\hat{\Theta}\ \hat{\Omega}_r\ \hat{\Omega}_g\ \hat{\beta}]^T$ is the state. The signal $\hat{V}$ is the wind speed acting as disturbance, and T_g and β_r are the control inputs.

4.3 Objectives and Control Scheme

A wind turbine normally works in different operating modes along the wind speed range [2]. These operating modes are illustrated in the power-wind speed curve of Fig. 4.4. The control objectives in these regions are substantially different. Below rated wind speed V_N (region 1), the objective is to capture as much energy as possible. In this case, the pitch angle is kept constant at its optimum value, whereas the rotational speed is varied in proportion to the wind speed by properly

Fig. 4.4 Wind turbine
operating regions
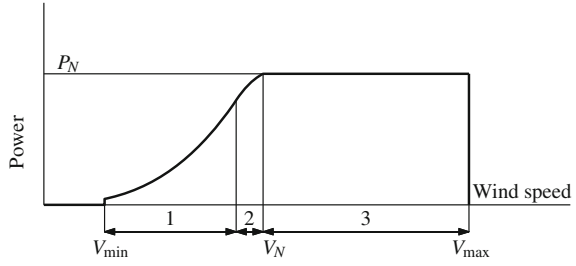
controlling the generator torque. Above rated wind speed (region 3), the objective
is to regulate the rotational speed and power at their rated values in order to protect
the wind turbine from high mechanical loads and excessive electrical currents. In
this region, the rotational speed is regulated acting on the pitch angle, whereas the
generator torque is kept constant at its rated value. Between these two regions,
there is a transition zone (region 2), in which the objectives and control structure
exhibit significant changes.

The operating locus of the wind turbine corresponding to the power-wind
strategy of Fig. 4.4 can be conveniently represented on a torque-rotational speed-
pitch angle space. This graph is shown in Fig. 4.5. In this figure, the projection of
this 3D curve onto the torque-rotational speed plane is also depicted. The three
operating regions can be easily identified.

- In region 1, the objective is energy capture maximization. Both the tip-speed
  ratio and the pitch angle should be maintained as close as possible to their
  optimum values: $C_P(\lambda_o, \beta_o) = C_{P_{max}}$. To this end, the generator torque is
  conventionally chosen to follow a quadratical relationship with the rotational
  speed, i.e.,

$$T_g = \left(\frac{\pi \rho R^5}{2\lambda_o^3} C_{P max} \right) \Omega_g^2 = k_t \cdot \Omega_g^2. \tag{4.7}$$

- The transition region 2 commonly comprises two subregions. Once the rota-
  tional speed reaches the lower limit $\underline{\Omega}_{lim}$, the torque increases proportionally
  until the rated value T_N. Beyond the upper limit $\overline{\Omega}_{lim}$, the torque is maintained
  constant at the rated value. The objective in this region is to decouple as much
  as possible the control laws for regions 1 and 3.
- In region 3, the generator torque is kept constant at the rated value whereas the
  pitch angle is used to regulate the rotational speed.

In the literature, several control schemes covering the entire operating range
have been proposed. Basically, two approaches can be identified among the
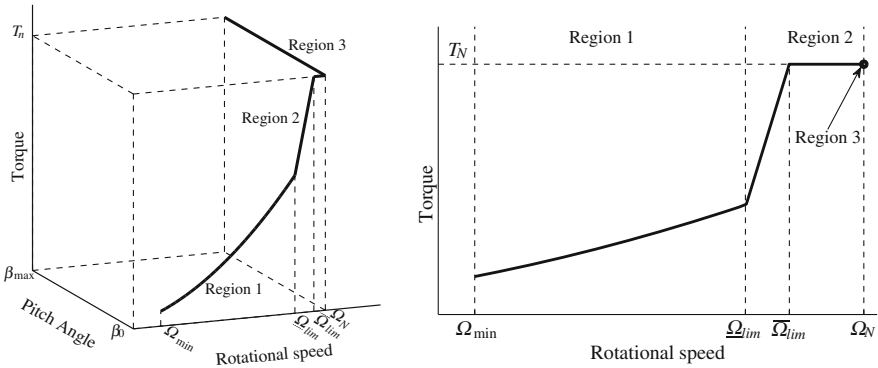
Fig. 4.5 Typical torque-rotational speed curve for a variable-speed variable-pitch wind turbine

proposals. In one of them, two different controllers for low and high wind speeds together with a switching strategy are designed (see for example, [8, 9]). Simple controllers can be used in each region at the cost of a bumpless or anti-windup compensation to reduce undesirable transients in the transition region. The other approach consists of just one control law (generally nonlinear) covering the whole operating envelope (see for example, [2, 5]). This approach yields more complex controllers, hence requiring more advanced control techniques. Furthermore, these controllers are usually more conservative and quite complex to implement.

The control scheme covering the entire operating range presented in this chapter is based on the first approach. It is sketched in Fig. 4.6. As previously mentioned, the generator torque follows the law in Eq. 4.7 below rated wind speeds. This control law is implemented as a look-up table, the LUT block in Fig. 4.6. While the rotational speed evolves well below rated (Ω_N), the pitch angle remains saturated at its lower limit β_o. Only after speed reaches Ω_N or approaches it fast enough, the pitch control becomes active. This pitch control is designed here using H_∞ optimal control tools. A gain scheduling technique is used to deal with the nonlinearity of the aerodynamic torque. In addition, anti-windup compensation is also included to smooth the transients in the transition region. This compensation is only active when the pitch angle saturates in order to recover optimally and softly the non saturated loop condition. The damping filter is commonly added to increase the damping of the drive-train oscillation mode. This filter is active in the three regions and it must be considered when the pitch controller is designed.

Figure 4.7 depicts the coefficients B_r, k_V and k_β as functions of wind speed over the operational wind speed range of the 5 MW wind turbine [6]. In particular, the intrinsic damping B_r and pitch gain k_β are of special interest since they affect the stability and performance of the closed loop system. To compensate for the nonlinearity in the pitch action, the inverse of the coefficient k_β (k_β^{-1}) is inserted in the loop. Besides, the intrinsic damping B_r is considered an uncertain parameter instead of a nonlinear function of the operating point. In this way, by canceling the nonlinearity in k_β and covering with uncertainty the nonlinearity in B_r, the
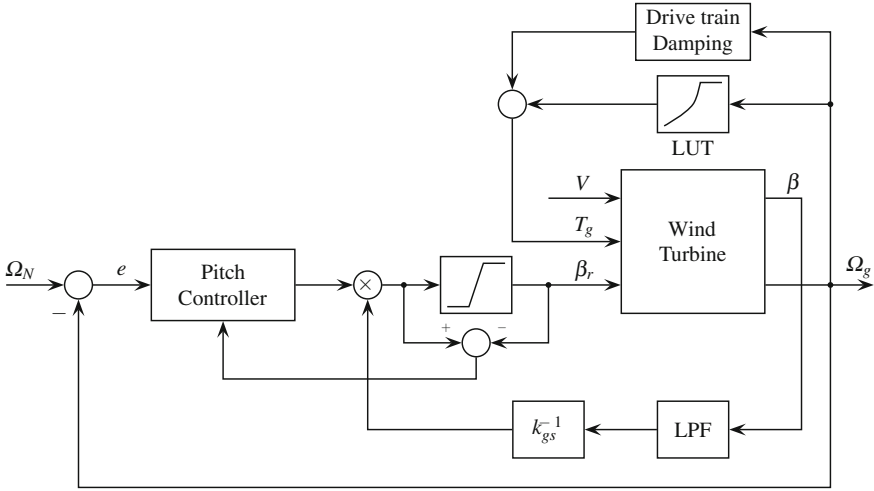
Fig. 4.6 Control scheme covering the entire operating range

rotational speed can be regulated with a linear time-invariant (LTI) controller. That is, an LTI controller designed for a given operating point can be used for the whole operating locus. To deal with the parameter uncertainty, H_∞ optimal control tools will be used.

To implement this control strategy, it is necessary to invert k_β, which is parameterized by wind speed. Recall, however, that wind speed in not measurable. To overcome this problem, the one-to-one correspondence between wind speed and pitch angle that exists in region 3 of the operating locus of Fig. 4.5 can be exploited. In fact, this one-to-one correspondence means that $\bar{\beta}$ suffices to uniquely determine the operating point in this region. Particularly, it means that k_β can be parameterized just in terms of $\bar{\beta}$. This allows computing k_β^{-1} as function of a measurable variable. To simplify this computation, the coefficient k_β can be approximated by

$$k_\beta(\bar{\beta}) = k_{\beta 0} k_{\mathrm{gs}}(\bar{\beta})$$

The gain $k_{\beta 0}$ is k_β evaluated at operating point where the LTI controller is designed, whereas $k_{\mathrm{gs}}(\cdot)$ is a second order polynomial of the form

$$k_{\mathrm{gs}}(\bar{\beta}) = c_2 \bar{\beta}^2 + c_1 \bar{\beta} + c_0$$

computed by curve fitting. The values of $k_\beta / k_{\beta 0}$ and the approximation k_{gs} for the 5 MW NREL wind turbine can be seen in Fig. 4.8. To avoid loop interactions, the scheduling parameter $\bar{\beta}$ is obtained by passing the pitch angle through a low pass filter (LPF).

Before describing the control design, a brief review of H_∞ optimal control concepts is provided in the next section.

Fig. 4.7 Values of the
linearization coefficients B_r,
k_V and k_β in the entire wind
speed range
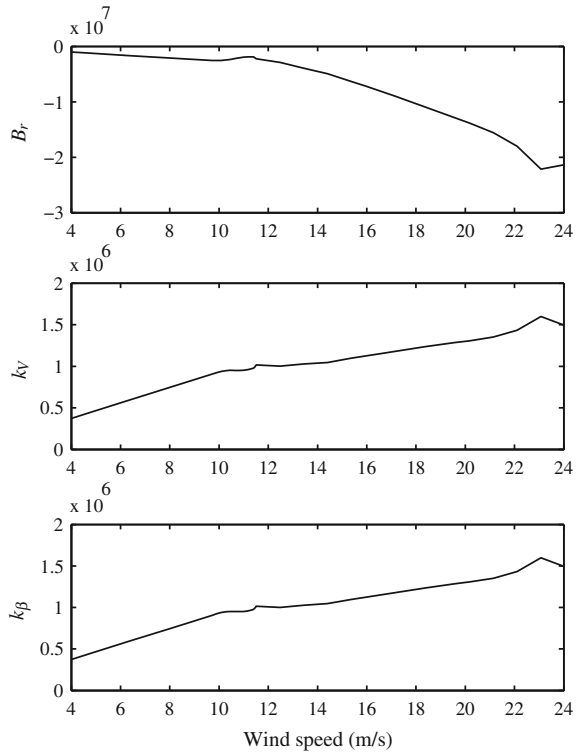
Fig. 4.8 Values of $k_\beta/k_{\beta 0}$ for
several wind speeds and the
second order polynomial
approximation
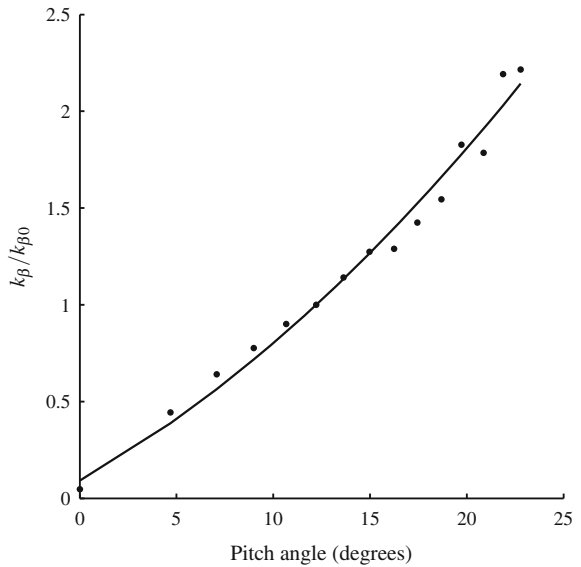
4.4 H_∞ Optimal Control Background

Consider an LTI system with the following state space realization

$$\begin{aligned}
\dot{x} &= Ax + B_w w + B_u u \\
z &= C_z x + D_{zw} w + D_{zu} u \\
y &= C_y x + D_{yw} w + D_{yu} u
\end{aligned} \tag{4.8}$$

where $A \in \mathbb{R}^{n \times n}$, $D_{zw} \in \mathbb{R}^{n_z \times n_w}$ and $D_{yu} \in \mathbb{R}^{n_y \times n_u}$. The signal u is the control input and w is the disturbance. The signal y is the controlled variable and z is a fictitious output signal that serves to state the control objectives. The signal z is commonly named as the performance output.

It is assumed that system in Eq. 4.8 is stabilizable and detectable. That is, there exists a control law $u = K(s)y$ that stabilizes the closed loop system

$$T_{zw}(s) = G_{zw}(s) + G_{zu}(s)K(s)(I + G_{yu}(s)K(s))^{-1}G_{yw}(s)$$

with I the identity matrix and $G(s)$ the transfer function of the system in Eq. 4.8 partitioned as

$$G(s) = \begin{bmatrix} G_{zw}(s) & G_{zu}(s) \\ G_{yw}(s) & G_{yu}(s) \end{bmatrix} = \left[\begin{array}{c|cc} A & B_w & B_y \\ \hline C_z & D_{zw} & D_{zu} \\ C_y & D_{yw} & D_{yu} \end{array} \right].$$

The γ-suboptimal H_∞ synthesis problem consists in finding an internally stabilizing control law $u = K(s)y$ that guarantees an ∞-norm of the closed-loop transfer function from the disturbance w to the performance output z lower than γ. Being $T_{zw}(s)$ being the closed-loop transfer function from w to z, the control objective can be formalized as

$$\|T_{zw}\|_\infty < \gamma, \tag{4.9}$$

where $\|\cdot\|_\infty$ denotes the infinity norm. For a stable system with transfer function $G(s)$, the ∞-norm is defined as

$$\|G(s)\|_\infty = \max_\omega \sigma_{max}(G(j\omega))$$

where σ_{max} is the maximum singular value and ω is the frequency [10]. In other words, the ∞-norm is basically the maximum gain of the frequency response of the transfer function $G(s)$.

There are several solutions for the γ-suboptimal H_∞ synthesis problem, but the most popular nowadays is the formulation as an optimization problem with linear matrix inequalities (LMIs) constraints [11]. Considering a controller with a state-space realization

$$K(s) = \left[\begin{array}{c|c} A_k & B_k \\ \hline C_k & D_k \end{array}\right],$$

the controller matrices can be found by solving the following optimization problem:

minimize $\gamma(R, S, \hat{B}_k, \hat{C}_k, D_k)$,
   subject to

$$\begin{bmatrix} AR + B_u\hat{C}_k + (\star) & \star & \star \\ (B_w + B_y D_k D_{yw})^T & -\gamma I_{n_w} & \star \\ C_z R + D_{zu}\hat{C}_k & D_{zw} + D_{zu}D_k D_{yw} & -\gamma I_{n_z} \end{bmatrix} < 0,$$

$$\begin{bmatrix} (SA + \hat{B}_k C_y) + (\star) & \star & \star \\ (SB_w + \hat{B}_k D_{yw})^T & -\gamma I_{n_w} & \star \\ C_z + D_{zu}D_k C_y & D_{zw} + D_{zu}D_k D_{yw} & -\gamma I_{n_z} \end{bmatrix} < 0,$$

$$\begin{bmatrix} R & I \\ I & S \end{bmatrix} > 0,$$

with ">" and "<" denoting positive and negative definite matrices, respectively, and $\star$ represents the matrices needed to obtain a symmetric matrix.

After finding the positive definite matrices R and S and matrices $\hat{B}_k$, $\hat{C}_k$ and D_k, the controller matrices can be computed from

$$A_k = -(A + B_u D_k C_y)^T + \begin{bmatrix} SB_w + \hat{B}_k D_{yw} & C_z + D_{zu}D_k C_y \end{bmatrix}$$
$$\begin{bmatrix} -\gamma I & (D_{zw} + D_{zu}D_k D_{yw})^T \\ D_{zw} + D_{zu}D_k D_{yw} & -\gamma I \end{bmatrix}^{-1} \begin{bmatrix} (B_w + B_y D_k D_{yw})^T \\ C_z R + D_{zu}\hat{C}_k \end{bmatrix}$$
$$B_k = N^{-1}(\hat{B}_c - SB_u D_c),$$
$$C_k = (\hat{C}_k - D_k C_y R)M^{-T},$$

with $MN^T = I - RS$.

The optimization problem involved in the H_∞-synthesis can be effectively solved with available software such as Sedumi [12] and YALMIP [13]. It is also available as a command in the Robust Control Toolbox for Matlab. Therefore, the design process of an H_∞ optimal control requires only to put the control specifications in terms of the minimization of the norm in Eq. 4.9, i.e., to construct the
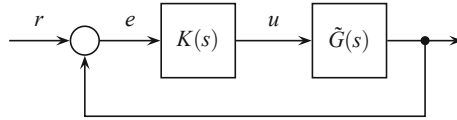
Fig. 4.9 Closed loop system with uncertain plant

augmented plant (Eq. 4.8) by selecting the performance output z and the disturbance w. More details about this process will be given in the next following sections.

One of the most common uses of H_∞-synthesis is the design of robust controllers. The dynamics of a system can be described by a model, but this description is always an approximation. There always exists discrepancy between system behavior and response predicted by the model, caused for example for changes in some parameters or unmodeled phenomena. To consider this situation, the system is described as a family of models in the form

$$\tilde{G}(s) = G_o(s) + W_\Delta(s)\Delta, \quad \|\Delta\|_\infty < 1, \tag{4.10}$$

where G_o is the nominal model and W_Δ is a filter describing the modeling error at different frequencies. Δ is an unknown LTI system with ∞-norm bounded by 1. It can be proved that the closed loop comprising system $\tilde{G}(s)$ and controller $K(s)$ (Fig. 4.9) is stable for all $\|\Delta\|_\infty < 1$ if the ∞-norm of the transfer function from r to u is lower than 1, i.e.,

$$\|K(s)(I + G(s)K(s))^{-1}\|_\infty < 1. \tag{4.11}$$

When a controller $K(s)$ ensures stability for all plants in the set in Eq. 4.10, it is said that the closed loop is robustly stable and Eq. 4.11 is the robust stability condition associated to the uncertainty representation in Eq. 4.10. Notice that there are other uncertainty representations, but Eq. 4.10 is one of the most commonly used (for more details see for example, [10]).

4.5 Wind Turbine Control Design

In this section, we present an H_∞ pitch controller. As said before, an anti-windup controller was added to avoid undesirable behavior caused by pitch saturation in the transition from region 1 to region 3. The controller is designed following a two-step process. First, the H_∞ pitch controller is designed disregarding the pitch saturation. Then, the anti-windup controller is designed for a suitable performance in the transition region.

4.5.1 $\mathbf{H}_\infty$ *Optimal Pitch Control*

As described in the previous section, the first step in the design of an H_∞ optimal control is to state the augmented plant. This implies stating the specifications in terms of the norm-minimization of the mapping between the performance output z and the disturbance w. Model uncertainty can be covered by properly choosing these signals, thus ensuring robust stability. Therefore, before describing the augmented plant, we find the model uncertainty representation to cover the variation of the parameter B_r and other errors caused by the approximation of the wind turbine behavior with a low-order model. The use of the scheduling gain $k_{\mathrm{gs}}^{-1}(\bar{\beta})$ allows canceling the variation of the linearized aerodynamic torque with respect to the operating conditions. However, the variations in B_r are not so simple to compensate for, since they affect the eigenvalues of the linear model.

For control design purposes, the wind turbine can be modeled, after applying the scheduling gain in the control input, by the following parameter dependent transfer function

$$
G(s) = \left[\begin{array}{cccc|c}
0 & 1 & -1/N_g & 0 & 0 \\
-K_s/J_r & (B_r(\bar{\beta})-B_s)/J_r & B_s/J_r & k_{\beta 0}/J_r & 0 \\
K_s/J_gN_g & B_s/J_gN_g & -B_s/J_gN_g^2 & 0 & 0 \\
0 & 0 & 0 & -1/\tau & 1/\tau \\
\hline
0 & 0 & 1 & 0 & 0
\end{array}\right].
$$

Figure 4.10 shows the frequency response of this transfer function for several operating points in region 3. These results correspond to the 5 MW wind turbine previously mentioned. It can be seen that these variations can be covered by additive uncertainty of the form in Eq. 4.10 with the weighting function $W_A(s)$ shown in the right plot of Fig. 4.10. In the uncertainty set, the scheduling gain errors caused by the polynomial approximation and the high-frequency unmodeled oscillation modes can also be covered.

In high wind speeds, the control objectives are the regulation of the rotational speed close to the rated value Ω_N and the reduction of the pitch activity to avoid high mechanical stresses. In the H_∞ optimal control framework, these objectives lead to the augmented plant of Fig. 4.11. In this case, the control input u is the pitch command and the controlled signal y is the rotational speed error $e = \Omega_N - \Omega_g$. Then, the performance signal is $z = [\tilde{e}, \ \tilde{\beta}_r]^T$ and the disturbance is the rotational set-point $w = \Omega_N$. Notice that the wind speed could also be considered as a disturbance. However, this would not improve the performance, but only increase the controller complexity.
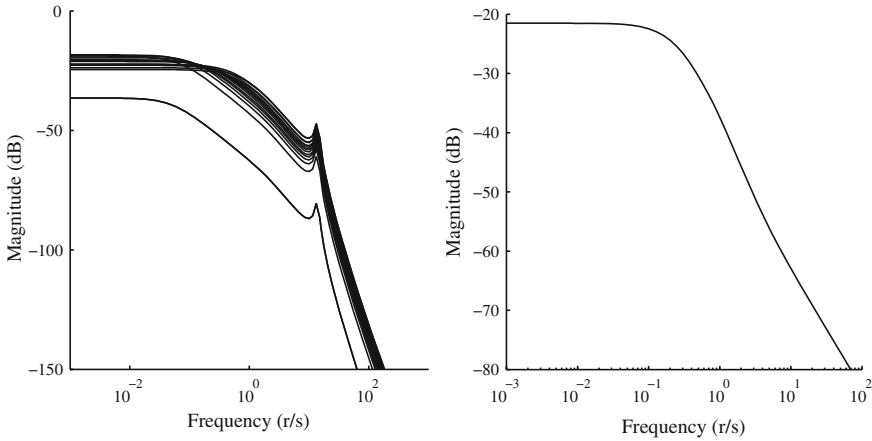
Fig. 4.10 *Left* frequency response of $G(s)$ corresponding to several operating points in region 3. *Right* weighting function W_Δ of the additive uncertainty representation Eq. 4.10
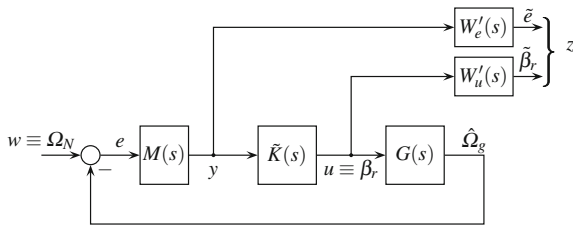
Fig. 4.11 Controller design setup augmented with weighting functions

The speed regulation results in the minimization of the low frequency components of the speed error $\tilde{e} = W'_e(s)(\Omega_N - \Omega_g)$, where

$$W'_e(s) = M(s)W_e(s) \tag{4.12}$$

with W_e a stable transfer function. If M includes integral action, the weight W_e can be a simple constant, such as,

$$M(s) = 1/s, \quad W_e = k_e.$$

The integral action ensures a zero steady-state error and penalizes the rotational speed error in low frequencies. Tracking error in high frequencies is not recommended because it would expose the wind turbine to excessive mechanical loads. The factorization in Eq. 4.12 is necessary for satisfying stabilizability conditions [10]. The controller actually applied to the wind turbine is
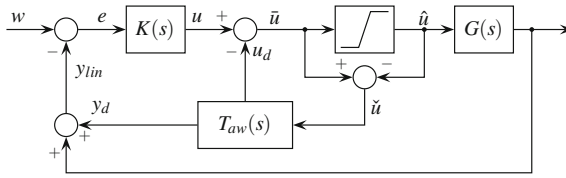
Fig. 4.12 Anti-windup compensation scheme

$$K(s) = M(s)\tilde{K}(s)$$

with $\tilde{K}(s)$ the controller produced by the optimization algorithm.

The weighting function $W_u(s)$ is a high pass filter such as

$$W_u(s) = k_u \frac{s/0.1\omega_u + 1}{s/\omega_u + 1}$$

with k_u and ω_u design parameters. This transfer function penalizes the high frequency components of the control signal, thus limiting the pitch activities. High frequency control action must be also avoided to prevent from rate pitch saturation. Since the modeling errors are covered by additive uncertainty, robust stability and the limitation of the pitch activity can be expressed as a constraint on the same closed loop transfer function. Therefore, the weighting function $W_u'(s)$ in Fig. 4.11 is the most restrictive function between $W_u(s)$ and $W_\Delta(s)$.

Notice that if the drive-train damping controller is considered, the plant $G(s)$ in Fig. 4.11 must include its dynamics in order to guarantee close loop stability.

Since the pitch controller is only active in region 3, an anti-windup controller is necessary to ensure good behavior during the transition from region 1 to region 3. With this purpose an optimal anti-windup controller is added. This controller is not shown in Fig. 4.6 for a matter of clarity. The anti-windup controller connection is shown in Fig. 4.12.

4.5.2 Anti-windup Compensation

In the control scheme of Fig. 4.6, the pitch controller will be in saturation during the low wind speed intervals. So, anti-windup compensation is absolutely necessary. To achieve high performance compensation, the anti-windup scheme proposed by [14, 15] is adopted here. It can be seen in Fig. 4.12. This scheme offers a good trade-off between stability margin and smooth recovery from saturation.

As can be seen in Fig. 4.12, the anti-windup compensator produces two terms: y_d acting on the controller input and another u_d acting on the control output. It can
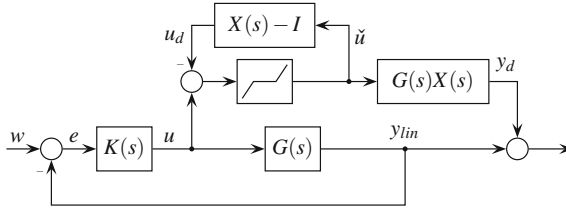
Fig. 4.13 Equivalent representation of the anti-windup compensation scheme in Fig. 4.12

be proved, after some system manipulations, that the block diagram in Fig. 4.13 is equivalent to the scheme in Fig. 4.12 by defining

$$\begin{bmatrix} u_d(s) \\ y_d(s) \end{bmatrix} = T_{aw}(s)\check{u}(s) = \begin{bmatrix} X(s) - I \\ Y(s) \end{bmatrix} \check{u}(s), \tag{4.13}$$

where X and Y are the coprime factors of G, i.e., $G = X^{-1}Y$. Therefore, the anti-windup compensator can be expressed as

$$T_{aw}(s) = \left[\begin{array}{c|c} A + B_u F & B_u \\ \hline F & 0 \\ \hline C_y + D_{yu}F & D_{yu} \end{array} \right] \tag{4.14}$$

where F is chosen for $A + B_u F$ to be Hurwitz.

In this way X must be designed to ensure the closed-loop stability of $X - I$ and the deadzone nonlinear operator. At the same time, X must be designed to minimize the effect of y_d on the controlled variable. It can be proved that using the Lyapunov function $V(x_{aw}) = x_{aw}^T P x_{aw} > 0$ and forcing

$$\dot{V}(x_{aw}) + y_d^T y_d - vu^T u < 0, \tag{4.15}$$

with x_{aw} the state of the system T_{aw}, the previously mentioned objectives are satisfied. Because of the sector boundedness of the dead-zone nonlinearity, the following condition is satisfied

$$2\check{u}^T U^{-1}(u - Fx_{aw} - \check{u}) \geq 0, \tag{4.16}$$

with U a diagonal matrix.

After some mathematical manipulations, the problem of finding an anti-windup compensator is reduced to a state feedback F satisfying the following optimization problem with LMI constraints:

minimize $v(Q, U, L)$,
subject to

$$
\begin{bmatrix}
(AQ + B_u L) + (\star) & B_u U - QF^T & 0 & QC_y^T + L^T D_{yu}^T \\
\star & -2U & I & UD_{yu}^T \\
\star & \star & -vI & 0 \\
\star & \star & \star & -vI
\end{bmatrix} < 0,
$$

$$Q = Q^T > 0,$$

where $\star$ are inferred by symmetry. The state feedback gain is then obtained as $F = LQ^{-1}$ (see [16] for more details).

4.6 Results

The system behavior was evaluated by simulation on the 5 MW NREL wind turbine benchmark [6]. Simulations were performed in the FAST/Simulink®/ Matlab® environment. A more complete 16 degrees-of-freedom model available in FAST [7] was used as a way to assess the robustness of the proposed control scheme against unmodeled dynamics. The wind turbine data are given in Table 4.1, whereas the limit values of the operating locus are listed in Table 4.2.

The pitch controller was designed according to the control setup in Fig. 4.11 with

$$
W_e'(s) = M(s)W_e(s) = \frac{1}{s}k_e, \, W_u' = k_u \frac{s/0.1\omega_u + 1}{s/\omega_u + 1}
$$

where $k_e = 0.3$, $\omega_u = 50$ and $k_u = 0.25$. The frequency response of the weights W_e', W_Δ and W_u are shown in Fig. 4.14. Remember that W_u' must be more demanding than W_u and W_Δ at every frequency. So, as can be seen in Fig. 4.14, it suffices to choose $W_u' = W_u$.

The ∞-norm of the closed loop transfer function T_{zw} resulted in 0.977. In particular, the norm of the transfer function from Ω_N to the control signal β, i.e.,

$$
||K(I + KG)^{-1}||_\infty = 0.972.
$$

As the norm is lower than 1, stability against covered modeling errors is guaranteed.

Table 4.1 Wind turbine parameters

Parameter value	Description
$P_N = 5.5967$ MW	Rated power
$N_p = 3$	Blades number
$R = 63$ m	Rotor radius
$N_g = 97$	Gear box ratio
$B_s = 6{,}210$ KNm/(r/s)	Drive-train damping
$J_r = 38{,}759{,}227$ kgm^2	Rotor inertia
$J_g = 534.2$ kgm^2	Generator inertia
$K_s = 867{,}637$ KN/r	Drive-train stiffness
$V_{min} = 3$ m/s	Cut-in wind speed
$V_{max} = 25$ m/s	Cut-out wind speed
$\beta_{min} = 0°$	Minimum pitch angle
$\beta_{max} = 30°$	Maximum pitch angle
$|\dot{\beta}|_{max} = 10°/s$	Maximum pitch rate
$\Omega_N = 1{,}173.7$ rpm	Rated speed
$T_N = 43093.55$ Nm	Rated torque

Table 4.2 Operating curve values

Parameter description	Value
V_{min}	3 m/s
V_{max}	25 m/s
$\underline{\Omega}_{lim}$	1,079 rpm
$\overline{\Omega}_{lim}$	1,115 rpm
Ω_N	1,173.7 rpm
T_N	43,093.55 Nm

Fig. 4.14 Weight functions used in the pitch control design
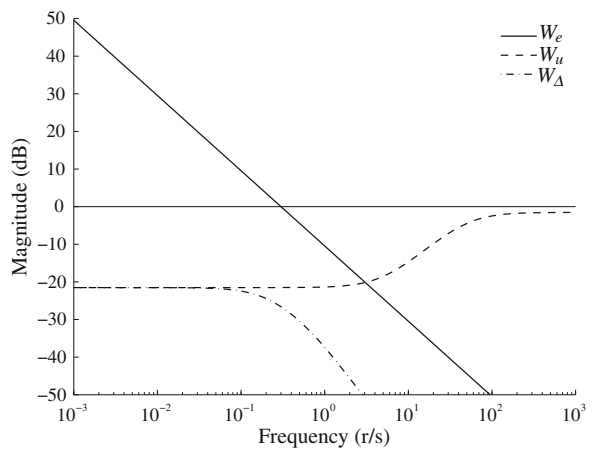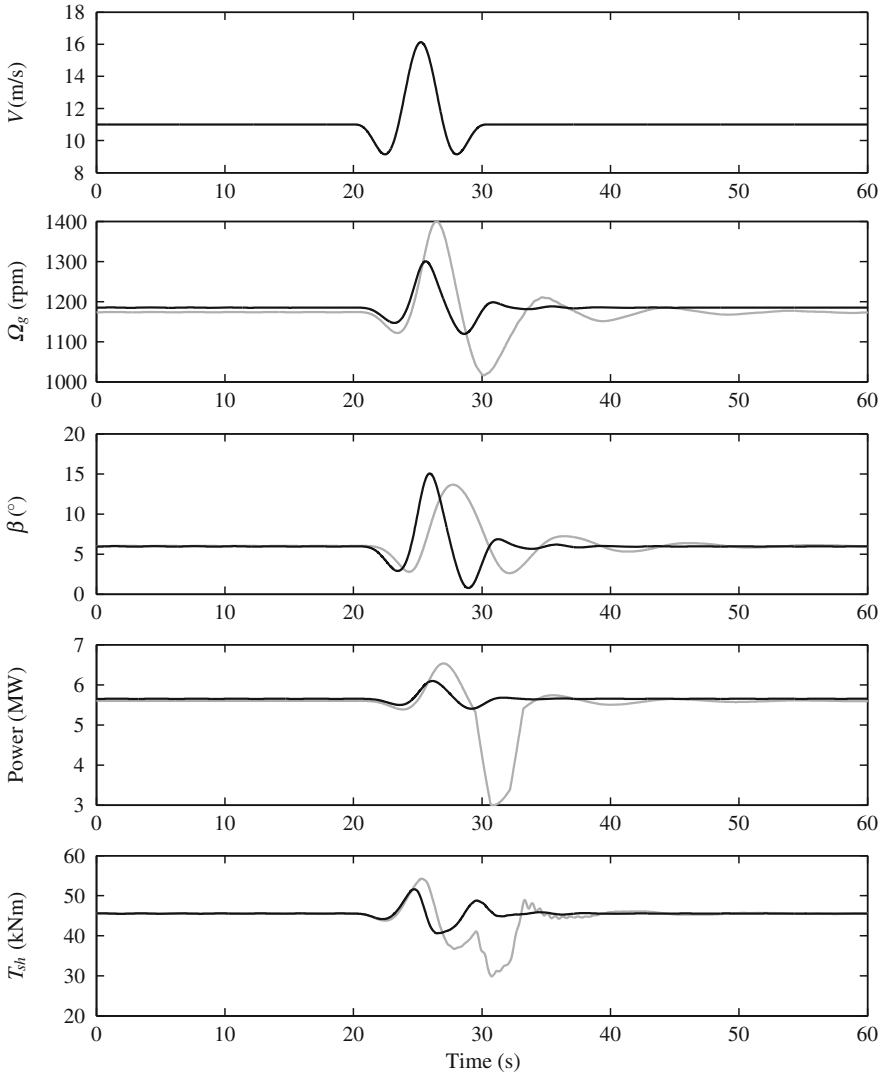
Fig. 4.15 System response to a wind gust profile. *Gray lines* PI controller, *black lines* H_∞ controller

After designing the pitch controller, the anti-windup compensation was computed by solving the optimization problem described in Sect. 5.2. The optimization problems for obtaining the H_∞ controller and the anti-windup compensation were solved using the Robust Control Toolbox for Matlab, Sedumi [12] and YALMIP [13].

For the sake of comparison, a classical gain-scheduled PI controller was also implemented and simulated. This PI, widely used in the literature as benchmark
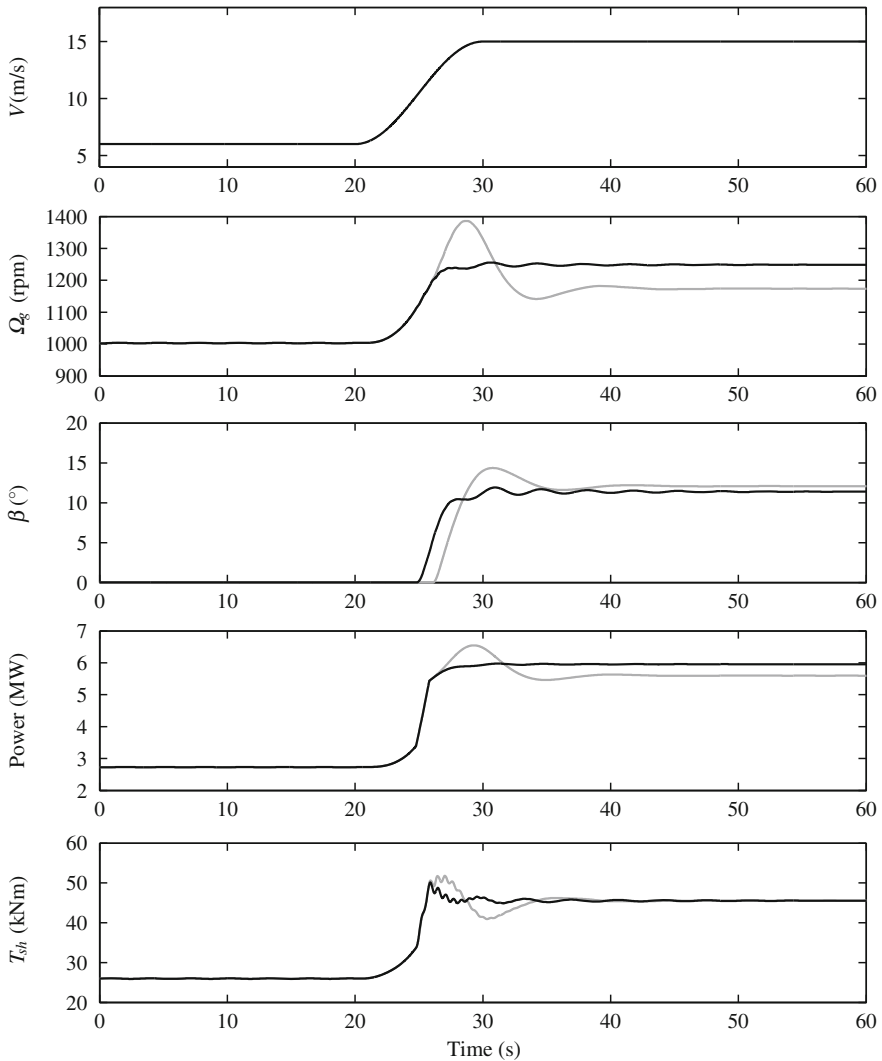
Fig. 4.16 System response to a wind rise profile. *Gray lines* PI controller, *black lines* H_∞ controller

controller, was designed following the guidelines in [6, 17]. Basically, the PI controller was tuned as in [6] after linearizing the wind turbine model at the operating point $(\bar{V}, \bar{\beta}, \bar{\Omega}_r) = (11.4 \, \text{m/s}, \, 0, \, 12.1 \, \text{rpm})$. The controller gains were calculated to achieve appropriate damping (0.7) and natural frequency (0.6 rad/s) [17]. As the controller ensures the desired behavior only at the design operating point, a pitch-dependent gain is applied to compensate for the nonlinear rotor torque. This gain is a function of β obtained by fitting the values of k_β along the
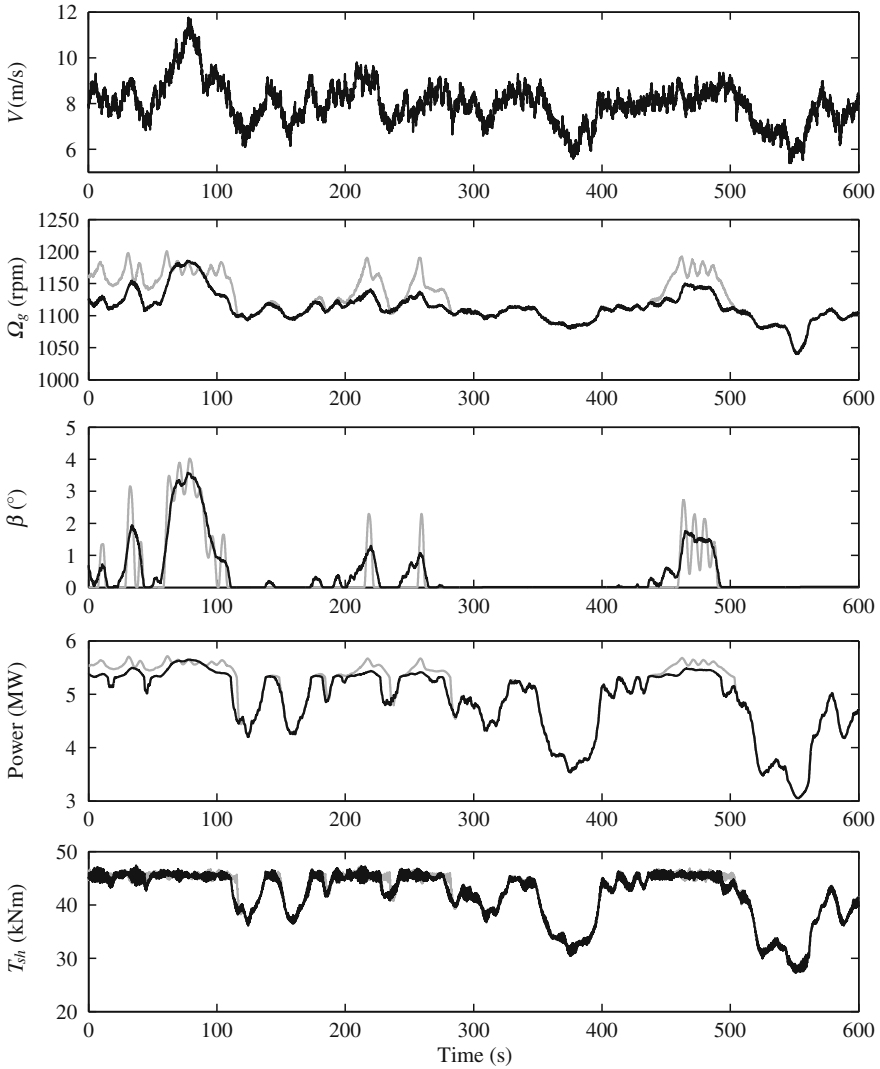
Fig. 4.17 System response to a realistic wind profile. *Gray lines* PI controller, *black lines* H_∞ controller

operating locus. In addition, a classical anti-windup compensation was added to improve the transient between regions 1 and 3. The PI tuning constants are $K_P(\beta = 0) = 0.01882681$ s, $K_I(\beta = 0) = 0.008068634$. The function that makes the gain scheduling is $f(\beta) = 1/(1 + \beta/\beta_k)$, where β is the pitch angle and $\beta_k = 6.30236$ is the blade pitch angle when the rotor power has doubled. The generator torque control is the same as in the H_∞ approach.

Three scenarios were simulated to assess the control performance. The first scenario is aimed at evaluating the performance of the controllers in region 3. To this end, the wind gust suggested in the IEC 61400-1 standard was used. This gust is very pitch demanding. The second scenario is mainly intended to assess the performance of the anti-windup compensator, i.e., the performance in the transition region. To this end, the wind rise proposed also in IEC 61400-1 standard was used. The last scenario illustrates the behavior of the controller under a realistic wind speed profile.

The simulation results obtained in the first scenario are presented in Fig. 4.15. As can be seen, the pitch controllers are always active. The H_∞ controller achieves better speed regulation with lower pitch activity than the PI controller. The speed overshoot is 16.86 % in the H_∞ case and 19.25 % in the PI case. Additionally, the H_∞ controller offers smoother responses in output power and shaft torque.

The results obtained in the second scenario are shown in Fig. 4.16. The wind profile rising from 6 to 13 m/s in 10 s makes the wind turbine to operate along the three regions. Again, it can be seen that the H_∞ controller achieves a better speed regulation with less pitch activity. Note that H_∞ with the anti-windup starts pitching the blades a bit before the PI with classical anti-windup does. The speed overshoot is 25.49 % in the H_∞ case and 32.96 % in the PI case. Like in the first scenario, the H_∞ controller offers smoother responses in output power and shaft torque.

The results for the last scenario are shown in Fig. 4.17. The 10 min wind speed field was generated with Turbsim [18]. The 8 m/s mean wind speed was selected so that the wind turbine operates in all the three operating regions, but most of the time in the transition one. It can be seen in the figure that the H_∞ controller achieves better speed regulation with significant less pitch activity.

4.7 Conclusion

This chapter presents a robust H_∞ pitch control design for variable-pitch variable-speed wind turbines operating along the entire wind speed range.

The main nonlinearities of the wind turbine dynamics are either canceled by inversion or covered with uncertainty so that an LTI H_∞ controller designed for a given operating point can be applied to the whole operating locus. The controller design guarantees robustness against unmodeled dynamics, cancelation errors and parameter uncertainties.

The system behavior was assessed by numerical simulations of a high-order wind turbine benchmark under three very demanding scenarios. Under these scenarios the H_∞ controller achieves better speed regulation with lower pitch activity than classical PI control. This lower pitch activity leads to lower mechanical stress spreading the wind turbine lifetime and also resulting in softer output power.

4.8 Future Research

The conservativeness inherent to the applied linearization, particularly due to the low-frequency uncertainty, can be eliminated by replacing the LTI design with the linear parameter varying (LPV) one. At the cost of a bit more complex implementation, better results particularly in speed regulation can be obtained. The complexity of the controller can be increased in order to consider more specifications as attenuating additional oscillation modes by adding more sensing signals.

References

1. Bossanyi EA (2003) Wind turbine control for load reduction. Wind Energy 6(3):229–244
2. Bianchi FD, De Battista H, Mantz RJ (2010) Wind turbine control systems: principles, modelling and gain scheduling design. Advances in industrial control. Springer-Verlag London Ltd., London
3. Muhando E, Senjyu T, Uehara A, Funabashi T (2011) Gain-scheduled H_∞ control for WECS via lmi techniques and parametrically dependent feedback part II: controller design and implementation. IEEE Trans Industr Electron 58(1):57–65
4. Munteanu I, Bratcu A, Cutululis N, Ceangă E (2007) Optimal control of wind energy systems: towards a global approach. Springer-Verlag London Ltd., London
5. Østegaard KZ, Stoustrup J, Brath P (2008) Linear parameter varying control of wind turbines covering both partial load and full load conditions. Int J Robust Nonlinear Control 19:92–116
6. Jonkman J, Butterfield S, Musial W, Scott G (2009) Definition of a 5-MW reference wind turbine for offshore system development. Technical report, NREL, 2009
7. Jonkman J (2013) NWTC computer-aided engineering tools (FAST). http://wind.nrel.gov/designcodes/simulators/fast/. Accessed 26 Aug 2013 (Last modified 27 Feb 2013)
8. Lescher F, Jing-Yun Z, Borne P (2006) Switching LPV controllers for a variable speed pitch regulated wind turbine. J Comput Commun Control 4:73–84
9. Yao X-j, Guo C-C, Li Y (2009) LPV H-infinity controller design for variable-pitch variable-speed wind turbine. In: Proceedings of the IEEE 6th international power electronics and motion control conference (IPEMC), pp 2222–2227, 2009
10. Sánchez Peña RS, Sznaier M (1998) Robust systems theory and applications. Wiley, New York
11. Gahinet P, Apkarian P (1994) A linear matrix inequality approach to H_∞ control. Int J Robust Nonlinear Control 4:421–448
12. Sturm J (1999) Using SeDuMi 1.02, a Matlab toolbox for optimization over symmetric cones. Optim Methods Softw 11–12:625–653
13. Löfberg J (2004) YALMIP: a toolbox for modeling and optimization in MATLAB. In: Proceedings of the CACSD conference, Taipei, Taiwan, 2004
14. Turner MC, Postlethwaite I (2004) A new perspective on static and low order anti-windup synthesis. Int J Control 77(1):27–44

15. Weston PF, Postlethwaite I (2000) Linear conditioning for systems containing saturating actuators. Automatica 36(9):1347–1354
16. Skogestad S, Postlethwaite I (2005) Multivariable feedback control: analysis and design. Wiley, UK
17. Hansen M, Hansen A, Larsen T, Øye S, Sørensen P, Fuglsang P (2005) Control design for a pitch-regulated, variable speed wind turbine. Technical report, RISØ, 2005
18. Kelley N, Jonkman B (2013) NWTC computer-aided engineering tools (TurbSim). http:// wind.nrel.gov/designcodes/preprocessors/turbsim/. Accessed 28 Aug 2013 (Last modified 30 May 2013)

Chapter 5
Design of Robust Controllers for Load Reduction in Wind Turbines

Asier Díaz de Corcuera, Aron Pujana-Arrese, Jose M. Ezquerra, Aitor Milo and Joseba Landaluze

Abstract This chapter proposes a methodology to design robust control strategies for wind turbines. The designed controllers are robust, multivariable and multi-objective to guarantee the required levels of stability and performance considering the coupling of the wind turbine. The proposed robust controllers generate collective pitch angle, individual pitch angle and generator torque control signals to regulate the electrical power production in the above rated power production zone and to mitigate the loads in the components of the wind turbines, like the drive train, tower, hub or blades, to increase their lifetime. The synthesis of these controllers is based on the H_∞ norm reduction and gain scheduling control techniques via Linear Matrix Inequalities. A wind turbine non-linear model has been developed in the GH Bladed software package and it is based on a 5 MW wind turbine defined in the Upwind European project. The family of linear models extracted from the linearization process of the non-linear model is used to design the proposed robust controllers. The designed controllers have been validated in GH Bladed and an exhaustive analysis has been carried out to calculate fatigue load reduction on wind turbine components, as well as to analyze load mitigation in some extreme cases.

A. Díaz de Corcuera (✉) · A. Pujana-Arrese · J.M. Ezquerra · A. Milo · J. Landaluze
IK4-IKERLAN, Arizmendiarreta, 2, 20500 Arrasate-Mondragon,
The Basque Country, Spain
e-mail: adiazcorcuera@ikerlan.es

A. Pujana-Arrese
e-mail: apujana@ikerlan.es

J.M. Ezquerra
e-mail: jmezquerra@ikerlan.es

A. Milo
e-mail: amilo@ikerlan.es

J. Landaluze
e-mail: jlandaluze@ikerlan.es

Nomenclature

A_n, B_n, C_n, D_n	State space matrices of system n
a_{Tfa}	Tower top fore-aft acceleration
a_{Tss}	Tower top side-to-side acceleration
C	Coleman transformation
C^{-1}	Anti-Coleman transformation
D_{ux}	Scalar constant in the control x channel
D_{ex}	Scalar constant in the output x channel
D_{dx}	Scalar constant in the disturbance x channel
e_{wg}	Generator speed error
K_{opt}	Optimum constant in below rated zone
M_{oop}	Blade root out-of-plane moment
M_{flap}	Blade root flapwise moment
M_{edge}	Blade root edgewise moment
M_{tilt}	Tilt moment in the rotor plane
M_{yaw}	Yaw moment in the rotor plane
p	Varying parameter
T	Generator torque
T_{DTD}	Torque contribution from drive train damping filter
T_{br}	Torque set-point in below rated zone
T_{sp}	Generator torque set-point
Unc	Uncertainty
w_g	Generator speed
β_{sp}	Pitch angle set-point
β_{col}	Collective pitch angle
B_{fa}	Pitch contribution from tower fore-aft damping filter
β_{tilt}	Pitch tilt angle in the rotor plane
β_{yaw}	Pitch yaw angle in the rotor plane
ψ	Azimuth angle
θ_T	Twist angle in the blade root section

5.1 Introduction

The continuous increase of the size of wind turbines, due to the demand of higher power production installations, has led to new challenges in the design of the turbines. Moreover, new control strategies are being developed. Today's strategies trend towards being multivariable and multi-objective, in order to fulfill the

numerous control design specifications in the non-linear and hardly coupled wind turbine system. To be more precise, one important specification is to mitigate loads in the turbine components to increase their life time.

This chapter presents different strategies to design robust, multivariable and multi-objective collective and individual blade pitch angle controllers and generator torque controllers. These controllers are based on the H_∞ norm reduction and gain scheduling control techniques to mitigate loads in wind turbines without affecting the electric power production. A wind turbine non-linear model has been developed using the GH Bladed software package and it is based on a 5 MW wind turbine defined in the Upwind European project [1]. The family of linear models extracted from the linearization process of the non-linear model is used to design the robust controllers. The designed controllers have been validated in GH Bladed and an exhaustive analysis has been carried out to calculate fatigue load reduction on wind turbine components, as well as to analyze load mitigation in some extreme cases.

The presented chapter is divided into four main sections, where the first one is this introduction. The second section presents general control concepts for wind turbines and the selected Upwind 5 MW wind turbine used to design the proposed controllers is briefly analyzed. Also, a baseline control strategy for the Upwind 5 MW based on classical control methods in wind turbines is carefully explained in this section. The third section shows the process to design the proposed multivariable robust controllers. These controllers are based on the research presented in [2] and they work in the above rated power production control zone. Their closed loop performance is analyzed in MATLAB. The designed robust controllers are:

- Generator Torque Controller based on the H_∞ norm reduction to mitigate the loads in the drive train and tower [3].
- Collective Pitch Controller based on the H_∞ norm reduction to mitigate loads in the tower and to regulate the generator speed at the nominal value [4]. The regulation of the generator speed is improved with a gain scheduling of three H_∞ controllers designed in three operating points. The gain scheduling is developed with a complex problem solved via Linear Matrix Inequalities (LMI).
- Individual Pitch Controller based on the H_∞ norm reduction [5] to mitigate loads in the tower and to align the rotor plane in the turbine.

The fourth section analyzes simulation results in GH Bladed using the different designed controllers compared to the baseline control strategy. Fatigue loads in DLC1.2 case and extreme loads in DLC1.6 and DLC1.9 cases are analyzed [6]. The last sections summarize the conclusions and the future of the work described in this chapter.

5.2 General Control Concepts for Wind Turbines

Wind turbines with generator variable speed regulation based on blade pitch angle control have been commonly used over the last few years by wind turbine manufactures. The wind turbine control system is divided into two layers: the wind farm supervisory control, which generates external electric power demand set-points for each wind turbine, and the wind turbine supervisory control for each individual wind turbine. Furthermore, the wind turbine supervisory control is also divided into four operating states: startup, shutdown, park and power production. The control strategy in the electric power production zone is determined by a curve where the generator speed and the generator torque values are carefully related [7–9]. Figure 5.1 shows this curve for the 5 MW wind turbine explained in Sect. 5.2.1. The power production zone is defined by the curve *ABCD* to be more time working at the optimum power coefficient value. The vertical sections *AB* and *CD* are implemented with generator torque controllers to regulate the generator speed at the references existing in the points *A* and *C* respectively. Between *B* and *C* points, the control zone is called below rated and it is implemented using a *look up table* control to work with the optimum power coefficient value while the pitch angle is fixed at the fine pitch angle, which is usually zero. However, in the *D* zone, the generator speed is regulated with a collective blade pitch angle control and the generator torque is kept at the nominal value. The transition between the generator torque control in the zone *CD* (transition zone) and the collective pitch control in zone *D*, called above rated, has to be soft to improve the controller performance [7, 10]. Sometimes, the rotor rotational frequencies $1P$, $2P$ and $3P$ are equal to other wind turbine structural modes in the tower, blades or drive train. If this coincidence exists, these modes can be dangerously excited. In [9, 11, 12], a strategy to avoid this coincidence is proposed, where the below rated zone is divided into five sub-zones: *BE* and *GC* to work in the power coefficient optimum value, *EF* and *GH* to regulate the generator speed outside the forbidden speed zone *EG* with a generator torque control.

Figure 5.2 shows the generator speed and electric power signals for the 5 MW wind turbine model in the different zones at the power production state. Also, the collective pitch angle and generator torque control signals are shown in next figures and they vary according to the wind operating point.

As it is mentioned in the introduction, the continuous increase of the size of wind turbines has led to new challenges in the design of wind turbine control systems beyond the main objective of electric power production. Today's control strategies trend towards being robust, multivariable and multi-objective in order to fulfill the numerous control design specifications considering the hardly coupling effects existing in a wind turbine non-linear system. One of the most important specifications is to mitigate loads in the turbine structural components. In spite of the coupling existing in wind turbines, classical control strategies for wind turbines in the power production zone uncouples the control problem into different Single Input Single Output (SISO) control loops to make easier the control system design:
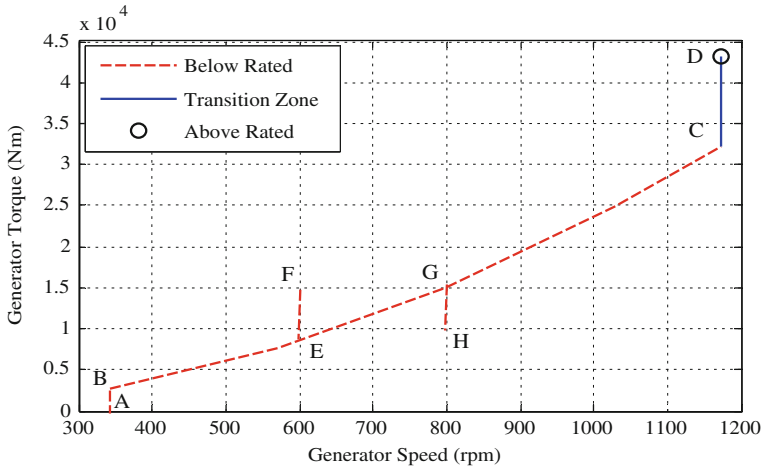
Fig. 5.1   Power production curve for upwind wind turbine
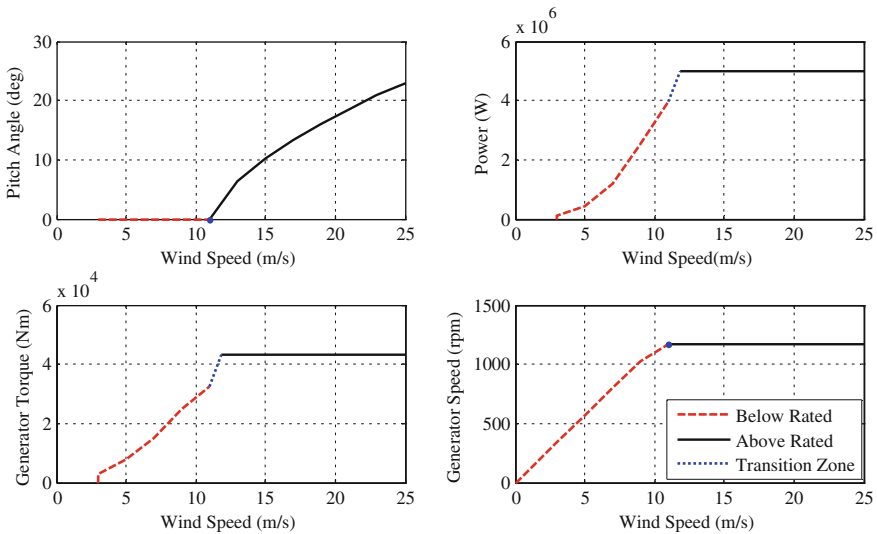
Fig. 5.2   Operating points for the upwind wind turbine

- Generator speed regulation varying the generator torque in *AB* and *CD* zones.
- Generator speed regulation varying the collective pitch angle in above rated zone.
- Drive train mode damping varying the generator torque to mitigate loads in the drive train.
- Tower fore-aft first mode damping varying the collective pitch angle and tower side-to-side first mode damping varying the generator torque to mitigate loads in the tower.

- Individual pitch angle control (IPC) to reduce loads caused by the misalignment of the rotor due to the stochastic dimensional wind, the wind shear, the yaw angle error and the tower shadow.

Over the last few years, several modern control techniques have been proposed to replace the classical SISO control loops with more complex Multi-Input Multi-Output (MIMO) controllers and to consider the real coupling existing in the wind turbine from a multi-objective control design point of view. These techniques are based on fuzzy control [13], adaptive control [14], Linear Quadratic control [15], QFT control [16], Linear Parameter Varying (LPV) control [17, 18] and control synthesis based on the H_∞ norm reduction [19]. H_∞ and LPV control techniques are robust and they can be multivariable and multi-objective, so their application in wind turbines offers a lot of advantages and interesting experimental results can be achieved using them [20]. Next section, where the design of different robust controllers is explained, is focused on two of these control techniques, control synthesis based on the H_∞ norm reduction and gain scheduling control techniques, and their application in the above rated power production zone of wind turbines, where the system non-linearities are more relevant.

The classical control design process for wind turbines is similar to the one used in other mechatronic systems and it is based on the design of a Linear Time Invariant (LTI) controller in different operating points of the non-linear model. Initially, the wind turbine non-linear model is needed to design and validate the controllers in simulation before experimental tests. The wind turbine non-linear model can be carried out from analytical models or making a closed loop identification of the system [21, 22]. Specific software packages exist to develop wind turbine complex analytical models (GH Bladed and FAST are the most well-known ones). GH Bladed [23] is commercialized by Garrad Hassan, whereas FAST [24] is an open source developed by the National Renewable Laboratory (NREL). Once the wind turbine is modeled as a non-linear system, this system is linearised in different operating points. Then, the generator torque and blade pitch angle controllers are designed in different operating points where they work. Finally, the designed controller performance is analyzed in the different operating points and they are discretized and tested using the initial non-linear model. The validation of the wind turbine control loops requires a load analysis based on the analysis of the fatigue damage and different extreme load cases [6].

5.2.1 Wind Turbine Non-Linear Model

The Upwind wind turbine defined inside the Upwind European project has been modelled in GH Bladed 4.0 software package and it is the reference wind turbine non-linear model used to design the controllers presented in this chapter. The Upwind model consists of a 5 MW offshore wind turbine [1] with a monopile structure in the foundation. It has three blades and each blade has an individual

pitch actuator. The rotor diameter is 126 m, the hub height is 90 m, it has a gear box ratio of 97, the rated wind speed is 11.3 m/s, the cut-out wind speed is 25 m/s and the rated rotor rotational speed is 12.1 rpm, so the nominal generator speed is 1,173 rpm. The family of linear models of this wind turbine is obtained in different operating points from the wind turbine non-linear model using the linearization tool of this software. Twelve operating points are defined according to wind speeds from 3 to 25 m/s. Once the non-linear model has been linearized, a modal analysis of the structural and non-structural modes of the wind turbine is essential to carry out a good control system. For example, the most important modes of the Upwind wind turbine in the operating points with wind speeds of 11 and 19 m/s are represented in Table 5.1. The $1P$ non-structural mode is related to the rotor rotational speed, which nominal value is 0.2 Hz for this wind turbine.

The plants of the family of linear models are expressed by the state-space matrices (Eq. 5.1) and they have different inputs and outputs. The inputs $u(t)$ are the collective pitch angle $\beta(t)$, the individual pitch angle in each blade $\beta_1(t)$, $\beta_2(t)$, $\beta_3(t)$, the generator torque control $T(t)$ and the disturbance input $w(t)$ caused by the wind speed. The outputs $y(t)$ are the sensorized measurements used to design the controller. The outputs used in the different designs shown in this chapter are the generator speed $w_g(t)$, the tower top fore-aft acceleration $a_{Tfa}(t)$, the tower top side-to-side acceleration $a_{Tss}(t)$ and the bending flapwise $M_{flap}(t)$ and the bending edgewise $M_{edge}(t)$ moments in the blade roots. Due to the non-linear model complexity, and the number of modes taken into account, the order of the linear models is 55.

$$\dot{x}(t) = A_x x(t) + B_u u(t) + B_w w(t)$$
$$y(t) = C_x x(t) + D_u u(t) + D_w w(t)$$

$$(5.1)$$

Figure 5.3 shows the SISO family of linear plants of the Upwind wind turbine model which relates the collective pitch angle control signal to the measured generator speed. Three operating points in the above rated zone are presented to demonstrate the differences between them for wind speeds of 13, 19 and 25 m/s due the non-linearities of the wind turbine in this control zone.

5.2.2 Baseline Control Strategy

The baseline control strategy to regulate the electric power production for the Upwind 5 MW wind turbine developed in this chapter is based on the *ABCD* curve shown in Fig. 5.1 and the control loops explained in [10]. This strategy is named *C1* and it is used to be compared with the robust controllers described in next sections. In the below rated zone, the generator torque control depends on the generator speed measurement (Eq. 5.2). The generator torque T_{br} is proportional to the square of the generator speed by a constant K_{opt}, where K_{opt} is 2.14 Nm/(rad/s^2) for the Upwind model. In this way, the wind turbine works with the optimum power coefficient value.

Table 5.1 Modal analysis for the upwind 5 MW wind turbine

Element	Mode	Frequency (Hz) at 11 m/s	Frequency (Hz) at 19 m/s
Rotor	In-plane 1st collective	3.68	3.69
	In-plane 2st collective	7.85	7.36
	Out-of-plane 1st collective	0.73	0.73
	Out-of-plane 2nd collective	2.00	2.01
Drive train	Drive train	1.66	1.63
Tower	1st tower side-to-side	0.28	0.28
	1st tower fore-aft	0.28	0.28
	2nd tower side-to-side	2.85	2.87
	2nd tower fore-aft	3.05	3.04
Non-structural	1P	0.2	0.2
	3P	0.6	0.6
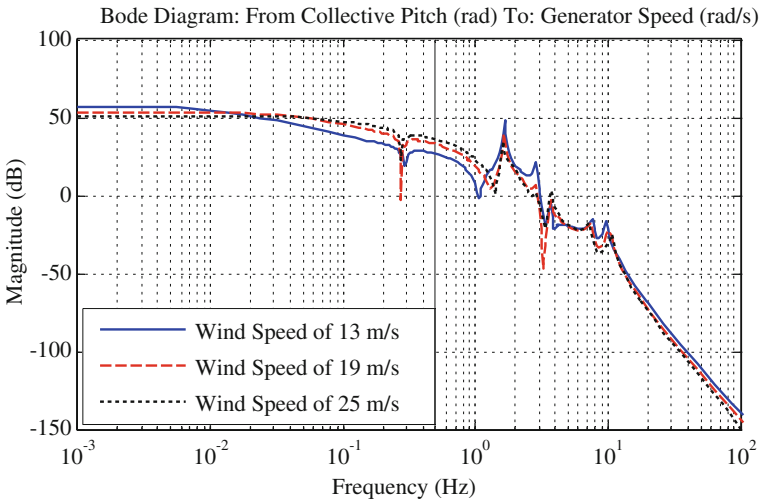
Fig. 5.3 Family of linear models for the upwind wind turbine

$$T_{br} = K_{opt} \cdot w_g^2 \tag{5.2}$$

A Drive Train Damping filter (DTD) is essential in the control design of wind turbines and it has to be firstly designed because the drive train mode is critically coupled in most control loops. The aim of the DTD is to damp the drive train mode and it has to be used in all control zones during the power production. The DTD used in the baseline control strategy for the Upwind model (Eq. 5.3) consists of

one gain, with one differentiator, one real zero and a pair of complex poles. In the designed DTD, K_1 is 641.45 Nms/rad, w_1 is 193 rad/s, w_2 is 10.4 rad/s and ξ_2 is 0.984.

$$T_{\text{DTD}}(s) = \left(K_1 \frac{s\left(1 + \frac{1}{w_1}s\right)}{\left(\left(\frac{1}{w_2}\right)^2 s^2 + 2\xi_2 \frac{1}{w_2}s + 1\right)} \right) w_g(s) \tag{5.3}$$

On the other hand, the objective in the transition zone is the regulation of generator speed varying the generator torque. In the baseline control strategy, it can be developed by using a proportional-integral (PI) controller (Eq. 5.4). In the baseline control strategy, called C1 in this chapter, the PI values in the transition zone (operating point with wind speed of 11 m/s) used in the Upwind baseline controller are w_T and K_T (Eq. 5.4), where $T(s)$ is the generator torque control signal, $e_{\text{wg}}(s)$ is the generator speed error. In this case, w_T is 0.5 rad/s and K_T is 2,685.2 Nm/rad.

$$T(s) = K_T \frac{\left(1 + \frac{1}{w_T}s\right)}{s} e_{\text{wg}}(s) \tag{5.4}$$

The main objective in the above rated zone is the regulation of the generator speed control at the nominal value of 1,173 rpm varying the collective pitch angle in the blades and keeping the electric power at the nominal value of 5 MW. The control structure used in this baseline control strategy in the above rated zone is shown in Fig. 5.4. This regulation of the generator speed is based on a Gain-Scheduled (GS) collective pitch angle PI controller. In this case, the controller input $e_{\text{wg}}(s)$ is the generator speed error, and the controller output $\beta_{\text{col}}(s)$ is the collective pitch angle control signal. The linear plants used to tune the gain-scheduled PI controller are the plants which relate pitch angle and generator speed. These plants have different gains (see Fig. 5.3), so gain-scheduling is used to guarantee the stability of the closed loop system in spite of these differences. Two PI controllers (Eq. 5.5), in two operating points with wind speeds of 13 and 21 m/s, are designed and then a GS is applied to interpolate them. For 13 m/s, K_{B13} is 0.00158 and w_{B13} is 0.2 rad/s and, for 21 m/s, K_{B21} is 0.00092 and w_{B21} is 0.2 rad/s.

$$\beta_{\text{col}} = K_B \frac{\left(1 + \frac{1}{w_B}s\right)}{s} e_{\text{wg}}(s) \tag{5.5}$$

The gain scheduling interpolation is developed according to an average of the measured pitch angle in the blades. Nowadays, new sensors that provide information about the present wind speed in front of the hub of the wind turbine, like LIDARs [25], are being included in the pitch control systems improving the
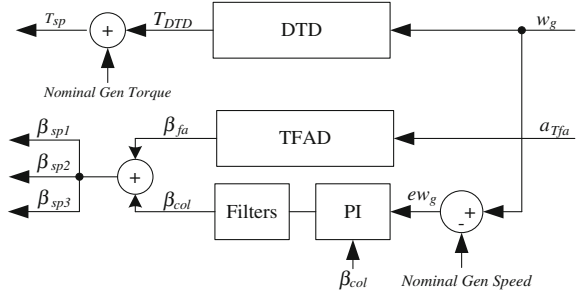
regulation of the generator speed and reducing the loads in the wind turbine. The corresponding steady-state collective pitch angle in the operating points where the collective pitch PI controllers are designed are 6.42° and 18.53° respectively. Next, some series notch filters are included in the regulation loop to improve the PI controller response [26]. Classical design criteria [27] are established to tune these controllers in these operating points, for instance: output sensitivity peak of 6 dB approximately, open loop phase margin between 30° and 60°, open loop gain margin between 6 and 12 dB and keeping constant the PI zero frequency.

Finally, a Tower Fore-Aft Damping filter (TFAD) is designed to reduce the wind effect in the tower fore-aft first mode in the above rated power production zone [28]. For the Upwind baseline controller, the filter (Eq. 5.6) consists of a gain with one integrator, a pair of complex poles and a pair of complex zeros. The input of the TFAD is the fore-aft acceleration measured in the tower top a_{Tfa} and the output is the pitch contribution β_{fa} to the collective pitch angle. For the designed TFAD, K_{TD} is 0.035, w_{T1} is 1.25 rad/s, ς_{T1} is 0.69, w_{T2} is 3.14 rad/s and ς_{T2} is 1.

$$\beta_{\text{fa}}(s) = K_{\text{TD}} \frac{1}{s} \left(\frac{1 + \left(2\varsigma_{T1}s/w_{T1} \right) + \left(s^2/w_{T1}^2 \right)}{1 + \left(2\varsigma_{T2}s/w_{T2} \right) + \left(s^2/w_{T2}^2 \right)} \right) a_{\text{Tfa}}(s) \qquad (5.6)$$

As Fig. 5.4 shows, the individual pitch angle set-point to each blade β_{sp1}, β_{sp2} and β_{sp3} are equals and they are made up of the control signals β_{fa} and β_{col}, and the generator torque set-point T_{sp} is obtained adding the nominal generator torque in above rated and the torque contribution of the DTD filter T_{DTD}.

5.3 Design of Robust Controllers

The robust control design process for load reduction in wind turbines is shown in Fig. 5.5. The robust control techniques applied are based on the H_∞ norm reduction and gain scheduling interpolation. Initially, the non-linear model is linealized to extract the family of linear models. Next, the modal analysis is carried out to analyze the structural and non-structural modes of the system.
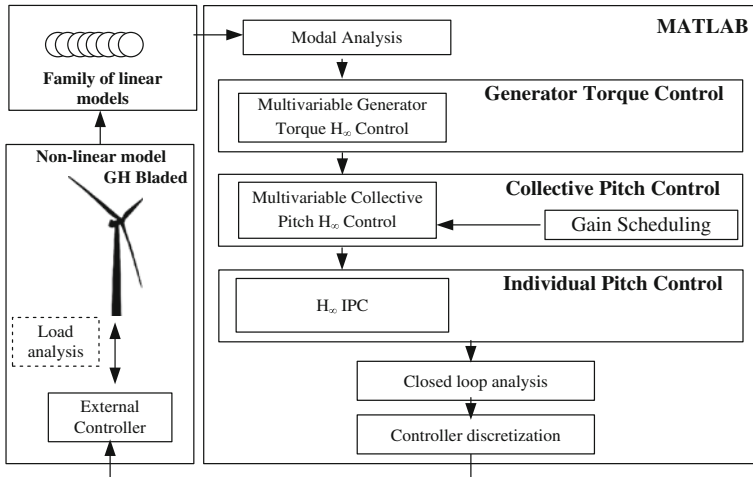
Fig. 5.5 Robust control design process for load reduction in wind turbines

The designed control loops are the generator torque control, the collective pitch control and the individual pitch control (IPC). Only one MIMO H_∞ control is proposed to develop the generator torque control. A MIMO H_∞ control and gain scheduling of different H_∞ controllers via LMI solution are proposed to carry out the collective pitch angle control. Also, a MIMO H_∞ control is finally proposed to perform a promising IPC. The controller design sequence is essential because the generator torque control has to be considered when designing the pitch angle control loops due to the couplings inherent to the system, mainly due to the hardly coupling of the drive train mode.

Once the controllers are obtained, they are reduced and validated by a closed loop analysis in different operating points with the family of linear models. Finally, they are discretized with a sample time of 0.01 s, which is commonly used by wind turbine manufactures and, afterwards, they are included in the custom-written controller to work with the non-linear wind turbine model. A load analysis is carried out to analyze the load reduction in different components of the wind turbine. Table 5.2 shows the control objectives of the different proposed robust controllers in the above rated zone.

5.3.1 Design of H_∞ Robust Controllers

Controllers based on the H_∞ norm reduction are robust from the control design point of view, so their application is very powerful for control systems design due to the fact that real engineering systems are vulnerable to external disturbances and noise measurements and due to the differences between the real systems and the mathematical models. A controller design requires a fixed certain performance

Table 5.2 Objectives of the designed robust controllers

Order	Controller name	Control objectives
I	Generator torque H_∞ control	To reduce the wind effect in the drive train and tower side-to-side first modes
II	Collective pitch H_∞ control	To improve the regulation of the generator speed and to reduce the wind effect in the tower fore-aft first mode
III	Collective pitch gain scheduled control	To improve the regulation of the generator speed
IV	Individual pitch H_∞ control	To reduce the wind effect in the tower side-to-side first mode and to align the rotor plane

level when facing the disturbance signals, noise interferences, no-modelled plant dynamics and plant parameter variations. These design objectives can be achieved using a feedback control mechanism, but it introduces the need of sensors, bigger system complexity and a guarantee of system stability. Since the 80s, many authors researched the controller design using the H_∞ norm [29, 30] and the applications of these controllers in different non-linear real systems. Currently, the MATLAB Robust Toolbox [31] is a useful tool to solve mathematically the H_∞ controller synthesis problem.

The designed H_∞ controllers are LTI systems and the controller performance is defined using weight functions, scale constants [32] and defining a nominal plant among the family of linear plants where the controller synthesis is made. The most usual feedback control problem is expressed as a mixed sensitivity problem. The mixed sensitivity problem is based on a nominal plant and three weight functions and it can be considered in SISO or MIMO systems. These matrices of weight functions $W_1(s)$, $W_2(s)$ and $W_3(s)$ define the performance of the sensitivity functions $S(s)$, $T(s)$ and $U(s)$ respectively in a classical mixed sensitivity problem scenario (Fig. 5.6), where $S(s)$ is the output sensitivity, $T(s)$ is the input sensitivity and $U(s)$ is the control sensitivity. The scale constants are used to make the scaling of the different channels of the system. The difference between the family of plants can be modeled as uncertainties and they can be structured or unstructured. The unstructured uncertainties considered in the H_∞ robust control design are commonly modeled in different representations: additive uncertainly, input multiplicative uncertainly, output multiplicative uncertainty, inverse additive uncertainty, input inverse multiplicative uncertainty and output inverse multiplicative uncertainty. The selected one in this chapter is the additive representation. Finally, the calculation of the $K(s)$ controller based on the H_∞ norm reduction in this mixed sensitivity problem consists of the resolution of two *Ricatti* equations, which can be solved with the MATLAB Robust control toolbox.

In the case of the wind turbine control design, two MISO (2×1) mixed sensitivity problems are necessary to design the MISO proposed generator torque and collective pitch controllers based on the H_∞ norm reduction. This control scenario is based on the augmented plant (Eq. 5.7) which is divided into the nominal plant $G(s)$, scale constants D_u, D_{d1}, D_{d2}, D_{e1}, D_{e2} and weight functions $W_{11}(s)$, $W_{12}(s)$, $W_2(s)$, $W_{31}(s)$ and $W_{32}(s)$. The nominal plant is the plant used to design the
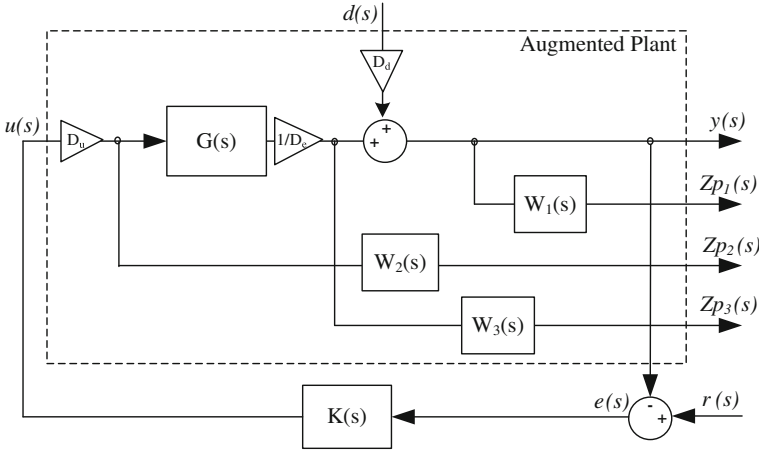
Fig. 5.6 Mixed control sensitivity problem

controller. The other plants of the family are considered as additive uncertainties in the pitch control design because these plants present differences. The inputs of the augmented plant are the output disturbances $d_1(s)$, $d_2(s)$ and the control signal $u(s)$. The outputs are the $y_1(s)$ and $y_2(s)$ from the scaled plant and the performance output channels $Z_{p11}(s)$, $Z_{p12}(s)$, $Z_{p2}(s)$, $Z_{p31}(s)$ and $Z_{p32}(s)$.

$$
\begin{pmatrix}
Z_{p11}(s) \\
Z_{p12}(s) \\
Z_{p2}(s) \\
Z_{p31}(s) \\
Z_{p32(s)} \\
y_1(s) \\
y_2(s)
\end{pmatrix}
=
\begin{pmatrix}
-(D_{d1}/D_{e1})W_{11}(s) & 0 & (D_u/D_{e1})G_{11}(s)W_{11}(s) \\
0 & -(D_{d2}/D_{e2})W_{12}(s) & (D_u/D_{e2})G_{12}(s)W_{12}(s) \\
0 & 0 & W_2(s) \\
0 & 0 & (D_u/D_{e1})G_{11}(s)W_{31}(s) \\
0 & 0 & (D_u/D_{e2})G_{12}(s)W_{32}(s) \\
-(D_{d1}/D_{e1}) & 0 & (D_u/D_{e1})G_{11}(s) \\
0 & -(D_{d2}/D_{e2}) & (D_u/D_{e2})G_{12}(s)
\end{pmatrix}
\begin{pmatrix}
d_1(s) \\
d_2(s) \\
u(s)
\end{pmatrix}
$$

$$(5.7)$$

5.3.1.1 Multivariable Generator Torque H_∞ Control

The H_∞ Torque Controller solves two of the control objectives: to reduce the wind effect in the drive train mode and to reduce the wind effect in the first tower side-to-side mode. The H_∞ Torque Controller has two inputs (generator speed w_g and tower top side-to-side acceleration a_{Tss}) and one output (generator torque $T_{H\infty}$).

The selected nominal plant to design the controller is the linearized plant at the 19 m/s wind speed operational point because it is a representative plant in the above rated zone. The nominal plant has the input of generator torque and two outputs: generator speed and tower top side-to-side acceleration. This nominal plant $G(s)$ (Eq. 5.8) is represented by the state space matrices A_{PT}, B_{PT}, C_{PT} and D_{PT} and it has 55 states. Uncertainties are not considered because the nominal plant is valid for all operating points in the above rated zone.

$$\dot{X}(t) = A_{\text{PT}}X(t) + B_{\text{PT}}T(t)$$
$$\begin{pmatrix} w_g(t) \\ a_{\text{Tss}}(t) \end{pmatrix} = C_{\text{PT}}X(t) + D_{\text{PT}}T(t) \tag{5.8}$$

The nominal plant is generalized including the performance output channels and the scale constants (Eq. 5.9) D_u, D_{d1}, D_{d2}, D_{e1}, D_{e2} to scale the different channels of the mixed sensitivity scenario.

$$D_u = 90$$
$$D_{e1} = 0.1; \quad D_{e2} = 1 \tag{5.9}$$
$$D_{d1} = 0.1; \quad D_{d2} = 1$$

Finally, five weight functions are included in the generalized plant. In this mixed sensitivity problem, $W_{11}(s)$, $W_{12}(s)$, $W_2(s)$ are used. The weight functions $W_{31}(s)$ and $W_{32}(s)$ are not used, so their value is the unit when using the MATLAB Robust Toolbox. Like Fig. 5.7 shows, $W_{11}(s)$ is an inverted notch filter centered at the drive train frequency to mitigate the wind effect in this mode, $W_{12}(s)$ is an inverted notch filter centered at the tower side-to-side first mode to also mitigate the wind effect in this mode and $W_2(s)$ is an inverted low pass filter to reduce the controller activity in high frequencies.

After developing the controller synthesis, the obtained controller has to be re-scaled to adapt the input and the output to the real non-scaled plant. A high pass filter is included in the DTD channel if the input of the controller is changed to be the generator speed value instead of the generator speed error. The gain of this controller channel is reduced at low frequencies with this high pass filter. As it is defined in the augmented plant, the designed H_∞ Torque Controller has two inputs (generator speed in rad/s and tower top side-to-side acceleration in m/s^2) and one output (generator torque contribution $T_{H\infty}$ in Nm). This designed controller is state space represented and its order is 39. Finally, the controller is reduced to order 25 without losing important information in its dynamics. After reducing, the last step is the controller discretization using a sample time of 0.01 s. The Bode diagram of the discretized state space represented controller (Eq. 5.10) is shown in Fig. 5.8.

$$X(k+1) = A_{\text{TD}}X(k) + B_{\text{TD}}\begin{pmatrix} w_g(k) \\ a_{\text{Tss}}(k) \end{pmatrix}$$
$$T_{H\infty}(k) = C_{\text{TD}}X(k) + D_{\text{TD}}\begin{pmatrix} w_g(k) \\ a_{\text{Tss}}(k) \end{pmatrix} \tag{5.10}$$

5.3.1.2 Multivariable Collective Pitch H_∞ Control

The H_∞ Pitch Controller solves two control objectives: the generator speed regulation increasing the output sensitivity bandwidth and reducing the output sensitivity peak compared to the classical control design, and to reduce the wind effect
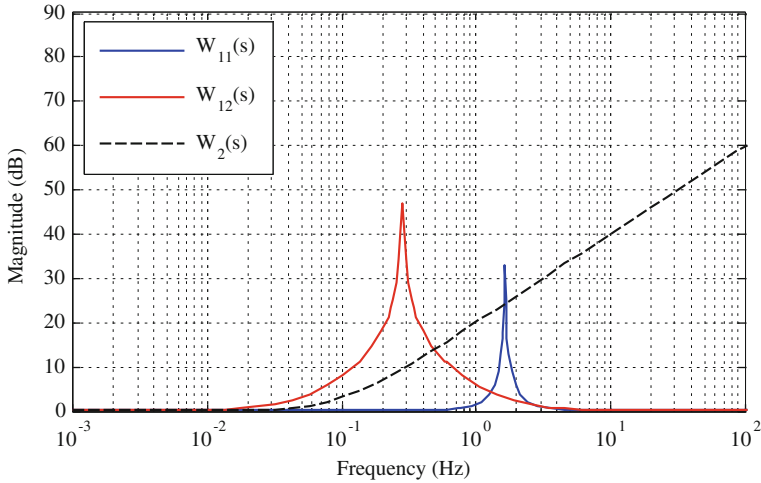
Fig. 5.7 Weight functions in the design of the generator torque H_∞ control
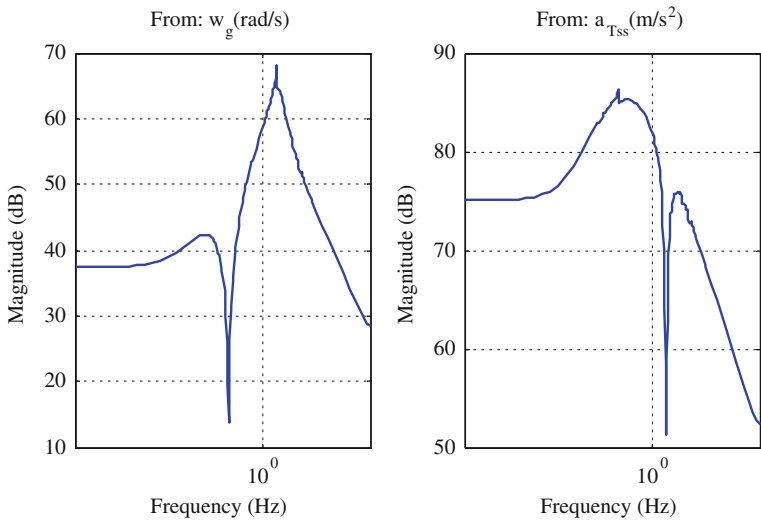
Fig. 5.8 Bode diagram of the generator torque H_∞ control

in the tower first fore-aft mode. Some notch filters are included in the pitch controller dynamics to reduce the excitation in some frequencies in the open loop response. The H_∞ Pitch Controller has two inputs (generator speed w_g and tower top fore-aft acceleration a_{Tfa}) and one output (collective pitch angle $\beta_{H\infty}$).

The selected nominal plant to design the controller is the linearized plant at the 19 m/s wind speed operational point. The nominal plant has one input: collective pitch angle and two outputs: generator speed and tower top fore-aft acceleration.

This nominal plant $G(s)$ (Eq. 5.11) is represented by the state space matrices A_{PP}, B_{PP}, C_{PP} and D_{PP} and it has 55 states. The differences of the family of linear plants compared to the nominal plant are considered as additive uncertainties. These differences appear due to their non-linear behavior of the plant which relates the pitch angle and the generator speed.

$$\dot{X}(t) = A_{PP}X(t) + B_{PP}\beta(t)$$
$$\begin{pmatrix} w_g(t) \\ a_{\mathrm{Tfa}}(t) \end{pmatrix} = C_{PP}X(t) + D_{PP}\beta(t) \tag{5.11}$$

The nominal plant is generalized including the performance output channels and the scale constants D_u, D_{d1}, D_{d2}, D_{e1}, D_{e2} (Eq. 5.12) to scale the different channels of the MISO mixed sensitivity scenario.

$$\begin{aligned} D_u &= 1 \\ D_{e1} = 10; &\quad D_{e2} = 0.1 \\ D_{d1} = 10; &\quad D_{d2} = 0.1 \end{aligned} \tag{5.12}$$

Five weight functions are included to create the generalized plant. In this mixed sensitivity problem, the $W_{11}(s)$, $W_{12}(s)$, $W_2(s)$ are only used (see Fig. 5.10). $W_{11}(s)$ is an inverted high pass filter and it is used to define the closed loop output sensitivity performance, $W_{12}(s)$ is an inverted notch filter centered at the first tower fore-aft mode to mitigate the wind effect in this mode and $W_2(s)$ is an inverted low pass filter to reduce the controller activity in high frequencies. Some inverted notch filters are included in $W_2(s)$ to include notch filters in the controller dynamics. These filters are centered at the rotational frequencies 1P (0.2 Hz) and 3P (0.6 Hz) and at other structural modes.

The controller obtained by using the MATLAB Robust toolbox has to be re-scaled to adapt the inputs and output to the real non-scaled plant. The designed H_∞ Pitch Controller has two inputs (generator speed error in rad/s and tower top fore-aft acceleration in m/s^2) and one output (collective pitch angle $\beta_{H\infty}$ in rad). This designed controller is state space represented and its order is 45. Finally, the controller is reduced to order 24 without losing important information in its dynamics. After reducing, the last step is the controller discretization using a sample time of 0.01 s. The Bode diagram of the discrete state space controller (Eq. 5.13) appears in Fig. 5.9.

$$X(k+1) = A_{BD}X(k) + B_{BD}\begin{pmatrix} ew_g(k) \\ a_{\mathrm{Tfa}}(k) \end{pmatrix}$$
$$\beta_{H\infty}(k) = C_{BD}X(k) + D_{BD}\begin{pmatrix} ew_g(k) \\ a_{\mathrm{Tfa}}(k) \end{pmatrix} \tag{5.13}$$
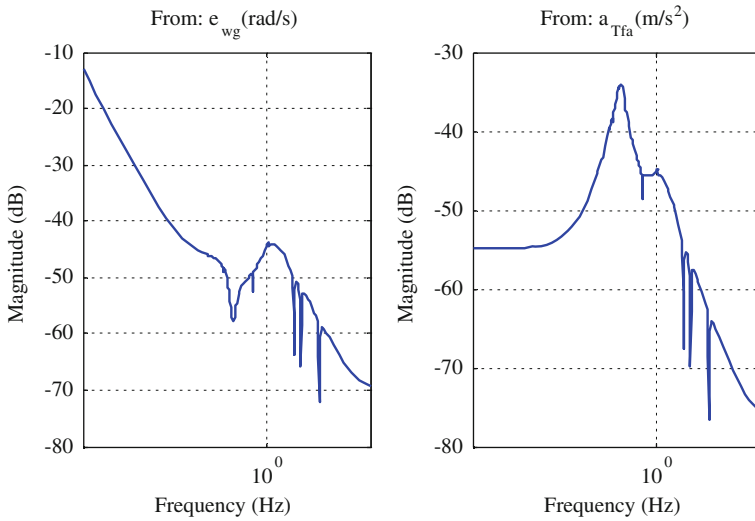
Fig. 5.9 Bode diagram of the collective pitch H_∞ control
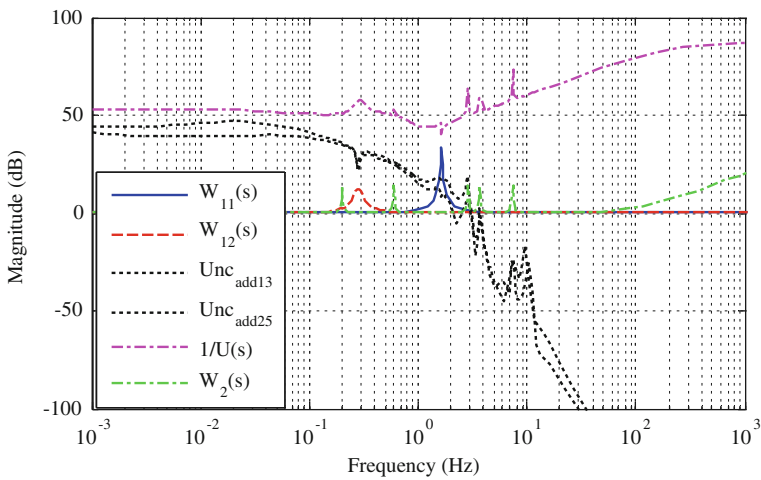
Fig. 5.10 Weight functions, uncertainties and control sensitivity function in the design of the collective pitch H_∞ control

After obtaining the pitch controller, the stability robustness of the closed loop for all plant in the family of linear models has to be analyzed. As it is proved in the small gain theorem [29], the inverse of the control sensitivity function has to be an upper limit of the modeled additive uncertainties (Fig. 5.10) to guarantee the robustness of the control in all operating points in the above rated zone.

Gain Scheduled Collective Pitch H_∞ **Control**

The interpolation of LTI controllers is an important task in control systems design for non-linear applications. In literature, the interpolation is commonly applied to low ordered LTI controllers and it can be divided into two approaches [33]: Gain Scheduling approach and LPV approach. The first one uses the family of linear models extracted from the non-linear model to design LTI controllers in different operating points to finally interpolate the designed controllers [34]. On the other hand, the LPV approach needs LPV models [35] of the plant to design LPV controls for the specified model [36]. The work presented in this section is focused on the first approach and it is based on gain scheduling of LTI controllers solving a LMI system. This technique guarantees the stability from the control design point of view because it is considered in the formulation of the LMI system. The adaptability of the presented gain scheduled control, which varies its behaviour according to the different operating points in wind turbines non-linear systems, improves the closed loop performance compared to LTI control techniques.

The non-linearities of wind turbines are more presented in the above rated zone, mainly in the pitch angle based generator speed regulation loop. To improve the control performance of the LTI H_∞ Pitch Controller, three collective pitch H_∞ controllers are designed to regulate the generator speed in three operating points in the above rated zone for wind speeds of 13, 19 and 25 m/s respectively. So, the above rated zone is divided into three sub-zones in this control design and each controller is optimized in performance for each zone guaranteeing the closed loop stability. Although the order of these controllers is high, they are perfectly interpolated without losing the stability and performance in all trajectories of the above rated zone solving an LMI system carefully proposed in [37]. The varying parameter p to develop the gain scheduling in the above rated zone is based on an adaptation of the measured pitch angle to work in the range $[-6, 6]$, which extreme points are calculated from the stationary pitch values of the operating points with wind speeds of [13 m/s, 25 m/s]. Figure 5.11 shows the bode diagram of discrete gain scheduling controller in three operating points where it is designed. The representation of the gain scheduled controller via LMI solution is based on a gain vector which interpolates the three state space LTI controllers previously adapted to make this interpolation.

5.3.1.3 Multivariable Individual Pitch H_∞ Control

One of the most well-known control loops developed to mitigate loads in wind turbines is the IPC. It consists of a controller which generates individual pitch set-points for each blade. The main objective of the IPC is to reduce the asymmetrical loads which appear in the rotor due to its misalignment caused by phenomena like wind shear, tower shadow, yaw misalignment or rotational sampling of turbulence. In [10, 38], decentralized d-q axes controllers based on proportional-integral (PI) controllers are proposed to solve this main objective using the
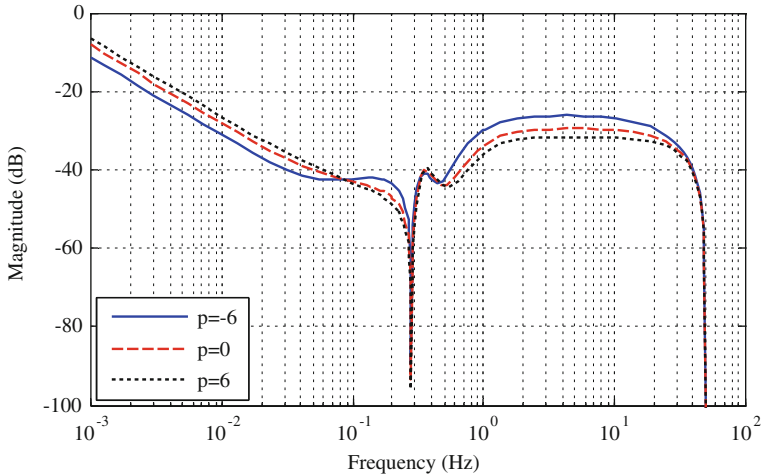
Fig. 5.11 Bode diagram of the gain scheduled collective pitch H_∞ controller in different operating points

Coleman transformation. The IPC to align the rotor frame has been field tested not only in the CART2 wind turbine [39], but it has also recently tested in the CART3 turbine with very promising results [40]. The load mitigation in the tower can be also considered as a control objective in the design of the Individual Pitch Controller. The tower side-to-side damping is commonly carried out with a generator torque contribution from measured side-to-side nacelle acceleration. This torque contribution affects to the quality of the generated electric power. In [41–43], different control strategies based on IPC are proposed to make the tower side-to-side damping with IPC signals. The interaction between the supervisory control and the IPC of the wind turbine is very important to reduce the loads in some components for shutdown and load sensor failure cases [10].

The IPC presented in this section, called H_∞ IPC, is composed of one MIMO controller based on the H_∞ norm reduction to generate individual pitch set-point signals for each blade with a multi-objective point of view (to align the rotor plane and to reduce the wind effect in the tower side-to-side first mode).

The first step when designing the H_∞ IPC is to create the nominal plant which will be included in the mixed sensitivity problem to make the H_∞ controller synthesis. To create this plant, firstly, the flapwise and edgewise moments extracted from strain gauges in the blade roots are transformed [44] to the out-of-plane moment M_{oop} using the transformation T (Eq. 5.14), where θ_T and β are the twist and pitch angles at the blade root section. The M_{tilt} and M_{yaw} rotor tilt and yaw moments are obtained using the transformation (Eq. 5.15) where ψ is the azimuth angle in each blade and M_{oop1}, M_{oop2} and M_{oop3} the out-of-plane moments in each blade. The tilt and yaw moments show how the blade loads developed in a rotating reference frame are transferred to a fixed reference frame. In this case, the Coleman transformation [45] C is used, and it is a transformation from a rotating to

a fixed reference frame, so M_{tilt} and M_{yaw} are proportional to the Coleman transformation outputs and the controller can be easily scaled. The inverse of the Coleman transformation C^{-1} is used to transform the fixed frame to the frame in blades.

$$
\begin{pmatrix} M_{oop1} \\ M_{oop2} \\ M_{oop3} \end{pmatrix} = \begin{pmatrix} \cos(\theta_T + \beta) & \sin(\theta_T + \beta) & 0 & 0 & 0 & 0 \\ 0 & 0 & \cos(\theta_T + \beta) & \sin(\theta_T + \beta) & 0 & 0 \\ 0 & 0 & 0 & 0 & \cos(\theta_T + \beta) & \sin(\theta_T + \beta) \end{pmatrix} \begin{pmatrix} M_{flap1} \\ M_{edge1} \\ M_{flap2} \\ M_{edge2} \\ M_{flap3} \\ M_{edge3} \end{pmatrix}
$$

$$
= T \begin{pmatrix} M_{flap1} \\ M_{edge1} \\ M_{flap2} \\ M_{edge2} \\ M_{flap3} \\ M_{edge3} \end{pmatrix}
$$

$$(5.14)$$

For the 'Upwind' model $\cos(\theta_T + \beta) = 0.8716$ and $\sin(\theta_T + \beta) = 0.4903$

$$
\begin{pmatrix} M_{tilt} \\ M_{yaw} \end{pmatrix} = \begin{pmatrix} \cos\psi_1 & \cos\psi_2 & \cos\psi_3 \\ \sin\psi_1 & \sin\psi_2 & \sin\psi_3 \end{pmatrix} \begin{pmatrix} M_{oop1} \\ M_{oop2} \\ M_{oop3} \end{pmatrix}
\tag{5.15}
$$

$$
P_{ipc} = C^{-1}PTC = PT \tag{5.16}
$$

The new plant P_{ipc} (Eq. 5.16) uses the mathematical properties of the Coleman transformation to simplify the construction of the plant. P_{ipc} has three outputs (a_{Tss}, M_{tilt} and M_{yaw}) and two inputs (β_{tilt} and β_{yaw}). The plant P_{ipc} linearized at the operating point of 19 m/s is used in the H_∞ IPC control design.

In this case, one MIMO (3 × 2) mixed sensitivity problem is necessary to design a MIMO controller based on the H_∞ norm reduction. The scale constants are shown in (Eq. 5.17). The weight functions used in this mixed sensitivity problem are $W_{11}(s)$, $W_{12}(s)$, $W_{13}(s)$, $W_{21}(s)$ and $W_{22}(s)$. The weight functions $W_{31}(s)$, $W_{32}(s)$, $W_{33}(s)$ are not used, so their value is the unit when using the MATLAB Robust Toolbox. Regarding to the weigh functions, $W_{11}(s)$ is an inverted notch filter centered at the tower first side-to-side mode frequency to reduce the wind effect in this mode, $W_{12}(s)$ and $W_{13}(s)$ are inverted high pass filters to guarantee the integral control activity to regulate the tilt and yaw moments. $W_{21}(s)$ and $W_{22}(s)$ are inverted low pass filters to reduce the controller activity in high frequencies with an inverted notch filter at the first blade in-plane mode frequency to include a notch filter at this frequency in the controller dynamics. Figure 5.12 shows the Bode diagrams of these weight functions.
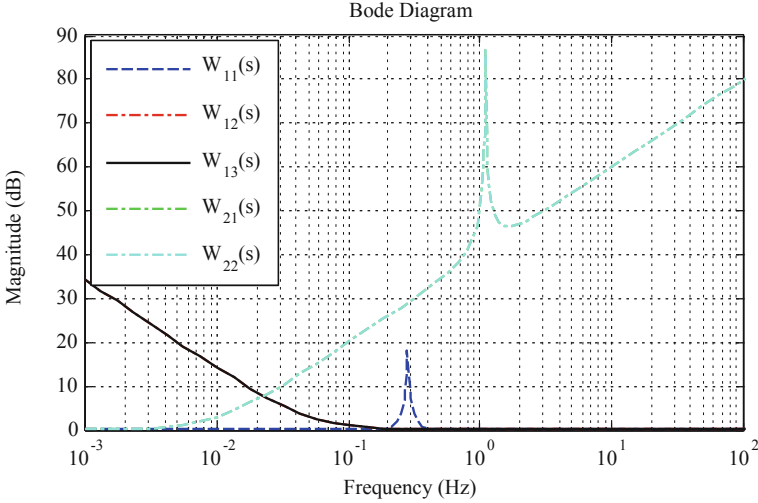
Fig. 5.12 Weight functions in the design of the individual pitch H_∞ control

$$D_{u1} = 0.001; \, D_{u2} = 0.001;$$
$$D_{d1} = 0.1; \, D_{d2} = 1e6; \, D_{d3} = 1e6; \qquad (5.17)$$
$$D_{e1} = 0.1; \, D_{e2} = 0.5e6; \, D_{e3} = 0.5e6;$$

After finishing the controller synthesis, the obtained controller has to be re-scaled to adapt the inputs and the outputs to the real non-scaled plant. The designed H_∞ IPC controller has three inputs (tower top side-to-side acceleration a_{Tss} in m/s^2, tilt moment in the rotor M_{tilt} in Nm and yaw moment in the rotor M_{yaw} in Nm) and two outputs (pitch angle in the rotor reference frame β_{tilt} in rad and yaw pitch angle β_{yaw} in the rotor reference frame in rad). This designed controller is state space represented and its order is 54. The reduction of the order of multivariable controllers is difficult due to coupling between the channels, so this controller is not reduced. The last step is the controller discretization with a sample time of 0.01 s. The Bode diagram of the discretized state space represented controller (Eq. 5.18) is shown in Fig. 5.13. Finally, the Coleman and its inverse have to be included in the control strategy to calculate the individual pitch angle contribution for each blade β_{rot1}, β_{rot2} and β_{rot3}. Figure 5.14 shows the complete control scheme of the IPC strategy from the signals from the loads in the blade roots to the individual pitch angle contributions. These pitch contributions for each blade are added to the collective pitch angle set-point obtained in the previously designed collective pitch angle controllers.
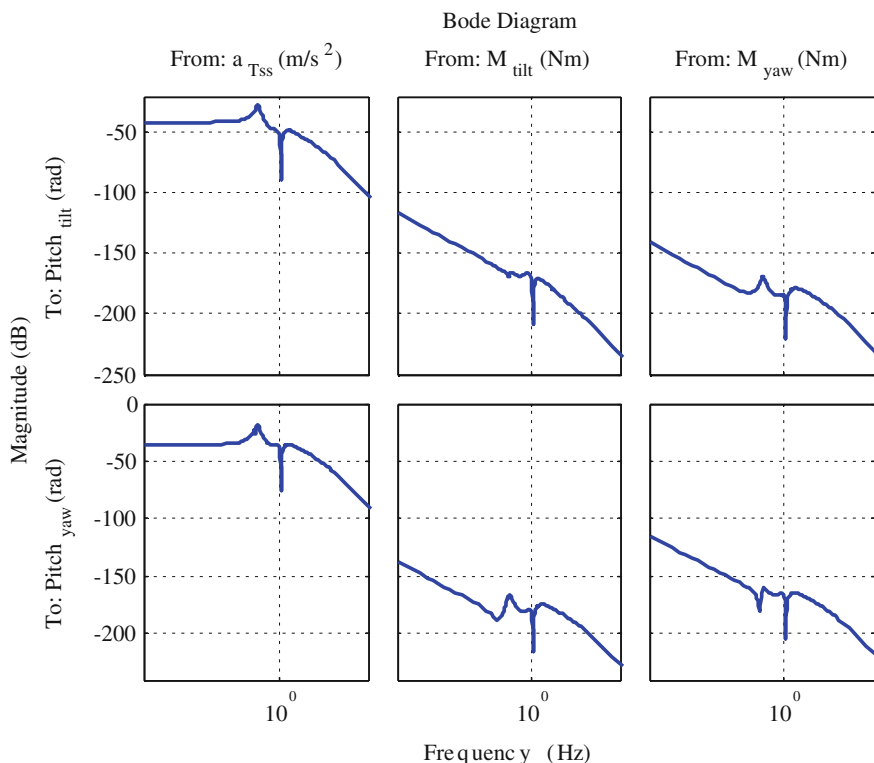
Bode Diagram

Fig. 5.13 Bode diagram of the individual pitch H_∞ control
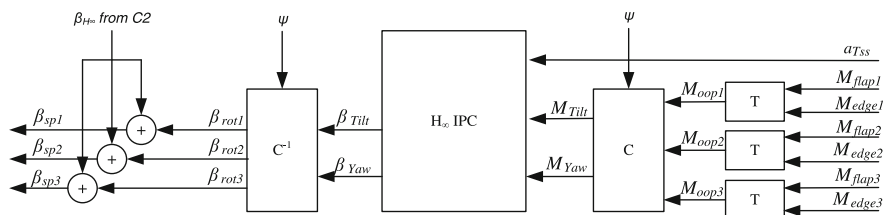
Fig. 5.14 Diagram of the individual pitch control strategy

$$x(k+1) = A_{\text{ipc1}}x(k) + B_{\text{ipc1}} \begin{pmatrix} a_{\text{Tss}}(k) \\ M_{\text{tilt}}(k) \\ M_{\text{yaw}}(k) \end{pmatrix}$$

$$\begin{pmatrix} \beta_{\text{tilt}}(k) \\ \beta_{\text{yaw}}(k) \end{pmatrix} = C_{\text{ipc1}}x(k) + D_{\text{ipc1}} \begin{pmatrix} a_{\text{Tss}}(k) \\ M_{\text{tilt}}(k) \\ M_{\text{yaw}}(k) \end{pmatrix}$$

(5.18)

5.3.2 Closed Loop Analysis of the Designed Robust Controllers

The closed loop analysis is an important step before including the designed controllers to work with the wind turbine non-linear model. Some control structures based on the designed controllers in this chapter are proposed to be analyzed not only in this closed loop analysis, but they will be also analyzed in the simulations shown in next section with the non-linear model. In all structures, the control strategy in the below rated zone is the same (baseline) but they present important differences in the above rated zone. These control structures in the above rated zone are:

$C1$ Baseline control strategy based on gain scheduled PI pitch controller with DTD and TFAD filters

$C2$ Robust control strategy based on two MISO H_∞ MISO LTI controllers: H_∞ Pitch Controller and H_∞ Torque Controller (see Fig. 5.15)

$C3$ Robust control strategy based on two controllers. The generator torque control is the same as in $C2$. However, the collective pitch control is based on the gain scheduling of three H_∞ controllers via LMIs resolution (see Fig. 5.15)

$C4$ It is an extension of the $C2$ robust control strategy with an extra-pitch angle contribution in each blade from the MIMO IPC H_∞ IPC (see Fig. 5.14)

The first analysis of the closed loop studies the output sensitivity function of the generator speed regulation loop. Table 5.3 shows the peaks and the bandwidth of this function in different operating points with the collective pitch angle controllers included in the control strategies $C1$, $C2$ and $C3$. The gain scheduled controller provides a larger bandwidth in the output sensitivity function, mainly at parameter values between -4 and 4, with an interesting decrease of the output sensitivity peak in all operational points. This is a good performance from a load mitigation point of view in wind turbines, mainly for extreme changes of wind.

The damping of the drive train mode is very important and it can be developed using the baseline DTD filter in $C1$ or with the H_∞ Torque Controller in $C2$, $C3$ and $C4$. Figure 5.16 shows the bode diagram of the response of the generator speed from the generator torque control signal with these generator torque controllers in the operating point of 19 m/s. The drive train mode is perfectly damped with $C1$ and $C2$.

Figures 5.17, 5.18, 5.19 and 5.20 show the wind effect in different controlled signals of the wind turbine with the different control schemes at the operating point of 19 m/s. Figure 5.17 shows the wind effect in the generator speed. The regulation of this variable is better using the $C3$ control strategy at 19 m/s operating point due to the high bandwidth of this control loop (Table 5.3). Figure 5.18 shows the mitigation of wind effect in the tower fore-aft first mode with the $C1$ and $C2$ control strategies. Figure 5.19 shows the ability of mitigating the wind effect in the tower side-to-side first mode with a generator torque control in $C2$ control strategy or with an individual pitch controller developed in the $C4$ strategy. Finally, Fig. 5.20 shows the regulation of the rotor tilt moment using the IPC included in the $C4$ control scheme. Similar regulation is achieved in the rotor yaw moment with this strategy.
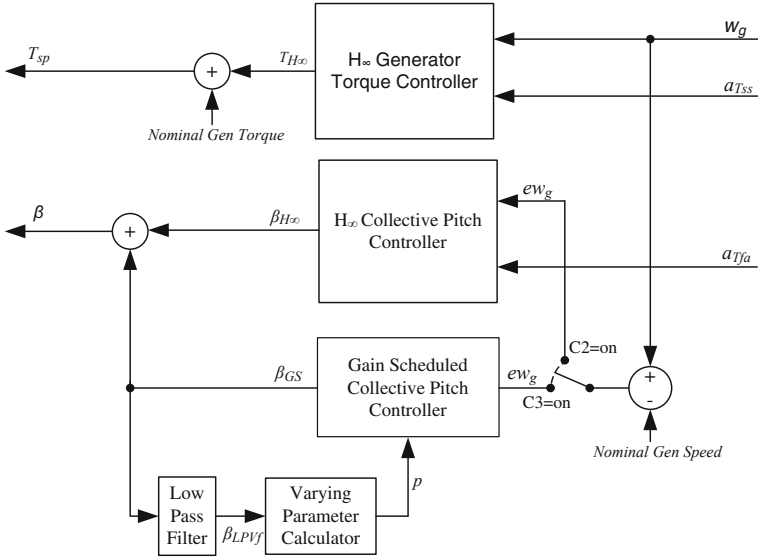
Fig. 5.15 Diagram of $C2$ and $C3$ control strategies

Table 5.3 Frozen output sensitivity analysis

Wind speed (m/s)	p value	Output sensitivity peak (dB)			Output sensitivity bandwidth (Hz)		
		$C1$	$C2$	$C3$	$C1$	$C2$	$C3$
13	−6	6.06	3.35	2.52	0.037	0.035	0.037
15	−4	6.06	3.59	2.87	0.045	0.044	0.059
17	−2	6.09	4.31	3.12	0.052	0.057	0.074
19	0	6.31	5.29	3.31	0.058	0.070	0.085
21	2	6.00	5.78	3.50	0.061	0.078	0.090
23	4	6.05	6.70	3.67	0.065	0.089	0.097
25	6	6.04	7.84	3.93	0.069	0.10	0.105

5.4 Simulation Results in GH Bladed

The control schemes explained in the closed loop analysis are included in the External Controller [46] in GH Bladed and different simulations are carried out using the *Upwind* non-linear wind turbine model with special wind conditions. The simulation analysis with the non-linear model is divided into two main steps:

- The analysis of a power production wind in above rated zone, in this case with a mean wind speed of 19 m/s, to see the time domain response of regulated signals. Also, the Power Spectral Density (PSD) of different signals within the
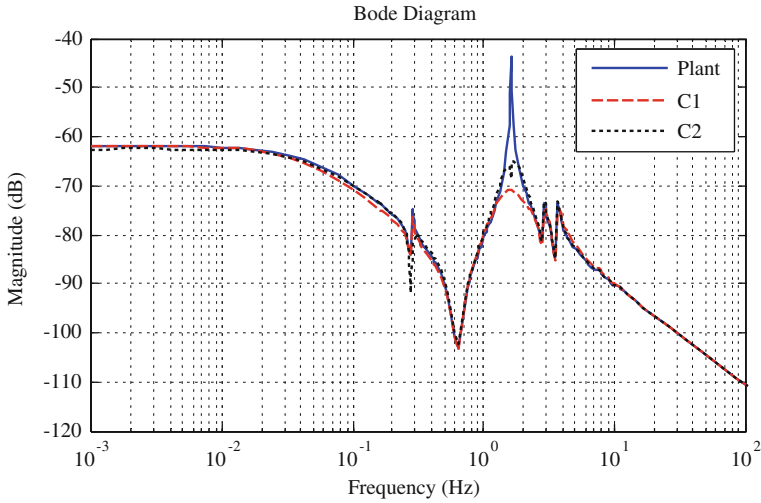
Fig. 5.16 Bode diagram of the plant "From: Generator Torque To: Generator Speed"
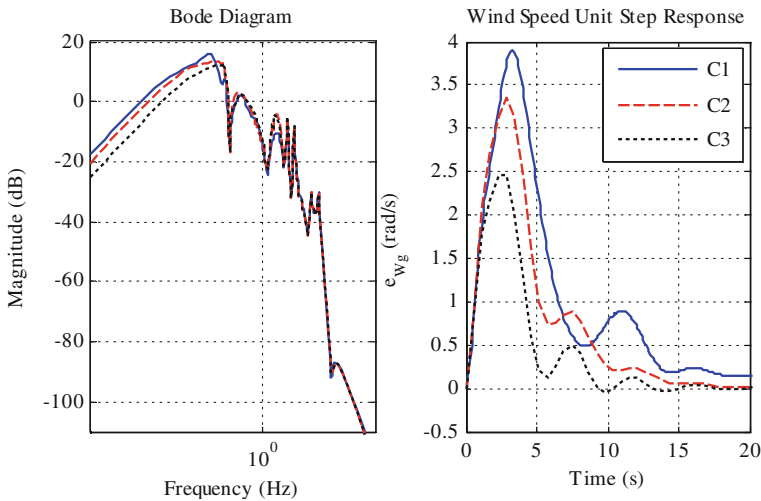
Fig. 5.17 Response of the generator speed for a wind input

control system is analyzed to see the control influence in the frequency domain
representation of these signals.

- The load analysis to see the extreme and fatigue load mitigation achieved with
  these control strategies. The rain flow counting algorithm [47, 48] is used to
  carry out the load equivalent analysis to determine the fatigue damage on the
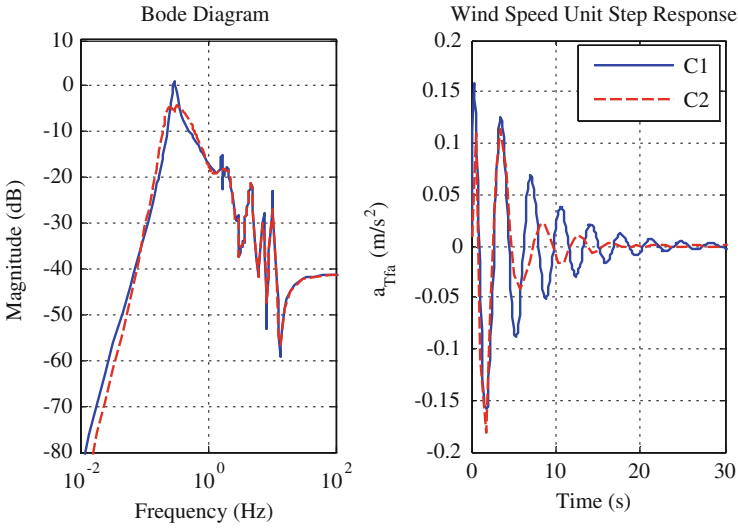
Fig. 5.18 Response of the tower top fore-aft acceleration for a wind input
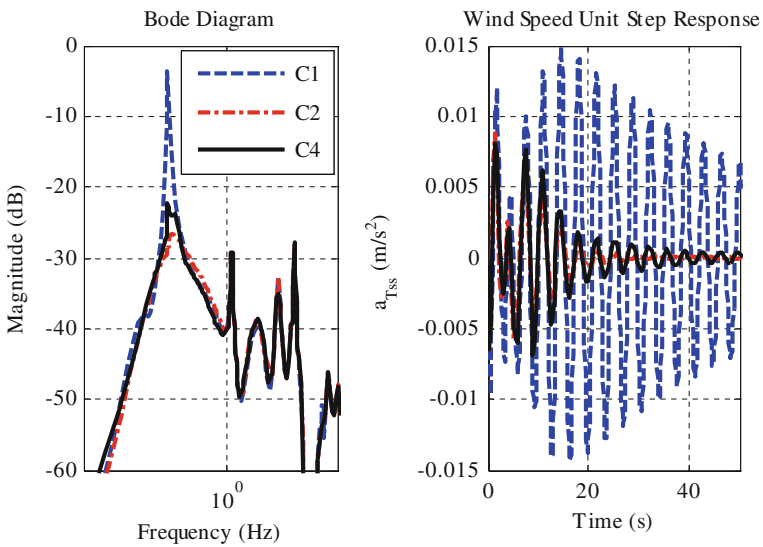
Fig. 5.19 Response of the tower top side-to-side acceleration for wind input

wind turbine components according to the constant of material m. The wind scenarios used to develop the fatigue analysis are based on 12 simulations of 600 s with power productions wind speeds with averages from 3 to 25 m/s. Also, a statistical analysis is usually carried out to see the mean and standard deviation of different signals in the wind turbine according to these twelve
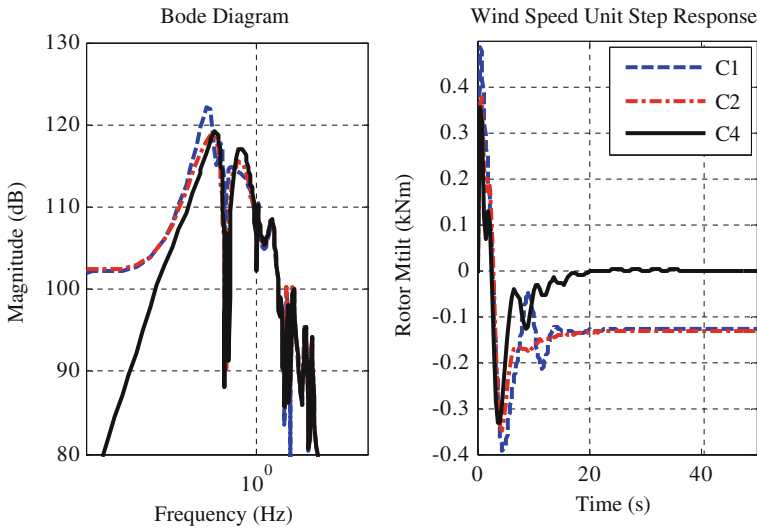
Fig. 5.20 Response of the rotor tilt moment for wind input

power production winds. On the other hand, two extreme load cases are ana-
lyzed: DLC1.6 and DLC1.9 cases. In these two analyses, the wind inputs are
different gusts and ramps respectively. Other extreme load cases are not taken
into account because results depend especially on the stop strategy, which has
not been very affected by the designed robust controllers.

According to the first step in the simulation analysis, one simulation is carefully
analyzed. The input of this simulation is a turbulent power production wind with a
mean speed of 19 m/s (Fig. 5.21). The increase of the bandwidth of the output
sensitivity function in the pitch control loop achieved using the robust controllers,
mainly with the gain scheduled control in $C3$ (see Table 5.3), improves the reg-
ulation of the generator speed near to the nominal value of 1,173 rpm for this wind
input (Fig. 5.22).

Different signals are also analyzed in the frequency domain using the PSD
analysis. Figures 5.23 and 5.24 are focused on showing the influence of the
designed feedback robust control loops to load mitigation in wind turbines in
different variables. In this case, the $C3$ control strategy is not considered because
the improvement in the generator speed regulation does not considerably affect to
the load mitigation in power production wind cases. Figure 5.23 shows the pitch
contribution of the IPC in the pitch control angle set-points using $C4$ control
scheme. In this figure, the generator torque oscillations are reduced when the tower
side-to-side first mode damping is developed using the IPC instead of with the
generator torque control in $C2$ control strategy. The quality of the generated
electric power is better if the oscillations in the torque control are avoided using
$C4$ because the regulation of the generator speed is not affected by the pitch
contributions in each blade generated with the IPC.
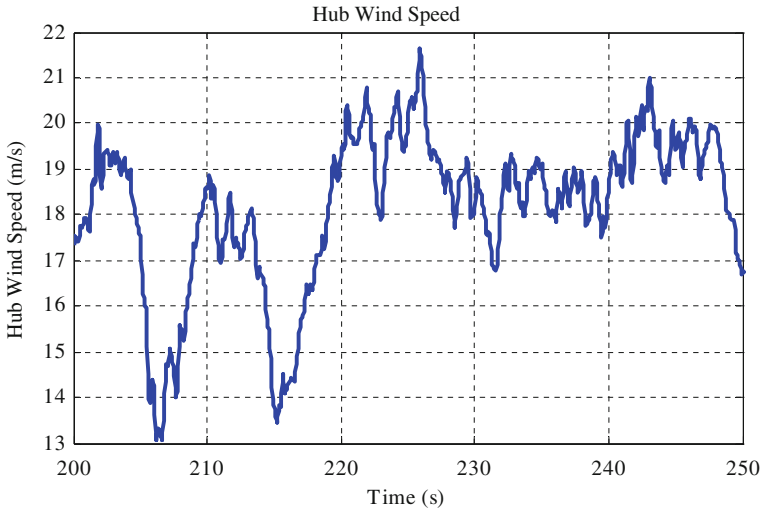
Fig. 5.21 Speed of the power production wind with mean of 19 m/s
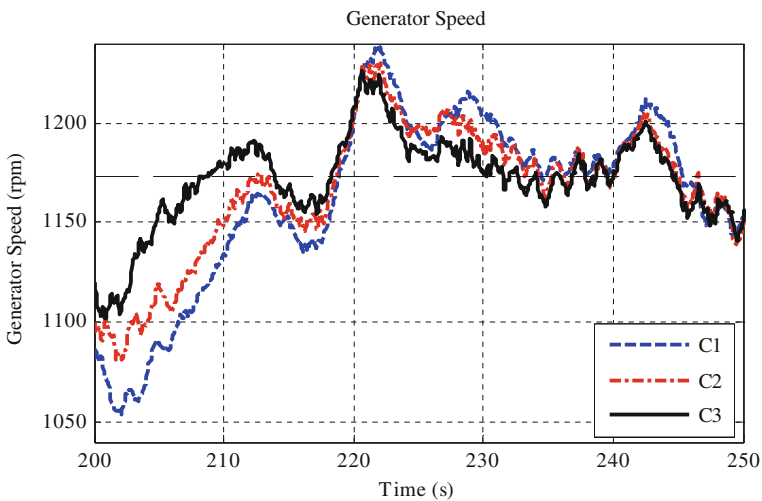
Fig. 5.22 Generator speed regulation for the power production wind

Figure 5.24 shows some important moments in different components of the wind turbine. The co-ordinate systems of blades, tower and hub are explained in [46]. The $C4$ control strategy reduces the activity at the $1P$ frequency in the blade out-of-plane moment M_{oop} and mitigates the activity of the M_{flap} moment around $1P$. However, the M_{edge} moment hardly depends on the $1P$ frequency and it is very difficult to mitigate loads in this variable. If the pitch actuator bandwidth was bigger, the activity of the blade first in-plane moment at 1.1 Hz in M_{edge} could be
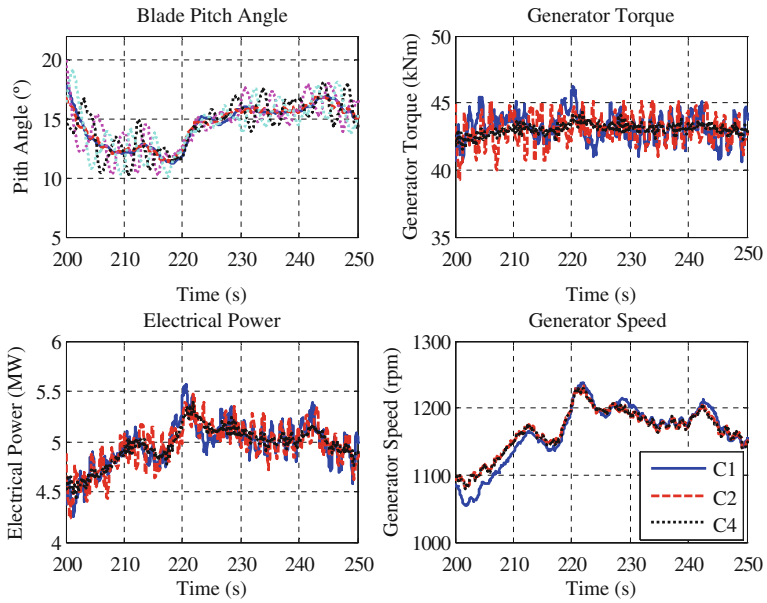
Fig. 5.23 Different signals for the power production wind
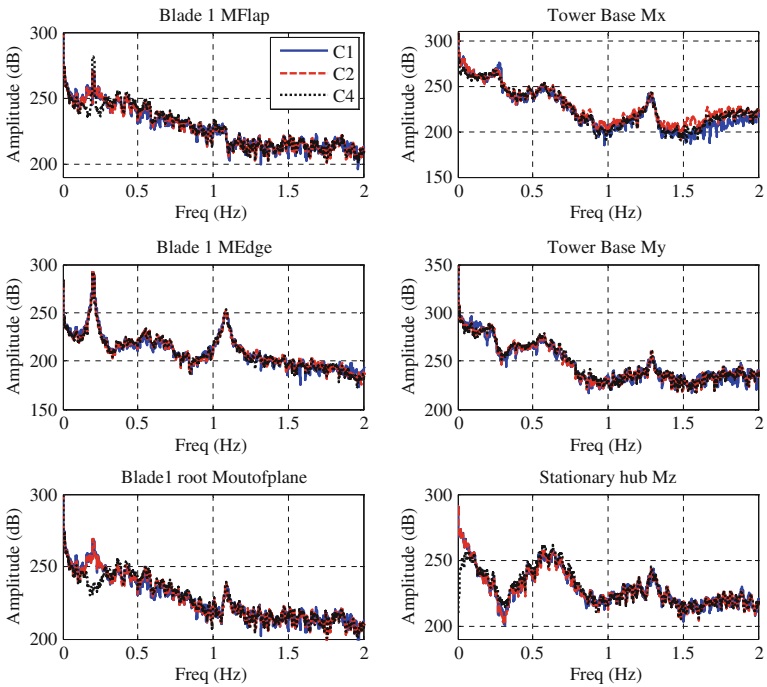
Fig. 5.24 Moments in different components for the power production wind speed
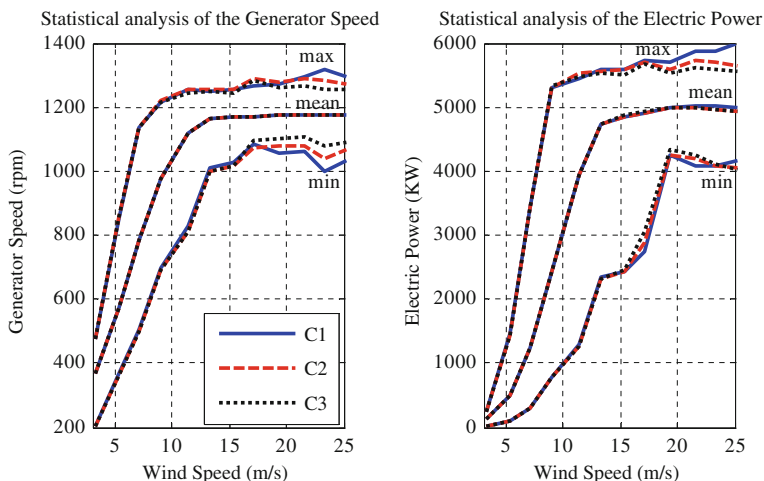
Fig. 5.25 Statistical analysis

reduced, but the pitch actuator bandwidth of the 'Upwind' model is only 1 Hz. The activity of the tower base moment in x is reduced with the C4 control strategy at the tower side-to-side first frequency, and the stationary hub moment in z is hardly mitigated at small frequencies due to the correct alignment of the rotor plane with IPC.

Figure 5.25 shows an statistical analysis of the regulated variables of generator speed and electric power. The maximum, minimum and mean values of these signals in different power production wind simulations are represented in Fig. 5.25. The regulation of the generator speed is better using C3 control scheme because the maximum and minimum values are closer to the nominal generator speed than with other strategies. Inherently, the regulation of the electric power is also better using C3 in spite of the difference in the generator torque control loop.

Table 5.4 represents the fatigue analysis with the four control schemes. C1 is considered as the reference to calculate the percentage of fatigue load reduction in different moments in the wind turbine components with the other control strategies. The m constant of material is 3 for the tower, m is 9 for the hub and for the yaw system and m is 12 for the blades. The inclusion of the generator torque contribution using the H_∞ torque controller in C2 reduces the fatigue load in the tower base moment in x axis in 11.9 % without important load increase in other components. The improvement in the generator speed regulation using C3 does not involve enhanced profits in the fatigue load analysis. On the other hand, the IPC based feedback control loop included in the C4 control strategy considerably affects to the fatigue loads. The fatigue loads are reduced in 7.5, 5.9, 5.3 and 5.5 % in the blade root moment in y axis, stationary hub moment in z axis and yaw bearing x and y moments respectively compared to the C2 control scheme. The load reduction in the tower base moment in x axis due to the reduction of the wind

Table 5.4 Fatigue load analysis

	m	C1	C2	C3	C4
Blade MFlap	12	100	100	102.1	98.6
Blade MEdge	12	100	100	100.1	99.5
Blade root Mx	12	100	99.9	100.0	101.0
Blade root My	12	100	98.8	98.9	91.3
Blade root Mz	12	100	98.3	101.0	99.0
Stationary hub Mx	9	100	100	99.8	99.0
Stationary hub My	9	100	99.2	99.6	92.8
Stationary hub Mz	9	100	99.9	101.0	94.0
Yaw bearing Mx	9	100	101.3	98.4	99.2
Yaw bearing My	9	100	99.2	99.3	93.9
Yaw bearing Mz	9	100	99.5	99.6	94.0
Tower base Mx	3	100	88.1	86.2	85.2
Tower base My	3	100	95.0	95.2	97
Tower base Mz	3	100	99.9	100.0	108.8

effect in the tower side-to-side first mode is a 2.9 % better using the IPC in $C4$ than with the generator torque control loop in $C2$. The control effort to align the rotor plane developed by the IPC of the $C4$ control scheme involves a load increment of 8.9 % in the tower base moment in z axis.

Lastly, Tables 5.5 and 5.6 show the extreme load analyses using the four control schemes. These analyses are very influenced by the activation and deactivation of the controllers, mainly of the IPC, when the wind turbine arrives to work in the above rated zone, so the results using IPC in $C4$ control scheme could be improved using better start-up strategies of the control system.

In the extreme DLC1.6 load case analysis, the blade root edgewise moment is hardly reduced due to the faster response of the collective pitch robust controller to regulate the generator speed. This rapidity also reduces other loads in blades, hub, yaw and tower. The $C3$ control strategy does not present important improvements compared to the $C2$ (only the blade root flapwise moment is reduced). On the other hand, the activation of the IPC in $C4$ control strategy involves important load reduction of 28.72 and 22.8 % compared to $C2$ in the DLC1.6 case in stationary hub moment in y axis and in the tower base moment in x axis respectively. Also, the $C4$ control strategy activation involves load increments in blade root moment in x axis, yaw bearing moment in z axis and tower base moment in z axis due to the extra-effort to align the rotor plane with the IPC.

The extreme load DLC1.9 analysis present important extreme load reductions in the x axis of the moments analyzed in Table 5.5 using the $C2$ control strategy compared to the $C1$. Also, the activation of the $C3$ control scheme with the collective pitch gain scheduled robust control improves the regulation of the

Table 5.5 Extreme load DLC1.6 analyses

	C1	C2	C3	C4
Generator speed	100	91.62	90.5	92.3
Blade MFlap	100	97.11	92.4	92.7
Blade MEdge	100	76.29	77.5	77.4
Blade root Mx	100	94.98	93.0	108.9
Blade root My	100	96.89	91.6	93.4
Blade root Mz	100	89.63	86.2	90.1
Stationary hub Mx	100	85.52	83.0	85.1
Stationary hub My	100	95.02	94.8	66.3
Stationary hub Mz	100	103.36	104.1	105.8
Yaw bearing Mx	100	86.00	84.9	87.3
Yaw bearing My	100	84.95	94.0	84.2
Yaw bearing Mz	100	106.36	105.6	115.5
Tower base Mx	100	87.92	85.7	65.1
Tower base My	100	98.60	97.5	98.8
Tower base Mz	100	106.34	105.6	115.4

Table 5.6 Extreme load DLC1.9 analyses

	C1	C2	C3	C4
Generator speed	100	100.59	95.6	100.7
Blade MFlap	100	100.18	94.7	95.5
Blade MEdge	100	101.66	97.7	99.3
Blade root Mx	100	99.14	97.5	97.1
Blade root My	100	99.81	94.3	95.0
Blade root Mz	100	100.45	89.6	107.4
Stationary hub Mx	100	99.05	99.0	98.9
Stationary hub My	100	99.31	89.7	56.0
Stationary hub Mz	100	90.95	103.9	98.1
Yaw bearing Mx	100	99.40	99.1	97.7
Yaw bearing My	100	104.31	94.1	93.4
Yaw bearing Mz	100	93.31	105.5	101.1
Tower base Mx	100	98.29	96.7	73.1
Tower base My	100	98.89	93.9	98.5
Tower base Mz	100	93.31	105.5	101.1

generator speed in 4.44 % but the loads are increased in the z axis in the different moments analyzed. The activation of the IPC in $C4$ reduces the loads in the stationary hub moment in y axis and tower base moment in x axis in 43.3 and 25.1 % respectively compared to the results using the $C2$ control scheme. In this extreme load analysis, the loads in blade root moment in z axis are increased using the $C4$ control strategy.

5.5 Conclusions

This chapter proposes one process to design different multivariable robust controllers for load mitigation in wind turbines. These controllers are compared with a baseline control strategy named $C1$, which is based on classical control methods used in wind turbines, not only in the controller design process, but also in the validation process with different complex analyses from simulations with the wind turbine non-linear model in GH Bladed. Some conclusions can be extracted from the work presented in this chapter:

- The control objectives of each control strategy are summarized in Table 5.1. The $C1$, $C2$ and $C3$ control strategies need a generator speed sensor and a tower top accelerometer to use them in the developed generator torque and collective pitch angle controllers. However, the $C4$ control strategy also needs blade root sensors to solve the specific control objectives including the IPC.
- The robustness of the generator torque and collective pitch controllers included in the $C2$ control scheme is carefully analyzed in Sect. 5.2. The mixed sensitivity problems to develop the controller syntheses are explained from the nominal plants to the definition of the weight functions. The proposed generator torque and collective pitch blade controllers perfectly mitigate the loads in the desired components of the wind turbine and they extract the nominal electric power value during the power production in the above rated zone.
- In the gain scheduled control included in $C3$ control scheme, the three LTI H_∞ controllers are perfectly interpolated without losing the stability and performance in all trajectories of the above rated zone solving an LMI system. These controllers perfectly improve the regulation of the generator speed compared with the LTI H_∞ controller in $C2$. The parameter adaptation in this gain scheduled controller is not optimized for gust inputs. Other variables with a faster response than the pitch angle signal, like generator speed error, can be taken into account to calculate the varying parameter value to improve the generator speed regulation in extreme wind gust cases.
- The multivariable robust IPC included in the $C4$ control strategy satisfies the proposed control objectives: to reduce the asymmetrical loads which appear in the rotor due to its misalignment and to mitigate the load in the tower reducing the wind effect in the tower side-to-side first mode. The load mitigation in the tower reducing the wind effect in the tower side-to-side first mode using the $C4$

control strategy improves the load reduction results comparing to the $C2$ and $C1$ baseline control strategies. Furthermore, the quality of the electrical power using the $C4$ control strategy is better than using the $C2$ control strategy because the tower side-to-side first mode damping is developed with an IPC instead of with a generator torque control. A start-up algorithm for the Individual Pitch Controller is necessary to have a softly activation of this control loop to reduce the extreme loads during the transition from the below rated to the above rated control zones.

- The designed feedback control strategies, which reduce the wind effect in some structural modes, mainly mitigate the fatigue loads in the wind turbine variables they are controlling. Other control loops like the rotor alignment and the generator speed regulator affect not only the variable they are trying to control. The effect of the increment of the bandwidth of the output sensitivity function in the generator speed regulation considerably affects the mitigation of the extreme loads. The collective pitch angle control responds quickly and the wind turbine rapidly changes the pitch angle in the blades to regulate the generator speed.

- The designed robust controllers have an important dependence from the nominal plants and these plants do not take into account the wind turbine rotational modes ($1P$, $3P$…) because they are not considered in the linearization process in GH Bladed. The robust control strategies can be improved if the plants consider these modes. This consideration can be developed by model identification from real data from the wind turbine or with complex analytical models.

- The proposed control strategies have been validated in GH Bladed for production and under extreme wind cases.

5.6 Future Work

Some of the work explained in this chapter has been towards numerical algorithms for the design of H_∞ and gain scheduled controllers. These algorithms are not totally matured and they need further research in different areas. The future work to continue with the work carried out in this chapter and to continue with the improvement of the load mitigation in wind turbines could be as follows:

- To use wind turbine models from the identification of real data of a wind turbine. These models are less ordered and the non-structural modes, like $1P$ or $3P$, are included in them. It is usefull to design controllers to mitigate the wind effect in these modes and the computational cost to make the control synthesis will be smaller.

- To estimate the wind speed with a Kalman filter or other techniques, or to use LIDAR sensors. The inclusion of the wind speed measurement in the control strategies is an advantage because the main disturbance of the system can be

known. This wind input can be used to be varying parameter of the gain scheduled controllers to adapt quickly their dynamics to the present wind.

- To improve the individual pitch controllers. If the pitch actuator bandwidth increases, the performance of individual pitch controller would be better because the wind effect in the blade modes can be mitigated.
- To improve the gain scheduled controllers in the above rated zone including new operational points in the family of linear models when the wind turbine do not work in the operational points of the curve of power production (Fig. 5.1).
- To improve gain scheduled controllers for wind gust inputs including a new parameter dependence with a faster response than the pitch angle signal, like the generator speed error, to have a better generator speed regulation in extreme wind cases.

References

1. Jonkman JM, Butterfield S, Musial W, Scott G (2009) Definition of a 5-MW reference wind turbine for offshore system development. NREL Technical Report NREL/TP-500-38060
2. Díaz de Corcuera A (2013) Design of robust controller for load reduction in wind turbines. Thesis. University of Mondragon, The Basque Country, Spain, 2013
3. Díaz de Corcuera A, Pujana-Arrese A, Ezquerra JM, Segurola E, Landaluze J (2012) H_∞ based control for load mitigation in wind turbines. Energies 2012(5):938–967
4. Díaz de Corcuera A, Nourdine S, Pujana-Arrese A, Camblong H, Landaluze J (2011) GH BLADED'S linear models based H-infinity controls for off-shore wind turbines. In: EWEA Offshore 2011. Nov 2011. Amsterdam (Holland)
5. Díaz de Corcuera A, Pujana-Arrese A, Ezquerra JM, Segurola E, Landaluze J (2012) Wind turbine load mitigation based on multivariable robust control and blade root sensors. In: The Science of Making Torque from Wind. October 2012. Oldenburg (Germany)
6. International Standard IEC 61400-1 Second Edition 1999-02 Wind turbine generator systems. Part 1: Safety requirements
7. Bossanyi EA (2000) The design of closed loop controllers for wind turbines. Wind Energy 3(3):149–163
8. Laks JH, Pao LY, Wright A (2009) Control of wind turbines: past, present, and future. In: American control conference 2009. June 2009. St. Louis (USA)
9. Pao LY, Johnson KE (2009) A tutorial on the dynamics and control of wind turbines and wind farms.In: American control conference 2009. June 2009. St. Louis (USA)
10. Bossanyi EA (2009) Controller for 5 MW reference turbine. European Upwind Project Report. www.upwind.eu. Accessed Feb 2013
11. Schaak P, Corten GP, van der Hooft EL (2003) Crossing resonance rotor speeds of wind turbines. ECN Wind Energy, Paper ECN-RX–03-041
12. Van der Hooft EL, Schaak P, van Engelen TG (2003) ECN Technical Report. DOWEC-F1W1-EH-03-0940

13. Caselitz P, Geyler M, Giebhardt J, Panahandeh B (2011) Hardware-in-the-Loop development and testing of new pitch control algorithms. In: Proceeding of European wind energy conference and exhibition (EWEC), Brussels, Belgium, Mar 2011; pp 14–17

14. Johnson KE, Pao LY, Balas MJ, Kulkarni V, Fingersh LJ (2004) Stability analysis of an adaptive torque controller for variable speed wind turbines. In: Proceeding of IEEE conference on decision and control, Atlantis, Bahamas, Dec 2004; pp 14–17

15. Nourdine S, Díaz de Corcuera A, Camblong H, Landaluze J, Vechiu I, Tapia G (2011) Control of wind turbines for frequency regulation and fatigue loads reduction. In: Proceeding of 6th Dubrovnik conference on sustainable development of energy, water and environment systems, Dubrovnik, Croatia, Sept 2011; pp 25–29

16. Sanz MG, Torres M (2004) Aerogenerador síncrono multipolar de velocidad variable y 1.5 MW de potencia: TWT1500. Rev. Iberoamer. Automática Informática 1:53–64

17. Bianchi FD, Battista HD, Mantz RJ (2007) Wind turbine control systems. In: Principles, modelling and gain scheduling design. Springer, London

18. Díaz de Corcuera A, Pujana-Arrese A, Ezquerra JM, Segurola E, Landaluze J (2013) Linear models based LPV (Linear parameter varying) control algorithms for wind turbines. EWEA 2013. Jan 2013. Vienna (Austria)

19. Geyler M, Caselitz P (2008) Robust multivariable pitch control design for load reduction on large wind turbines. J Sol Energy Eng 2008(130):12

20. Fleming PA, van Wingerden JW, Scholbrock AK, van der Veen G (2013) Field testing a wind turbine drivetrain/tower damper using advanced design and validation techniques. In: American control conference (ACC) 2013 (Washington: USA)

21. Iribas M, Landau (2009) Closed loop identification of wind turbines models for pitch control. In: 17th Mediterranean conference on control and automaton. June 2009. Thessaloniki (Greecce)

22. Iribas M (2011) Wind turbine identification in closed loop operation. European Upwind Project Report. www.upwind.eu. Accessed Feb 2013

23. Garrad Hassan GL (2011) V4 Bladed Theory Manual. ©Garrad Hassan & Partners Ltd, Bristol

24. Jonkman JM, Marshall L, Buhl Jr (2005) FAST user's guide. NREL Technical Report NREL/TP-500-38230

25. Harris M, Hand M, Wright A (2005) LIDAR for turbine control. NREL Technical Report NREL/TP-500-39154

26. Van der Hooft EL, Schaak P, van Engelen TG (2003) Wind Turbine Control Algorithms; DOWEC-F1W1-EH-03094/0; Technical Report for ECN: Petten, The Netherlands, 2003

27. Ogata K (1993) Ingeniería de Control Moderna, 2 edn. Pearson Prentice Hall, Mexico

28. Bossanyi EA (2003) Wind turbine control for load reduction. Wind Energy 2003(6):229–244

29. Doyle JC, Francis BA, Tannenbaum AR (1992) Feedback control theory. MacMillan, New York

30. Scherer CW, El Ghaoui L, Niculescu S (eds) (2000) Robust mixed control and LPV control with full block scaling. In: Recent advances on LMI methods in control, SIAM (2000)

31. Balas G, Chiang R, Packard A, Safonov M (2010) Robust control toolbox. User's guide Mathworks. http://www.mathworks.es/es/help/robust/index.html. Accessed Feb 2013

32. Skogestad S, Postlethwaite I (2010) Mutivariable feedback control. Analysis and design, 2 edn. Willey, Chichester

33. Rugh WJ, Shamma JS (2000) Research on gain scheduling. Automatica 36(10):1401–1425

34. Bianchi FD, Mantz RJ, Christiansen CF (2004) Control of variable-speed wind turbines by LPV gain scheduling. Wind Energy 7(1):1–8

35. Díaz de Corcuera A, Pujana-Arrese A, Ezquerra JM, Segurola E, Landaluze J (2012) LPV model of wind turbines from GH Bladed's linear models. In: 26th European conference on modelling and simulation. ECMS 2012. May 2012. Koblenz (Germany)

36. Ostergaard KZ, Brath P, Stoustrup J (2008) Linear parameter varying control of wind turbines covering both partial load and full load conditions. Int J Robust Nonlinear Control 19:92–116

37. Bianchi FD, Sanchez Peña RS (2011) Interpolation for gain-scheduled control with guarantees. Automatica 47:239–243
38. Van Engelen TG, van del Hooft EL (2005) Individual pitch control inventory. ECN-C-030-138. Technical report for ECN. The Netherlands, 2005
39. Bossanyi EA, Wright A, Fleming P (2010) Controller field tests on the NREL CART2 Turbine. NREL/TP-5000-49085. Technical Report for NREL. Colorado, CO, USA, Dec 2010
40. Bossanyi EA, Wright A, Fleming P (2013) Validation of individual pitch control by field tests on two- and three-bladed wind turbines. IEEE Trans Control Systems Technol 21(2): 1067–1078
41. Stol KA, Zhao W, Wright AD (2006) Individual blade pitch control for the controls advanced research turbine (CART). J Sol Energy Eng 128(2):498–505
42. Wortmann S, (2010) REpower field test of active tower damping. In: European Upwind Project Report; Garrad Hassan & Partners Ltd., Bristol, UK
43. Heß F, Seyboth G (2010) Individual Pitch Control with tower side-to-side damping. In: Proceeding of 10th German wind energy conference, Bremen (Germany), Nov 2010
44. Nam Y (2011) Control system design, wind turbines. Ibrahim Al-Bahadly (ed), ISBN: 978-953-307-221-0
45. Coleman RP, Feingold AM (1957) Theory of self-excited mechanical oscillations of helicopter rotors with hinged blades. NASA TN 3844, NASA, 1957
46. Garrad Hassan GL (2011) V4 Bladed User Manual. ©Garrad Hassan & Partners Ltd, Chichester
47. Frandsen ST (2007) Turbulence and turbulence generated structural loading in wind turbine clusters. Ph.D. Thesis, Technical University of Denmark, Roskilde, Denmark, 2007
48. Söker H, Kaufeld N (2004) Introducing low cycle fatigue in IEC standard range pair spectra. In: Proceeding of 7th German wind energy conference, Wilhelmshaven, Germany, Oct 2004; pp 20–21

Chapter 6
Further Results on Modeling, Analysis, and Control Synthesis for Offshore Wind Turbine Systems

Hamid Reza Karimi and Tore Bakka

Abstract Renewable energy is a hot topic all over the world. Nowadays, there are several sustainable renewable power solutions out there; hydro, wind, solar, wave, and biomass to name a few. Most countries have a tendency to want to become greener. In the past, all new wind parks were installed onshore. During the last decade, more and more wind parks were installed offshore, in shallow water. This chapter investigates a comparative study on the modeling, analysis, and control synthesis for the offshore wind turbine systems. More specifically, an $\mathcal{H}_\infty$ static output-feedback control design with constrained information is designed. Constrained information indicates that a remarkable performance can be achieved by considering less information in the control loop or in the case of sensor failures in practice. Therefore, a special structure is imposed on the static output-feedback gain matrix in the contest of constrained information. A practical use of such an approach is to design a decentralized controller for a wind turbine. This will also benefit the controller in such a way that it is more tolerant to sensor failure. Furthermore, the model under consideration is obtained by using the wind turbine simulation software FAST. Using Linear Matrix Inequality ($\mathcal{LMI}$) method, some sufficient conditions to design an $\mathcal{H}_\infty$ controller are provided. Finally, a comprehensive simulation study will be carried out to illustrate the effectiveness of the proposed methodology for different cases of the control gain structures.

Keywords Wind turbine system · Control design · Modeling · Simulation · LMI

H.R. Karimi (✉) · T. Bakka
Department of Engineering, Faculty of Engineering and Science,
University of Agder, 4879 Grimstad, Norway
e-mail: hamid.r.karimi@uia.no

T. Bakka
e-mail: tore.bakka@uia.no

Nomenclature

β Blade pitch angle
C_p Power coefficient
F_t Thrust force
λ Tip-speed-ratio
P_a Extracted electrical power from the wind
ω_r Rotational speed of the rotor
R Rotor radius
ρ Air density
T_a Aerodynamic torque
υ Wind speed acting on the blades

6.1 Introduction

The wind turbine has been in use for several centuries. The first wind machines were only used for mechanical labor, such as grinding corn or pumping water. The first who benefited from the wind turbine in an electrical way, was James Blyth in Scotland in 1887. He used it to charge his batteries, in order to have light in his cabin. The modern wind power industry did not start until the late 1970s, and from this point, the research within wind power has accelerated.

In these green times, renewable power sources are a popular topic all over the world. The growth in the wind power industry has been tremendous over the last decade and it is nowadays one of the most promising sources for renewable energy. Since the early 1990s, wind power industry has enjoyed a renewed interest, and the total installed capacity is increasing heavily every year. According to The World Wind Energy Association's (WWEA) 2012 half-year report, the top world leading countries are China, USA, Germany, Spain, and India. Together, they represent 74 % of the total global capacity. Figure 6.1 illustrates the total installed capacity world wide since 2001, the figure shows an increase of about 21 % each year. In order to sustain this growth in the wind industry sector, advanced control is one area where this can be achieved. Although the majority of the world wide installed wind parks are situated onshore, there is an interest to install new offshore wind parks. The wind velocities are both higher and more stable in offshore environments. Offshore turbines are often either fixed to the soil or they stand on monopoles or other structures. These structures are installed in shallow waters, typical depths up to 60 m. For many countries, it would be beneficial to also be able to install wind turbines in deeper waters, in depths up to 1000 m. Hywind is one example for a floating wind turbine solution. This is a turbine which is currently in operation and is located right off the Norwegian west coast. It is a model of Hywind this chapter is dealing with.

Wind turbines are complex mechanisms. In general, they consist of four major components: rotor, transmission, generator, and a support structure. In addition,

Fig. 6.1 Total installed wind power capacity from 2001 to 2011 in [MW]
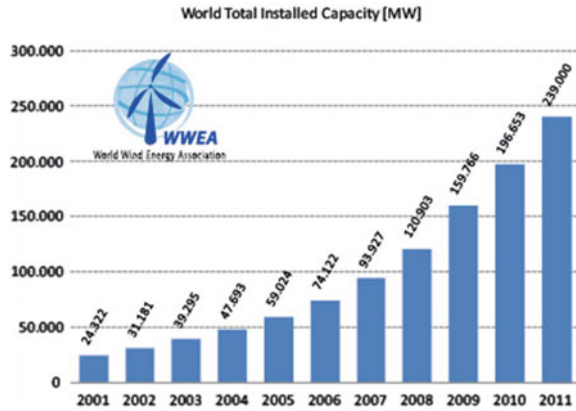
there is a control system causing the turbine to behave in a suitable manner. Over the years, there have been presented many ways to model the wind turbine, for instance, single mass models [1], multiple mass models [19], and complex flexible multibody models. The latter seems to have gained a lot of interest in recent years, much because these methods are incorporated into special wind turbine simulation software, such as HAWC2 [16], Cp-Lambda [8] and FAST [13]. Recently, a robust data-driven fault detection approach is proposed with application to a wind turbine benchmark [24]. More recently, modeling and optimization of a passive structural control design for a spar-type floating wind turbine is addressed in [22]. Besides, an application of adaptive output-feedback control design to wind turbine collective pitch control and load mitigation is proposed in [18]. In this work, the main objective is the design of an output-feedback controller without wind speed estimation, ensuring that the generator speed tracks the reference trajectory with robustness to uncertain parameters and time-varying disturbances.

The region of operation for a typical wind turbine is often divided into four regions, shown in Fig. 6.2. In region I ($v < v_{cut-in}$) the wind speed is lower than the cut–in wind speed and no power can be produced. In region II ($v_{cut-in} < v < v_{rated}$) the blade pitch is usually kept constant, while the generator torque is the controlling variable. In region III ($v_{rated} < v < v_{cut-out}$) the main concern is to keep the rated power and generator speed by pitching the blades. In region IV ($v > v_{cut-out}$) the wind speed is too high, and the turbine is shut down. This chapter is focused on the above-rated wind speed scenario, i.e., region III.

It is tempting to just put a well-designed onshore controller and install it on an offshore turbine. In principle, one can do this, but there is no guarantee that the closed-loop system will be stable. The major difference between the onshore and the offshore turbine is the natural frequencies. The natural frequencies will decrease significantly once the turbine is mounted on a floating foundation. First, lets say the turbine is located onshore. Then, the lowest tower frequency is typically 0.5 Hz, which is the tower fore-aft bending mode. Once this turbine is put

Fig. 6.2 Region of operation
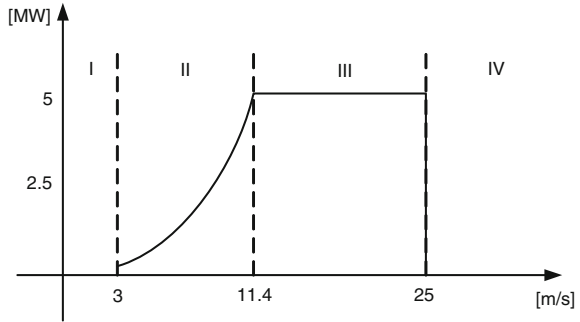
offshore, some additional vibration modes appear, see Fig. 6.4. These are much more low frequent, and the lowest frequencies are in the area $0.01-0.04$ Hz. When the turbine is designed, the designers already know the wind and wave frequencies in the area, and design the turbine structure accordingly. This is to make sure that the surrounding environment will not excite any of the structural vibration modes. For nonfloating turbines, the soil also plays a major role in relation to the structural natural frequencies, as discussed in [2]. A controller for an onshore turbine, typically has a frequency of 0.1 Hz, i.e., lower than the tower fore-aft bending mode. If this controller was implemented on the offshore turbine, then the controller would be faster than the tower vibration modes. This can cause a stability issue once the wind speed is above rated. One can quite easily visualize why this becomes a problem. It is known that, in the above-rated wind speed conditions the controlling variable is the blade pitch angle. When the wind speed increases, the blades will pitch out of the wind in order not to gain higher generator speed. This means that the aerodynamic forces acting on the tower will decrease and it will start to move forward. It is during this motion the stability issue occurs and it is directly related to the pitching frequency of the blades. Let us consider two scenarios: (1) the onshore controller is being used, (2) the offshore controller is being used. In the first scenario, the blades are being pitched out of the wind at a higher frequency than the tower is moving forward. The consequence is that the tower will lose most of its aerodynamic damping. The result is that the tower and eventually the generator will start to oscillate and eventually become unstable. In the second scenario, the blades are being pitched out of the wind with a lower frequency than the tower is moving forward. Therefore, the tower will not loose as much of the aerodynamic damping, and the overall system will maintain its stability.

In today's industry, PI or PID controllers are commonly used. These are designed by keeping in mind these critical frequencies. Pole placement is one way of getting the closed-loop system poles at the right locations. The control design proposed in this chapter does not directly include these stability constraints, but they are indirectly included since the proposed controller design is model based and guarantees stability. This problem will be demonstrated in the simulation results.
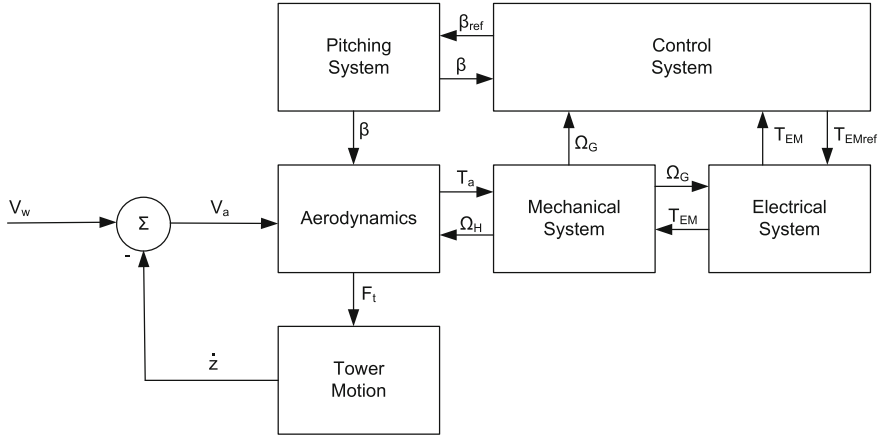
Fig. 6.3 Interconnected subsystems

The wind turbine is a highly nonlinear system. The nonlinearity is caused by the conversion of wind to electrical power. According to [10], the extracted electrical power from the wind can be formulated as

$$P_a = \frac{1}{2}\rho\pi R^2 \upsilon^3 C_p(\lambda, \beta). \tag{6.1}$$

The dimensionless tip-speed-ratio (TSR) λ is defined as

$$\lambda = \frac{\omega_r R}{\upsilon}, \tag{6.2}$$

where ω_r is the rotational speed of the rotor, R is the rotor radius and υ is the wind speed acting on the blades. From (1) the expressions for the aerodynamic torque and thrust force are found as follows:

$$T_a = \frac{1}{2}\rho\pi R^3 \upsilon^2 \frac{C_p(\lambda, \beta)}{\lambda}, \tag{6.3}$$

$$F_t = \frac{1}{2}\rho\pi R^2 \upsilon^2 C_T(\lambda, \beta). \tag{6.4}$$

where T_a is the aerodynamic torque, F_t is the thrust force, ρ is the air density and β is the blade pitch angle. C_p is known as the power coefficient and depends on how the turbine is designed. It is an expression describing the relationship between power available in the wind and how much it is possible to extract. It is not possible to extract all the wind. If this were to happen, then the wind would have to completely stop after hitting the blades. The theoretical upper limit for the power extraction is known as the Betz limit. Albert Betz showed that only 59.3 % of the

theoretical power can be extracted, no matter how well designed the turbine is. In reality, after all the losses and friction are accounted for, only about 40–50 % is actually extracted. C_T has a similar explanation, but dealing with thrust force. Both expressions depend on the TSR λ and the blade pitch angle β.

Typical wind turbines are built up by five major components; tower, nacelle, rotor, generator, and drive train. The nacelle is on top of the tower and houses the drive train and the generator. The drive train is divided into two parts, the low-speed shaft and the high-speed shaft. The rotor is attached to the low-speed shaft and is driven by the wind. The velocity of the low-speed shaft is geared up typically about hundred times. The low-speed shaft drives the induction generator and electrical power is produced. Although lately, drive trains without gearboxes are being developed. These are called direct drive solutions, where the wind directly drives a permanent magnet synchronous generator. Recently, a novel mathematical modeling and parameter tuning of the OC3-Hywind spar-type floating wind turbine with a tuned mass damper (TMD) installed in nacelle is proposed in [21].

A variety of control techniques are often solved by formulating the problem in terms of Linear Matrix Inequalities ($\mathcal{LMI}s$) [9]. Formulating the problem in such a way gives an opportunity to impose a special structure on the $\mathcal{LMI}$ variables. This comes in very handy when it comes to constrained information systems. This means that it is possible to design a controller which can handle the fact that not all the information in the feedback loop is used. There can be several reasons for this, i.e., some of the information is simply not needed, some of the sensors are especially prone to failure, switching between controllers and they do not need the same information, etc. State-feedback is widely used in control applications, but in practice full state measurement is usually not possible. A more practical approach is output-feedback. However, the output gain matrix is not computed as easily as in the state-feedback case, where a simple change of variables converts a nonconvex problem into a convex problem. In the output-feedback case, the gain matrix is not directly isolated from the other $\mathcal{LMI}$ variables. In [25–27], they proposed an explicit solution to calculate the gain matrix. In [20], an even simpler solution is found. With the solution found in [20], it is possible to impose zero-nonzero constraints on the $\mathcal{LMI}$ variables. An application of these developed methods to wind turbines has been investigated in [4, 5, 7]. Other solutions to make the system more tolerant to failures have been suggested in [23] and [15]. Faults in the grid can also cause the turbine to behave in a nonsatisfactory manner, this is discussed and dealt with in [28].

Nowadays, modern wind turbines are getting bigger and bigger and are often located in harsh environments. This leads to larger loads on critical parts and the possibility of sensor failure is always present. This chapter tries to alleviate these two issues. A traditional controller might force the turbine to shut down completely, if a sensor in the feedback loop should fail. With the controller designed in this chapter, the turbine is able to stay in operation, although the failed sensor should of course be fixed as soon as possible. This is not managed without consequences, as will be discussed later in the chapter. The main contributions of this chapter are

twofold: First, an $\mathcal{H}_\infty$ controller is designed to minimize the effect of disturbance on the controlled output, practically this means it is possible to dampen unwanted oscillations on critical parts due to turbulent wind; and second, the controller is designed as a priori to reduce effects of sensor failures that might occur.

This chapter is organized as follows. Section 6.2 describes the model under consideration and how the wind turbine model and blade pitch actuators are interconnected. Section 6.3 goes into the control design and how it is possible to calculate the constrained gain matrix. Simulation results for both the linear model and the nonlinear model are presented in Sect. 6.6. Finally, concluding remarks and suggestions to future work are discussed in Sect. 6.5.

Notation. Throughout this chapter, the notations $\mathcal{R}^n$ and $\mathcal{R}^{n \times m}$ denote, respectively, the n dimensional Euclidean space and the set of all $n \times m$ real matrices. Superscript "**T**" denotes matrix transposition and I and 0 are the identity matrix and the zero matrix with compatible dimensions, respectively. The symbol $\otimes$ denotes Kronecker product. The notation $P > 0$ means that P is real symmetric and positive definite and the symbol * denotes the transpose elements in the symmetric positions. diag$\{\cdots\}$ represents a block diagonal matrix and the operator sym(A) represents $A + A^{\mathrm{T}}$. All $\mathcal{LMI}$ variables are written with boldface font.

6.2 Model Description

A wind turbine system can be divided into several interconnected subsystems, see Fig. 6.3. The complexity of the subsystems are often related to the control strategy. A model for control purpose should not be overly complicated, but it should still describe the most important dynamics. Which dynamics that are important or not, will differ depending on the control objective. The model under consideration is obtained from FAST (Fatigue, Aerodynamics, Structures, and Turbulence) [13], which is a fully nonlinear wind turbine simulation software developed at the National Renewable Energy Laboratory (NREL) in Denver, USA. The code models the wind turbine as a combination of both rigid and flexible bodies. These bodies are then connected with several degrees of freedoms (DOFs). The code provides with a nonlinear model with up to 24 DOFs. The turbine model is floating and is rated for 5 MW, the main specifications are summarized in Table 6.1. More detailed information about the specifications can be found in [14]. Figure 6.4 shows the floating wind turbine. The platform DOFs are also indicated on the figure, they include; translational heave, sway and surge motion and rotational yaw, pitch and roll motion. Heave movement is defined along the z-axis, sway is along the y-axis, and surge is along the x-axis. Yaw motion is defined about z-axis, pitch is about the y-axis and roll is about the x-axis. This gives six DOFs.

Four more DOFs are related to the tower, two for longitudinal direction and two for lateral direction. Yaw motion of the nacelle provides one DOF. Variable generator- and rotor speeds gives another two DOFs, this also includes drive train

Fig. 6.4 Floating wind
turbine [12]
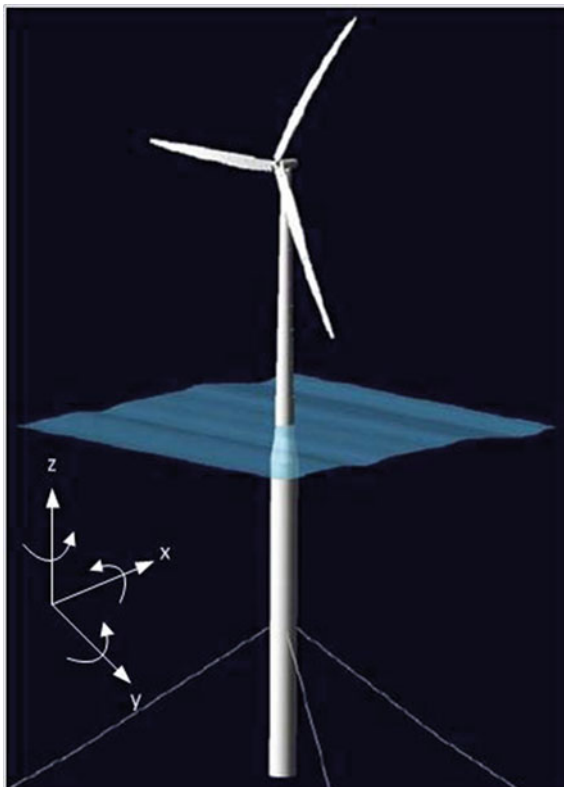
Table 6.1 Basic facts of
NREL's OC3 turbine

Rated power	5 MW
Rated wind speed	11.6 m/s
Rated rotor speed	12.1 RPM
Rotor radius	63 m
Hub hight	90 m

flexibility. Nine DOFs for the blades, that is; three for blade flapwise tip motion for
the first mode, three for tip displacement for each blade for the second flapwise
mode, and another three for the blade edgewise tip displacement for the first
edgewise mode. The last two DOFs are for rotor- and tail furl. In total, this adds up
to 24 DOFs.

In order to utilize linear control techniques, a linear model is needed. The linear
model is also obtained form FAST. A model with a low number of DOFs is
preferred for the controller design, otherwise the model is simply too complicated
in order to get a feasible solution. Three DOFs are selected for the linear model,
they are; platform pitch (1 DOF) and drive train (2 DOFs). The drive train includes

the rotor and generator inertia, which are connected with springs, dampers, and a gearing. FAST is not equipped with any blade pitch actuators, these are therefore added to the model after the linearization. A blade pitch actuator is the mechanism that physically rotates the turbine blade. The linear model obtained from FAST without any pitch actuators is in the following standard state-space form.

$$
\begin{aligned}
\dot{x} &= Ax + Bu, \\
y &= Cx,
\end{aligned}
\tag{6.5}
$$

where x is the state vector with dimensions $\mathcal{R}^{n \times 1}$, u is the control signal with dimensions $\mathcal{R}^{p \times 1}$, y is the model outputs with dimensions $\mathcal{R}^{m \times 1}$ and A, B and C are the state-space matrices with dimensions $\mathcal{R}^{n \times n}$, $\mathcal{R}^{n \times p}$ and $\mathcal{R}^{m \times n}$, respectively. y contains measurements for platform pitch angle, rotor speed, and generator speed. The specific dimensions for system (5) are; $n = 6$, $p = 3$, and $m = 3$.

This chapter deals with individual pitch control, therefore three blade pitch actuators are added to the linear model. The three second-order actuators are considered to be equal to each other, their properties are specified in the appendix. The DOFs for the updated model are; blade I actuator, blade II actuator, blade III actuator, platform pitch, drive train and generator. This gives a total of six DOFs with twelve states, i.e., one position- and velocity state for each degree of freedom. Then, an augmented system can be derived and represented in the following state-space formulation

$$
\begin{aligned}
\dot{X} &= A_t X + B_1 \omega + B_t u, \\
z &= C_z X + D_z u, \\
y &= C_t X,
\end{aligned}
\tag{6.6}
$$

where X is an augmented state vector which contains all the aforementioned 12 states and w and z are disturbance and controlled output, respectively. The updated dimensions for system (6) are; $n = 12$, $p = 3$, and $m = 3$. The state-space matrices A_t, B_t and C_t are defined as follows:

$$
A_t = \begin{bmatrix} I_3 \otimes A_a 0 \\ B \otimes C_a A \end{bmatrix}, \; B_t = \begin{bmatrix} I_3 \otimes B_a \\ 0 \end{bmatrix}
\tag{6.7}
$$
$$
C_t = \begin{bmatrix} 0 & C \end{bmatrix},
$$

where A_a, B_a and C_a are the state-space matrices for the pitch actuator, the matrix values can be found in the appendix. The rest of the state-space matrices B_1, C_z and D_z are defined in Sect. 6.4.

In this chapter, a static output-feedback controller $u = Ky$ is to be determined under constrained information, i.e., a zero-nonzero structure on the control gain matrix by utilizing $\mathcal{LMIs}$ such that the following requirements are met:

1. The following closed-loop system is asymptotically stable;

$$\begin{pmatrix} A_{cl} & B_{cl} \\ C_{cl} & 0 \end{pmatrix} = \begin{pmatrix} A_t + B_t K C_t & B_1 \\ C_z + D_z K C_t & 0 \end{pmatrix}. \tag{6.8}$$

2. Under zero initial condition, the closed-loop system satisfies $\|z(t)\|_2 < \gamma \|\omega(t)\|_2$ for any nonzero $\omega(t) \in L_2[0, \infty)$ where γ is a positive scalar.

6.3 Controller Design

$\mathcal{H}_\infty$ control is chosen because of its ability to minimize any energy-bounded disturbance on the controlled output. Also, since the linear model is of low order and the nonlinear model is of high order, this so-called advanced control design technique can catch a part of the unmodeled dynamics. The main issue in this section is to design a controller, which is able to handle constrained information, i.e., only a part of the available information will be used to calculate the control signal. In this case, that is to design a decentralized controller. What is meant with decentralized control, is that none of the calculated control signals should directly interfere with each other. The considered system consists of three inputs and three outputs, this indicates that the gain matrix is square and of dimension $\mathcal{R}^{3 \times 3}$. By imposing a diagonal structure on the gain matrix, this is possible. The solution found in [20], makes it possible to impose zero-nonzero constraints on the $\mathcal{LMI}$ variables. The control problem is formulated in terms of $\mathcal{LMIs}$, and are solved using YALMIP [17] interfaced with MATLAB.

The $\mathcal{H}_\infty$ performance constraints for a state-feedback system formulated in terms of $\mathcal{LMIs}$ are as follows:

$$\begin{pmatrix} \text{sym}(A_t X + B_t Y) + \gamma^{-2} B_1 B_1^T & * \\ C_z X + D_z Y & -I \end{pmatrix} < 0, \tag{6.9}$$
$$X > 0.$$

Remark 1 In a manner similar to [3], it is possible to present a new $\mathcal{H}_\infty$ performance criterion for the robust stability analysis of the system (6) with norm-bounded time-varying parameter uncertainties in the state-space matrices.

For the state-feedback case, the gain matrix is calculated as $\tilde{K} = YX^{-1}$. In the output-feedback case, the state gain matrix factors as the product $\tilde{K} = KC_t$, where

C_t is given from the state-space system. Now, when the output gain matrix is required, a solution to (9) needs to be found such that the product $\mathbf{Y}\mathbf{X}^{-1}$ factors as

$$\mathbf{Y}\mathbf{X}^{-1} = KC_t. \tag{6.10}$$

To solve this, [20] suggests the following change of variables

$$\mathbf{X} = Q\mathbf{X}_Q Q^{\mathrm{T}} + R\mathbf{X}_R R^{\mathrm{T}}, \tag{6.11}$$

$$\mathbf{Y} = \mathbf{Y}_R R^{\mathrm{T}}, \tag{6.12}$$

where $\mathbf{X}_Q$ and $\mathbf{X}_R$ are symmetric matrices with dimensions $\mathcal{R}^{(n-m)\times(n-m)}$ and $\mathcal{R}^{m\times m}$, respectively, and $\mathbf{Y}_R$ has dimension $\mathcal{R}^{p\times m}$. The matrix Q is the null-space of C_t and R can be calculated as follows:

$$R = C_t^{\mathrm{T}} \left(C_t C_t^{\mathrm{T}} \right)^{-1} + QL, \tag{6.13}$$

where L is an arbitrary matrix with dimensions $\mathcal{R}^{(n-m)\times m}$.

In order to obtain a diagonal structure on the gain matrix K, simply force a diagonal structure on $\mathbf{X}_R$ and $\mathbf{Y}_R$, while $\mathbf{X}_Q$ is a full matrix.

$$\mathbf{X}_R = \mathrm{diag}\{\mathbf{X}_{R1}, \mathbf{X}_{R2}, \mathbf{X}_{R3}\}, \tag{6.14}$$

$$\mathbf{Y}_R = \mathrm{diag}\{\mathbf{Y}_{R1}, \mathbf{Y}_{R2}, \mathbf{Y}_{R3}\}. \tag{6.15}$$

In order to solve the $\mathcal{LMIs}$ (9), first define $v = \gamma^{-2}$. Then, maximize v and solve the $\mathcal{LMIs}$ in terms of $\mathbf{X}_Q, \mathbf{X}_R, \mathbf{Y}_R$. Once $\mathbf{X}$ and $\mathbf{Y}$ from (11, 12) are calculated it is possible to find the gain matrix $K = \mathbf{Y}_R \mathbf{X}_R^{-1}$, satisfying $\mathbf{Y}\mathbf{X}^{-1} = KC$. Additional information and proofs about this can be found in the aforementioned references.

6.4 Simulation Results

In this section, the proposed control design methodology is applied to the wind turbine system. The simulation is divided into two parts, one dealing with the linear model and one dealing with the nonlinear model. First, both the full information gain and the constrained gain are tested with the linear model. Second, the constrained gain controller is tested with the nonlinear model. The figures contain plots for simulations done with the constrained controller and with the baseline controller. The baseline is intended as a reference plot and is included in the FAST package. But first of all, suitable matrix values for B_1, C_z and D_z need to be found.

The effect of disturbance on the linear model is assumed to affect the platform pitch angle and the rotor- and generator speed. In this analysis, the disturbance vector is chosen to be:

$$B_1 = \begin{bmatrix} 0_{1 \times 9} & 0.1 & 1 & 1 \end{bmatrix}^{\mathrm{T}}. \tag{6.16}$$

This means that the platform pitch speed will not be as influenced by the disturbance as the rotor- and generator speed. The performance measure matrices are considered as

$$C_z = \begin{bmatrix} 97C_{t1} - C_{t2} \\ C_{t3} \\ (.) \end{bmatrix}, \tag{6.17}$$

$$D_z = \mathrm{diag}\{100, 80, 10\}, \tag{6.18}$$

where $(.) = \begin{bmatrix} 10 & 0 & 10 & 0 & 10 & 0 & 0_{1 \times 6} \end{bmatrix}$ and C_{ti} represent the i-*th* row of C_t. The first row of C_z handles drive train oscillations. Rotor speed times the gearing ratio minus the generator speed should be kept zero, i.e., minimizing oscillations. In row 2, the platform pitch movement is penalized and row 3 handles the blade pitch motion. Suitable results were found with a diagonal structure on the matrix D_z.

Figures 6.5 and 6.6 show the outputs (first column) and the blade pitch angles (second column) for the closed-loop linear system. Simulation is carried out with initial values for platform pitch angle, generator speed and rotor speed. In Fig. 6.5, no faults occur in the system and both controllers achieve an acceptable performance. In Fig. 6.6, a sensor failure is imposed on the system. For the full structure of the control gain K, values for all three blades are calculated and the output values are not too different from the results in Fig. 6.5. For the diagonal structure of the control gain K, only values for blades 1 and 2 are calculated, the value for blade 3 is depending on a working sensor nr. 3. In the case of a failure in sensor nr. 3, the two systems do not behave too different. It is worth mentioning that scenarios where sensor nr. 1 and nr. 2 fails have also been investigated. Only one sensor fails at the time. Now, the behavior of the two systems become very different. Results from these scenarios show that the system with the diagonal gain is stable regardless of which of the sensors that fails. In contrast to tests done with the full gain, where the system becomes unstable if sensor nr. 1 or nr. 2 fails, but as the figure shows, stays stable when sensor nr. 3 fails.

The full and the diagonal controllers are given in (19) and (20), respectively, and the γ-values for the two cases are compared in Table 6.2.

$$K_{\text{full}} = \begin{bmatrix} -0.9676 & 0.01 & 0 \\ 0.0037 & 0 & -0.0125 \\ 0.1988 & -0.0021 & 0.0043 \end{bmatrix}, \tag{6.19}$$

Fig. 6.5 System outputs and blade pitch angle, no faults
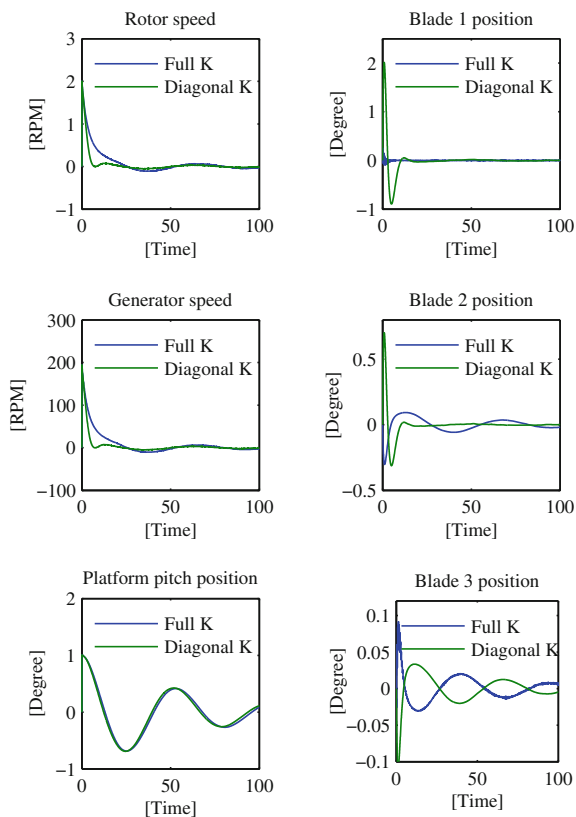
$$K_{\text{diagonal}} = \text{diag}\{0.0470, 0.0003, -0.0042\}. \tag{6.20}$$

Simulation of the nonlinear model is carried out in MATLAB/Simulink interfaced with FAST. 27 DOFs are now available, counting the 24 DOFs from FAST and the 3 DOFs extra from the pitch actuators. The input to the model is turbulent wind, and the wind profile is obtained from the software Turbsim [11], which also is a software developed at the NREL. The profile is a 1-year extreme case with an average speed of 18 m/s and a turbulence intensity of 6 %, see Fig. 6.7. Significant wave height is 6 m with a peak wave period of 10 s. The time-series are of 600 s, but the first 200 s are taken out due to transient behavior. The gain matrix in the feedback loop is now constrained to have diagonal structure. A fault is introduced to the system after 200 s. This fault causes sensor nr. 3 to stop working, i.e., blade nr. 3 is not moving. This fault only happens to simulations with the constrained controller, and not for the baseline simulation. It may be noted that the γ-value is considerably higher when the diagonal structure constraint is imposed. This makes sense because the number of $\mathcal{LMI}$ variables have now decreased and there are a lower number of variables available when it comes to finding the lowest γ-value.

Fig. 6.6 System outputs and blade pitch angle, sensor 3 has failed
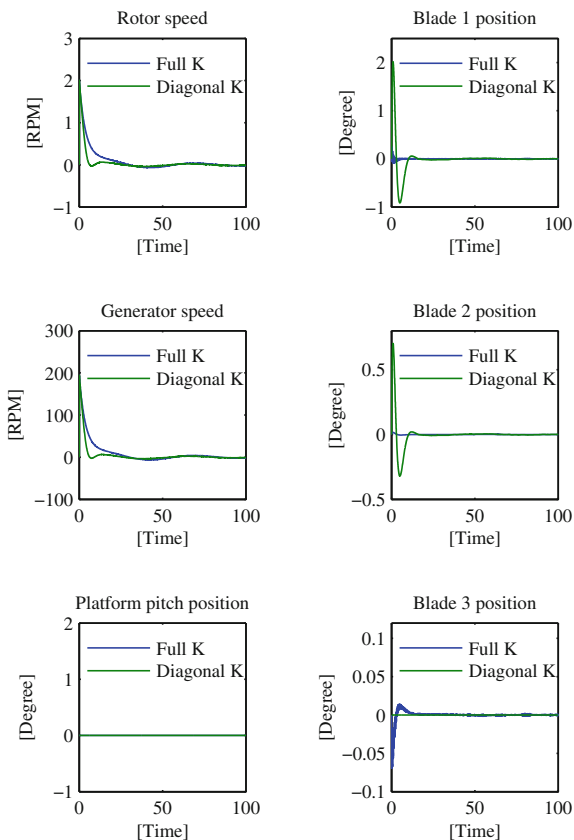
γ-value for full gain	γ-value diagonal gain
208	6331

Table 6.2 γ-values

Simulation done with the baseline controller is also included in the figures as a reference plot. This baseline controller comes with the FAST package and is a gain-scheduled PI controller. The controller proposed in this chapter is individual pitch in contrast to the baseline which is a collective pitch controller.

In order to evaluate the drive train oscillations, the standard deviation of the speed difference between rotor—and generator—speed is calculated. The values are normalized in such a way that the value for the baseline controller is used as reference and given value 1, see Table 6.3.

By using an individual pitch controller, it is possible to have a controller which handles events such as sensor failure in a good way. That is; if one of the

Fig. 6.7 Wind profile
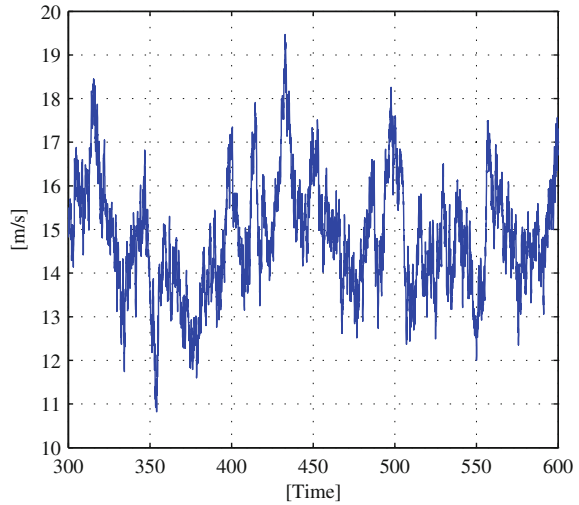
Table 6.3 Normalized values for standard deviation of drive train oscillations

Baseline	Constrained gain
1	0.93

This means, in terms of standard deviation, the constrained gain is 7 % better than the baseline.

Fig. 6.8 Generator speed
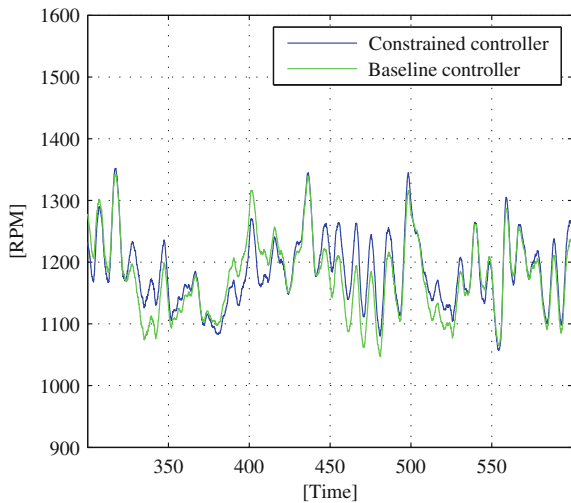
sensors in the feedback loop fails, only one of the blades will directly experience this failure. This can be achieved with a decentralized individual pitch controller. It is seen from Figs. 6.8, 6.9, 6.10, 6.11 and 6.12 that the controller behaves in a

Fig. 6.9 Platform pitch
angle
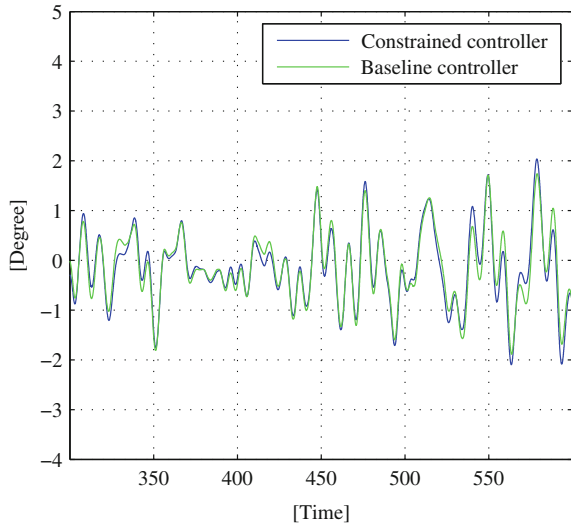
Fig. 6.10 Blade pitch angle
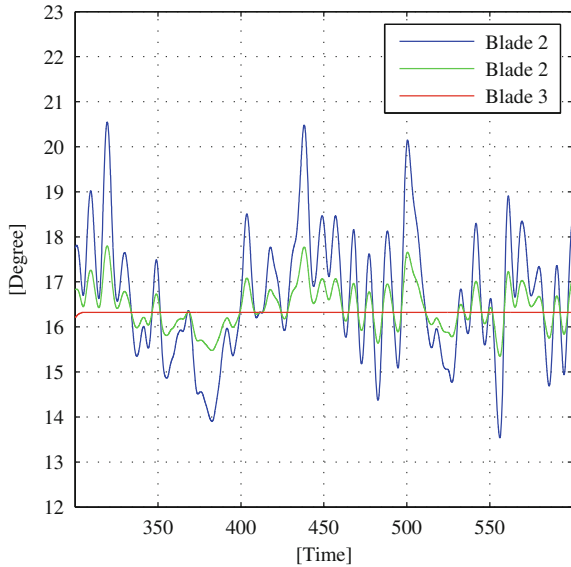
satisfactory manner and the overall system is stable, even if blade 3 is not moving. The behavior of the system is not as steady as in the references [3–6], but the main advantage with the approach proposed in this chapter is that the system is much more robust when it comes to sensor failures.

From Fig. 6.12 it is seen that the thrust force has some peaks below zero, this means the tower is moving forward. That is, the tower experiences negative

Fig. 6.11 Generated power
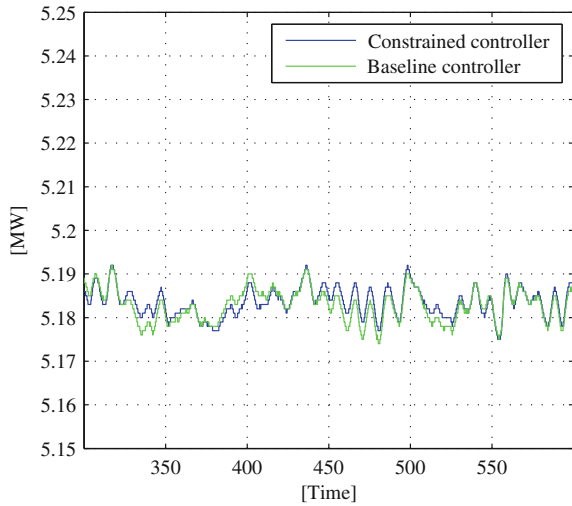
Fig. 6.12 Rotor thrust force
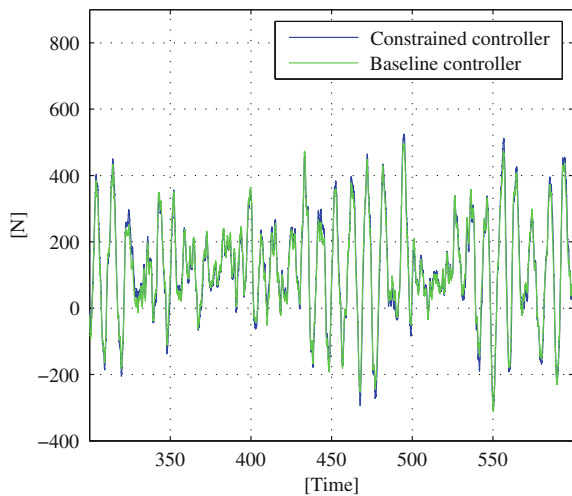
Table 6.4 Critical natural frequencies

Platform surge	0.015 Hz
Platform pitch	0.049
Platform heave	0.1
Blade pitch	0.03

aerodynamic damping. This issue was discussed in the introduction of this chapter. As the plots show, and Table 6.4 imply, enough aerodynamic damping is acting on the tower. Hence, the overall system remains stable.

Fig. 6.13 Normalized
standard deviations for
selected time-series
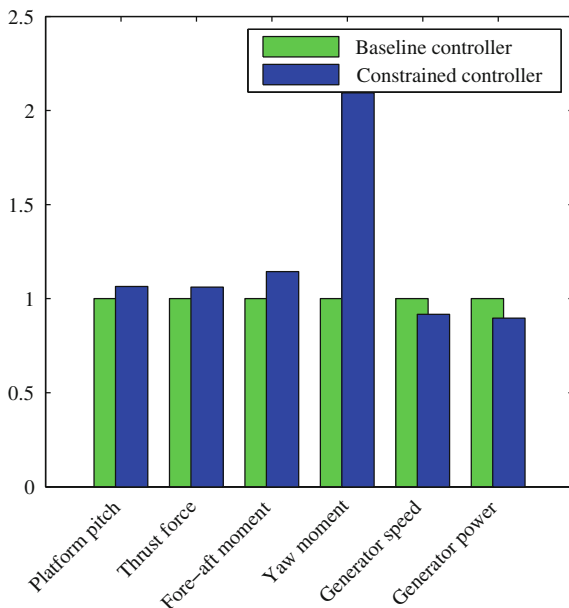
Fig. 6.14 Normalized mean
values for selected
time-series
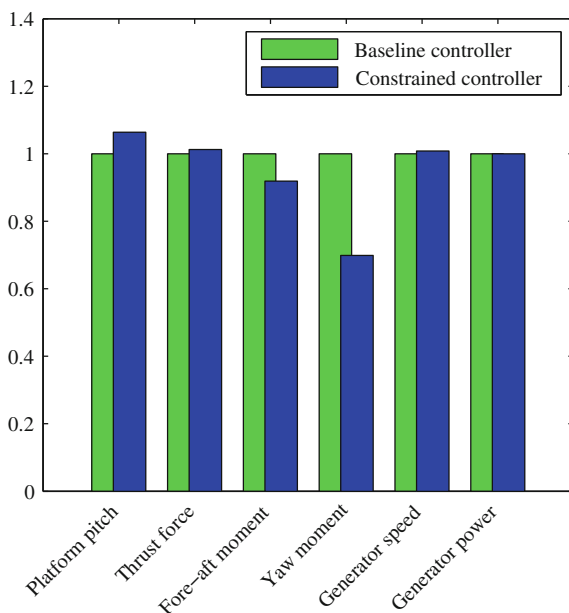
Figure 6.13 shows the normalized standard deviations from selected time-series. By allowing the turbine to stay in operation even if one of the sensors fail, is not without consequence. The force acting on the structure is now much more

unsymmetrical than if all three blades were pitching. This will introduce additional fluctuations in the yaw moment, as seen from the histogram. Although, the mean value is almost 40 % lower than the baseline value, see Fig. 6.14.

A table describing the most critical natural frequencies are shown in Table 6.4. These are found by calculating the Fast Fourier Transform (FFT) from the closed-loop time-series. From the discussion about critical frequencies in the introduction, it is seen from the table that the natural frequencies are where they should be.

6.5 Conclusions

This chapter studied modeling, analysis, and control design for offshore floating wind turbine systems. To this aim, an individual pitch static output-feedback controller is designed for the system under consideration with constrained information. The constrained information can be utilized in the case of sensor failures and from mathematical point of view means that a special zero-nonzero structure is imposed on the output-feedback gain matrix. In the considered system, there are three inputs and three outputs. If one sensor fails, only one blade pitch actuator will be influenced. The model under consideration is obtained from the software FAST. The model is fully nonlinear and in addition to the added pitch actuators the model consists of 27 DOFs. A linear model is obtained in order to perform the controller design, and simulations are carried out to verify the design. Simulation results performed both on the linear model and on the fully nonlinear system are presented in order to show the effectiveness of the controller design methodology.

6.6 Future Work

It is noted that the extensions of the proposed method to the observer-based controller design for wind turbine control systems deserve further investigation. Also, considering the delay in actuators and its effect in the performance of the closed-loop system will be part of our future works. Besides, application of the developed method for wind farm control systems can be addressed as an interesting further work.

A.1 6.7 Appendix

A dynamic model is constructed for each of the three linear pitch actuators:

$$\dot{x}_a = \underbrace{\begin{bmatrix} -2\omega_n\zeta & -\omega_n^2 \\ 1 & 0 \end{bmatrix}}_{A_a} x_a + \underbrace{\begin{bmatrix} 1 \\ 0 \end{bmatrix}}_{B_a} u_1, \tag{6.21}$$

$$y = \underbrace{\begin{bmatrix} 0 & \omega_n^2 \end{bmatrix}}_{C_a} x_a, \tag{6.22}$$

where the natural frequency is $\omega_n = 0.88\,\text{rad/s}$ and the damping ratio is $\zeta = 0.9$.

References

1. Abdin ES, Xu W (2000) Control design and dynamic performance analysis of a wind turbine induction generator unit. IEEE Trans Energy Convers 15(1):91–96
2. AlHamaydeh M, Hussain S (2011) Optimized frequency-based foundation design for wind turbine towers utilizing soil-structure interaction. J Franklin Inst 348:1470–1487
3. Bakka T, Karimi HR (2012) Robust H_∞ dynamic output-feedback control synthesis with pole placement constraints for offshore wind turbine systems. Math Probl Eng Article ID 616507
4. Bakka T, Karimi HR (2012) Multi-objective control design with pole placement constraints for wind turbine systems. In: Advances on analysis and control of vibrations—theory and applications. INTECH 2012 ISBN 978-953-51-0699-9, p 179–194
5. Bakka T, Karimi HR (2013) H_∞ Static output-feedback control design with constrained information for offshore wind turbine system. J Franklin Inst 350(8):2244–2260
6. Bakka T, Karimi HR, Duffie NA (2012) Gain scheduling for output H_∞ control of offshore wind turbine. In: Proceedings of the twenty-second international offshore and polar engineering conference, pp 496–501
7. Bakka T, Karimi HR, Christiansen S (2014) Linear parameter-varying modeling and control of an offshore wind turbine with constrained information. IET Control Theory Appl 8(1):22–29
8. Bottasso CL, Croce A (2009) Cp-Lambda user manual. Dipartimento di Ingnegneria Aerospaziale, Politecnico di Milano, Italy
9. Boyd S, Ghaoui LE, Feron E, Balakrishnan V (1994) linear matrix inequalities in systems and control theory. SIAM Studies in Applied Mathematics, vol 15, SIAM, Philadelphia
10. Eggleston DM, Stoddard FS (1987) Wind turbine engineering design. Van Nostrand Reinhold, New York
11. Jonkman BJ (2009) TurbSim users guide: version 1.50. Technical report NREL/EL-500-46198, National Renewable Energy Laboratory
12. Jonkman J (2010) Definition of the floating system for phase IV of OC3. Technical report NREL/TP-500-47535, National Renewable Energy Laboratory
13. Jonkman J, Buhl ML Jr (2005) FAST users guide. Technical report NREL/EL-500-38230, National Renewable Energy Laboratory
14. Jonkman J, Butterfield S, Musial W, Scott G (2009) Definition of a 5-MW reference wind turbine for offshore system development. Technical report NREL/TP-500-38060, National Renewable Energy Laboratory
15. Kamal E, Aitouche A, Ghorbani R, Bayrat M (2012) Robust fyzzy fault-tolerant control of wind energy conversion systems subjected to sensor faults. IEEE Trans Sustain Energy 3(2):231–241
16. Larsen TJ (2009) How 2 HAWC2, the user's manual, Risø-R-1597(ver. 3–9)(EN)
17. Lfberg J (2004) YALMIP a toolbox for modeling and optimization in MATLAB. In: Proceedings of the CACSD conference, Taipei, Taiwan

18. Li D, Song Y, Cai W, Li P, Karimi HR (2014) Wind turbine pitch control and load mitigation using an L_1 adaptive approach. Math Probl Eng 2014(Article ID 719803):11
19. Muyeen SM, Ali MH, Takahashi R, Murata T, Tamura J, Tomaki Y, Sakahara A, Sasano E (2007) Comparative study on transient stability analysis of wind turbine generator system using different drive train models. IET Renew Power Gener 1(2):131–141
20. Rubió-Massegú J, Rossell JM, Karimi HR, Palacios-Quiñonero F (2013) Static output-feedback control under information structure constraints. Automatica 49(1):313–316
21. Si Y, Karimi HR, Gao H (2013) Modeling and parameter analysis of the OC3-Hywind floating wind turbine with a tuned mass damper in nacelle. J Appl Math 2013(Article ID 679071):10
22. Si Y, Karimi HR, Gao H (2014) Modelling and optimization of a passive structural control design for a spar-type floating wind turbine. Eng Struct 69:168–182
23. Sloth C, Esbensen T, Stoustrup J (2011) Robust and fault-tolerant linear parameter-varying control of wind turbines. Mechatronics 21(4):645–659
24. Yin S, Wang G, Karimi HR Data-driven design of robust fault detection system for wind turbines. Mechatronics. doi: 10.1016/j.mechatronics.2013.11.009
25. Zečević AI, Šiljak DD (2004) Design of robust static output feedback for large-scale systems. IEEE Trans Autom Control 11:2040–2044
26. Zečević AI, Šiljak DD (2008) Control design with arbitrary information structure constraints. Automatica 44(10):2642–2647
27. Zečević AI, Šiljak DD (2010) Control of complex systems: structural constraints and uncertainty. Springer, Berlin
28. Zhang F, Leithead WE, Anaya-Lara O (2011) Wind turbine control design to enhance the fault ride-through capability. In: IET conference on renewable power generation, pp 1–6

Chapter 7
A Fault Tolerant Control Approach to Sustainable Offshore Wind Turbines

Montadher Sami Shaker and Ron J. Patton

Abstract The main challenges for the deployment of wind turbine systems are to maximise the amount of good quality electrical power extracted from wind energy. This must be ensured over a significantly wide range of weather conditions simultaneously with minimising both manufacturing and maintenance costs. In consequence to this, the fault tolerant control (FTC) and fault detection and diagnosis (FDD) research have witnessed a steady increase in interest in this application area as an approach to maintain system sustainability with more focus on offshore wind turbines (OWTs) projects. This chapter focuses on investigations of different aspects of operation and control of wind turbine systems and the proposal of a new FTC approach to sustainable OWTs. A typical non-linear state space model of a wind turbine system is described and a Takagi-Sugeno (T-S) fuzzy model of this system is also presented. A new approach to active sensor fault tolerant tracking control (FTTC) for OWT described via T-S multiple models. The FTTC strategy is designed in such way that aims to maintaining nominal wind turbine controller without change in both fault and fault-free cases. This is achieved by inserting T-S proportional state estimators augmented with multiple-integral feedback (PMI) fault estimators to be capable to estimate different generator and rotor speed sensors fault for compensation purposes. The material in this chapter is presented using a non-linear benchmark system model of a wind turbine offered within a competition led by the companies Mathworks and KK-Electronic.

Keywords Wind turbine control · Active fault tolerant control · Fault estimation · T-S fuzzy systems · Tracking control

M.S. Shaker (✉)
Department of Electrical Engineering, University of Technology, Baghdad, Iraq
e-mail: m.s.shaker@uotechnology.edu.iq

R.J. Patton
School of Engineering, University of Hull, Hull HU6 7RX, UK
e-mail: r.j.patton@hull.ac.uk

Nomenclature

$P_{\text{cap}}, P_{\text{wind}}$	Aerodynamic, wind power
ρ	Air density
R	Rotor radius
C_p, C_q	Power, torque coefficients
β, β_r	Actual, reference blade pitch angle
$\lambda, \lambda_{\text{opt}}$	Actual, optimal tip-speed-ratio
$v, v_{\text{min}}, v_{\text{max}}$	Point, minimum, and maximum wind speed
$\omega_r, \omega_{\text{min}}, \omega_{\text{max}}, \omega_{r\text{opt}}$	Actual, minimum, maximum, and optimal rotor speed
T_a	Aerodynamic torque
$T_g, T_{gr}, T_{gm},$	Actual, reference, measured generator torque
J_r, J_g	Rotor, generator inertia
B_r, B_g	Rotor, generator external damping
ω_g	Generator speed
n_g	Gearbox ratio
$K_{\text{d}t}, B_{\text{d}t}$	Torsion stiffness, damping coefficients
θ_Δ	Torsion angle
ζ	Damping factor
ω_n	Natural frequency
τ_g	Generator time constant
$C_{p\text{max}}$	Upper bound of power coefficient
$\mathcal{A}_{\text{wind}}, \mathcal{A}, \mathcal{A}_2$	Upstream, disc, downstream, areas
P^+, P^-	Pressure before, after actuator disc
F_d	Thrust exerted on the actuator disc
α	Axial interference factor
t_b, t_w	Blade, turbulence times
S	Length of the disturbed wind
n	Number of blades
f_s	Sensor fault signal
e_t, e_x, e_v	Tracking, state estimation, wind measurement errors
$K(p), L_a(p)$	Controller, observer gains
$P_1, P_2, \gamma, \mu, X_1$	LMI variables
$A(p), B, E(p), C, D_f$	System matrices
$\bar{A}(p), \bar{B}, \bar{E}(p), R, \bar{C}, \bar{D}_f$	System matrices augmented with tracking error integral
$A_a(p), B_a, E_a(p), R_a, G, C_a$	Observer augmented matrices

7.1 Introduction

Owing to inherent limitations in different kinds of the well-known fossil fuel and nuclear energy sources, e.g. carbon footprint, rapidly increasing fuel prices or the probability of catastrophic effects of nuclear station malfunction, the last two decades have witnessed a rapid growth in the use of wind energy. Although, it is considered a promising source of energy, depending on naturally generated wind forces, there are several very significant challenges to efficient wind energy conversion for electrical power transformation.

Wind turbine systems demand a high degree of reliability and availability (sustainability) and at the same time are characterised by expensive and safety critical maintenance work [3, 14, 20, 30]. The recently developed offshore wind turbines (OWTs) are foremost examples since OWT site accessibility and system availability is not always ensured during or soon after malfunctions, primarily due to changing weather conditions. Indeed, maintenance work for OWTs is more expensive than the maintenance of onshore wind turbines by a factor of 5–10 times [46]. Hence, to be competitive with other energy sources, the main challenges for the deployment of wind turbine systems are to maximise the amount of good quality electrical power extracted from wind energy over a significantly wide range of weather and operation conditions and minimise both manufacturing and maintenance costs.

Since regular and corrective maintenance are among the factors that increase the overall cost of wind projects, the most efficient way of reducing these costs would be to continuously monitor the condition of these systems. This condition monitoring-based preventive maintenance allows for early detection of the degeneration of the wind turbine health, facilitating a proactive response, minimising downtime, and maximising productivity. However, the wind energy technical reports [49] show that some of the currently available signal-based monitoring techniques are unreliable and not suitable for wind turbine applications because of the stochastic nature of the wind that affects the fault decision-making. Moreover, the simultaneous increase of wind turbine accidents with the increase of wind turbine size, which are clearly shown in the failure records, such as the survey of failures in Swedish wind power plant presented in [35] (see Fig. 7.1), as well as the steady increase of the number of OWTs projects have all stimulated research into fault tolerant control (FTC) and fault detection and diagnosis (FDD) in this application area since the ability to detect wind turbine faults and to control turbines in the presence of faults are important aspects of decreasing the cost of wind energy and increasing penetration into electrical grids [3, 12, 20, 30, 38, 39, 42].

Although the significance of wind turbine control on the overall system behaviour is well investigated in the literature [5, 9, 10, 26], nominal control systems lack the ability to ensure system sustainability during components and/or system faults. Clearly, improvements in FDD and FTC can play an important role to ensure the availability of wind turbines during different normal or abnormal operation conditions, minimise the number of unscheduled maintenance operation, and prevent development of minor fault into failure especially for OWTs.
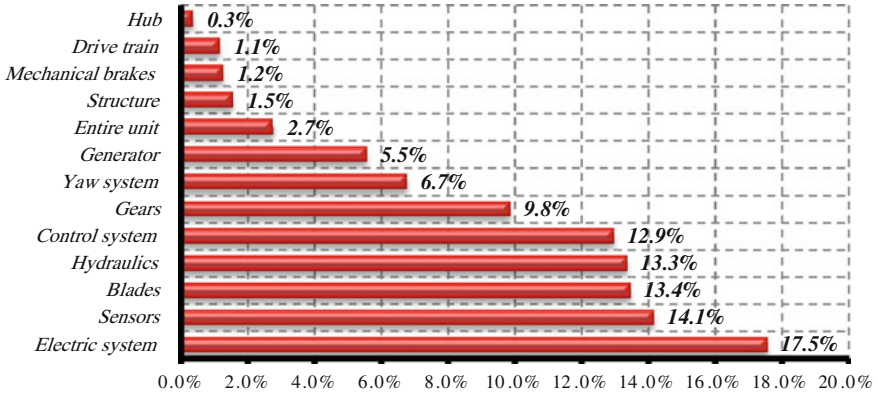
Fig. 7.1 Distribution of number of failure for Swedish wind power plants [35]

For example, the wind turbine benchmark in [29, 30] involves rotor and generator speed parameter scaling and stuck sensor faults. These faults have a direct effect on the reference torque signal provided by the controller. Consequently, the controller will start to drive the wind turbine away from its optimal operation, which in turn leads to lower conversion efficiency or may even prevent the turbine from converting energy (cutoff).

This chapter focuses on investigations of different aspects related to a fault tolerant control approach to sustainable wind turbine systems, as well as the presentation of FTC strategies for OWTs based on the T-S fuzzy framework. A typical non-linear state space model of a wind turbine system is described and a T-S fuzzy model of this system is also presented. The investigations are based on a 4.8 MW benchmark model proposed by [29, 30].

7.2 Structure and Approaches to FTC Systems

Generally, the nominal controller (sometimes referred to as the 'baseline' controller, see [32]) aims to stabilise and achieve the required closed-loop performance during normal operating conditions. To give the controlled system the ability to tolerate fault effects, additional inherent ability of the controller and/or extra assistant blocks should be inserted in the control loop. Figure 7.2 illustrates the main structure of the fault tolerant system.

Generally, two steps are required to provide the system with the capability to tolerate faults:

- Equip the system with some mechanism to make it able to detect the fault once it occurs, provide information about the location, identification of faulty component and decide the required remedial action in order to maintain acceptable operation performance (Supervision level).
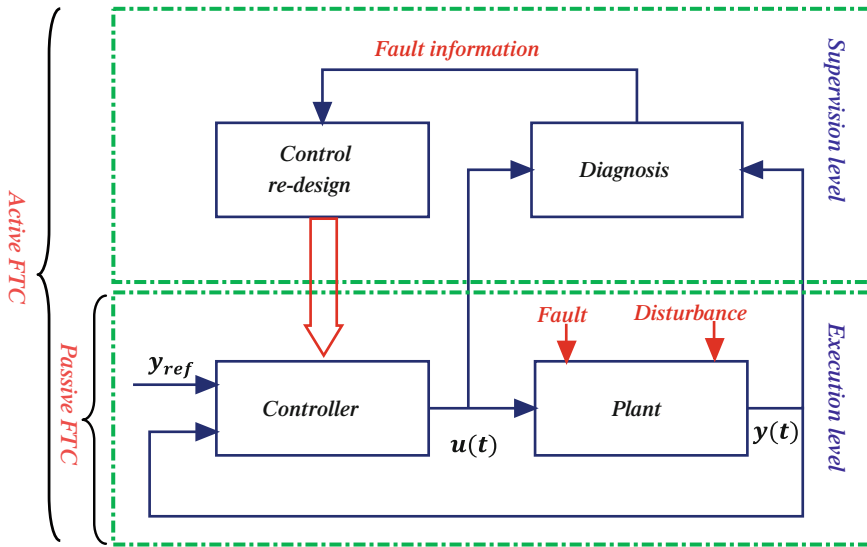
Fig. 7.2 Schematic of the fault tolerant system [6]

- Make use of the information obtained from the supervision level and adapt the controller parameters and/or reconfigure the structure of the controller so that the required remedial activity can be achieved (Execution level).

Hence, the FTC loop extends the usual feedback controller by a *supervision level*. In the absence of a fault, the system matches its nominal response so that the nominal controller attenuates the disturbance and ensures good reference following and other requirements on the closed-loop system. In this situation, the diagnostic block recognises that the closed-loop system is fault-free and no change of the control law is necessary.

If a fault occurs, the *supervision level* makes the control loop fault-tolerant. The diagnosis block identifies the fault and the control re-design block adjusts the controller to the new controller parameter set. Following this, the reconfigured system continues to satisfy the control target.

Thus, FTC is the control loop that has the ability to fulfil the required system performances even if faults occur through utilising the help provided by the supervision level. Approaches for synthesizing the FTC loop are classified as either a passive FTC (PFTC) or active FTC (AFTC). In the PFTC approach, the control loop is designed to tolerate some anticipated types of faults. The effectiveness of this strategy, that usually handles anticipated faults scenarios, depends upon the robustness of the nominal closed-loop system. Additionally, since the robustness of the closed-loop system to the fault is considered during the design cycle of the nominal controller, this may lead to post-fault degraded performance of the closed-loop system. However, it is interesting to note that the PFTC system does not require the FDD and controller reconfiguration and hence it has the ability

to avoid the time delay due to online diagnosis of the faults and reconfiguration of the controller. In fact, this is very important in practice where the time windows during which the system remains stabilisable in the presence of faults are very short, e.g. the unstable double inverted pendulum example [27, 50]. Most of the PFTC methods have been proposed mainly based on robust control theory. However, the fundamental difference between the traditional robust control and the PFTC lies in the fact that robust control deals with small parameter variations or model uncertainties, whilst PFTC deals with more drastic changes in system configuration caused by faults [4, 17, 34, 41, 47, 48, 53]. It should be noted that in the early literature the PFTC approach was referred to as 'reliable control' [47, 48].

In order to improve the post-fault control performance and cope with severe faults that break the control loop, it is commonly advantageous to switch to a new controller that is on-line or designed off-line to control the faulty plant.

In the AFTC approach, two conceptual steps are required: *FDD* and *controller adjustment* so that the control law is reconfigured to achieve performance requirements, subsequent to faults [6, 32, 36, 56]. An AFTC system compensates for faults either by selecting a pre-computed control law (projection-based approaches) [7, 25, 40, 55] or by synthesizing a new control strategy online (online automatic controller redesign approaches) [1, 2, 22, 23, 37, 52, 57]. Another widely studied method is the fault compensation approach, where a fault compensation input is superimposed on the nominal control input [8, 15, 19, 28, 31, 54].

It should be noted that owing to the ability of the traditional adaptive control methods to automatically adapt controller parameters to changes in system parameters, adaptive control has been considered as a special case of AFTC that obviates the need for diagnosis and controller re-design steps [45, 51]. Figure 7.3 shows a general overview of the main approaches used to achieve FTC for each class.

7.3 Wind Turbine Modelling

The principle aim of control in the wind turbine systems operation is to optimise wind energy conversion to mechanical energy which in turn is used to produce electricity. These systems are characterised by non-linear aerodynamic behaviour and depend on a stochastic uncontrollable wind force as a driving signal. To conceptualise the system from analysis and control designs to real application, an accurate overall mathematical model of the turbine dynamics is required. Normally, the model is obtained by combining the constituent subsystem models that together make up the overall wind turbine dynamics. This Section describes the combination of a flexible low speed shaft model together with a two-mass conceptual model of a wind turbine.

The aerodynamic torque (T_a) acting within the rotor represents the principal source of non-linearity of the wind turbine. T_a depends on the rotor speed ω_r, the
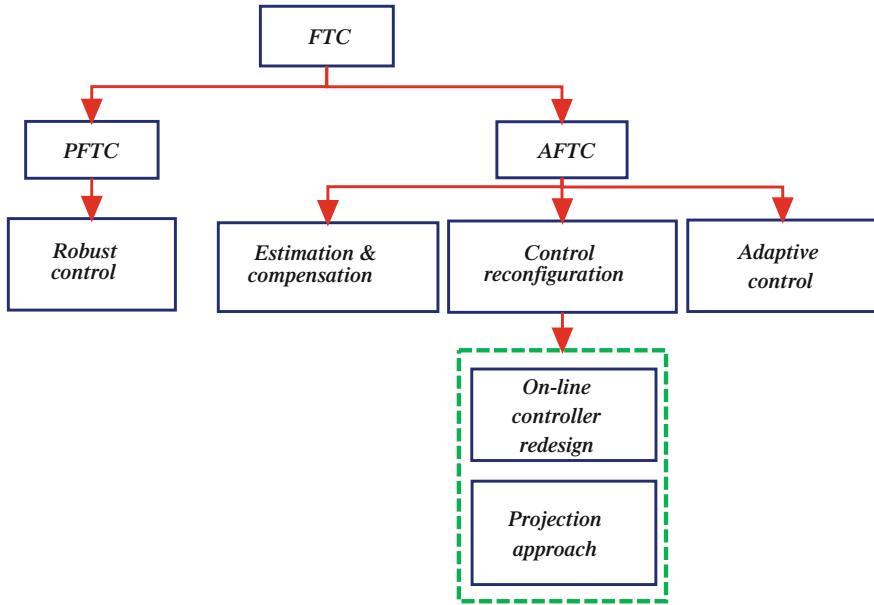
Fig. 7.3 General classification of FTC methods

blade pitch angle β and the wind speed v. The aerodynamic power captured by the rotor is given by:

$$P_{\text{cap}} = \frac{1}{2}\rho\pi R^2 C_p(\lambda, \beta)v^3 \tag{7.1}$$

where ρ is the air density, R is the rotor radius, and C_p is the power coefficient that depends on the blade pitch angle (β) and the tip-speed-ratio (λ) (TSR) defined as:

$$\lambda = \frac{\omega_r R}{v} \tag{7.2}$$

The aerodynamic torque is thus:

$$T_a = \frac{1}{2}\rho\pi R^3 C_q(\lambda, \beta)v^2 \tag{7.3}$$

where $C_q = \frac{C_p}{\lambda}$ is the torque coefficient.

The drive train is responsible for gearing up the rotor rotational speed to a higher generator rotational speed. The drive train model includes low and high speed shafts linked together by a gearbox modelled as a gear ratio. The state space model of the wind turbine drive train has the form:

$$
\begin{bmatrix} \dot{\omega}_r \\ \dot{\omega}_g \\ \dot{\theta}_\Delta \end{bmatrix} = \begin{bmatrix} a_{11} & a_{12} & a_{13} \\ a_{21} & a_{22} & a_{23} \\ a_{31} & a_{32} & a_{33} \end{bmatrix} \begin{bmatrix} \omega_r \\ \omega_g \\ \theta_\Delta \end{bmatrix} + \begin{bmatrix} b_{11} & 0 \\ 0 & b_{22} \\ 0 & 0 \end{bmatrix} \begin{bmatrix} T_a \\ T_g \end{bmatrix} \tag{7.4}
$$

where:

$$
a_{11} = -\frac{(B_{dt} + B_r)}{J_r} \quad a_{12} = \frac{B_{dt}}{n_g J_r} \quad a_{13} = -\frac{K_{dt}}{J_r} \quad a_{21} = \frac{B_{dt}}{n_g J_g}
$$

$$
a_{22} = -\frac{(B_{dt} + n_g B_g)}{n_g^2 J_g} \quad a_{23} = \frac{K_{dt}}{n_g J_g} \quad a_{31} = 1 \quad a_{32} = -\frac{1}{n_g}
$$

$$
a_{33} = 0 \qquad\qquad b_{11} = \frac{1}{J_r} \qquad b_{22} = -\frac{1}{J_g}
$$

where J_r is the rotor inertia, B_r is the rotor external damping, J_g is the generator inertia, ω_g and T_g are the generator speed and torque, B_g is the generator external damping, n_g is the gearbox ratio, K_{dt} is the torsion stiffness, B_{dt} is the torsion damping coefficient, and θ_Δ is the torsion angle.

The hydraulic pitch system is modelled as a second-order transfer function between the pitch angle β and its reference β_r as follows:

$$
\beta = \frac{\omega_n^2}{s^2 + 2\zeta\omega_n s + \omega_n^2} \beta_r \tag{7.5}
$$

where ζ is the damping factor and ω_n is the natural frequency. A transfer function is associated with each of the three pitch systems.

Finally, the generator subsystem is given by the following linear relation:

$$
\dot{T}_g = -\frac{1}{\tau_g} T_g + \frac{1}{\tau_g} T_{gr} \tag{7.6}
$$

Where T_{gr} is the generator torque reference signal and τ_g is the time constant.

For controller design purposes, the state space model of wind turbine is required. The non-linear model of a wind turbine is established by combining the individual systems given above. However, it is clear that the main source of non-linearity is the aerodynamic subsystem which is usually linearised in order to predict its effects on all model states. Hence, the state space model of wind turbine is given as:

$$
\left.\begin{array}{l} \dot{x} = Ax + Bu + Ev \\ y = Cx \end{array}\right\} \tag{7.7}
$$

where

$$A = \begin{bmatrix} -\frac{1}{\tau_g} & 0 & 0 & 0 & 0 & 0 \\ 0 & 0 & I & 0 & 0 & 0 \\ 0 & -\omega_n^2 I & -2\zeta\omega_n I & 0 & 0 & 0 \\ 0 & \frac{1}{J_r}\frac{\partial T_a}{\partial \beta} & 0 & -\frac{(B_{dt}+B_r)}{J_r}+\frac{1}{J_r}\frac{\partial T_a}{\partial \omega_r} & \frac{B_{dt}}{n_g J_r} & -\frac{K_{dt}}{J_r} \\ -\frac{1}{J_g} & 0 & 0 & \frac{B_{dt}}{n_g J_g} & -\frac{(B_{dt}+n_g B_g)}{n_g^2 J_g} & \frac{K_{dt}}{n_g J_g} \\ 0 & 0 & 0 & 1 & -\frac{1}{n_g} & 0 \end{bmatrix}$$

$$B = \begin{bmatrix} \frac{1}{\tau_g} & 0 \\ 0 & 0 \\ 0 & \omega_n^2 I \\ 0 & 0 \\ 0 & 0 \\ 0 & 0 \end{bmatrix}, \; E = \begin{bmatrix} 0 \\ 0 \\ 0 \\ \frac{1}{J_r}\frac{\partial T_a}{\partial v} \\ 0 \\ 0 \end{bmatrix}, \; C = \begin{bmatrix} 1 & 0 & 0 & 0 & 0 & 0 \\ 0 & 1 & 0 & 0 & 0 & 0 \\ 0 & 0 & 0 & 1 & 0 & 0 \\ 0 & 0 & 0 & 0 & 1 & 0 \end{bmatrix}, \; x = \begin{bmatrix} T_g \\ \beta \\ \dot{\beta} \\ \omega_r \\ \omega_g \\ \theta_\Delta \end{bmatrix},$$

$$u = \begin{bmatrix} T_{gr} \\ \beta_r \end{bmatrix}$$

$$\frac{\partial T_a}{\partial \beta} = \frac{1}{2\omega_r}\rho A v^3 \frac{\partial C_p}{\partial \beta}$$

$$\frac{\partial T_a}{\partial \omega_r} = \frac{1}{2\omega_r}\rho A v^3 \frac{\partial C_p}{\partial \omega_r} - \frac{1}{2\omega_r^2}\rho A v^3 C_p$$

$$\frac{\partial T_a}{\partial v} = \frac{1}{2\omega_r}\rho A v^3 \frac{\partial C_p}{\partial v} + \frac{3}{2\omega_r}\rho A v^2 C_p$$

where T_g is the generator torque, β is the pitch angle, ω_r and ω_g are the rotor and generator speed respectively, and θ_Δ is the torsional angle. It is clear from the state space model given in Eq. (7.7) that the system matrix A and the disturbance matrix E are not fixed matrices and depend on state variables, the uncontrollable input v, and the partial derivatives of the usually non-analytical function of λ and β, C_p. Hence, to cope with system non-linearity, a non-linear control strategy is required to achieve the aim and objectives of wind turbine operation.

Multiple-model based non-linear control is one of the approaches to verify non-linear controllers. The basic concept is to design local controller responsible for controlling the local behaviour of the non-linear system. In the literature, the Takagi-Sugeno (T-S) fuzzy inference modelling approach for dynamical systems [43] is an important and systematic tool for multiple model control. The T-S fuzzy model consists of a set of IF-THEN rules which represent local linear model of the non-linear system. The main feature of this approach is that it can express the local dynamics of each fuzzy rule by a linear system model. The overall fuzzy model is achieved by connecting the local linear model of each rule by membership

functions yielding the global model of the system. Details about T-S fuzzy modelling and control can be found in [44].

Several reasons lead to satisfaction that a Takagi-Sugeno (T-S) fuzzy non-linear control can cope with wind turbine control requirements, these are:

- The T-S fuzzy control makes use of a linear control strategy locally to produce a non-linear controller through fuzzy inference modelling, in terms of fuzzy multiple-modelling.
- By increasing the number of premise variables, the T-S fuzzy model can cover a wider range of operation scenarios which cannot be considered with a linear robust controller. For example, a linear robust controller is designed based on the linearised model derived at a specific operation point belong to the ideal operation curve given in Fig. 7.4. Hence, all other operating regions are considered as regions with modelling uncertainty, this controller design always degrades the nominal required performance in order to take good care of the modelling uncertainty. On the other hand, by considering the wind speed and the rotor speed as premise variables in the low wind speed range (*Region2*), the T-S fuzzy model can approximate the wind turbine model not only during its ideal operation curve but it can additionally cover the operation scenarios in which the system inputs and outputs deviated from ideal operation trajectory. This scenario usually happens during wind turbine operation, specifically for large inertia wind turbines, since the variation of wind speed is faster than rotor speed variations.
- The structure of the non-linear state space model given in Eq. (7.7) is characterised by its common input (B) and common output (C) matrices. This fact plays a vital role in simplification and conservatism reduction of T-S fuzzy
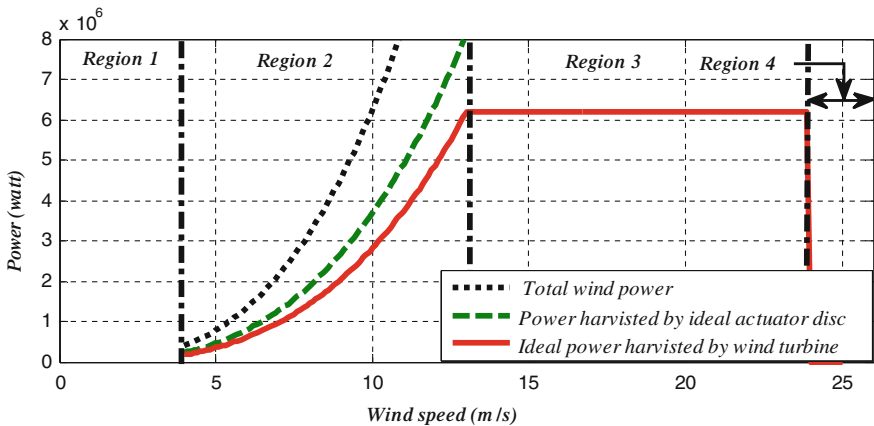
Fig. 7.4 Wind turbine region of operation

controller design. For example, the quadratic parameterisation dynamic output feedback controller can correspondingly be reduced to a linear parameterisation dynamic output feedback controller to control the wind turbine.

The aim is to develop a controller whose gain varies with wind speed. For example, in the low wind speed range of operation the control aim is to maximise the amount of power extracted from the available wind power through tracking the optimal rotor rotational speed reference signal. Hence, to derive the T-S model with minimum uncertainty, the wind speed (v) and the rotor speed (ω_r) are considered as fuzzy premise variables.

During the low wind speed of operation (*Region 2*) v varies within the operating range:

$$v \in [v_{\min}, v_{\max}]\text{m s}^{-1}$$

where in the benchmark wind turbine considered in this thesis $v_{\min} = 4\,\text{m s}^{-1}$ and $v_{\max} = 12.5\,\text{m s}^{-1}$. According to these limits the other premise variable (ω_r) is bounded by:

$$\omega_r \in [\omega_{\min}, \omega_{\max}]rad\,s^{-1}$$

where $\omega_{\min} = 0.56\,\text{rad s}^{-1}$ and $\omega_{\max} = 1.74\,\text{rad s}^{-1}$. The bounds of ω_r are determined using Eq. (7.2) using $\lambda_{\text{opt}} = 8$.

The membership function is selected as follows:

$$\left.\begin{aligned}
M_1 &= \frac{\omega_r - \omega_{\min}}{\omega_{\max} - \omega_{\min}} \\
M_2 &= 1 - M_1 \\
N_1 &= \frac{v - v_{\min}}{v_{\max} - v_{\min}} \\
N_2 &= 1 - N_1
\end{aligned}\right\} \tag{7.8}$$

Based on the two premise variables four local linear models of the wind turbine can be determined to approximate the non-linear system at different operating points in the low range of wind speed. Hence, Eq. (7.9) gives the four rule T-S fuzzy model of the non-linear wind turbine in Eq. (7.7):

$$\left.\begin{aligned}
\dot{x} &= \sum_{i=1}^{r} h_i(v, \omega_r)[A_i x + Bu + E_i v] \\
y &= Cx
\end{aligned}\right\} \tag{7.9}$$

where $h_1 = M_1 \cdot N_1, h_2 = M_1 \cdot N_2, h_3 = M_2 \cdot N_1$, and $h_4 = M_2 \cdot N_2$.
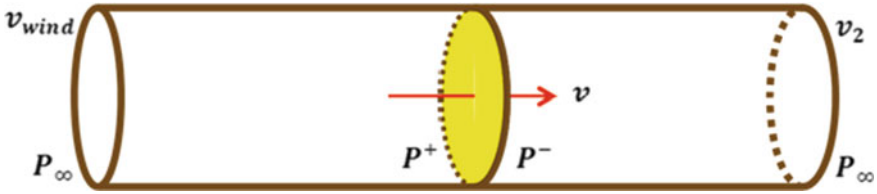
Fig. 7.5 Actuator disc

7.4 Wind Turbine Aerodynamic and Control

In order to best understand the wind turbine control challenges, the fundamental theory of the wind power extraction process and the upper bound of conversion efficiency $C_{p\max}(\lambda, \beta)$ of the wind power P_{wind} to mechanical power P_{cap} must first be clarified.

Basically, actuator disc theory is used to derive the P_{cap} given in Eq. (7.1) and the maximum $C_p(\lambda, \beta)$. The actuator disc is a generic device that has the ability to extract wind energy when it is immersed in streamlined airflow passing through a virtual tube (see Fig. 7.5).

Therefore, due to energy extraction, the downstream wind speed is necessarily slower than the upstream wind speed. However, the mass flow rate must be the same everywhere in the tube. Hence,

$$\rho \mathcal{A}_{\text{wind}} v_{\text{wind}} = \rho \mathcal{A} v = \rho \mathcal{A}_2 v_2 \tag{7.10}$$

where $\mathcal{A}_{\text{wind}}$, $\mathcal{A}$, and $\mathcal{A}_2$ are the upstream, disc, and downstream areas, respectively. The force or thrust (F_d) exerted by the wind on the actuator disc is given as:

$$F_d = \rho \mathcal{A} v (v_{\text{wind}} - v_2) \tag{7.11}$$

Equivalently, F_d can also be defined in term of pressure difference before (P^+) and after (P^-) the disc. Based on Bernoulli's equation, the total energy of the flow remains constant provided no work is done on the fluid. Hence, this equation can be applied upstream and downstream of the actuator disc as follows:

$$\left. \begin{aligned} \frac{1}{2}\rho v_{\text{wind}}^2 + P_\infty &= \frac{1}{2}\rho v^2 + P^+ \\ \frac{1}{2}\rho v_2^2 + P_\infty &= \frac{1}{2}\rho v^2 + P^- \end{aligned} \right\} \tag{7.12}$$

by taking the difference between expressions in Eq. (7.12), F_d can be rewritten as follows:

$$F_d = \mathcal{A}(P^+ - P^-) = \frac{1}{2}\rho \mathcal{A}(v_{\text{wind}}^2 - v_2^2) \tag{7.13a}$$

Assuming that v can be represented as:

$$\frac{v_2 + v_{\text{wind}}}{2} = v \tag{7.14b}$$

It then follows that the wind speed at the disc v and the downstream wind v_2 are related to the upstream wind v_{wind} as follows:

$$\left. \begin{array}{l} v = (1 - \alpha)v_{\text{wind}} \\ v_2 = (1 - 2\alpha)v_{\text{wind}} \end{array} \right\} \tag{7.15}$$

where α is known as the axial interference factor defined as the fractional increase in wind velocity between the free stream and the rotor plane. Using Eqs. (13) and (15) the power captured by the actuator disc is given by:

$$P_{\text{cap}} = \frac{1}{2}\rho A v^3 (4\alpha - 8\alpha^2 + 4\alpha^3) \tag{7.16}$$

the maximum power captured is obtained when $\frac{dP_{\text{cap}}}{d\alpha} = 0$, for which $\alpha = \frac{1}{3}$. Hence, by substituting α in Eq. (7.16) the ideal power captured by disc actuator will be:

$$P_{\text{cap}} = \frac{1}{2}\rho A v^3 \frac{16}{27} = 0.59 P_{\text{wind}} \tag{7.17}$$

Clearly, the three blade variable speed-variable pitch wind turbines are a special case of the actuator disc. In this special structure of actuator disc, the blade pitch angles (β), wind speed (v) and the rotor rotational speed (ω_r) are the main variables that affect the amount of the power captured. See Fig. 7.6.

Generally, wind turbine control objectives are functions of wind speed. For low wind speeds, the objective is to optimise wind power capture through the tracking of optimal generator speed signals. Once the wind speed increases above its nominal value the control objective moves to the rated regulating power. See Fig. 7.4.

Usually, the wind speed and rotor rotational speed ω_r are given in terms of the tip speed ratio λ (or TSR). Hence, the variation of power conversion efficiency with respect to λ and β is given either as a mathematical polynomial or as look-up table.
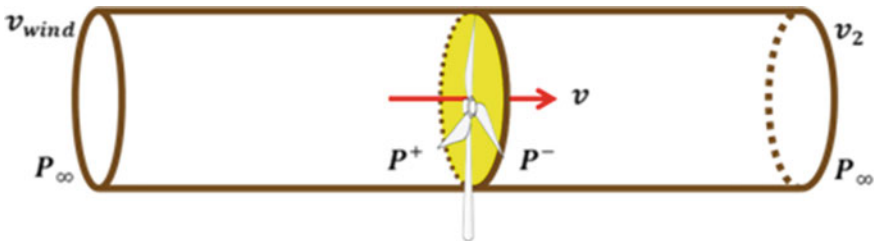
Fig. 7.6 Wind turbine power extraction
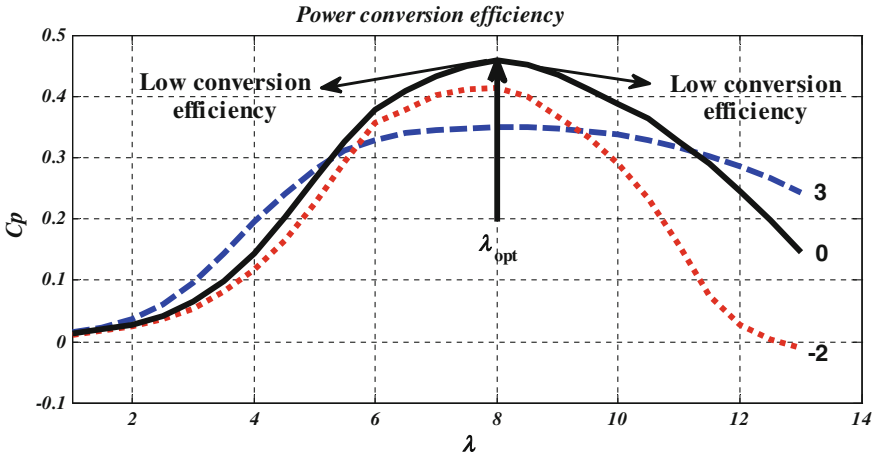
Fig. 7.7 Variation of C_p with respect to λ for $\beta = -2,0,3°$

Figure 7.7 below shows this relationship for the benchmark wind turbine considered in this chapter.

From Fig. 7.6 two points must be highlighted:

1. For low wind speeds, to maximise the amount of the captured wind power, the blade pitch angle β must be held at a fixed angle corresponding to maximum allowable conversion efficiency curve at which ($\beta = 0$). Additionally, the rotor speed must vary in proportional to the wind speed variation so that λ is kept in the vicinity of it optimal value (λ_{opt}). Specifically, the generator subsystem represents the actuator of the aerodynamic subsystem in the low range of wind speed that decelerates or just releases the aerodynamic subsystem rotation to adjust the variation of rotor speed, so that good tracking of the optimal rotor speed ensured. It should be noted that exact tracking of the optimal rotor speed leads to increasing the load on the drive train shafts and hence minimises the drive train life time. Moreover, exact tracking will also produce a highly fluctuating output power and produce a varying direction reference torque signals that can lead to abnormal generator operation [26].
2. For high wind speeds, it is possible to dissipate some proportion of the available wind power by changing the blade pitch angle to prevent the wind turbine operation from crossing over the rated power. However, to ensure good regulation performance, some control strategies use the generator torque control as a supplementary control signal to overcome the limited rate of change of blade pitch actuator.

The λ_{opt} is determined by relating the blade time t_b and the turbulence time t_w. t_b is the time required by the blade to take the position of the previous one and t_w is the time required to remove the disturbed wind component generated by the movement of the blade. See Fig. 7.8.

Fig. 7.8 The philosophy of λ_{opt}

$$t_b = \frac{2\pi}{n\,\omega r}$$
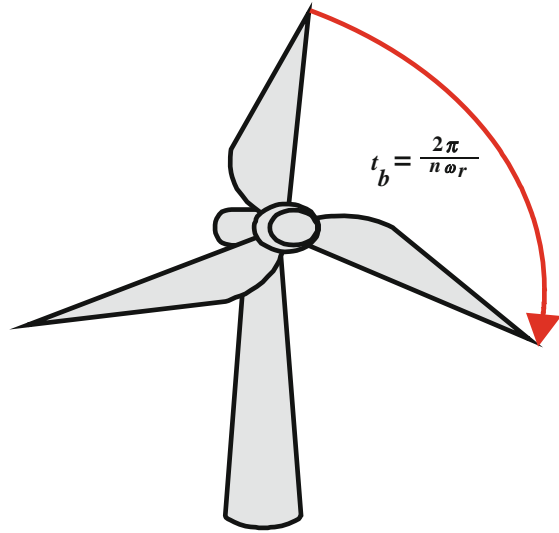
According to these two times, three operation scenarios can be recognised [11], these are:

1. $t_b > t_w$: This scenario corresponds to slow rotation in which some undisturbed wind passes the area swept by the rotor without harvesting its power content.
2. $t_b < t_w$: This scenario corresponds to fast rotation in which the blade passes through the disturbed wind component generated by the previous blade. In this case, the rotor acts as a rigid obstacle and prevents the undisturbed wind from passing through the rotor.
3. $t_b \approx t_w$: This scenario corresponds to the optimal operation in which the blade harvests the power from the re-established wind component.

Suppose the length of the disturbed wind is $S(m)$ and n is the number of blades, then t_b and t_w are obtained as follows:

$$\left.\begin{aligned} t_b &= \frac{2\pi}{\omega_r n} \\ t_w &= \frac{S}{v} \end{aligned}\right\} \tag{7.18}$$

by setting t_b equal to t_w, the optimal rotational speed thus given as:

$$\omega_{ropt} = \frac{2\pi v}{nS} \tag{7.19}$$

then λ_{opt} can be obtained as follows:

$$\lambda_{\text{opt}} = \frac{2\pi R}{nS} \tag{7.20}$$

Hence, wind turbines must be properly controlled to operate at their optimal wind tip speed ratio in order to extract as much wind power as possible. It should be noted that λ_{opt} is determined empirically by the wind turbine manufacturer since it is clear that all the parameters in Eq. (7.20) are dependent on the wind turbine structure. Consequently, the dependence of λ_{opt} on S causes a serious challenge in wind turbine control since S is highly dependent on the blade design. Hence, with turbine ageing any deformation in the blade structure causes permanent uncertainty in the value of λ_{opt}.

7.5 Investigation of the Effects of Some Faults Scenarios

As stated in Sect. 1.4, the controller optimises the power captured by controlling the rotor rotational speed by varying the reference generator torque T_{gr} so that the wind turbine rotor speed ω_r follows the optimal rotor speed given by:

$$\omega_{r\text{opt}} = \frac{\lambda_{\text{opt}} v}{R} \tag{7.21}$$

where $\omega_{r\text{opt}}$ and λ_{opt} are the optimal rotor speed and the optimal tip speed ratio. Moreover, the controller must be designed to have fault tolerance capability against probable fault scenarios that degrade the required closed-loop performance.

The following faults are considered and the proposed control strategies need to tolerate the fault effects so that good tracking performance to $\omega_{r\text{opt}}$ can be maintained.

- *Rotor speed sensor scaling fault:* the sensor scaling fault (decreasing or increasing) drive the turbine away from the optimal operation. It is very clear that the controller is designed to provide good tracking of $\omega_{r\text{opt}}$ (i.e. $e_t = \omega_{r-\text{measured}} - \omega_{\text{opt}} \approx 0$). However, due to the scale factor fault the controller now tries to force the faulty measurement to follow $\omega_{r\text{opt}}$ (i.e. if the scale faults are $\pm 10\%$ then $1.1 * \omega_r - \omega_{\text{opt}} \approx 0$ or $0.9 * \omega_r - \omega_{\text{opt}} \approx 0$) causing a decelerating or accelerating of the actual rotor speed and hence causing the wind turbine to operate away from the optimal value ω_{opt}. Additionally, more sever sensor scale faults can affect the structure of the wind turbine or guide the wind turbine to the cut-off region. For example, severe scale-down sensor faults cause the turbine to rotate faster according to the available wind speed. Hence, the fast rotation scenario means that the blade passes through the turbulence component of the previous blade before re-establishing the undisturbed wind speed. This induces excessive vibration of the overall structure of the wind turbine. On the other hand,
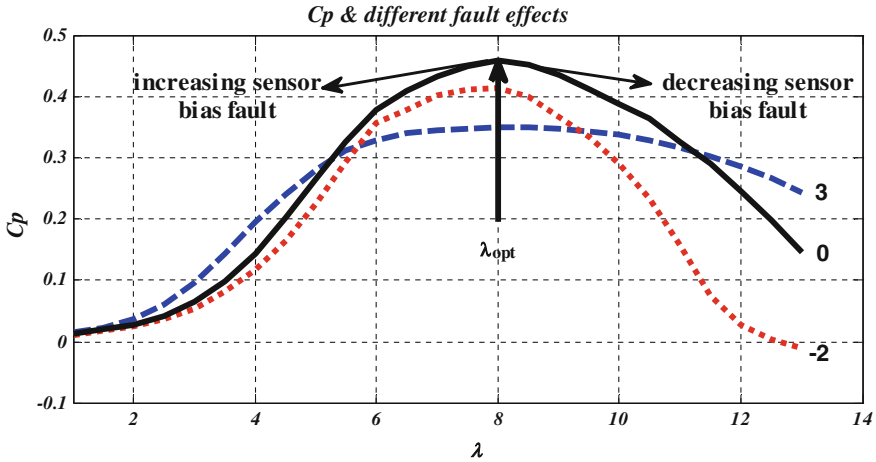
Fig. 7.9 The effect of sensor faults on power optimisation

in the scale-up sensor fault the control system slows down the rotor rotational speed. This in turn may lead to the wind turbine entering the cut-off region.

- *Fixed rotor speed sensor fault:* the effect of this fault scenario differs based on the fixed measured rotor speed (magnitude of stuck fault) and ω_{ropt} which in turn depends on wind speed. If ω_{ropt} is lower than the fixed rotor speed measurement then the controller will force the system to slow-down and this in turn may lead to the cut-off rotational speed being reached. On the other hand, if ω_{ropt} is higher than the fixed rotor speed then the controller will simply release the turbine to rotate according to the available wind speed without control.
- *Generator speed sensor bias fault:* the sensor bias fault (decreasing or increasing) affects the closed-loop performance of the wind turbine and hence the wind power conversion efficiency. However, the expected effect of this fault is probably less than the effect of the rotor speed sensor faults since the generator speed signal is part of the feedback signal and not compared directly with the reference optimal speed (i.e. not the objective signal).
- *Generator torque bias fault:* the effect of torque bias fault is similar to the effect of the rotor speed sensor fault. In this fault scenario the inner-loop generator controller minimises the difference between the T_{gr} and the measured generator torque T_{gm}. In fact, T_{gm} is not directly measured but obtained via soft sensing. Therefore, any bias in this measurement results in driving the system away from optimal operation. This results in a decrease of the wind turbine power conversion efficiency. Fortunately, from a global control standpoint, this fault appears as a scale actuator fault.

Figure 7.9 shows the effects of different fault scenarios on the optimal operation of wind turbine.

Clearly, the generator and rotor speed sensor scaling faults emulate the effect of the λ_{opt} uncertainty problem which arises in part due to wind turbine ageing and

blade deformation. Hence, even if the scaling fault is minor and does not lead to structural damage, the detection and tolerance of this fault can lead to maintain the harvested power at its optimal value.

Generally, the aim of all proposed FTC strategies in this chapter is to maintain the same control law during both faulty and fault-free cases. Estimators are used to simultaneously estimate the sensor fault signals and tolerate their effects on the output signal delivered to the input of the controller.

While the proposal makes use of measured wind speed, the fault estimator in these strategies is designed to be robust against the expected error between the measured wind speed and the effective wind speed (EWS). This is because the measured wind speed signal does not exactly represent the EWS signal.

7.6 T-S Fuzzy PMIO-Based Sensor FTC

This section describes a T-S fuzzy observer-based sensor FTC scheme designed to optimise the wind energy captured in the presence of generator and rotor speed sensor faults. To ensure good estimation of a wider than usual range of sensor faults, the FTTC strategy utilises the fuzzy PMIO. The nominal fuzzy controller remains unchanged during the faulty and fault-free cases. Although the proposed strategy is dedicated to controlling the wind turbine within the low range of wind speed (below rated wind speed), the proposed controller is useful as a supplementary control to assist the pitch control system as a means of regulating the rotor speed above the rated wind speed.

Recently, T-S fuzzy observer-based sensor FTC design has been proposed in [21], see Fig. 7.10. The method is based on evaluation of *two* residual signals generated using the *generalised observer* concept of [33] to switch the estimation from faulty to healthy observers with the assumption that no simultaneous sensor faults are occur. It is clear that switching between two different observers produces
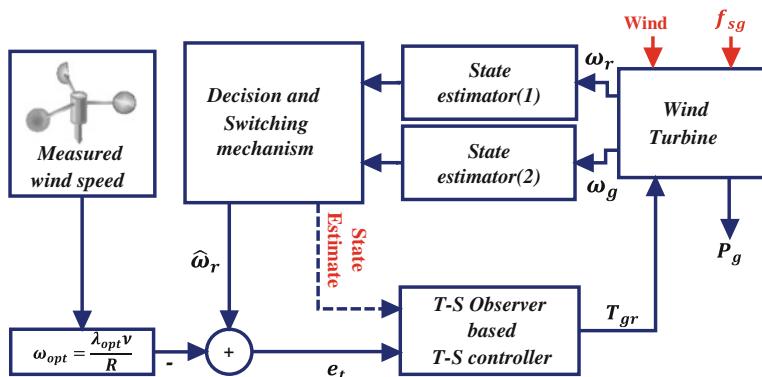
Fig. 7.10 Generalised observer-based wind turbine AFTC
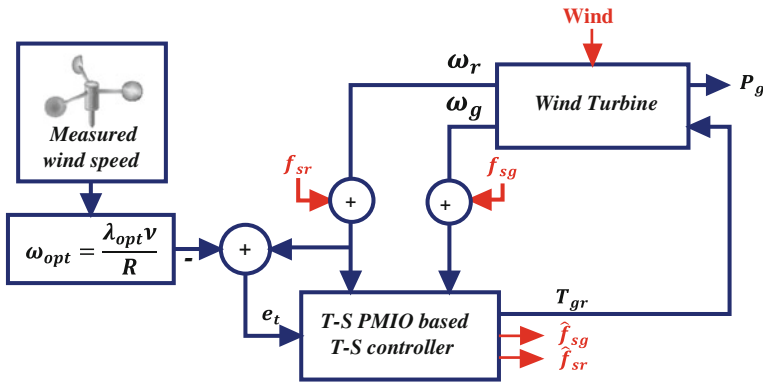
Fig. 7.11 Wind turbine PMIO based sensor FTC scheme

unavoidable spikes that specifically affect the drive train torsion of low inertia wind turbines. Also the performance of the proposed FTC strategy is highly affected by the robustness and the computation time of the residual evaluation unit. Moreover, the T-S model in this reference is derived based on measured wind speed which in turn causes clear modelling uncertainty since the wind varies stochastically and faster than wind turbine dynamic and hence it cannot schedule the controller commands appropriately. Furthermore, there is a significant probability of simultaneous occurrence of generator and rotor speed sensor faults.

Within the framework of the proposed strategies, the use of wind speed and rotor rotational speed as scheduling variables will ensure that the T-S fuzzy model can represents a wide range of operation scenario. Specifically, the model can cover cases in which the system operates away from the ideal power/wind speed characteristic shown in Fig. 7.4. In fact, large inertial wind turbines frequently operate away from their ideal power/wind characteristics and hence the use of two scheduling variables is the best approach to handle this challenge.

The main contributions involved in the proposed strategy are: (1) the use of the PMIO to hide or implicitly compensate the effect of drive train sensor faults. This obviates the need for residual evaluation and observer switching (see [21] for example). (2) The PMIO simultaneously estimates the states and the sensor fault signals. Hence, information about the fault severity can also be provided through the fault estimation signals. (3) The fuzzy PMIO scheme is shown to give good simultaneous state and abrupt sensor fault estimate. Figure 7.11 schematically illustrates the proposed strategy.

In this strategy, the controller forces the generator rotational speed to follow the optimal generator speed. Additionally, this strategy makes use of the measured wind speed as an approximation of the EWS.

As derived in Sect. 1.2, the T-S fuzzy model of the non-linear wind turbine system given in Eq. (7.20) with additive sensor can be expressed as:

$$\left. \begin{array}{l} \dot{x} = A(p) + Bu + E(p)v \\ y = Cx + D_f f_s \end{array} \right\} \tag{7.22}$$

$A(p) \in \mathcal{R}^{n*n}(= \sum_{i=1}^{r} h_i(p)A_i), B \in \mathcal{R}^{n*m}, E(p) \in \mathcal{R}^{n*m_v}(= \sum_{i=1}^{r} h_i(p)E_i), D_f \in \mathcal{R}^{l*g}$ and $C \in \mathcal{R}^{l*n}$ are known system matrices. r is the number of fuzzy rules and the term $h_i(p)$ is the weighting function of the ith fuzzy rule (as defined in Sect. 1.2) satisfying $\sum_{i=1}^{r} h_i(p) = 1$, and $1 \geq h_i(p) \geq 0$, for all i.

An augmented system consisting of the Eq. (7.22) and the tracking error integral $(e_t = \int (y_r - Sy))$ is defined as:

$$\left. \begin{array}{l} \dot{\bar{x}} = \bar{A}(p)\bar{x} + \bar{B}u + \bar{E}(p)v + Ry_r \\ \bar{y} = \bar{C}\bar{x} + \bar{D}_f f_s \end{array} \right\} \tag{7.23}$$

$$\bar{A}(p) = \begin{bmatrix} 0 & -SC \\ 0 & A(p) \end{bmatrix}, \bar{x} = \begin{bmatrix} e_t \\ x \end{bmatrix}, \bar{B} = \begin{bmatrix} 0 \\ B \end{bmatrix}, \bar{E}(p) = \begin{bmatrix} 0 \\ E(p) \end{bmatrix}, R = \begin{bmatrix} I \\ 0 \end{bmatrix}$$

$$\bar{C} = \begin{bmatrix} I_q & 0 \\ 0 & C \end{bmatrix}, \bar{D}_f = \begin{bmatrix} 0 \\ D_f \end{bmatrix}$$

where $S \in \mathcal{R}^{w*l}$ is used to define which output variable is considered to track the reference signal. Hence, the tracking problem is transferred to a fuzzy state feedback control, for which the proposed control signal is:

$$u = K(p)\hat{\bar{x}} \tag{7.24}$$

where $K(p) \in \mathcal{R}^{m*(n+w)}(= \sum_{i=1}^{r} h_i(p)K_i)$ is the controller gain and $\hat{\bar{x}} \in \mathcal{R}^{(n+w)}$is the estimated augmented state vector.

As described in [16], if it can be assumed that the qth derivative of the sensor fault signal is bounded, then an augmented state system comprising the states of the original local linear system and the qth derivative of the f_s, is given as follows:

$$\varphi_i = f_s^{q-i}(i = 1, 2, \ldots, q), \dot{\varphi}_1 = f_s^q; \dot{\varphi}_2 = \varphi_1; \dot{\varphi}_3 = \varphi_2; \ldots; \dot{\varphi}_q = \varphi_{q-1}$$

Then the system of Eq. (7.22) with the augmented fault derivative states will become:

$$\left. \begin{array}{l} \dot{x}_a = A_a(p)x_a + B_a u + E_a(p)v + R_a y_r + G f_s^q \\ y_a = C_a x_a \end{array} \right\} \tag{7.25}$$

where

$$x_a = \begin{bmatrix} \bar{x}^T & \varphi_1^T & \varphi_2^T & \varphi_3^T & \cdots & \varphi_q^T \end{bmatrix}^T \in \mathcal{R}^{\bar{n}}$$

$$A_a(p) = \begin{bmatrix} \bar{A}(p) & 0 & \cdots & 0 & 0 \\ 0 & 0 & \cdots & 0 & 0 \\ 0 & I & \cdots & 0 & 0 \\ \vdots & \vdots & \ddots & \vdots & \vdots \\ 0 & 0 & \cdots & I & 0 \end{bmatrix} \in \mathcal{R}^{\bar{n} \times \bar{n}}$$

$$B_a = \begin{bmatrix} \bar{B}^T & 0 & 0 & \cdots & 0 \end{bmatrix}^T \in \mathcal{R}^{\bar{n} \times m}$$
$$E_a(p) = \begin{bmatrix} \bar{E}^T & 0 & 0 & \cdots & 0 \end{bmatrix}^T \in \mathcal{R}^{\bar{n} \times m_v}$$
$$G = \begin{bmatrix} 0 & I_k & 0 & \cdots & 0 \end{bmatrix}^T \in \mathcal{R}^{\bar{n} \times g}$$
$$C_a = \begin{bmatrix} \bar{C} & 0 & 0 & \cdots & \bar{D}_f \end{bmatrix} \in \mathcal{R}^{l * \bar{n}}$$
$$\bar{n} = (n + w) + gq$$

The following T-S fuzzy PMIO is proposed to simultaneously estimate the system states and sensor faults:

$$\left.\begin{array}{l} \dot{\hat{x}}_a = A_a(p)\hat{x}_a + B_a u + E_a(p)v + R_a y_r + L_a(p)(y_a - \hat{y}_a) \\ \hat{y}_a = C_a x_a \end{array}\right\} \tag{7.26}$$

The state estimation error dynamics are obtained by subtracting Eq. (7.26) from Eq. (7.25) to yield:

$$\dot{e}_x = (A_a(p) - L_a(p)C_a)e_x + Gf_s^q + E_a(p)e_v \tag{7.27}$$

where e_v is the difference between the effective wind speed and the measured wind speed (v). The augmented system combining the augmented state space system [25], the controller [24], and the state estimation error [27] is given by:

$$\dot{\tilde{x}}_a(t) = \sum_{i=1}^{r} h_i(p)\{\tilde{A}_i \tilde{x}_a + \tilde{N}_i \tilde{d}\} \tag{7.28}$$

where:

$$\tilde{A}_i = \begin{bmatrix} \bar{A}(p) + \bar{B}K(p) & -\bar{B}[K(p)0_{m \times q}] \\ 0 & A_a(p) - L_a(p)C_a \end{bmatrix}$$

$$\tilde{x}_a = \begin{bmatrix} \bar{x} \\ e_x \end{bmatrix}, \tilde{N}_i = \begin{bmatrix} \bar{E}(p) & 0 & R & 0 \\ 0 & E_a(p) & 0 & G \end{bmatrix}, \tilde{d} = \begin{bmatrix} v \\ e_v \\ y_r \\ f_s^q \end{bmatrix}$$

The objective here is to compute the gains $L_a(p)$ and $K(p)$ such that the effect of the input $\tilde{d}$ in Eq. (7.28) is attenuated below the desired level γ, to ensure robust stabilisation performance.

Theorem 8.1: For $t > 0$ and $h_i(p)h_j(p) \neq 0$, The closed-loop fuzzy system in [28] is stable and the H_∞ performance is guaranteed with an attenuation level, provided that the signal $(\tilde{d})$ is bounded, if there exist SPD matrices P_1, P_2, matrices H_{ai}, Y_i, and scalar satisfying the following LMI constraints (7.29) and (7.30):

Minimise, such that:

$$P_1 > 0, \ P_2 > 0 \tag{7.29}$$

$$
\begin{bmatrix}
\Psi_{11} & \Psi_{12} & \bar{E}(p) & 0 & R & 0 & 0 & 0 & 0 & 0 & 0 & X_1 C_p^T \\
* & -2\mu\bar{X}_1 & 0 & 0 & 0 & 0 & \mu I & 0 & 0 & 0 & 0 & 0 \\
* & * & -2\mu I & 0 & 0 & 0 & 0 & \mu I & 0 & 0 & 0 & 0 \\
* & * & * & -2\mu I & 0 & 0 & 0 & 0 & \mu I & 0 & 0 & 0 \\
* & * & * & * & -2\mu I & 0 & 0 & 0 & 0 & \mu I & 0 & 0 \\
* & * & * & * & * & -2\mu I & 0 & 0 & 0 & 0 & \mu I & 0 \\
* & * & * & * & * & * & \Psi_{55} & 0 & E_a(p) & 0 & P_2 G & 0 \\
* & * & * & * & * & * & * & -\gamma I & 0 & 0 & 0 & 0 \\
* & * & * & * & * & * & * & * & -\gamma I & 0 & 0 & 0 \\
* & * & * & * & * & * & * & * & * & -\gamma I & 0 & 0 \\
* & * & * & * & * & * & * & * & * & * & -\gamma I & 0 \\
* & * & * & * & * & * & * & * & * & * & * & -\gamma I
\end{bmatrix} < 0
$$

$$\tag{7.30}$$

where: $K_i = Y_i X_1^{-1}, L_a = P_2^{-1} H_{ai}, X_1 = P_1^{-1}, \bar{X}_1 = \text{diagonal}(X_1, I_{q \times q})$
$\Psi_{11} = \bar{A}_i X_1 + (\bar{A}_i X_1)^T + \bar{B} Y_i + (\bar{B} Y_i)^T; \Psi_{12} = [-\bar{B} Y_i \quad 0];$
$\Psi_{55} = P_2 A_{ai} + (P_2 A_{ai})^T - H_{ai} C_a - (H_{ai} C_a)^T.$

Proof From Theorem 1, to achieve the performance and required closed-loop stability of 27, the following inequality must hold [13]:

$$\dot{\upsilon}(\tilde{x}_a) + \frac{1}{\gamma} \tilde{x}_a^T C_p^T C_p \tilde{x}_a - \gamma \tilde{d}^T \tilde{d} < 0 \tag{30}$$

where $\dot{v}(\tilde{x}_a)$ is the time derivative of the candidate Lyapunov function $(v(\tilde{x}_a) = \tilde{x}_a^T \bar{P} \tilde{x}_a$, where $\bar{P} > 0$) for the augmented system 27. Using Eq. (7.27), inequality 30 becomes:

$$\dot{v}(\tilde{x}_a) = \sum_{i=1}^{r} \left\{ \tilde{x}_a^T \left(\tilde{A}_i^T \bar{P} + \bar{P} \tilde{A}_i \right) \tilde{x}_a + \tilde{x}_a^T \bar{P} \tilde{N}_i \tilde{d} + \tilde{d}^T \tilde{N}_i^T \bar{P} \tilde{x}_a \right\} \tag{7.31}$$

After simple manipulation, inequality Eq. (7.30) implies that the inequality Eq. (7.32) must hold:

$$\begin{bmatrix} \tilde{A}_{ij}^T \bar{P} + \bar{P} \tilde{A}_{ij} + \frac{1}{\gamma} I & \bar{P} \tilde{N}_{ij} \\ \tilde{N}_{ij}^T \bar{P} & -\gamma I \end{bmatrix} < 0 \tag{7.32}$$

To be consistent with [27] $\bar{P}$ is structured as follows:

$$\bar{P} = \begin{bmatrix} P_1 & 0 \\ 0 & P_2 \end{bmatrix} > 0 \tag{7.33}$$

Then after simple manipulation and using the variable change $(H_{ai} = P_2 L_a(p))$ the inequality [32] can be re-formulated as:

$$\Pi_{ij} = \begin{bmatrix} \Omega_{11} & -P_1[\bar{B}K_j 0] & P_1 \bar{E}(p) & P_1 R & 0 \\ * & \Omega_{22} & 0 & 0 & P_2 G \\ * & * & -\gamma I & 0 & 0 \\ * & * & * & -\gamma I & 0 \\ 0 & (P_2 G)^T & 0 & 0 & -\gamma I \end{bmatrix} < 0 \tag{7.34}$$

where:

$$\Omega_{11} = \bar{A}_i X_1 + (\bar{A}_i X_1)^T + \bar{B} Y_i + (\bar{B} Y_i)^T + \frac{1}{\gamma} C_p^T C_p$$

$$\Omega_{22} = P_2 A_{ai} + (P_2 A_{ai})^T - \bar{H}_i C_a - (\bar{H}_i C_a)^T$$

A single step design formulation of the matrix inequality in [34] is proposed to avoid the complexity of separate design steps characterised by repeated iteration to determine the gains required. Hence, Π_{ij} as shown in [34] becomes:

$$\Pi_{ij} = \begin{bmatrix} \Pi_{11} & \Pi_{12} \\ * & \Pi_{22} \end{bmatrix} \tag{7.35}$$

where

$$\Pi_{11} = \Omega_{11}; \Pi_{12} = \begin{bmatrix} -P_1 \begin{bmatrix} \bar{B} K_j & 0 \end{bmatrix} & P_1 \bar{E}(p) & P_1 R & 0 \end{bmatrix}$$

$$\Pi_{22} = \text{lower right block}$$

to do variable change, the following Lemma is required:

Lemma 1 (Congruence) *Consider two matrices P and Q, if P is positive definite and if Q is a full column rank matrix, then the matrix* $Q * P * Q^T$ *is positive definite.*

Let $Q = \begin{bmatrix} P_1^{-1} & 0 \\ 0 & X \end{bmatrix}$, and $X = \begin{bmatrix} \bar{X}_1 & 0 & 0 & 0 \\ 0 & I & 0 & 0 \\ 0 & 0 & I & 0 \\ 0 & 0 & 0 & I \end{bmatrix}$

Then $Q * \Pi_{ij} * Q^T < 0$ is also true and can be written as:

$$\begin{bmatrix} P_1^{-1} \Pi_{11} P_1^{-1} & P_1^{-1} \Pi_{12} X \\ * & X \Pi_{22} X \end{bmatrix} < 0 \tag{7.36}$$

Inequality [36] implies that $\Pi_{22} < 0$ so that the following inequality holds true [18, 24]:

$$\left(X + \mu \Pi_{22}^{-1} \right)^T \Pi_{22} \left(X + \mu \Pi_{22}^{-1} \right) \le 0 \Leftrightarrow X \Pi_{22} X \le -2\mu X - \mu^2 \Pi_{22}^{-1} \tag{7.37}$$

where μ is a scalar.

By substituting [37] into [36] and using the Schur complement Theorem, then [36] holds if the following inequality holds:

$$\begin{bmatrix} P_1^{-1} \Pi_{11} P_1^{-1} & P_1^{-1} \Pi_{12} X & 0 \\ X \Pi_{12} P_1^{-1} & -2\mu X & \mu I \\ 0 & \mu I & \Pi_{22} \end{bmatrix} < 0 \tag{7.38}$$

After substitution for $\Pi_{11}, \Pi_{12}, \Pi_{12}, \Pi_{22}$ from [35] and by simple manipulation, the LMI in [29] is obtained. This completes the proof

7.6.1 Simulation Results

The rotor and generator sensor faults are represented by two-scale errors. The scale factors of 1.1 and 0.9 are multiplied by the simulated real generator and rotor rotational speeds. The expected fault effects represent a deviation of the wind turbine from the optimal operation. Figure 7.2 shows how the wind turbine operation is affected by the two fault scenarios and helps to illustrate the success of
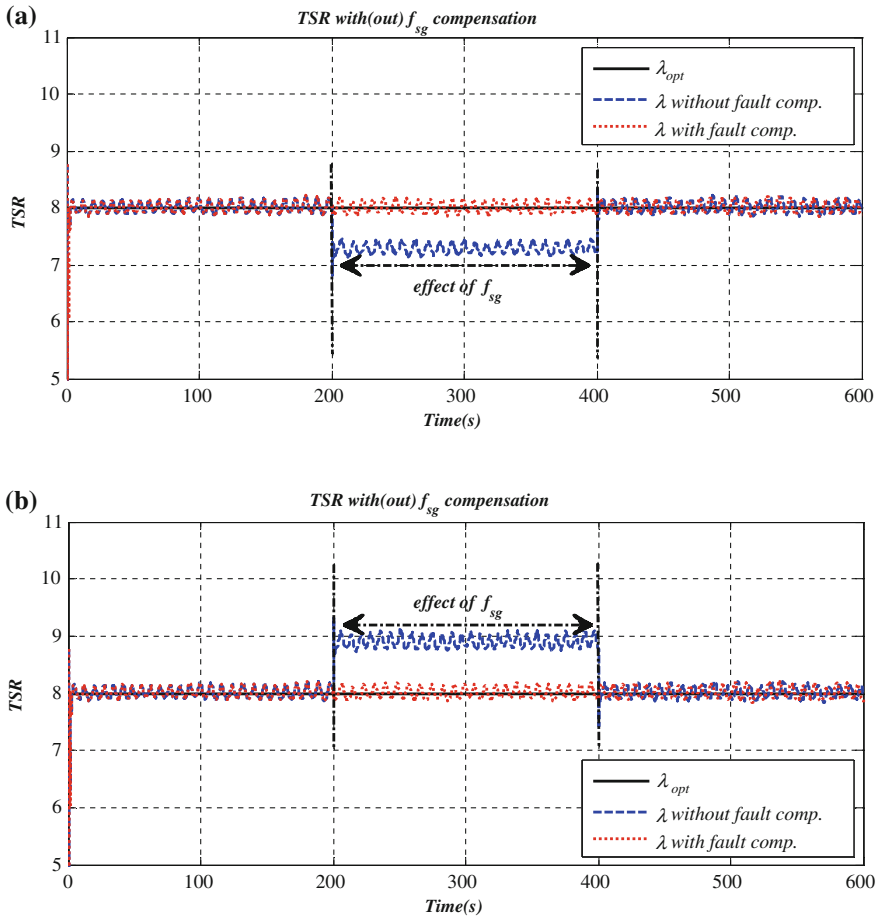
Fig. 7.12 Effect of 1.1 **a** and 0.9 **b** sensor scale faults with(out) fault compensation

the proposed strategy to tolerate the effects of sensor faults and maintain optimal wind turbine operation (Fig. 7.12).

It is clear that the 1.1 scale sensor fault causes a deceleration of ω_r & ω_g. Based on the faulty measurement, the controller forces the turbine to reduce the rotational speed by increasing the reference generator torque (the generator acts with a breaking torque that can decelerate or release the aerodynamic subsystem) which in turn increases the drive train load. Hence, although the sensor fault is a scale-up fault, the actual rotational speeds of the generator and rotor are decelerated as a result of the dependence of the controller on the faulty measured signal. The effect of this fault scenario is shown in Fig. 7.13 without sensor fault compensation.

Conversely, the 0.9 scale sensor fault causes acceleration of ω_r & ω_g since, based on faulty measurement; the controller releases the aerodynamic subsystem

(a)

(b)
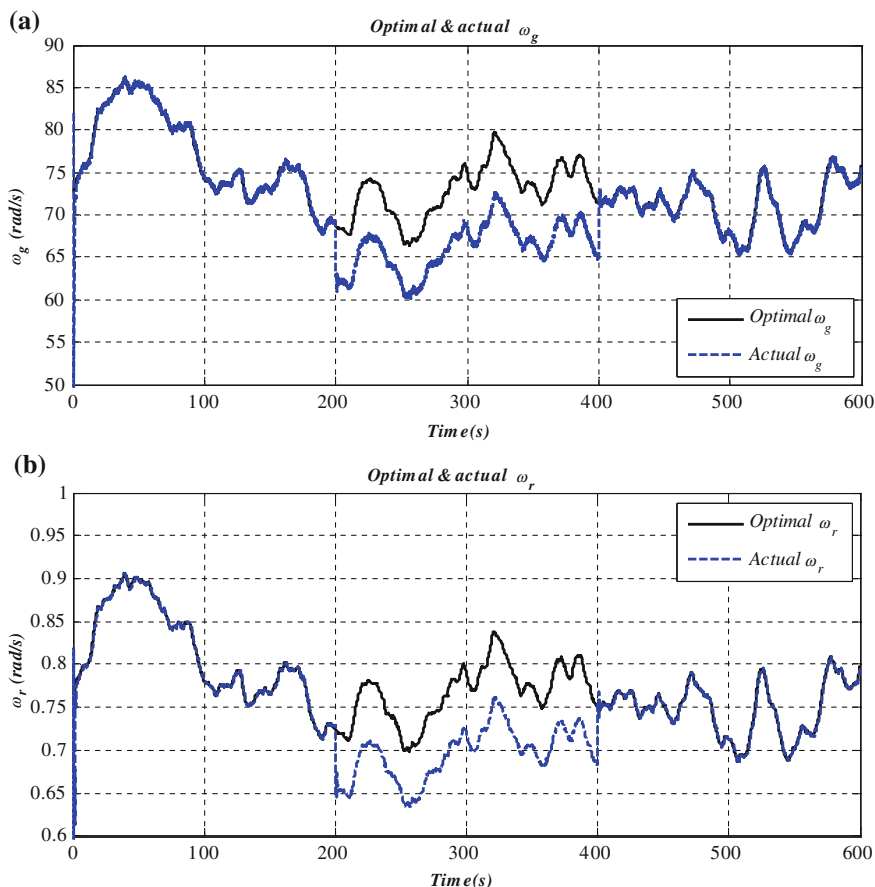
Fig. 7.13 1.1 sensor scale fault decelerate ω_g **a** and ω_r **b**

to rotate according to the available wind speed. Figure 7.14 shows the effect of the 0.9 sensor fault without compensation. On the other hand Fig. 7.15, shows the time variations of ω_r & ω_g in response to the proposed sensor FTTC strategy.

The generator rotational speed sensor fault estimation signals for both 0.9 and 1.1 scale factor fault scenarios are shown in Fig. 7.16.

The T-S PMIO can provide information about the fault severity via the fault estimation signal. This is achieved through taking the ratio between the measured generator speed and the estimated signal. Hence, if there are no faults the ratio should be 1 otherwise any deviation from unity indicates the occurrence of the fault and the magnitude of the deviation represents the fault severity. Figure 7.17 shows the fault evaluation signal for both fault scenarios.

It should be noted that maintaining state estimation without changes during the whole range of operation is due to the fact that the fuzzy PMIO performs implicit
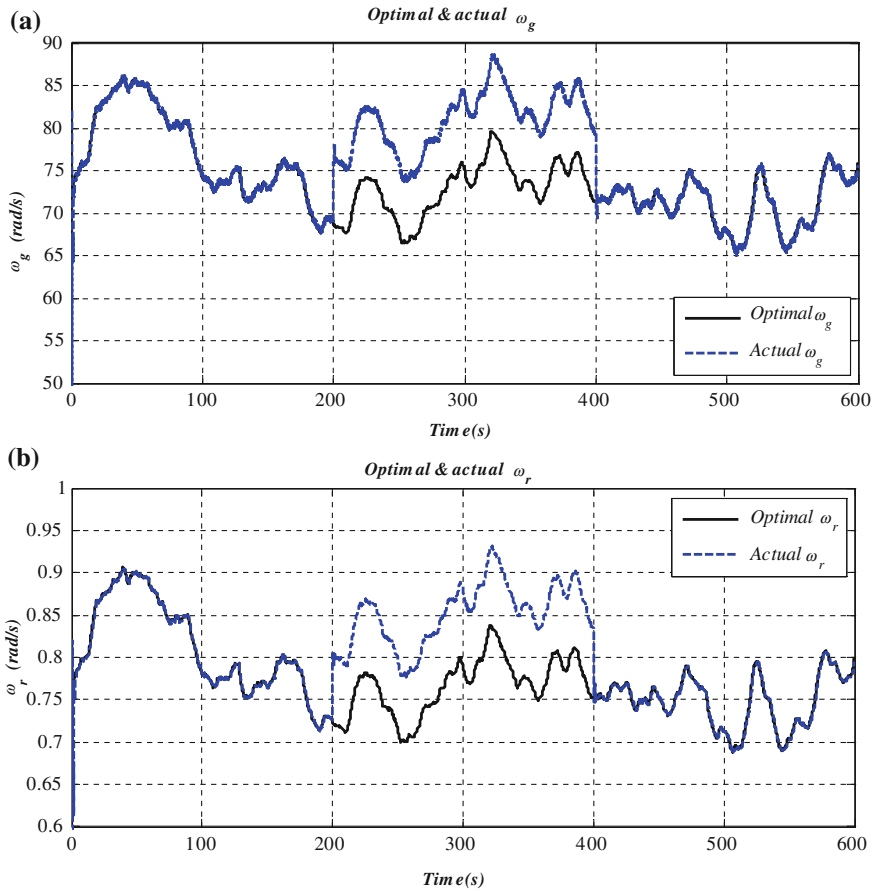
Fig. 7.14 0.9 sensor bias fault accelerate ω_g **a** and ω_r **b**

fault estimation and compensation of sensor faults from the input of PMIO. This fact is clearly interpreted from the error signal $(y_a - C_a \hat{x}_a)$ which can be rewritten as $(\bar{C}\bar{x} + \bar{D}f_s - \bar{C}\hat{\bar{x}} - \bar{D}\hat{f}_s)$, then as long as there are no sensor faults, $\hat{f}_s = 0$. However, once a sensor fault occurs the fault estimation $\hat{f}_s$ compensates the effect of the fault signal f_s and hence the observer always receives a fault-free error signal.
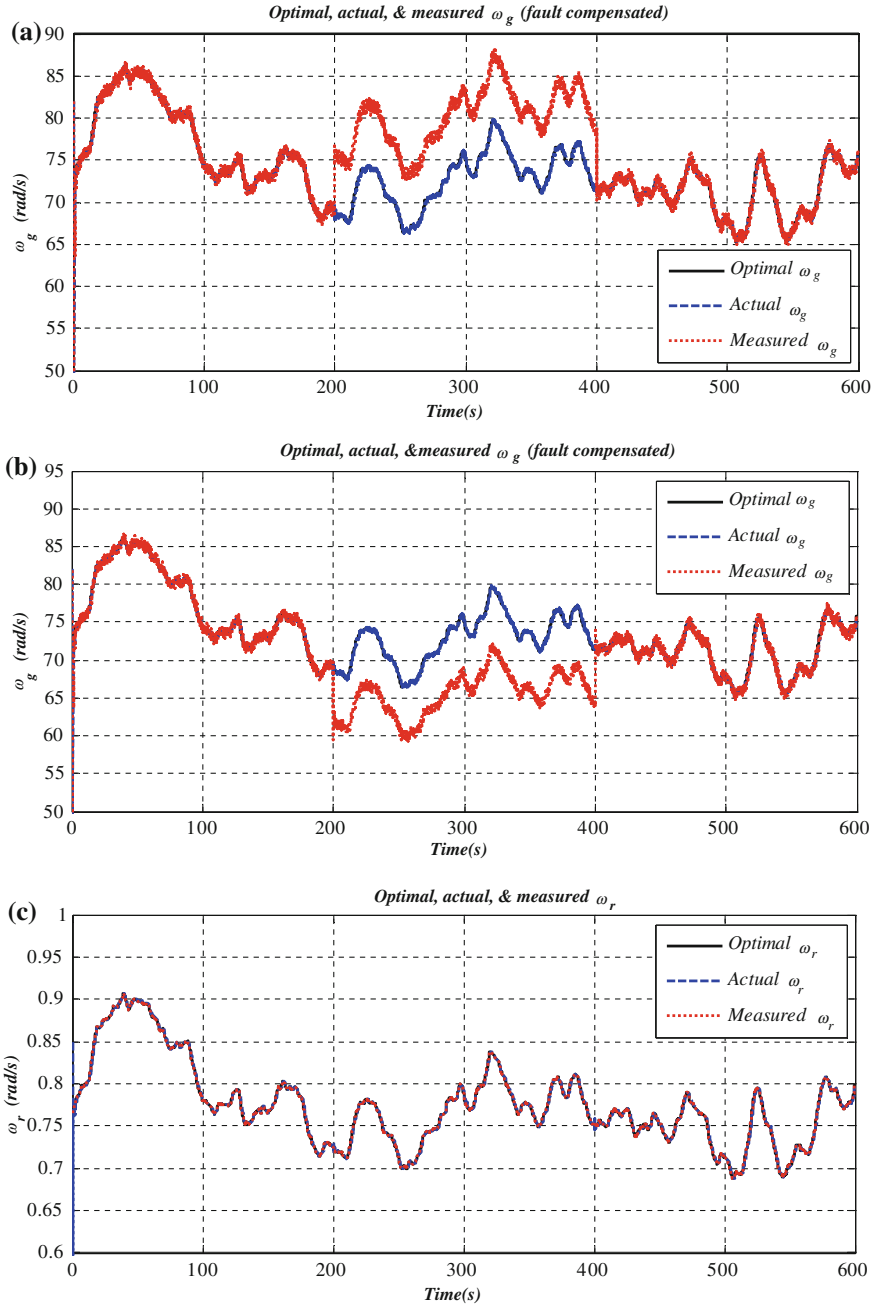
Fig. 7.15 Actual, optimal, and measured ω_g **a**, **b** and ω_r **c** using the proposed sensor FTC strategy
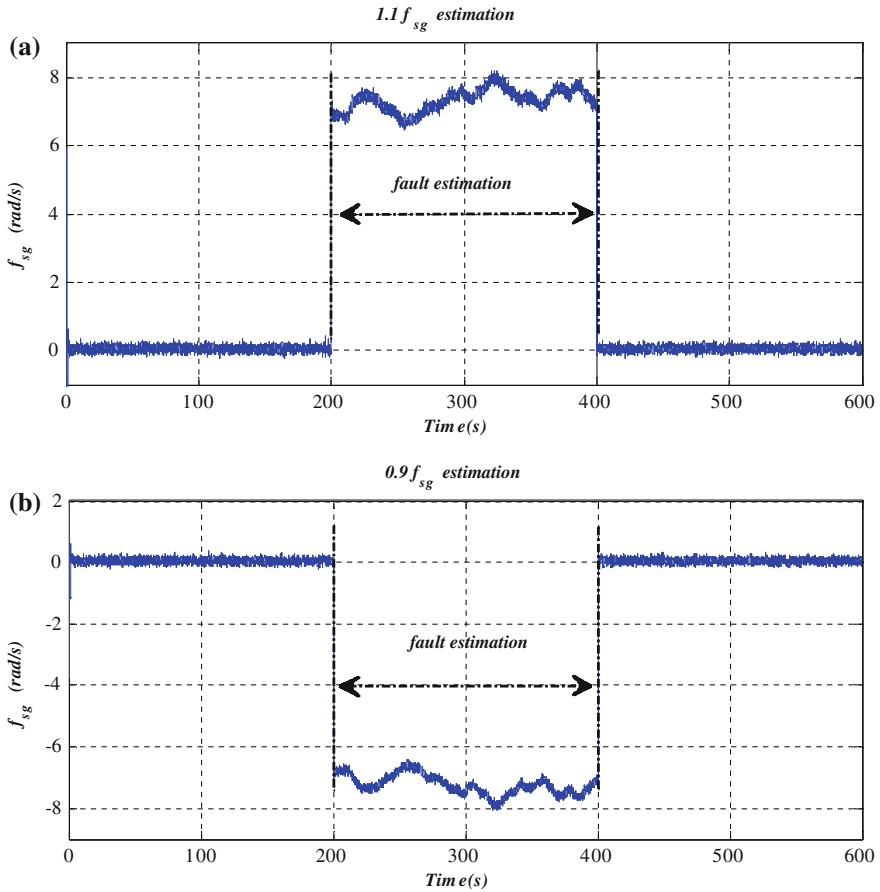
Fig. 7.16 Estimation of 1.1 **a** and 0.9 **b** sensor bias faults

7.7 Conclusions

In this chapter, the concept of wind turbine operation, the definition of the control problems, modes of operation and the non-linear and T-S fuzzy model of wind turbine are presented.

Generally, wind turbine control objectives are functions of wind speed. For low wind speeds, the objective is to optimise wind power capture through the tracking of optimal rotor speed signals. Once the wind speed increases above its nominal value the control objective moves to the rated regulating power.

Specifically, in the low wind speed range of operation, the controller optimises power capture through controlling the generator torque so that the wind turbine rotor speed follows the optimal rotor speed.

(a)

(b)
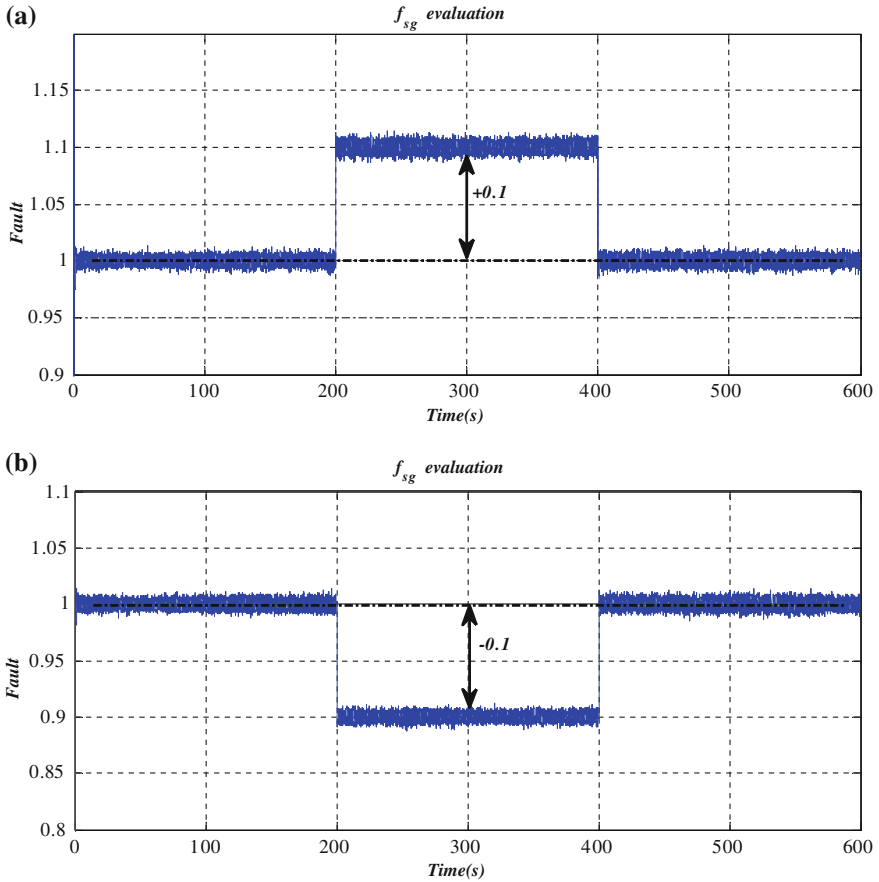
Fig. 7.17 Deviation of 1.1 (**a**) and 0.9 (**b**) sensor measurements from unity

In fact, from a control stand point, the power optimisation problem is a tracking control problem. However, several design constraints must be taken into account in the design of the wind turbine power maximization controller, these are:

a. Wind turbines are characterised by their non-linear aerodynamics and have a stochastic and uncontrollable driving force as input in the form of EWS. This limits the ability of linear control strategies to maintain acceptable performance over a wide range of wind speed.
b. Due to the common input common output matrices of wind turbine model the conservatism of T-S fuzzy estimation and control is highly reduced.
c. Owing to the direct effect of wind turbine components faults on the wind power conversion efficiency, the designed control strategy must be capable of tolerating different expected fault effects.

In addition to an evaluation of the fault effects, this chapter presents several contributions to the problem of sustainable wind turbine based on FTTC. The advantages of the use of PMIO based sensor FTC over the generalised observer-based sensor FTC are clearly given as: (i) Obviate the need for residual evaluation and observer switching; (ii) Ability to tolerate simultaneous generator and rotor rotational speed sensor faults; (iii) The PMIO simultaneously estimates the states and the sensor fault signals. Hence, information about the fault severity can also be obtained through the fault estimation signals, and (iv) The new fuzzy PMIO scheme is shown to cover a wide range of sensor fault scenarios.

7.8 Future Research

Although in this chapter new strategy has been proposed to overcome several challenges involved within the FTC framework, some improvements are still required to handle further challenges. Further research suggestions are addressed as follows:

- Owing to the presence of several redundant measurements in wind turbine systems, designing an integrated FDD/FTC based static virtual sensor is one of the approaches that can maintain the nominal performance of wind turbine control over a wide range of operation conditions.
- The problem of uncertainty of λ_{opt} due to turbine ageing and blade deformation together with the uncertainty in the measured wind speed represent real challenges to power optimisation control problem. Therefore, robust estimation of these variables based on the wind turbine aerodynamic subsystem can ensure good power transformation performance.
- Due to the ability of sliding mode control (SMC) to tolerate matched faults without the need for additional analytical redundancy, the use of SMC within fault estimation and compensation framework could substantially enhance the fault tolerance capability of the control system.

References

1. Ahmed-Zaid F, Ioannou P, Gousman K, Rooney R (1991) Accommodation of failures in the F-16 aircraft using adaptive control. IEEE Control Syst 11(1):73–78
2. Alwi H, Edwards C (2008) Fault tolerant control using sliding modes with on-line control allocation. Automatica 44(7):1859–1866
3. Amirat Y, Benbouzid MEH, Al-Ahmar E, Bensaker B, Turri S (2009) A brief status on condition monitoring and fault diagnosis in wind energy conversion systems. Renew Sustain Energy Rev 13(9):2629–2636
4. Benosman M, Lum KY (2010) Passive actuators' fault-tolerant control for affine nonlinear systems. IEEE Trans Control Syst Technol 18(1):152–163

5. Bianchi DF, De Battista H, Mantz JR (2007) Wind turbine control systems: principles. Springer, Modelling and Gain Scheduling Design
6. Blanke M, Kinnaert M, Lunze J, Staroswiecki M (2006) Diagnosis and fault-tolerant control. Springer, London
7. Boskovic JD, Mehra RK (1999) Stable multiple model adaptive flight control for accommodation of a large class of control effector failures. In: Proceedings of the American control conference, San Diego, California, 2–4 June 1920–1924
8. Boskovic, JD, Mehra RK (2002) An adaptive retrofit reconfigurable flight controller. In: Proceedings of the 41st IEEE conference on decision and control, Las Vegas, Nevada, 1257–1262. 10–13 Dec 2002
9. Bossanyi EA, Ramtharan G, Savini B (2009) The importance of control in wind turbine design and loading. In: 17th Mediterranean conference on control and automation, Thessaloniki, Greece, 1269–1274. 24–26 June 2009
10. Burton T, Sharpe D, Jenkins N, Bossanyi E (2001) Wind energy handbook. Wiley, Chichester
11. Carriveau R (2011) Fundamental and advanced topics in wind power. Intech, Rijeka
12. Caselitz P, Giebhardt J (2005) Rotor condition monitoring for improved operational safety of offshore wind energy converters. J Solar Energy Eng 127(2):253–261
13. Ding SX (2008) Model-based fault diagnosis techniques design schemes, algorithms, and tools. Springer, Berlin
14. Djurovic S, Crabtree CJ, Tavner PJ, Smith AC (2012) Condition monitoring of wind turbine induction generators with rotor electrical asymmetry. Renew Power Generation, IET 6(4):207–216
15. Gao Z, Ding SX (2007) Actuator fault robust estimation and fault-tolerant control for a class of nonlinear descriptor systems. Automatica 43(5):912–920
16. Gao Z, Ding SX, Ma Y (2007) Robust fault estimation approach and its application in vehicle lateral dynamic systems. Optim Control Appl Methods 28(3):143–156
17. Guang-Hong Y, Dan Y (2010) Reliable H_∞ control of linear systems with adaptive mechanism. IEEE Trans Automatic Control 55(1):242–247
18. Guerra TM, Kruszewski A, Vermeiren L, Tirmant H (2006) Conditions of output stabilization for nonlinear models in the Takagi-Sugeno's form. Fuzzy Sets Syst 157(9):1248–1259
19. Jiang B, Staroswiecki M, Cocquempot V (2006) Fault accommodation for nonlinear dynamic systems. IEEE Trans Autom Control 51(9):1578–1583
20. Johnson KE, Fleming PA (2011) Development, implementation, and testing of fault detection strategies on the National Wind Technology Center's controls advanced research turbines. Mechatronics 21(4):728–736
21. Kamal E, Aitouche A, Ghorbani R, Bayart M (2012) Robust fuzzy fault-tolerant control of wind energy conversion systems subject to sensor faults. IEEE Trans Sustainable Energy 3(2):231–241
22. Li JL, Yang GH (2012) Adaptive actuator failure accommodation for linear systems with parameter uncertainties. IET Control Theory Appl 6(2):274–285
23. Lunze J, Steffen T (2006) Control reconfiguration after actuator failures using disturbance decoupling methods. IEEE Trans Autom Control 51(10):1590–1601
24. Mansouri B, Manamanni N, Guelton K, Djemai M (2008) Robust pole placement controller design in LMI region for uncertain and disturbed switched systems. Nonlinear Anal Hybrid Syst 2(4):1136–1143
25. Maybeck PS, Stevens RD (1991) Reconfigurable flight control via multiple model adaptive control methods. IEEE Trans Aerosp Electron Syst 27(3):470–480
26. Munteanu I, Bratcu A, Cutululis N-A, Ceanga E (2008) Optimal control of wind energy systems: towards a global approach. Springer, London
27. Niemann H, Stoustrup J (2005) Passive fault tolerant control of a double inverted pendulum—a case study. Control Eng Pract 13(8):1047–1059
28. Noura H, Sauter D, Hamelin F, Theilliol D (2000) Fault-tolerant control in dynamic systems: application to a winding machine. IEEE Control Syst 20(1):33–49

29. Odgaard PF, Stoustrup J, Kinnaert M (2009) Fault tolerant control of wind turbines: A Benchmark model. In: 7th IFAC symposium on fault detection, supervision and safety of technical processes Safeprocess 2009, Barcelona, 155–160. 30 June–3 July 2009
30. Odgaard PF, Stoustrup J, Kinnaert M (2013) Fault-tolerant control of wind turbines: a Benchmark model. IEEE Trans Control Syst Technol 21(4):1168–1182
31. Patton R, Putra D, Klinkhieo S (2010) Friction compensation as a fault-tolerant control problem. Int J Syst Sci 41(8):987–1001
32. Patton RJ (1997) Fault tolerant control: the 1997 situation. IFAC Safeprocess '97, Hull, United Kingdom, pp 1033–1055
33. Patton RJ, Frank PM, Clark RN (1989) Fault diagnosis in dynamic systems: theory and application. Prentice Hall, New York
34. Puig V, Quevedo J (2001) Fault-tolerant PID controllers using a passive robust fault diagnosis approach. Control Eng Pract 9(11):1221–1234
35. Ribrant J, Bertling LM (2007) Survey of failures in wind power systems with focus on Swedish wind power plants during 1997–2005. IEEE Trans Energy Convers 22(1):167–173
36. Richter JH (2011) Reconfigurable control of nonlinear dynamical systems a fault-hiding approach. Springer, Berlin
37. Richter JH, Schlage T, Lunze J (2007) Control reconfiguration of a thermofluid process by means of a virtual actuator. IET Control Theory Appl 1(6):1606–1620
38. Sami M, Patton RJ (2012a) An FTC approach to wind turbine power maximisation via T-S fuzzy modelling and control. In: 8th IFAC symposium on fault detection, supervision and safety of technical processes, Mexico City, Mexico, pp 349–354. 29–31 Aug 2012
39. Sami M, Patton RJ (2012b) Wind turbine sensor fault tolerant control via a multiple-model approach. In: The 2012 UKACC international conference on control, Cardiff, 3–5 Sept 2012
40. Sanchez-Parra M, Suarez DA, Verde C (2011) Fault tolerant control for gas turbines. In: 16th International conference on intelligent system application to power systems, pp 1–6. 25–28 Sept 2012
41. Šiljak DD (1980) Reliable control using multiple control systems. Int J Control 31(2):303–329
42. Sloth C, Esbensen T, Stoustrup J (2011) Robust and fault-tolerant linear parameter-varying control of wind turbines. Mechatronics 21(4):645–659
43. Takagi T, Sugeno M (1985) Fuzzy identification of systems and its applications to modeling and control. IEEE Trans Syst Man Cybern 15(1):116–132
44. Tanaka K, Wang HO (2001) Fuzzy Control Systems Design and Analysis: A Linear Matrix Inequality Approach. Wiley, New York
45. Tao G, Chen S, Tang X, Joshi SM (2004) Adaptive control of systems with actuator failures. Int J Robust Nonlinear Control
46. Van Bussel GJW, Zaaijer MB (2001) Reliability, availability and maintenance aspects of large-scale offshore wind farms, a concepts study. In: Marine renewable energies conference, Newcastle, pp 119–126. 27–28 Dec 2001
47. Veillette RJ (1995) Reliable linear-quadratic state-feedback control. Automatica 31(1):137–143
48. Veillette RJ, Medanic JB, Perkins WR (1992) Design of reliable control systems. IEEE Trans Autom Control 37(3):290–304
49. Verbruggen TW (2003) Wind turbine operation and maintenance based on condition monitoring. Energy Research Center of the Netherlands, Technical report ECN-C-03-047
50. Weng Z, Patton RJ, Cui P (2007) Active fault-tolerant control of a double inverted pendulum. J Syst Control Eng 221(6):221, 895
51. Yang G-H, Ye D (2011) Reliable control and filtering of linear systems with adaptive mechanisms. Taylor and Francis, London
52. Yen GG, Liang-Wei H (2003) Online multiple-model-based fault diagnosis and accommodation. IEEE Trans Ind Electron 50(2):296–312
53. Yew-Wen L, Der-Cheng L, Ti-Chung L (2000) Reliable control of nonlinear systems. IEEE Trans Autom Control 45(4):706–710

54. Zhang K, Jiang B, Staroswiecki M (2010) Dynamic output feedback-fault tolerant controller design for Takagi-Sugeno fuzzy systems with actuator faults. IEEE Trans Fuzzy Syst 18(1):194–201
55. Zhang Y, Jiang J (2001) Integrated active fault-tolerant control using IMM approach. IEEE Trans Aerosp Electron Syst 37(4):1221–1235
56. Zhang Y, Jiang J (2008) Bibliographical review on reconfigurable fault-tolerant control systems. Annu Rev Control 32(2):229–252
57. Zhang YM, Jiang J (2002) Active fault-tolerant control system against partial actuator failures. IEE Proc Control Theory Appl 149(1):95–104

Part III
Monitoring and Fault Diagnosis

Chapter 8
Monitoring Ice Accumulation and Active De-icing Control of Wind Turbine Blades

Shervin Shajiee, Lucy Y. Pao and Robert R. McLeod

Abstract Ice accumulation on wind turbines operating in cold regions reduces power generation by degrading aerodynamic efficiency and causes mass imbalance and fatigue loads on the blades. Due to blade rotation and variation of the pitch angle, different locations on the blade experience large variation of Reynolds number, Nusselt number, heat loss, and nonuniform ice distribution. Hence, applying different amounts of heat flux in different blade locations can provide more effective de-icing for the same total power consumption. This large variation of required heat flux highly motivates using distributed resistive heating with the capability of locally adjusting thermal power as a function of location on the blade. Under medium/severe icing conditions, active de-icing with accurate direct ice detection is more energy efficient and effective in keeping the blade ice-free. This chapter includes: (1) A literature study on different methods of ice detection and a review on passive and active anti/de-icing techniques on wind turbines, (2) Development of an optical ice sensing method for direct detection of ice on the blade, including experimental results, (3) Development of an aero/thermodynamic model, which predicts how much heat flux is needed locally for de-icing under variable atmospheric conditions, (4) Experimental results showing a proof of concept of closed-loop de-icing using distributed optical ice sensing and resistive heating, and (5) Numerical modeling of ice melting on a blade for different distributed heater layouts and geometries in order to optimize thermal actuation strategy, improve de-icing efficiency, and reduce power consumption. We

S. Shajiee
Department of Aerospace Engineering Sciences, University of Colorado, Boulder, CO 80309, USA
e-mail: shervin.shajiee@colorado.edu

L.Y. Pao (✉) · R.R. McLeod
Department of Electrical, Computer, and Energy Engineering, University of Colorado, Boulder, CO 80309, USA
e-mail: pao@colorado.edu

R.R. McLeod
e-mail: robert.mcleod@colorado.edu

conclude with discussions of future directions on distributed ice sensing and thermal actuation for the next generation of de-icing systems on wind turbines.

Keywords Active de-icing · Distributed actuation · Localized heating · Optical ice sensing · Optical frequency domain reflectometry

Nomenclature

AoA	Angle of attack
c	Chord length of the blade
$d\tau$	Transform-limited time resolution of an optical measurement
$e_j(t)$	Error signal j between desired blade temperature and actual blade temperature
h	Natural convective heat transfer coefficient of air
J	Performance cost function
K_d	Derivative gain of a PID controller
K_g	Gain of the op-amp circuit
K_i	Integral gain of a PID controller
K_p	Proportional gain of a PID controller
K	Thermal conductivity
k_{air}	Thermal conductivity of air
Nu_x	Local Nusselt number on the airfoil
n	Total number of thermal resistors in the network
P	Rated power produced by the wind turbine
P_{total}	Total average power consumption for the distributed thermal resistor network
q	Input heat flux to the thermal resistor
q_{conv}	Convective loss heat flux
q_{max}	Maximum resistor heat flux at maximum applied voltage
R_i	Resistance of heater element i
R_{tip}	Span-wise radius of the blade tip
r	Span-wise distance from the blade hub
$T_{a_i}(t)$	Current temperature on the blade for channel i at time t
T_{amb}	Ambient temperature
T_d	Maximum desired blade temperature
T_{max_b}	Maximum global temperature applied to the blade structure during de-icing
t	Time after switching on the resistor network
t_{di}	De-icing time
u_w	Wind speed
V_{ice}	Volume of ice residue
$V_{T>T0}$	Volume of the blade experiencing temperature higher than T_d
v	Input voltage to the resistors
v_i	Applied voltage to resistor i
v_{max}	DC input voltage to the resistor at maximum power

W_m	Weighting matrix in de-icing performance cost function
X	De-icing performance state vector
x	Chord-wise distance from the leading edge of the blade
x_b	Chord−wise blade axis along resistor columns
y_b	Span−wise blade axis along resistor rows
ω	Angular velocity of the rotating blade

8.1 Introduction

With good wind resources often in cold and wet regions, installation of wind turbines in these regions has been growing faster than the total installed wind power capacity in the world. From the year 2008 to 2011, the global total installed capacity of wind turbines approximately doubled while the installed capacity in cold regions increased more than three times from 3 GW to more than 10 GW. Many regions of North America (Minnesota, Alaska, Canada, etc.) and Europe experience more than 50 days per year of icing conditions.

Atmospheric icing causes several problems on wind turbine operation in cold climates. It causes (1) significant reduction of the energy production because it lowers aerodynamic efficiency of the wind turbine blades, (2) errors in sensing wind speed and direction, (3) mechanical failure by increasing load and mass imbalance on the blades and tower and also increasing high amplitude structural vibrations and resonances, (4) electrical failure by snow infiltration in the nacelle, and (5) safety hazard issues when ice sheds off the blades. Seifert and Richert studied the effect of different amounts of ice accretion at the leading edge of the blade tip on aerodynamic efficiency of wind turbines [1]. Their analysis showed, for the case of severe ice accumulation, that more than 40 % of the average generated power may be lost for the wind speed range of 5–20 m/s for a typical 300 KW wind turbine using pitch control. This was based on different power curves calculated using the aerodynamic characteristics of the various iced sections found in wind tunnel tests and linear interpolation along the radius of the blade (Fig. 8.1). This analysis can be extended for a range of turbine sizes by updating the power curve versus wind speed at hub height. Figure 8.2 shows examples of ice build-up accretion and some of the issues that result [2, 3].

This chapter includes 11 sections. In Sect. 8.2, we introduce different types of atmospheric ice accretions on wind turbine blades. In Sect. 8.3, we describe background information on existing ice sensing and thermal actuation techniques and compare their effectiveness for active de-icing of wind turbines. In Sect. 8.4, we present calculations of heat flux requirements for de-icing. We describe a proposed method of ice detection using optical sensors in Sect. 8.5 and further discuss our experimental results on detection of different types of ice using a particular class of optical sensors. Our optical sensing method allows direct and
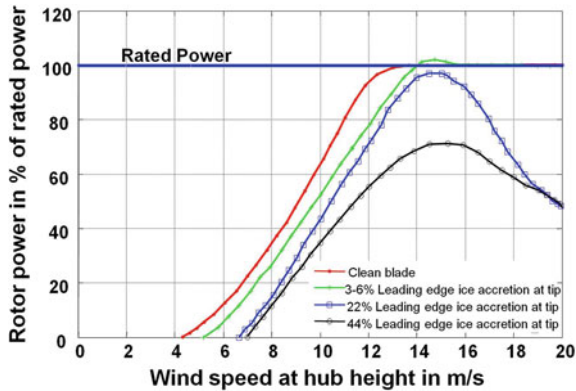
Fig. 8.1 Power loss estimation due to icing at different wind speeds under different icing conditions (reproduced based upon Seifert and Richert, 1997) [1]
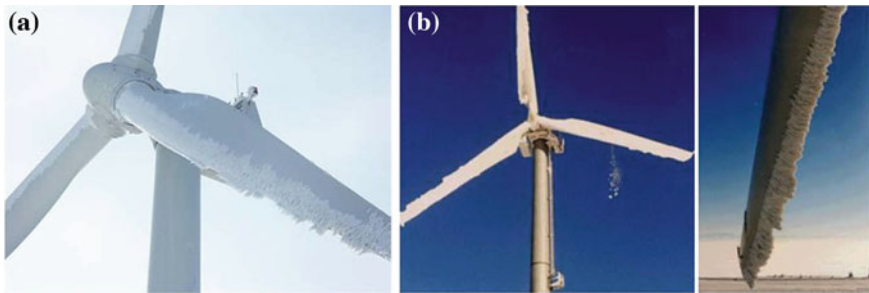
Fig. 8.2 a Ice accumulation on the leading edge of wind turbine blades causes reduced turbine availability, and if operated, potentially damaging loading and increased public safety concerns. Photo by: Kent Larsson, ABvee (SE) from Ref. [2]; permission received from Goran Ronsten; **b** Ice accumulation may either fall off or be thrown off, causing safety issues for persons, animals, or properties that may be nearby. Photos are of 150 KW Grenchenberg turbines in Switzerland; photographs from Ref. [3]; permission received from Robert Horbaty

local detection of ice on the blade and thus provides a suitable test bed for localized active de-icing. In Sect. 8.6, we describe our proposed method of active thermal control for ice mitigation using distributed resistive heating. In Sect. 8.7, we describe the components of our experimental setup including a custom icing chamber, distributed optical ice and temperature sensors, thermal actuators, and data acquisition hardware as well as our closed-loop control scheme for active de-icing. We then discuss a computational model for evaluating distributed heating in Sect. 8.8. In Sect. 8.9, different heater layouts and geometries are numerically evaluated and compared in terms of de-icing performance. In Sect. 8.10, we present closed-loop experimental results of active de-icing including comparing the performance of continuous Proportional, Integral, and Derivative (PID) control with high-intensity pulsed actuation. Finally, in Sects. 8.11 and 8.12, we give

conclusions and discuss our ongoing and future work in developing a closed-loop de-icing strategy.

8.2 Atmospheric Icing

There are traditionally three main types of atmospheric ice accumulation on wind turbine blades: in-cloud icing, precipitation icing, and frost [4–8]. In-cloud icing consists of soft rime, hard rime, and glaze ice, while precipitation icing includes freezing rain and wet snow.

In-cloud icing occurs when small, supercooled, airborne water droplets, which make up clouds and fog, freeze upon impacting a surface. These water droplets can remain liquid in the air at temperatures down to −35 °C due to their small size, but will freeze upon striking a surface [9]. Different types of rime and glaze ice are formed depending on the droplet sizes and the energy balance of the surface. For small droplets with almost instantaneous freezing, soft rime forms. With medium sized droplets and slightly slower freezing, hard rime forms. If the buildup of rime is such that a layer of liquid water is present on the surface during freezing, glaze ice forms [10]. Accretions are different in size, shape, and property, depending on the number of droplets in the air (liquid water content—LWC) and their size (median volume diameter—MVD), the temperature, the wind speed, the duration of icing event, the chord length of the blade, and the collection efficiency. Rime ice forms at colder temperatures of accretion, while glaze forms at warmer temperatures [8]. Rime and glaze have different thermodynamic characteristics and therefore require different heat fluxes for melting. Hard rime ice is denser than soft rime and is more difficult to remove. The ability to not only detect the presence of ice, but the specific character, could enable significant energy savings by tailoring the response of a de-icing system.

8.3 Sensing and Actuation Background: Existing Methods

8.3.1 Ice Sensing

There are two different types of ice detection: indirect and direct. Typical methodologies for detecting ice in current wind turbine systems are called indirect (passive) sensing. They use weather stations on the tower or nacelle of the turbine. Humidity and temperature measurements are correlated with measured wind speeds to determine whether icing is likely to occur [11]. Another example of indirect ice sensing is monitoring the power output during the wind turbine operation to detect an icing event. However, on many occasions, indirect ice sensing methods are neither accurate nor have enough spatial resolution for active de-icing [12]. Furthermore, icing is most likely to occur on the far reach leading

edges of the blades themselves, not on the tower, leading to inaccuracies when trying to correlate the weather station data on the tower or nacelle to the active portions of the blade. Wind velocity is another factor which affects ice formation and accumulation on the blade which is not taken into account in most existing indirect ice detection methods.

Direct ice sensing methods are more accurate for direct detection of ice on the blade with better spatial resolution. Some examples of direct ice sensing methods are resistance, impedance, and capacitance based methods, as well as optical techniques. In Ref. [10], capacitance, inductance, and impedance sensing are introduced as effective on-blade ice sensing methods for wind turbines. These sensors can detect ice formation within a localized area, and their thin sensing elements or electrodes can conform to blade surfaces [10, 13]. More information on these methods are available in [12] and [14]. Ice removal technology coupled with an early detection of ice formation on the blade for reducing aerodynamic degradation (shown in Fig. 8.1) appears to be an essential feature for future generations of wind turbines in cold climates. There are currently no widely available and sufficiently reliable ice detection systems suitable for wind turbines [10, 15]. Figure 8.3 shows a summary of different approaches to ice sensing and anti-icing and de-icing [12–14], including our technique which will be detailed further in this chapter. Direct sensing and active actuation methods are the most energy efficient methods of de-icing. In Sect. 8.5, we discuss our experimentally demonstrated optical ice sensing method which is capable of high resolution and fast detection of ice existence, type, and thickness with micron-range accuracy.

8.3.2 Thermal Actuation

De-icing and anti-icing methods in the literature can be divided into active and passive methods. While many wind turbines operating in cold climates encounter icing conditions, very few of them are equipped with active de-icing and/or anti-icing systems. Currently, wind turbines installed in cold regions use passive methods such as ice repellant (ice-phobic) coatings on the blades. However, these coatings are only effective for short-term operations in slight icing conditions and are not effective in harsh cold conditions with varying forms of ice. As an example, silicon paints exhibit promising ice repellant characteristics on soft rime under slight icing conditions; however, hard rime ice exhibits greater adhesion strength to silicon paint than an uncoated surface. In addition, these passive ice prevention techniques have been shown to have poor durability when tested on wind turbines [15, 16].

Active heating systems are more effective for ice prevention. After sensing and detecting icing conditions, anti/de-icing systems are activated to mitigate turbine downtime. Active heating systems either affect the aerodynamic efficiency and/or the generation capacity of the turbine. Both hot air injection and resistive heaters can consume more than 10 % of the generated power [12, 17].
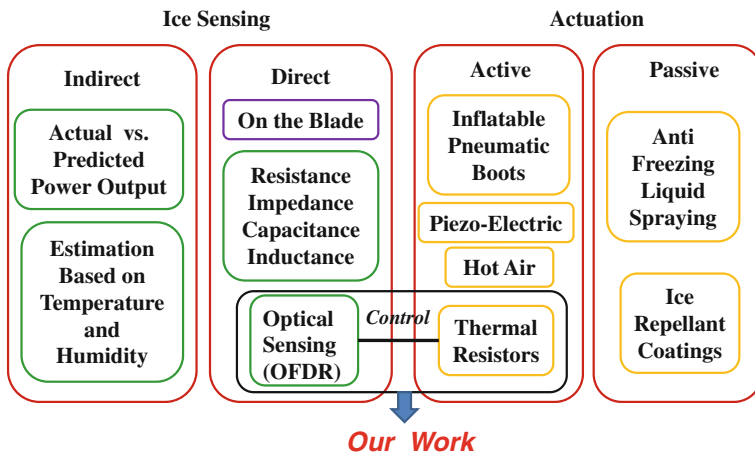
Fig. 8.3 Summary of different approaches to ice sensing and anti-icing and de-icing. Among all of the direct ice sensing methods to date, our optical ice sensing method provides the most complete information (ice existence, type, and thickness) for local de-icing

Table 8.1 shows a high-level qualitative comparison of different active de-icing methods on wind turbines, where the advantages and disadvantages of each method in a number of categories are listed. There are very limited technical data available in the literature related to the active control of icing for wind turbines. Among all of the mentioned active de-icing techniques, only thermal resistors and hot air techniques have been successfully tested on wind turbines in cold climates with available commercial kits.

Different types of ice have different thermodynamic and adhesion characteristics and need different amounts of heat flux for de-icing [5]. Direct detection of ice on the blade, as opposed to estimating ice accumulation on the blades using sensors on the nacelle, also provides a more accurate method for applying thermal control for de-icing. This highlights the need for improved sensing methodologies. We aim to demonstrate a de-icing method using combined on-the-blade optical and temperature sensors and electrothermal actuation, as shown in Fig. 8.4. Our de-icing experimental setup consists of a distributed optical sensor network that allows for precise local measurements of ice existence and type. Our ice sensors are responsive (0.5 Hz response time) and accurate in measuring ice thickness (36 micrometer thickness resolution) and hence are able to detect ice in the very early stages of ice formation. Leveraging the ability to quickly measure and react to changing conditions, we then develop a suite of control solutions optimized for any type of ice accumulation. Temperature sensors, installed close to the blade leading edge area, are used for calculating the input thermal power for a distributed network of heaters.

Table 8.1 Comparison of different methods for active de-icing of wind turbines

Performance categories	Active de-icing method				
	Thermal resistors	Hot air	Inflatable pneumatic boots	Liquid surface coatings	Microwave
Energy consumption (1 for the smallest and 5 for the highest)	4	5	2	3	1
Effect on aerodynamic efficiency of the turbine	(Good) Does not create negative aerodynamic effect on the blades	(Medium) Hot air layer under the ice does not create negative effects. Blowing external hot air may degrade aerodynamic efficiency	(Poor) Temporarily disrupts the flow when actuating and therefore decreases aerodynamic efficiency	(Medium) Might slightly degrade the aerodynamic efficiency	(Good) Does not create negative aerodynamic effect on the blades
Operating cost	Moderate	Moderate	Moderate	High	Low
Maintenance cost	Moderate	Moderate	Moderate	High due to frequent clogging of membrane holes	Not known
Negatively affected by centrifugal force during blade rotation	No	No	Yes (inflates itself)	Yes (is quickly removed)	No
Environmentally harmful	No	No	No	Yes	No
Noise creation	Low	Low	High	Low	Not known

(continued)

Table 8.1 (continued)

Performance categories	Active de-icing method				
	Thermal resistors	Hot air	Inflatable pneumatic boots	Liquid surface coatings	Microwave
Effective for different types of icing	Effective from light to severe icing conditions	Effective from light to severe icing conditions	Effective from light to severe icing conditions	Only effective from light to moderate icing conditions	Only effective for light icing conditions
Capability of distributing thermal energy "optimally" from hub to tip of the blade	Moderate (depending on the number of resistors and distances between them)	Low (difficult to optimally control external hot air flow over the blade from hub to tip)	Low	Low	Not known
Modification of the blade	Few	Few	Much	Few	Few
Ice prevention durability	Long	Long	Long	Short	Not known
Successfully tested on wind turbines	Yes	Yes	No successful wind turbine application to our knowledge	No	Concept has been proven, no successful wind turbine application to our knowledge
Commercial kit for wind turbines	Available	Available	Not available to our knowledge	Not available	Not available
Advantages	Energy distribution, implementation, minimal blade modification	Direct deflection of cold water droplets	Fast reaction time for de-icing	Minimal system complexity	Very low thermal power

Table 8.1 (continued)

Performance categories	Active de-icing method				
	Thermal resistors	Hot air	Inflatable pneumatic boots	Liquid surface coatings	Microwave
Disadvantages	Higher local thermal stress due to direct contact of resistors and blade structure	Poor optimal distribution of thermal energy	High noise, possible self inflation due to centrifugal force	Short durability, quickly removed by centrifugal force	Not effective for moderate and severe icing conditions
Current overall commercial ranking for wind turbines	1	2	3	4	5

Fig. 8.4 Schematic diagram showing thermal control system using direct optical sensing

Combined Optical Ice/Temperature Sensors and Electro-thermal Resistors are Embedded on the Blades

On-Blade Ice and Temperature Sensors

Ice Presence, Type, Thickness, and Temperature

Feedback Control Algorithm

Commands to Distributed Electro-thermal Actuators
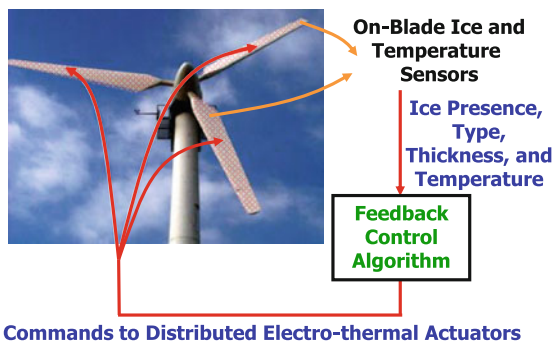
8.4 Blade Thermodynamics

Different areas on wind turbine blades need significantly different levels of thermal power and flux for de-icing (Fig. 8.5). Thus, optimally distributing the required thermal energy across the blade can save a significant amount of thermal energy in de-icing systems. The highest heat flux required is at the leading edge of the tip of the blade. As such, a preliminary step in designing a suitable thermal actuation method for de-icing is calculating the heat flux requirement for this most critical region of the blade. Figure 8.5 shows the calculated heat flux requirement (due to convection loss) versus nondimensional chord position x/c and nondimensional span-wise radius r/R_{tip} at a given atmospheric condition. The required parameters are angle of attack AoA of the blade, blade geometry, angular velocity ω of the blade, and wind speed u_w. Figure 8.5 shows the characteristics and behavior of the convection loss for laminar flow over the blade. Negative values of x/c are for the lower blade surface, positive values of x/c are for the upper blade surface, and $x/c = 0$ is leading edge of the blade. The peak value of heat flux at the leading edge of the blade tip for this simulation is about 1,800 W/m^2 for a 500 KW wind turbine. This calculation uses experimental local values of Nusselt numbers at different Reynolds numbers and Prandtl numbers for a NACA 63421 airfoil using experimental convective heat correlations [18]. This airfoil has a nonsymmetrical profile which creates different trends below and above the stagnation point for Nusselt numbers and the convective heat transfer coefficient [18].

The convective coefficient of heat transfer (h) at each point is calculated as

$$h = \frac{Nu_x k_{air}}{c} \tag{8.1}$$

where Nu_x is the local Nusselt number on the airfoil, k_{air} is the thermal conductivity of air, and c is the chord length of the blade.

The convective loss heat flux (q_{conv}) is calculated as
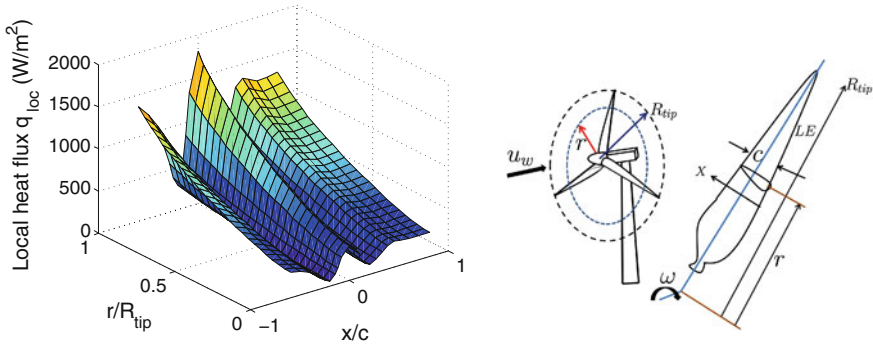
Fig. 8.5 Simulated heat flux requirement (due to convection loss) versus nondimensional chord position x/c (negative values are for the lower surface and positive numbers are for the upper surface of the blade) and nondimensional span-wise radius (distance from hub) r/R_{tip}. The heat flux plotted is the amount needed from a de-icing system to compensate for convection loss from the blade; $T_{\text{amb}} = -30\,°C$, $\omega = 20$ RPM, $u_w = 12$ m/s, $R_{\text{tip}} = 25$ m, $AoA = 0$, $P = 500$ KW, where T_{amb} is ambient temperature, ω is angular velocity of the rotating blade, u_w is wind speed, R_{tip} is the span-wise radius at the blade tip, AoA is angle of attack, and P is rated power produced by the wind turbine

$$q_{\text{conv}} = h(T_d - T_{\text{amb}}) \tag{8.2}$$

where T_d is the maximum desired blade temperature and T_{amb} is the ambient temperature.

The thermodynamic behavior of convection loss changes once the flow becomes turbulent over the blade. This was investigated in [19] where it was shown that the effect of a transition to turbulent flow at the leading edge is to increase the required heat transfer by an average factor of 2.5. Therefore, laminar and turbulent flow conditions need to be detected throughout the blade for different turbine operating conditions for active de-icing.

A de-icing system must provide enough thermal energy to compensate for convection heat loss, sensible heat to increase the initial temperature of ice to its melting temperature, and latent heat for the phase change from solid ice to liquid water. The latent heat flux required for the phase change of ice is dominant compared to the sensible heat flux even when the initial ice temperature is significantly below zero. Calculations show that for ice with an initial temperature of $-30\,°C$, the amount of heat required to change its temperature to $0\,°C$ is only 18 % of the heat required for the phase change. Since the phase change of ice requires much higher thermal flux than sensible heat flux, it is not profitable to melt the entire ice layer formed on the blade. Thus, one strategy for reducing thermal energy expenditure is to only melt a thin layer of ice and then shed off the remaining ice by using centrifugal force from the blade rotation [17].

Figure 8.6 shows a plot of the summation of sensible and latent heat flux of ice required for de-icing versus melting time for a 1 mm soft rime ice at two different initial ice temperatures. It is seen that this heat flux exponentially decreases when

Fig. 8.6 Total (sensible + latent) heat flux versus melting time for a 1 mm soft rime ice layer at different initial ice temperatures
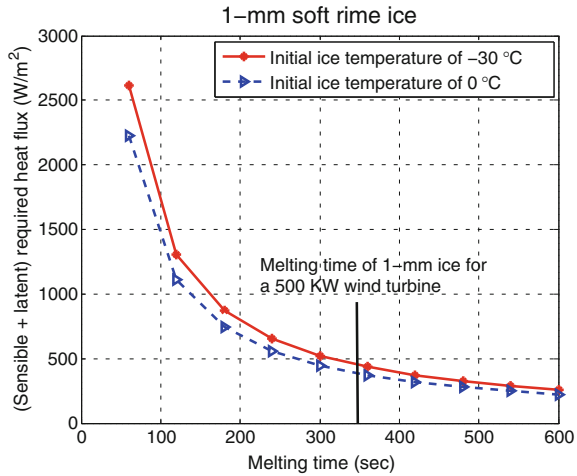
melting time increases. Assuming thermal resistive heating with a maximum heat flux generation capability of 2,000 W/m^2 (approximately 500 W/m^2 for the summation of latent and sensible heat fluxes and 1,500 W/m^2 to compensate for the convection loss at the leading edge), this calculation shows that 6 min is a reasonable melting time for a 500 KW wind turbine.

It is shown in Fig. 8.5 that the required heat flux for de-icing significantly decreases from the blade tip to the blade root. Experimental data is reported in the literature on the required heat flux for de-icing at different blade regions, as tested by VTT (The Technical Research Center of Finland) and Kemijoki Ltd. in 1993. They tested a de-icing system using a thermal resistor on a 450 KW turbine in extreme conditions in Finnish Lapland in order to keep the rotors free of ice. This is likely the world's first documented test of a heat-based de-icing system for commercial wind turbines [15, 20]. Their data shows de-icing power consumption of 5 % of the 450 KW turbine's rated power with peak heating power of 4,500 W/m^2 at the blade tip versus 350 W/m^2 at the blade root (13/1 ratio). Heating elements covered a maximum of 15 cm from the leading edge. Heating power was sufficient in most cases to keep off rime ice in the winter; however, this system was unable to prevent icing in the (rare) cases of freezing rain.

8.5 Direct Optical Ice Sensing

As discussed earlier in Sect. 8.3.1, indirect ice sensing methods do not have enough spatial resolution and accuracy for active localized de-icing. Still there are no implementations to directly measure the presence and type of ice accurately on the blade.

We have applied a newly developed optical sensing technique to enable detecting early stages of ice formation, including both the type of ice and the thickness (to an

accuracy within 36 microns). Direct ice detection requires measurement of the region just outside the blade surface. To accomplish this thickness measurement, optical signals directed normal to the surface reflect from the upper surface of the ice to reveal its presence, thickness, and type. Thickness could be measured by time of flight of a short pulse, referred to as time-domain reflectometry (TDR) of sub-mm films. TDR requires optical pulses of approximately 100 fs duration which are costly to generate and tend to disperse rapidly in solids. Conversely, optical frequency domain reflectometry (OFDR), as shown in Fig. 8.7, uses continuous laser light with a swept frequency which is easier to generate and can be directed through optical fiber [21, 22]. Fiber coupled sources allow for many sensors to be multiplexed on a single fiber running down the full length of the blade, greatly reducing complexity. Additionally, recent advances in all-fiber, rapidly tuning laser sources [21] promise to reduce the cost and delicacy of the lasers while increasing the measurement speed. OFDR can measure multiple simultaneous returns in different time windows. The optical signal to each sensor is thus delayed by a unique delay such that the entire array can be measured in a single interrogation.

To demonstrate the efficacy of OFDR for the detection of icing on a blade surface, we use the instrument whose schematic is shown in Fig. 8.7 to monitor the thickness of an evaporating water film on a solid substrate, as shown in Fig. 8.8. Gradient-index (GRIN) lenses with an antireflective coating are used as our optical ice sensors. Many such probes can be queried by a single OFDR system, providing spatially resolved icing data [14, 23]. The transform-limited time resolution of the measurement is $d\tau = 1/dv = 121$ fs which corresponds to a spatial resolution of 36 μm in air.

As shown in Fig. 8.8, top, the system can easily distinguish both the presence and thickness of the material on the surface.

We have recently shown [22] the use of phase information in the OFDR to simultaneously measure thickness to ± 61 nm precision and the index of refraction to $\pm 2 \times 10^{-6}$. Since variations in the ice type are reflected in their refractive index, this suggests that both type and thickness of ice can be detected.

The sensor area must be sufficiently large to average over ice crystal size, entrapped air, and other spatial variations. The 10 μm diameter of a fiber core is thus too small and will not return a repeatable signal. Thus, we used a fiber collimator consisting of a graded index collimating lens attached to the end of the optical fiber. The lens is covered by an anti−reflective coating and we detect water and ice which sits on top of the sensor. The collimating lens has a circular detection diameter of 3 mm.

Figure 8.9 presents experimental optical sensing results, demonstrating that the sensor can distinguish between air, water, glaze ice, and rime ice on the blade. For the case of air, the measured signal is symmetric with a small peak due to the existence of the anti−reflective coating (Fig. 8.9a). In this case, there is no volume scatter and the peak of the signal corresponds to the airfoil-air boundary. For the case of liquid water, two smooth peaks are captured with no volume scatter (Fig. 8.9b). For the case of glaze ice (Fig. 8.9c), a smooth peak is captured followed by a small scattered signal. The first peak corresponds to the airfoil/ice boundary,
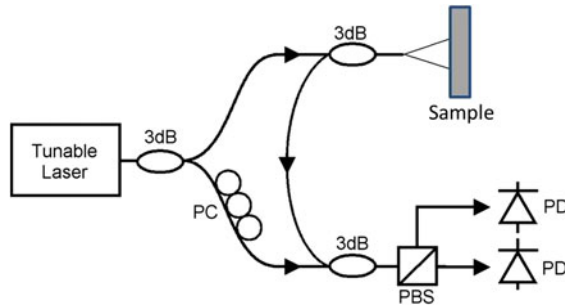
Fig. 8.7 Layout of an optical frequency domain reflectometer [22]. Light from the tunable laser is reflected from the sample and interfered with a reference arm. As the frequency of the laser is swept, interference fringes are detected that indicate the amplitude and round-trip delay of reflections from the sample. 3db = 50/50 fiber coupler, PC = polarization controller, PBS = polarization beam splitter, PD = photodiode
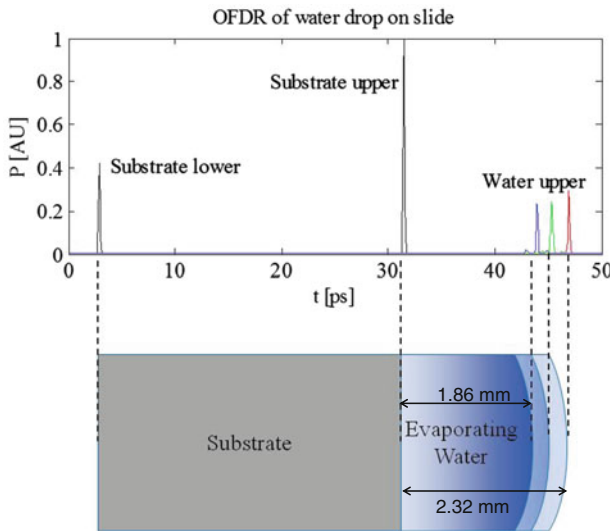
Fig. 8.8 Optical frequency domain reflectometry of a variable thickness water layer deposited on a substrate. The water layer, which was allowed to evaporate over the course of approximately 1 h, was measured at three times to have thickness 2.32, 2.08, and 1.86 mm with a transform-limited precision of 0.036 mm. The vertical axis is the amplitude of reflection. On the horizontal axis, 1 ps corresponds to a round-trip travel time for the laser in 112.5 µm of water [14]

and the small scattered signal corresponds to the rough ice/air interface. Rime ice (Fig. 8.9d) has a highly nonsymmetric shape and distinctive volume scatter due to the increased air volume within the ice and irregular shape of the ice crystals. These signals can be recognized and categorized in signal processing to identify type and thickness. The peak magnitudes and corresponding times where these peaks occur are numerically calculated. A magnitude filter is applied to reject noise while being
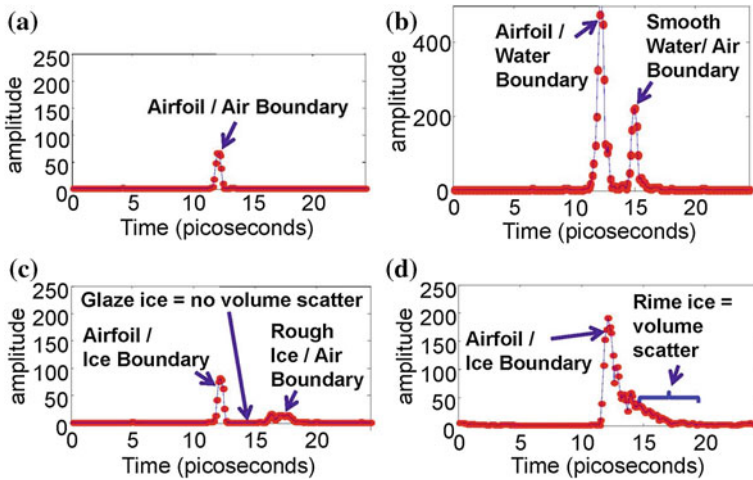
Fig. 8.9 OFDR measurements yield distinct signals for different conditions: **a** No water/ice on the blade. **b** Liquid water on the blade. **c** Glaze ice on the blade. **d** Rime ice on the blade. Y-axis is arbitrary scale proportional to the amplitude of the reflected optical electric field. X-axis is round-trip optical time of flight from the fiber exit to the particular layer. 1 ps corresponds to a round-trip travel time for the laser in 112.5 μm of water [14]. For ice thickness calculation, the same index of refraction is assumed for ice and water

able to capture the volume scatter due to rime ice. The signal processing algorithm looks at the number of captured peaks, peak magnitudes, magnitude of time integral of the signals, and symmetrical/asymmetrical shape of the signals around their peaks in order to detect the type of ice. For the case of water (Fig. 8.9b), the thickness of the water droplet is calculated by multiplying the speed of light by the peak time difference between airfoil/water and water/air boundaries. For the case of glaze ice (Fig. 8.9c), the thickness of ice is calculated by multiplying the speed of light by the peak time difference between airfoil/ice boundary and the first captured peak of ice/air boundary. When there is rime ice (Fig. 8.9d), the thickness is calculated by multiplying the speed of light by the time difference between the airfoil/ice boundary up to the time that volume scatter ends in the captured signal.

In summary, our demonstrated optical method is capable of direct detection of ice existence, classification of ice type, and ice thickness measurement with 36 micrometer resolution.

8.6 Distributed Localized Heating

Due to varying amounts of heat loss in different regions of a rotating blade, an energy efficient active de-icing method requires different amounts of thermal power in different blade regions which motivates using distributed heating with adjustable local heat flux to reduce power consumption for de-icing. The aerothermodynamic

analysis presented in Sect. 8.4 shows this noticeable variation of required heat power for different locations, with the highest value at the leading edge of the tip of the blade (Fig. 8.5). These calculations show that heating the entire blade using this locally adjusted heat flux consumes approximately 7–10 % of the rated power of the wind turbine [14]. Equally heating the entire blade, such as using a hot air technique, consumes even more power (about 15 % of the rated power) as reported in Refs. [17] and [24]. Many active and passive anti/de-icing methods are in development, but few are available on the market. Active heating of blades using resistive thermal heaters is the most tested, used, and reliable way to prevent icing effects [8]. It is often used in parallel with a passive hydrophobic coating to lower energy consumption. While accurate and direct ice sensing and distributed resistive thermal actuation have not yet been tested on wind turbines, it is now a growing research area because it could significantly reduce de-icing energy consumption by providing locally adjusted thermal power only in the regions where ice exists.

In our preliminary experimental test bed, we use flexible resistive thermal heating elements with a maximum heating capability of 10 W/in^2. A similar thermal resistor has also been used by a wind energy research laboratory at the University of Quebec in Canada for their preliminary study of electrothermal de-icing of wind turbine blades [25]; however, these are large heaters which heat the bulk of the blade based on coarse environmental conditions. We use many small local heaters on the surface of the blade, capable of heating in short time frames by heating only a thin layer and not the bulk material. This allows to enhance the intelligence of the control system while using established thermal actuation technologies. In Sect. 8.7, we explain our fabricated experimental setup for active de-icing using distributed ice and temperature sensors and resistive heaters.

8.7 Experimental Setup

We have built an experimental setup to create different types of ice on a blade and to implement active de-icing using combined optical ice and temperature sensors and distributed resistive heating with adjustable heat flux in different blade locations using feedback control. This section describes the components of the experimental setup, including resistive heaters, optical ice sensors, custom fabricated icing chamber, and amplifier circuit board.

De-icing is investigated under a fixed blade pitch angle for a non−rotating blade inside a thermally insulated custom cooling chamber (Fig. 8.10a). Different types of ice can be created by controlling temperature, humidity, and wind speed inside the chamber. The benefit of this custom cooling chamber over an icing wind tunnel is that it is less expensive to operate. However, there are some limitations such as stationary blade installation and longer time for ice creation inside the chamber compared to an icing wind tunnel. The experimental results of de-icing for a stationary blade can be extended to a rotating blade using further computational simulations. Wind is generated by a box fan installed inside the test
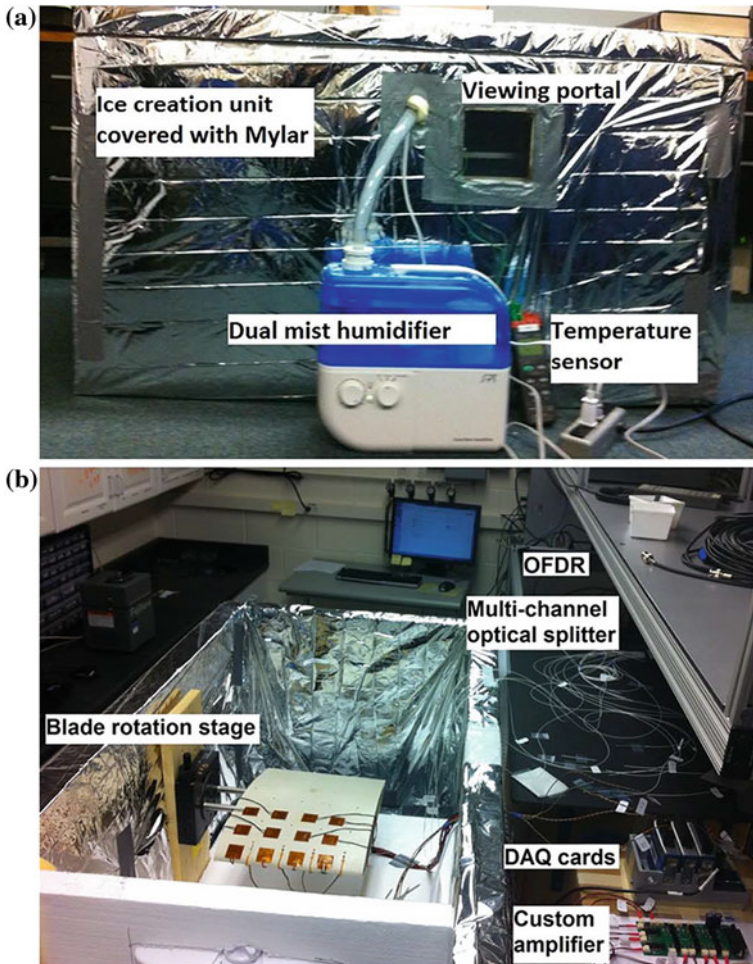
Fig. 8.10 **a** Cooling chamber for ice creation on the blade surface. **b** Different components of our test setup at a glance

section. Blade pitch angle can be changed between tests by a rotation stage inside the chamber which affects pressure distribution and convection heat loss at different blade locations. This allows us to investigate de-icing performance under different aerodynamic and heat loss conditions.

Thin flexible electrothermal heaters [26] with 5 watt and 10 watt power ratings are used in different regions of the blade for thermal actuation. These resistors have the maximum power density of 5 W/in^2 (7,750 W/m^2) and 10 W/in^2 (15,500 W/m^2), which is still much higher that the maximum required power density for de-icing in any region of the blade. A finite difference code is developed to determine the transient heat conduction on the blade for computing the optimal distance between heaters. This calculation satisfies de-icing controllability on

different regions (by sending required heat flux to different blade regions) within a reasonable amount of de-icing time (20 min–1 h) given the conductivity of the blade. The local required heat flux is a function of blade location, pitch angle, and environmental conditions (altitude, ambient temperature, wind speed, and direction). Twelve resistive heaters (ten 5 watt and two 10 watt) are mounted from the leading edge up to 1/3 of the chord length of our blade with the higher power resistors placed at the leading edge.

Optical ice sensors are distributed on the blade such that each thermal actuator is surrounded by four sensors. Optical fibers terminate in GRIN lenses mounted flush with the surface of the blade. Ice sensors (3 mm in diameter and 6 mm in height) are installed in drilled holes of the same size and attached with water resistant glues for environmental stability (Fig. 8.10b).

At ice temperatures below 0 °C, before any melting occurs, optical ice sensors cannot provide enough information for control gain calculation since the ice thickness and type do not change by heating. Therefore, combined temperature and optical ice sensors are used for closed-loop thermal control before any phase change of ice. Below the melting temperature, optical ice sensors determine which actuator should be active while temperature information is used to calculate the controller gains. Alternatively, ice thickness information provided by the ice sensors can be used to calculate control gains during ice thickness variation. Four thermocouples [26] are placed close to the leading edge ice sensors for gain calculation of the PID control that is a function of the difference between desired temperature (slightly above 0 °C) and instantaneous local temperature. It is economically preferable to use fewer temperature sensors on the blade. Hence, distributed temperature sensors are only installed on the leading edge area. Thin temperature sensors are used to prevent aerodynamic degradation in this work.

Figure 8.11 shows distributed optical sensors and resistive heaters on the blade. Ultimately for active de-icing implementation on a full-scale wind turbine, it is necessary to have distributed resistors embedded inside the composite blade to lower the risk of damage by lightning. As mentioned earlier, distributed resistive heating provides an efficient local control of heat flux on the blade. However, due to a large number of actuators and sensors in this methodology, the possibility of a fault in the network should be carefully considered in the design as an area of future work.

Under some very cold conditions, instant freezing of the runback water might occur at the edges of the heating elements or on some cold blade areas that are not covered by heating elements. This could form a barrier at the edges of the heating element. The edge barriers may tend to grow toward the leading edge as horns without contact with a heating element. Those horns that happen to grow on the optical sensors could immediately be detected and de-iced by locally increasing thermal flux using the surrounding heating elements. Intuitively, using a staggered array configuration of heaters instead of an aligned array can be more efficient (Fig. 8.12) for preventing these local horns to grow all the way toward the leading edge where icing leads to large aerodynamic losses. In addition, placing resistive heaters in both upper and lower surfaces of the blade close to the leading edge area can be considered to even further reduce the potential threat of ice horn residues in
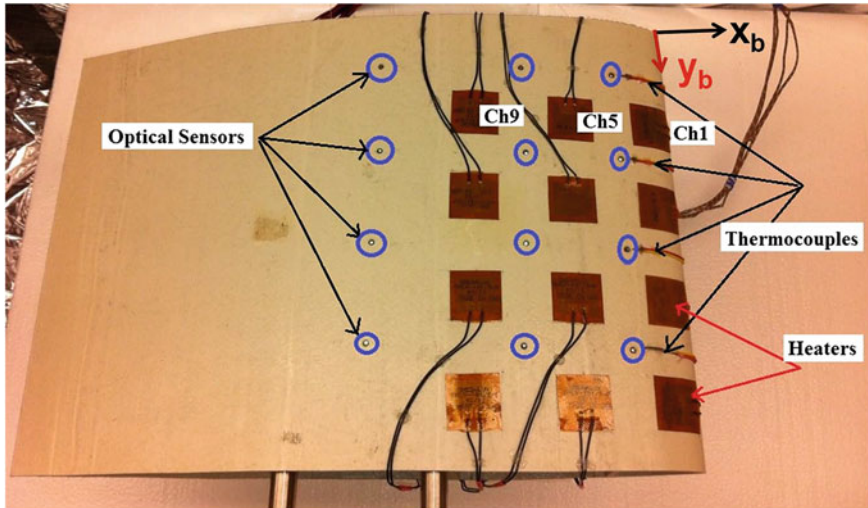
Fig. 8.11 Distributed optical ice sensors, leading edge temperature sensors, and resistive heaters on a blade segment. Resistor rows are along the y_b axis, and resistor columns are along the x_b axis. The optical sensor and the resistor in the top column closest to the blade leading edge are both labeled as channel 1
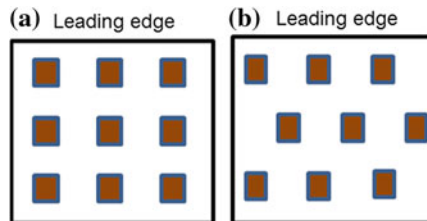
Fig. 8.12 Heating elements in: **a** Aligned array and **b** Staggered array

this region. The ice/water dynamics including melting and refreezing are potentially quite complex. In Sect. 8.9, we study the optimization of the layout of heaters in greater detail. Because of lower relative wind speed, Reynolds number, convective heat loss, and contribution to power production, the first two-thirds of the blade (toward the blade root) is less important to be de-iced. Installing distributed heating elements only on the last third outboard section of the blade enables decreasing equipment costs and de-icing power consumption while maintaining 90 % of the aerodynamic performance of the clean blade with only 30 % of the length de-iced [27].

Figure 8.13 shows a schematic diagram of the closed-loop control. Numerical signal processing [28] detects the ice existence, type, and thickness by each optical ice sensor based on the magnitude of the peak, the signal asymmetry, and backscatter level. Each optical scan (for all the channels) including numerical detection
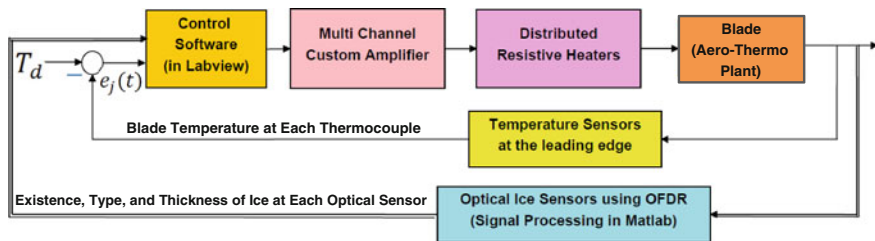
Fig. 8.13 Closed-loop control schematic diagram. $T_d = 2\ °C$ is the desired blade surface temperature and $e_j(t)$ is the error signal between the desired blade temperature T_d and the actual blade temperature at the jth thermocouple

takes less than 2 s in the loop. As such, we use a closed-loop control update rate of 0.5 Hz. This is sufficiently fast for the desired thermal response bandwidth of 0.001–0.01 Hz for the actuation network. Both the control system software and OFDR software have been developed in LabVIEW [29].

The result of the numerical ice detection algorithm is sent to the closed-loop control system at 0.5 Hz. The command voltage output of the control software is amplified through a custom fabricated multichannel op-amp circuit and fed to the distributed resistors on the blade.

8.8 Computational Model Validation with Experiments

Accurate prediction of the aero/thermodynamic response of a rotating blade covered with ice/snow and distributed electrothermal resistors is complex due to the coupled nonlinear dynamics of turbulent wind, the ice/water phase change, and multiple distributed heat sources on the blade. Experimental validation is required to achieve a reasonably accurate dynamic model for such a complex system. In this section, we compare the transient thermal response of a composite blade undergoing distributed thermal actuation using a computational model in ANSYS [30] with results from an experimental run performed using our test setup. The geometry of the hollow blade with distributed resistors is modeled in SolidWorks [31]. This geometry is imported into the ANSYS Workbench environment for computational simulations (Fig. 8.14). The transient thermal module in ANSYS is used to compute the temperature variation as a function of time on the blade for different heater layouts. In the simulations explained in Sect. 8.9.2, a variable time step is implemented with a minimum time step of 0.05 s and maximum time step of 0.5 s. In the ANSYS analysis setting, heat and temperature convergence modes are activated to achieve better stability and convergence in the numerical simulations.

For our experiment, a temperature sensor is placed between two of the middle resistors in the second and third row to record the variation of the temperature (Fig. 8.15). Figure 8.16 shows the experimentally applied input voltage to all of
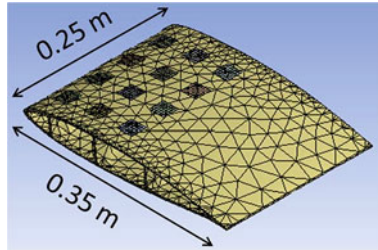
Fig. 8.14 Created blade geometry, with a volume of 5.33×10^{-4} m^3, in SolidWorks for computational analysis
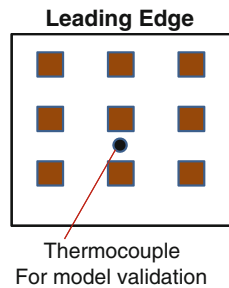
Fig. 8.15 Location of a temperature sensor installed for experimental validation of the computational ANSYS model in an aligned heater layout

the resistors as a function of time created by a PID control to increase the initial temperature of the blade from 24.9 °C to about 30 °C. Then, a fifth-order polynomial curve, shown in Fig. 8.16, was fit to the input voltage using a least squares curve fitting method. Using this fitted input voltage, the generated heat flux from each resistor (q (W/m^2)) is calculated as

$$q = q_{max} \cdot \left(\frac{v}{v_{max}}\right)^2 \tag{8.3}$$

where q_{max} is the maximum resistor heat flux (W/m^2) at maximum applied voltage, v is the input voltage to the resistors (volts), and v_{max} is the DC input voltage to the resistor at maximum power (volts).

The calculated input heat flux was later applied to the heater network in the ANSYS model. This experiment was done under a natural air convection condition, with no forced wind velocity to the blade. This natural convection is caused by buoyancy forces due to density differences caused by temperature variations in the air. The natural convective heat transfer coefficient of air is in the range $h = 5$–25 W/(m^2·°C), and the range of the thermal conductivity for a typical composite material is $K = 0.2$–1 W/(m·°C). Assuming natural convection on the

Fig. 8.16 Experimental input voltage to the resistive heaters
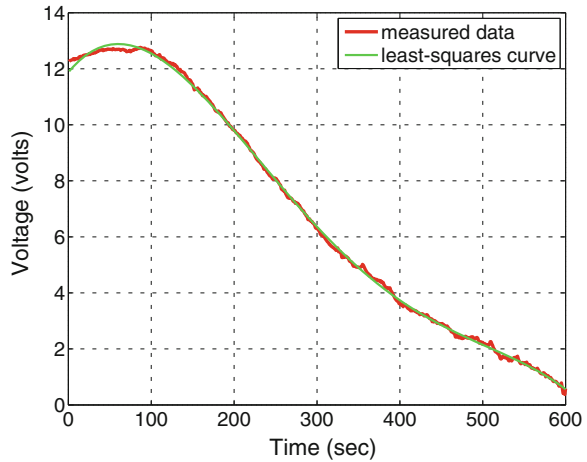
upper and lower surfaces of the blade, we simulated the temperature variation on the blade at the location of the temperature sensor for both $h = 6$ W/(m^2·°C) and $h = 7$ W/(m^2·°C), and with a composite blade thermal conductivity of $K = 0.3$ W/(m·°C). Figure 8.17 shows the temperature comparison between our recorded experimental data and the simulated values in ANSYS, showing a reasonably close match between the numerical simulations and the experimental data.

8.9 Optimizing the Layout of Distributed Heaters

In this section, we explore several heater geometries and layouts (Fig. 8.18) and show that there are de-icing efficiency advantages to circular heaters in a staggered layout. Circular heaters generate uniform heat flux in all radial directions, and square heaters generate uniform heat flux along their two axes of symmetry. Figure 8.18 shows different heater layouts modeled for ANSYS computational analysis. For the created staggered layouts, only heaters in the second row are shifted in the y_b direction shown in Fig. 8.11. For the staggered alignments, in order to keep the geometry symmetric about the axis that connects the midpoint leading edge to the midpoint trailing edge, two half-area resistors are used at each end in the second row of resistors (Fig. 8.18b, d). The total heating area and total input heat flux are equal for all of the resistor shapes and layouts considered in Fig. 8.18 and in the results that will be discussed in Sect. 8.9.2.

We also investigated other heater geometries. It was observed that the de-icing performance of other regular polygon-shaped heaters (pentagon, hexagon, etc.) is between square and circular heaters. Therefore, the performance of only square and circular heaters will be discussed in Sect. 8.9.2 as the lower and upper bound of the de-icing performance.
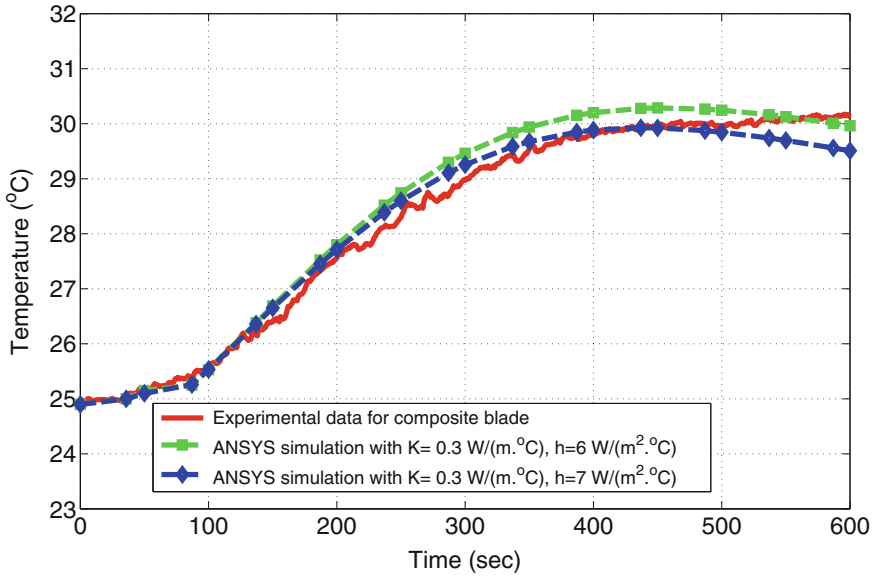
Fig. 8.17 Validation of the computational model developed in ANSYS with the experiments

Fig. 8.18 Different heater
layouts. **a** Aligned square
layout. **b** Staggered square
layout. **c** Aligned circular
layout. **d** Staggered circular
layout
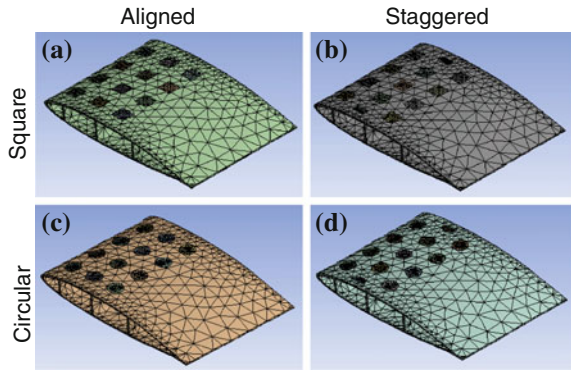
A uniform 3 mm glaze ice layer on the blade from the leading edge to 40 % of
the chord length is incorporated into the numerical model, as shown in Fig. 8.19.
The ice layer covers all of the distributed resistors mounted on the blade. This
uniform ice thickness model is assumed for the purpose of optimizing the heater
layout. However, a nonuniform ice layer based on experimental field data is
needed for the purpose of investigating aerodynamic efficiency degradation and
calculating lift and drag coefficients for an icy airfoil, which is not the focus of this
chapter. The physical properties of the glaze ice layer and the composite blade
were carefully modeled in ANSYS, including the melting point, density as a
function of temperature, specific heat as a function of temperature, and thermal
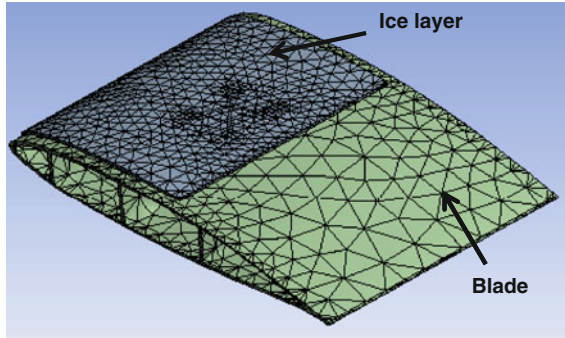
Fig. 8.19 ANSYS model of accumulated ice with a uniform thickness of 3 mm with initial volume $V_{ice} = 1.17 \times 10^{-4}$ m^3, covering the *upper* surface of the blade from the leading edge to about 40 % of the blade chord length

conductivity. The heater material was assumed to be "structural steel" from the ANSYS material library in creating the models.

8.9.1 De-icing Performance Metric

In order to quantitatively evaluate the de-icing performance of distributed thermal actuation, a performance metric is needed. This performance cost function should consider the de-icing time [t_{di} (sec)], maximum global temperature to the blade structure during de-icing [T_{max_b} (°C)], the volume of the blade experiencing higher than a certain temperature [30 °C here as $V_{T>30}$ (m^3)], and thermal power consumption. Both T_{max_b} and $V_{T>30}$ give indications of the level of thermal stress on the blade due to the localized heating. A more advanced metric may also consider additional parameters such as setting priority for de-icing in those regions on the blade with higher contributions to the aerodynamic torque production (regions closer to the leading edge and the blade tip), cost of the heaters, etc. In general, the total cost of a heater network is a function of wind turbine size, blade dimension, and total number of heaters on a full-scale blade. This financial cost has not been included in the performance cost function in this chapter and is an area of future work.

In order to compare de-icing performance between different heater layouts, assuming the same amount of thermal power consumption, a quadratic performance cost function J is defined as

$$J = X^T W_m X \tag{8.4}$$

where $X = [t_{di}, V_{T>30}, T_{max_b}]^T$ is the de-icing performance state vector, and W_m is a diagonal weighting matrix

$$W_m = \begin{bmatrix} \dfrac{1}{1350^2} & 0 & 0 \\ 0 & \dfrac{1}{(3.48 \times 10^{-5})^2} & 0 \\ 0 & 0 & \dfrac{1}{56.31^2} \end{bmatrix}. \qquad (8.5)$$

This weighting matrix W_m was chosen such that, for the aligned square heater layout, the three performance variables inside the de-icing performance state vector X contribute equally to the cost, resulting in a total cost of $J = 3$. A smaller value of J is desirable. For the analysis discussed in Sect. 8.9.2, ice residues in different areas on the blade are assumed to have equal weighting in the de-icing performance. The de-icing time t_{di} is defined as the time when the total volume of the ice residue becomes smaller than 10^{-7} m^3. In Sect. 8.9.2, the performance cost function J will be calculated for the other heater geometries and layouts to quantitatively compare de-icing performance.

8.9.2 De-icing Performance Comparison for Different Heater Layouts

In this section, the computational modeling of ice melting and de-icing performance comparison is investigated for the different heater shapes and layouts explained at the beginning of Sect. 8.9. In the following simulations, distributed heaters are placed on both upper and lower surfaces of the blade region starting from the leading edge for the first 40 % chord length. By investigating different geometries in AN-SYS, it is noticeable that placing heaters on both sides of the blade, while using the same amount of total thermal power (meaning using half of the heat flux for each individual resistor) provides a more uniform de-icing especially for those blade geometries that have smaller cavities, or are less thermally conductive. Intuitively, placing resistors on both upper and lower sides of the blade also provides a more effective de-icing when ice accumulates on both sides of the blade.

For the following simulations in this section, the thickness of the resistors is 0.5 mm. Resistors are modeled as a volume, where each face has a heat flux magnitude of 400 W/m^2. No convection is assumed in the boundary conditions for these simulations. By performing several simulations in ANSYS, it is observed that these modifications expedite the simulation time while not fundamentally changing the outcome of the de-icing performance comparison between different heater layouts and the layout optimization. In Figs. 8.20, 8.21, 8.22, and 8.23, the ice layer residue is shown for different heater layouts. For all of these simulations, the ice thickness is divided into four layers (in the mesh setting) in order to accurately capture the ice thickness variation during the melting process. Figure 8.20 shows the ice residue at $t = 200$ s after switching on the resistor network. It is seen that ice melting starts faster for circular heaters than square heaters, especially in the areas
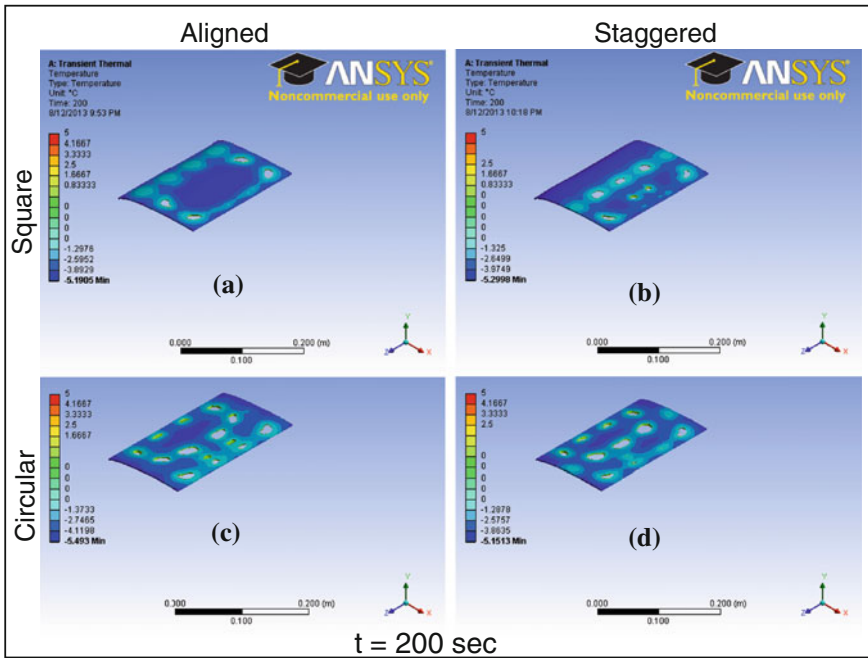
Fig. 8.20 Ice residue for different layouts at $t = 200$ s after switching on the resistors with an input heat flux of $q = 400$ W/m^2. **a** Aligned square layout with $V_{ice} = 1.145 \times 10^{-4}$ m^3. **b** Staggered square layout with $V_{ice} = 1.15 \times 10^{-4}$ m^3. **c** Aligned circular layout with $V_{ice} = 9.95 \times 10^{-5}$ m^3. **d** Staggered circular layout with $V_{ice} = 9.78 \times 10^{-5}$ m^3

close to the leading edge due to faster diffusion of the heat flux in those regions. The circular heaters also diffuse the flux more uniformly throughout the ice layer. The staggered circular layout is slightly faster than the aligned circular layout in melting the ice in the middle area of the modeled ice layer. The staggered square configuration does a relatively poor job compared to the other configurations in de-icing the areas close to the leading edge.

Figure 8.21 shows ice residue at $t = 400$ s after switching on the resistor network. It is observed that the square staggered layout does not effectively provide the required heat flux for melting the ice at the leading edge area, but instead transports higher heat flux at the second row of the heaters. This is aerodynamically less efficient compared to the other layouts. The aligned square layout results in a more effective ice melting close to the leading edge but it can not effectively de-ice the region in the middle of the ice layer. However, de-icing at the middle region is not as crucial as the leading edge area in terms of recovering the aerodynamic efficiency of the blade. Similar behavior is seen in the different layouts after this time until de-icing is completed for the accessible regions to the heat flux diffusion (Figs. 8.22, 8.23).

Figure 8.23 shows ice residue on the blade at $t = 800$ s for the different heater layouts. Among the four compared cases, the circular heaters provide the fastest

Fig. 8.21 Ice residue for different layouts at $t = 400$ s after switching on the resistors with an input heat flux of $q = 400$ W/m^2. **a** Aligned square layout with $V_{ice} = 7.64 \times 10^{-5}$ m^3. **b** Staggered square layout with $V_{ice} = 8.72 \times 10^{-5}$ m^3. **c** Aligned circular layout with $V_{ice} = 4.97 \times 10^{-5}$ m^3. **d** Staggered circular layout with $V_{ice} = 5.58 \times 10^{-5}$ m^3

de-icing times t_{di} of less than 800 s assuming that there is no convection loss on the blade surface. Adding equal forced convection loss does not change the outcome of layout performance comparison. Furthermore, the ANSYS simulation results show that the de-icing times t_{di} for aligned square and staggered square layouts are 1,350 and 1,116 s, respectively. Although the staggered square layout melts the ice layer faster than the aligned square layout, it is not capable of removing ice from the leading edge area for a long time. Therefore, the aligned square layout is preferable to the staggered square layout for localized active de-icing because it removes the ice first from the leading edge area.

The values of the performance cost function *J* based on Eq. (8.4) for different heater layouts and geometries are shown in Table 8.2. These results show that staggered circular heaters achieve the best performance with 40 % faster de-icing and 39.3 % smaller maximum blade temperature compared to aligned square heaters. Furthermore, $V_{T>30}$ is reduced from 6.5 % to 0.5 % of the blade volume using staggered circular heaters compared to aligned square heaters. Comparing aligned circular heaters to aligned square heaters shows 39.8 % faster de-icing, 29.5 % reduction in T_{max_b}, and reduction of $V_{T>30}$ from 6.5 % to 1.15 % of the blade volume for aligned circular heaters. Other polygon heaters (pentagonal and
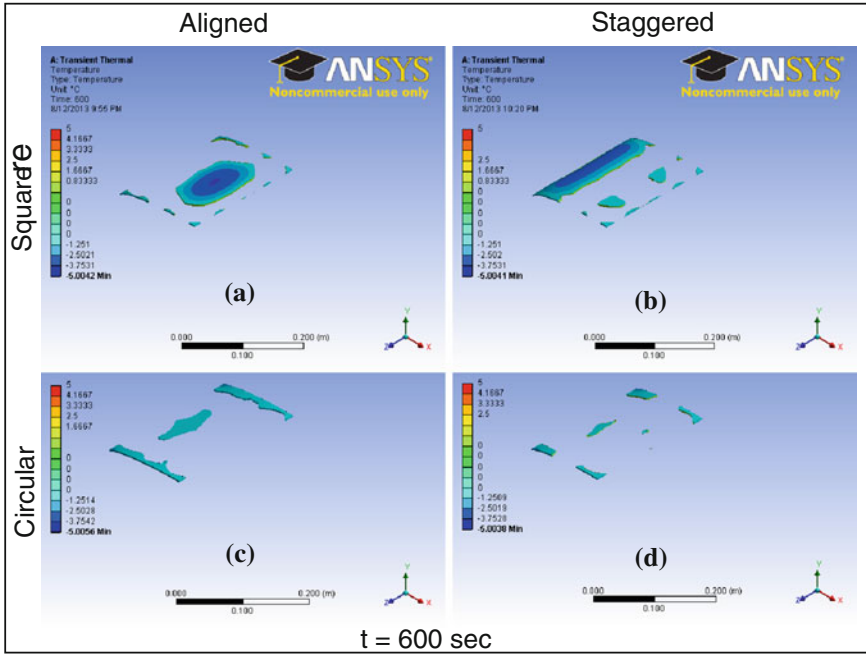
Fig. 8.22 Ice residue for different layouts at $t = 600$ s after switching on the resistors with an input heat flux of $q = 400$ W/m^2. **a** Aligned square layout with $V_{ice} = 3.46 \times 10^{-5}$ m^3. **b** Staggered square layout with $V_{ice} = 4.57 \times 10^{-5}$ m^3. **c** Aligned circular layout with $V_{ice} = 1.58 \times 10^{-5}$ m^3. **d** Staggered circular layout with $V_{ice} = 8.1 \times 10^{-6}$ m^3

hexagonal) were investigated and it was observed that their de-icing performance cost value J is between the performance costs of the square and circular heaters in Table 8.2.

Besides minimizing the total de-icing time and improving ice melting efficiency in the leading edge area, decreasing the amount of applied thermal stress is another important factor to be considered in the design of distributed active de-icing systems. Our calculations show that aligned layouts induce higher thermal stress than staggered layouts, which result in higher maximum temperatures and larger areas with higher temperature on the blade. This observation is more subtle due to the partial absorption of the generated heat flux in the upper surface of the blade by the ice layer. In summary, in the case of using aligned heaters for de-icing, more careful considerations are needed in the selection of closed-loop control gains to avoid high thermal stress induction to the blade structure. Clearly, having reliable and accurate on-the-blade optical sensing prevents this high thermal stress induction by switching off those resistors near the regions where ice does not exist.

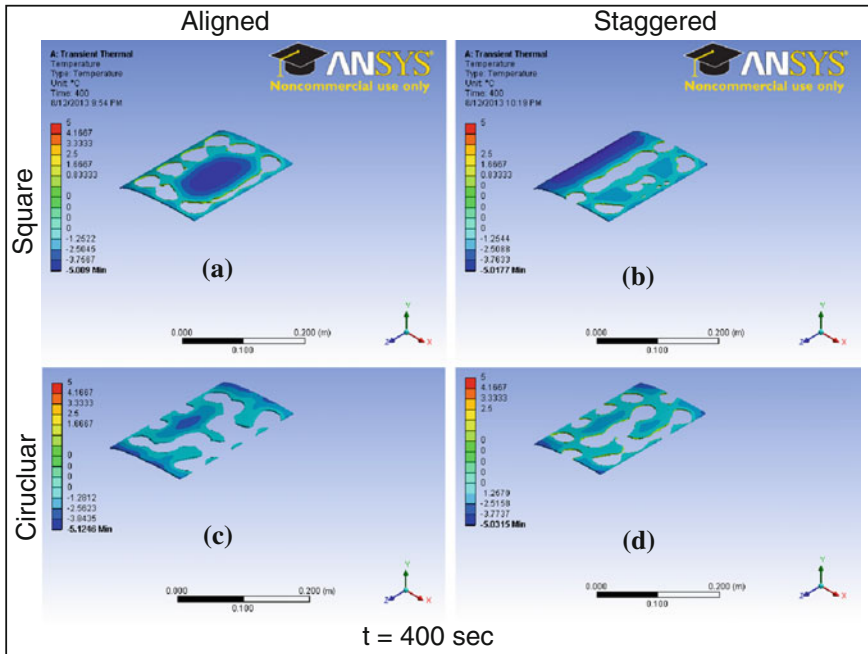Aligned   Staggered

t = 800 sec
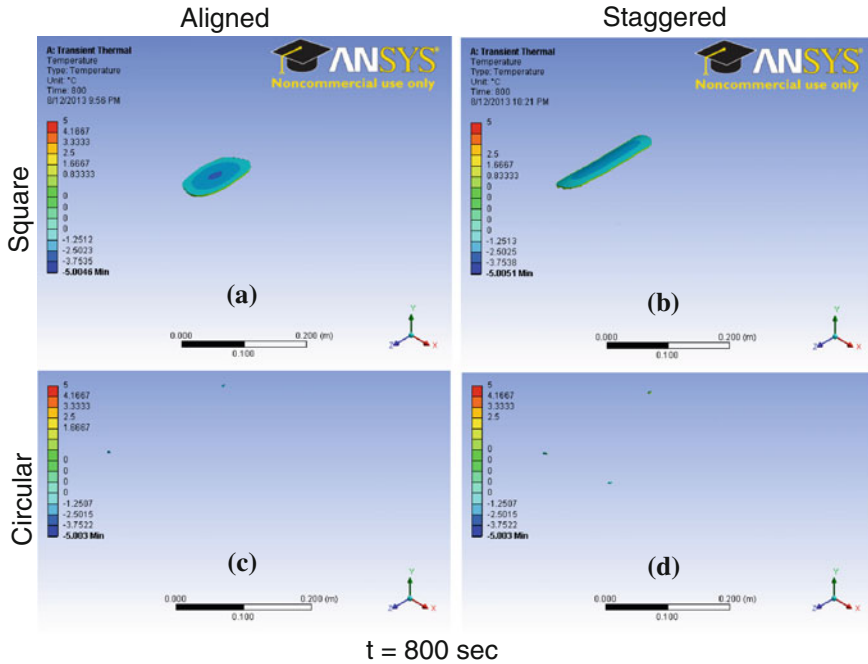
Fig. 8.23 Ice residue for different layouts at $t = 800$ s after switching on the resistors with an input heat flux of $q = 400$ W/m^2. **a** Aligned square layout with $V_{ice} = 2.1 \times 10^{-5}$ m^3. **b** Staggered square layout with $V_{ice} = 2.48 \times 10^{-5}$ m^3. **c** Aligned circular layout with $V_{ice} = 1.55 \times 10^{-8}$ m^3. **d** Staggered circular layout with $V_{ice} = 9.63 \times 10^{-8}$ m^3

Table 8.2 Quantitative performance cost comparison (Percentage reductions for each parameter relative to aligned square layout is written in the parenthesis)

Heater layouts	t_{di} (sec)	$T_{\max_b}$ (°C)	$V_{T>30}$ m^3	J
Aligned square	1,350	56.31	3.48×10^{-5}	3
Staggered square	1,116 (-17.33 %)	41.59 (-26.14 %)	1.73×10^{-5} (-50.29 %)	1.48 (-50.66 %)
Aligned circular	813 (-39.78 %)	39.70 (-29.50 %)	6.02×10^{-6} (-82.70 %)	0.89 (-70.33 %)
Staggered circular	798 (-40.89 %)	34.18 (-39.30 %)	2.85×10^{-6} (-91.81 %)	0.72 (-76.00 %)

8.10 Preliminary De-icing Experimental Results

In the first part of this section, we describe the closed-loop experimental results of active de-icing using an initial distributed PID controller with combined ice and temperature sensing. We will discuss the total amount of consumed energy relative to the size of our blade. In Sect. 8.10.2, we compare experimental results of this

PID controller with a higher intensity pulse amplitude modulation (PAM) actuation that uses the same amount of electrical energy. The magnitude and duty cycle of the PAM signal are updated at each time step based on the magnitude of the continuous PID signal to match the consumed energy over one signal period.

8.10.1 Distributed Closed-Loop Control Experiments

For the results described in this section, each heater receives information from the two adjacent optical ice sensors, and the heater stays on only if both of the adjacent ice sensors detect ice. Ultimately, we can use information from all four surrounding optical ice sensors adjacent to each resistor if necessary; however, this makes the closed-loop controller slower by adding computations required for signal processing. The initial control systems discussed here only use ice existence information. Further experimental investigation is needed for a characterization of the thermodynamic characteristics of different types of ice. Ice type and thickness information provided by the OFDR ice sensing system can be used in future versions of the control system design.

The control gains for each heater at the leading edge are calculated based on the temperature information from the adjacent temperature sensors. For the initial closed-loop test of de-icing, since there is only one temperature sensor for each "column" of thermal resistors in the chord-wise direction of the blade, the same voltage was applied for each column of resistors. Figure 8.24 shows different stages of ice formation on the blade before the active de-icing control system was switched on in the icing chamber. Figure 8.24a shows rime and glaze ice formed on the blade in the icing chamber. Glaze ice was created in the chamber by directly pumping humidity to the blade surface under the condition of no wind. Uniform rime ice is created on the blade when there is nonzero wind velocity in the icing chamber (from a fan).

A PID control has been implemented to each column of resistors in the network. The applied voltage to resistor j is:

$$v_j = K_g \left[K_p e_j(t) + K_i \int_0^t e_j(\tau) d\tau + K_d \frac{d}{dt} e_j(t) \right] \qquad (8.6)$$

where K_g is the gain of the op-amp circuit, $e_j(t)$ is the error between the desired temperature (T_d) and current temperature $(T_{a_j}(t))$ on the blade for channel j at time t, K_p is the proportional gain, K_i is the integral gain, and K_d is the derivative gain.

Figure 8.25 shows the time history of the voltage and temperature for channel 1 (see Fig. 8.11) from the beginning to the end of the activated PID control for de-icing using distributed resistors, optical ice sensors, and temperature sensors, where the maximum voltage indicates that approximately half of the maximum power capability of the individual kapton resistor has been used. Similar behavior has been captured with the remaining resistors. It takes approximately 3 min until
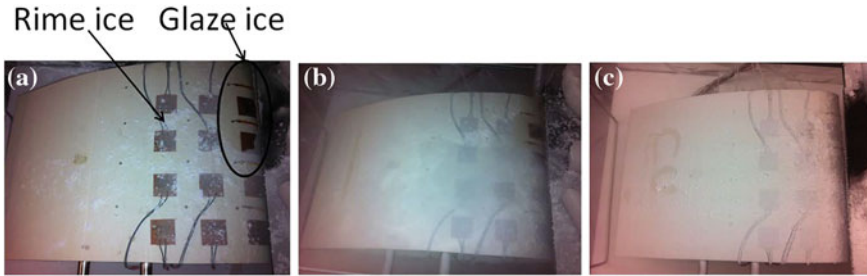
Fig. 8.24 Different stages of ice formation on the blade before switching the controller on. **a** Rime and glaze ice started to form on the blade at $t = 0$. **b** Blade slightly covered with rime ice at $t = 17$ min. **c** Blade covered with 5 mm thick rime ice at $t = 90$ min
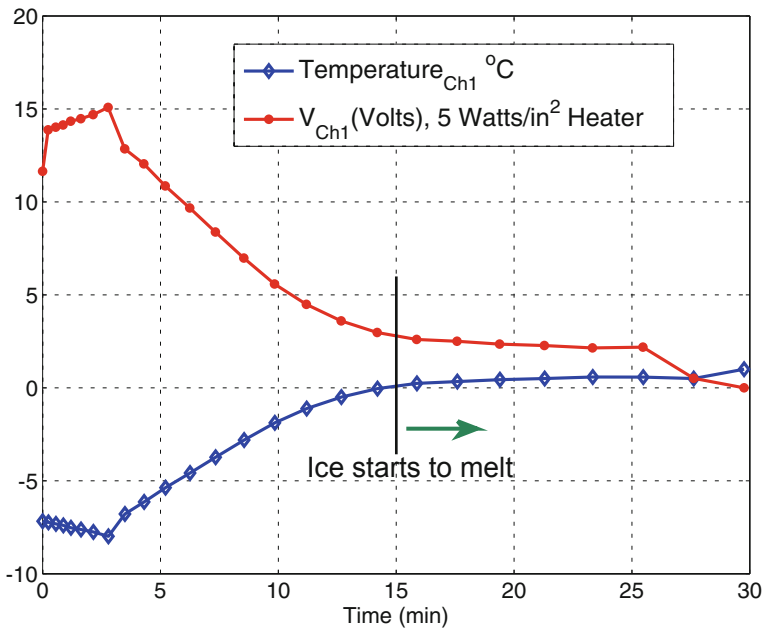
Fig. 8.25 Time history of voltage and temperature for a selected channel when using distributed PID control for de-icing, using approximately half of the maximum power capability of the actuation system with empirically tuned PID gains of $K_p = -0.5$ v/(°C), $K_d = -0.01$ v/(°C/s), $K_i = -0.001$ v/(°C·s), and closed-loop update rate of 0.5 Hz

the resistive heaters start to increase the local temperature at the leading edge, 2 cm away from the edge of the boundary of the leading edge resistors. Then the voltage on the resistor decreases as the temperature increases toward the desired temperature (+2 °C). After de-icing and satisfying a no ice condition on both of the optical channels 1 and 2, the control system automatically shuts down the corresponding resistor 1. This de-icing took about 30 min in an ambient temperature of

approximately $-10\,°C$ inside the icing chamber while the outer blade surface temperature reached the desired temperature (T_d) at the corresponding channel 1 thermocouple. Ice melting started to happen approximately 15 min after switching on the controller.

The total average power consumption from time 0 to t for the distributed resistor network is calculated as

$$P_{\text{total}} = \sum_{j=1}^{n=12} \frac{1}{R_j t} \int_0^t v_j^2(\tau)\mathrm{d}\tau. \tag{7}$$

where n is the total number of thermal resistors in the network, R_j is the resistance of heater element j, and v_j is the applied voltage to element j. The total power consumption for the network of 12 resistors using distributed PID control in our test was about 4 W. Our blade dimension is approximately 1/100 of a blade on a 500 KW wind turbine. Simply scaling up, a similar PID controller and de-icing network on a three-bladed 500 KW wind turbine needs about 1,200 W of de-icing power which is only about 0.24 % of the rated power, which is similar but somewhat less than the experimental study in [32]. This is a very small power consumption for an active de-icing system which could improve the net average annual power capture significantly by improving aerodynamic efficiency and reducing wind turbine downtime under icing conditions [12, 33]. The fractional power consumption for this localized heating is only about 10 % of the power consumed when uniformly heating the entire blade.

8.10.2 High Intensity Pulse Amplitude Modulation

A number of tests have been performed to compare de-icing performance between the low intensity continuous PID actuation described in Sect. 8.10.1 and a higher intensity PAM actuation. PAM actuation is preferable and more efficient compared to duty cycle modulation with constant amplitude as long as we ensure that the amount of thermal power does not cause large local thermal stresses that can hurt the blade structure. Much higher signal amplitudes for de-icing are initially required when the outer blade surface temperature may be much lower than the desired blade outer surface temperature. In PAM, the signal amplitude goes to zero as the desired blade outer surface temperature is reached.

Figure 8.26 shows pictures of de-icing results for these two actuation methods over time. Ice is first "grown" on the blade to approximately 5 mm thickness across both resistive heaters. Then the two different control strategies are turned on simultaneously on the two different resistive heaters with an update rate of 10 Hz. For this experiment, optical ice sensors were switched off from the closed-loop controller since we started with the known initial ice condition on the blade. Therefore, a much faster update rate of 10 Hz was implemented compared to the results shown in Fig. 8.25, where an update rate of 0.5 Hz was used with active
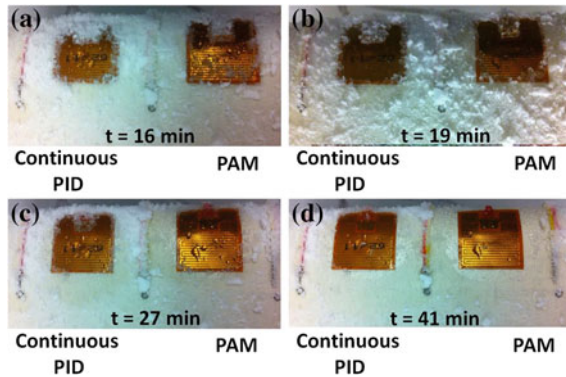
Fig. 8.26 Visual comparison of low intensity continuous PID actuation versus higher intensity PAM actuation with the same amount of electrical energy expenditure. The PAM frequency is 0.1 Hz. Over each period, the PAM actuation has a 40 % duty cycle, and a pulse magnitude that is 1.581 times larger than the continuous PID signal. The icing chamber temperature is slightly higher than −10 °C throughout the test. More rime ice residue can be seen on the heater for the lower intensity continuous PID control compared to the PAM control at all times. **a** $t = 16$ min. **b** $t = 19$ min. **c** $t = 27$ min. **d** $t = 41$ min

optical ice sensors (and associated signal processing algorithms) in the closed-loop. In Fig. 8.26, both of the resistors use the same amount of electrical energy. It is shown visually that PAM provides better de-icing results and faster thermal energy propagation through the composite blade. Running several analogous experiments generated repeatable results.

Figure 8.27 shows the applied voltage and temperature variation for these two different actuation techniques. It is seen that PAM actuation has a better de-icing performance than continuous PID control when using the same amount of electrical energy by yielding a higher temperature at the closest thermocouple at all times. These two temperature sensors are mounted diagonally from the corner of each resistive heater with the same distance. The improved performance of the PAM controller is due to a high thermal inertia of the resistive heaters that can hold the required heat for a while (more than 15 s) even after switching off before the generated thermal energy is dissipated by convection loss. Further investigations are needed for different wind speeds and blade pitch angles. These test results are for a no wind condition (natural convection) and a nonrotating (stationary) blade where convection loss is normally less compared to a rotating wind turbine under similar environmental conditions.

8.11 Conclusion

Optical ice sensing and distributed resistive heating have been investigated for active de-icing of wind turbines. Distributed electrothermal actuation is capable of locally adjusting the thermal power at different blade locations in order to reduce
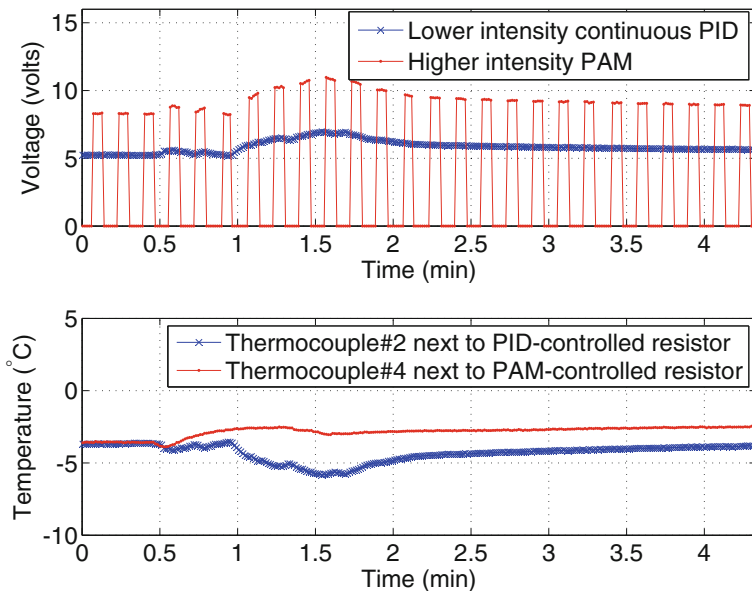
Fig. 8.27 **a** Lower intensity continuous PID controller applied voltage (resistor channel 2) with the gains $K_p = -0.25$ v/(°C), $K_d = -0.005$ v/(°C/s), $K_i = -0.0005$ v/(°C•s), and PAM applied voltage (resistor channel 3) with the same electrical energy over one signal period. Both are 10-W resistors. Lower PID gains are selected compared to the previous subsection (shown in Fig. 8.25) to assure that the higher intensity PAM signal is amplified within the operational linear range of our custom amplifier, before reaching the saturation limit, and to prevent causing large thermal stresses in the *blade structure*. **b** Temperature variation at thermocouple 2 adjacent to resistor channel 2 with lower intensity continuous PID signal and at thermocouple 4 adjacent to resistor channel 3 with higher intensity PAM signal with the same amount of electrical energy expenditure. The time axis denotes the time after both PID and PAM controllers are simultaneously turned on

the energy consumption for efficient active de-icing. The feasibility of this method has been experimentally demonstrated. Development of an aero/thermodynamic model for a blade with distributed heat sources is extremely beneficial for the implementation of an optimal closed-loop control as well as for reducing instrumentation costs by removing the requirement for temperature sensors on the blade. However, developing a fully analytical model for such a complex dynamical system is very difficult, if possible at all.

A computational thermodynamic model for distributed resistive heaters was developed using ANSYS. This computational model was validated with experimental results using a continuous PID control for thermal actuation. Further, different heater geometries (square, circular, and hexagonal) for two different heater layouts (aligned and staggered) were modeled in ANSYS. Our simulations show faster and more uniform de-icing for circular heaters, and lower thermal stress to the blade structure for staggered layouts under constant input heat flux to the resistor network.

Experimental results of closed-loop distributed de-icing were also presented on a stationary turbine blade part at a fixed pitch angle inside a custom icing chamber. Scaling up the experimental results showed that using combined OFDR with temperature sensing and distributed PID control uses a total power expenditure of less than 0.5 % of the rated power under light/medium icing conditions; de-icing could yield a larger percentage of power improvement and a longer turbine uptime in cold regions. The power consumption for this localized heating was only about 10 % of the power used when uniformly heating the blade. Furthermore, de-icing performance of high-intensity pulsed actuation versus continuous low intensity actuation was investigated. The results show that using high intensity pulse amplitude modulation (PAM) actuation achieves better de-icing performance than continuous PID control.

8.12 Future Work

In future work, in order to optimize the heater layout design on a full-scale blade of a specific wind turbine, we will look at the effect of different ice shapes, sizes, and locations on lift, drag, and power using a computational fluid mechanics approach. Optimal layout design of the heaters for active de-icing depends on the blade size, thermal properties, and the cost of heaters, which can vary from the results discussed in Sect. 8.9. In addition, we will use the computational model for the development of a pseudo−analytical aero/thermodynamic model that can be used to estimate leading edge temperatures instead of requiring temperature sensors. The temperature estimates can then be used to calculate closed-loop commands for each individual resistor. Furthermore, this model will be very useful in designing suitable closed-loop control strategies under known faulty resistors in the network.

References

1. Seifert H, Richert F (1997) Aerodynamics of iced airfoils and their influence on loads and power production. In: Proceedings of European wind energy conference
2. Baring-Gould I, Tallhaug L, Ronsten G, Horbaty R, Cattin R, Laakso T, Durstewitz M, Lacroix A, Peltola E, Wallenius T (2009) Recommendations for wind energy projects in cold climates. Technical report, International Energy Agency
3. Laakso T, Baring-Gould I, Durstewitz M, Horbaty R, Lacroix A, Peltola E, Ronsten G, Tallhaug L, Wallenius T (2009) State-of-the-art of wind energy in cold climates. Technical report, International Energy Agency
4. Boluk Y (1996) Adhesion of freezing precipitates to aircraft surfaces. Transport Canada, pp 44
5. Fikke S et al (2006) Atmospheric icing on structures: measurements and data collection on icing: state of the art. MeteoSwiss 75:110
6. ISO-12494 (2001) Atmospheric icing of structures. ISO copyright office, Geneva, p 56
7. Richert F (1996) Is Rotorcraft icing knowledge transferable to wind turbines? BOREAS III. FMI, Saariselkä, pp 366–380
8. Ilinca A (2011) Analysis and mitigation of icing effects on wind turbines. In: Al-Bahadly I (ed) Wind turbines, 1st Edn. InTech, Rijeka
9. Mason J (1971) The physics of clouds. Technical report. Oxford University Press, London
10. Homola M, Nicklasson P, Sundsbo P (2006) Ice sensors for wind turbines. J Cold Reg Sci Technol 46:125–131
11. Makkonen L (2000) Jn Detektointi Kosteusmittauksen Avulla [Detection of Ice from Humidity Measurements]. Technical report, Report in Finnish to the Vilho, Yrj and Kalle Visl Foundation, Helsinki
12. Parent O, Ilinca A (2011) Anti-icing and de-icing techniques for wind turbines: critical review. J Cold Reg Sci Technol 65:88–96
13. Geraldi J, Hickman G, Khatkhate A, Pruzan D (1996) Measuring ice distribution on a surface with attached capacitance electrodes. Technical report, United States Patent number 5,551,288
14. Shajiee S, Wagner P, Pao L Y, Mcleod R R (2012) Development of a novel ice sensing and active de-icing method for wind turbines. In: Proceedings of AIAA aerospace sciences meeting, Nashville, 15 p
15. Walsh M (2010) Accretion and removal of wind turbine icing in polar conditions. Masters Thesis, AALTO University, Helsinki
16. Mulherin N, Richter-Menge J, Tantillo T, Gould L, Durell G, Elder B (1990) Laboratory test for measurement of adhesion strength of spray ice to coated flat plates. Cold regions research and engineering, Laboratory report 90-2, US Army Corps of Engineers
17. Battisti L, Baggio P, Fedrizzi R (2006) Warm-air intermittent de-icing system for wind turbines. Wind Eng 30(5):361–374
18. Wang X (2008) Convective heat transfer and experimental icing aerodynamics of wind turbine blades. Ph.D. Thesis, University of Manitoba
19. Marjaniemi M, Peltola E (1998) Blade heating element design and practical experiences. In: BOREAS IV conference on wind energy production in cold climates, Yllas
20. Makinen J (1996) Ice detection and de-icing system improves the economics of a wind turbine in the Arctic weather conditions. In: BOREAS III conference on wind energy production in cold climates, Saariselka
21. Huber R, Wojtkowski M, Fujimoto JG (2006) Fourier domain mode locking (FDML): a new laser operating regime and applications for optical coherence tomography. J Opt Express 14:3225–3237
22. Moore ED, McLeod RR (2011) Phase-sensitive swept-source interferometry for absolute ranging with application to measurements of group refractive index and thickness. J Opt Express 19:8117–8126

23. Fuhr PL, Huston DR (1993) Multiplexed fiber optic pressure and vibration sensors for hydroelectric dam monitoring. Smart Mater Struct 2:260
24. Laakso T, Peltola E (2005) Review on blade heating technology and future prospects. In: BOREAS VII FMI, Saariselkä, pp 2–13
25. Mayer C, Illinca A, Fortin G, Perron J (2007) Wind tunnel study of electro-thermal de-icing of wind turbine blades. Int J Offshore Polar Eng 17:182–188
26. Omega Eng. www.Omega.com
27. Hochart C, Fortin G, Perron J, Ilinca A (2008) Wind turbine performance under icing conditions. Wind Energy 11:319–333
28. MathWorks. http://www.mathworks.com
29. National Instruments Corporation. http://www.ni.com
30. ANSYS Inc. www.ANSYS.com
31. Dassault Systemes SolidWorks Corp. www.SolidWorks.com
32. Dierer S, Oechslin R, Cattin R (2011) Wind turbines in icing conditions: performance and prediction. Adv Sci Res 6:245–250
33. Shajiee S, Pao LY, Wagner P, Moore ED, McLeod RR (2013) Direct ice sensing and localized closed-loop heating for active de-icing of wind turbine blades. In: Proceedings of American control conference, pp 634–639, Washington, D.C.

Chapter 9
Structural Health Monitoring of Wind Turbine Blades

Hui Li, Wensong Zhou and Jinlong Xu

Abstract Wind turbine blades usually achieve a very long operating life of 20–30 years. During their operation, the blades encounter complex loading with a high number of cycles as well as severe weather. All of these factors result in accumulated damage, acceleration of fatigue damage, and even sudden blade failure, which can cause catastrophic damage to the wind turbine. In recent years, many structural health monitoring (SHM) techniques, including global and local methods, have been developed and applied as important and valid tools to detect the damage of wind turbine blades. This chapter provides a comprehensive review and analysis on the state of the art of SHM for blades. Then, the SHM techniques are described in detail. For the global method, this chapter discusses mainly the vibration-based damage detection problem for wind turbine blades given the rotation effects. For the local methods, a fatigue damage detection system used for wind turbine blade is developed using high spatial resolution differential pulse-width pair Brillouin optical time-domain analysis (DPP-BOTDA) sensing system and PZT sensors is introduced to detect the tiny damage under static loading.

Keywords Wind turbine blades · Damage detection · Vibration-based method · DPP-BOTDA · PZT

H. Li (✉) · W. Zhou · J. Xu
School of Civil Engineering, Harbin Institute of Technology, 150090 Harbin, China
e-mail: lihui@hit.edu.cn

W. Zhou
e-mail: zhouwensong@hit.edu.cn

J. Xu
e-mail: jinlongxu@hit.edu.cn

Nomenclature

A	Section area of elements
$b_{\max,k}$	The largest length of the signal curve of every time series as the interval time is k
$b_{\min,k}$	The length of the signal curve which pass through no damaged region as the interval time is k
C	System damping matrix
E	Elastic modulus, the residual error
$FD_{\max}$	The largest value of estimated FD of the curve of each time series
J	FD-based damage acuteness index
K	System stiffness matrix
K_s	The structural stiffness
K_d	The additional stiffness
K_0	Is the normal modal stiffness matrix
$K_1(\alpha)$	The stiffness matrix of the geometric nonlinearities
L	The length of time series of PZT signal
M	System mass matrix
n	The degrees of freedom of the structure, the refractive index of the fiber core
NI	The damage index based on PCA method
$\bar{NI}$	The mean value of NI
t	Time
T	The loading matrix
u_0	The displacement in x direction
v	The external force
V_a	The velocity of the acoustic wave
v_B	The Brillouin frequency shift
v_0	The displacement in y direction
X	The scores matrix
$\hat{X}$	The reconstructed data
Y	The compressed data
Z	The displacements of the degrees of freedom of the structure
$\dot{Z}$	The velocities of the degrees of freedom of the structure
$\ddot{Z}$	The accelerations of the degrees of freedom of the structure
U	The potential energy of strain
α	The modal coordinate, the first Rayleigh damping coefficients
β	The second Rayleigh damping coefficients
ε	The normal strain
λ	The eigenvalues, the vacuum wavelength of the pump light
σ	Standard deviation
ω	The angular frequency
$[]$	The Gauss' notation

9.1 Introduction

Wind energy has been developed rapidly throughout the world. According to the World Wind Energy Report 2010 of the World Wind Energy Association, in the year 2010, the wind capacity reached 196 GW worldwide, after 159 GW in 2009, 120 GW in 2008, and 93 GW in 2007, and the trend wherein the installed wind capacity more than doubles every third year continues. However, as more wind turbines are built worldwide, the number of accidents recorded increases as well. During the last 10 years, more than 1,000 wind turbine accidents have been reported as well as 132 accidents per year from 2007 to 2011 inclusive. As the most critical and expensive components of the wind turbine system, wind turbine blades often suffer damage. According to the Caithness Windfarm Information Forum, by far the greatest number of incidents found was due to blade failure. "Blade failure" can arise from a number of possible sources and results in either whole blades or pieces of blade being thrown from the turbine. A total of 234 separate incidences were found up to March 2012.

Wind turbine blades usually achieve a very long operating life of 20–30 years. They are the only part of the turbine designed specifically for the wind energy industry. During their operation, blades encounter complex loading with a high number of cycles, such as aerodynamic loads, centrifugal inertia forces, changing gravity moments, braking force, and accidental impacts as well as severe weather such as moisture absorption, wind gusts, or lightning strikes. All of these factors result in accumulated damage, acceleration of fatigue damage, and even sudden blade failure, which can cause catastrophic damage to the wind turbine. At the same time, the downtime of the blades for extended repair and maintenance resulting from undiscovered damage can lead to large economical losses. Thus, much research effort is now focused on real-time monitoring techniques. In recent years, many structural health-monitoring (SHM) techniques, including vibration-based, optical fiber sensing, and piezoelectric techniques, have been developed and applied as important and valid tools.

Currently, a number of techniques are being investigated for damage detection of wind turbine blades. Optical fiber Bragg grating (OFBG) sensors have been used to measure strain at various spatial locations and to detect severe damage modes, such as the failure of adhesive joints or the delamination and failure of blades due to their excellent sensing and mechanical performance and their capability of online monitoring [1–4]. OFBG sensors can be patched on the surface of the blades or embedded into textile-reinforced composites [5, 6]. They can be integrated with other sensors as well [7, 8]. However, OFBG sensors can still only measure the local deformation, but not the damage, such as the impacted damage or active cracks, which are far away from the location of sensors. In the meantime, the distributed optic sensors based on Brillouin scattering show great advantages of environmentally stable, immunity to electromagnetic interference, and distributed sensing over extremely long distances with increasingly high accuracy. The scheme of Brillouin optical time-domain analysis (BOTDA) is much preferable

due to its high signal-to-noise ratio (SNR) and high accuracy. Usually, BOTDA employs two counterpropagating lights, i.e., a pump pulse and a CW probe wave, to induce stimulated Brillouin scattering (SBS) and its spatial resolution is determined by the pump pulse width [48]. Shorter pulse width means higher spatial resolution but lower accuracy. Shorter pulse will get weaker Brillouin signal, broaden the Brillouin gain spectrum (BGS), and decrease the SNR, which results in a 1 m spatial resolution limitation for the distributed optic sensors. In 2008, Li W and Bao X et al. proposed the differential pulse-width pair (DPP) technique in BOTDA achieving high-spatial resolution by using a small difference in the pulse pair based on the mechanism of prepumping the acoustic wave [49]. The spatial resolution of the DPP-BOTDA system is determined by the differential pulse, i.e., the pulse-width difference of the pulse pair, rather than the original pulses [49, 50]. Other local sensing techniques, such as PZT-based techniques, have also been investigated frequently. With these techniques, an array of sensors can capture the stress waves passively generated by active damage to identify the type or location of the damage [9–13]. On the other hand, sensor arrays are also used for receiving stress waves generated by the actuator arrays to actively detect the damage in the path of wave propagation [14, 15].

In addition, global vibration-based monitoring methods are also employed to detect structural damage to blades, which might occur far from the location of the sensors. The global vibration-based methods can identify damage inside the blade without having to map over the surface of the entire blade with a sensor. Gross et al. verified the damage detection method using modal response data from a wind turbine blade [16]. They loosened the bolts at the root of one of the three blades to simulate a damaged blade and acquired the structural response data using accelerometers mounted on the blade. Three damage detection techniques making use of the strain energy, modal flexibility matrix, and differences in mode shapes have been used. Ghoshal et al. tested four vibration-based damage detection techniques on a section of a fiberglass blade. The structural damage was simulated by a steel plate (additional mass) clamped to the blade. A periodic signal with a frequency bandwidth of 100–500 Hz was used to excite the blade and the frequency response function, transmittance function, operational deflection shape, and resonant comparison were compared between the damaged and healthy structure [17]. Kraemer and Fritzen presented a three-step concept for the structural health monitoring of offshore wind energy plants [18]. The basic idea is also based on the global approach and involves vibration measurements, the stochastic subspace fault detection method, and the multivariate autoregressive model. Whelan et al. proposed an integrated monitoring of wind plant systems, which consisted of a wireless network and a large array of multiaxis accelerometers to evaluate the modal properties of the system as well as individual members [19]. Dolinski and Krawczuk described a vibration-based method for damage localization in a composite wind turbine blade based on a one-dimensional continuous wavelet analysis applied to mode shapes. They simulated a series of different localizations and sizes of damage. The results were obtained from both numerical simulation and a scale model [20]. Frankenstein et al. also employed the global damage

detection method based on an analysis of the low-frequency structural vibration and combined the local damage detection methods. In their works, the modal identification was implemented by means of the so-called operational modal analysis methods [15].

For vibration-based damage detection methodologies, the initial assumption is that the structural vibration properties are affected only by structural damage, which results in changes in the structural stiffness and/or structural mass. It has been proven that vibration-based methodologies are valid for most mechanical and aerospace structures. However, more than 10 years ago, in the civil engineering community, it was found that for real full-scale engineering structures, varying environmental factors such as temperature, prestress, traffic load, wind, and humidity, can also affect the structural vibration properties. These environmental factors may mask the changes caused by structural damage [21–30]. If the effect of these environmental or operational variations is not taken into account in the damage detection process, a false-positive or negative damage diagnosis may occur such that vibration-based damage detection becomes unreliable.

For a wind turbine blade in operational condition, uniform temperature effects can be ignored because it is a cantilever beam structure, and gradient temperature effects will be small due to its continuous motion and relatively small section size. However, rotational motion interferes with the detection of damage in a wind turbine blade because it changes the vibrational characteristics of the blade. Compared to nonrotating structures, the stiffness of the wind turbine blades will increase due to both stretching caused by centrifugal inertia forces caused by the rotational motion and the increment of the bending stiffness of the structure, which results in the variation of the natural frequencies and mode shapes [31–34]. Osgood [33] and Park et al. [34] demonstrated that the natural frequencies of wind turbine blades may change with their rotational speed. In this case, vibration-based damage detection methods will be invalid because the structural modal properties vary with the rotational speed of wind turbine blades and not only due to structural damage.

Furthermore, it is well known that all vibration-based damage detection processes rely on vibration data with inherent uncertainties, which are due to the mechanical model, the data acquisition system, and other process noise; thus, it makes sense to use statistical methods to handle damage problems. A few methods of this type have been developed [35–38]. The purpose of the current study is to make use of a methodology based on principal component analysis (PCA), which is able to reject the rotational effect to detect damage using vibration data from a healthy and damaged structure. This method was proposed by Yan et al. for structural damage diagnosis under varying environmental conditions [23]. In this method, the influencing variables need not be measured in advance, and their effects will be removed during the damage detection procedure. The remaining minor components were used to detect the damage.

This chapter descripts structural health monitoring of wind turbine blades using three frequently used techniques including PZT-based, vibration-based, and optical sensor-based damage detection methods.

9.2 Vibration-Based Damage Detection of Rotational Wind Turbine Blades

9.2.1 Structural Dynamic Model of Rotating Blades

A general horizontal axis wind turbine (HAWT) consists of three basic parts: the tower, the nacelle, and the blades. The blades are fixed to the hub; see Fig. 9.1. In general, this system can be considered as flexible bodies attached to moving supports, which have been described in a number of technical papers considering rotating machinery, helicopter rotor blades, and so on.

A stationary linear dynamical model for the blade in still conditions is generally suitable for structural dynamic analysis:

$$M\ddot{Z}(t) + C\dot{Z}(t) + KZ(t) = v(t) \tag{9.1}$$

where M, C and K are the mass, damping, and stiffness matrices, respectively, their dimensions are $n \times n$, which is the degrees of freedom of the structure. Z collects the displacements of the degrees of freedom of the structure, and its dimension is $n \times 1$; the external force v is modeled as a nonstationary white noise.

However, for a rotational blade, because of the axial loads, such as centrifugal forces and changing gravity forces, on the blade effect the lateral and torsional deflections, the out-of-plane stiffness of a structure can be significantly affected by the state of in-plane stress in the structure. This coupling between the in-plane stress and transverse stiffness known as stress stiffening (or dynamic stiffening and geometric stiffening), first proposed by Kane et al. [39], is most pronounced in the blade structure. In this case, the conventional small-deflection theory models used in the nonrotating structures is no longer suitable. Kane et al. considered the system stiffness to be $K = K_s + K_d$, in which K_s is the structural stiffness and K_d depends on the angular velocity, based on the accurate description of the deformation of an elastic beam with a large overall motion [39]. In the past 20 years, a number of researchers have observed and investigated this topic, and several analytical approaches have been proposed to include stress stiffening terms in the
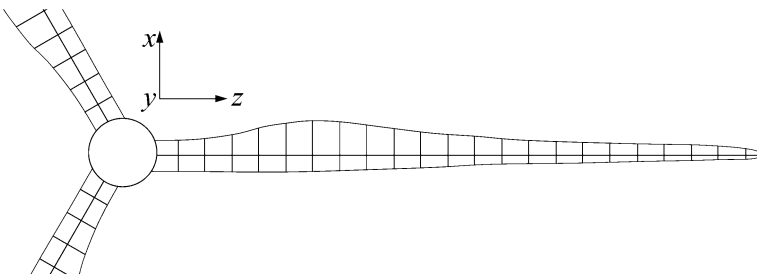
Fig. 9.1 Typical horizontal axis wind turbine blades

dynamic formulations of structures, such as the methodology based on the constraint of geometrical deformation [39], geometric nonlinearities [40], and initial stress [41].

The geometric nonlinearities considering the relation between the strain and deformation are nonlinear because the stiffness matrix of flexible bodies should be a function of motion status and stress. Therefore, the nonlinear relationship between the strain and deformation should be retained. For an elastic plane beam, the relation between the strain and deformation for one arbitrary point on the nonmidline is given by:

$$\varepsilon_{xx} = \frac{\partial u_0}{\partial x} - y\frac{\partial^2 v_0}{\partial x^2} + \frac{1}{2}\left(\frac{\partial v_0}{\partial x}\right)^2 \tag{9.2}$$

where u_0 and v_0 are the longitudinal and transverse deformations of the corresponding point on the midline, respectively. Thus, the corresponding potential energy of strain is also nonlinear. Bakr and Shabana reserved cubic terms without considering quartic ones [40] and presented the corresponding potential energy of strain:

$$U = \frac{1}{2}\int_0^L EA\left(\frac{\partial u_0}{\partial x}\right)^2 dx + \frac{1}{2}\int_0^L EA\frac{\partial u_0}{\partial x}\left(\frac{\partial v_0}{\partial x}\right)^2 dx$$
$$+ \frac{1}{2}\int_0^L EI\left(\frac{\partial^2 v_0}{\partial x^2}\right)^2 dx \tag{9.3}$$

where E is elastic modulus, A the section area, and I the moment of inertia.

Mayo retained the quartic terms in the expression of the potential energy of strain [42]:

$$U = \frac{1}{2}\int_0^L EA\left(\frac{\partial u_0}{\partial x}\right)^2 dx + \frac{1}{2}\int_0^L EA\frac{\partial u_0}{\partial x}\left(\frac{\partial v_0}{\partial x}\right)^2 dx$$
$$+ \frac{1}{2}\int_0^L EI\left(\frac{\partial^2 v_0}{\partial x^2}\right)^2 dx + \frac{1}{2}\int_0^L \frac{1}{4}EA\left(\frac{\partial v_0}{\partial x}\right)^4 dx \tag{9.4}$$

The total stiffness matrix derived from the potential energy of strain can be written as

$$K = K_0 + K_1(\alpha) \tag{9.5}$$

where K_0 is the normal modal stiffness matrix, which is a constant matrix, and $K_1(\alpha)$ is the stiffness matrix of the geometric nonlinearities, which is a function of the modal coordinate.

Therefore, the structural dynamic equation-based geometric nonlinearities method instead of Eq. 9.1 can be expressed with modal coordinates as

$$M\ddot{\alpha} + C\dot{\alpha} + [K_0 + K_1(\alpha)]\alpha = Q \tag{9.6}$$

where α is the modal coordinate. $K_1(\alpha)$ can be expanded based on the Taylor theorem as

$$K_1(\alpha) = K_1(0) + \frac{1}{2!}K_G(\alpha) + \frac{1}{3!}K_B(\alpha) \tag{9.7}$$

where $K_G(\alpha)$ is a linear function of modal coordinate α and $K_B(\alpha)$ is its quadratic function. Based on the method proposed by Sharf, the total stiffness matrix can be calculated iteratively.

In this chapter, a finite element analysis considering the effect of stress stiffening is employed to simulate the dynamic behavior of rotational blades. The effect of stress stiffening is taken into account by generating and then using an additional stiffness matrix, hereinafter called the stress stiffness matrix. The stress stiffness matrix is added to the regular stiffness matrix to determine the total stiffness.

9.2.2 Damage Detection Methodology: Principal Component Analysis

A principal component analysis (PCA) is a method based on the idea of reduced order whose purpose is to reduce the dimensionality of the data, while retaining as much as possible the characteristics of the original dataset. PCA has been applied in structural health monitoring [43], modal analysis [44], and the elimination of environmental effects in damage detection [23, 24]. In the present work, it will be shown that this method is useful for eliminating the effects of rotation in the vibration-based damage detection of wind turbine blades.

The variations in environmental conditions (such as the rotational speed and temperature) are known to have considerable effects on vibrational features. Let us denote the n-dimension vector x_k as a set of vibration features identified at time t_k, ($k = 1\ldots N$) with N being the number of samplings. All of the x_k are collected in a matrix $x \in \Re^{n \times N}$, where n represents the number of selected modes, while the natural frequencies are chosen as the vibrational features. Then, PCA can compress the data by reducing the original dimension n to a lower dimension m:

$$Y = TX \tag{9.8}$$

where X is called the scores matrix and $T \in \Re^{m \times n}$ is the loading matrix; the dimension m is considered the number of principal components that affect the

feature. Using this dimension reduction process, the embedded relation between the rotational speed and the features can be captured.

A practical method to obtain the matrix T is extracting the main m eigenvectors that correspond to the largest m eigenvalues $\lambda_k (k = 1, \ldots, m)$, where the eigenvalues are written in decreasing order:

$$\lambda_1 \geq \lambda_2 \geq \cdots \geq \lambda_m \geq \lambda_{m+1} \geq \cdots \geq \lambda_n \to 0 \tag{9.9}$$

In most practical situations, we select $m < n$, and the cumulative contribution $\sum_{k=1}^{m} \lambda_k \Big/ \sum_{k=1}^{n} \lambda_k$ reaches a certain proportion (say, 80 or 95 %) [45], which means the m factors have a significant influence on the vibration features. In this work, the rotational speed will be the only significant factor, which means that m is equal to 1. In some other practical applications, where the number of environmental factors is unknown or difficult to determine by observing the eigenvalues, choosing a series of order m for verification may be considered.

Finally, T is the m eigenvectors corresponding to the m eigenvalues in decreasing order. Then, we can use T in Eq. 9.8 to project the features into the principal components space. The loss of information in this process can be assessed by reconstitution of the projected data back to the original space:

$$\hat{X} = T^T Y \tag{9.10}$$

.

According to the analysis above, Eq. 9.8 is a dimension reduction process; Eq. 9.10 is a reconstruction process. The PCA method is shown in Fig. 9.2. The residual error between the original data and the reconstructed data is estimated as [46]:

$$E = X - \hat{X} \tag{9.11}$$

The damage index is defined from the prediction error vector E_k obtained at time t_k using the Euclidean norm [47]:

$$NI_k = \|E_k\| \tag{9.12}$$

If it is further assumed that the Euclidean indices are normally distributed, statistical analysis may be performed. Defining $\overline{NI}$ and σ as the mean value and standard deviation of NI for the prediction in the reference state, respectively, the upper and lower control limits (UL and LL) can be defined as [23]:

$$\begin{aligned} CL &= \overline{NI} \\ UL &= CL + \alpha\sigma \\ LL &= CL - \alpha\sigma \end{aligned} \tag{9.13}$$

$$\begin{bmatrix} x_1 \\ x_2 \\ \vdots \\ x_n \end{bmatrix} \xrightarrow{\begin{bmatrix} t_1 & t_2 & \cdots & t_m \end{bmatrix}^T} \begin{bmatrix} y_1 \\ y_2 \\ \vdots \\ y_n \end{bmatrix} \xrightarrow{\begin{bmatrix} t_1 & t_2 & \cdots & t_m \end{bmatrix}} \begin{bmatrix} \hat{x}_1 \\ \hat{x}_2 \\ \vdots \\ \hat{x}_n \end{bmatrix}$$

Input data   Dimension reduction   Reconstruct process
                                     process
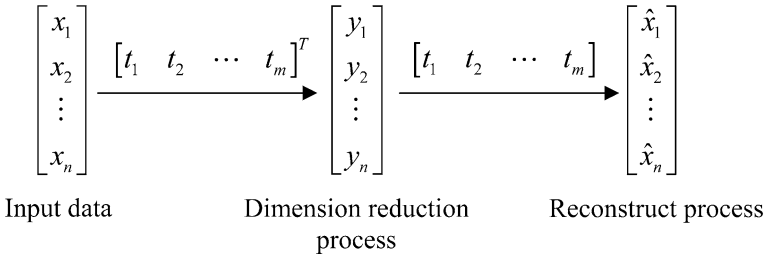
Fig. 9.2 The main steps of PCA

where α corresponds to a confidence interval of 95 % with the assumption of a normal distribution. Outlier statistics indicates that the prediction errors overpass the limits; in healthy conditions, the vibration features should lie in the hyperplane, and the outlier statistics value of the data should remain at the same level as for the reference data. On the contrary, if damage occurs, the features should deviate from the original hyperplane, and the outlier statistics should increase significantly. A geometric interpretation about above method in a two-dimensional case was given by Yan [23].

9.2.3 Numerical Example

9.2.3.1 The Wind Turbine Blade Model and Structural Dynamic Response Simulation

To test the validity of the proposed damage detection and variability rejection methods, in this section, some numerical results obtained with the proposed methods on a simulated blade are provided. The FE model of the blade was created according to a real, small blade with a length of 2.05 m, which is assembled in a small wind turbine with a power of approximately 1 kW. The blade was modeled as a cantilever beam with finite element analysis software ANSYS using shell63 elements, which is available for use in stress stiffening and large deflection. The damage is simulated as the reduction in the stiffness of some elements. More precisely, the damaged elements in three levels, whose location is 0.5 m from the end, are modeled as a reduction of the material elastic modulus by 5, 10, 20, and 30 %. In addition, Rayleigh damping, whose coefficients are $\alpha = 1.73$ and $\beta = 0.00015$, was applied to the finite element model during the dynamic simulation. Figure 9.3 shows the FE model of the blade.

Simulation scenarios for both the undamaged cases, which serve as the reference signal for the subsequent damage detection, and the damaged cases are considered. For each undamaged and damaged case, different rotational speeds about the global Cartesian Y axes, from $\omega = 1$ rad/s to 40 rad/s with an increment

Fig. 9.3 FE model of the wind turbine blade
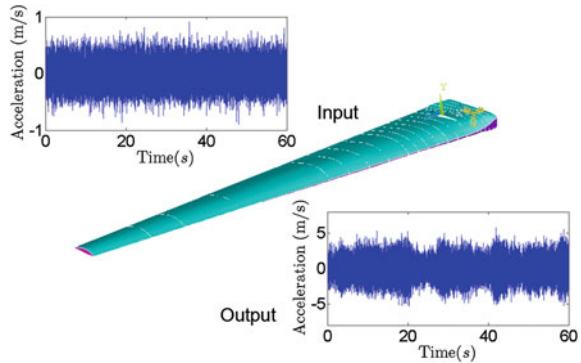
of 1 rad/s, are applied within ANSYS. Thus, a total of 200 scenarios were simulated. The simulations are performed by a prestressed transient dynamic analysis with ANSYS. The stress stiffening and large deformation effects were turned on during the modal analysis. A high-performance computer with eight processors is used to implement all of the simulations. Five sensors are uniformly placed on the top side of this blade to measure the acceleration in the y direction. The sampling frequencies for all sensors are 1,000 Hz, and 60,000 data points within 60 s are recorded for each sensor. A typical vibration signal (y direction) is shown in Fig. 9.3.

9.2.3.2 Results of Modal Analysis

To verify and investigate the finite elements model and analysis considering the rotational effects, a modal analysis was conducted prior to vibration simulation and damage detection. Figure 9.4 shows the varying frequency of the first four modes at different rotational speeds for both the undamaged and damaged status. This

Fig. 9.4 Varying frequencies w.r.t. rotational speed
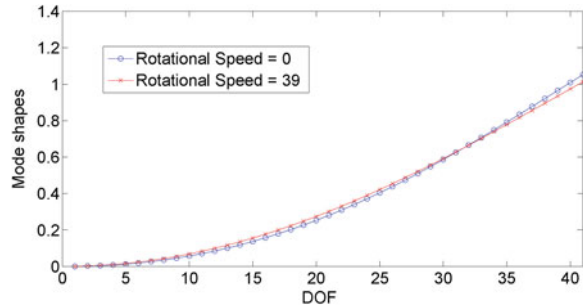
figure indicates that the rotational speed significantly affects the modal frequency
of the blade. Due to the augmentation of structural stiffness as a result of the
centrifugal force, the modal frequency increases with the rotational speed gradu-
ally. For the undamaged structure, the first frequency is increased by approxi-
mately 11.35 % when the rotational speed changes from 1 to 50 rad/s. At the same
time, the modal frequencies decrease due to structural damage. Therefore, in some
cases, the usual damage detection method will mistake the rotational speed drop
for structural damage. Figure 9.5 shows the effects of the rotational speed on the
mode shapes for the first mode. As the figure shows, the presence of additional
stiffness also changes the mode shapes.

9.2.3.3 Results of Damage Detection Based on PCA

As stated above, the method presented in this chapter was applied to a simulation
of a small wind turbine blade. Structural vibration responses were obtained under
different rotational speeds by using ANSYS. After collecting all of the simulation
output, the steps in the proposed damage detection and modal variation rejection
algorithm may be summarized as follows:

1. Compute the loading matrix T using a set of reference data;
2. Apply the PCA method on the undamaged cases to obtain the damage index
   NI_u, control limits UL and LL;
3. Run the PCA method on the test data to obtain their damage indexes NI_t;
4. Estimate whether the NI_t are within the control limits.

   The results for undamaged state obtained with the PCA method are shown in
Fig. 9.6; three straight lines correspond to UL, CL and LL, as defined in Eq. 9.11.
The 200 nodes on the polyline correspond to the specific rotational speeds, which
are within the range from 0 to 50 rad/s under healthy conditions. Not all nodes lie
on a straight line due to the nonlinear relationship between the frequencies and
rotational speeds. In fact, we expect to obtain a straight line that is independent of
the rotational speed such that the effect of the rotational speed can be removed.
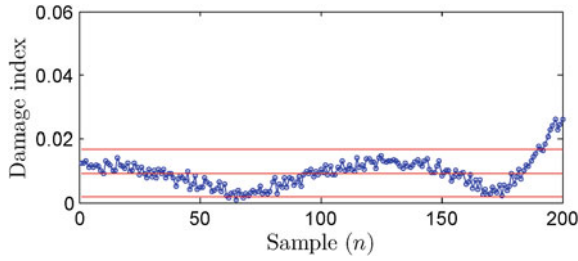
Fig. 9.6 The Novelty Index at different rotational speeds under undamaged conditions

The following results show that the effect of this nonlinearity is minor comparing to the effect of damage.

Figure 9.7 shows the damage index under different damaged levels. The curves from bottom to top correspond to damage indices in the healthy state and 5, 10, 20, and 30 % damage magnitudes, respectively. According to this figure, the minor damage, such as a 5 % stiffness reduction, has a more significant influence on the damage index. At the same time, the rotational speed has little effect on these indices. It should be noted that all indices in Fig. 9.7 were obtained from the structural modal frequencies under known damage levels and rotational speeds. Figure 9.8 was obtained for unknown damage levels and rotational speeds because this methodology was designed to address this type of situation. In this case, for a certain damage level, the modal frequencies with respect to 50 random rotational speeds were used to calculate the damage indices, which are shown in Fig. 9.8. Because the rotational speeds were unknown, the corresponding indices were plotted from the beginning of the x-axis, and in fact, they were not obtained from 0 to 12.5 rad/s. Finally, Fig. 9.8 shows that the damage indices increase remarkably with the unknown damage level. The damage detection problem for wind turbine blades under varying rotational speeds is solved by the methodology presented.

Fig. 9.7 Novelty Index under different damaged levels
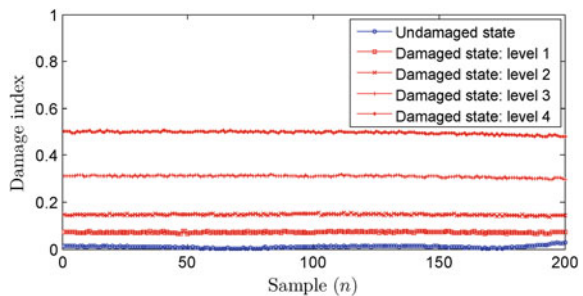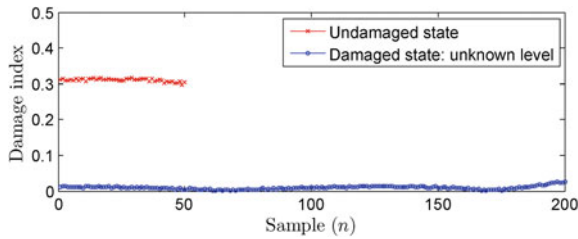
Fig. 9.8 Novelty Index under unknown damaged levels

9.2.4 Experimental Example

9.2.4.1 Composite Blade and Experimental Setup

An experiment was designed to demonstrate effects of stiffening and structural damage on the structural modal parameters. Furthermore, all modal parameters were processed by the PCA method described above to distinguish the structural damage.

Three prototypes of 1.25-m glass fiber reinforced plastic (GFRP) composite wind turbine blades were used in this experiment. They were mounted vertically in the wind turbine tower. The accessories shown in Fig. 9.9 include the blades, the ring flange, the rotating shaft, the slip ring, the wheel boss, the footstock, and the tower. The three blades were integrated with the ring flange through bolts and were then installed on the rotating shaft. The slip ring with 24 channels can conduct the electric signal of the sensors on the rotating blades to fixed signal wires, which solves the problem in which signal wires intertwine together when the blades are rotating. The wind turbine tower is a hollow steel tube with a thick wall that is installed on the ground with bolts. There is a cowling in front of the wind turbine blades, which can reduce the windward resistance.

Three accelerometers, type B&K 4507B, were used for the measurement of the vibration motion of the blades. They were attached to the tip of each blade. According to the direction that the sensors were fixed, the acceleration signal measured in the test corresponds to the vibration perpendicular to the rotating
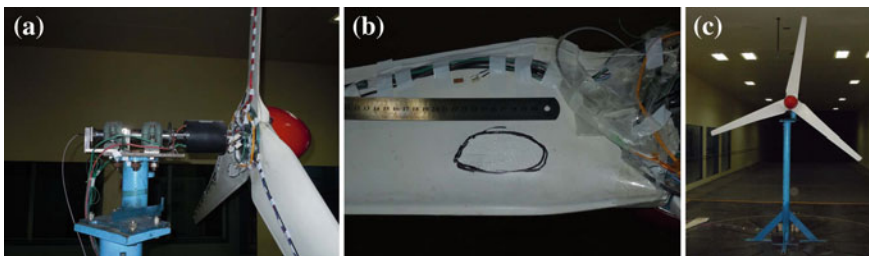
Fig. 9.9 The wind turbine used in experiment

plane, and all of the frequencies are flapping frequencies. A data acquisition system, type NI PXI-4472, was used and the sampling frequency was 1,000 Hz.

The start-up wind velocity of the wind turbine is 3 m/s; the rated wind velocity and rated rotating speed are 8 m/s and 400 rad/s, respectively. The test is conducted in the wind tunnel laboratory at the Harbin Institute of Technology, China. The vibration responses of blades under different wind velocities were measured to determine the relations between the frequency and rotating speed. Six cases of wind velocity were used in this test: 0, 4, 5, 6, 7, and 8 m/s. The duration under each wind velocity is approximately 3 min. When the wind velocity is 0, the vibration signals are measured by rapping the blades.

Structural damage was simulated by abrasing laminations from the surface of one blade. Figure 9.9b shows the artificial damage on the blade. Damage levels were controlled by different abrasion depths and areas. It should be noted that this damage cannot be quantified.

9.2.4.2 Damage Detection Results Based on Experimental Data

Modal frequencies of the first three modes corresponding to different wind speeds and damage levels are shown in Fig. 9.10, which shows that both rotation and damage change the modal frequencies of the blades. The first damage level has slight effect on the first mode. Anyway, in some cases, it is difficult to distinguish whether the decrease in frequencies is due to the decrease in rotational speed or structural damage according to data in Fig. 9.10.

After using the PCA algorithm, Fig. 9.11 shows the damage index under different damaged levels for the experimental data. X-axis indicates number of the wind speed samples. From Fig. 9.11, the effects of rotation have largely been removed. The damage indices for the damaged cases are separated from the undamaged ones, but the different levels of damage are not clearly detected.

9.3 Fatigue Damage Detection Based on High Spatial Resolution DPP-BOTDA

9.3.1 Principles of DPP-BOTDA

The schematic of DPP-BOTDA sensing system is shown in Fig. 9.12. BOTDA system employs a stimulated Brillouin scattering (SBS) technique [48]. Two counterpropagating laser beams, i.e., a pump pulse and a CW probe wave, are injected from both ends of the sensing fiber. The two laser beams have certain frequency differences which are near the Brillouin frequency of sensing fiber. Thus acoustic wave can be excited by the interaction of these two laser beams. The pump pulse is backscattered by the phonons, and part of its energy is transferred to the CW. The power gain of the CW, i.e., Brillouin gain signal, is measured at the output end of the probe light. The relation between Brillouin gain of the CW and
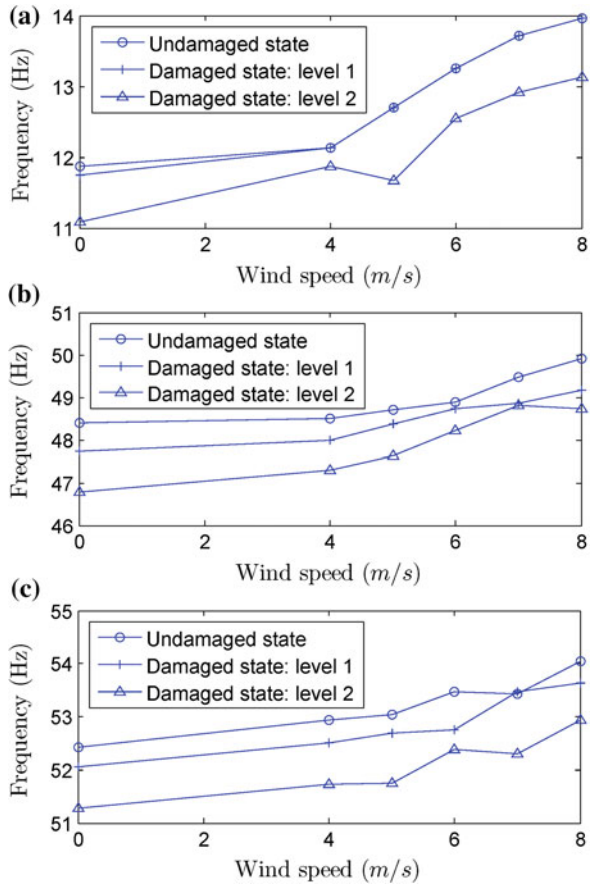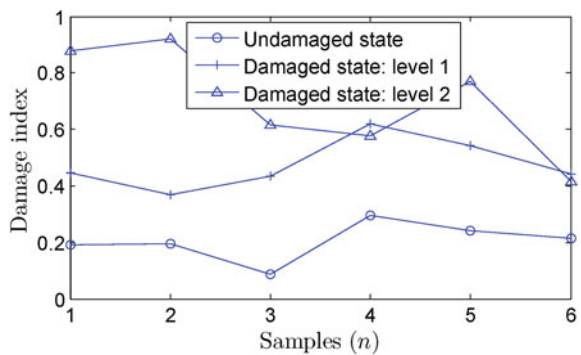
the frequency difference of the two laser beams is called the Brillouin gain
spectrum (BGS), which can be obtained by sweeping the frequency of the probe
light. The value of the strain can be estimated by measuring the peak frequency of
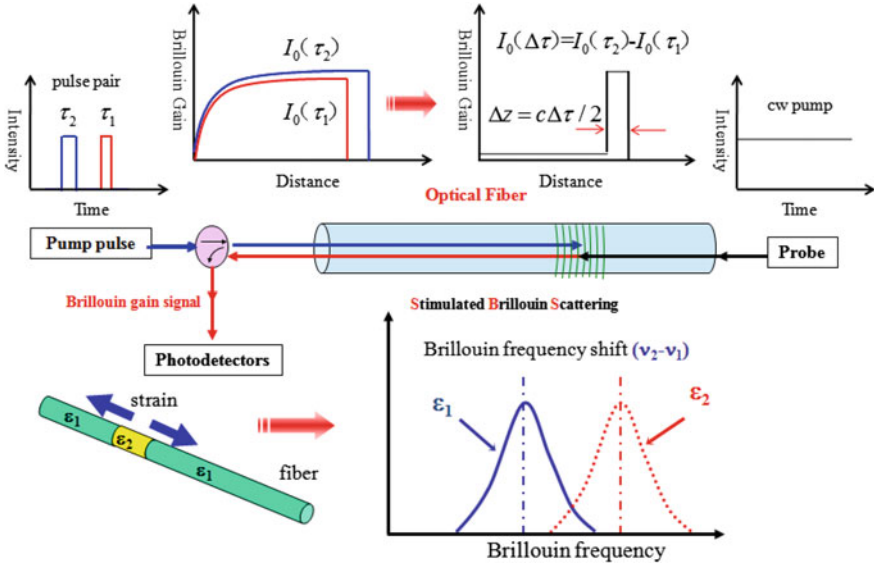
Fig. 9.12 Schematic of DPP-BOTDA sensing system

BGS (Brillouin frequency), while its position along the fiber is calculated from the light round-trip time. The differential pulse-width pair (DPP) technique in BOTDA is implemented as follows [49, 50]: first, two time traces of the Brillouin signal $(I_0(\tau_1), I_0(\tau_2))$ are obtained by using two pulses (τ_1, τ_2) with different pulse widths; second, the differential signal $(I_0(\Delta\tau))$ is obtained by making a subtraction between the two Brillouin signals, and then the differential Brillouin spectra can be obtained by sweeping the frequency offset in the vicinity of the Brillouin frequency shift (BFS). In the differential Brillouin spectra, the spatial resolution is determined by the differential pulse, i.e., the pulse-width difference of the pulse pair, rather than the original pulses. So a high spatial resolution can be achieved by using a small difference of the pulse pair.

The peak frequency of the BGS, called the Brillouin frequency shift is given by [51]:

$$v_B = 2nV_a/\lambda \tag{9.14}$$

where n is the refractive index of the fiber core, V_a is the velocity of the acoustic wave, and λ is the vacuum wavelength of the pump light. Brillouin frequency shift increases linearly with strain and temperature, so the Brillouin frequency shift at position z is expressed as [52]:

$$v_B(z) = v_B(0) + C_s\varepsilon(z) + C_t(t(z) - t_r) \tag{9.15}$$

where $\varepsilon(z)$ is the axial strain along the optical fiber, $t(z)$ is temperature and t_r is the reference temperature. C_s and C_t are the proportionality constants of strain and temperature. $v_B(0)$ is the initial Brillouin frequency in a strain-free state at the reference temperature t_r. Since the Brillouin frequency shift depends on both the strain and temperature applied to the optical fiber, the Brillouin frequency shift due to strain change could not be easily distinguished from that caused by temperature change. This study used the unstrained part of the optic fiber that attached to the surface of the blade to compensate the frequency shifts due to the temperature change. The strain distribution is calculated from the following equation:

$$\varepsilon(z) = \frac{v_B(z) - v_B(z_0)}{C_s} \tag{9.16}$$

where $v_B(z_0)$ is the Brillouin frequency shift at reference position z_0, i.e., z_0 is the unstrained part of the optic fiber that attached to the surface of the blade.

9.3.2 Fatigue Damage Detection Test

9.3.2.1 Experimental Setup

The experimental setup of DPP-BOTDA is shown in Fig. 9.13. A narrow linewidth 2 kHz fiber laser operating at 1550 nm is used as the light source. A 3-dB coupler is used to split the output light into two parts, providing the pump and the probe waves, respectively. An electro-optic modulator (EOM1) with high extinction ratio ($ER > 40$ dB) is used to generate the optical pulse, which is then amplified by an erbium-doped fiber amplifier before being launched into the sensing fiber. The microwave generator outputs microwave signals to modulate the light through EOM2, and the first-order lower sideband is chosen as the probe wave by a narrow bandwidth fiber Bragg grating. A 7-m polarization-maintaining fiber ($C_s = 0.0483$ MHz/$\mu\varepsilon$), whose BFS is 10.845 GHz at room temperature (20 °C), is used as the sensing fiber to remove the polarization fading and improve the effective signal-to-noise ratio (SNR). Two polarization controllers are used to ensure that the pump and probe waves are launched into the same principal axis of the sensing fiber. A 3.5 GHz bandwidth detector with a transition time (10–90 %) of 115 ps, which thus can resolve the cm-order variation in strain or temperature, is used to detect the Brillouin signal. The sampling rate of the digitizer is set at 10 GHz s-1, which corresponds to 1 cm/point in the optical fiber. The double pulse pair used is 39.5 and 41.5 ns and the pulse-width difference is 2 ns, so the special resolution of the DPP-BOTDA system is 20 cm.

A 1.25 m prototype glass fiber reinforced plastic (GFRP) composite wind turbine blade was used in the fatigue test. The blade was mounted horizontally in a flap direction with its root fixed and the low-pressure blade surface facing down. An electric motor was mounted on the blade tap at the free end. Fatigue loading
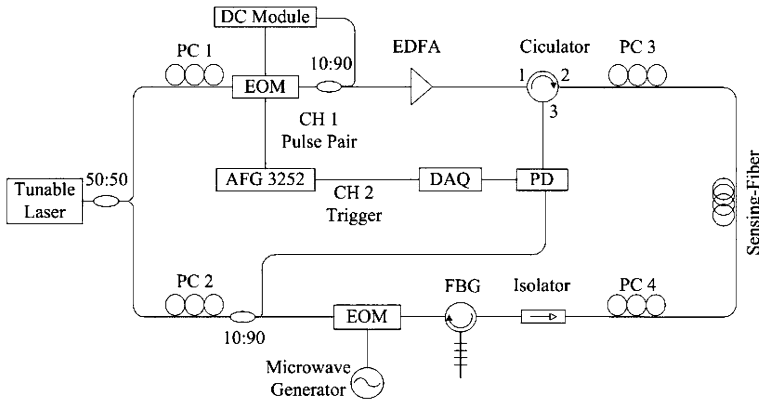
Fig. 9.13 Experimental setup. *PD* Photodetector, *PC* Polarization controller, *EOM* Electro-optic modulator, *EDFA* Erbium-doped fiber amplifier, *DAQ* Data acquisition

Fig. 9.14 Photo of the blade fatigue test setup
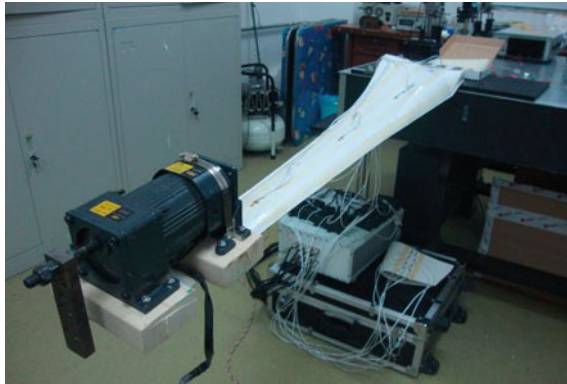
was induced by the electric motor using single-axis resonance method. Figure 9.14 shows the photography of the blade fatigue test setup.

The layout of optic fiber sensors and strain gages on the blade is shown in Fig. 9.15. Polarization-maintaining optical fibers (PMF) were glued two circuits on both sides of the blade surface, along the spanwise axis, to measure the longitudinal strain distribution. PMF can transmit optical power with very low loss and maintain a stable performance over large temperature and strain range. Its polarization-maintaining characteristic can remove the polarization fading of the Brillouin signal and increase the SNR of the DPP-BOTDA system. In order to increase the reliability of the optic fiber-sensing system, two optical fibers (Optical Fiber 1 and Optical Fiber 2), of the same kind and length, went similar path on the blade, monitoring the similar place with two lines of the single optical fiber. Simultaneously, eight strain gauges are patched on the surface of the composite
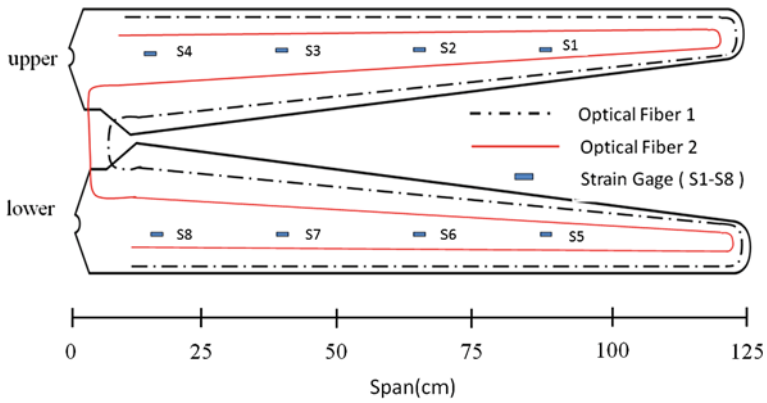
Fig. 9.15 Layout of optic fiber sensors and strain gauges

blade along with optical fiber to validate the measurement accuracy of the distributed sensing and continuously monitor the condition of the blade. Hence, the measurement taken is stable and reliable during the blade fatigue test process.

9.3.2.2 Summary of Test Procedure

Figure 9.16 shows the fatigue test loading system for wind turbine blade based on single-axis resonance method [53]. An electric motor, connected with a 1 kg mass, was mounted approximately at 115 cm from the blade root using wooden saddles. The motor was driven to excite the first flap frequency and induce a cyclic load in the blade. The loading cycle frequency is about 2.6 c/s. The initial strain amplitudes of the fatigue loading along the spanwise axis on both side of the blade are shown in Fig. 9.17.

Fig. 9.16 Schematic of the fatigue loading system
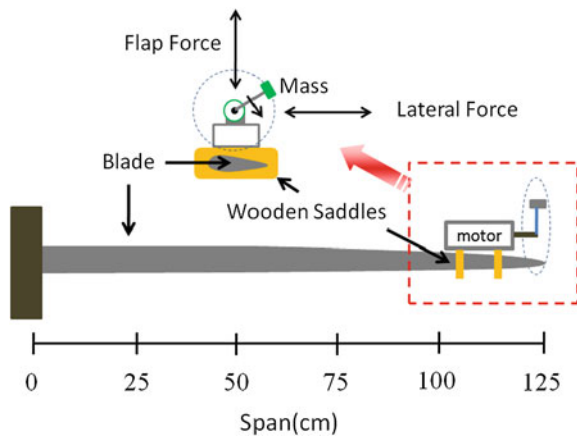
Fig. 9.17 Initial strain amplitude along the blade. **a** Upper surface, **b** lower surface
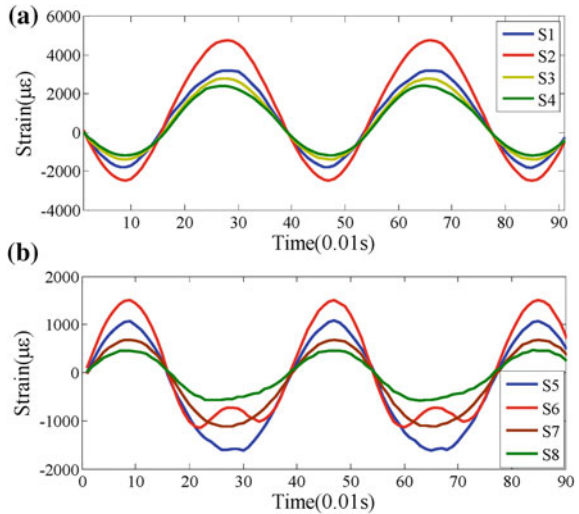
First, the blade was carried out statist test. An 80 N force, which is approximately 15 % of the bearing capacity, was loaded on the top of the blade (115 cm from the blade root). The stain distribution under this fixed loading was obtained by the DPP-BOTDA sensing system. The test result was used as the baseline for damage detection. Then the blade underwent fatigue excitation from undamaged state to failure. The fatigue loading system was paused after fixed fatigue cycle for blade inspection and the blade was carried out the same statist test as the first step. At first, the fatigue loading system was paused every 4 h ($\sim$40,000 cycles). After 28 h ($\sim$260,000 cycles), a multitude of gel-coat cracks and some larger visible cracks were identified on the blade. The resonance frequency decreased to 2.2 Hz, as the stiffness degradation and accumulated cracks reduced the local flexural stiffness of the blade. Then the fatigue loading system was paused every 2 h ($\sim$20,000 cycles) to carefully study the signal changes of DPP-BOTDA system near the failure moment. Comparisons of the stain distribution and specific response of the DPP-BOTDA at different fatigue cycle count were used as a feature to track the progression of structural change over the course of the fatigue test.

9.3.3 Test Results and Discussions

9.3.3.1 Blade Failure Scenario and Mechanism

The blade was failed after 310,000 cycles (34 h) and the fatigue damage, i.e., adhesive joint failure between skins at the leading edge, was visually identified at 75 cm from the root, which was also the high strain region of the blade. The blade
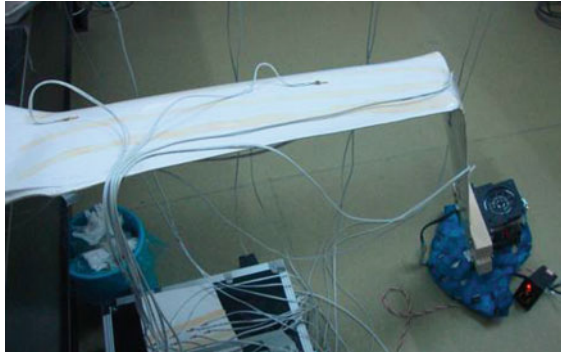
Fig. 9.18 Photo of the blade failure
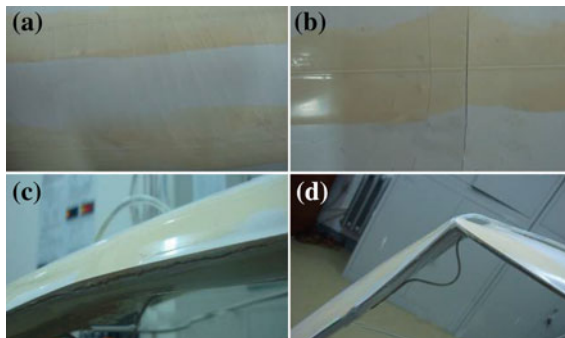
Fig. 9.19 Photograph of the fatigue damage process, **a** gel-coat cracks appearance, **b** gel-coat cracks development, **c** adhesive joint failure, **d** blade failure

lost its structural integrity and the top and bottom halves flattened before allowing the blade to fold (as shown in Fig. 9.18).

Figure 9.19 shows the fatigue damage process of the blade. Starting at about 40,000 cycles, a multitude of fine gel-coat cracks developed on the high-pressure (upward facing) side and the cracks were most apparent at the 70–80 cm span of the blade, which was the high strain region of the blade according to the strain distribution obtained by the DPP-BOTDA system in the statist test. From 80,000 to 260,000 cycles, these gel-coat cracks progressed in length and gap width. Some of the gel-coat cracks near the high strain region turned to larger visible cracks. Between 260,000 and 300,000 cycles, adhesive joint failure between skins at the leading edge was visually identified at 75 cm from the root. As the crack of adhesive joint failure progressed in length, the blade lost its structural integrity and failed at about 310,000 cycles.

9.3.3.2 Damage Detection Results of the DPP-BOTDA System

The strain distributions of the wind turbine blade along the optical fibers, which were obtained by the DPP-BOTDA system at different fatigue cycle counts, are presented in Figs. 9.20 and 9.21. The horizontal axis is the distance from one end of the optical fiber and the vertical axis is the longitudinal strain along the optical fiber. The test results consist of four sensing segments A, B, C, and D. Segments A and D represent the strain distributions obtained by the optical fibers near the leading edge. Segments B and C represent the strain distributions obtained by the optical fibers near the trailing edge. The zero parts between segments are the turnarounds of the strain-free fibers. In undamaged state (0 cycle), the test results reveal that the strain near the leading edge (A, D), both the tensile strain on the upper surface and compressive strain on the lower surface, are higher than those near the trailing edge. The high strain region of the blade was at 70–80 cm from the root. These characteristics indicate severe fatigue damage near the leading edge at high strain region. Soon after the fatigue test started (starting at about 40,000 cycles), a multitude of fine gel-coat cracks developed on the upper surface, and the cracks were most apparent at the 70–80 cm span of the blade which was the high strain region of the blade. The gel-coat cracks reduced the local flexural stiffness and resulted in a higher tensile strain near the damaged region. As shown in the test results of strain distributions at 80,000 cycles, the strain changed significantly in the high strain region, especially near the leading edge side. Hence, these test results demonstrated the effectiveness of the DPP-BOTDA sensing system in the initial fatigue damage detection location. From 80,000 to 260,000 cycles, these gel-coat cracks progressed in length and gap width. Some of the gel-coat cracks near the high strain region turned to larger visible cracks. These cracks further reduced the local flexural stiffness and resulted in a much higher
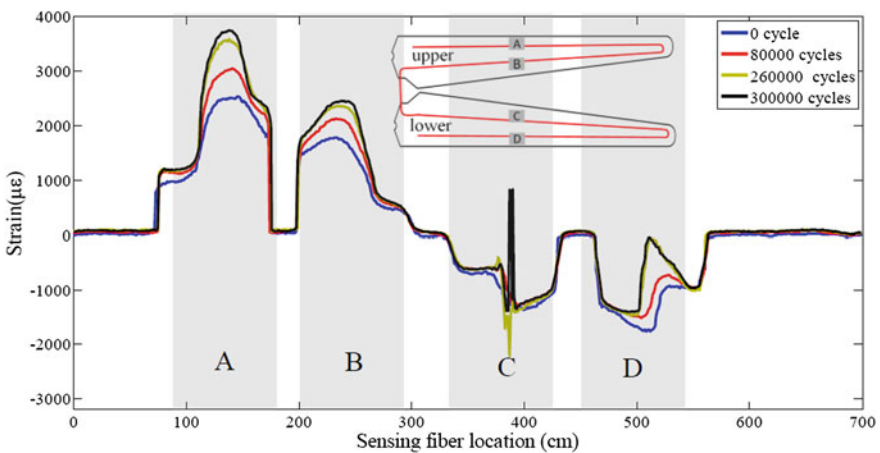
Fig. 9.20 The strain distributions at different fatigue cycle count obtained by Optical Fiber 1
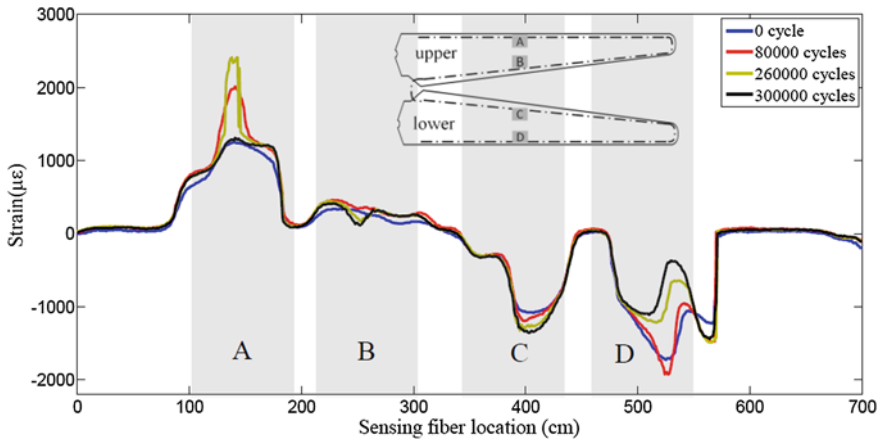
Fig. 9.21 The strain distributions at different fatigue cycle count obtained by Optical Fiber 2

tensile strain near the damaged region. As shown in the test results of strain distributions at 260,000 cycles, the strain in the initial fatigue damage region continuously increased. Especially near the leading edge side of the high strain region on the upper surface (segment A of Optical Fiber 2), the strain was extremely high, which indicated a further damage in this position. Between 260,000 and 300,000 cycles, adhesive joint failure between skins at the leading edge was visually identified at 75 cm from the root, where was exactly the extremely high strain position in segment A of Optical Fiber 2. Adhesive joint failure broke the structure integrity and released the stress near the damage region, which led to a sudden decrease of the stain near adhesive joint location. As shown in the test results of strain distributions at 300,000 cycles, the strain near the failed adhesive joint significantly decreased (segment A of Optical Fiber 2), which show the effectiveness of severe fatigue damage detection in DPP-BOTDA system. As the crack of adhesive joint failure progressed in length, the blade lost its structural integrity and failed at about 310,000 cycles. The strain distributions obtained by the DPP-BOTDA system at different fatigue cycle count validated the effectiveness of the developed system in damage detection and distributed sensing.

The Brillouin gain spectra (BGS) is the foundation of all the Brillouin sensors. According to the principle of Brillouin scattering-based strain and temperature measurement, only the Brillouin frequency shift determines the final measurement results of strain and temperature. But other parameters of the BGS in the sensing fiber, like width, amplitude, even the shape of the BGS, contain more information about the local strain field, as these parameters are influenced by the local strain gradient and the nonuniformity of the strain distribution. Then, these parameters also can be used to detect and locate damage [54, 55].

The normalized fitted BGS, obtained by the DPP-BOTDA system at different fatigue cycle count, along the leading edge are shown in Fig. 9.22. In undamaged state (0 cycle), the test results reveal that BGS along the leading edge have a similar
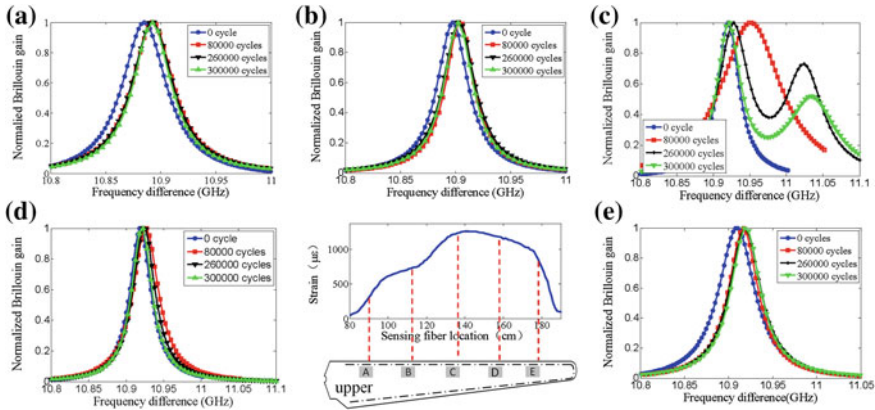
Fig. 9.22 Differences in the fitted BGS along the leading edge at different fatigue cycle counts: **a** results in point a, **b** results in point b, **c** results in point c, **d** results in point d.

single peak Lorenz shape. As the development of the gel-coat cracks (from 40,000 to 80,000 cycles), the stiffness degradation and accumulated cracks reduced the local flexural stiffness and changed the local strain gradient, which broadened the width of the BGS near the damaged region. As shown in the test results of 80,000 cycles, the width of the BGS near the damage region (point C) changed significantly, while the BGS near the undamaged region kept its initial shape. The test results reveal that fatigue damage introduced local strain gradient change will broaden the width of the BGS, which can be used to detect and locate fatigue damage. As these gel-coat cracks progressed in length and gap width, from 80,000 to 260,000 cycles, the local flexural stiffness near the damaged region further decreased, which resulted in a steeper strain gradient. Hence, the shape of the BGS further changed. As shown in the test results of 260,000 cycles, the BGS near the damage region (point C) changed from single peak to double peak, which indicated a very steep local strain gradient and high nonuniform strain. The appearance of the double-pick BGS indicated further damage in this region. Then, the adhesive joint failure was visually identified at point C, between 260,000 and 300,000 cycles, which further validates the effectiveness of damage detection base on the BGS shape change.

9.4 Damage Detection under Static Loading Using PZT Sensors

9.4.1 Test Description

The glass fiber reinforced plastic composite wind turbine blade in this test was a prototype of a 2.1 meter blade. During the test, the blade was mounted horizontally in a flap direction with its attached to a rigid steel mounting assembly. An actuator

Fig. 9.23 The photograph of configuration of the experiment setup
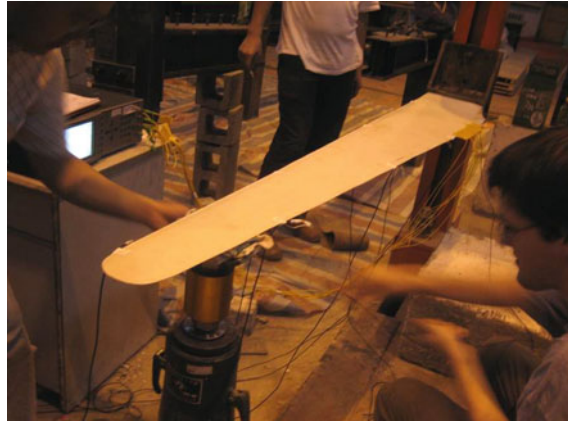
connected with a load transducer was attached at the free end. This actuator was capable of exerting a force about 1000kN, with a maximum displacement of twenty centimeters. The actuator was operated manually, and the force can be read by the load transducer. Figure 9.23 shows the photograph of configuration of the experiment setup.

A total of eight piezoelectric transformers were used in this test to detect the damage propagation. Another eight optical fiber sensors were used to measure the strain through the blade. All sensors were applied to the blade with epoxy glue. Sensors arrangement is shown in Fig. 9.24.

The test consisted of two steps. The first part of this test was an incremented loading procedure from 0 to 433 N, with steps of 33 N. The actuator was a mechanical floor jack, hand operated, and the loading steps were determined by the force sensor reading. After 13 steps, at a load of 433 N, the blade held the load without failing. This first loading process validated the testing procedure, and the functionality of each sensor was also confirmed at this time. The load was gradually removed and the blade returned to its neutral position. The second part of the

Fig. 9.24 Location of all sensors on the blade
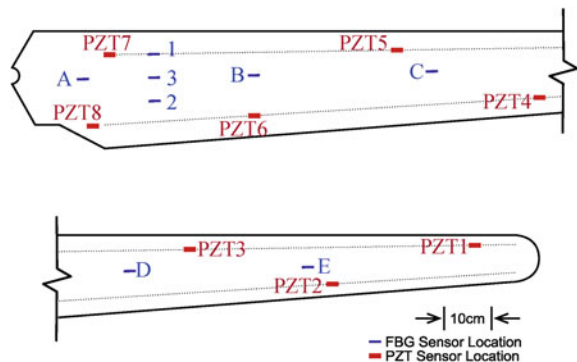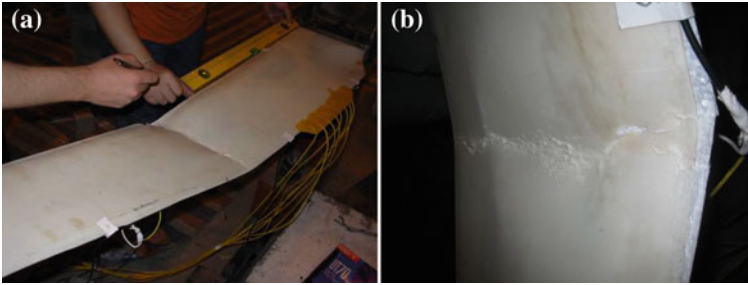
Fig. 9.25 Photography of the broken blade: **a** normal view, **b** close-up view.

static test was then carried out. The actuator footing was given a positive offset of 8 cm, so that it could bend the blade to the failure point while staying within its 20 cm stroke range. During the second half of the static testing, which was carried out with the same increment-based loading as the first, the load cell reading reflected a maximum force of 500 N at the loading point before the blade's failure occurred.

Failure of the turbine blade happened when the resin bond between the top and bottom layers of glass fiber reinforcement failed due to shear stress. The upper and lower halves of the blade slipped in opposite directions approximately perpendicular to the long edge of the blade. This separation is seen in detail in the close-up view of Fig. 9.25. After this failure occurred on the leading and trailing edges of the blade, it lost its structural integrity and the top and bottom halves flattened before allowing the blade to fold.

9.4.2 Experimental Results and Discussion

9.4.2.1 Results of Optical Fiber Sensors

Figure 9.26 shows the output of all eight FBG optical strain sensors during the second part of the testing procedure. Because of the initial load on the blade, each sensor started this test segment with an initial strain dependent upon its location on the blade. As described in the procedure section, loading was performed in 33 N increments which were applied gradually. A delay of several seconds was used in between increments to allow any signs of failure to be noticed. The short segments of constant strain are indicative of these delay periods. At approximately 580 s, failure occurred at 0.74 m from the fixed end of the blade, which is closest to sensor C. The reading of sensor C at this time shows the highest strain of all the optical sensors.

Figure 9.27 is a graph confirming the linear relationship between strain at FBG sensor A and the load applied to the blade.

Fig. 9.26 Strain versus time *curve* of the blade
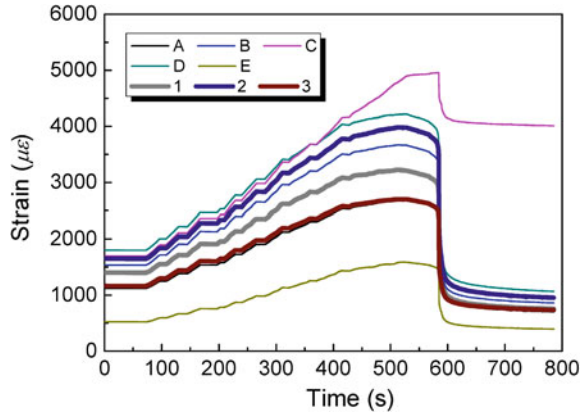
Fig. 9.27 Strain versus force *curve* of the blade
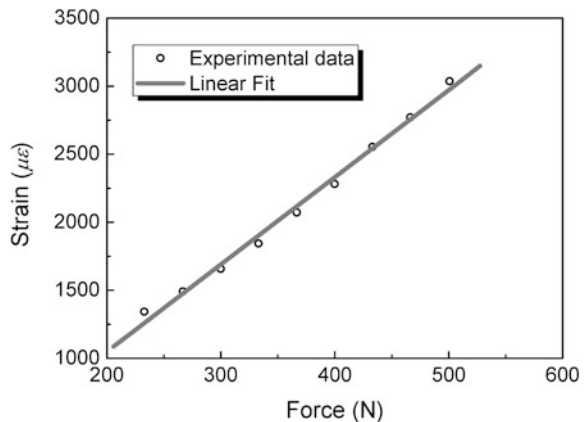
9.4.2.2 Results of PZT Transformer

The eight PZT sensors were attached to a data acquisition system and recorded to a laptop computer. The data were filtered and analyzed with MATLAB software, employing an FIR-based high pass filter of 60 Hz to reduce noise. By establishing a threshold of 4 mV, acoustic emission events whose RMS amplitude exceeded this value could be logged for further analysis. Data from each event were also collected, including arrival time, event duration, rise time, and peak value. The counts of the number of events that occurred according to each sensor versus time in the static loading tests are displayed in Fig. 9.28.

In the first loading test, sensors 1 and 7 registered no emissions and in both loading tests sensor 5 most frequently detected emissions. Sensor 5 was also the closest sensor to the point of failure on the surface of the blade. Between the first
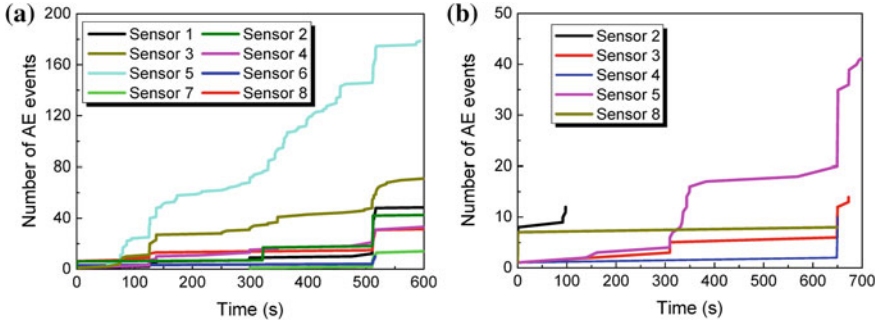
Fig. 9.28 Acoustic emission arrival times and magnitudes load: **a** the second loading stage, **b** the first loading stage.

and second loadings, the closest sensor to the actuator, sensor 2, was destroyed as the actuator was repositioned and had to again be bonded.

Overall, it seems the odd numbered sensors counted more AE events, which may have occurred due to the geometry of the blade; the foreword positions of these sensors along the airfoil made the thickness of the blade at those points larger than at the even positions. The blade was also hollow at the odd locations, which may have affected how the waves at the recorded frequencies moved across the blade's surface and thus affected the AE counts.

9.4.3 Fractal Theory-Based Damage Detection Method and Results

In this section, a damage acuteness index based on fractal theory is presented. The length of time series of PZT signal, X_k^m, can be defined as follows [56]:

$$L_m(k) = \left\{ \left(\sum_{i=1}^{[(N-m)/k]} |(X(m+ik) - X(m+(i-1)k)|) \cdot \frac{N-1}{[(N-m)/k].k} \right\} / k$$

(9.17)

where [] denotes the Gauss' notation and both k and m are integers, which indicated the initial time and the interval time, respectively. For a time interval equal to k, we get k sets of new time series and the certain length of the curve of the signal.

We define the length of the curve for the time interval k, $< L(k) >$, as the average value over k sets of $L_m(k)$. If $< L(k) > \alpha k^{-FD}$, then the curve is fractal with the dimension FD. As shown in Fig. 9.29, the signal of PZT sensor has obvious fractal feature because the straight line is fitted to the points by the least-square method.
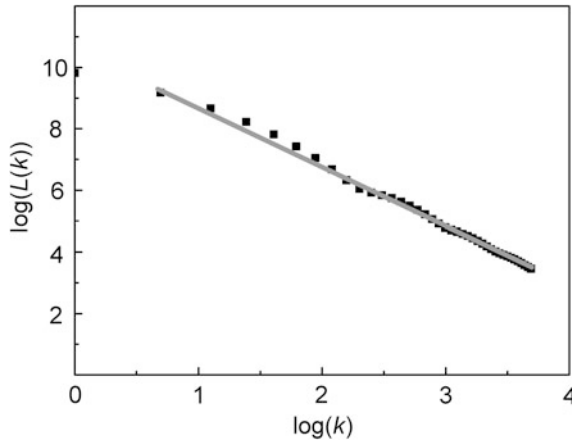
Fig. 9.29 The logarithm of the curve length $\log(L(k))$ versus $\log(k)$

We define FD-based damage acuteness index as follows:

$$J = \left(b_{\mathrm{max,k}}/bx_{\mathrm{min,k}}\right)^{\mathrm{FD_{max}}} - 1 \tag{9.18}$$

where $b_{\mathrm{max},k}$ is the largest length of the signal curve of every time series as the interval time is k; $b_{\mathrm{min},k}$ is the length of the signal curve which passes through no damaged region as the interval time is k; FD_{max} is the largest value of estimated FD of the curve of each time series.

Finally, the proposed damage acuteness index was applied to the data from the PZT sensors 5 and 6 during the second part of the testing procedure. The results are shown in Fig. 9.30, where the x and y axis represent respectively the time and the damage index. These two figures show that the damage index increases greatly
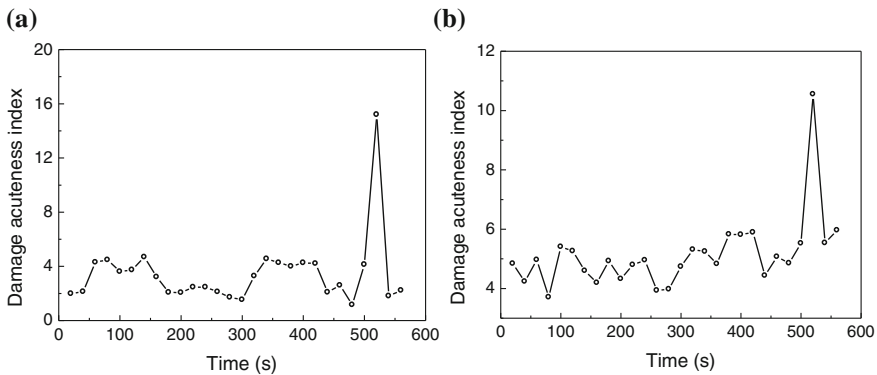
Fig. 9.30 The damage acuteness index J along the loading time: **a** the damage index calculated from PZT sensor 5, **b** the damage index calculated from PZT sensor 6

Fig. 9.31 The damage acuteness index J at the failure time of the structure for different PZT sensors
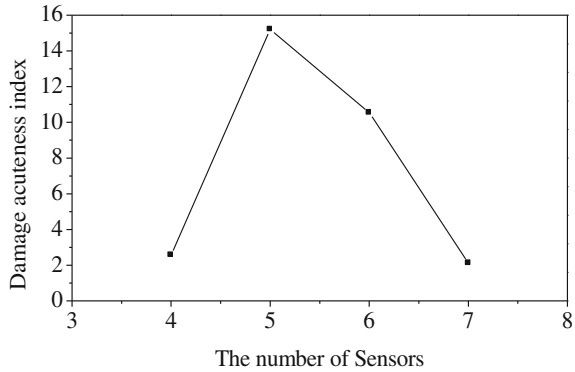
which means the structure is failed. Before the structure was failed, the damage index fluctuates at similar value, which means the damage developed with similar acuteness. The results indicate that the proposed method is able to assess the damage development in the composite wind blade.

The damage acuteness index J for different PZT sensors at the failure time of the structure is shown in Fig. 9.31. It is demonstrated that sensor 5 has the largest value which indicates the structure failed close to sensor 5. As the distance from the failure location become larger, the value of J becomes smaller.

9.5 Conclusions and Future Work

Three kinds of damage detection methods, vibration-based, BOTDA-based, and PZT-based methods, are employed to implement structural health monitoring of wind turbine blades. Above methods have their advantages, respectively. Vibration-based method is able to detect the damage of the large structure with few sensors. BOTDA-based techniques show their distributed sensing ability over extremely long distance with increasingly high accuracy. They can measure the structural strain directly. While PZT-based techniques can detect the tiny local damage with high sensitivity.

(1) For the vibration-based damage detection method, a PCA-based method was introduced to implement the damage detection of rotational blades. The finite element modal analysis of the wind blade indicates that the modal parameters (frequencies and mode shapes) of the rotational blade depend on the rotational speed. The detailed theory foundation and operating procedures of the PCA-based method are introduce. Then, it was tested on a detailed FE model of a wind turbine blade. The results indicate that the algorithm is able to detect the simulated damage in the blade in operational condition despite the weak nonlinear relationship between modal frequencies. Subsequently, an experiment was designed to obtain the modal parameters under the rotational

condition to further verify the proposed method in this work. The experimental results obtained were similar w.r.t. modal parameters. An analysis shows that the proposed method is able to largely remove the effects of rotation.

(2) Fatigue damage detection system using a high spatial resolution DPP-BOTDA is successfully developed and experimentally validated. Polarization-maintaining optical fibers were bonded on the surface of wind turbine blade to form the distributed sensing network. The strain distributions obtained by the DPP-BOTDA system at different fatigue cycle count validated the effectiveness of the developed system in damage detection and distributed sensing. The shape of the BGS was sensitive to fatigue damage as the stiffness degradation and accumulated cracks change local strain gradient which can be used to locate the serious fatigue damage. The developed system shows its potentiality for developing highly reliable wind turbine monitoring system.

(3) An experiment is designed to study the damage detection techniques based on optical fiber sensors, PZT sensors, and the fractal dimension-based damage detection method. From the direct results of optical fiber sensors, it can observe the strain increase and also determine the strain distribution through the blade surface. This information is important to study concerned topic on the static and dynamic properties of this composite blade, for example, the fatigue characteristic, etc. From the results of PZT sensors, in the later part of the test when the cracks produce, it can obviously detect the signal from cracks. Then, the fractal dimension-based damage detection method was employed to calculate the damage index and results are encouraged.

It should be pointed out that the most important and difficult problems for structural health monitoring and damage detection are the actual application of the above techniques. Such as the data measured under changing environmental and operational conditions will be effected by noise and so on, the application also requires the fast decision based on the damage detection algorithms. These approaches should be further developed for online monitoring of wind blades.

References

1. Schroeder K, Ecke W, Apitz J et al (2006) A Fibre Bragg Grating sensor system monitors operational load in a wind turbine rotor blade. Meas Sci Technol 17(5):1167–1172
2. Krämer SGM, Wiesent B, Müller MS et al (2008) Fusion of a FBG-based health monitoring system for wind turbines with a Fiber-optic lightning detection system. In: Proceeding of SPIE 7004, 19th international conference on optical fibre sensors, 70040O; doi:10.1117/12.783602
3. Ecke W, Schröder K (2008) Fiber Bragg Grating sensor system for operational load monitoring of wind turbine blades. In: Proceeding of SPIE 6933, Smart Sensor Phenomena, Technology, Networks and Systems, 69330I; doi:10.1117/12.783602

4. Bang H-J, Shin H-K, Ju Y-C (2010) Structural health monitoring of a composite wind turbine blade using Fiber Bragg Grating sensors. In: Proceeding of SPIE 7647, Sensors and Smart Structures Technologies for Civil, Mechanical, and Aerospace Systems, 76474H; doi:10.1117/12.847557

5. Krebber K, Habel W, Gutmann T et al (2005) Fiber Bragg Grating sensors for monitoring of wind turbine blades. Proc SPIE 5855:1036–1039

6. Eum SH, Kageyama K, Murayama H et al (2008) Process/health monitoring for wind turbine blade by using FBG sensors with multiplexing Techniques. Proc SPIE 7004:70045B

7. Rohrmann RG, Rucker W, Thons S (2007) Integrated monitoring systems for offshore wind turbines. In: Proceedings of the sixth international workshop on structural health monitoring. Stanford, US

8. Mcgugan M, Sorensen BF (2007) Fundamentals for remote condition monitoring of offshore wind turbine blades. In: Proceedings of the sixth international workshop on structural health monitoring. Stanford, US

9. Joosse P, Blanch M, Dutton A et al (2002) Acoustic emission monitoring of small wind turbine blades. J SolEnergy Eng 124(4):446–454

10. Blanch M, Dutton A (2003) Acoustic emission monitoring of field tests of an operating wind turbine. In: Proceedings of the 5th international conference on damage assessment of structures. Southampton, UK

11. Kirikera GR, Schulz MJ, Sundaresan MJ (2007) Multiple damage identification on a wind turbine blade using a structural neural system. Proc SPIE 6530:65300T

12. Rumsey MA, Paquette JA (2008) Structural health monitoring of wind turbine blades. Proc SPIE 6933:69330E

13. Zhou W, Huang Y, Li H (2008) Damage propagation monitoring of composite blade under static loading. In: Proceeding of 2nd Asia-Pacific workshop on structural health monitoring. Melbourne, Australia

14. Sundaresan MJ, Schulz MJ, Ghoshal A (2002) Structural health monitoring static test of a wind turbine blade. National Renewable Energy Laboratory March, Subcontractor Report NREL/SR-500-28719

15. Frankenstein B, Schubert L, Meyendorf N (2009) Monitoring system of wind turbine rotor blades. Proc SPIE 7293:72930X

16. Gross E, Simmermacher T, Rumsey M et al (1999) Application of damage detection techniques uing wind turbine modal data. American society of mechanical engineers wind energy symposium, AIAA 99-0047: 230-235

17. Ghoshal A, Sundaresan MJ, Schulz MJ (2000) Structural health monitoring techniques for wind turbine blades. J Wind Eng Ind Aerodyn 85:309–324

18. Kraemer P, Fritzen CP (2007) Concept for structural damage identification of offshore wind energy plants. In: Proceedings of the sixth international workshop on structural health monitoring. Stanford, US

19. Whelan MJ, Janoyan KD, Qiu T (2008) Integrated monitoring of wind plant systems. In: Proceeding of SPIE 6933, smart sensor phenomena, technology, networks, and systems, 69330F. doi: 10.1117/12.776753

20. Dolinski L, Krawczuk M (2009) Damage detection in turbine wind blades by vibration based methods. J Phys Conf Ser 181:12–86

21. Peeters B, Maeck J, Roeck GD (2001) Vibration-based damage detection in civil engineering: excitation sources and temperature effects. Smart Mater Struct 10(3):518

22. Peeters B, Roeck GD (2001) One-year monitoring of the Z24-bridge: environmental effects versus damage events. Earthquake Eng Struct Dynam 30(2):149–171

23. Yan AM, Kerschen G, Boe PD, Golinval JC (2005) Structural damage diagnosis under varying environmental conditions - part I: a linear analysis. Mech Syst Sig Process 19(4):847–864

24. Yan AM, Kerschen G, Boe PD, Golinval JC (2005) Structural damage diagnosis under varying environmental conditions - part II: local PCA for non-linear cases. Mech Syst Sig Process 19(4):865–880

25. Xia Y, Hao H, Zanardo G, Deeks A (2006) Long term vibration monitoring of an RC slab: temperature and humidity effect. Eng Struct 28(3):441–452
26. Kim JT, Park JH, Lee BJ (2006) Vibration-based damage monitoring in model plate-girder bridges under uncertain temperature conditions. Eng Struct 29(7):1354–1365
27. Liu C, DeWolf JT (2007) Effect of temperature on modal variability of a curved concrete bridge under ambient loads. J Struct Eng 133(12):1742–1751
28. Deraemaeker A, Reynders E, Roeck GD et al (2008) Vibration-based structural health monitoring using output-only measurements under changing environment. Mech Syst Sig Process 22(1):34–56
29. Balmes E, Basseville M, Bourquin F et al (2008) Merging sensor data from multiple temperature scenarios for vibration monitoring of civil structures. Struct Health Monit 7(2):129–142
30. Basseville M, Bourquin F, Mevel L (2010) Handling the temperature effect in vibration monitoring: two subspace-based analytical approaches. J Eng Mech 136(3):367–378
31. Yoo HH, Shin SH (1998) Vibration analysis of rotating cantilever beams. J Sound Vib 212(5):807–828
32. Bucher I, Ewins DJ (2001) Modal analysis and testing of rotating structures. Philos Trans Roy Soc London Ser A Math Phys Eng Sci 359(1778):61–96
33. Osgood RM (2001) Dynamic characterization testing of wind turbines. Technical Report, National Renewable Energy Laboratory, NREL/TP-500-30070, 2001
34. Park JH, Park HY, Jeong SY (2010) Linear vibration analysis of rotating wind-turbine blade. Curr Appl Phys 10(2, Supplement 1):332–334
35. Sohn H, Czarnecki JA, Farrar CR (2000) Structural health monitoring using statistical process control. J Struct Eng 126(11):1356–1363
36. Sohn H, Farrar CR, Hunter NF (2001) Structural health monitoring using statistical pattern recognition techniques. J Dyn Syst Meas Contr 123(4):706–711
37. Lei Y, Kiremidjian AS, Nair KK et al (2003) Statistical damage detection using time series analysis on a structural health monitoring benchmark problem. In: Proceedings of the 9th international conference on applications of statistics and probability in civil engineering. San Francisco, CA, USA
38. Basseville M, Mevel L, Goursat M (2004) Statistical model-based damage detection and localization: subspaced-based residuals and damage-to-noise sensitivity ratios. J Sound Vib 275(3–5):769–794
39. Kane TR, Ryan RR, Banerjee AK (1987) Dynamics of a cantilever beam attached to a moving base. J Guid Control Dyn 10:139–151
40. Bakr EM, Shabana AA (1986) Geometrically nonlinear analysis of multibody system. Comp Struct 23:739–751
41. Wallrapp O, Schwertassek R (1991) Representation of geometric stiffening in multibody system simulation. Int J Numer Meth Eng 32:1833–1850
42. Mayo J, Dominguez J, Shabana AA (1995) Geometrically nonlinear formulation of beams in flexible multibody dynamics. J Vibr Acoust 117(4):501–509
43. Park S, Lee J-J, Yun C-B, Inman DJ (2008) Electro-mechanical impedance-based wireless structural health monitoring using PCA-Data compression and k-means clustering algorithms. J Intell Mater Syst Struct 19(4):509–520
44. Han S, Feeny BF (2002) Enhanced proper orthogonal decomposition for the modal analysis of homogeneous structures. J Vib Control 8(1):19–40
45. Mei C, Fan J (2006) Methods for data analysis. Higher Education Press, Beijng
46. Ma J, Niu Y, Chen H (2006) Blind signal processing. National Defense Industry Press, Beijing
47. Bao X, Chen L (2011) Recent progress in Brillouin scattering based fiber sensors. Sensors 11(4):4152–4187
48. Horiguchi T, Tateda M (1989) Optical-fiber-attenuation investigation using stimulated Brillouin scattering between a pulse and a continuous wave. Opt Lett 14:408–410

49. Li W, Bao X, Li Y et al (2008) Differential pulse-width pair BOTDA for high spatial resolution sensing. Opt Express 16:21616–21625
50. Dong Y, Bao X, Li W (2009) Differential Brillouin gain for improving the temperature accuracy and spatial resolution in a long-distance distributed fiber sensor. Appl Opt 48:4297–4301
51. Cotter D (1983) Stimulated Brillouin scattering in monomode optical fiber. J Opt Commun 4(1):10–19
52. Horiguchi T, Shimizu K, Kurashima T et al (1995) Development of a distributed sensing technique using Brillouin scattering. J Lightw Technol 13(7):296–302
53. White D (2004) New method for dual-axis fatigue testing of large wind turbine blades using resonance excitation and spectral loading. National Renewable Energy Laboratory, NREL/TP-500-35268
54. Minakuchi S et al (2009) Barely visible impact damage detection for composite sandwich structures by optical-fiber-based distributed strain measurement. Smart Mater Struct 18(8):085018
55. Minakuchi S et al (2011) Life cycle monitoring of large-scale CFRP VARTM structure by fiber-optic-based distributed sensing. Compos A 42(6):669–676
56. Higuchi T (1988) Approach to an irregular time series on the basis of the fractal theory. Physica D 31(2):277–283

Chapter 10
Sensor Fault Diagnosis in Wind Turbines

Manuel Gálvez-Carrillo, Laurent Rakoto and Michel Kinnaert

Abstract This chapter addresses the early detection and isolation of sensor faults in a systematic and unified way and illustrates the approach on wind turbine simulation data. Three problems are successively considered: individual signal monitoring, fault detection and isolation (FDI) in redundant sensors, and FDI based on analytical redundancy. In all three cases, a specific approach to generate fault indicators, also called residuals, is presented and combined with an online statistical change detection/isolation algorithm. The considered case studies consist of wind turbine generator speed monitoring, as well as FDI in the stator current and voltages of a wind-driven doubly fed induction generator. For the latter problem, the fact that the three-phase signals are balanced allows one to determine a simple signal model from which a multiobserver scheme is designed for residual generation.

Keywords Sensor fault detection and isolation · Statistical change detection/isolation algorithm · Multiobserver scheme · Three-phase signals · Doubly fed induction generator

Nomenclature

$\mathbf{e}_j$	jth standard basis vector
f	Additive sensor fault
g	Decision function
$\mathbf{i}_{s,abc}$, $\mathbf{i}_{r,abc}$	Stator and rotor three-phase currents
k_0	Fault occurrence time

M. Gálvez-Carrillo (✉)
ELIA System Operator S.A., Boulevard de L'Empereur 20, 1000 Brussels, Belgium
e-mail: manuel.galvez@elia.be

L. Rakoto · M. Kinnaert
Université Libre de Bruxelles (ULB), 50 Ave. F.D. Roosevelt, 1050 Brussels, Belgium
e-mail: laurent.rakoto@ulb.ac.be

M. Kinnaert
e-mail: michel.kinnaert@ulb.ac.be

$p_\theta(r(i))$	Probability density function of $r(i)$ that depends on the vector parameter θ
q	Quantization error
$r(i)$	ith sample of the residual vector
$s(r(i))$	Log-likelihood ratio for $\mathbf{r}(i)$
t_a	Alarm time instant
$\mathbf{u}_{s,abc}$, $\mathbf{u}_{r,abc}$	Stator and rotor three-phase voltages
$\mathbf{v},\mathbf{w}$	Process and measurement noise vectors respectively
$\mathbf{x}$	State vector
$\mathbf{y}$	Output vector
$\hat{}$	Stands for estimate
m	As an upper index indicates measurement
abc	As a lower index indicates three-phase signals
s	As a lower index indicates a stator signal (voltage or current)
r	As a lower index indicates a rotor signal (voltage or current)
$*$	As an upper index indicates a reference signal within a closed loop
$\mathscr{L}(r(i))$	Probability law of $r(i)$
N_p	Number of encoder pulses per revolution
$\mathscr{N}(\mu_0, \Sigma)$	Normal distribution with mean μ_0 and variance Σ
Q_s^*	Reactive power reference
R_v, R_w	Variance of $\mathbf{v}$ and $\mathbf{w}$ respectively
$\mathscr{R}_1^k$	Set of k independent residual samples
$\mathscr{S}(\mathscr{R}_1^k)$	Log-likelihood ratio for the data set $\mathscr{R}_1^k$, assuming a change in the mean at time k_0
T_{sc}	Time window used for speed estimation
T_s	Sampling period
T_g^*	Generator torque reference
$\mathscr{U}(a,b)$	Probability law of a uniform statistical distribution in the interval $[a,b]$
$\Lambda_{k_0}(\mathscr{R}_1^k)$	Likelihood ratio for the data set $\mathscr{R}_1^k$, assuming a change in the mean at time k_0
ω	Frequency
Ω_g	Generator speed
η	Portion of the damaged bars of a code wheel
θ_s	Angle that fulfills $\omega_s = \dfrac{d\theta_s}{dt}$
θ	Vector that parameterizes a probability density function

10.1 Introduction

Fault diagnosis systems aim at detecting and locating degradations in the operation of wind turbine components as early as possible. This way, maintenance operations can be performed in due time, and during time periods with low wind speed. Therefore, maintenance costs are reduced as the number of costly corrective maintenance actions decreases. Besides, the loss of production due to maintenance operations is minimized.

Fault detection and isolation (FDI) in wind turbines has been the subject of a large number of publications notably stimulated by different benchmark problems [1, 2]. In those benchmarks, the authors mostly consider various sensor and actuator faults like sensor faults on pitch position and generator speed measurements, pitch actuator faults, and converter faults. Structural health monitoring has also been considered for wind turbines specifically. The aim is to detect changes such as delamination and cracks in the structural parts of the turbine, namely the tower and the blades. Presently, visual inspection through regular maintenance operations is the usual approach. Yet specific robots are being developed to make this task easier, and the permanent monitoring, thanks to appropriately placed sensor networks for strain and displacement measurement, is also under investigation [3, 4]. Last but not least, vibration monitoring techniques have been thoroughly studied for the monitoring of the gearbox, the bearings, and the generator. Commercial products have been developed for these components, specially since gearbox is responsible for the largest downtime [5, 6].

A complete monitoring system should have a modular structure with appropriate methods for each component, as depicted in Fig. 10.1. The lower layer within this architecture consists of measurement validation modules. The latter aim at detecting and locating (or isolating) sensor faults. These different measurement validation modules will be the focus of this chapter. A short section will address faults that can be detected by analyzing the measurement samples issued by a single sensor. This includes excessive noise on the measurements, flat signals, and outliers. However, the focus of this chapter will be on incipient faults like small sensor bias and drifts, which typically require the use of several sensor signals to achieve FDI. Two approaches can be distinguished depending on the instrumentation: hardware redundancy and analytical redundancy. The first approach applies for redundant sensors, namely groups of sensors that are measuring the same physical quantity. A sensor exhibiting a significant discrepancy with respect to the others will be discarded. A way to handle this issue within a proper statistical framework will be discussed. On the other hand, analytical redundancy amounts to detecting incoherencies between a model of the supervised system and data recorded online on this system [7]. A systematic approach to handle sensor faults in the voltage and current sensors that equip a wind-driven doubly fed induction generator (DFIG) will be used to illustrate this class of methods.
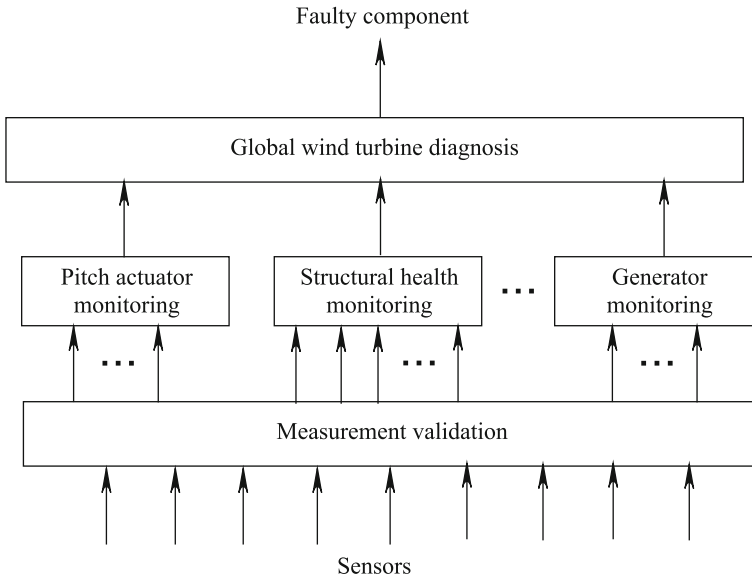
Fig. 10.1 Hierarchical structure of a fault detection and isolation system

The approaches that are used in this chapter rely on statistical change detection/isolation algorithms. Hence, the second section provides a review of the relevant material. In Sect. 10.4, single sensor monitoring is briefly discussed. Section 10.5 then addresses sensor FDI based on hardware redundancy. Finally, the last section is dedicated to the use of analytical redundancy for sensor FDI.

10.2 Statistical Change Detection/Isolation Algorithms

The FDI systems that are presented below consist of two parts, a residual generator and a decision system. The first generates signals called residuals, namely fault indicators, that are designed in such a way that they have zero mean in the absence of fault and non-zero mean in the presence of faults. Besides, the residual sequence is made of statistically independent data samples. Residual generation will be addressed separately in the case of hardware redundancy and analytical redundancy. However, in both cases, the decision system relies on statistical change detection/isolation algorithms to decide on the presence of a fault (fault detection) and to indicate the faulty component (fault isolation). Therefore, the tools used in the decision system are first presented before dealing with the two types of redundancy. In the following sections, fault detection is first addressed, next a detection/isolation algorithm is presented.

10.2.1 Fault Detection

The following hypothesis testing problem is the basis for the development of fault detection algorithms.

Data: A set of independent random vectors $\mathscr{R}_1^k = \{\mathbf{r}(1), \mathbf{r}(2), \ldots, \mathbf{r}(k)\}$, where k denotes the present time instant, characterized by the probability density function $p_\theta(\mathbf{r}(\mathbf{i}))$. The latter depends on a parameter vector θ that takes value θ_0 in fault free mode and θ_1 in faulty mode, with $\theta_1 \neq \theta_0$. Typically θ will be the mean or the variance of the probability distribution in the sequel.

Problem: choose between the following two hypotheses:

$$
\begin{aligned}
\mathscr{H}_0 \quad & \mathscr{L}(\mathbf{r}(i)) = p_{\theta_0}(\mathbf{r}(i)) && \text{for } i = 1, \ldots, k \\
\mathscr{H}_1 \quad & \mathscr{L}(\mathbf{r}(i)) = p_{\theta_0}(\mathbf{r}(i)) && \text{for } i = 1, \ldots, k_0 - 1 \\
& \quad\quad\quad\quad = p_{\theta_1}(\mathbf{r}(i)) && \text{for } i = k_0, \ldots, k
\end{aligned}
$$

where k_0 is the fault occurrence time which is actually unknown, and $\mathscr{L}(\mathbf{r}(k))$ denotes the probability law of $r(k)$.

By Niemann Pearson's lemma, the relevant test to decide between the two hypotheses is based on the likelihood ratio [8]. In our specific setting, assuming that k_0 is known, this can be written as:

$$
\begin{aligned}
\Lambda_{k_0}(\mathscr{R}_1^k) &= \frac{\prod_{i=1}^{k_0-1} p_{\theta_0}(r(i)) \prod_{i=k_0}^{k} p_{\theta_1}(r(i))}{\prod_{i=1}^{k} p_{\theta_0}(r(i))} \\
&= \prod_{i=k_0}^{k} \frac{p_{\theta_1}(r(i))}{p_{\theta_0}(r(i))}
\end{aligned}
$$

where the mutual independence of the samples $\mathbf{r}(i), i = 1, \ldots, k$ has been accounted for. The test can be stated as follows:

Accept hypothesis $\mathscr{H}_0$ when $\Lambda_{k_0}(\mathscr{R}_1^k) \leq \lambda_\alpha$, otherwise accept $\mathscr{H}_1$, where λ_α is a user defined threshold that depends of the acceptable probability of false alarm α.

Taking the natural logarithm of both sides of the above expression yields an equivalent test which is often easier to implement, particularly with distributions belonging to the exponential family, like the Gaussian distribution. The following notation will be used to denote the resulting log-likelihood ratio:

$$
S_{k_0}(\mathscr{R}_1^k) = \ln \Lambda_{k_0}(\mathscr{R}_1^k) = \sum_{i=k_0}^{k} \ln \frac{p_{\theta_1}(r(i))}{p_{\theta_0}(r(i))} = \sum_{i=k_0}^{k} s(i) \tag{10.1}
$$

where $s(i)$ denotes the log-likelihood ratio for the i-th sample. The test obviously becomes:

Accept hypothesis $\mathscr{H}_0$ when $S_{k_0}(\mathscr{R}_1^k) \leq h_\alpha$, otherwise accept $\mathscr{H}_1$, where $h_\alpha = \ln \lambda_\alpha$.

Now, as k_0 is actually unknown, it is substituted by its maximum likelihood estimate. The resulting decision function at time k can then be written as:

$$g(k) = \max_{1 \le j \le k} S_j(\mathscr{R}_1^k) \tag{10.2}$$

An alarm is triggered at the time instant t_a defined as:

$$t_a = \min\{k : g(k) > h_\alpha\} \tag{10.3}$$

and the estimated fault occurrence time can be determined from

$$\hat{k}_0 = \arg \max_{1 \le j \le t_a} S_j(\mathscr{R}_1^k) \tag{10.4}$$

This test can be implemented recursively in order to handle the increasing number of data as time elapses. The derivation of this recursive algorithm is explained in [8], and we only describe the algorithm here.

CUSUM algorithm—recursive form

$$g(k) = \max(0, g(k-1) + s(k)) \quad g(0) = 0 \tag{10.5}$$

$$d(k) = d(k-1)1_{\{g(k-1) > 0\}} + 1 \quad d(0) = 0 \tag{10.6}$$

$$t_a = \min\{k : g(k) > h_\alpha\} \tag{10.7}$$

$$\hat{k}_0 = d(t_a) \tag{10.8}$$

where $1_{\{x\}}$ is the indicator function of event x. It is equal to 1 when x is true and to zero otherwise.

As an example, let us consider the case where the residual is normally distributed.

10.2.1.1 Example

In fault free mode, the probability law of the n_r-dimensional residual vector is assumed to be

$$\mathscr{L}(\mathbf{r}(i)) = \mathscr{N}(\mu_0, \Sigma)$$

while upon occurrence of a fault, it is given by

$$\mathscr{L}(\mathbf{r}(i)) = \mathscr{N}(\mu_1, \Sigma)$$

where $\mathcal{N}(\mu, \Sigma)$ denotes the multinormal distribution with mean μ and variance Σ. The associated probability density function is the following:

$$p(\mathbf{r}(i)) = \frac{1}{\sqrt{(2\pi)^{n_r} \det \Sigma}} \exp\left(-\frac{1}{2}(\mathbf{r}(i) - \mu)^T \Sigma^{-1}(\mathbf{r}(i) - \mu)\right) \qquad (10.9)$$

Straightforward computations yield the following expression for $s(i)$ in this case:

$$s(i) = (\mu_1 - \mu_0)^T \Sigma^{-1}\left(\mathbf{r}(i) - \frac{1}{2}(\mu_1 + \mu_0)\right) \qquad (10.10)$$

Notice that the factor $(\mu_1 - \mu_0)^T \Sigma^{-1}$ can be seen as a vector form of signal-to-noise ratio that weights the contributions of the different components of $\mathbf{r}(i)$.

Let us now turn to the situation where several faults can possibly occur.

10.2.2 Detection/Isolation Algorithm

The problem amounts to generating an alarm when one out a set of n_f possible faults can occur, given a sequence of independent samples of a residual vector $\{\mathbf{r}(1), \mathbf{r}(2), \ldots, \mathbf{r}(k)\}$. The corresponding hypothesis testing problem can be stated as follows.

Data: A set of independent random vectors $\mathcal{R}_1^k = \{\mathbf{r}(1), \mathbf{r}(2), \ldots, \mathbf{r}(k)\}$ where k denotes the present time instant characterized by the probability density function $p_\theta(\mathbf{r}(i))$. The latter depends on a parameter vector θ that takes value θ_0 in fault free mode and $\theta_\ell, \ell = 1, \ldots, n_f$ in fault mode ℓ (with $\theta_\ell \neq \theta_q, 0 \leq q \neq \ell \leq n_f$)

Problem: Choose between the following $n_f + 1$ hypotheses:

$$
\begin{array}{lll}
\mathcal{H}_0 & \mathcal{L}(\mathbf{r}(i)) = p_{\theta_0}(\mathbf{r}(i)) & \text{for } i = 1, \ldots, k \\
\mathcal{H}_\ell, \ell = 1, \ldots, n_f & \mathcal{L}(\mathbf{r}(i)) = p_{\theta_0}(\mathbf{r}(i)) & \text{for } i = 1, \ldots, k_0 - 1 \\
& \quad\quad\quad\quad\quad = p_{\theta_\ell}(\mathbf{r}(i)) & \text{for } i = k_0, \ldots, k
\end{array}
$$

In order to decide that a fault of type ℓ has occurred, the log-likelihood ratio between fault ℓ and all other possible fault modes, as well as the fault free mode should be larger than a threshold h_ℓ. The test function for fault ℓ can thus be written:

$$g_\ell^*(k) = \max_{1 \leq j \leq k} \min_{0 \leq q \neq \ell \leq n_f} (S_j^{\ell q}(\mathcal{R}_1^k))$$

where the exponent ℓq refers to the log-likelihood ratio between hypotheses ℓ and q. As above, the maximization over j aims at determining the most likely fault occurrence time. An alarm for fault $\ell \in \{1, \ldots, n_f\}$ will be triggered at time t_a^ℓ such that

$$t_a^\ell = \inf\{k \geq 1 : g_\ell^*(k) > h^\ell\}$$

where h^ℓ is a user-defined threshold that depends on the specifications regarding the probability of false alarm and missed isolation. It turns out that the decision function can be implemented in a recursive way while guaranteeing attractive optimality properties of the algorithm [9, 10]. Let us introduce the following notation for the decision function of the CUSUM algorithm between hypothesis $\mathscr{H}_\ell$ and $\mathscr{H}_0$:

$$g_{\ell 0}(k) = \max(0, g_{\ell 0}(k-1) + s_{\ell 0}(k)) \tag{10.11}$$

where $s_{\ell 0}(k) = \ln \frac{p_{\theta_\ell}(r(k))}{p_{\theta_0}(r(k))}$. Then recursive computation of the decision functions can be written:

$$g_\ell^*(k) = \min_{0 \leq q \neq \ell \leq n_f} (g_{\ell 0}(k) - g_{q0}(k)) \quad \ell = 1, \ldots, n_f \tag{10.12}$$

where $g_{0,0}(k) = 0$, and an alarm is generated when

$$g_\ell^*(k) > h^\ell \quad \text{for some } \ell = 1, \ldots, n_f \tag{10.13}$$

The detection/isolation algorithm can be summarized as follows:

- *Initialization*:
  Set $g_{\ell 0}(0) = 0, \ell = 1, \ldots, n_f$.
- *Upon receipt of the kth residual sample*,
  perform the following operations:

  – Compute the n_f CUSUM test functions according to Eq. (10.11).
  – Decision

     Compute $g_\ell^*(k)$ from Eq. (10.12), for $\ell = 1, \ldots, n_f$.
     If $g_\ell^*(k) > h^\ell$, then an alarm for fault ℓ is issued at the kth time instant and the algorithm stops.

We now turn to some practical issues.

10.2.3 Practical Issues

Two issues have to be discussed, namely the setting of the parameters of the recursive algorithm and the actions to be taken once an alarm has been generated, in order to detect a possible fault disappearance.

As far as the setting of the parameters is concerned, one should distinguish the choices of θ_0, $\theta_\ell, \ell = 1, \ldots, n_f$ and the thresholds h^ℓ. θ_0 is normally determined from a set of data obtained in healthy operation. These data are processed by the residual generators to be described next, in order to generate a residual set $\{\mathbf{r}(1), \ldots, \mathbf{r}(N)\}$. θ_0 is then determined as an empirical estimate of the corresponding characteristics (mean or variance for instance), of the probability density function of the residual. For what regards $\theta_\ell, \ell = 1, \ldots, n_f$, the fault magnitude is usually not known; yet one has to quantify the effect of the fault on the residual in order to set $\theta_\ell, \ell = 1, \ldots, n_f$. This is achieved typically by considering the fault $\ell, \ell = 1, \ldots, n_f$ with the smallest magnitude one wishes to detect and isolate. This magnitude will depend in the end on its effect on the technical-economic performance of the system, which is yet to be determined, and is outside the framework of this chapter. The fault is superimposed to the recorded measurements (provided the sensor is not used within a closed loop) or simulated via a model of the supervised process; a residual vector is computed from these data and the parameter vector of the residual probability density function, namely θ_ℓ, is estimated from this residual sequence.

The choice of the threshold can be performed in two steps. An a priori setting of the threshold values can be determined from analytical expressions of the mean detection/isolation delays in terms of the thresholds and a measure of the distance between the statistical distribution of the residual in fault free and faulty modes [10, 11]. This a priori value can be fine tuned from a set of experimental data in fault free mode, and possibly in faulty mode. By processing the residual generated from these data with the decision system, one should notably check that the mean time between false alarms meets the specifications and possibly increase the threshold if too many false alarms are observed.

As far as detection of a possible fault disappearance is concerned, two approaches can be distinguished. In the case of the CUSUM algorithm given by Eqs. 10.5–10.8 aimed at fault detection, once a change from $\mathcal{H}_0$ to $\mathcal{H}_1$ has been detected, it is natural to look for the opposite change, namely:

Choose between the following two hypotheses:

$$
\begin{aligned}
\mathcal{H}_0 \quad & \mathcal{L}(\mathbf{r}(i)) = p_{\theta_1}(\mathbf{r}(i)) && \text{for } i = t_a, \ldots, k \\
\mathcal{H}_1 \quad & \mathcal{L}(\mathbf{r}(i)) = p_{\theta_1}(\mathbf{r}(i)) && \text{for } i = t_a, \ldots, k_1 - 1 \\
& \qquad\qquad = p_{\theta_0}(\mathbf{r}(i)) && \text{for } i = k_1, \ldots, k
\end{aligned}
$$

where k_1 is the unknown fault disappearance time, and t_a is the alarm time instant.

A recursive algorithm that performs this choice is easily obtained by noticing that the likelihood ratio of $\mathbf{r}(k)$ associated to the above problem is the inverse of the likelihood ratio for the initial problem. In terms of log-likelihood ratio, this corresponds to a sign change. Hence, the following strategy is proposed to detect possible fault disappearance. From time instant $t_a + 1$, run the following recursive CUSUM algorithm

$$g_{\text{dis}}(k) = \max(0, g_{\text{dis}}(k-1) - s(k)) \quad g_{\text{dis}}(t_a + 1) = 0 \tag{10.14}$$

$$d(k) = d(k-1)1_{\{g(k-1) > 0\}} + 1 \quad d(t_a + 1) = 0 \tag{10.15}$$

$$t_{a,\text{dis}} = \min\{k : g_{\text{dis}}(k) > h_\alpha\} \tag{10.16}$$

$$\hat{k}_1 = d(t_{a,\text{dis}}) \tag{10.17}$$

On the other hand, when the detection/isolation algorithm given by Eqs. 10.11–10.13 is used, the detection of fault disappearance corresponds to a new hypothesis test, which cannot be translated into a simple transformation of this algorithm, like a sign change. Therefore, the easiest way to proceed is to re-initialize all the n_f decision functions computed from Eq. 10.11 to zero each time a threshold is crossed in Eq. 10.13, and to keep issuing an alarm as long as periodic crossing of the threshold is observed.

Let us now consider the application of the above tools to handle sensor fault detection first.

10.3 Individual Signal Monitoring

Usual alarm systems check whether the signal issued by a sensor lies within the measurement range. Yet somewhat more involved verifications can be made on a single signal before resorting to hardware or analytical redundancy to look for small magnitude faults. We will illustrate this claim by using a recursive CUSUM algorithm for variance change detection in order to detect the appearance of an excessive measurement noise on a signal. The same type of algorithm can also be used to detect a flat signal.

10.3.1 Excessive Noise

Let us assume that the measured signal can be modeled as:

$$y(t) = cx(t) \tag{10.18}$$

$$y^m(kT_s) = y(kT_s) + v(kT_s) \tag{10.19}$$

where the first equation corresponds to the measurement process with $t \in \mathbb{R}$ the continuous time, $x(t)$ is the physical signal which is measured, c is the sensor gain and $y(t)$ the sensor output. The second equation models the data acquisition system operating at the sampling period T_s. $v(kT_s)$ denotes the measurement noise, supposed to be a normally distributed zero mean white noise sequence with variance σ^2. kT_s will be replaced by k below, for the sake of concision.

An excessive noise is characterized by an increase in the noise variance to $\gamma\sigma^2$ where $\gamma > 1$. Such an increase may occur notably due to a poor contact in an electric connection. It induces an increase in the variance of $y(k)$. Hence monitoring this variance is a natural way to detect excessive noise. To determine an empirical estimate of the variance, an empirical estimate of the mean of $y(k)$ is needed. Yet this estimation step will be avoided here by exploiting typical properties of $x(t)$. Indeed, the spectrum of $x(t)$ is normally concentrated in the low frequency range with regard to measurement noise. Hence, it is reasonable to assume that, within a time window around time kT_s, the physical signal can be described as

$$x(t) = a_1 t + a_0 \quad \text{with} \quad t \in [(k - W/2)T_s, (k + W/2)T_s]$$

where $a_0, a_1 \in \mathbb{R}$ and W is an even integer corresponding to the window size. Under this hypothesis, the trends within the signal $y(t)$ can be filtered out by considering its second derivative $\frac{d^2 y(t)}{dt^2}$. Translating this procedure on the measurement sequence amounts to computing

$$r(k) = \frac{y^m(k+1) - 2y^m(k) + y^m(k-1)}{T_s^2} \tag{10.20}$$

which is an approximation of the second derivative of $y(t)$ at time kT_s. Given the white noise hypothesis, the variance of $r(k)$ is equal to $\sigma_r^2 = 6\sigma^2/T_s^4$. Notice that division by T_s^2 can be omitted in Eq. 10.20 without affecting the removal of the trend. This corresponds the approach used in Sect. 10.4.2.

It is then straightforward to detect the change in the variance of σ_r^2 by using the recursive form of the CUSUM algorithm given by Eqs. 10.5–10.8 applied to the following hypothesis test:

Choose between the following two hypotheses:

$$\begin{aligned} \mathscr{H}_0 \quad & \mathscr{L}(\mathbf{r}(i)) = \mathscr{N}(0, 6\sigma^2/T_s^4) \quad \text{for } i = 1, \dots, k \\ \mathscr{H}_1 \quad & \mathscr{L}(\mathbf{r}(i)) = \mathscr{N}(0, 6\sigma^2/T_s^4) \quad \text{for } i = 1, \dots, k_0 - 1 \\ & \qquad\qquad = \mathscr{N}(0, 6\gamma\sigma^2/T_s^4) \quad \text{for } i = k_0, \dots, k \text{ and } \gamma > 1 \end{aligned}$$

where k_0 is the unknown fault occurrence time.

Straightforward computations yield the following expression for the log-likelihood ratio $s(k)$ in Eq. 10.5:

$$s(k) = \ln\frac{1}{\sqrt{\gamma}} - \frac{r(k)^2}{2}\frac{T_s^4}{\sigma^2}\left(\frac{1}{6\gamma} - \frac{1}{6}\right) \tag{10.21}$$

This method is illustrated by a case study in the next section.

10.3.2 Application to Incremental Encoder Fault

The detection of excessive noise is applied to generator speed measurements for a wind driven DFIG. Such measurements are typically determined from an incremental encoder. The generator speed estimate, $\hat{\Omega}_g(k)$, is then obtained by computing the frequency of the encoder pulses over a time window T_{sc} as

$$\hat{\Omega}_g(k) = \frac{60\Delta N(k)}{N_p T_{sc}}[\text{rpm}]$$

where N_p is the number of pulses per revolution and $\Delta N(k)$ is the measured number of pulses over the time window.

The quantization error on this speed estimate is given by $q_h = \frac{60}{N_p T_{sc}}[\text{rpm}]$, [12]. An excessive noise can be due to imperfections of the encoder code wheel. For instance, when a portion $\eta \in]0,1[$ of the bars of the code wheel is damaged, a reduction to $(1-\eta)N_p$ of the number of pulses per revolution can be induced. This imperfection generates an increase of the quantization error to $q_f = \frac{60}{(1-\eta)N_p T_{sc}}[\text{rpm}]$.

To illustrate the algorithm for excessive noise detection, a wind turbine is simulated with the AERODYN and FAST software [13]. The main data of the variable-speed variable-pitch wind turbine are represented in Table 10.1. The weather conditions correspond to a mean wind speed equal to 14.2 m/s and a 18 % wind turbulence intensity. The incremental encoder parameters are $N_p = 1,024$ and $T_{sc} = 0.01$ s. In the wind turbine simulator, the quantization error on the generator speed measurement is modeled by an additive uniformly distributed white noise in the interval $[-q,0]$, namely $\mathcal{L}(v(kT_s)) = \mathcal{U}(-q,0)$ [12]. q is equal to q_h (q_f) when the encoder is healthy (faulty). The simulation represents the occurrence of an excessive noise with η equal to 10 % at time instant 10 s.

The algorithm described by Eqs. 10.5–10.8, in which Eq. 10.21 is substituted for the log-likelihood ratio, is applied to $r(k)$ with $\sigma^2 = q_h^2/12$ and the increase factor in the variance $\gamma = 1/(1-\eta)^2$. Note that the division by T_s^2 is omitted in the computation of Eq. 10.20 for $r(k)$. η is set to 10 % as the algorithm is intended to detect a damage affecting at least 10 % of the bars of the code wheel.

Table 10.1 Main wind turbine data

Parameter	Value
Nominal power, P_n	1,250 KW
Nominal speed, v_{wn}	12.5 m/s
Generator reference speed, Ω_g^{ref}	1,116 rpm

The generator speed measurement is represented in the upper subplot of Fig. 10.2. The second subplot represents the estimation of the second derivative of the generator speed, from the measurements. At the appearance time of the excessive noise (10 s), the decision function $g(k)$ (third subplot in Fig. 10.2) increases and exceeds the threshold, set at 10, around the time instant 15 s. The alarm is then switched to 1 and the decision function $g_{\mathrm{dis}}(k)$ is activated for detecting the fault disappearance (see lower subplots in Fig. 10.2). For the chosen algorithm parameters, the detection delay of an excessive noise on the incremental encoder is around 5 s.

10.3.2.1 Note

The algorithm for excessive noise detection is based on the detection of a variance change under the hypothesis of white Gaussian noise. Nevertheless, even with an additive uniform white noise, the algorithm performance is not significantly affected due to the fact that the pdf of $r(k)$ is close to a Gaussian distribution (see Fig. 10.3).

10.4 Fault Detection and Isolation Based on Hardware Redundancy

Hardware redundancy can notably be encountered for wind turbine speed measurements. Indeed, both rotor speed and generator speed are measured, and they are directly linked through the gear ratio. Besides, redundant measurements of the generator speed are quite usual. We successively address the issue of residual generation and residual evaluation in the following sections.

10.4.1 Residual Generation

A given physical quantity, say x (a temperature, a pressure, a flow, a position, a velocity, …) is measured by a set of sensors, possibly based on different sensing principles. The mathematical model describing the measurement process can be written as:
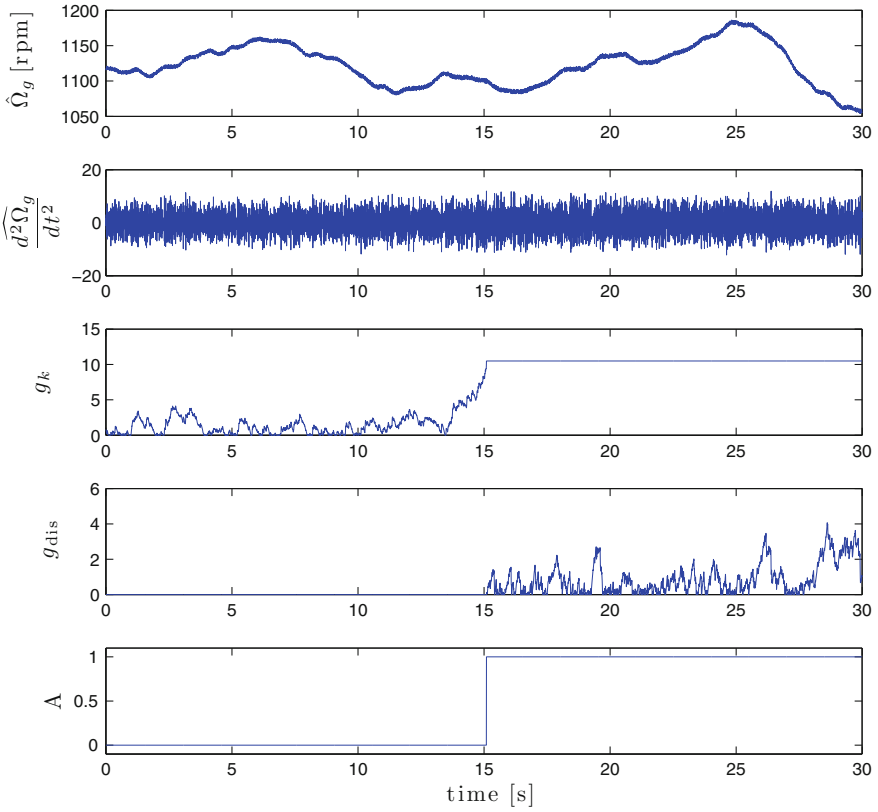
Fig. 10.2 Detection of excessive noise on the incremental encoder for the generator speed, $\hat{\Omega}_g$: the estimated speed; $\widehat{\frac{d^2\Omega_g}{dt^2}}$: the estimated second derivative of the generator speed; $g(k)$ and $g_{\text{dis}}(k)$: decision functions of the presence and disappearance of excessive noise, respectively; A: alarm signal indicating the presence of excessive noise

$$\mathbf{y}^m(k) = \mathbf{C}x(k) + \mathbf{v}(k) + \mathbf{f}(k) \qquad (10.22)$$

with $x \in \mathcal{R}$, $\mathbf{y}(k) \in \mathcal{R}^p$, $\mathbf{v}(k) \in \mathcal{R}^p$, $\mathbf{f}(k) \in \mathcal{R}^p$. $\mathbf{y}^m(k)$ denotes the vector made of the p sensor measurements. $\mathbf{v}(k)$ stands for the measurement noise vector. It is a zero mean white noise vector with variance Σ. $\mathbf{f}(k)$ is a vector of additive faults that can notably represent a bias or a drift on the sensors. Finally $\boldsymbol{C}$ is a $p \times 1$ matrix of sensor gains. If the measurement noises on the different sensors are assumed to be independent, matrix Σ takes the form $\Sigma = \text{diag}_{j=1,p}\{\sigma_j^2\}$ and the scalars σ_j^2 can be chosen in accordance with the precision class of the instrument notably.
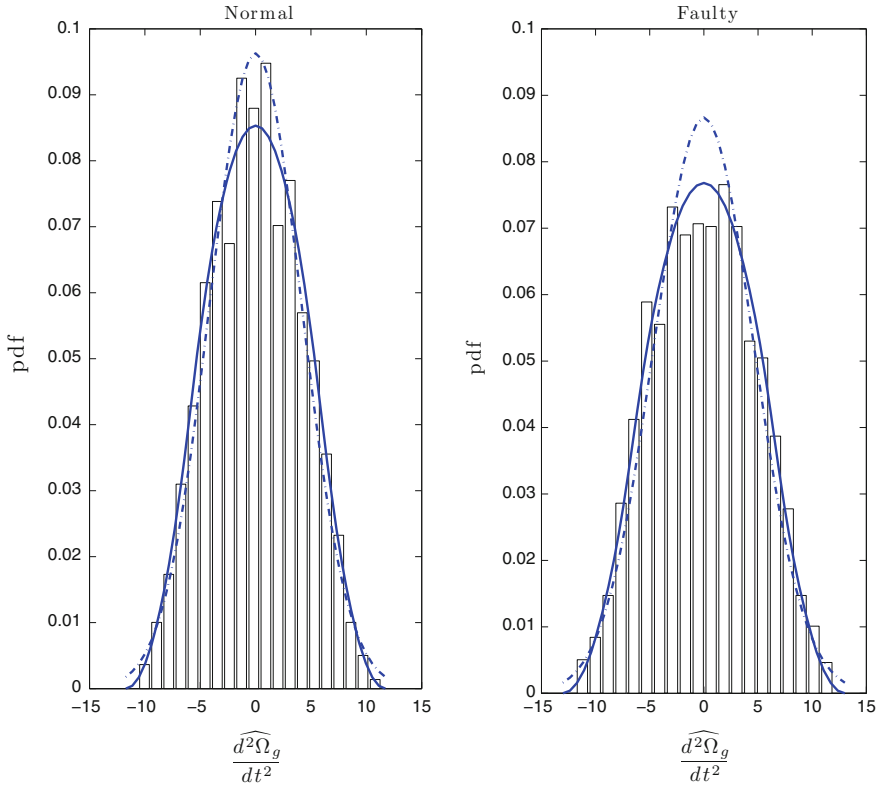
Fig. 10.3 Histogram of the estimated derivative of the generator speed; dashed line, pdf of the normal distribution $\mathcal{N}(0, q^2/2)$; *solid line*, theoretical pdf of $r(k)$ for uniform white noises $\mathcal{U}(-q, 0)$. *Left* normal healthy condition, $q = q_h = \frac{60}{N_p T_{sc}}$, *Right* presence of excessive noise, $q = q_f = \frac{60}{(1-\eta)N_p T_{sc}}$ where $\eta = 10\%$

To generate fault indicators, the unknown quantity x has to be eliminated from Eq. 10.22. To this end, let us consider a full row rank matrix N_C such that $N_C C = 0$. Thus the rows of N_C span the left null space of matrix C. Multiplying Eq. 10.22 on the left by N_C yields:

$$N_C \vec{y}(k) = N_C \vec{v}(k) + N_C \vec{f}(k) \tag{10.23}$$

Let us set

$$\mathbf{r}(k) \equiv N_C \mathbf{y}(k) \tag{10.24}$$

as a candidate residual vector. It is indeed easily seen from Eq. 10.23 that the probability law for $\mathbf{r}(k)$ is

$$\mathscr{L}(\mathbf{r}(k)) = \mathscr{N}(\mathbf{0}, N_C \Sigma N_C^T) \quad \text{when } \mathbf{f}(k) = 0$$
$$\mathscr{L}(\mathbf{r}(k)) = \mathscr{N}(N_C \mathbf{f}(k), N_C \Sigma N_C^T) \quad \text{when } \mathbf{f}(k) \neq 0$$

$\mathbf{r}(k)$ can thus be used as a fault indicator.

A hypothesis on the fault type is needed to be able to apply the decision system described in Sect. 10.3 in order to process the residual vector defined in Eq. 10.24. Bias-like faults will be considered from now on. In this case, the fault vector $\mathbf{f}(k)$ can be written $\mathbf{f}(k) = \pm b_j \mathbf{e}_j 1_{\{k \geq k_0\}}$ where $\mathbf{e}_j = \begin{bmatrix} 0 & \dots & 0 & 1 & 0 & \dots & 0 \end{bmatrix}^T$ is the jth standard basis vector, b_j is the fault magnitude and $1_{\{k \geq k_0\}}$ is the indicator function of event $\{k \geq k_0\}$. Notice that both positive and negative bias should be detected and isolated; hence, the $\pm$ symbol in the expression of $\mathbf{f}(k)$. In these conditions, the change in the mean due to the fault can be detected and isolated using the algorithm presented in Sect. 10.3.2 in which the number of faults is $n_f = 2p$. The required log-likelihood ratio for each residual sample takes the form

$$s_{\ell 0}(k) = \mathbf{e}_j^T N_C^T b_j (N_C \Sigma N_C^T)^{-1} (\mathbf{r}(k) - \frac{1}{2} N_C b_j \mathbf{e}_j) \quad \ell = 1 \dots, p$$
$$s_{\ell 0}(k) = -\mathbf{e}_j^T N_C^T b_j (N_C \Sigma N_C^T)^{-1} (\mathbf{r}(k) + \frac{1}{2} N_C b_j \mathbf{e}_j) \quad \ell = p+1 \dots, 2p$$

By insertion of these expressions into Eq. 10.11, Eqs. 10.11–10.13 yield the required decision system.

10.5 Fault Detection and Isolation Based on Analytical Redundancy

In this section, the relationships between different physical quantities is exploited through a mathematical model in order to achieve detection and isolation of incipient faults on the measurements of these quantities. This is the principle of analytical redundancy. The approach is illustrated for the monitoring of stator current and voltage measurements in a wind-driven DFIG. A specific property of these signals is exploited, namely the fact that they consist of balanced three-phase signals. This feature is very helpful for detecting and locating small additive faults. Notice that the monitoring of the rotor current sensors has to be performed with a more involved approach. Indeed, due to closed-loop control, a sensor fault on a rotor current is attenuated and propagates to the other measurement channels, while this situation is not so pronounced with stator current and voltage measurements. Therefore, the monitoring of stator voltages and currents sensors can be performed without resorting to a model of the DFIG. A simple signal model is

used which is not subject to parameter variations. The reader is referred to [14, 15] for a detailed description of a method for rotor current monitoring, where the DFIG model is used and the parameter variations are accounted for.

The following sections successively address modeling of a balanced three-phase system, residual generation for three-phase signals, and application to the monitoring of stator voltages and currents for a wind-driven DFIG.

10.5.1 Model of a Balanced Three-Phase System

Consider a sinusoidal signal with amplitude M_o, frequency ω_o and phase ϕ_o, represented by:

$$y(t) = M_o \sin(\omega_o t + \phi_o) \tag{10.25}$$

This particular signal can be modeled by the following state-space representation

$$\begin{bmatrix} \dot{x}_1(t) \\ \dot{x}_2(t) \end{bmatrix} = \underbrace{\begin{bmatrix} 0 & \omega_o \\ -\omega_o & 0 \end{bmatrix}}_{\mathbf{A}_o} \underbrace{\begin{bmatrix} x_1(t) \\ x_2(t) \end{bmatrix}}_{\mathbf{x}(t)} \tag{10.26}$$

$$y(t) = \underbrace{\begin{bmatrix} 1 & 0 \end{bmatrix}}_{\mathbf{C}_o} \begin{bmatrix} x_1(t) \\ x_2(t) \end{bmatrix} \tag{10.27}$$

where $\mathbf{x}(0) = [M_o \sin(\phi_o), M_o \cos(\phi_o)]^T$ is the initial state.

The idea behind the modelling of a sinusoidal signal is now used to model a three-phase balanced system. Consider a balanced three-phase sinusoidal electric system (current or voltage). All the signals have identical amplitudes (M) and frequencies (ω_e), and their mutual phase shift is $2\pi/3$. They can be described by:

$$y_a(t) = M \sin(\omega_e(t)t + \phi_a) \tag{10.28a}$$

$$y_b(t) = M \sin\left(\omega_e(t)t + \phi_a - \frac{2\pi}{3}\right) \tag{10.28b}$$

$$y_c(t) = M \sin\left(\omega_e(t)t + \phi_a + \frac{2\pi}{3}\right) \tag{10.28c}$$

where ϕ_a is the initial phase of $y_a(t)$. Notice that although we consider the same frequency for all the signals, the value of ω_e can be time-varying as explicitly indicated above. Since the system in Eqs. 10.28a–10.28c is balanced, the summation of the three signals must be equal to zero:

$$y_a(t) + y_b(t) + y_c(t) = 0 \tag{10.29}$$

which means that one of the signals $y_j(t)$, for $j \in \{a, b, c\}$, can be computed from the other two.

Taking into account this property, and exploiting model described in Eqs. 10.26–10.27, any balanced three-phase sinusoidal system can be generated by a state-space model of the following form:

$$\dot{\mathbf{x}}(t) = \mathbf{A}(\omega_e(t))\mathbf{x}(t) \tag{10.30}$$

$$\mathbf{y}(t) = \mathbf{C}\mathbf{x}(t) \tag{10.31}$$

with state vector $\mathbf{x}(t) = [x_1(t), x_2(t)]^T$, output vector $\mathbf{y}(t) = [y_a(t), y_b(t), y_c(t)]^T$, and initial state $\mathbf{x}(0) = [M \sin(\phi_a), M \cos(\phi_a)]^T$. Matrices $\mathbf{A}(\omega_e(t))$ and $\mathbf{C}$ are defined by:

$$\mathbf{A}(\omega_e(t)) = \begin{bmatrix} 0 & \omega_e(t) \\ -\omega_e(t) & 0 \end{bmatrix}, \quad \mathbf{C} = \begin{bmatrix} 1 & 0 \\ -\frac{1}{2} & -\frac{\sqrt{3}}{2} \\ -\frac{1}{2} & \frac{\sqrt{3}}{2} \end{bmatrix} \tag{10.32}$$

Model described by Eqs. 10.30–10.32 can be extended to a balanced three-phase system with multiple harmonics, for which the monitoring methodology described below extends in a straightforward way [16]. The above model is used for the design of residual generators in the following section.

10.5.2 Residual Generation

The presence of sensor faults in a balanced three-phase system can be modeled as follows. First, model given by Eqs. 10.30–10.32 is discretized with sampling period T_s. Adding the effect of electromagnetic disturbances and measurement noise to the resulting discrete-time model yields:

$$\mathbf{x}(k+1) = \Phi(\omega_e(k))\mathbf{x}(k) + \mathbf{w}(k) \tag{10.33}$$

$$\mathbf{y}^m(k) = \mathbf{C}\mathbf{x}(k) + \mathbf{v}(k) + \mathbf{f}(k) \tag{10.34}$$

with $\Phi(\omega_e(k)) = \exp(\mathbf{A}(\omega_e(k))T_s)$, where $\omega_e(k)$ is assumed to be constant over the sampling period T_s. Vectors $\mathbf{w}(k)$ and $\mathbf{v}(k)$ are uncorrelated zero-mean Gaussian white noise sequences with covariance matrices $\mathbf{R_w}$ and $\mathbf{R_v}$, respectively. $\mathbf{f}(k) = [f_a(k), f_b(k), f_c(k)]^T$ is a vector containing the faults, with $f_i(k)$ the fault in the i-th sensor, for $i \in \{a, b, c\}$. The three-phases will alternatively be indexed with $i \in \{1, 2, 3\}$ below.

Multiple observer strategies can be used to detect and isolate sensor faults on the basis of model in Eqs. 10.33–10.34. Two classical schemes can be distinguished, namely the Dedicated Observer Scheme (DOS) and the Generalized Observer Scheme (GOS) [7, 17]. Both schemes are presented in Fig. 10.4.

The residual generation system per three-phase signals consists of three observers when using the GOS or the DOS. The i-th observer, $i \in \{1, 2, 3\}$ is designed on the basis of model dynamics described by Eq. 10.33 with the following output equation:

$$\tilde{\mathbf{y}}_i^m(k) = \tilde{\mathbf{C}}_i \mathbf{x}(k) + \tilde{\mathbf{v}}_i(k) + \tilde{\mathbf{f}}_i(k) \tag{10.35}$$

For the GOS, $\tilde{\mathbf{y}}_i^m(k)$ denotes vector $\mathbf{y}^m(k)$ without the i-th measurement, $\tilde{\mathbf{f}}_i(k)$ denotes vector $\mathbf{f}(k)$ without the i-th component, and $\tilde{\mathbf{C}}_i$ stands for matrix $\mathbf{C}$ without the i-th row. For the DOS, $\tilde{\mathbf{y}}_i^m(k)$ is the i-th measurement in vector $\mathbf{y}^m(k)$, $\tilde{\mathbf{f}}_i(k)$ is the i-th fault or the i-th component in $\mathbf{f}(k)$, and $\tilde{\mathbf{C}}_i$ is the i-th row of $\mathbf{C}$. $\tilde{\mathbf{v}}_i(k)$ is a zero-mean Gaussian white noise sequence with covariance matrix $\mathbf{R}_{\tilde{\mathbf{v}}i}$. It turn out that, for both schemes, the pair $(\tilde{\mathbf{C}}_i, \Phi(\omega_e))$ is observable when ω_e is a non zero constant, or uniformly completely observable when $\omega_e(t)$ is varying within an interval $[\omega_{\min}, \omega_{\max}]$ with $\omega_{\min}, \omega_{\max} \in \mathbb{R}^+$. Hence, both schemes can be implemented in the considered application.

For residual generation purposes, the observers are Kalman filters described as [18]

$$\hat{\mathbf{x}}_i(k|k-1) = \Phi(\hat{\omega}_e(k-1))\hat{\mathbf{x}}_i(k-1) \tag{10.36}$$

$$\mathbf{M}_i(k|k-1) = \Phi(\hat{\omega}_e(k-1))\mathbf{M}_i(k-1)\Phi(\hat{\omega}_e(k-1))^T + \mathbf{R}_\mathbf{w} \tag{10.37}$$

$$\hat{\mathbf{y}}_i(k) = \tilde{\mathbf{C}}_i\hat{\mathbf{x}}_i(k|k-1) \tag{10.38}$$

$$\mathbf{K}_i(k) = \mathbf{M}_i(k|k-1)\tilde{\mathbf{C}}_i\left(\tilde{\mathbf{C}}_i\mathbf{M}_i(k|k-1)\tilde{\mathbf{C}}_i^T + \mathbf{R}_{\tilde{\mathbf{v}}i}\right)^{-1} \tag{10.39}$$

$$\hat{\mathbf{x}}_i(k) = \hat{\mathbf{x}}_i(k|k-1) + \mathbf{K}_i(k)(\tilde{\mathbf{y}}_i^m(k) - \hat{\mathbf{y}}_i(k)) \tag{10.40}$$

$$\mathbf{M}_i(k) = \mathbf{M}_i(k|k-1) - \mathbf{K}_i(k)\tilde{\mathbf{C}}_i\mathbf{M}_i(k|k-1) \tag{10.41}$$

In Eqs. 10.36–10.41, the frequency $\omega_e(k)$ has been replaced by its estimate $\hat{\omega}_e(k)$. This estimation can be obtained, for instance, by a frequency-locked loop (FLL) as described in [19].

The i-th residual can be set as the innovation of the i-th Kalman filter (KF), namely a two-dimensional vector when using the GOS or a scalar signal when using the DOS:
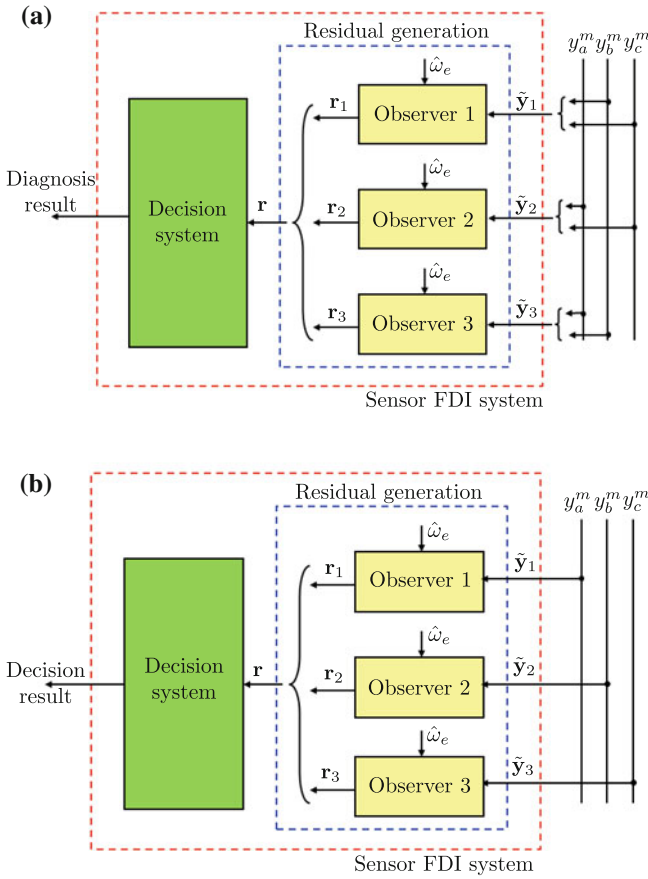
Fig. 10.4 Sensor FDI system with residual generation based on the **a** GOS, **b** DOS

$$\mathbf{r}_i(k) = \tilde{\mathbf{y}}_i^m(k) - \hat{\mathbf{y}}_i(k) \tag{10.42}$$

As it is not easy to distinguish the effect of $\mathbf{w}(k)$ and $\tilde{\mathbf{v}}_i(k)$ on the measured signals, the covariance matrices $\boldsymbol{R}_w$ and $\boldsymbol{R}_{\tilde{v}_i}$ are used as tuning parameters. They are selected in order to adjust the residual transient response and its sensitivity to faults. Specifically, the i-th KF gain $\mathbf{K}_i(k)$ is designed so that the effect of a single fault on the residuals produced by the GOS (DOS) corresponds to the the incidence Table 10.2 (3). In these tables, a '1' in row i and column j indicates that residual $\mathbf{r}_i$ changes significatively upon occurrence of fault f_j, whereas a '0' means that the residual presents very low sensitivity to fault f_j, for $j \in \{1, 2, 3\}$.

Per three-phase signals (currents or voltages), three residual vectors $\mathbf{r}_i$, $i \in \{1, 2, 3\}$, are obtained. By stacking the three residual vectors, we can define vector $\mathbf{r}(k) = [\mathbf{r}_1(k)^T, \mathbf{r}_2(k)^T, \mathbf{r}_3(k)^T]^T$, which can be processed by a decision

system of the form presented in Sect. 10.3.2. $\mathbf{r}(k)$ is a 6-dimensional vector when using the GOS, and a three-dimensional vector when using the DOS. The residual vector resulting from these two schemes can be written as:

$$\mathbf{r(k)} = \mathbf{r}_0(k) + v_\ell \boldsymbol{\Gamma}_\ell 1_{\{k \geq k_0\}} \tag{10.43}$$

where $\mathbf{r}_0(k)$ can be considered as a zero-mean Gaussian white noise sequence with known variance $\Sigma_r(k)$ that corresponds to fault free measurements, $\boldsymbol{\Gamma}_\ell$ is the ℓ-th column of the incidence table and v_ℓ stands for the magnitude of the fault effect on the residual. v_ℓ is supposed to be constant and equal to its steady state value, for the sake of simplicity. Transient effects could be accounted for as in [11].

Thus the fault detection/isolation problem can be stated as the following hypothesis test.

Choose between:

$$
\begin{array}{lll}
\mathscr{H}_0 & \mathscr{L}(\mathbf{r}(i)) = \mathscr{N}(\mathbf{0}, \Sigma_r(i)) & \text{for} \quad i = 1, \ldots, k \\
\mathscr{H}_\ell, \ell = 1, \ldots, n_f & \mathscr{L}(\mathbf{r}(i)) = \mathscr{N}(\mathbf{0}, \Sigma_r(i)) & \text{for} \quad i = 1, \ldots, k_0 - 1 \\
& \quad\quad\quad\;\; = \mathscr{N}(v_\ell \boldsymbol{\Gamma}_\ell, \Sigma_r(i)) & \text{for} \quad i = k_0, \ldots, k
\end{array}
$$

where k_0 is the unknown fault occurrence time.

This is exactly the form of the problem statement in Sect. 10.3.2, except that the variance of the residual is time-varying. Yet this can be accounted for in a straightforward way in the computation of the the log-likelihood ratios [14, 15].

Remark Due to the fact that $\boldsymbol{R}_w$ and $\boldsymbol{R}_{\tilde{v}_i}$ are used as tuning parameters for the Kalman filters, the whiteness of the residual sequence is not guaranteed. However, the CUSUM algorithm is known to be robust to this hypothesis [20].

In the next section, a validation example for voltage and current sensor FDI on a DFIG is presented.

10.5.3 Fault Detection and Isolation in the Stator Voltage and Current Sensors of a Wind Driven DFIG

The presentation of the case study consists of the problem statement, the design of the residual generator and the decision system, and their validation in simulation.

10.5.3.1 Problem Statement

The controlled DFIG depicted in Fig. 10.5 is considered. The rotor side controller (RSC) aims at reaching the desired reference generator torque T_g^* and the stator

Table 10.2 Incidence table using the GOS

r	f_1	f_2	f_3
$\mathbf{r}_{1,1}$	0	1	0
$\mathbf{r}_{1,2}$	0	0	1
$\mathbf{r}_{2,1}$	1	0	0
$\mathbf{r}_{2,2}$	0	0	1
$\mathbf{r}_{3,1}$	1	0	0
$\mathbf{r}_{3,2}$	0	1	0

reactive power Q_s^* exchanged between the DFIG and the grid. As is usual for control purposes, the measured three-phase stator voltages $u_{s,abc}^m$, stator current $i_{s,abc}^m$ and rotor currents $i_{r,abc}^m$ are transformed into the appropriate rotating dq frame by the Park transformation represented by the dq/abc blocs in the figure [21]. $\hat{\theta}_s$ and $\hat{\theta}_r$ represent estimates of θ_s and θ_r. These two angles are defined with respect to a suitable reference axis and they fulfill $\frac{d\theta_s}{dt} = \omega_s$, $\frac{d\theta_r}{dt} = \omega_r$ where ω_s and ω_r are respectively the stator and rotor signal frequencies. The symbols $\mathbf{v}$ and $\mathbf{f}$, indexed by a signal name, correspond to the measurement noise and the additive fault affecting this signal, in accordance with the measurement Eq. 10.34. Finally Ω_g denotes the generator speed. The design of the RSC controller is described in Chapter 5 of [15].

Our aim is to design a diagnostic system that detects and isolates faults on the stator voltages $v_{s,abc}^m$ and the stator currents $i_{s,abc}^m$ while being insensitive to possible faults on the rotor currents. This diagnostic system should work properly in the whole operating range of the wind-driven DFIG. All the fault magnitudes are expressed as a percentage of the peak value of the signal at the rated operating point. The nominal faulty situation (minimum fault to be detected) is defined as the presence of an offset in the stator current (stator voltage) sensor with magnitude equal to 5 % (2 %). The choice of a lower nominal fault amplitude for the stator voltage is justified as follows. A fault in the stator voltages not only affects the computation of the control law since the stator voltages are used for both state estimation and computation of the stator active and reactive power, but also affects the estimated angle for the *Park* transformation which is obtained by a phase-locked loop/frequency-locked loop. This is the reason why a lower fault magnitude is considered for the stator voltages than for the stator currents. The error on the estimated angle for the Park transformation due to a bias or phase unbalance in the stator voltages has been studied in [22]. Finally, a mean detection/isolation delay of $\bar{\tau}_\ell \leq 0.04$ s is imposed for all six sensor faults.
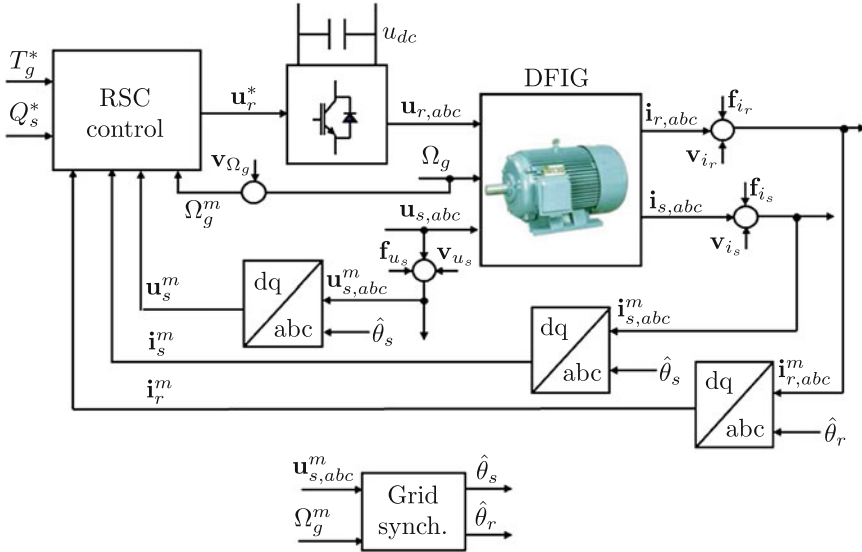
Fig. 10.5 Faults affecting the three-phase signals in a controlled DFIG

10.5.3.2 Residual Generator and Decision System Design

Let us denote by f_1, f_2, and f_3 the faults affecting $u_{s,a}$, $u_{s,b}$ and $u_{s,c}$ respectively, and by f_4, f_5, and f_6 the faults affecting $i_{s,a}$, $i_{s,b}$, and $i_{s,c}$. Then by combining two GOS schemes, one for monitoring the stator voltages and one for monitoring the stator currents, a 12-dimensional residual vector is obtained that complies with the incidence matrix of Table 10.4. Indeed, each observer output $\mathbf{r}_\ell(k)$, where $\ell \in \{1, 2, 3\}$ for the stator voltages and $\ell \in \{4, 5, 6\}$ for the stator currents, is a two-dimensional vector. Both three-phase systems are assumed to have constant frequency $\omega_e = 2\pi f_s$ rad/s, with $f_s = 50$ Hz the synchronous frequency for the design of the Kalman filter based on model described by Eqs. 10.33 and 10.35.

The residual vector can be processed by the multi-CUSUM algorithm described by Eqs. 10.11–10.13 to detect and isolate faults. To this end, the mean and covariance of the residual vector have to be evaluated in fault free mode and for the nominal fault to be detected.

From a first set of 5 s of simulated data in healthy conditions, with the system in its rated operating point, the value of the covariance matrix ($\boldsymbol{\Sigma}$) for the residual vector $\mathbf{r}(k)$ is obtained. The residual mean presents negligible values, so $\boldsymbol{\mu}_0$ is set to zero. On the basis of the indicated minimum fault magnitudes, each $\boldsymbol{\mu}_\ell$, for $\ell = 1, 2, \ldots, 6$, is calculated, assuming that vector $\boldsymbol{\Gamma}_\ell$ is the ℓ-th column in Table 10.3. The thresholds are set to $h^\ell = 3 \times 10^4$ for $\ell \in 1, 2, 3$ and $h^\ell = 6 \times 10^3$ for $\ell \in \{4, 5, 6\}$, to comply with the required mean detection/isolation delay.

Table 10.3 Incidence table for single faults using the DOS

r	f_1	f_2	f_3
r_1	1	0	0
r_2	0	1	0
r_3	0	0	1

10.5.3.3 Simulation Scenario

The performance of the designed FDI system is tested via simulations where additive sensor faults in the stator currents and voltages, changes in the reference variables (T_g^* and Q_s^*) and in the disturbances (Ω_g), as well as additive sensor faults in the rotor currents are carried out. Changes in the reference of the generator torque T_g^* and in the generator speed Ω_g are related to changes in the mean wind speed ($\bar{V}$) since the wind-driven DFIG is operating according to its ideal power curve shown in Fig. 10.6a. Changes in operating points can also be characterized in terms of the slip of the DFIG, which is defined as $s = (\omega_s - n_p\Omega_g)/\omega_s$ with n_p the number of pole pairs of the generator (see Fig. 10.6b).

For validation purposes, a simulation of the DFIG including parameter variations, as described in [15] is performed. To avoid too lengthy simulations, given the small step size needed for the numerical resolution of the differential equations describing the generator dynamics, the variations of the operating point that are simulated are much faster than the ones expected in a real wind turbine. Indeed, for a wind turbine the operating point variations depend mainly on the wind speed variations, that lie in the low frequency range (up to 10 Hz). In addition, according

Table 10.4 Incidence table using GOS

r	f_1	f_2	f_3	f_4	f_5	f_6
$r_{1,1}$	0	1	0	0	0	0
$r_{1,2}$	0	0	1	0	0	0
$r_{2,1}$	1	0	0	0	0	0
$r_{2,2}$	0	0	1	0	0	0
$r_{3,1}$	1	0	0	0	0	0
$r_{3,2}$	0	1	0	0	0	0
$r_{4,1}$	0	0	0	0	1	0
$r_{4,2}$	0	0	0	0	0	1
$r_{5,1}$	0	0	0	1	0	0
$r_{5,2}$	0	0	0	0	0	1
$r_{6,1}$	0	0	0	1	0	0
$r_{6,2}$	0	0	0	0	1	0
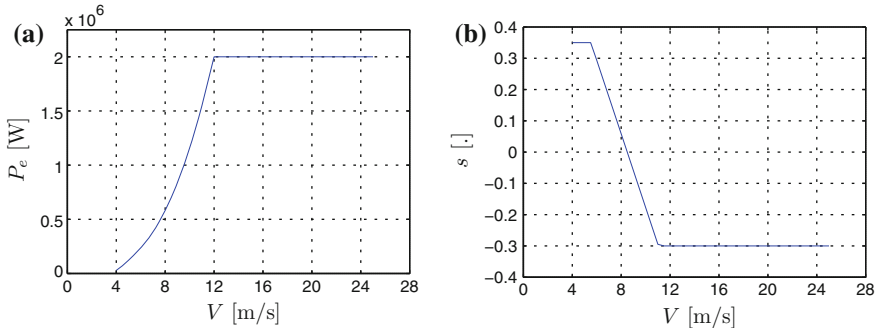
Fig. 10.6 Operating conditions for a wind-driven DFIG: **a** Ideal power curve: active power (P_e) versus wind speed (V). **b** Slip (s) versus wind speed (V)

to some grid codes, the resulting power changes (that are related to both the generator torque and speed) must be smaller than 0.1 p.u./min (see p. 122 of [23]). We can expect that, if the sensor FDI system can cope with such fast operating point variations, it will achieve good performance for slower variations as well.

Changes in the generator speed Ω_g are depicted in the form of slip changes in Fig. 10.7a. We can see that a wide range of operating conditions are covered. The first 6 s of the simulation correspond to supersynchronous operation ($s < 0$), at $t = 6$ s the machine drifts toward synchronism ($s = 0$) and at $t = 8$ s the machine is forced to operate at subsynchronous values of speed ($s > 0$).

Three faults are simulated, each affecting one of the three sets of sensors measuring, respectively $i_{r,abc}$, $v_{s,abc}$ and $i_{s,abc}$, as presented in Fig. 10.7b. First, between $t = 1$ s and $t = 2$ s, a fault of 5 % in the sensor $\ell = 8$ occurs, which corresponds to the measurement of $i_{r,b}$. Recall that the rotor currents are not monitored. Then, between $t = 4$ s and $t = 5$ s, a fault of 2 % in the sensor $\ell = 1$ occurs, which corresponds to the measurement of $u_{s,a}$. Finally, between $t = 8.5$ s and $t = 9.5$ s, a fault of 5 % in the sensor $\ell = 6$ occurs, which corresponds to the measurement of $i_{s,c}$.

The applied changes in the reference of T_g and the resulting generator torque is depicted in Fig. 10.8a. The reference of the stator reactive power Q_s is set to zero for the first 8 s of simulation, and at $t = 8$ s, a step change of 0.05 [p.u.] is made, as presented in Fig. 10.8b.

In both the controlled variables, T_g and Q_s, the effect of the additive faults are clearly noticeable. The presence of bias in the measurement of a stator or rotor three-phase signal produces oscillations in the dq components of the measured signal. These oscillations have a frequency equal to the frequency of the faulty stator or rotor signal. Since the dq components are used for computing the control law as well as the controlled variables, oscillations around the reference value of both T_g and Q_s appear in the presence of the faults.

Fig. 10.7 **a** Imposed slip.
b Faulty sensor
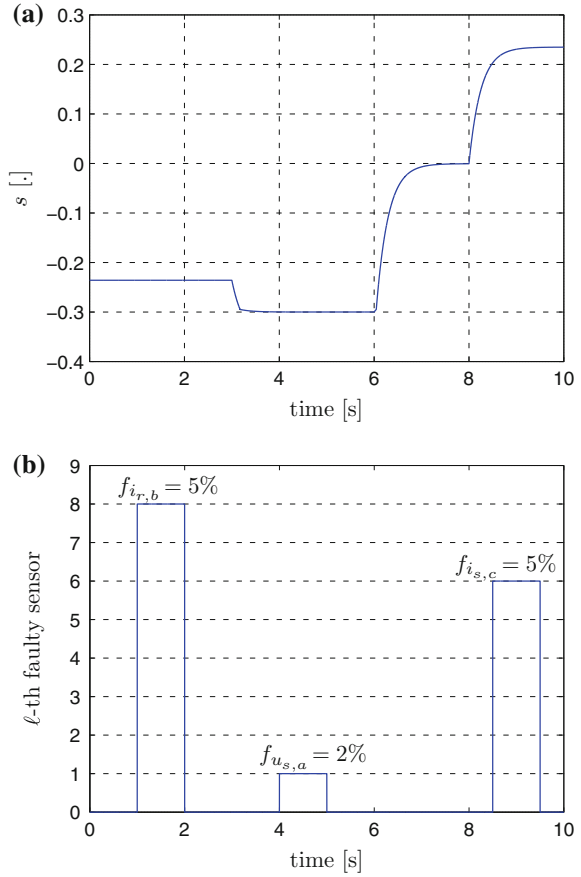
10.5.3.4 Results and Discussion

The outputs of the two GOS are depicted in Fig. 10.9a for the stator voltages
($\ell \in \{1, 2, 3\}$) and in Fig. 10.9b for the stator currents ($\ell \in \{4, 5, 6\}$). In
Fig. 10.9a, the fault in sensor 1 ($u_{s,a}$) between $t = 4$ s and $t = 5$ s produces a
change in the mean in components $\mathbf{r}_{2,1}$ and $\mathbf{r}_{3,1}$, which is consistent with the
incidence Table 10.4. In Fig. 10.9b, the mean of components $\mathbf{r}_{4,2}$ and $\mathbf{r}_{5,2}$ presents
a sustained change only between $t = 8.5$ s and $t = 9.5$ s, which corresponds to the
fault in sensor 6 ($i_{s,c}$). All the residuals $\mathbf{r}_\ell$ for $\ell \in \{4, 5, 6\}$ are affected by the other
sensor faults because of their propagation due to the control algorithm, but their
means remain close to zero. The same behavior occurs in the presence of changes
in the references and in the disturbance.

The decision functions resulting from treating the resulting 12-dimensional
residual vector $\mathbf{r}(k)$ using the multi-CUSUM algorithm are presented in
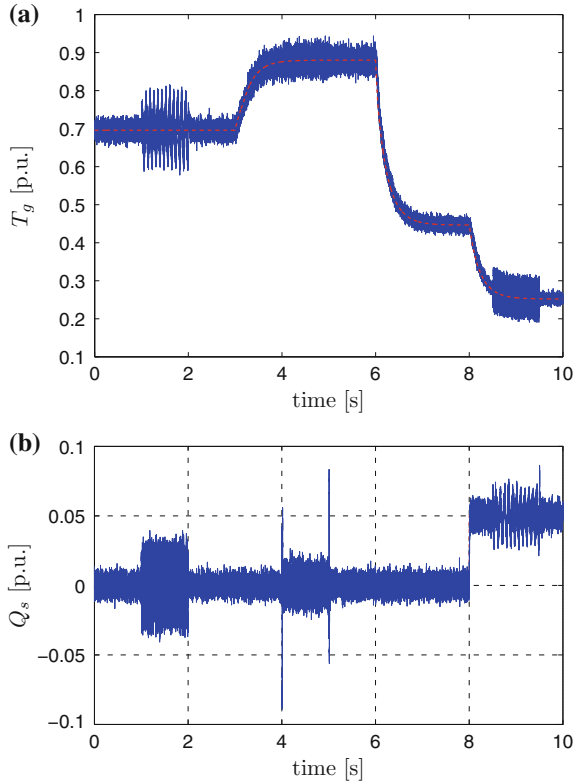
Fig. 10.10a for the stator voltages ($\ell \in \{1, 2, 3\}$) and in Fig. 10.10b for the stator currents ($\ell \in \{4, 5, 6\}$). For the presentation of the decision functions in Figs. 10.10a, b we have used the thresholds h_ℓ as normalization factor.

In Fig. 10.10a, only g_1^*, corresponding to fault in the sensor measuring $u_{s,a}$ crosses the threshold after $t = 4$ s. Therefore, this fault is correctly detected and isolated. From Fig. 10.10b, only g_6^*, corresponding to fault in the sensor measuring $i_{s,c}$ crosses the threshold after $t = 8.5$ s. Notice the repeated crossing of the threshold while the fault is present, due to the re-initialization strategy in Sect. 10.3.3. The fault in sensor $\ell = 8$ ($i_{r,b}$) produces positive values in g_ℓ^* for $\ell \in \{4, 5, 6\}$. In addition, changes in the reference and in the disturbance produce transients of small amplitude in these decision functions. However, in both cases, the decision functions do not cross the corresponding threshold. Again, we can conclude that the fault in the stator current $i_{s,c}$ is correctly detected and isolated. In addition for both faults are detected and isolated within the required detection/isolation delay.

Fig. 10.9 Residual vectors $\mathbf{r}_i(k)$ **a** for stator voltages **b** for stator currents
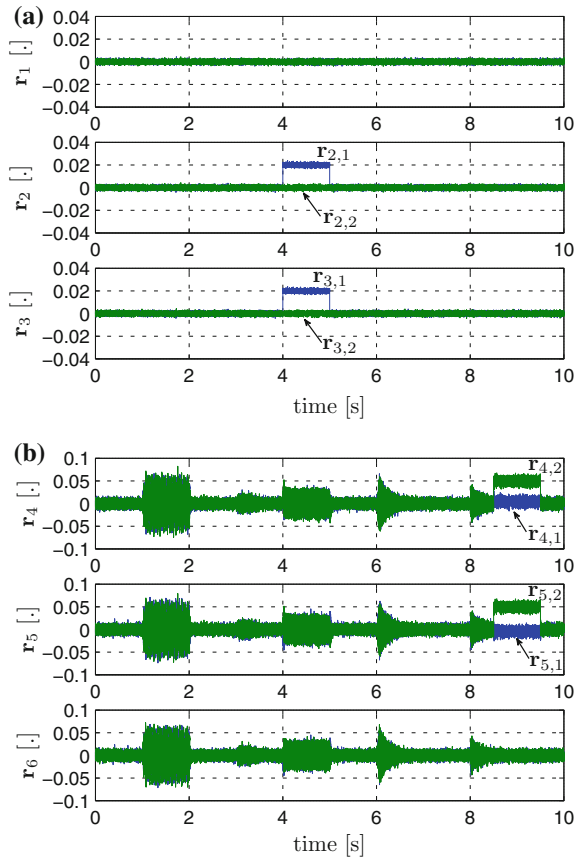
Simulations with fault magnitudes of 2, 3, 5, 8 % for the stator voltages, 5, 8, 10, 15 % for the stator currents have been performed. In all the cases, the decision algorithm was able to detect and isolate all the faults, with a detection/isolation delay lower than the required one. We can conclude that, with the proposed sensor FDI system based on the model of the three-phase signals, sensor FDI for the stator voltages and currents can be achieved. The performance is not affected by either changes in the references or in the disturbance, or by faults in the rotor currents.

Faults in the rotor currents are compensated by the control algorithm; so the effect of the fault in the signals is not noticeable as in the case of faults affecting the stator voltages and the stator currents. This is shown in Fig. 10.11.

Figure 10.11a depicts the measured stator and rotor currents when the fault in sensor $i_{s,c}$ ($\ell = 6$) is present between $t = 8.5$ s and $t = 9.5$ s, while Fig. 10.11b presents both currents when the fault in sensor $i_{r,b}$ is present between $t = 1$ s and $t = 2$ s. Notice in Fig. 10.11a that the measurement of $i_{s,c}$ presents a change in its mean, and that the fault does not produce significative changes in the mean

of the other stator current measurements, nor in the rotor current measurements. On the contrary, Fig. 10.11b shows that upon occurrence of an additive fault on the sensor measuring $i_{r,b}$ ($\ell = 8$), the fault is propagated, due to the control algorithm to the other two rotor currents, and it affects the mean of all three rotor currents. Finally, the stator currents are also affected by the fault in sensor $\ell = 8$. Oscillations with frequency equal to the rotor current frequency ($\omega_r = \omega_s - n_p \Omega_g$ [rad/s]) appear, but the means of the stator currents remain unchanged.

Because of these observations, the approach described in Sect. 10.6.2 cannot be applied to perform sensor FDI in the rotor currents. A method based on a model of the DFIG, as described in [14, 15], is needed in this case. Nevertheless, using such a model will imply being sensitive to variations in the electrical parameters (mainly as function of the temperature) due to the large variation in the operating conditions. A proper handling of this issue is proposed in the indicated references.

Fig. 10.11 Measured stator
and rotor currents during
a fault in sensor $i_{s,c}$ **b** fault in
sensor $i_{r,b}$
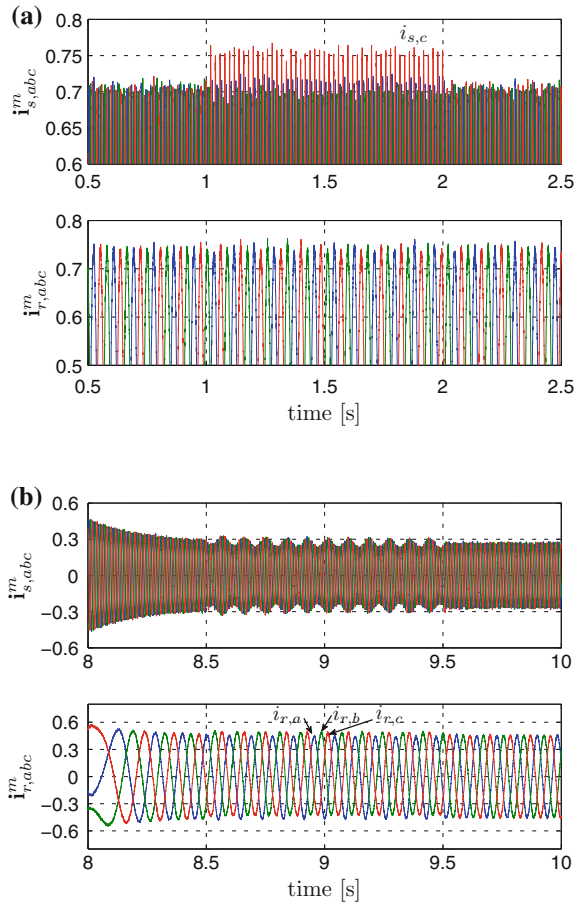
10.6 Conclusion

Three issues have successively been considered, namely single sensor monitoring,
FDI in redundant sensors, and analytical redundancy for sensor FDI. In all cases, a
decision system based on a recursive statistical change detection/isoltion algorithm
has been used.

The algorithm for excessive noise detection has been applied to generator speed
measurements in a wind driven DFIG. These data were obtained from a wind
turbine simulation corresponding to realistic wind conditions.

Analytical redundancy has been applied to FDI of stator voltage and current
sensors. It has been emphasized that a simple signal model can be used, accounting
for the balanced nature of the three-phase signals. This allows one to avoid the use
of a model of induction generator, which is subject to parameter changes, for FDI.
In the validation involving simulated data from a controlled DFIG, the

performance of the resulting sensor FDI system is not affected by changes in the reference signals and by disturbance variations. In addition, faults affecting the rotor currents do not degrade the performance of the sensor FDI system. Besides, it was observed that the control algorithm partially hides the fault affecting a particular rotor current sensor, and the effect of the fault is propagated to the other two rotor current sensors.

10.7 Future Work

As wind turbines are growing larger and larger, the concern for online structural health monitoring is increasing. This can notably be achieved through sensor networks. Therefore, sensor monitoring for sensor networks appears to be an important issue. This raises new problems such as the development of decentralized methods allowing to handle a large number of sensors, and the determination of proper ways to handle transmission delays and packet losses in sensor networks in the framework of sensor monitoring. Initial work on this topic goes into two directions: data-based methods [24], and model based methods [25]. In the later case, the available results on decentralized state observers appears to be an interesting starting point [26, 27, 28]. Open issues include the generalization of classical multiobserver schemes, such as the generalized observer scheme and the dedicated observer scheme, to sensor network while accounting for scalability and decentralization. The extension of statistical change detection/isolation algorithms to this context is also just starting to be tackled [29]. Another issue concerns the integration, in the design of the FDI system, of the notion of risk (namely the probability that a certain fault appears) and of the potential impact of a fault on the process performance. The choice of the decision threshold should notably account for risk and fault impact. This would allow one to go toward risk-based maintenance.

References

1. Odgaard PF, Stoustrup J, Kinnaert M (2013) Fault tolerant control of wind turbines: a benchmark model. IEEE Trans Control Syst Technol 21:1168–1182
2. Simani S, Castaldi P (2013) Active actuator fault-tolerant control of a wind turbine benchmark model. Int J Robust Nonlinear Control. doi:10.1002/rnc.2993
3. Ciang CC, Lee J-R, Bang H-J (2008) Structural health monitoring for a wind turbine system: a review of damage detection methods. Meas Sci Technol 19:122001. doi:10.1088/0957-0233/19/12/122001
4. Sattar TP, Rodriguez HL, Bridge B (2009) Climbing ring robot for inspection of offshore wind turbines. Industr Robot: Int J 36:326–330
5. Crabtree CJ (2010) Survey of commercially available condition monitoring systems for wind turbines. http://www.supergen-wind.org.uk/docs/. Survey of commercially available CMS for WT.pdf. Cited 4 Dec 2013

6. Ribrant J, Bertling L (2007) Survey of failures in wind power systems with focus on Swedish wind power plants during 1997–2005. In: Proceedings of the 2007 IEEE power engineering society general meeting, Tampa, USA
7. Blanke M, Kinnaert M, Lunze J, Staroswiecki M (2006) Diagnosis and fault-tolerant control, Second edn. Springer, Berlin
8. Basseville M, Nikiforov I (1993) Detection of abrupt changes: theory and application. Prentice-Hall, Englewood Cliffs
9. Nikiforov I (1995) A generalized change detection problem. IEEE Trans Inf Theory 41:171–187
10. Nikiforov I (1998) A simple recursive algorithm for diagnosis of abrupt changes in signals and systems. In: Proceedings of the 1998 American control conference, Philadelphia, USA, vol 3, pp 1938–1942
11. Kinnaert M, Vrancic D, Denolin E, Juricic J, Petrovcic J (2000) Model-based fault detection and isolation for a gas-liquid separation unit. Control Eng Pract 8:1273–1283
12. Li Y, Gu F, Harris G, Ball A, Bennett N, Travis K (2005) The measurement of instantaneous angular speed. Mech Syst Signal Process 19:786–805
13. NWTC Computer-Aided Engineering Tools (FAST by Jonkman J, PhD). http://wind.nrel.gov/designcodes/simulators/fast/
14. Boulkroune B, Galvez-Carrillo M, Kinnaert M (2013) Combined signal and model based fault diagnosis for a doubly fed induction generator. IEEE Trans Control Syst Technol 21:1771–1783
15. Galvez M (2011) Sensor fault diagnosis for wind-driven doubly-fed induction generators. PhD thesis, Université libre de Bruxelles (ULB)
16. Galvez-Carrillo M, Kinnaert M (2010) Sensor fault detection and isolation in three-phase systems using a signal-based approach. IET Control Theory Appl 4:1838–1848
17. Patton R, Frank P, Clark R (1989) Fault diagnosis in dynamic systems: theory and applications. Prentic-Hall, Englewood Cliffs
18. Franklin G, Powell J, Workman M (1998) Digital control of dynamic systems, Third edn. Addison-Wesley, Reading
19. Rodriguez P, Luna A, Ciabotaru M, Teodorescu R, Bjaabjerg F (2006) Advanced grid synchronization system for power converters under unbalanced and distorted operating conditions. In: Proceedings of the 32nd annual conference of the IEEE industrial electronic society—IECON 2006, Orlando, USA, pp 5173–5178
20. Basseville M, Benveniste A (1983) Design and comparative study of some sequential jump detection algorithms for digital signals. IEEE Trans Acoust Speech Signal Process 31:521–535
21. Krause P, Wasynczuck O, Sudhoff S (2002) Analysis of electric machinery and drive systems, second edn. Wiley-IEEE Press, New York
22. Chung S (2000) A phase tracking system for three-phase utility interface inverters. IEEE Trans Power Electron 15:431–438
23. Matevosyan J, Ackermann T, Bolik S (2005) Technical regulations for the interconnection of wind farms to the power system. In: Ackermann T (ed) Wind power in power systems. Wiley, Chichester, pp 115–142
24. Kullaa J (2010) Sensor validation using minimum mean square error estimation. Mech Syst Signal Process 24:1444–1457
25. Chabir K, Sauter D, Al-Salami IM, Aubrun C (2012) On fault detection and isolation design for networked control systems with bounded delay constraints. In: Proceedings of the 8th IFAC symposium on fault detection, supervision and safety of technical processes (SAFEROCESS), Mexico City, Mexico
26. Alriksson P, Rantzer A (2006) Distributed Kalman filter using weighted averaging. In: Proceedings of the 17th international symposium on mathematical theory of networks and systems, Kyoto, Japan
27. Cattivelli FS, Sayed AH (2010) Diffusion strategies for distributed Kalman filtering and smoothing. IEEE Trans Autom Control 55(9):2069–2084

28. Olfati-Saber R (2005) Distributed Kalman filter with embedded consensus filters. In: Proceedings of the 44th IEEE conference on decision and control, 2005 and 2005 European control conference
29. Noumir Z, Guépié KB, Fillatre L, Honeine P, Nikiforov I, Snoussi H, Richard C, Jarrige PA, Campan F (2014) Detection of contamination in water distribution network. In: Advances in hydroinformatics. Springer Hydrogeology, Singapore, pp 141–151

Chapter 11
Structural Load Analysis of Floating Wind Turbines Under Blade Pitch System Faults

Rannam Chaaban, Daniel Ginsberg and Claus-Peter Fritzen

Abstract High performance and reliability are required for floating wind turbines due to the fact that they operate under hard conditions with minimum access for maintenance and high cost of repair. Therefore, the assessment of the severity of possible faults on the floating turbine structure will provide good guidelines once they occur either to employ the appropriate protective strategies such as turbine shutdown, or to continue power operation at reduced or full capacity. Furthermore, it will motivate the development of fault-oriented identification algorithms and fault-tolerant control systems that enhance the floating turbine reliability. As the pitch system has the highest failure rate, the faults of such system are of great interest. Several pitch system faults are considered and compared in this chapter including blade pitch sensor bias and gain faults, in addition to the performance degradation of the pitching mechanism, actuator stuck, and actuator runaway. Regardless of the origin of the fault inside the pitch system, these faults lead to an increased rotor imbalance which has different effects on the turbine structure and the platform motion. A utility-scale turbine mounted on the barge platform concept, and modeled using an aero-hydro-servo-elastic simulation tool is used to simulate these faults, and to study their effects as function of the fault magnitude and the mean wind speed in the full load region.

Keywords Floating wind turbines · Structural load analysis · Pitch system faults · Damage equivalent loading · Fault modeling

R. Chaaban (✉) · C.-P. Fritzen
Center of Sensor Systems (ZESS), Institute of Mechanics and Control Engineering-
Mechatronics, University of Siegen, Paul-Bonatz-Strasse 9-11, 57076 Siegen, Germany
e-mail: rannam.chaaban@uni-siegend.de

C.-P. Fritzen
e-mail: claus-peter.fritzen@uni-siegen.de

D. Ginsberg
Department of Mechanical Engineering, Institute of Mechanics and Control Engineering-
Mechatronics, University of Siegen, Paul-Bonatz-Strasse 9-11, 57076 Siegen, Germany
e-mail: daniel.ginsberg@uni-siegen.de

Nomenclature

β	Blade pitch angle
β_{ref}	Reference blade pitch angle
C	Damping coefficient
$C_{P,\text{max}}$	Maximum power coefficient
$e(t)$	Error signal
η	Generator efficiency
h	Hub height
I_D	Drive-train inertia
J	Turbine inertia term about platform pitch axis
K	Stiffness coefficient
K_P	Proportional gain
K_I	Integral gain
λ	Tip speed ratio
N	Gearbox ratio
Ω_g	Generator speed
$\Omega_{g,\text{rated}}$	Rated generator speed
Ω_r	Rotor speed
$\Omega_{r,\text{rated}}$	Rated rotor speed
ω_n	Natural frequency
P_{rated}	Rated output power of the generator
$\frac{\delta P}{\delta \theta}$	Sensitivity of the rotor aerodynamic power to the scheduling parameter
R	Rotor radius
ρ	Air density
T	Aerodynamic rotor thrust
T_0	Aerodynamic thrust over the rotor at the linearization point
T_g	Generator torque
t_d	Time delay
θ	Scheduling parameter
V	Average wind speed over the rotor disk
$w(t)$	Noise
$\dot{x}$	Tower top (hub) velocity
ξ	Platform pitch angle
$\dot{\xi}$	Platform pitch angular velocity
$\ddot{\xi}$	Platform pitch angular acceleration
ζ	Damping ratio

11.1 Introduction

With the steady increase in wind power worldwide, offshore wind farms are most likely to be a sizable contributor of electricity production in some countries due to the high quality of offshore wind resources and their proximity to the big shore cities. To date, offshore wind turbines are limited to shallow water supported by conventional fixed-bottom substructures [1]. Different types of substructures are used according to water depth such as gravity bases for water depth to about 10 m, fixed-bottom mono-piles for water depth to about 30 m, and tripods and lattice frames used in water to about 50 m in depth [1]. For deeper water more than 60 m, these support structures are no longer economically feasible and new types of turbine support are needed. Floating support platforms are one of the potential solutions. Numerous configurations of the floating support platforms are available from the offshore oil and gas (O&G) industry. The technical feasibility of developing offshore floating wind turbines platforms is out of question as the O&G industry has already proven the long-term survivability of such support structures. However, the main concern regarding this new trend to invade deep water is the development of a cost-effective offshore floating wind turbine that can find its way into the competitive energy market. This concern motivates the research for optimized designs while making use of the gained knowledge from the offshore O&G industry.

Floating substructures could be divided into three main concepts according to the method used to achieve stability in pitch and roll. These three primary concepts are the tension leg platform (TLP), spar buoy and barge (Fig. 11.1). The TLP uses mooring lines combined with excess buoyancy to provide restoring pitch and roll moments, the spar buoy platform provides similar moments by its deep draft and ballast, while the barge platform uses its shallow draft combined with the large water-plane area moment to generate the needed restoring moments. Hybrid
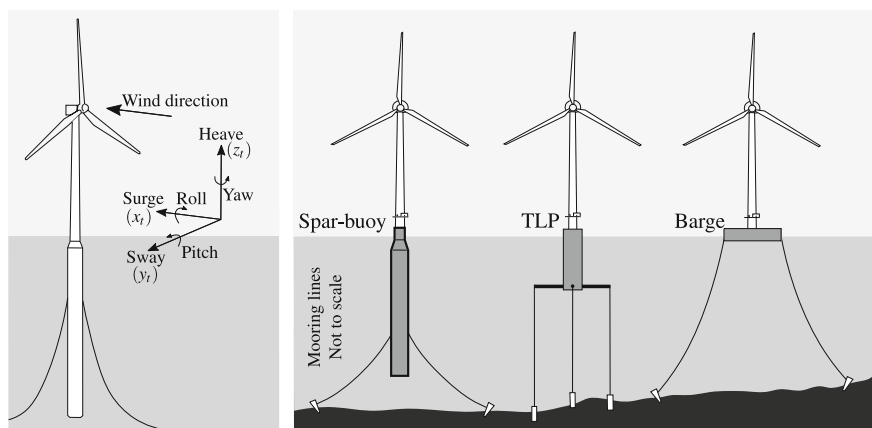
Fig. 11.1 Floating platforms concepts

concepts of these main three platforms are also possible [2]. In June 2009, the world's first spar buoy supported floating wind turbine was installed off the coast of Norway in 220-m deep water [3].

The floating platform introduces six new degrees of freedom (DOFs) to the system; these added DOFs, if not taken into account actively or passively, can negatively affect the power production and turbine structural loading. The load comparison between land-based and floating turbines shows dramatic increase in the loading of the floating structure, basically, in tower base fore-aft and side-side bending moments, blade flap-wise and edge-wise bending moments, and drive-train torsional loading [4]. This overall increase in structural loading is related to the motion of the platform in the fore-aft direction (platform pitch motion) that induces the oscillatory wind inflow relative to the rotor, and excites the gyroscopic yaw moment in combination with the spinning inertia of the rotor. The turbine motion in the fore-aft direction in combination with the blade pitch control engaged in the above-rated region results in a servo-induced negative damping to the pitch motion. Considering, for example, a single DOF model of the floating wind turbine where the platform pitch angle is the only considered DOF (assuming rigid body model for tower, blades, drive-train, and platform). The equation of motion of such simple model could be written as

$$J\ddot{\xi} + C\dot{\xi} + K\xi = hT \tag{11.1}$$

where $\xi, \dot{\xi}, \ddot{\xi}$ are the platform pitch angle, rotational velocity and rotational acceleration, respectively, J is the inertia term that combines the turbine and platform pitch inertia in addition to the added inertia due to hydrodynamic radiation in pitch, C is the damping term that combines the damping associated with the hydrodynamic radiation in pitch and the linearized damping associated with the hydrodynamic viscous drag in pitch, K is the stiffness term that combines the hydrostatic restoring in pitch and the linearized hydrostatic restoring in pitch from all mooring lines, h is the hub height, and T is the aerodynamic rotor thrust.

The aerodynamic rotor thrust depends on the relative wind speed at the hub height, blade pitch angle β and rotor speed Ω_r. Assuming a slow change in hub translation, and using the first-order Taylor series expansion, then

$$T \approx T_0 - \frac{\partial T}{\partial V}\dot{x} \tag{11.2}$$

with V is the average wind speed over the rotor disk, $\dot{x}$ is the tower top (hub) velocity, and T_0 is the aerodynamic thrust over the rotor at the linearization point. The hub translation and the platform pitch angle are related such as

$$x = h\xi. \tag{11.3}$$
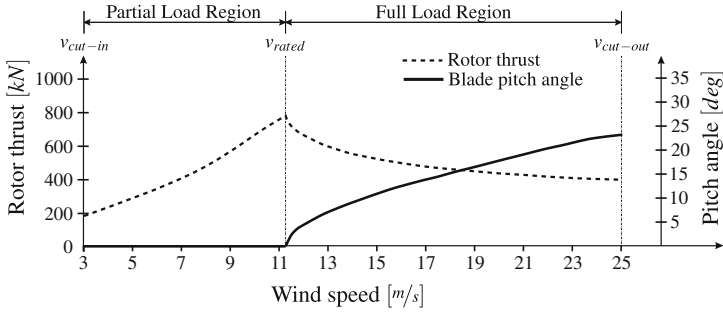
Fig. 11.2 Rotor thrust over operating regions, maximum at rated wind speed and blade pitch angle active in full load region

Using Eqs. (11.2) and (11.3) in the equation of motion (11.1) then

$$\frac{J}{h^2}\ddot{x} + \left(\frac{C}{h^2} + \frac{\partial T}{\partial V}\right)\dot{x} + \frac{K}{h^2}x = T_0 \qquad (11.4)$$

An interesting result obtained from this simple model is the dependency of the damping term on the thrust sensitivity to wind speed $\frac{\partial T}{\partial V}$. Using a closed-loop blade-pitch speed-regulation controller along with the 5 MW mounted on the barge platform as an example, the sensitivity of the closed loop could be "ideally" estimated from the slope of the steady-state thrust versus wind speed response presented in Fig. 11.2. The maximum negative slope can be found directly above the rated wind speed; moreover, the maximum thrust over the rotor is at the rated wind speed [5]. The decrease in thrust sensitivity in the full load region is due to the engagement of the pitch control loop in this region (Fig. 11.2). This control loop changes the blade pitch angle such as to adapt the rotor aerodynamic efficiency with the above-rated wind speeds, which in turn will also affects the damping term in Eq. (11.4).

The negative damping of the platform pitch motion affects the turbine performance, as this motion induces the oscillatory wind inflow relative to the rotor, and in combination with the spinning inertia of the rotor it excites the gyroscopic yaw moment which turns the turbine away from the wind. Several publications explored the negative damping behavior and suggested some guidelines for controller design to avoid it, yet, the most interesting result is presented by Larsen and Hansen which states that, to avoid negative damping implied by a conventional controller, the controller frequency should be less than the natural frequency of the floating wind turbine, and the decreased performance of controlling power and rotational speed can be compensated by a nonlinear gain on the pitch regulator [6]. Using this result, Jonkman updated the baseline gain-scheduled proportional integral (GSPI) controller developed originally for land-based turbines to suit the new conditions of floating platforms [5]. Other methods to stabilize platform

motion either using the individual blade pitching (IBP) [7, 8], or making the rotor speed changing as function of platform pitch velocity [9] are also studied in the literature.

Furthermore, many quantitative studies of wind turbine reliability have been carried out in the past 10 years. One of the recent studies is the *Reliawind* project survey that studied wind turbine subassembly reliability information from of 35,000 down events obtained from 350 onshore wind turbines operating for varying length of time [10]. The Reliawind survey shares the well-known failure rates to the public domain, where the pitch system failure rate dominates by more than 20 % failures/turbine/year. The power module takes a considerable share of the failure rates, while sensors take the highest rate of failures in the control and communication module. Partial results of this survey for submodules with failure rates higher than 2 % are shown in Fig. 11.3.

As the conventional control methods developed to decrease platform motions depend heavily on controlling the blade pitch angle, and with the high failure rates of the pitch system along with the failure rates of the sensors needed for the control loop, this raises the question about the possible effects of a malfunctioning blade pitch system on the floating wind turbine in terms of performance and structural loading. Very recently, this topic starts to draw the attention of the research community aiming to analyze the dynamic response of wind turbines during different fault scenarios, and comparing their structural loading to the loading created
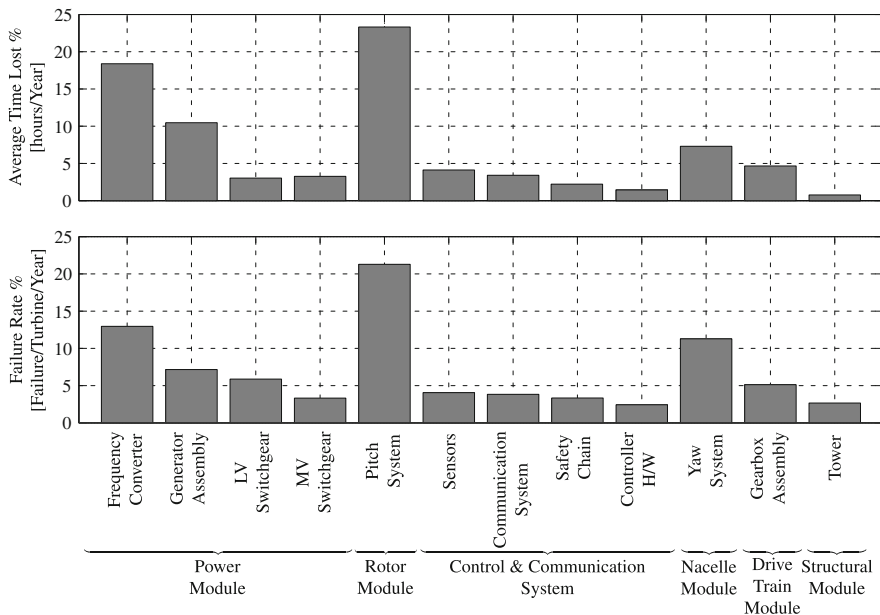
Fig. 11.3 Normalized failure rate and average downtime of subsystems and assemblies for turbine of multiple manufacturers. Failures with failure rate less than 2 % are excluded, and full results are available in [10]

during normal operation or extreme events in order to estimated the severity of each fault on the turbine structure.

Bachynski et al. [11] studied the dynamic response of the floating wind turbine subject to three different faults, the first fault is the blade seize where the pitch actuator of one blade is blocked, the second one is the blade seize, recognized by the controller and followed by shutdown (grid disconnection and aerodynamic braking), and the last fault is the grid loss followed by shutdown. The faults are assumed to be detected within a short period of the fault event. A utility-scale wind turbine mounted on different floating platforms are used, and platform motions in addition to the structural loading caused by fault events are compared to loads encountered during normal operation and during selected extreme weather conditions. The main results of this study indicate that the platform motions and mooring loads are dominated by the extreme wave conditions and hardly affected by the faults, while the tower bending moments are more affected by fault conditions; moreover, they found that blade bending loads in flap-wise direction are sensitive to the imbalance while in edge-wise direction are sensitive to shutdown. This study, though it is limited to the actuator seize and the shutdown process directly after it, gives a good idea about the floating system dynamic response to the fault-induced imbalance in the rotor and its effects on the platform motions.

In another study, Etemaddar et al. [12] investigated the effect of the magnitude of different faults on a land-based wind turbine where the faults are assumed to proceed through the simulation undetected. While Bachynski et al. used a collective blade pitch controller, Etemaddar et al. used an individual blade pitch controller in their work. The sensitivity of each control method to faults depends on the fault origin and type which should be taken into account when comparing the results. The presented results by Etemaddar et al. indicate that the individual blade pitch control can reduce the penalty term of pitch sensor and pitch actuator faults on output power and thrust load; however, the main effect of pitch sensor fault is on the shaft main bearing bending loads. Moreover, the study did not mention the effect of the faults on the tower loading.

Nevertheless, modern wind turbine control systems are equipped with condition monitoring and fault detection and isolation systems, once the fault is detected and isolated the common approach is to deploy the condition monitoring system and shut down the turbine. However, not all faults share the same severity on the turbine, some faults change the characteristics of a component such as the slower performance of the pitching system, this change in the performance can be adapted if the turbine is equipped with a fault-tolerant control system, or it might be just monitored without engaging any preventive procedure in case of well-known effects of such fault. Most condition monitoring systems and fault detection systems in wind turbines are signal-based, which makes fault detection and isolation more challenging knowing that different faults may show similar signals. This last point draws particular attention to the undetected occurring faults in wind turbines and their effects on its structure. This chapter examines the effects of undetected occurring pitch system faults on floating wind turbines. These faults lead to an imbalance in the aerodynamic loading over the rotor disk, which will affect not

only the rotor and the nacelle assembly, but also the tower and the floating plat-form. However, the effects depend on how the rotor imbalance is built up, the operating condition, and the fault magnitude.

This chapter is organized as follows: Sect. 11.2 describes the considered ref-erence floating wind turbine model used in simulation along with its operating region and the implemented controller, in addition to the considered pitch system model. The sensor and actuator faults of the pitch system are presented in Sect. 11.3. Section 11.4 goes through the simulation setup, the environmental conditions (ECs) in addition to the addressed fault scenarios. The obtained sim-ulation results are discussed and analyzed in Sect. 11.5. Finally, Sect. 11.6 states the final conclusion of this chapter.

11.2 Wind Turbine

11.2.1 Reference Wind Turbine

The NREL offshore 5-MW baseline turbine [13] model mounted on the barge platform is used as a reference wind turbine (RWT). The turbine is a fictitious 5-MW machine with its properties based on a collection of existing wind turbines of similar rating since not all turbine properties are published by manufacturers. The barge is a rectangular platform designed to be a cost effective and easy to install platform suitable for shallow water. It utilizes the buoyancy due to its large water-plane area to maintain stability. Since most of the platform is above the water, it is very sensitive to incident waves. The main properties of this turbine and the barge platform are listed in Table 11.1.

11.2.2 Regions of Operation

The variable-pitch variable-speed wind turbine operates typically in two different regions, namely the full load region where the wind speed is above its rated value, and the partial load region where the wind speed is less than its rated value (Fig. 11.4). In the full load region (known also as the above-rated region), the wind has enough energy to run the turbine at its rated rotor speed, and the main task of the controller is to adapt the aerodynamic efficiency of the rotor by pitching the blades into or out of the wind in order to keep the rotor speed at its rated value. On the contrary, the maximum aerodynamic efficiency is maintained in the partial load region (also known as the under-rated region) where the wind speed is less than its rated value, and the controller task is to follow the maximum power production by changing the rotor speed and consequently the generator torque. The partial load region could also be divided into subregions in order to handle the transition at the cut-in wind speed where the rotor should be accelerated till it reaches the power

Table 11.1 Floating reference wind turbine properties [4, 22]

Turbine	
Rated power	5 MW
Rotor type, blades	Upwind/3 blades
Control	Variable speed and variable pitch
Rotor/hub diameter	126 m/3 m
Hub height	90 m
Cut-in/rated/cut-out wind speed	3/11.5/25 m/s
Rated rotor speed	12.1 rpm
Rated generator speed	1173.7 rpm
Blade pitch range	$-1°$ to $+90°$
Maximum blade pitch rate	± 8 deg/s
Barge platform	
Length	40 m
Width	40 m
Height	10 m
Draft	4 m
Water depth	150 m
Platform mass	5,452,330 kg
Roll and pitch inertia	726.9×10^6 kg·m^2
Yaw inertia	$1,454 \times 10^6$ kg·m^2
Number of mooring lines	8
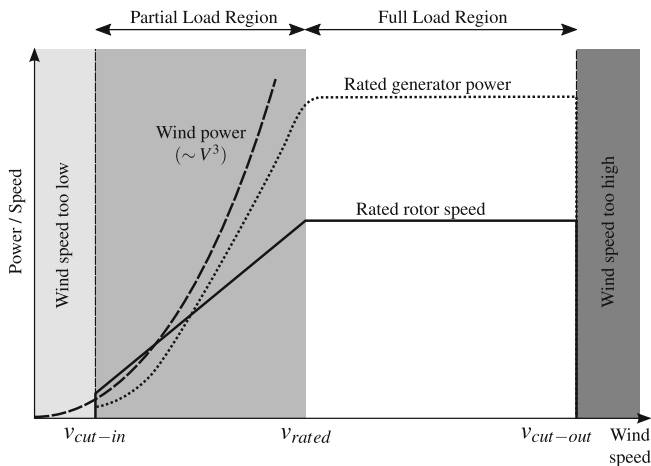
Fig. 11.4 Wind turbine operating regions

production speed, or the transition at the rated wind speed between the partial and full load regions (Fig. 11.2).

Blade pitching is activated only in the full load region, while in the partial load region the blades are kept at zero pitch angle in order to maintain the maximum aerodynamic efficiency of the rotor.

11.2.3 Wind Turbine Control

Two control methods for blade pitching are available, the first method is the collective blade pitching (CBP) which is the process of changing the pitch angle of all blades in the same time, or in other words, all blades have the same pitch angle at any time. The second method is the IBP where each blade is set to a different angle from the other blades. The use of each method depends on the set objective(s) of the controller in the full load region. If regulating rotor speed is the main task, CBP can do the job, however, if the task is extended to reduce blade loading or adapt to the varying aerodynamic loading over the rotor disk, the IBP is the right candidate [7, 14]. These two control methods pose different performance requirements over the blade pitch actuators, while the CBP is used to adjust the blades angles according to the slow changes in the wind speed which might happen once every few rotations, the IBP requests many adjustments of the blades angles per each rotation. This difference in performance requirement should be taken into account when faults are introduced, and in analyzing the results.

The controller design follows the classical linear design methods applied to a linearized wind turbine model at a number of operating points that spans over the different operating regions. Due to the change of the turbine characteristics over the operating regions, the gain-scheduling control methods are used successfully to control turbines.

The collective blade pitch GSPI is one of the first well-documented controllers that have been implemented to control floating wind turbines, it is used in the literature as a baseline controller to compare the obtained results. This work will follow the same steps and use the baseline GSPI controller to study the blade pitching system fault effects on the floating turbine.

The GSPI controller is a sophisticated collective pitch controller that employs a gain-scheduling technique to compensate for the nonlinearity in the turbine by changing the controller gain according to a scheduling parameter. This controller was originally developed by Jonkman for the standard land-based 5-MW turbine [13], and later was implemented to the same turbine mounted on the three main floating platforms [5]. The controller has two separate control loops, the first is the collective blade pitch control loop which employs the gain-scheduling technique to the proportional integral controller. This control loop is active only in the full load region. The second one is the generator torque control loop that switches the objective between the partial and the full load regions. The structure of the baseline GSPI is shown in Fig. 11.5.
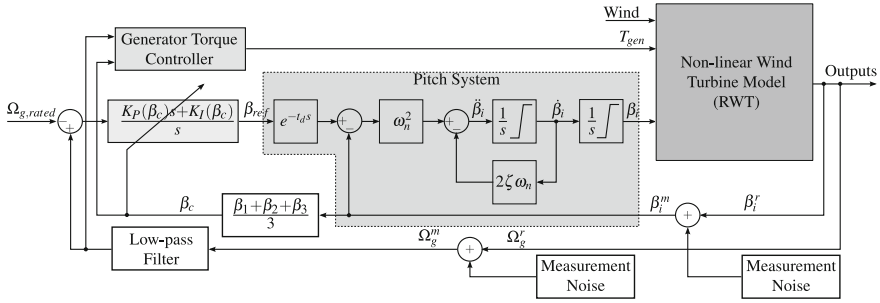
Fig. 11.5 GSPI control structure with pitch system model. Only one pitch system is included in this diagram. β_i^r is the noise-free blade pitch angle ($i = 1, 2, 3$), β_i^m is the pitch angle measurement, Ω_g^r is the noise-free generator speed, Ω_g^m is the generator speed measurement. $\beta_c = \frac{1}{3}(\beta_1 + \beta_2 + \beta_3)$ is the collective blade pitch angle. T_{gen} is the generator torque command, and β_i is the blade pitch command, s is Laplace complex variable

As the RWT does not have any model for the pitch system, the pitch system model block is added between the blade pitch controller and the turbine model. The measured outputs are the generator speed, generator torque, and the three blade pitch angles. A Gaussian noise with zero mean and given standard deviation is added to the deterministic output values in order to emulate measurement noise. The noise standard deviation depends on sensor type, and the difficulty to get the measurement. The blade pitch angles are measured for example on the cylinder of the pitch actuators in the hydraulic pitch systems, while the generator torque is provided by soft sensors in the converters, and the generator speed is measured using a speed encoder. The used standard deviations are for the generator speed noise 0.0158 rad/s, for the generator torque noise 45 Nm, and finally for the pitch angle measurement noise 0.2° [15].

11.2.3.1 Blade Pitch Control

The GSPI control law is given in Eq. (11.5) where $\beta(t)$ is the collective blade pitch control command, K_P is the proportional gain, K_I is the integral gain, both gains are functions of the scheduling parameter θ, while $e(t)$ is the error signal to be driven to zero. The error signal is given in Eq. (11.6) where Ω_g is the measured generator speed, and $\Omega_{g,\text{rated}}$ is the rated generator speed of the turbine. The scheduling parameter θ is taken to be the previous measured collective blade pitch angle. As the three pitch angles are measured, the collective pitch angle is obtained by averaging the measurements of all pitch angles.

$$\beta(t) = K_P(\theta)e(t) + K_I(\theta) \int_0^t e(\tau)d\tau \qquad (11.5)$$

$$e(t) = \Omega_g - \Omega_{g,\text{rated}}. \tag{11.6}$$

The proportional and integral gains are scheduled such as the rotor DOF has the same response of a closed-loop system defined by the natural frequency ω_0 and the damping ratio ζ_0 at each wind speed in the full load region. The scheduling gains are calculated using the following equations

$$K_P(\theta) = \frac{2I_D\Omega_{r,\text{rated}}\zeta_0\omega_0}{N\left(-\dfrac{\delta P}{\delta\theta}\right)} \tag{11.7}$$

$$K_I(\theta) = \frac{I_D\Omega_{r,\text{rated}}\omega_0^2}{N\left(-\dfrac{\delta P}{\delta\theta}\right)} \tag{11.8}$$

where I_D is the drive-train inertia, $\Omega_{r,\text{rated}}$ is the rated rotor speed, N is the gearbox ratio, and $\frac{\delta P}{\delta\theta}$ represents the sensitivity of the rotor aerodynamic power to the scheduling parameter (e.g., collective blade pitch angle). For further details on how the sensitivity is converted into a function of the scheduling parameter, the reader is referred to [4].

11.2.3.2 Generator Torque Control

The generator torque control is basically used in the under-rated region to follow the maximum power production by changing the rotor speed as the wind speed changes. In the above-rated region, two approaches are presently used, the first one uses constant generator torque (rated value), with this approach the power will be a function of the fluctuations of the rotor speed about its rated value as the wind speed changes, these speed fluctuations are minimized by the pitch controller. The second approach is to use a constant generator power, which means to adapt the generator torque within certain limits to the changes of the rotor speed in order to produce constant output power. This second approach assumes that the generator torque can move above its rated value to some maximum value, and the fluctuations are constrained to a maximum torque rate.

Considering maximum power production in the partial load region, the generator torque is a function of the rotor speed such as

$$T_g = \frac{\pi\rho R^5 C_{P,\text{max}}}{2\lambda^2 N^3}\Omega_g^2 \tag{11.9}$$

where ρ is the air density, R the rotor radius, $C_{P,\text{max}}$ is the maximum power coefficient, λ is the tip speed ratio corresponding to $C_{P,\text{max}}$. Considering the constant output power approach for the full load region, the generator torque is given as

$$T_g = \frac{P_{\text{rated}}}{\eta \Omega_g} \tag{11.10}$$

where P_{rated} is the rated output power of the generator, and η is the generator efficiency.

11.2.4 Pitch System

The pitch system adjusts the angle of the blade by rotating it. In a three-bladed wind turbine, three identical pitch systems are used. These systems could be electrical or hydraulic, and regardless of the system nature they share common components, system response, and fault symptoms. The common components include the actuator, the controller, and the sensors. The pitch system can be satisfactory modeled as a second-order system [16] with a time delay t_d and a reference signal β_{ref} such as

$$\ddot{\beta}(t) = -2\zeta\omega_n\dot{\beta}(t) - \omega_n^2(\beta(t) - \beta_{\text{ref}}(t - t_d)) \tag{11.11}$$

where t_d is the time delay related to the communication between the turbine controller and the pitch system controller, $\beta(t)$ is the pitch angle, $\beta_{\text{ref}}(t)$ is the reference pitch angle, ω_n and ζ are the natural frequency and damping ratio of the pitch system model, respectively. The block diagram that illustrates the pitch system model along with the constraints on the pitch slow rate and range is shown in Fig. 11.6. The constraints are added to represent the limitations of the actual pitch actuator.

The GSPI controller was originally designed [5] without considering the pitch system model in the turbine. As the considered pitch system model has higher dynamics than the turbine dynamics, the pitch system does not affect the controller design. Figure 11.7 shows the bode magnitude of the transfer function from the collective pitch angle to the generator speed for the RWT model with and without pitch system model. The transfer function is obtained from linearizing the non-linear model of the turbine implemented in FAST (All DOFs in FAST are enabled such as tower fore-aft and side-side modes, blade flap-wise and edge-wise modes,
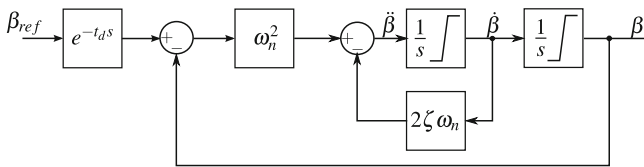
Fig. 11.6 Block diagram of pitch actuator including slow rate and range limitations. s is Laplace complex variable
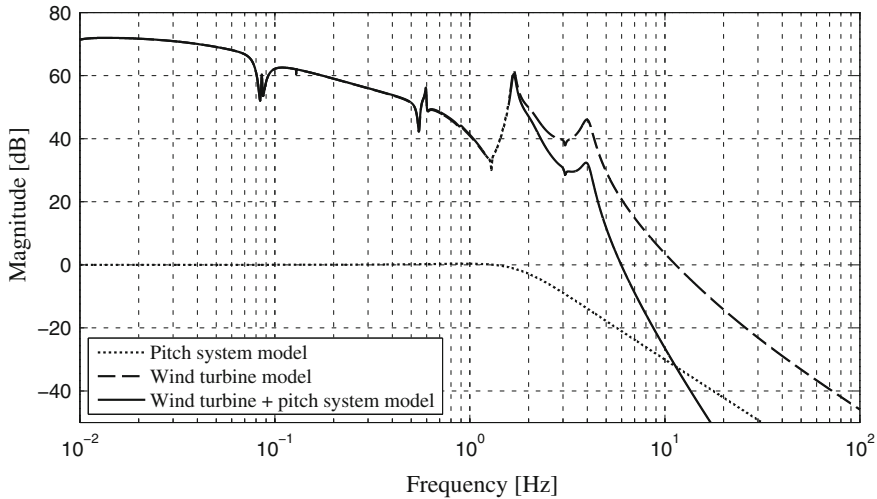
Fig. 11.7 Bode magnitude plot of the transfer function between the collective pitch angle and the generator speed for wind turbine model with (*continuous*) and without (*dashed*) actuator model. Actuator model (*dotted*) is considered as second-order model of natural frequency $\omega_n = 11.11$ rad/s and damping ratio $\zeta = 0.6$

drive-train torsional mode in addition to platform translational and rotational DOFs) at a chosen operating point in the middle of the full load region, e.g., the wind speed at the operating region is 18 m/s and the rotor speed is 12.1 rpm. A hydraulic pitch system is considered by a second-order model that has the natural frequency at $\omega_n = 11.11$ rad/s and damping ratio $\zeta = 0.6$ (see Table 11.5). It is clear that adding the pitch system model to the turbine model does not affect the dynamics of the system below 2 Hz. For this reason, the GSPI gains are not affected.

11.3 Faults

An undesired change in the characteristics of a component is normally called a fault. Faults in general could be categorized according to their temporal profile as incipient or abrupt. Incipient faults are slow to happen and progress slowly with time and system dynamics are gradually changed, on the contrary, abrupt faults are sudden and unexpected. Abrupt faults are generally more easier to detect than the incipient faults; however, they might have severe consequences on the system. Faults on wind turbines have different degrees of severity and accommodation. Once faults are detected, a safe and fast shutdown of the turbine might be necessary in response to some of them, while the turbine could be reconfigured to continue power production in response to other faults.

According to wind turbine reliability analysis (Fig. 11.3), the most common faults occur in the pitch system, power electronics and generator assembly and in turbine sensors. Faults in the pitch system and sensors result in structural loading of the turbine due to rotor imbalance and might affect the stability of the floating platform. These faults are originated by either electrical or mechanical anomalies, and they can result in different fault scenarios in sensors and pitch system. Furthermore, the optimal operation of wind turbines depends highly on the right rotor adjustment and balance, and the blade angles have a strong impact not only on the performance, but also on the emerging loads.

In order to model the faults, the pitch system/sensor equations are to be updated. The incipient faults are introduced gradually through their magnitude and rate of change. On the other side, the abrupt faults are modeled by rewriting the system and measurement equations such that the new equations correspond to the enforced changes by the introduced fault.

11.3.1 Sensor Faults

Sensor faults are more frequent compared to the turbine structure lifetime. As turbine monitoring and control uses the sensor data for decision, it is important that the data acquired are accurate and reliable. Generally, the fault-free sensor is modeled as

$$S_m(t) = S_r(t) + v(t) \tag{11.12}$$

where $S_m(t)$ is the fault-free sensor measurement (e.g., pitch angle or generator speed), $S_r(t)$ is the noise-free value, and $v(t)$ is the measurement noise. The dynamics of the sensor is ignored as it is too fast compared to the system dynamics. Sensors might produce different types of faults including—but not limited to—the following.

11.3.1.1 Bias

The bias could be represented with a constant value that is introduced to the final measurement such as

$$S_f(t) = S_r(t) + B + v(t) \tag{11.13}$$

where B is the bias value (constant), and $S_f(t)$ is the faulty sensor measurement.

11.3.1.2 Gain

The gain error is modeled as

$$S_f(t) = (1 + \alpha)S_r(t) + v(t) \tag{11.14}$$

where α could be constant or time-dependent gain.

11.3.1.3 Complete Failure

The sensor could generate suddenly a constant value A that might be contaminated with noise $w(t)$ such as

$$S_f(t) = A + w(t) \tag{11.15}$$

This fault is an abrupt fault, and it might rise due to a failure in the sensor electronics.

11.3.2 Pitch System Faults

The blade pitch system is affected by the measurements of the blade pitch angle; however, as a system the following faults could be recognized.

11.3.2.1 Performance Degradation

The performance of the pitching system might be changing with time, which could be seen by the change of the system response. The performance degradation is an incipient fault that could be introduced by changing the model parameter, Eq. (11.11), such as

$$\ddot{\beta}(t) = -2\zeta(\gamma)\omega_n(\gamma)\dot{\beta}(t) - \omega_n^2(\gamma)(\beta(t) - \beta_{\text{ref}}(t - t_d)) \tag{11.16}$$

where the damping ration ζ and the natural frequency ω_n are now functions of the parameter γ that is used to describe the change in system performance.

11.3.2.2 Actuator Stuck

The complete failure in the pitch actuator which will lead to loosing the ability of pitching the blade so it sticks in its current position which will cause the rotor imbalance. This fault is described as

$$\beta(t) = \beta_0 \tag{11.17}$$

where β_0 is the seize angle.

11.3.2.3 Pitch Runaway

The complete failure of the pitch sensor in such way that produces a constant value will make the pitch control loop unstable, and the output command follows a ramp function forcing the blade to pitch to feather at the maximum rate till it reaches the maximum range of $\beta_{\max} = 90°$, then the blade will stuck at this position. This fault is described as

$$\beta(t) = \min\left(\beta(TOF) + \dot{\beta}_{\max}(t - TOF), \beta_{\max}\right) \tag{11.18}$$

where $\beta(TOF)$ is the current pitch angle at the time of fault TOF, $\dot{\beta}_{\max}$ is the maximum pitch rate, and t is the time.

11.3.2.4 Bias Error

The bias error is a common problem in pitch systems that might originate from different sources such as a malfunctioning of the pitch sensor measurement (gain or bias), or a relative blade angle deviation in the rotor (rotor adjustment problem). When the bias is introduced, the pitch actuator model equation is modified as

$$\ddot{\beta}(t) = -2\zeta\omega_n\dot{\beta}(t) - \omega_n^2(\beta(t) - \beta_{\text{bias}}(t)) + \omega_n^2\beta_{\text{ref}}(t - t_d) \tag{11.19}$$

where $\beta_{\text{bias}}(t)$ is the bias angle value, which might be constant or depending on time according to the fault origin.

11.4 Simulation Setup

The state-of-the-art aero-hydro-servo-elastic simulation code FAST (Fatigue, Aerodynamics, Structures, and Turbulence) is a moderate complexity simulation code developed by the national renewable energy laboratory (NREL) [17]. This code is used by the research community and industry to analyze the structural dynamics of the horizontal axis wind turbines. FAST is built up of different modules such as the AeroDyn module which is used to calculate the aerodynamic loading of the wind over the turbine structure, the HydroDyn module that models the hydrodynamic interaction of the platform with waves and current, the Servo-Dyn model that includes the turbine control system, and the ElastoDyn module

that includes the structural dynamics. The full nonlinear RWT model is implemented in FAST, and the used barge platform model is as implemented by Jonkman [4]. However, the control part, faults, and simulation are developed and implemented by the authors in Matlab/Simulink.

11.4.1 Environmental Conditions

Three-dimensional turbulent wind fields according to the design load case *DLC*2.1 of the international standard *IEC*61400-3 (power production plus occurrence of faults) with different mean wind speeds in the full load region are used along with the corresponding wave conditions. The study is limited to the full load region as the pitch system is active only in this region (Fig. 11.2), and only undetected pitch system faults are included. All ECs are considered to be correlated as shown in Table 11.2 with wind and wave conditions for the North Sea. The direction of the wind is assumed to be aligned with the direction of the waves. The number and length of simulations are chosen according to the offshore wind turbine standards that suggests for statistical reasons 12 simulations with different wind and wave profiles with duration of 10 min each to be carried out for power production plus fault cases [18].

The turbulent wind profiles are generated using the TurbSim program [19] based on the Kaimal spectrum for IEC Class *C* along with a normal turbulence model (NTM) and wind shear according to the power law with power component of 0.14 [18]. Meanwhile, the simulated wave series are generated using JON-SWAP spectra for the incident wave kinematics model with significant wave height H_s and peak period T_p. Recorded simulation length is 10 min after introducing the fault at time step $TOF = 100$ s. Each simulation is repeated 12 times with different seeds for the turbulent wind and wave fields.

Table 11.2 Environmental conditions, U_{wind} is the mean wind speed, H_s is the significant wave height of incident waves, T_p is peak spectral period of incident waves, *TMax* is the simulation time after occurrence of fault

EC	$U_{\text{wind}}(\frac{\text{m}}{\text{s}})$	$H_s(\text{m})$	$T_p(\text{s})$	Turbine model	No. of simulations	TMax (s)
*EC*1	11.2	3.10	10.10	NTM	12	600
*EC*2	14.0	3.60	10.30	NTM	12	600
*EC*3	17.0	4.20	10.50	NTM	12	600
*EC*4	20.0	4.80	10.80	NTM	12	600
*EC*5	23.0	5.40	11.00	NTM	12	600

11.4.2 Fault Scenarios

The faults in the pitch system originate either from the internal faults in the system or from the pitch control loop in the GSPI controller as this loop sets the reference pitch angle. The bias and the gain faults in pitch sensor result in bias and gain in the final blade pitch angle, while the complete failure of the pitch sensor results in pitching the blade to feather. The pitch sensor fault also affects the GSPI pitch control loop, as the faulty pitch measurement affects the choice of the scheduled gains. Moreover, the generator speed faults will lead to either bias in the final blade pitch angle or in actuator runaway on the system level. Therefore, only the listed faults in Table 11.3 are considered.

Different magnitudes for each fault are simulated in order to estimate the severity of the fault as function of its magnitude. Some magnitudes depend on the corresponding environmental condition, other magnitudes are absolute. The dependency of the fault on the environmental condition is introduced in order to prevent losing rotor torque, which in turn will shut down the turbine (Table 11.4).

As the hydraulic pitch systems are common in utility-scale wind turbines, a hydraulic system is considered in order to study the performance degradation fault effects. The hydraulic pitch system consists of the main pump that provides the hydraulic pressure to the system, a set of valves that have different tasks such as the servo valves that control the position of the actuators and the blade pitch motion is achieved through an actuator, e.g., cylinder (Fig. 11.8). The system is also provided with a controller that accepts the error signal between the measured blade pitch angle and the set reference one and issues the appropriate command to the servo valves. The reference pitch angle is set by the baseline GSPI controller, and the basic implementation of the pitch system controller could be a proportional gain [16].

The performance degradation of the hydraulic pitch system might rise from different sources such as pump wear, hydraulic leakage, high air content in oil, and pressure drop [15, 20]. These faults lead to change in the system dynamics and consequently to performance degradation, and in case of total failure, it leads to actuator stuck in its current position. The change in the dynamics is pronounced by varying the nominal natural frequency ω_n and damping ratio ζ of the system into the new values $\omega_n(\gamma)$ and $\zeta(\gamma)$ where the parameter γ is used to identify the fault type shown in Table 11.5.

Table 11.3 List of considered pitch system faults

	Fault code	Fault	Fault type
Pitch sensor	B	Bias	Incipient
	C	Gain	Incipient
Pitch system	D	Performance degradation	Incipient
	E	Actuator stuck	Abrupt
	F	Actuator runaway	Abrupt

Table 11.4 List of magnitudes simulated for each fault

Fault code	Magnitude				Notes
	M1	M2	M3	M4	
B	−7°	−3°	3°	7°	Absolute
C	−0.10	−0.05	0.05	0.10	Absolute
D	see Table 11.5				Absolute
E	0 %	50 %	100 %	125 %	Of mean pitch in fault-free case
F	–	–	–	–	Only one magnitude (+90°)
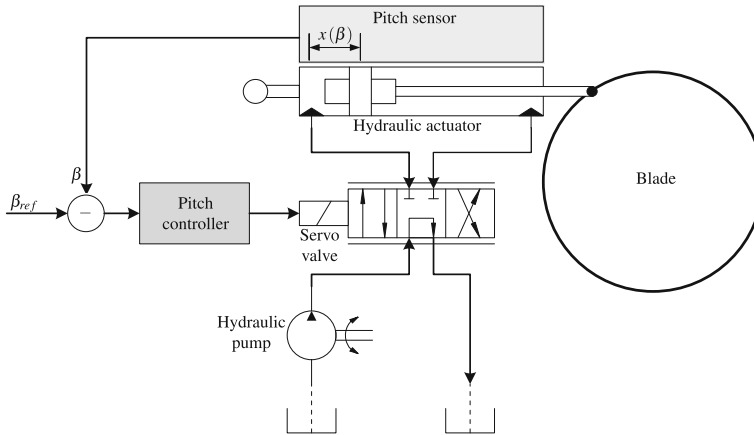
Fig. 11.8 Hydraulic blade pitch system structure. The pitch sensor measures, for example, the actuator stroke x as function of the blade pitch angle β. The pitch controller could be a simple proportional gain. β_{ref} is the set reference pitch angle

Table 11.5 Parameters for the hydraulic pitch system under different conditions [15, 20]	Faults	Parameters	
		ω_n (rad/s)	ζ
	No fault (fault-free)	11.11	0.6
	High oil content in the oil (M1)	5.73	0.45
	Pump wear (M2)	7.27	0.75
	Hydraulic leakage (M3)	3.42	0.9
	Pressure drop	3.42	0.9

Pump wear is an irreversible slow process over the years that results in low pump pressure. As this wear is irreversible, the only possibility to fix it is to replace the pump which will happen after pump wear reaches certain level. Meanwhile, the pump will still be operating and the system dynamics is slowly changing, while the turbine structure should be able to withstand the effects of this

fault. Pump wear after approximately 20 years of operation might result in pressure reduction to 75 % of the rated pressure, which is reflected by the faulty natural frequency $\omega_{pw} = 7.27$ rad/s and a fault damping ratio of $\zeta_{pw} = 0.75$.

Hydraulic leakage is another irreversible incipient fault, but is introduced considerably faster than the pump wear. When this fault reaches a certain level, system repair is necessary, and if the leakage is too fast, it will lead to a pressure drop and the preventive procedure is deployed to shut down the turbine before the blade is stuck in undesired position. The fast pressure drop is easy to detect and requires immediate reaction, yet the slow hydraulic leakage reduces the dynamics of the pitch system, and for a reduction of 50 % of the nominal pressure, the natural frequency under this fault condition is reduced to $\omega_{hl} = 3.42$ rad/s and the corresponding damping ratio is $\zeta_{hl} = 0.9$. If the hydraulic pressure is too low, the hydraulic system will not be able to move the blades which will cause the actuator to stuck in its current position resulting in blade seize.

On the contrary to pump wear and hydraulic leakage, high air content in the oil is an incipient reversible process, which means that the air content in the oil may disappear without any necessary repair to the system. The nominal value of the air content in the oil is 7 %, whereas the high air content in the oil corresponds to 15 %. The effect of such a fault is expressed by the new natural frequency $\omega_{ha} = 5.73$ rad/s and the damping ratio of $\zeta_{ha} = 0.45$ (corresponding to the high air content in the oil). The pitch system step response to each of the previously illustrated faults that induce a change in performance is shown in Fig. 11.9.

The performance degradation of the hydraulic system is simulated by updating the natural frequency and damping ratio of the first blade according to a given rate. This fault is introduced only to the first blade at time of fault *TOF*, and the natural frequency and damping ratio are changed gradually from their nominal values ω_n, ζ to their new values $\omega_n(\gamma), \zeta(\gamma)$ as in Eq. (11.16). The new values are reached within duration T_i.
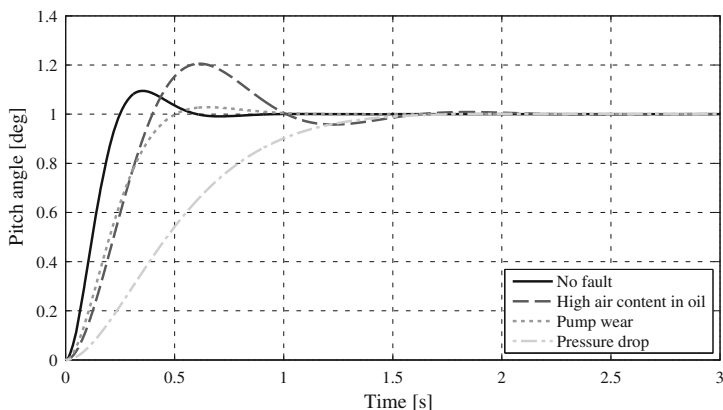

Fig. 11.9 Step response for the normal and fault conditions of the pitch system

The incipient faults are introduced gradually to the system between simulation time *TOF* and *TOF* + T_i where *TOF* is the time step at which the fault is introduced, and T_i is the time duration at which the fault propagates from the fault-free case to the faulty condition. The value of T_i does not represent the actual value as some faults, e.g., the pitch sensor bias, will develop slowly such as ± 1deg/month which could be considered as zero rate compared to the simulation time of 10 min. The time duration T_i is used to increase the development rate of the fault, which will not affect the results, as most of the important effects of the faults are introduced after the fault reaches the set magnitude. $T_i = 50$ s is considered in all simulations of incipient faults and this time is considered within the recorded simulation time.

In addition to the previously illustrated faulty cases with their magnitudes, the fault-free system is simulated at the above-mentioned environmental conditions, these fault-free cases are used as reference to estimate the severity of the fault on the normal operation of the turbine.

11.5 Results Discussion and Analysis

11.5.1 Performance Indices

To quantify the effects of each fault at each operating condition and at each fault magnitude, a set of performance indices are used to monitor the key components of the wind turbine. The performance indices involve two types of calculations, the root mean square (RMS) and the damage equivalent load (DEL) values. The calculation of the DEL requires using the rain flow counting algorithm [21], the fatigue DEL is calculated at a reference frequency of 1 Hz. All calculated indices are normalized to their corresponding fault-free values, then averaged over all simulations. A brief description of each performance index is given in the following

- Generator power error: the normalized RMS is calculated for the generator power error in order to study the fault effect on the output power as the GSPI controller follows a constant output power strategy in the above-rated region. A value larger than one for this index means that the fault will increase the error in the generated power.
- Blade pitch rate: the normalized RMS of the blade pitch rate is calculated in order to monitor the effect of the fault on the actuator usage. The index is calculated for the first blade where the fault is induced, and for the second blade which will be along with the third blade working as fault-free blades, however, they will be affected by the faulty first blade. A value larger than one for this index means higher actuator usage.
- Platform motion: the normalized RMS indices are calculated for platform rotational motions, roll, pitch, and yaw in order to monitor the fault effects on

the platform stability. An index value larger than one means that the fault excites the corresponding motion.

- Tower fore-aft, side-side, and torsional moments fatigue DEL: the damage equivalent loading index for the tower moments shows the fault effect on the tower loading. An index value larger than one means the rotor imbalance increases the dynamic loading over the tower and reduces the useful average lifetime.
- Low speed shaft (LSS) non-rotating bending fatigue DEL at the shaft tip at $0°$ direction (vertical) and at $90°$ direction (horizontal): this index shows the fault-induced rotor imbalance effect on the low speed shaft (LSS) bending moment. An index value higher than one means higher dynamic loading on the LSS.
- Blade root flap-wise and edge-wise bending moment DEL: this index monitors the fault-induced loading over the blades in flap-wise and edge-wise directions. An index higher than one means increase of the blade loading moment.

11.5.2 Blade Pitch Bias Fault

The bias in blade pitch angle causes rotor imbalance which affects the LSS and the tower bending moments. The GSPI controller performance is not affected that much with this bias as the collective blade pitch angle is used for gain scheduling only, which means minor deviations in the reference pitch angle. The bias fault has most effect at *EC*2 (Table 11.2) where the thrust force over the rotor disk is close to its maximum value (Fig. 11.10). As the GSPI pitch controller switches between the full and partial load control methods which means disabling the pitch control in the partial load region, this reduces the fault effects at *EC*1, yet the high thrust force. The fault effect also depends on the bias magnitude but not the sign. Furthermore, the blade flap-wise and edge-wise moments in addition to tower fore-aft and side-to-side moments show negligible response to this fault.
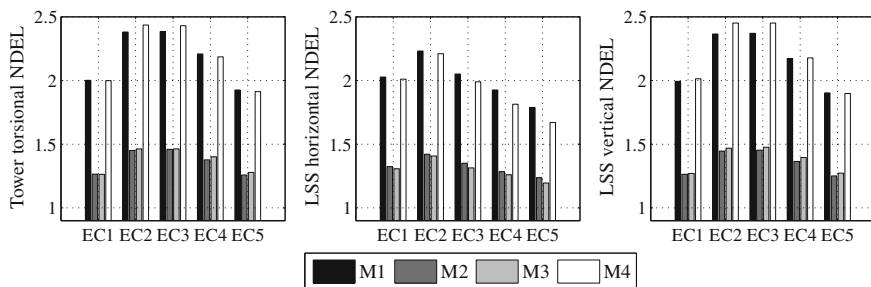
Fig. 11.10 Fault: blade pitch sensor bias. Normalized DEL (NDEL) of tower torsional and LSS moments. High DEL at maximum bias (absolute) and at EC2
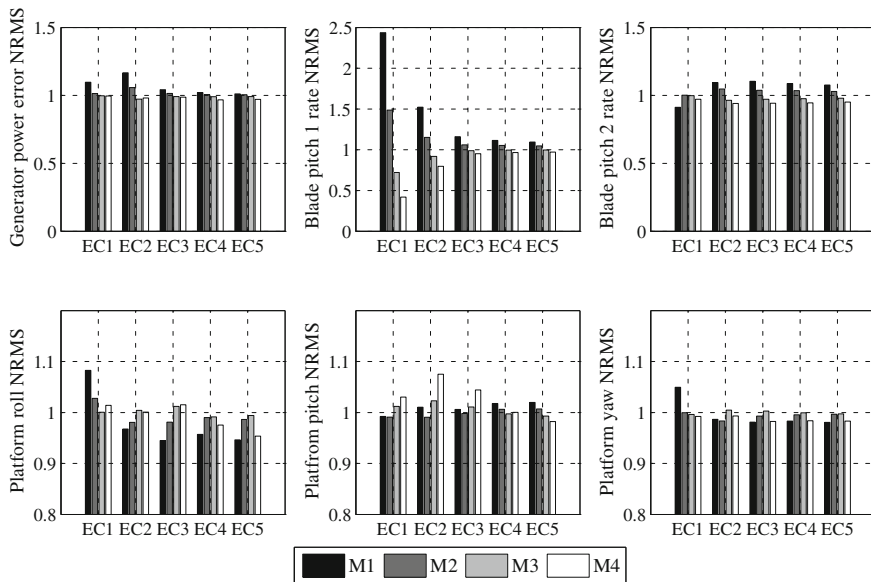
Fig. 11.11 Fault: blade pitch sensor bias. Normalized RMS (NRMS) of generator power error, blade pitch rates, and platform motion

Furthermore, the bias fault has minor effect on the power production with the exception of the first bias magnitude at *EC*1 and *EC*2 (see Fig. 11.11) where the error shows limited effect for the negative bias, this is due to the pre-switching between the operating regions. The bias fault also affects the faulty pitch actuator mostly at *EC*1, and this effect decreases with the increase of mean wind speed. Again, the main reason of this high effect is the switching of the GSPI pitch controller between the operating regions, with negative bias (magnitudes *M*1 and *M*2), the faulty blade starts to move after the healthy blades which means it should have high pitching rate in order to catch the set-point, the opposite happens to the positive bias (magnitudes *M*3 and *M*4).

The platform pitch and yaw motions show negligible response to the fault, while the roll motion is affected close to the switching region (*EC*1 and *EC*2) basically due to the usage of the generator torque in response to the increased power error. The big inertia of the platform minimizes the effects of the rotor imbalance on the platform motion, at the cost of increasing this effect on the tower torsional moment and the LSS moments. The faulty blade affects the rotor speed, and as far as the turbine is operating in the full load region where the constant output power strategy is engaged and the generator torque is changing according to rotor speed. With the negative bias in blade pitch angle, the controller is delayed in switching to the partial load region though the rotor speed is less than rated. This will increase the generator torque, which will excite the platform roll motion. The opposite effect happens with positive bias of the blade pitch angle when the turbine is operating far from the switching region (*EC*3 till *EC*5) where this effect

disappears. Furthermore, the effect of constant output power as control strategy is more pronounced in the higher part of the full load region, where the positive or negative bias leads to similar change in rotor speed and generator torque compared to the normal operating conditions.

11.5.3 Blade Pitch Gain Fault

The gain fault does not affect the blades root moments, neither the tower fore-aft and side-side moments. However, the fault effect is clear on the tower torsional moment and the LSS moments DEL which increase with the mean wind speed and the absolute magnitude of the fault (Fig. 11.12). The reduced effects of the fault on the $EC1$ are due to the switching between the operating regions. The effect increases with the wind speed as the measured pitch angle will increase for higher wind speeds, and the gain fault is becoming bigger. Therefore, the same gain fault for small measured pitch angles (such as in $EC1$ and $EC2$) does not produce higher effect on the structural response even though the aerodynamic thrust over the rotor disk is at its maximum value at $EC1$.

The gain fault also introduces minor effects on the RMS power error, and the platform motions. The effect seen by the bias fault at $EC1$ and $EC2$ in the generator power error and platform roll motion is not present here as there is no delay in switching between the operating regions, in addition to that, at $EC1$ the measured pitch angle is small, which means small fault due to the change in pitch sensor gain, and the resulting rotor imbalance is marginal (Fig. 11.13).

11.5.4 Actuator Performance Degradation

Only the third magnitude $M3$ of the performance degradation fault has an effect on turbine structure as it has slower response compared to the other magnitudes
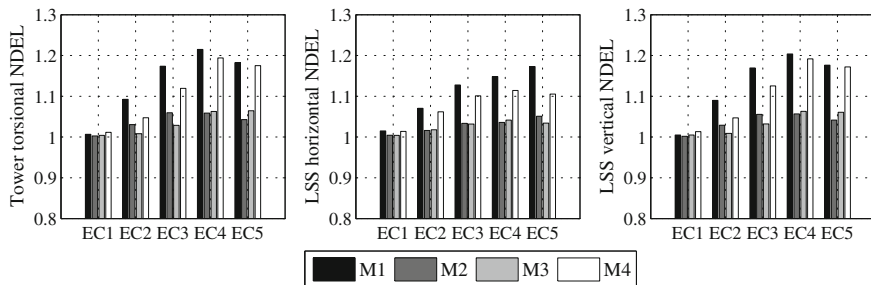
Fig. 11.12 Fault: blade pitch sensor gain. Normalized DEL (NDEL) of tower torsional and LSS moments. DEL increases with the wind speed and the absolute value of the gain error
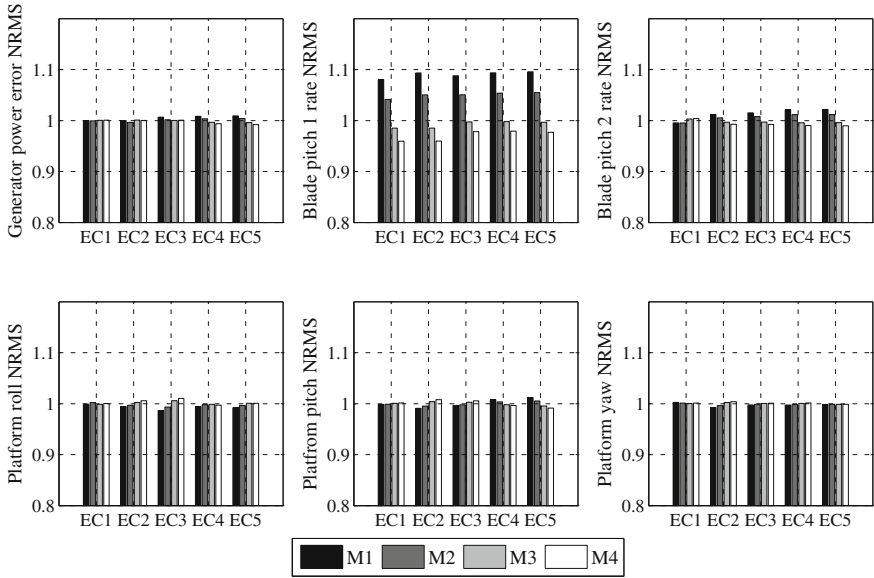
Fig. 11.13 Fault: blade pitch sensor gain. Normalized RMS (NRMS) of generator power error, blade pitch rates and platform motions. Platform motion is hardly affected by this fault

($M1$ and $M2$). This effect is clear by the increased tower torsional and LSS DEL indices. The slow performance of the actuator increases the rotor imbalance due to the late response of the faulty blade compared to the others (Fig. 11.14). However, the slow performance of the pitch system does not affect power production; moreover, its effects on platform motion are marginal. On the other side, the slow performance decreases the faulty blade pitch rate and introduces small increase to the rate of the healthy blades as they try to compensate for the slow behavior of the faulty one. The slow pitch system also works as a low-pass filter as it cannot respond to the high frequency measurement noise as the healthy blades do which is clear from Fig. 11.15.
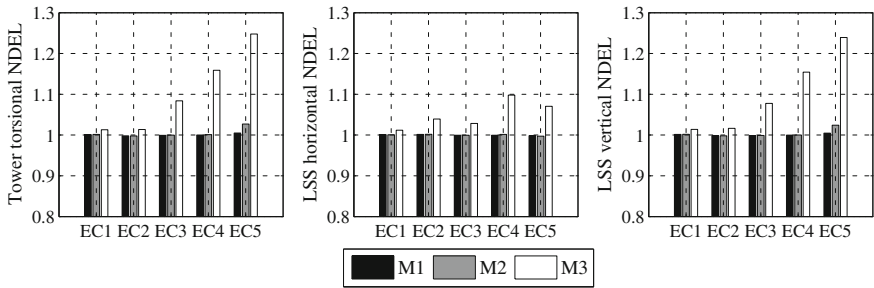
Fig. 11.14 Fault: actuator performance degradation. Normalized DEL (NDEL) of tower torsional and LSS moments
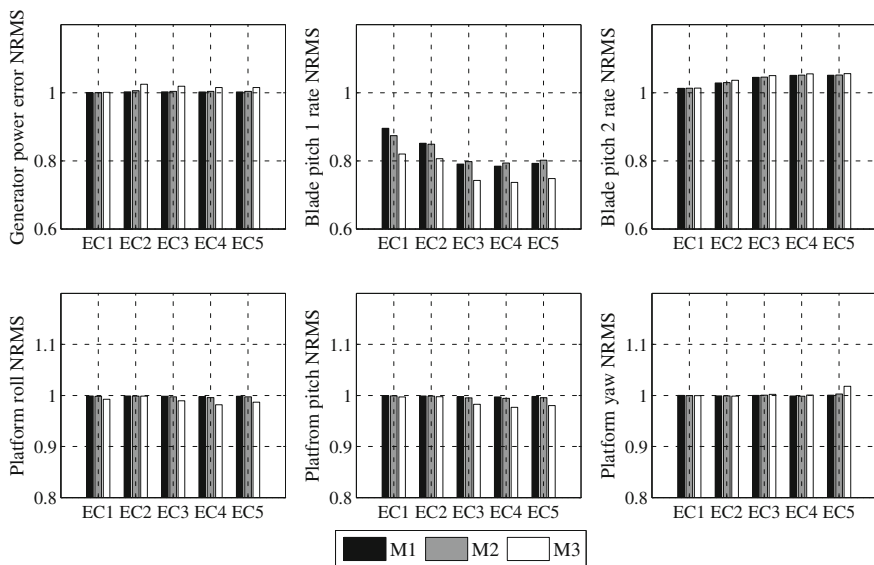
Fig. 11.15 Fault: actuator performance degradation. Normalized RMS (NRMS) of generator power error, blade pitch rates, and platform motions

11.5.5 Actuator Stuck

Actuator stuck has dangerous effects on the turbine structure, and the angle at which the blade seize plays a big roll in the total structural loading. The small stuck angles leave the blade at the maximum aerodynamic loading, which increase significantly the rotor imbalance, so the LSS and the tower torsional moments are mostly affected, with DEL going up to 5 times compared to the faulty-free turbine operating under the same condition. The fault also affects the faulty blade flap-wise and edge-wise bending moments. For example, the stuck angle at 0° represents the maximum aerodynamic loading over the faulty blade. As the turbine operates at EC1, the stuck angle will not increase the rotor imbalance as this angle is close to the mean pitch angle for a fault-free turbine operating under the same condition. The rotor aerodynamic loading will lose the balance as the faulty blade is always at maximum aerodynamic loading with the increase of mean wind speed in the full load region, while the faulty blade is still stuck at 0° and the other blades are pitching following the set-point of the GSPI pitch controller. This will result from one side to an increased root loading moment of the faulty blade, and from the other side due to rotor imbalance, the LSS and tower torsional loading moments are also increased as it is clear from Fig. 11.16.

The generator power is also affected by this fault, with minimum generator error RMS at EC1. The effect of this fault increases between EC2 and EC3 then it reduces for EC4 and EC5, the increase in generator error is related to the increased

Fig. 11.16 Fault: actuator stuck. Normalized DEL (NDEL) of tower, LSS, and blade root moments

fluctuations of the generator torque due to the fault-induced changes in the generator speed. This fault also excites the platform pitching motion, in particular if the actuator stuck at small pitch angles where the aerodynamic loading over the faulty blade is still high (*M*1 and *M*2). The platform pitching motion response for this fault is also affected by the mean wind speed, with higher response at *EC*3 and actuator stuck angle of 0° the platform pitch motion shows an increase of up to 25 %. The platform roll also demonstrates an increase in response of up to 13 % (Fig. 11.17).

11.5.6 Actuator Runaway

Once this fault is introduced to the turbine, the rotor speed is reduced gradually to zero, and the turbine is shut down due to the loss of the aerodynamic torque.
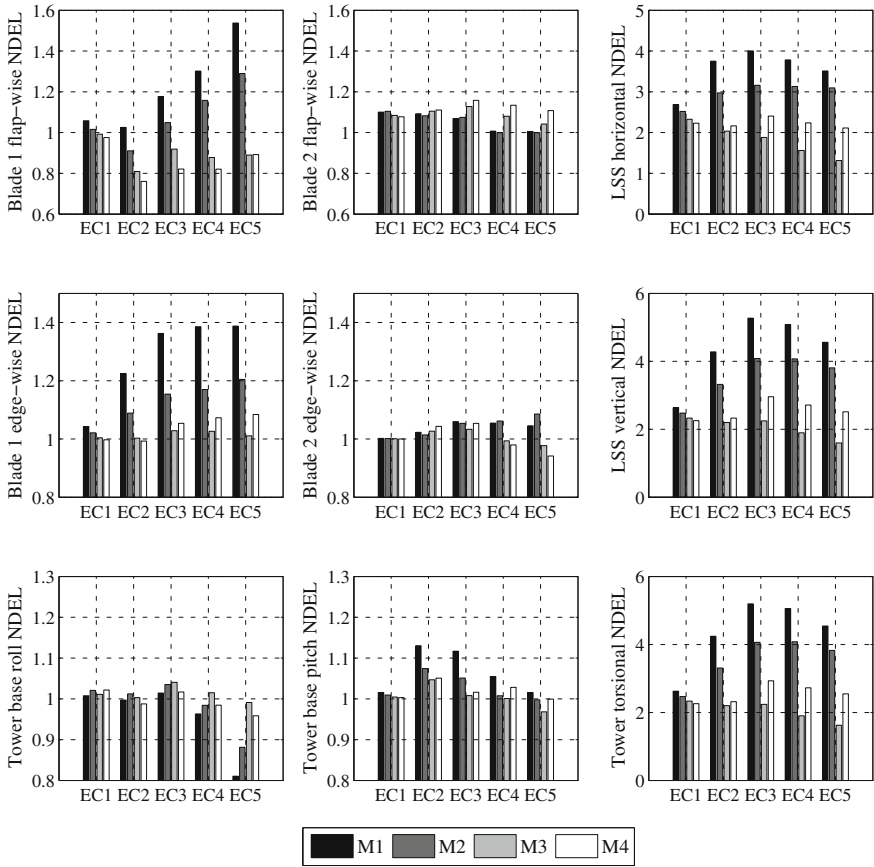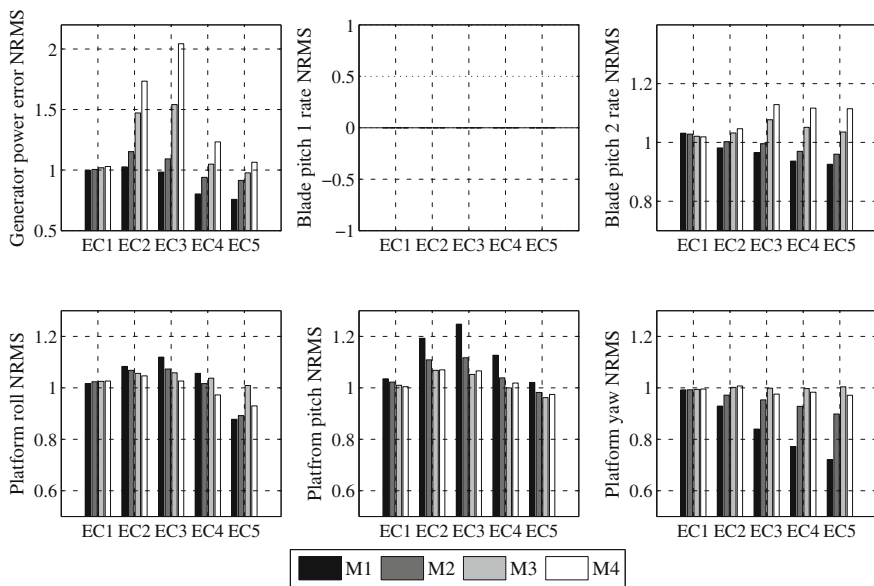
Fig. 11.17 Fault: actuator stuck. Normalized RMS (NRMS) of generator power, blade pitch rates, and platform motions

The GSPI pitch controller tries to restore the aerodynamic torque by pitching the healthy blades to 0° in order to increase the rotor moment, however, with the faulty blade is pitched to feather (90°) the aerodynamic moment is not enough to move the rotor. If the turbine goes in operation in such condition, the structure of the turbine will be very affected, especially the tower in addition to the LSS. The tower side-side (roll) bending moment DEL will be more than 3 times higher at $EC4$ and $EC5$, the tower fore-aft (pitch) moment DEL will be more than 2 times higher at $EC2$, while the maximum tower torsional DEL will be about 2.5 times higher at $EC1$, of course all compared to the normal operating condition (Fig. 11.18). The blade root moments in both directions, flap-wise and edge-wise, show a decrease in DEL for both faulty and healthy blades as the turbine is shutting down.

On the other side, platform motion is very affected by such fault. The platform pitching motion increases more than twice over the full load region, while the yaw motion is highly affected by higher wind speeds ($EC4$ and $EC5$) with more than 5 times compared to the normal operating conditions. The roll motion is less affected, but still above the normal level with up to 47 % more at $EC2$ and $EC4$. The direct dependency of the platform yaw motion excitation with the wind speed is clear, as this motion is mostly affected by the rotor imbalance with two blades are pitched to maximum aerodynamic efficiency and one blade is pitched to feather, this will create a difference between the aerodynamic thrust over the left and half side of the rotor disk according to the position of the blades, which, in turn, will build up a moment along the tower axis. As the rotor speed at $EC4$ and
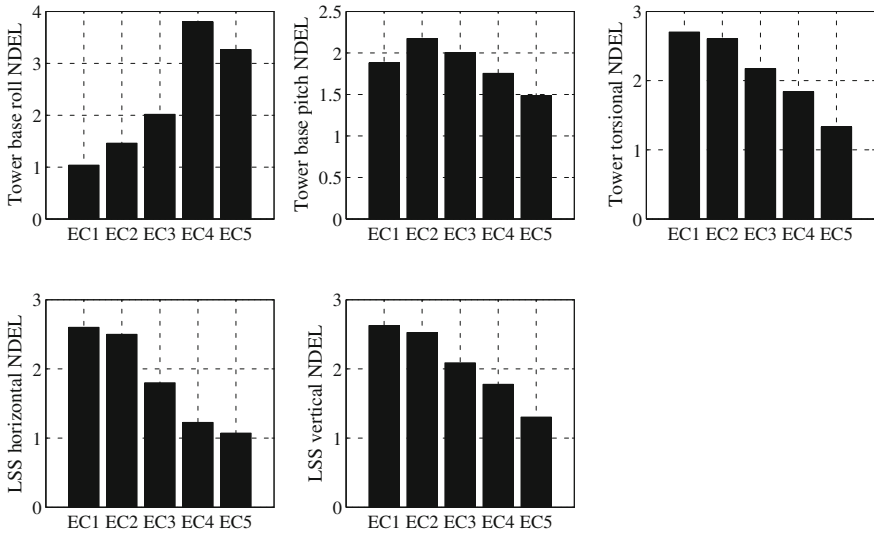
Fig. 11.18 Fault: actuator runaway. Normalized DEL (NDEL) of tower and LSS moments
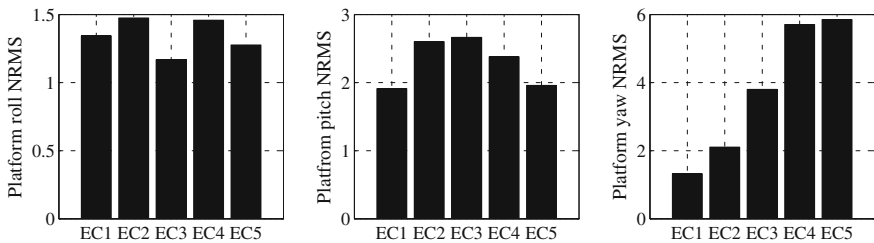
Fig. 11.19 Fault: actuator runaway. Normalized RMS (NRMS) of platform motion

*EC*5 is considerably lower than rated, the rate of the imbalance-induced moment will be lower, giving the platform yaw motion the time to respond to such excitation moment. The effect disappears at lower wind speeds (e.g., *EC*1) where the rotor speed is almost zero, and the moment built up due to the imbalanced aerodynamic loading is considerably less than at higher mean wind speed; at lower mean wind speeds, the imbalance moment is mostly dominated by the turbulent wind loading that has higher change rate so the platform yaw motion is not able to follow these changes which result in an increased tower torsional moment loading (Figs. 11.18 and 11.19).

As the rotor speed decreases the turbine loses the thrust force over the rotor disk, and the restoring moment due to buoyancy forces the turbine to pitch back to the vertical position. As the generator torque control algorithm uses the collective blade pitch angle to switch between the operating regions, this algorithm will always see the turbine to be operating at the full load region, even though the rotor
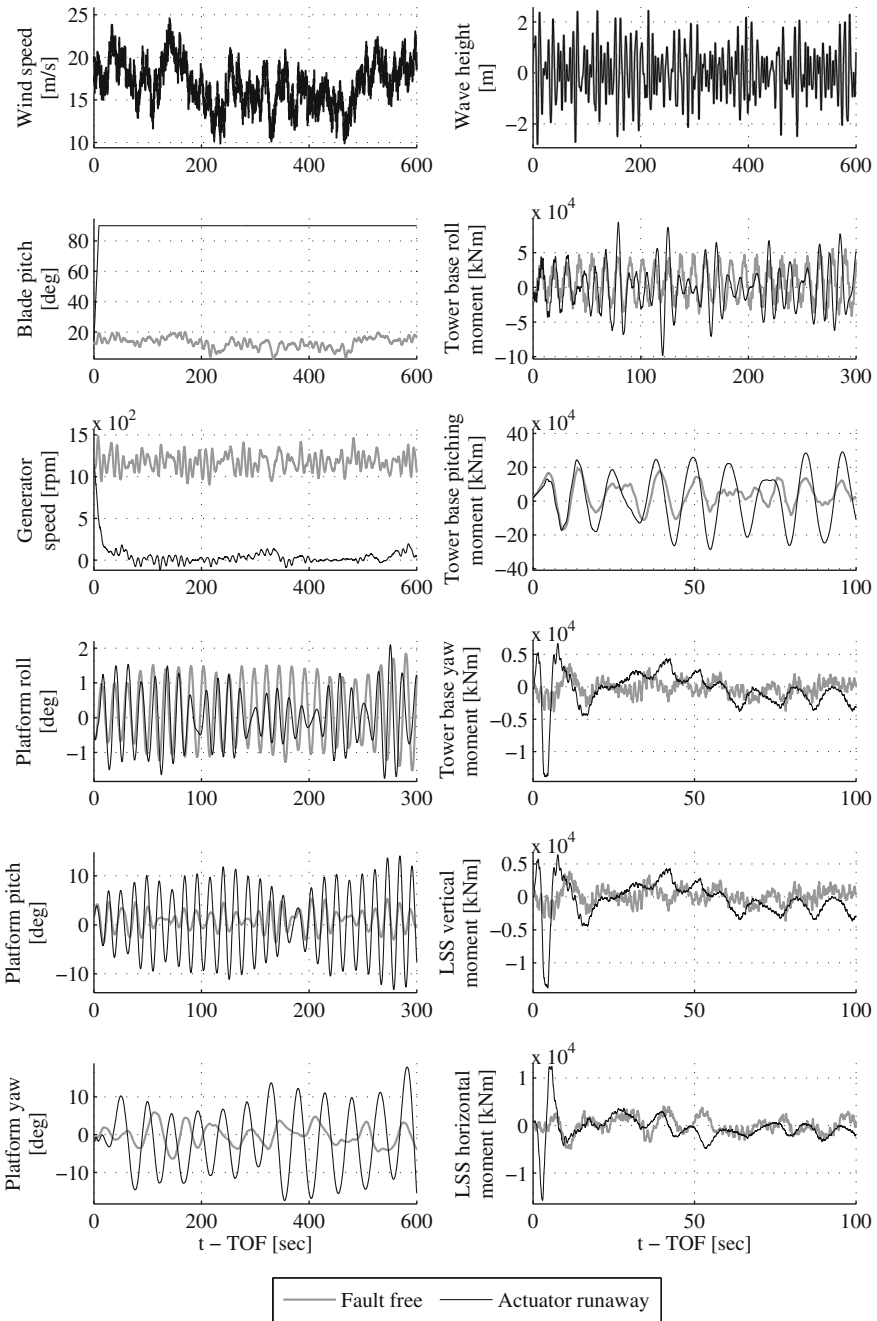
Fig. 11.20 Time series of actuator runaway fault. *t* is time and *TOF* time of fault

speed is down to zero, so the generator torque is always set to produce the rated output power. This will lead to a series of acceleration and decceleration of the rotor due to the induced inflow by the platform pitching and the changes of generator torque by the torque control loop, resulting in exciting the platform pitch motion.

The time series of the actuator runaway fault at $EC3$ are shown in Fig. 11.20. Once the fault is introduced at time step TOF, the faulty blade (blade 1) is pitched at maximum rated to feather leading to gradual decrease of generator speed to zero. The direct effect of such a fault is clear from the LSS moments, which shows high transient response with magnitudes up to 3 times the mean LSS moment. The same transient response is also clear on the tower torsional moment with similar high magnitudes as in LSS moments. The transient response settles down as the faulty blade stuck at feather, and the rotor imbalance effects over the turbine structure starts to dominate.

11.6 Conclusion

This chapter studies the structural loading effects of various pitch system faults in a floating wind turbine. The considered faults include the bias and gain errors in pitch sensor measurements, the performance degradation of the pitch actuator, in addition to the actuator stuck and actuator runaway faults. The simulations use the utility-scale 5-MW wind turbine mounted on the barge platform model subject to different wind and wave profiles that correspond to the full load region. The turbine is equipped with the standard GSPI controller with two control loops, the first for collective pitch control which is engaged in the full load region, and the second loop is for generator torque control that switches the control objective according to the operating region. Different fault magnitudes are also considered in order to assess the magnitude effect on the turbine. Moreover, different performance metrics are used to evaluate the fault effects on the turbine structure.

Regardless of the fault magnitude, LSS moments in addition to the tower torsional moment are the most affected measures by pitch sensor faults. However, the effect depends on the fault type, magnitude, and operating condition. While the pitch sensor bias has the maximum DEL in the middle of the full load region, the pitch sensor gain fault shows direct dependency of the DEL with wind speed.

Actuator performance degradation has effect on the turbine structure only if the actuator has very slow response ($M3$), otherwise, the effect is marginal as the faulty actuator dynamics are still higher than the turbine dynamics. This result is strongly related to the type of pitch controller used by the turbine for power production in the full load region. The implemented strategy employs the collective pitch control concept to pitch the blades away from the wind as the wind speed exceeds its rated value, which will reduce the aerodynamic efficiency as a result, and maintain the rotor speed close to its rated value. The used GSPI controller has reduced gains (compared to the gains used for similar controllers of

offshore turbines) in order to increase platform pitch motion damping, this in its turn, decreases the demand for the pitch system giving the chance even for the slow pitch system to follow—to some limit—the controller commands. Therefore, if the control strategy is changed, and the demands on the pitch system are increased, the slower pitch system response will fail to respond on time and rotor imbalance will build up resulting in an increase in structural loading. A good example for such increased demands on the pitch system is the usage of IBP control strategy to accommodate the changes in the turbulent wind profile, or to compensate the vertical wind shear, or even to use the IBP to build up a restoring moment over the rotor disk that can counteract the pitch moment of the platform due to waves.

Actuator stuck shows a different effect on the turbine structure, starting with the increased blade root loading of the faulty blade that stuck at angles close to zero and increases with the wind speed. LSS and tower bending and torsional moments are also affected by this fault where the moments are increased up to 5 times in some cases. Furthermore, actuator runaway has substantial effect on the turbine structure, namely on tower bending and torsional moments, and an LSS bending moments.

The barge platform motion is mainly affected by the actuator stuck and actuator runaway, while other faults show negligible influence. The actuator stuck excites the platform pitch motion as a response to the fault-induced increase in generator power error. However, the excited pitch motion is still small compared to that caused by the actuator runaway fault. This later fault also excites the platform roll and yaw motions with amplitudes that depend on the mean wind speed. Other platform concepts might show different response to these faults due to their own dynamics, which is different from the studied barge platform; therefore, the presented results are limited to the barge platform concept.

Finally, in some cases, the process that the fault affects the turbine structure is explained; in other cases, more work is needed to completely understand the connection between the introduced fault and obtained result due to the high complexity of the turbine dynamics and the coupling between the modes in addition to the aero-structural dynamical interaction where the fault is introduced.

References

1. Musial W, Butterfield S, Ram B (2006) Energy from offshore wind. In: Offshore technology conference, NREL/CP-500-39450, Houston, Texas
2. Jonkman J, Matha D (2009) A quantitative comparison of the responses of three floating platforms. In: European offshore wind 2009 conference and exhibition, NREL/CP-500-46726, Stockholm, Sweden
3. Biester D (2009) Hywind: siemens and statoilhydro install first floating wind turbine (online). http://www.siemens.com/press/pool/de/pressemitteilungen/2009/renewable_energy/ERE200906064e.pdf
4. Jonkman J (2007) Dynamics modeling and loads analysis of an offshore floating wind turbine. Ph.D. thesis, National Renewable Energy Laboratory
5. Jonkman JM (2008) Influence of control on the pitch damping of a floating wind turbine. National Renewable Energy Laboratory, NREL/CP-500-42589

6. Larsen TJ, Hanson TD (2007) A method to avoid negative damped low frequent tower vibrations for a floating, pitch controlled wind turbine. J Phys 75:1–11. doi:10.1088/1742-6596/75/1/012073

7. Chaaban R, Fritzen CP (2014) Reducing blade fatigue and damping platform motions of floating wind turbines using model predictive control. In: IX international conference on structural dynamics, Porto, Portugal

8. Namik H, Stol DK (2010) Individual blade pitch control of floating offshore wind turbines. Wind Energy 13:74–85

9. Lackner MA (2009) Controlling platform motions and reducing blade loads for floating wind turbines. Wind Eng 33(6):541–554. doi:10.1260/0309-524X.33.6.541

10. Wilkinson M, Hendriks B (2011) Reliability focused research on optimizing wind energy systems design, operation and maintenance: tools, proof of concepts, guidelines & methodologies for a new generation. Tech Rep, Reliawind. www.ReliaWind.eu, FP7-ENERGY-2007-1-RTD

11. Bachynski EE, Etemaddar M, Kvittem MI, Luan C, Moan T (2013) Dynamic analysis of floating wind turbines during pitch actuator fault, grid loss, and shutdown. In: 10th deep sea offshore wind R&D conference, Trondheim

12. Etemaddar M, Gao Z, Moan T (2012) Structural load analysis of a wind turbine under pitch actuator and controller faults. In: The science of making torque from wind, Oldenburg, Germany

13. Jonkman J, Butterfield S, Musial W, Scott G (2009) Definition of a 5-MW reference wind turbine for offshore system development. Tech Rep, National Renewable Energy Laboratory (NREL), NREL/TP-500-38060

14. Bossanyi EA (2003) Individual blade pitch control for load reduction. Wind Energy 6:119–128

15. Esbensen T, Sloth C (2009) Fault diagnosis and fault-tolerant control of wind turbines. Master's thesis, Aalborg University

16. Hansen MH, Kallesøe BS (2007) Servo-elastic dynamics of a hydraulic actuator pitching a blade with large deflections. J Phys Conf Ser 75:012077

17. Jonkman JM, Buhl ML Jr (2005) Fast user's guide. Tech Rep, National Renewable Energy Laboratory (NERL), NREL/EL-500-38230

18. International Electrotechnical Commission (2009) Wind turbines: Part 3: Design requirements for offshore wind turbines. IEC61400-3

19. Jonkman B (2009) Turbsim user's guide (version 1.5). Tech Rep, National Renewable Energy Laboratory (NREL)

20. Mohammadpour J, Scherer CW (2012) Control of linear parameter varying systems with applications. In: Adegas FD, Sloth C, Stroustrup J (eds) Chapter 12, Structured linear parameter varying control of wind turbines. Springer, Heidelberg

21. Downing S, Socie D (1982) Simple rainflow counting algorithms. Int J Fatigue 4(1):31–40. doi:10.1016/0142-1123(82)90018-4

22. Robertson A, Jonkman J (2011) Loads analysis of several offshore floating wind turbine concepts. In: International society of offshore and polar engineers 2011 conference, NREL/CP-5000-50539

Part IV
Vibration Mitigation

Chapter 12
Vibration Mitigation of Wind Turbine Towers with Tuned Mass Dampers

Okyay Altay, Francesca Taddei, Christoph Butenweg and Sven Klinkel

Abstract Because of its minor environmental impact, electricity generation using wind power is getting remarkable. The further growth of the wind industry depends on technological solutions to the challenges in production and construction of the turbines. Wind turbine tower vibrations, which limit power generation efficiency and cause fatigue problems with high maintenance costs, count as one of the main structural difficulties in the wind energy sector. To mitigate tower vibrations auxiliary measures are necessary. The effectiveness of tuned mass damper is verified by means of a numeric study on a 5 MW onshore reference wind turbine. Hereby, also seismic-induced vibrations and soil–structure interaction are considered. Acquired results show that tuned mass damper can effectively reduce resonant tower vibrations and improve the fatigue life of wind turbines. This chapter is also concerned with tuned liquid column damper and a semiactive application of it. Due to its geometric versatility and low prime costs, tuned liquid column dampers are a good alternative to other damping measures, in particular for slender structures like wind turbines.

Keywords Structural control · Tuned mass damper · Tuned liquid column damper · Semiactive · Soil–structure interaction

Nomenclature

In appearance order:

δ_s, δ_A	Logarithmic damping decrement-Structural and aerodynamic
D	Damping ratio
K_{FS}, C_{FS}, M_{FS}	Stiffness, damping coefficient, and mass of the foundation-soil system
S_{FS}	Dynamic stiffness of foundation-soil system
Ω	Excitation frequency

O. Altay (✉) · F. Taddei · C. Butenweg · S. Klinkel
Faculty of Civil Engineering, Chair of Structural Analysis and Dynamics,
RWTH Aachen University, Mies-van-der-Rohe-Str. 1, 52074 Aachen, Germany
e-mail: altay@lbb.rwth-aachen.de

u_F, P_F	Displacement and harmonic loading of foundation
G_S, ρ_S, υ_S	Shear modulus, density, and Poisson's ratio of soil
r_F	Equivalent radius of foundation
θ_φ, $\theta_{\varphi z}$	Rocking and torsional mass moments of inertia of foundation
K_x, K_y, K_z, $K_{\varphi z}$	Stiffness coefficients of foundation-soil system
C_x, C_y, C_z, $C_{\varphi z}$	Damping coefficients of foundation-soil system
f_D	Natural frequency of tuned mass damper/tuned liquid column damper
μ^*	Mass ratio between tuned mass damper and modal mass of structure
f_H	Natural frequency of structure
$f_{D,\mathrm{opt}}$, $D_{D,\mathrm{opt}}$	Optimal frequency and damping ratio of tuned mass damper/tuned liquid column damper
u, $\dot{u}$, $\ddot{u}$	Displacement, velocity, and acceleration of liquid column motion of tuned liquid column mass damper
δ_P	Pressure loss
ω_D	Fundamental circular frequency of tuned mass damper/tuned liquid column damper
γ_1, γ_2	1. and 2. geometric factor of tuned liquid column damper
$\ddot{x} + \ddot{x}_g$, $x + x_g$	Acceleration and displacement of structure caused by base excitation
L_1, L_2	1. and 2. effective length of liquid column
α	Angle of the liquid column
V, H	Vertical and horizontal length of the liquid column
A_V, A_H	Area of the vertical and horizontal liquid column
D_H, ω_H	Damping ratio and fundamental circular frequency of structure
μ	Mass ratio between tuned liquid column damper and modal mass of structure
$f(t)$	Dynamic excitation force
k_act, c_act	Stiffness and damping coefficient of seismic actuator
m_tf	Total mass of turbine and foundation
Ω_act	Frequency of seismic actuator
$f_g(t)$	Seismic excitation force
$x_{g,0}$, $\dot{x}_{g,0}$	Realized seismic foundation motions
$x_{g,seis}$, $\dot{x}_{g,seis}$	Desired seismic foundation motions

12.1 Introduction

Wind turbines count as one of the most important techniques of renewable energy production and perform an increasing share in the electric power market. According to the statistics presented in the annual report of Global Wind Energy

Council (GWEC), the energy generation capacity of the worldwide operating wind farms increased in 2012 by about 20 % and reached a total of 283 GW [16].

A further growth of the wind energy industry depends mainly on the technological developments, especially considering production and construction methods of the plants. From certification authorities, specified minimum design lifetime of a new wind turbine is currently only 20 years, which, compared with the production and maintenance costs economically is not sufficient enough. The main challenge to the design of a wind turbine is caused by alternation loadings initiated by wind, waves, and earthquake-induced dynamic excitation forces. For instance, the load change of the rotor blades and thereby of the entire tower structure of a wind turbine designed for 20 years corresponds to approximately $2 \cdot 10^8$ [18], which is about 100 times more than a standard highway bridge.

The performance of a wind turbine is primarily determined by its tower height and rotor diameter. With respect to lifetime problem and for the purpose of building higher and more effective plants, it is necessary to improve the structural dynamics of wind turbines. Several methods can be applied to mitigate the tower vibrations and achieve better structural response.

12.2 Tower Vibrations

Onshore wind turbine towers carry, besides static gravity loading from nacelle, also wind-induced loadings from rotor mainly in fore-aft direction. In side-to-side direction wind flow causes vortex-induced tower vibrations. Furthermore, in seismic regions turbine towers must withstand earthquake-induced extreme loads. These dynamic loadings threaten structural safety and affect the lifetime of plants.

Wind turbine towers show different dynamic responses depending on the utilized construction material. Hereby, besides material strength, the damping properties must also be considered. The dynamic characteristics of a wind turbine tower rely also on the structural properties. Especially, stiffness and mass, which determine the natural frequencies of the tower, are important for the resonant behavior of wind turbines.

12.2.1 Wind Loading

Depending on the wind speed and turbulence intensity wind induces different tower vibrations, which can be categorized as periodic vibrations of resonant behavior and transient vibrations.

During normal wind conditions at low wind speeds, tower vibrations are mainly characterized by resonant type of oscillations. At these wind speeds, the revolution frequency of rotor blades is usually quite near the fundamental frequency of the tower fore-aft modes. Wind turbines behave like a harmonically oscillated single
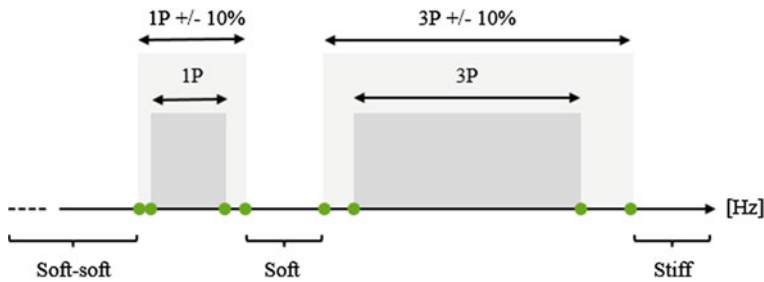
Fig. 12.1 Classification of wind turbine towers depending on the revolution frequencies of the rotor blades

degree Of freedom (SDOF) system. Because of low damping values enormous tower deflections can occur. During design process, in order to prevent these resonant vibrations, the stiffness and therefore the fundamental frequency of the tower are chosen depending on the rotor blade revolution frequencies. Hereby, the rotational frequency of the rotor is called one-per-revolution frequency (1P). Depending on the number of blades, the blade passing frequency is called two-per-revolution (2P) or three-per-revolution frequency (3P). As shown in Fig. 12.1, according to the relationship between tower fundamental frequency and the revolution frequencies of the rotor blades, wind turbine towers are classified as stiff, soft, and soft–soft. The 1P and 3P regions shown in Fig. 12.1 are defined by the cut-in and rated rotor speeds. Therefore, for instance, a soft tower can still response resonantly during start-up phase below cut-in wind speeds. Depending on the duration, this fatigue loading influences the lifetime of a wind turbine.

Turbulence wind loading depends on the average wind speed and turbulence intensity. For the load calculations, several wind models are described in certification documents for the wind turbines. Hereby, also the site-specific conditions and interactions with other wind turbines can be taken into account.

The amplitudes of the turbulence-induced tower vibrations depend mainly on the damping property of the plants, which consists of aerodynamic and structural damping. The damping ratio of a wind turbine can be calculated by the logarithmic damping decrement using the values in Table 12.1 [13]. According to this method, a steel turbine tower has approximately a damping ratio of 1.4 %.

As mentioned before, the load change in the entire tower structure of a wind turbine designed for 20 years corresponds to approximately $2 \cdot 10^8$ [18]. Half of the

Table 12.1 Logarithmic damping decrements and damping ratios of wind turbines [13]

Structural type	δ_S	δ_A	$\delta = \delta_S + \delta_A$	$D = \delta/2\pi$ (%)
Steel tower	0.015	0.070	0.085	1.4
Concrete tower	0.040	0.060	0.100	1.6

δ Logarithmic damping decrement
D Damping ratio

load change occurs during wind speeds below rated wind speed [18]. Therefore, it can be concluded that half of the fatigue loading is caused by periodic tower vibrations.

12.2.2 Seismic Loading

Annual installations of wind power have increased constantly across the world over the last decades, expanding the market toward seismically active areas. If a project is located at sites with relevant seismic hazard, the wind unit must be designed considering a reasonable likelihood of earthquake occurrence during the operational state or an emergency shutdown. In some cases, seismic plus operational loads may govern tower and foundation design. Figure 12.2 shows the representation of the seismic hazard in Europe in combination with the average wind speed at 50 m from the ground. The latter is a key issue for the site suitability assessment for wind power and must be greater than 5-6 m/s. The map reports also annotations of the wind power installations in European countries by the end of 2012 according to GWEC [16]. A large part of the south European coastal areas presents high seismic hazard and such wind conditions, which are sufficiently suitable for financial returns from modern wind turbines.

Norms and guidelines come to the aid of practitioners, providing general suggestions for the seismic design of wind turbines. However, an accurate approach for the superposition of earthquake and wind effects is still missing.

This topic has aroused the interest of researchers all over the world. Seismic design loads are less crucial than standard design loads under extreme wind conditions [7, 25, 26]. Therefore, the load combinations prescribed by the International Electrotechnical Commission (IEC) [19] provide also a seismic safe design.

Also, Ritschel compared the loads occurring during earthquakes with IEC design loads for the case of a 60 m hub height wind turbine [28]. Modal and transient analyses were also compared. The earthquake response was covered by the design load at most of the tower sections. However, a peak acceleration of 0.3 g may be considered the maximum seismic excitation, a 60 m hub height wind turbine can withstand. For the blades, earthquake loads are much lower (about 70 %) than the design loads, governed typically by the 50-years gust load case, therefore are not decisive. They found that the modal approach yields relatively conservative results near the tower base with respect to the results of transient analysis. This work confirmed the general rule that a frequency domain analysis produces more conservative results than a time domain analysis, because of the smaller number of considered participating modes. However, in the frequency domain, phase information gets lost and possible in-phase summation of wind and seismic signals cannot be detected. Transient analyses are generally preferred because of the higher accuracy and more realistic representation of the problem.
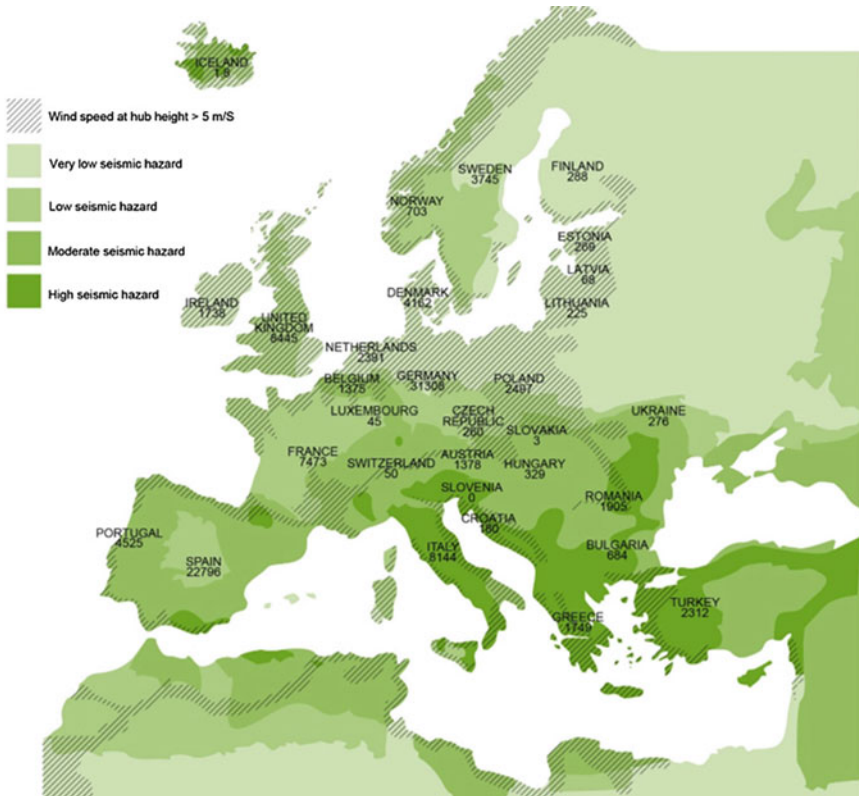
Fig. 12.2 Seismic hazard map of Europe with annotation of suitable site for wind power installation with average wind speed at 50 m from the ground >5 m/s and of wind power installed in each country by the end of 2012

In practice, the evaluation of earthquake effects can be performed through different approaches, depending on the aim of the investigation. Focusing on the treatment of seismic effects on wind turbine, besides the usual building codes such as Eurocode (EC), International Building Code (IBC), and German code (DIN), one may refer to the following special guidelines for wind turbine:

- IEC, EN 61400-1:2005 + A1:2010: Design requirements [19];
- Det Norske Veritas and Risø National Laboratory, Guidelines for Design of Wind Turbines 2002 [14];
- American Wind Energy Association-AWEA, ASCE/AWEA RP2011: Recommended Practice for Compliance of Large Land-based Wind Turbine Support Structures 2011 [6];
- Germanischer Lloyd Industrial Service-GL, Guideline for the certification of wind turbine GL-Chap. 2.4.2 [17];
- Danish Standards-DS, DS472 1992 [10];

- Deutsches Institut für Bautechnik-DIBt, Richtlinie für Windenergieanlagen Einwirkungen und Standsicherheitsnachweise für Turm und Gründung, 2012 [13].

The majority of the standard codes suggests an idealization of wind turbine as a vertical beam with a concentrated mass at the top. The latter includes the weight of rotor, nacelle, gear box, and a part of the tower.

Any analysis procedure is permitted for the evaluation of horizontal seismic forces: Equivalent lateral force, modal response spectrum, and response history analysis. The seismic forces are then combined with the operational loading equal to the greatest between:

1. Design load during normal power production at the rated wind speed and
2. Design load calculated for an emergency stop at rated wind speed.

The partial safety factors for all load components are set to 1.0.

A very conservative method is presented in Annex C of the IEC [19], where the natural frequencies higher than the first are neglected and the wind turbine is idealized as an SDOF system. Once the natural period of the SDOF system is determined, a correspondent spectral ordinate is selected from the standard design response spectrum. Multiplying the spectral acceleration by the mass of the SDOF, an equivalent static seismic load is obtained. In this case, a standard design response spectrum with a damping coefficient of 1 % is applied.

As described above, standard codes tend to suggest simplified techniques, which are suitable for normal civil buildings. However, a more detailed modeling of the seismic response of wind turbines can be achieved with the aid of computer-aided aerodynamic tools. Nowadays, aerodynamic computational tools are widely used and have become an indispensable support for design considerations, especially when dealing with nondeterministic phenomena, such as earthquake and wind.

12.2.3 Soil-Structure Interaction

The first step in any dynamic analysis is the determination of the structural dynamic properties. These depend on the performance of all components, from the tip of the rotor blades to the underlying ground. During this step, the interaction between the soil and the structure so-called soil-structure interaction (SSI) must be taken into account because of several interrelated effects:

- First of all the dynamic natural properties of the structure are modified by the presence of a compliant soil.
- Consequently, the minimum frequency separation between the natural frequency of the structure and the rotor operational frequency (1P) as well as the blade passing frequency (2P or 3P) may be violated and resonance effects may raise.
- On the one hand, the frequency content of the dynamic load may lead to vibration amplification or attenuation phenomena, with possible high shear force and overturning moment at the tower base.

- On the other hand, the compliance of the soil attributes a certain additional damping properties to the structural SSI system compared with the fixed base model, leading to energy dissipation.
- Moreover, large motions of the foundation may disturb the control processes of the machine leading to an inefficient production or even an emergency shutdown.

It is obvious from the above discussed points that the SSI effects can act in opposite directions and it is not possible to establish deductively whether the displacements of the tower will decrease or not. In general, for each specific configuration of wind unit and underlying soil, an exhaustive investigation is necessary. Norms and guidelines [6, 13, 14] provide only few suggestions in regard to the SSI analysis. Indeed, the awareness of these sophisticated aspects encounters hardly a straightforward application in practical regulations and therefore it is only roughly mentioned.

An all-encompassing dynamic analysis of a soil–wind turbine system appears certainly intricate. Anyway, it is possible to isolate the decisive aspects of the problem and reduce the number of variables at play.

In dynamic SSI, the modeling procedures can be classified into rigorous and approximate. The former are usually used in the substructure method, while the latter lend themselves to the direct method of analysis. In the substructure method, the soil and the structure are analyzed separately with different approaches and then coupled at the interface enforcing compatibility and equilibrium conditions, while in the direct methods the whole system is solved through a unique one-step technique.

Rigorous modeling satisfies the radiation condition for unbounded media, which enforce that the wave propagation energy is radiated toward infinity. This condition can be used to find the fundamental solution (also called Green's functions) of the wave propagation problem in each specific medium configuration (i.e., half space and full space). Finally, boundary integral equations can be built upon the fundamental solutions. The problem can be solved also numerically discretizing the interface in boundary elements. This procedure is called boundary element method (BEM). The main advantage of rigorous modeling is that the radiation condition is automatically satisfied and the problem size is reduced by one, as only the interface between soil and structure must be taken into account. Further explanations can be found in [24]. However, the fundamental solution is only available for the homogenous isotropic half space. For complicated soil configurations, the fundamental solutions can be found only numerically and no closed analytical form is available. For example, for the horizontally layered unbounded medium, one may resort to the thin layer method (TLM) [9] or to the precise integration method (PIM) [20] for computing the Green's functions.

Among approximate modeling methods, there are several combinations of finite element method (FEM) and artificial boundaries (transmitting, viscous, paraxial, etc.), which have highly energy absorption capabilities. Also, infinite elements can be used as an extension of the finite element method. The drawbacks of these

extended FEM are the large size of the model, as the soil boundary must be located far away from the structure and the residual error caused by the wave energy reflection at the model boundary.

Besides advanced numerical methods, the most popular approach in practice for SSI analysis applied to wind turbine is the spring-dashpot analog model. Here, the foundation-soil system can be converted into a mechanical model of springs, dashpots, and masses (Lysmer's analog), also called lumped parameter model (LPM). This model represents the soil trough in just two free parameters, the stiffness K_{FS} and the damping C_{FS} coefficients, and gives good results for the low and medium frequencies. The mass parameter M_{FS} can be added to obtain a better fit between the real system and the LPM. The dynamic stiffness S_{FS} of the LPM can be expressed as a function of the excitation frequency Ω as

$$S_{FS}(\Omega) = K_{FS} - \Omega^2 M_{FS} + i\Omega C_{FS} \qquad (12.1)$$

The dynamic stiffness relates the displacements of the foundation $u_F(\Omega)$ to the applied harmonic load $P_F(\Omega)$ as

$$u_F(\Omega) = \frac{P_F(\Omega)}{S_{FS}(\Omega)} \qquad (12.2)$$

The model can be enriched with additional lumped masses, dashpots, and springs, increasing the number of free parameters. This is especially important for layered half-space or stratum over bedrock.

Previous research works [1, 7, 8, 28, 33] proved that LPMs can predict accurately the dynamic response of soil-turbine systems in the case of a homogeneous isotropic medium. They confirmed that if the soil compliance is included, the natural frequencies of the system decrease with respect to the fixed base system and the most affected frequencies are those related to the second and third bending modes. Investigation of the influence of soil layering on the turbine dynamics can be found in [5, 30, 31], where rigorous methods were applied.

Standard codes usually suggest a representation of the foundation-soil influence in terms of a set of linear frequency-independent springs, connected the turbine model at the foot of the tower (Fig. 12.3).

Stiffness coefficients can be computed according to the DNV/Risø Guidelines [14] or to the DIBt Provisions [13], which refer to the recommendations of the Building Ground Dynamics Work Group [12]. Alternative coefficient formulas may be used if justified by rational engineering analysis.

The LPMs proposed by standard codes are generally made up of six uncoupled springs, one along each of the six degrees of freedom. They are frequency independent and no coupling between translational and rotational degrees of freedom is considered. The LPM can be implemented in structural multidegrees of freedom model in the form of diagonal stiffness and damping matrices. The matrix coefficients depend on the soil properties (shear modulus G_S, density ρ_s, Poisson's ratio υ_S) and on the foundation geometry (a representative length of the footing and

Fig. 12.3 Wind turbine model with soil springs for the soil–structure interaction influence

mass moment of inertia). The foundation geometry can be idealized as an equivalent rigid disk footing of radius r_F (Fig. 12.4) in order to simplify the calculation of mass moments of inertia.

The LPM proposed by the DNV/Risø [14] does not include dashpots or fictitious masses. The formulas for the soil spring coefficients address the case of homogeneous half space, stratum over bedrock, and stratum over half space. From the formulas it emerges that, the thinner the layer becomes the stiffer the generalized spring is. A comparison between the DNV model and rigorous model can be found in [32] (Fig. 12.5).

The DIBt coefficients can be computed according to the formulas in Table 12.2. Compared to the DNV/Risø model, the DIBt LPMs include also six dashpots (one along each of the six degrees of freedom).
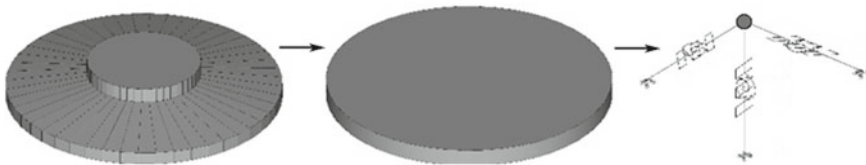
Fig. 12.4 Modeling of the foundation-soil system according to standard codes [13, 14]

Fig. 12.5 Comparison of vibration mitigation methods and tower vibration characteristics
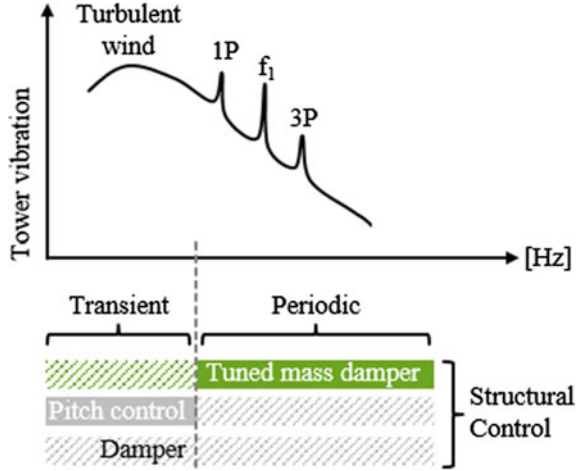
Table 12.2 Stiffness and damping coefficients for the modeling of the foundation-soil system [14]

	Stiffness coefficients	Damping coefficients
Horizontal translation	$K_x = K_y = \dfrac{8G_S r_F}{2 - v_S}$	$C_x = C_y = \dfrac{4.6 r_F^2}{2 - v_S}\sqrt{G_S \rho_S}$
Vertical translation	$K_z = \dfrac{4G_S r_F}{1 - v_S}$	$C_z = \dfrac{3.4 r_F^2}{1 - v_S}\sqrt{G_S \rho_S}$
Rocking	$K_\varphi = \dfrac{8G_S r_F^3}{3(1 - v_S)}$	$C_\varphi = \dfrac{0.8 r_F^4}{(1 - v_S)(1 + B_\varphi)}\sqrt{G_S \rho_S}$ $B_\varphi = \dfrac{3(1 - v_S)}{8}\dfrac{\theta_\varphi}{r_F^5 \rho_S}$
Torsion	$K_{\varphi z} = \dfrac{16 G_S r_F^3}{3}$	$C_{\varphi z} = \dfrac{2.3 r_F^4}{1 + 2B_{\varphi z}}\sqrt{B_{\varphi z} G_S \rho_S}$ $B_{\varphi z} = \dfrac{\theta_{\varphi z}}{r_F^5 \rho_S}$

In case of embedded foundations, a modification of the above reported coefficients is necessary. An investigation of the soil–structure interaction effects on the wind turbine dynamics is presented in Sect. 12.4.3.4.

12.3 Vibration Mitigation Methods

In order to mitigate wind turbine tower vibrations several systems are invented and applied. The most common methods can be classified as blade pitch control, auxiliary dampers, and tuned mass dampers (TMD). Figure 12.5 shows some of these methods and categorizes them according to the vibration characteristics by means of a soft tower. As discussed in Sect. 12.2.1, the dynamic tower response depends mainly on the wind speed and contains both transient and periodic components. The efficiency of a mitigation method relies on the response
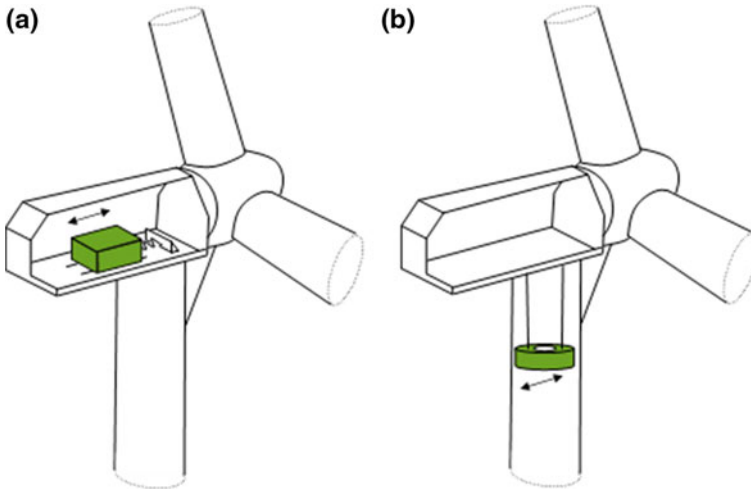
Fig. 12.6 Wind turbine with tuned mass damper (**a**) and pendulum damper (**b**)

characteristics of the tower. As known from other slender structures, TMD can dissipate especially periodic vibrations. Therefore, they count as an effective method to mitigate oscillations with definite frequencies like the revolution frequencies 1P and 3P, or vibrations of resonant nature, referred to as f_1 in Fig. 12.5.

12.3.1 Blade Pitch Control and Brake Systems

To prevent excessive tower vibrations and generating loading most of the modern wind turbines use blade pitch control and brake systems, which regulate automatically the angle and speed of rotor blades depending on the wind speed and operational conditions. By means of these measures, the turbines can generate constant power and avoid critical high rotor speeds. This vibration mitigation method is especially effective at high wind speeds inducing transient tower vibrations.

12.3.2 Dampers

Wind turbines feature very low damping characteristics compared with other structures. As shown in Sect. 12.2.1, the total damping ratio of a wind turbine resulting from structural and aerodynamic damping equals 1–2 %. With the use of auxiliary dampers, the structural damping properties can be improved. For instance, hydraulic dampers with viscose liquids as a passive application or with magnetorheological and electrorheological fluids as a semiactive damper can dissipate the

oscillation energy locally at installation spots of the turbine similar to the buffers used by the automobile industry. Hereby, due to their adaptation characteristic, semiactive dampers can mitigate vibrations over a broader frequency range compared with passive elements. In order to control tower vibrations in all directions, both passive and semiactive dampers are to be positioned in the inner side of the turbine tower in polar formation, which blocks the tower shaft and disturbs the accessibility of the nacelle. Material costs and necessary maintenance effort make the effective application of the auxiliary dampers difficult.

12.3.3 Tuned Mass Dampers

For conventional slender structures, the mitigation of wind-induced periodic vibrations is commonly achieved through TMD. A standard TMD consists of an auxiliary mass, which is attached to the main structure by means of spring and dashpot elements. The natural frequency of a TMD is defined by its spring constant and the damping ratio caused by the dashpot. The tuned parameter of the TMD enables the auxiliary mass to oscillate with a phase shift with respect to the motion of the structure, leading to damping forces on the structure. TMD can suppress especially periodic vibrations very effectively. Nevertheless, because of mechanical challenges, it is not easy to find a suitable spring element, which can be tuned to the fundamental frequencies of wind turbines, as they are generally lower than 0.4 Hz. Therefore, TMD can mainly be used to mitigate higher tower modes.

A pendulum damper counts also as a TMD and consists of an auxiliary mass, which can be hung below the nacelle of a wind turbine and supported by dampers or friction plates. The pendulum length is tuned to the natural frequencies of the turbine tower modes. For a wind turbine with a fundamental frequency of 0.4 Hz, the resulting pendulum length is according to Eq. 12.3 more than 1.5 m. Hereby, f_D is the damper frequency, L pendulum length, and g acceleration due to gravity. For lower frequencies this value increases exponentially. To solve this problem, multistep pendulum dampers can be used. Hereby, the auxiliary mass is attached to multiple pendula, which are interlinked to each other by various mechanical joints. Figure 12.6 shows a wind turbine with TMD and pendulum damper.

$$f_D = \frac{1}{2\pi}\sqrt{\frac{g}{L}} \tag{12.3}$$

12.3.3.1 Calculation of Optimal Parameters of Tuned Mass Damper

For the calculation of optimal TMD parameters, especially the criteria developed by Den Hartog and Warburton are commonly used [12, 32]. The results of these applied criteria are optimal values for the natural frequency and damping ratio of TMD.

Using the resonance curves of a harmonically excited SDOF oscillator, Den Hartog derived the optimal frequency and the damping ratio as in Eq. 12.4–12.5. Hereby, μ^* is the ratio between effective mass of TMD and modal mass of the structure. f_H is the natural frequency of the structure.

$$f_{D,\text{opt}} = f_H \frac{1}{1 + \mu^*} \tag{12.4}$$

$$D_{D,\text{opt}} = \sqrt{\frac{3\mu^*}{8(1 + \mu^*)^3}} \tag{12.5}$$

The same procedure can also be used with the tuning criterion of Warburton, who has enlarged the criterion of Den Hartog also for other stochastic excitations such as earthquake. The tuning parameters of a TMD attached to a stochastically excited SDOF can be calculated by Eq. 12.6–12.7.

$$f_{D,\text{opt}} = f_H \frac{\sqrt{1 - \mu^*/2}}{1 + \mu^*} \tag{12.6}$$

$$D_{D,\text{opt}} = \sqrt{\frac{\mu^*(1 - \mu^*/4)}{4(1 + \mu^*)(1 - \mu^*/2)}} \tag{12.7}$$

12.3.4 Tuned Liquid Dampers

Tuned liquid dampers such as tuned sloshing damper (TSD) and tuned liquid column damper (TLCD) count also as TMD. Figure 12.7 shows a wind turbine with a TSD and TLCD. These dampers have naturally very low fundamental frequencies and therefore can be easily tuned to the tower frequencies of wind turbines. As these dampers use commonly water as auxiliary masses and do not need any mechanical elements like springs or joints, they feature a better alternative to other vibration mitigation methods for wind turbines.

12.3.4.1 Tuned Sloshing Dampers

The TSD consists of an open tank filled with a Newtonian liquid such as water with antifreeze. Depending on the tank geometry and liquid depth, different natural frequencies can be achieved. In order to control the vibrations effectively, TSD should be installed like TMD and pendulum damper near the tower top, for instance in the nacelle. As the turbine tower starts to vibrate, the movement of TSD tank causes the liquid to slosh and develop waves, which dissipate the oscillation energy. Hereby, the fundamental frequency of TSD depends on non-linear phenomena, which are caused by sloshing and tank–liquid interaction.
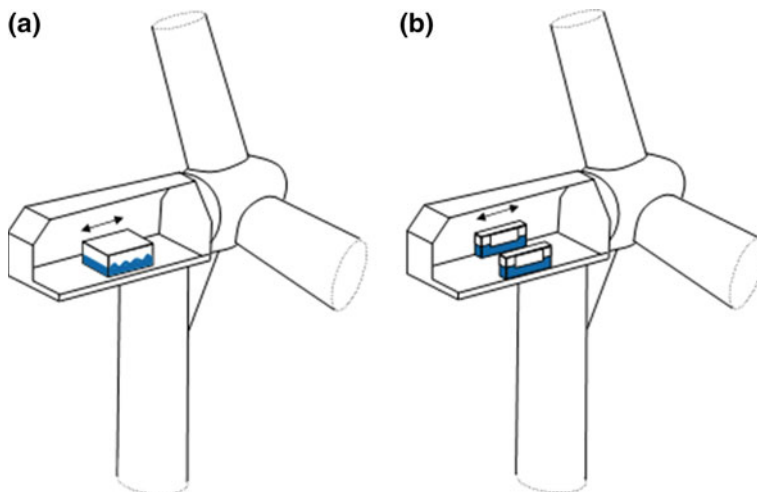
Fig. 12.7 Wind turbine with tuned sloshing damper (**a**) and tuned liquid column damper (**b**)

Further research is needed for a better prognosis of the efficiency of this damper for the wind turbines. A more stable vibration mitigation process can be achieved by TLCD, which is described in the following section. Figure 12.7 shows a wind turbine with a TSD.

12.3.4.2 Tuned Liquid Column Dampers

The TLCD, patented in 1910 by Frahm, consists of a U-shaped tank, which is filled similar to TSD with a Newtonian liquid [15]. Originally invented to mitigate rolling motions of ships, the TLCD counts as one the first damping devices. The vibration energy of the oscillating damper liquid dissipates by turbulence effects and friction caused local pressure loss. In civil engineering, TLCD became known first after the publications and patent application by Sakai [29]. In addition to low material and maintenance costs, because of the geometric flexibility, TLCD is assumed to be a better choice compared to other damping measures, particularly for slender structures like wind turbines.

Mathematical Description

Figure 12.8 shows a TLCD attached to a horizontally excited structure. The liquid motion and oscillation effects can be derived with the nonlinear Bernoulli equation, whereas the natural frequency of the liquid damper depends only on the geometry of the tank.
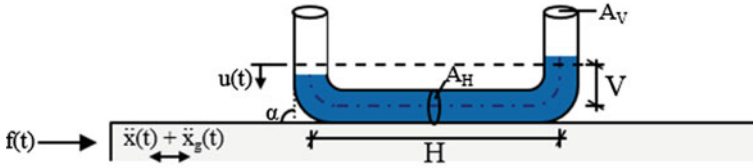
Fig. 12.8 A horizontally excited structure with a tuned liquid column damper

The equation of motion and the fundamental circular frequency of a TLCD are given in Eq. 12.8–12.9.

$$\ddot{u} + \delta_P|\dot{u}|\dot{u} + \omega_D^2 u = -\gamma_1(\ddot{x} + \ddot{x}_g) \tag{12.8}$$

$$\omega_D = \sqrt{\frac{2g}{L_1}\sin\alpha} \tag{12.9}$$

Hereby, the motion of the liquid column is defined by $u(t)$ and the motion of the structure, which is caused by a dynamic force and base excitation equal to $x(t) + x_g(t)$. The coefficient δ_P specifies the pressure loss, which is caused by turbulence and friction effects induced by changes in the stream direction and sectional area of the tank. The geometric factor γ_1 (Eq. 12.10) scales the interaction force between structure and TLCD depending on the geometry of the tank. The fundamental circular frequency ω_D of TLCD depends on the so-called effective length L_1 (Eq. 12.11) of the liquid column, inclination of the vertical tank parts α, and the acceleration g due to gravity. The geometric factor γ_1 and the effective length L_1 depend on the angle α, vertical length V and the horizontal length H of the liquid stream, and sectional areas A_V, A_H.

$$\gamma_1 = \frac{H + 2V\cos\alpha}{L_1} \tag{12.10}$$

$$L_1 = 2V + \frac{A_V}{A_H}H \tag{12.11}$$

The damping forces resulting from the impulse of the liquid mass are given in the following equation for a structure, which is idealized as an SDOF oscillator. Hereby, D_H and ω_H are the damping ratio and fundamental circular frequency of the structure, μ the mass ratio of liquid to modal mass of the structure, x_g the base motion, $f(t)$ an excitation force, and γ_2 a further geometric factor of TLCD.

$$\ddot{x} + 2D_H\omega_H\dot{x} + \omega_H^2 x = -\ddot{x}_g + f(t) - \underbrace{\mu(\ddot{x} + \ddot{x}_g + \gamma_2\ddot{u})}_{\text{Damping forces}} \tag{12.12}$$

$$\gamma_2 = \frac{H + 2V \cos\alpha}{L_2} \tag{12.13}$$

$$L_2 = 2V + \frac{A_H}{A_V}H \tag{12.14}$$

As described above, the fundamental frequency of TLCD depends on five geometric variables: V, H, A_V, A_H, and α. An increasing mass ratio μ causes an increase in the TLCD efficiency. The geometric factors γ_1 and γ_2 also influence the efficiency of TLCD. The damping effect reaches its maximum, if the geometric factor γ_1 scaled by γ_2 has its maximum. The interaction force of the structure acting on TLCD increases, if the geometric factor γ_1 also increases. Further, if the TLCD tank has a short height, the liquid can even slop over. To avoid this, it is better to keep γ_1 as low as possible and compensate the efficiency loss by maximizing the second geometric factor γ_2.

Calculation of Optimal Parameters of Tuned Liquid Column Damper

The optimal parameters of TLCD can be derived by applying tuning criteria of mechanical mass dampers, which can be easily adapted through analogy approaches. In order to use these equations with TLCD, the parameters of an equivalent TMD must be calculated. The analogy can be derived from the equation of motion of TLCD used by substituting liquid stream deflection u by $u^* = u/\gamma_1$. The mass ratio μ^* of TLCD can then be calculated as in Eq. 12.15. By using μ^* in the equations of Den Hartog or Warburton, the optimum frequency and damping ratio of TLCD can be found.

$$\mu^* = \frac{\mu\gamma_1\gamma_2}{1 + \mu(1 - \gamma_1\gamma_2)} \tag{12.15}$$

As the geometric factors γ_1 and γ_2 also influence the efficiency of TLCD, it is better to use an extended optimization approach, which also considers the mathematical description of the TLCD geometry within the tuning procedure as described in [2, 4].

Semiactive Tuned Liquid Column Dampers

Semiactive structural control systems can sense and adapt their dynamic behavior according to the actual condition of the main structure and environment. These adaptive devices offer a broad range of new application possibilities, which enable the trend toward design of economically more efficient and more esthetic structures. The adaptation of the damper parameters can be achieved by various methods.
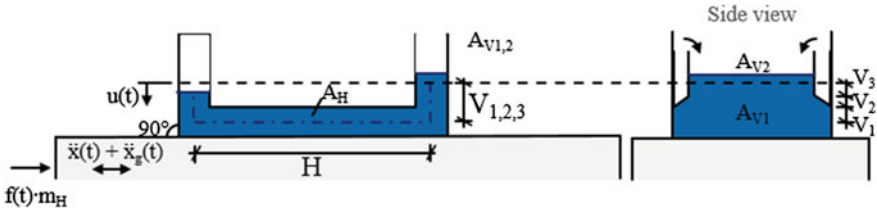
Fig. 12.9 Semiactive tuned liquid column damper [2, 3]

The semiactive Tuned Liquid Column Damper (S-TLCD) [2–4] uses the effects of the tank geometry to change both its natural frequency and damping ratio. Hereby, a control system identifies the dynamic properties of the turbine tower by sensors and calculates the optimum parameter of the damper. The semiactive damping system can tune itself to the changing tower dynamics, which are primarily caused by degradation effects, temperature, and soil conditions. To modify the frequency, S-TLCD uses movable panels, which change the flow area of the vertical sections of the damper tank. The damping ratio is adapted by using an orifice as patented by Sakai [29]. As a result, compared to a passive strategy, thanks of the permanent optimum tuning of the damper parameters, S-TLCD works more efficiently. Figure 12.9 shows the S-TLCD with a horizontally excited structure. In the side view of the damper the movable plates are illustrated.

The dynamic properties of S-TLCD can be determined using the Bernoulli equations as described in the last section for TLCD. Hereby, the effective lengths L_1 and L_2 are calculated by Eq. 12.16 and 12.17. The equation of motion and the frequency equation of TLCD (Eq. 12.8–12.9) can be used furthermore.

$$L_1 = 2V_3 + V_2 + \frac{A_{V2}}{A_{V1}}(2V_1 + V_2) + \frac{A_{V2}}{A_H}H \quad (12.16)$$

$$L_2 = 2V_3 + V_2 + \frac{A_{V1}}{A_{V2}}(2V_1 + V_2) + \frac{A_H}{A_{V2}}H \quad (12.17)$$

12.4 Reference Wind Turbine with Tuned Mass Damper

The effectiveness of TMD and TLCD is numerically verified by means of a 5 MW reference onshore wind turbine. In this chapter, the following calculations are presented:

- Onshore wind turbine with TMD
- Onshore wind turbine with TLCD
- Seismically excited onshore wind turbine with TMD
- Onshore wind turbine with TMD considering SSI

Table 12.3 Relevant system parameters of the reference wind turbine

System property	Parameter
Rating/configuration	5 MW/3 Blades
Control	Variable speed, collective pitch
Cut-in, rated and cut-out wind speed	3, 11.4, 25 m/s
Cut-in and rated rotor speed	6.9, 12.1 rpm
Hub height	90 m
Rotor diameter	126 m

12.4.1 System Properties of the Reference Wind Turbine

The turbine specifications are described by the U.S. Department of Energy's National Renewable Energy Laboratory (NREL). The relevant system properties are summarized in Table 12.3. Further specifications relating to the reference wind turbine can be found in the technical report by NREL [21].

The dynamic parameters of the turbine tower modes in fore-aft direction are listed in Table 12.4. In Fig. 12.10, the tower fundamental frequency and the number of rotor revolutions per minute are shown. As shown by this diagram, the first fore-aft tower frequency is placed between one- and three-per-revolution frequencies to avoid the occurrence of a resonant condition. However, the tower frequency is still quite near the three-per-revolution frequency. Therefore, especially by low wind speeds resonant tower vibrations are to be expected.

12.4.2 General Simulation Parameters

The simulation of the reference wind turbine with TMD is carried out by the aeroelastic dynamic horizontal axis wind turbine simulator FAST [22] with FAST-SC [23]. FAST is developed by NREL. FAST can simulate two fore-aft and two side-to-side bending modes of turbine tower. FAST-SC is an expanded code of FAST, which can simulate wind turbines with TMD and is developed by the University of Massachusetts. The wind turbine is simulated with a TMD connected in the nacelle to the tower top. TMD controls hereby vibrations in fore-aft direction. Seismic calculations are carried out combining FAST-Seismic [27] with FAST-SC and main program FAST.

Table 12.4 Natural frequencies, modal masses, and the structural damping ratio of tower fore-aft modes

	1. Mode	2. Mode
Natural frequency	$f_1 = 0.324$ Hz	$f_2 = 2.900$ Hz
Modal mass	$m_1 = 403.969$ t	$m_2 = 480.606$ t
Damping ratio	$D_1 = 1$ %	$D_2 = 1$ %

Fig. 12.10 One- and three-per-revolution frequencies of the reference wind turbine
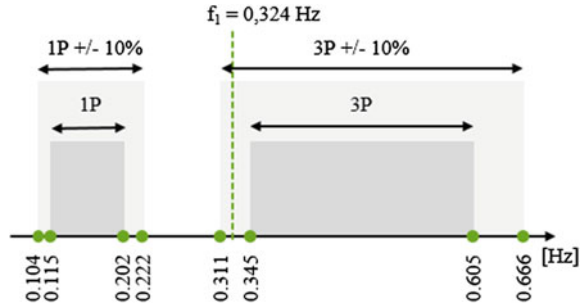
Table 12.5 Wind field simulation parameters

Number grid points	31×31
Grid dimension	145×145 m
Simulation time	1,030 s
Time step	0.05 s
Turbulence model	Kaimal
Turbulence type	Normal turbulence model
Wind profile type	Power law
Height of the reference wind speed	90 m
Mean wind speeds	3–25 m/s

The wind turbine is assumed to be in operation and system controls for variable speed and blade pitch are active. The simulations are carried out for normal wind conditions with a normal wind profile model as described in IEC 61400-1 [19]. The relevant simulation parameters of the wind field are listed in Table 12.5.

12.4.3 Simulation Results

12.4.3.1 Onshore Reference Wind Turbine with a Tuned Mass Damper

The first calculations are carried out by means of the onshore version of the reference wind turbine, which is assumed to be connected rigidly to the ground. In order to mitigate the first fore-aft tower bending mode vibrations, the TMD is tuned to the fundamental frequency of 0.324 Hz. The parameters of the turbine and TMD are summarized in Table 12.6.

Figure 12.11 compares the time histories of tower deflection with and without TMD for the cut-in, rated, and cut-out wind speeds. The frequency spectra of the tower responses are shown in Fig. 12.12. Hereby, resonant tower vibrations occur especially at the cut-in wind speed 3 m/s. This can be seen also in the frequency

Table 12.6 Parameters of the onshore reference wind turbine with TMD

Tower height	$h = 87.60$ m
Fundamental frequency of wind turbine	$f_H = 0.324$ Hz
Structural damping ratio of wind turbine	$D_H = 1$ %
Modal mass of wind turbine	$m_H = 403.969$ t
Mass ratio TMD/m_H	$\mu^* = 5$ %
Fundamental frequency of TMD	$f_{D,opt} = 0.309$ Hz
Damping ratio of TMD	$D_{D,opt} = 12.7$ %

Fig. 12.11 Tower deflection time histories of the onshore reference wind turbine for the cut-in, rated, and cut-out wind speeds
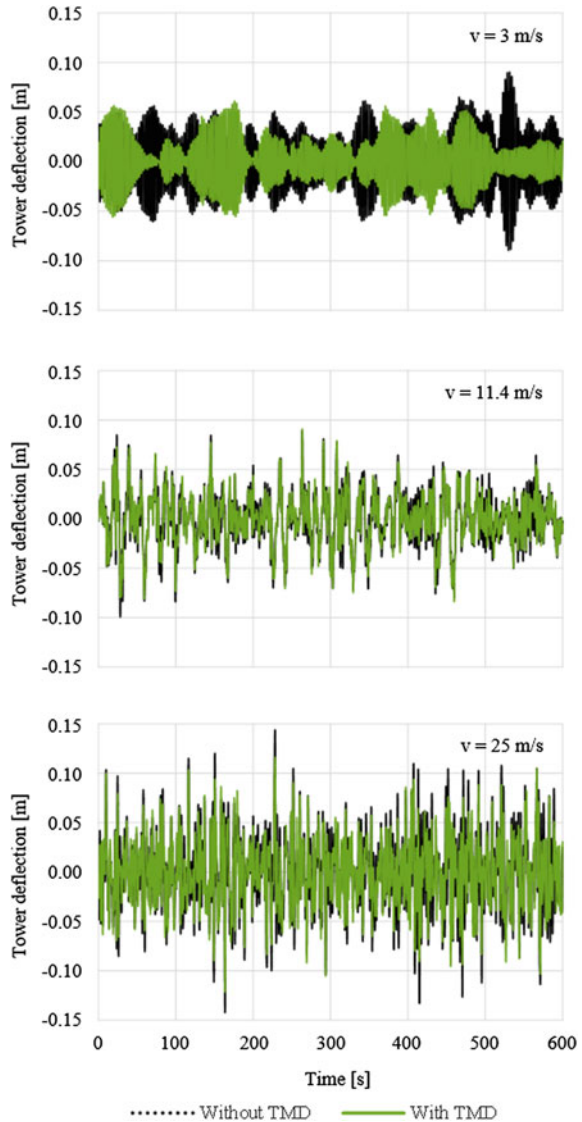
Fig. 12.12 Frequency
spectra of the onshore
reference wind turbine tower
response for the cut-in, rated,
and cut-out wind speeds
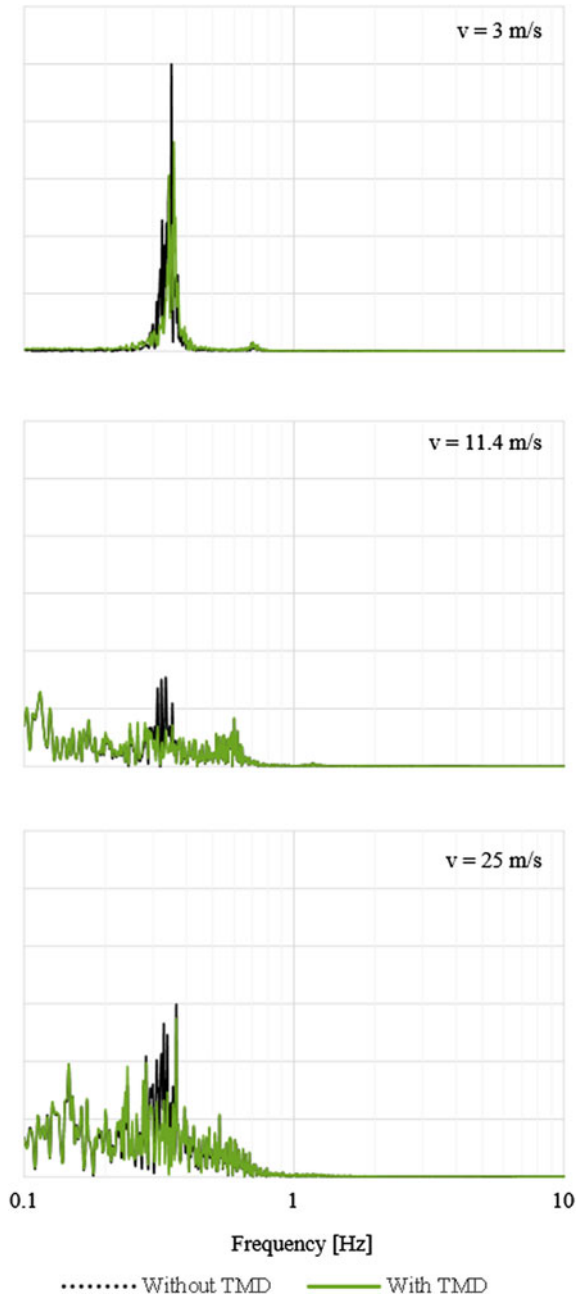
spectrum, where mainly two particular frequencies are being excited: the first
natural frequency of tower fore-aft mode and the 3P-frequency. At rated and cut-
out wind speeds, the response of the tower is more stochastic within broadband

Fig. 12.13 RMS-values of tower deflection of onshore reference wind turbine with and without TMD
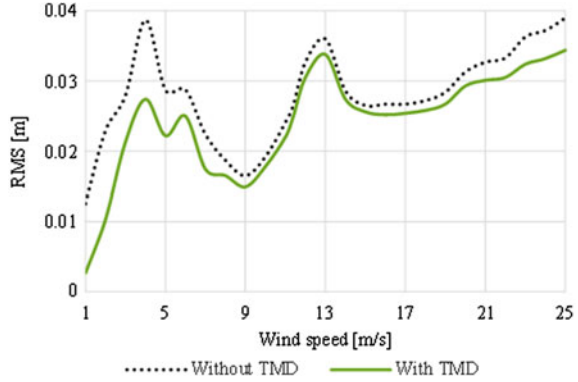
frequency spectra. TMD can suppress especially the resonant vibrations. Therefore, the efficiency of TMD at cut-in wind speed is much higher than at rated and cut-out speeds.

The efficiency of the TMD is evaluated by means of RMS-values of the turbine tower displacement in fore-aft direction. From the results with and without TMD, a reduction factor is calculated using Eq. 12.18. This factor is equivalent to the vibration energy, which is dissipated by TMD. From the total 1,000 s simulation time of the turbine response, the last 600 s is used for evaluation. Hereby, the specified time step of the simulations equals 0.0125 s. To eliminate the static tower deflection, which cannot be reduced by TMD, a high-pass filter is applied with a cutoff frequency at 0.1 Hz.

$$R = 1 - \frac{\text{RMS}_{\text{with TMD}}}{\text{RMS}_{\text{without TMD}}} \tag{12.18}$$

Figure 12.13 shows the resulting RMS-values. Figure 12.14 shows the difference between the RMS-values with and without TMD. The reduction factors for the analyzed wind speeds can be found in Fig. 12.15. As these graphs also summarize, the designed TMD mitigates the vibrations of the reference wind turbine, especially at wind speeds lower than 5 m/s. The reduction factor varies between 20 and 80 % (Fig. 12.15). At higher wind speeds, the tower vibrations are reduced slightly by means of the additional structural damping caused by TMD. Hereby, the reduction factor varies between 5 and 20 % (Fig. 12.15).

12.4.3.2 Onshore Reference Wind Turbine with a Tuned Liquid Column Damper

As described in Sect. 12.3.4.2 by means of the analogy, similar results can also be obtained using TLCD [4]. Table 12.7 lists the calculated optimum parameters of TLCD. Hereby, the active damper mass is, as for TMD, about 5 %. For the chosen

Fig. 12.14 Difference
between the RMS-values of
tower deflection of onshore
reference wind turbine with
and without TMD
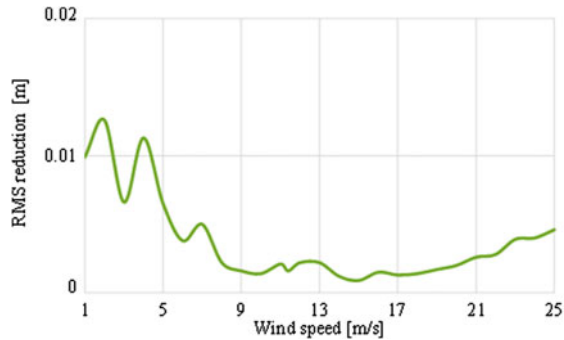
Fig. 12.15 Reduction factors
of TMD attached to the
onshore reference wind
turbine
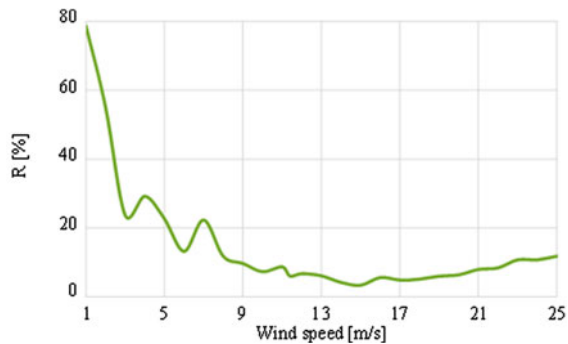
Table 12.7 Optimum TLCD
parameters

Horizontal length	$H = 9.932$ m
Vertical length	$V = 1$ m
Area of the horizontal section	$A_H = 3.086$ m^2
Area of the vertical section	$A_V = 1$ m^2
Inclination of the vertical tank parts	$\alpha = 90°$
Total damper mass	$m_D = 32.650$ t
Geometric factors	$\gamma_1 \cdot \gamma_2 = 0.58$

tank dimensions, a geometric factor $\gamma_1 \cdot \gamma_2$ of about 60 % is reached. With a distributed TLCD system or by changing the geometry, a further improvement of the damper efficiency can be achieved.

The calculated tower displacement for cut-in, rated, and cut-out wind speeds are presented in Fig. 12.16. Figure 12.17 shows the frequency spectra of these time histories. The results vary slightly from the vibration reduction reached by TMD. The main difference is caused by the liquid mass, which changes the natural frequencies of wind turbine and consequently influences also the dynamic response of the tower to certain wind speeds. The evaluation of the RMS-values is presented in Fig. 12.18.
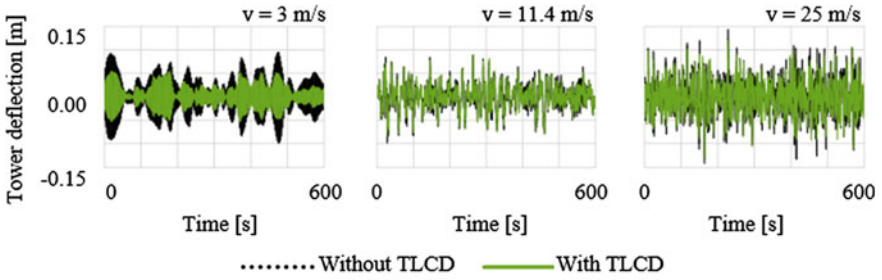
Fig. 12.16 Tower deflection time histories of the onshore reference wind turbine for the cut-in, rated, and cut-out wind speeds with and without TLCD
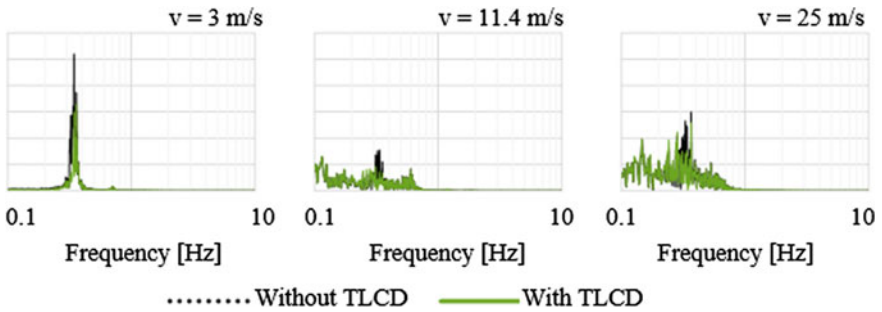
Fig. 12.17 Frequency spectra of the onshore reference wind turbine tower response for the cut-in, rated, and cut-out wind speeds with and without TLCD
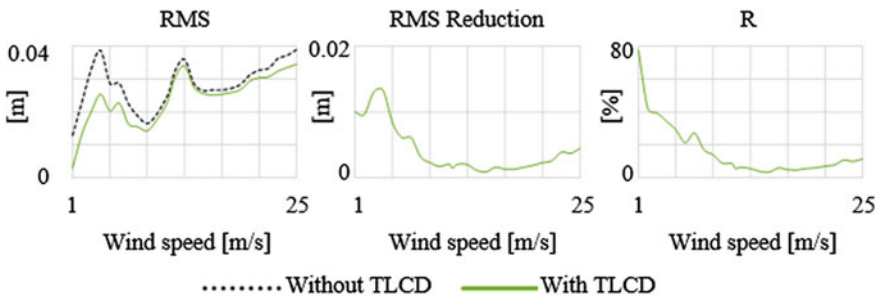
Fig. 12.18 RMS-values and reduction of tower deflection of onshore reference wind turbine with and without TLCD

12.4.3.3 Seismically Excited Onshore Reference Wind Turbine with Tuned Mass Damper

In the following paragraph, an example of seismic analyses of wind turbines is presented. These were carried out with the aid of the software FAST-Seismic [26, 27], which offers the possibility to consider the interaction between earthquake loadings and aerodynamics of wind turbines.

The FAST-Seismic is a modified version of FAST tool. In FAST-Seismic, it is possible to apply base shaking to the turbine model, which still includes all the feature of the normal FAST program. In FAST-Seismic, a damped oscillator of stiffness k_{act} is connected to the base of the turbine model. This damped actuator is used to translate specified motions into required seismic forces. The actuator stiffness k_{act} is calculated as

$$k_{act} = m_{tf}(2\pi\Omega_{act}) \tag{12.19}$$

where m_{tf} is the mass of turbine and foundation, and Ω_{act} is the actuator frequency. At each time step, the damped oscillator is subjected to seismic forces, calculated as

$$f_g(t) = k_{act}(x_{g,seis} - x_{g,0}) + c_{act}(\dot{x}_{g,seis} - \dot{x}_{g,0}) \tag{12.20}$$

where c_{act} is the actuator damping coefficient, $x_{g,0}$ and $\dot{x}_{g,0}$ are the realized foundation motions, $x_{g,seis}$ and $\dot{x}_{g,seis}$ are the desired seismic foundation motions. Tuning frequency and damping, the realized motions get closer to the desired seismic motions.

FAST-Seismic provides routines to modify the user-defined or synthetically generated input motions. The user can also manipulate the motions through baseline corrections and target response spectrum adjustments. For the calculations, five recorded accelerograms are applied in the fore-aft and side-to-side tower directions equally. The following historic earthquakes are used (Fig. 12.19):

El Centro Earthquake: 1979, recorded in Bonds Corner
Takochi Oki Earthquake: 1968, recorded in Hachinohe
Kobe Earthquake: 1995, recorded at KJMA
Kocaeli Earthquake: 1999, recorded in Düzce
Northridge Earthquake: 1994, recorded in Tarzana.

The time step is set to 0.005 s. The acquired results are presented for each earthquake in Figs. 12.20, 12.21, 12.22, 12.23, and 12.24. Similar to the previous calculations, from the 1,000 s total simulation time, a 600 s part of it is analyzed. Earthquakes started at 100 s. Depending on the excited frequencies, most of the earthquakes cause a significant tower vibration, which can be clearly separated from the wind-induced vibrations.

As shown in Figs. 12.25, 12.26, and 12.27, TMD causes an important improvement of the tower dynamics. Compared to previous results, the vibration
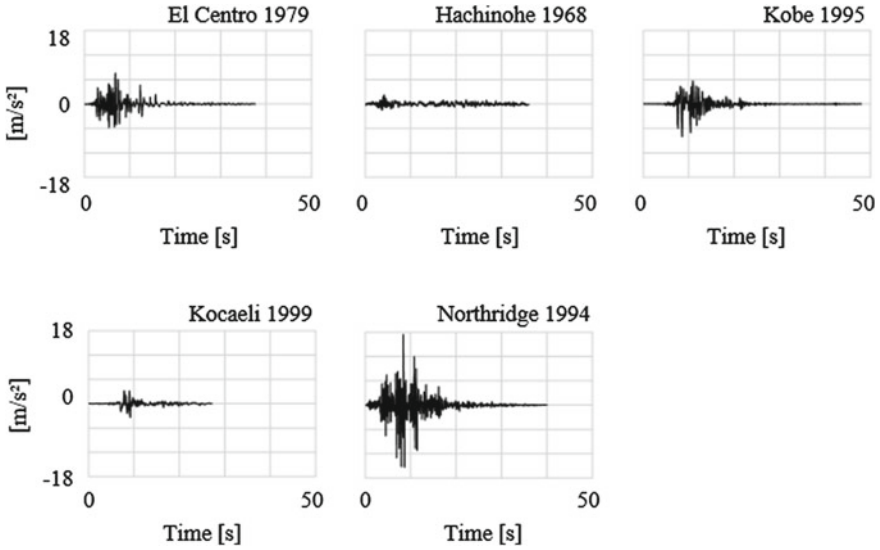
Fig. 12.19 Accelerograms of the analyzed earthquakes
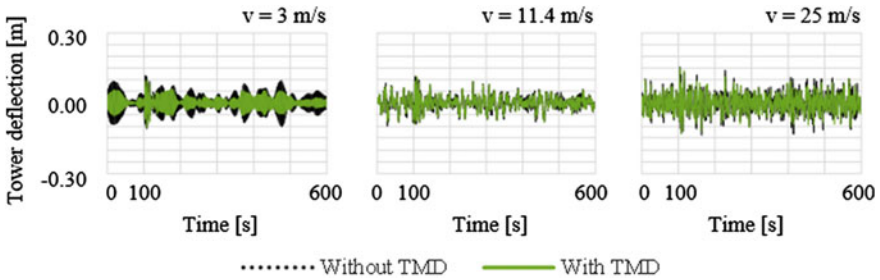
Fig. 12.20 Tower deflection time histories of the seismically excited onshore reference wind turbine for the cut-in, rated, and cut-out wind speeds—El Centro Earthquake
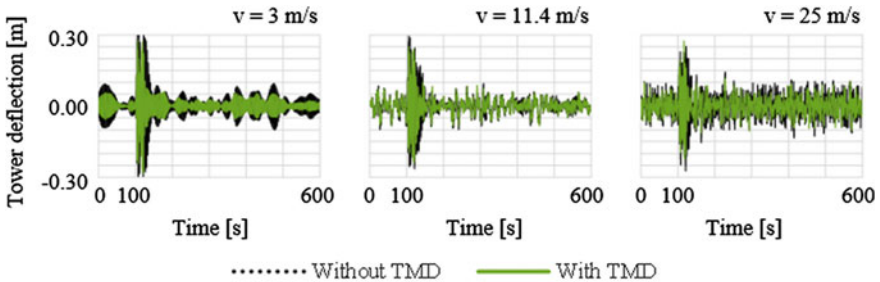
Fig. 12.21 Tower deflection time histories of the seismically excited onshore reference wind turbine for the cut-in, rated, and cut-out wind speeds—Hachinohe Earthquake
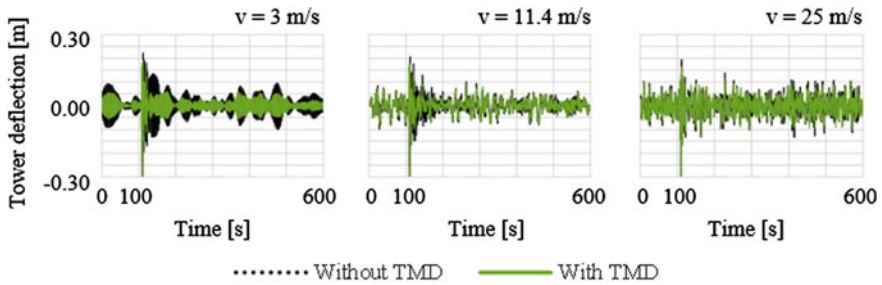
Fig. 12.22 Tower deflection time histories of the seismically excited onshore reference wind turbine for the cut-in, rated, and cut-out wind speeds—Kobe Earthquake
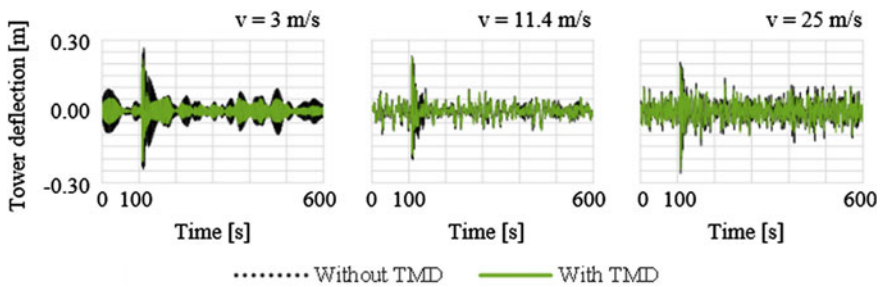
Fig. 12.23 Tower deflection time histories of the seismically excited onshore reference wind turbine for the cut-in, rated, and cut-out wind speeds—Kocaeli Earthquake
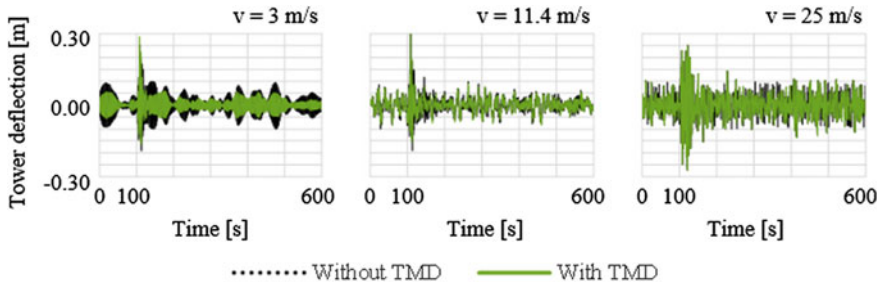
Fig. 12.24 Tower deflection time histories of the seismically excited onshore reference wind turbine for the cut-in, rated, and cut-out wind speeds—Northridge Earthquake

mitigation occurs at higher wind speeds. TMD shows a discrete efficiency regarding earthquake-induced vibrations that have caused resonant tower oscillations. The difference between El Centro and Hachinohe earthquakes shows the influence of earthquake parameters on the TMD efficiency. As the reference wind turbine responds to Hachinohe Earthquake with resonant vibrations, TMD reaches a much better result than during El Centro Earthquake.
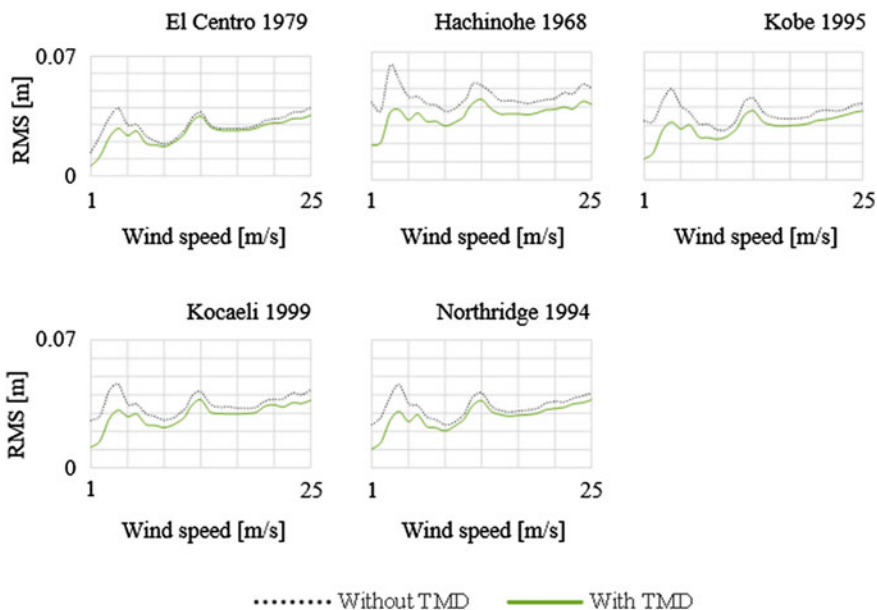
Fig. 12.25 RMS-Values of tower deflection of seismically excited onshore reference wind turbine with and without TMD
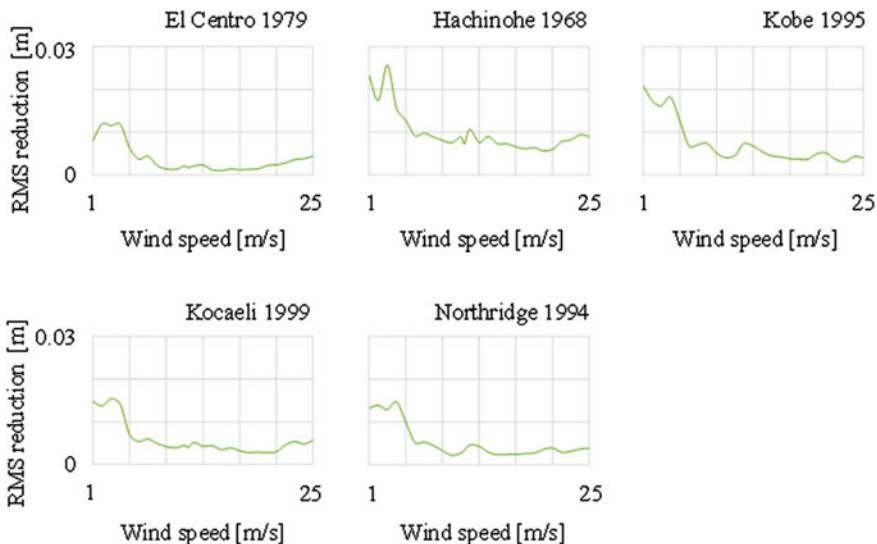
Fig. 12.26 Difference between the RMS-values of tower deflection of seismically excited onshore reference wind turbine with and without TMD
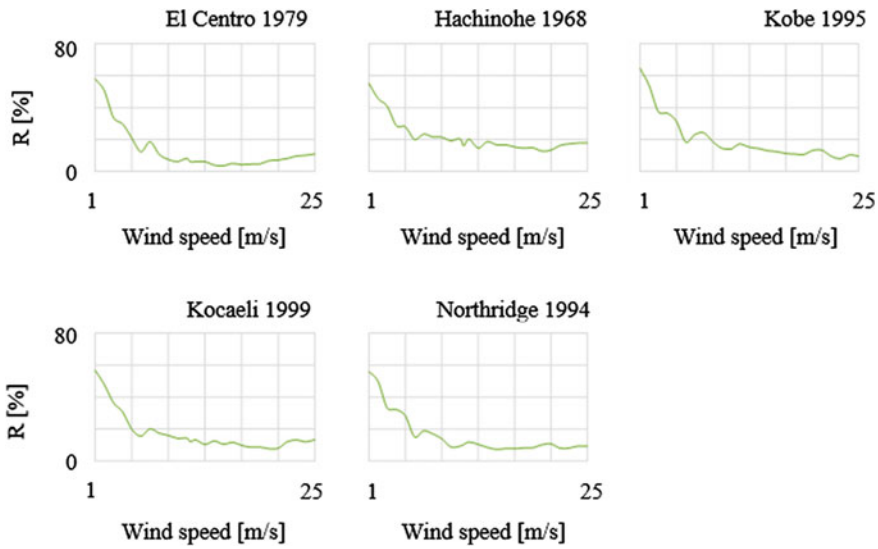
Fig. 12.27 Reduction factors of TMD attached to the seismically excited onshore wind turbine

12.4.3.4 Onshore Reference Wind Turbine with Tuned Mass Damper Considering Soil-Structure Interaction

In the following example, the SSI effects are presented for three different types of soil: soft, medium hard, and hard soil. The foundation of the turbine was assumed to be rigid and no embedment was considered. The soil properties are reported in Table 12.8, while the foundation properties are collected in Table 12.9.

Table 12.8 Soil properties

Soil properties	Soft soil	Medium hard soil	Hard soil
Shear modulus G_S in MN/m^2	3	120	5,000
Poisson's ratio υ_S	0.35	0.30	0.25
Soil density ρ_S in kg/m^3	1,600	1,900	3,000

Table 12.9 Foundation geometry and material properties

Foundation equivalent radius	$r_F = 11.30$ m
Density of the foundation material	$\rho_F = 2,500$ kg/m^3
Thickness of the foundation	$d_F = 2.50$ m
Foundation mass	$m_F = 2507187.29$ kg
Rocking mass moment of inertia	$\Theta_\varphi = 81341512.88$ kg m^2
Torsional mass moment of inertia	$\Theta_{\varphi z} = 160071372.35$ kg m^2

The stiffness coefficients are calculated according to Table 12.2 in Sect. 12.2.3. For example, the stiffness and damping coefficients for the translational degree of freedom of the platform over soft soil are obtained as

$$K_x = \frac{8G_S r_F}{2 - v_S} = \frac{8 \cdot 3 \cdot 10^6 \cdot 11.3}{2 - 0.35} = 1.644 \cdot 10^8 \text{ N/m} \tag{12.21}$$

$$C_x = \frac{4.6 r_F^2}{2 - v_S} \sqrt{G_S \rho_S} = \frac{4.6 \cdot 11.3^2}{2 - 0.35} \sqrt{3 \cdot 10^6 \cdot 1600} = 2.466 \cdot 10^7 \text{ Ns/m} \tag{12.22}$$

Repeating the calculation for each of the six degrees of freedom, the stiffness and damping matrices for the soft soil can be completed (Eq. 12.23–12.24). Table 12.10 contains the whole set of spring-dashpot coefficients for the three different soil types.

$$K = \begin{bmatrix} 0.164 & & & & & \\ 0 & 0.164 & & & \text{sym} & \\ 0 & 0 & 0.209 & & & \\ 0 & 0 & 0 & 17.759 & & \\ 0 & 0 & 0 & 0 & 17.759 & \\ 0 & 0 & 0 & 0 & 0 & 23.086 \end{bmatrix} \cdot 10^9 \text{ N/m} \tag{12.23}$$

$$C = \begin{bmatrix} 0.025 & & & & & \\ 0 & 0.025 & & & \text{sym} & \\ 0 & 0 & 0.046 & & & \\ 0 & 0 & 0 & 1.303 & & \\ 0 & 0 & 0 & 0 & 1.303 & \\ 0 & 0 & 0 & 0 & 0 & 0.918 \end{bmatrix} \cdot 10^9 \text{ N} \cdot \text{s/m} \tag{12.24}$$

Table 12.10 Spring-dashpot coefficients for the three soil types

Soil type	DOF	Stiffness K [N/m]	Damping C [N s/m]
Soft soil	Horizontal	$1.644 \cdot 10^8$	$2.466 \cdot 10^7$
	Vertical	$2.086 \cdot 10^8$	$4.627 \cdot 10^7$
	Rocking	$1.776 \cdot 10^{10}$	$1.303 \cdot 10^9$
	Torsional	$2.309 \cdot 10^{10}$	$9.178 \cdot 10^8$
Medium hard soil	Horizontal	$6.381 \cdot 10^9$	$1.650 \cdot 10^8$
	Vertical	$7.749 \cdot 10^9$	$2.961 \cdot 10^8$
	Rocking	$6.596 \cdot 10^{11}$	$8.337 \cdot 10^9$
	Torsional	$9.235 \cdot 10^{11}$	$6.325 \cdot 10^9$
Hard soil	Horizontal	$2.583 \cdot 10^{11}$	$1.300 \cdot 10^9$
	Vertical	$3.013 \cdot 10^{11}$	$2.242 \cdot 10^9$
	Rocking	$2.565 \cdot 10^{13}$	$6.468 \cdot 10^{10}$
	Torsional	$3.848 \cdot 10^{13}$	$4.949 \cdot 10^{10}$

The calculated tower displacements are presented for each soil type in Figs. 12.28, 12.29, and 12.30. The simulation time equals to 1,000 s and 600 s of it are used for the evaluation. To improve the numeric accuracy, the time step is reduced for hard soil to 0.001 s and for other soil types to 0.005 s. Tower vibrations with hard soil and medium hard soil show only a minor difference,
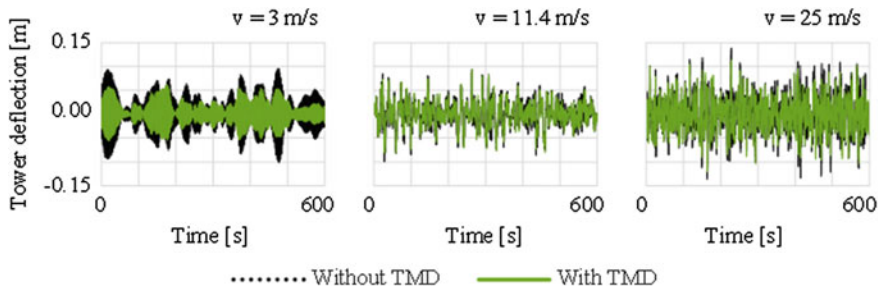
Fig. 12.28 Tower deflection time histories of the onshore reference wind turbine for the cut-in, rated, and cut-out wind speeds—Hard soil
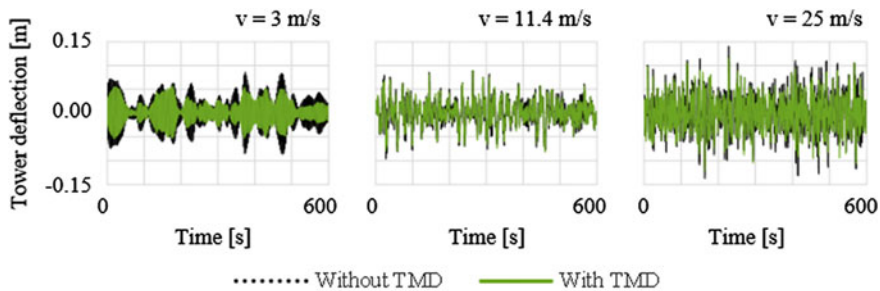
Fig. 12.29 Tower deflection time histories of the onshore reference wind turbine for the cut-in, rated, and cut-out wind speeds—Medium hard soil
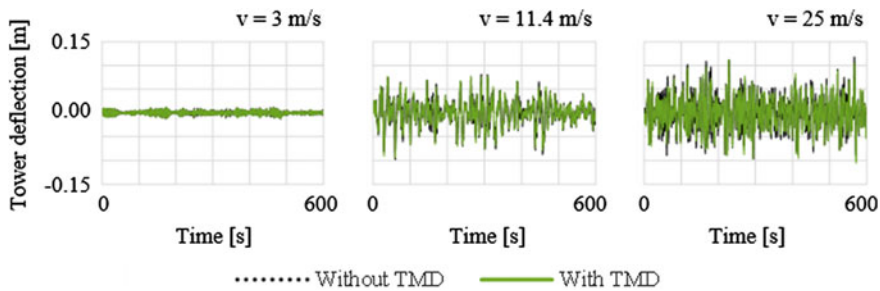
Fig. 12.30 Tower deflection time histories of the onshore reference wind turbine for the cut-in, rated, and cut-out wind speeds—Soft soil

when compared to the presented results with rigid ground connection in Sect. 12.4.
3.1. On the other hand, soft soil causes a significant change in the tower response.
The main reason for this major change is the frequency shift. As the difference
between the fundamental frequency of tower bending mode and the 3P-frequency
grows, the possibility of resonant vibrations reduces. This can be clearly identified
in the time history of tower vibration at cut-in wind speed 3 m/s (Fig. 12.30).

The evaluation of RMS-values of tower vibrations is presented in Figs. 12.31,
12.32, and 12.33. As discussed in Sect. 12.4.3.1, TMD reduces especially the
resonant vibrations efficiently. Therefore, the vibration mitigation of the wind
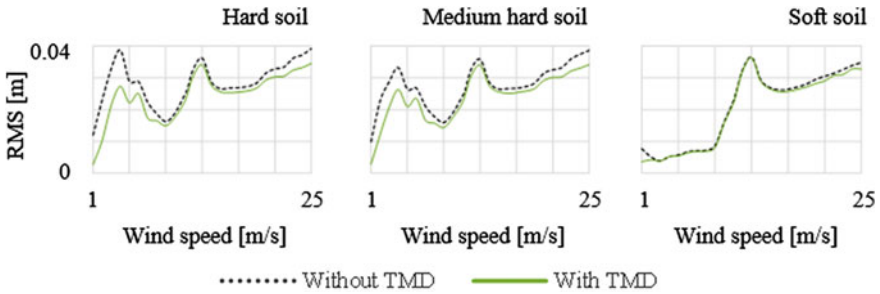
Fig. 12.31 RMS-values of onshore wind turbine tower deflection with and without TMD
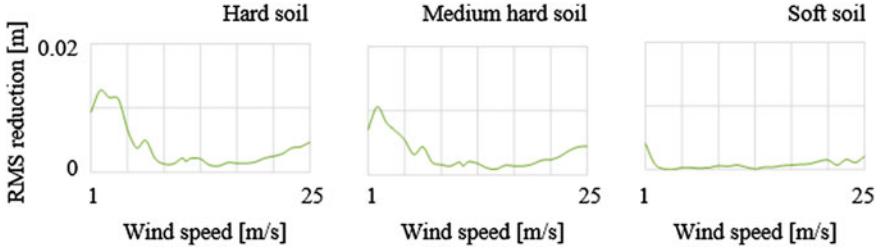
Fig. 12.32 Difference between the RMS-values of onshore wind turbine tower deflection with
and without TMD
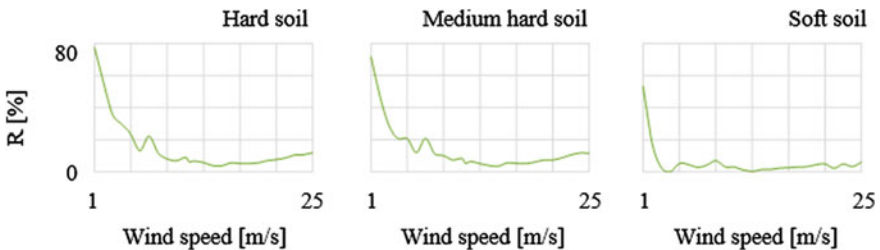
Fig. 12.33 Reduction factors of TMD attached to the onshore wind turbine for different wind
speeds

turbine on soft soil is quite insignificant. This confirms also the importance of SSI for the dynamic response of turbine towers. The acquired results of medium hard and hard soil are similar to the previous results calculated with rigid ground connection. The TMD is highly efficient at wind speeds, which cause resonant tower vibrations.

12.5 Conclusion

Tower vibrations occur in fore-aft direction depending on the wind speed and structural properties in the form of periodic and transient oscillations. These vibrations threaten the structural stability and reduce the lifetime of wind turbines significantly. To mitigate tower vibrations, several methods have been investigated. In this chapter, the efficiency of tuned mass damper (TMD) is analyzed for wind and earthquake-induced tower vibrations of onshore wind turbines. Furthermore, tuned liquid column damper (TLCD), which belongs also to the group of TMD, has been studied. The numerical verification of efficiency of the analyzed damper is carried out by means of a 5 MW reference onshore wind turbine. Hereby, four calculation campaigns are presented: Onshore Turbine with TMD and TLCD, seismically excited onshore turbine with TMD and onshore turbine considering soil–structure interaction (SSI) with TMD.

As known from other conventional slender structures, TMD can especially mitigate resonant vibrations effectively. The acquired results of onshore with TMD and TLCD enhance this phenomenon. During low wind speeds, the 3P frequency of the reference wind turbine is quite near the fundamental frequency of the tower bending mode in fore-aft direction. Therefore, near the cut-in wind speed 3 m/s, the reference wind turbine responses is mainly characterized by resonant tower vibrations. By using a TMD or TLCD these vibrations can be effectively reduced. The vibration energy level reduced by TMD and TLCD amounts to a value hereby between 20 and 80 % depending on the wind speed. At higher wind speeds, the resonant nature of the vibrations disappears and tower oscillations become more transient. The efficiency of a damping at transient vibrations mainly depends on the auxiliary damping added to the main structure. At higher wind speeds, the vibration energy reduction acquired by TMD and TLCD reaches up to 20 %.

Also, in seismic regions electricity generation using wind power is getting remarkable. Therefore, in order to numerically verify the efficiency of TMD, the onshore reference wind turbine is seismically excited. Hereby, five historic earthquakes are used: El Centro, Hachinohe, Kobe, Kocaeli, and Northridge. With the exception of El Centro each earthquake causes resonant tower vibrations. It is observed that similar to the transient wind-induced vibrations, the efficiency of TMD during seismic impact caused motion is nominal. On the other hand, calculated results show that by using a TMD, resonant tower vibrations, which usually occur during the post-earthquake phase, can be effectively reduced.

The last calculation campaign deals with the SSI effects on the efficiency of TMD. Indeed, because of the frequency shift caused by soil stiffness, the dynamic response of the turbine tower can change remarkably, which affects also the TMD efficiency. Therefore, during the design phase of a vibration mitigation system local SSI effects should always be considered.

The load change of the rotor blades and thereby of the entire tower structure of a wind turbine designed for 20 years corresponds to approximately $2 \cdot 10^8$. About the half the fatigue loading is caused by periodic tower vibrations, which occur especially during wind speeds below the rated wind speed. As the acquired results show that TMD and TLCD can effectively reduce resonant tower vibrations, it can be concluded that using these devices the fatigue life of wind turbines will be significantly improved.

Semiactive structural control systems can sense and adapt themselves to the changing structural properties. Therefore, these intelligent dampers operate more efficiently compared to passive systems. In this chapter, a semiactive tuned liquid column damper (S-TLCD) is also presented, which can modify its frequency and damping properties. Especially for slender structures, like wind turbines with changing dynamic properties, semiactive dampers offer new possibilities.

12.6 Future Work

The transient tower vibrations caused by turbulent wind can be reduced by improving the damping properties of the tower. Therefore, the future work will consist mainly on the development of such dampers, which should be integrated in the filigree construction of the wind turbine. Either as a passive or as a semiactive application, the material cost and the maintenance effort of these dampers should be kept affordable.

References

1. Adhikari S, Bhatacharya S (2011) Vibrations of wind turbines considering soil-structure interaction. Wind Struct 14(2):85–112
2. Altay O (2013a) Flüssigkeitsdämpfer zur Reduktion periodischer und stochastischer Schwingungen turmartiger Bauwerke. Dissertation, RWTH Aachen University
3. Altay O (2013b) Semiaktives Flüssigkeitssäulendämpfungssystem. German patent application AZ 10201300595.1, 26 June 2013
4. Altay O, Butenweg C, Klinkel S (2014a) Vibration mitigation of wind turbine towers by tuned liquid column dampers. In: Proceedings of the IX international conference on structural dynamics, Porto, Portugal

5. Anderson L (2011) Assessment of lumped-parameter models for rigid footings. Comput Struct 88(23):1567–1578
6. ASCE/AWEA (2011) Recommended practice for compliance of large land-based wind turbine support structures, Washington, DC
7. Bazeos N, Hatzigeorgiou GD, Hondros ID et al (2002) Static, seismic and stability analyses of a prototype wind turbine steel tower. Eng Struct 24:1015–1025
8. Cao Q, Hao Z (2010) The research of the affecting factors on the seismic response of wind turbine tower. In: International conference on mechanic automation and control engineering. Nanjing, China
9. Chen L (2013) Two parameters to improve the accuracy of the Green's functions obtained via the thin layer method. In: Proceedings of the international conference on SeDIF. Aachen, Germany
10. Danish Standard Committee (1992) Last og sikkerhed for vinmøller DS472. Dansk Ingeniørforening og Ingeniør-Sammenslutningen
11. Den Hartog JP (1947) Mechanical vibrations. McGraw-Hill, New York
12. DGGT (2002) Recommendations of the Building Ground Dynamics Work Group, Deutsche Gesellschaft für Geotechnik e.V. (DGGT), Berlin
13. DIBt (2012) Richtlinie für Windenergieanlagen- Einwirkungen und Standsicherheitsnachweise für Turm und Gründung, DIBt-B8
14. DNV/Risø (2002) Guidelines for design of wind turbines. 2nd edn. Det Norske Veritas and Risø National Laboratory
15. Frahm H (1910) Means for damping the rolling motion of ships, US Patent 970,368, 13 Sept 1910
16. Fried L, Sawyer S, Shukla S et al (2013) Global wind report—Annual market update 2012. Global Wind Energy Council (GWEC). Brussels, Belgium
17. GL (2005) Guideline for the certification of offshore wind turbines. Germanischer Lloyd Industrial Services GmbH Renewables Certification
18. Hau E (2008) Windkraftanlagen. Springer, Berlin
19. IEC (2010) 61400-1-am1 Wind turbines-Part 1 Design requirements. 3rd edn. International Electrotechnical Commission
20. Lin G, Han Z (2013) A 3D Dynamic impedance of arbitrary-shaped foundation on anisotropic multi-layered half-space. In: Proceedings of the International Conference SeDIF. Aachen, Germany
21. Jonkman J, Butterfield, Musial W et al (2009) Definition of a 5-MW reference wind turbine for offshore system development. Technical report NREL/TP-500-38060, National Renewable Energy Laboratory, Golden, Colorado
22. Jonkman J (2013) NWTC computer aided engineering tool FAST. http://wind.nrel.gov/designcodes/simulators/fast. Accessed 28 Dec 2013
23. Lackner MA (2012) FAST-SC modified version of FAST. http://www.umass.edu/windenergy/research.topics.tools.software.fastsc.php. Accessed 28 Dec 2013
24. Mykoniou K, Taddei F, Han Z (2012) Dynamic foundation-soil interaction: A comparative study. Bauingenieur DACH Bullettin 87:9–13
25. Prowell I, Paul V (2009) Assessment of wind turbine seismic risk: existing literature and simple study of tower moment demand, Technical Report. Sandia National Laboratories, California
26. Prowell I, Asareh MA (2011) Seismic loading for FAST, subcontract report NREL/SR-5000-53872. Missouri University of Science & Technology Rolla, Missouri
27. Prowell I, Asareh MA (2012) NWTC design code FAST-Seismic. http://wind.nrel.gov/designcodes/simulators/seismic. Accessed 28 Dec 2013
28. Ritschel U, Warnke I, Kirchner J, Meussen B (2003) Wind turbines and earthquakes. In: 2nd world wind energy Conference, Cape Town
29. Sakai F, Takaeda S, Tamaki T (1991) Damping device for tower-like structure, US Patent 5,070,663, 10 Dec 1991

30. Taddei F, Meskouris K (2013) Seismic analysis of onshore wind turbine including soil-structure interaction effects. In: Proceedings of the International Conference on SeDIF. Aachen, Germany
31. Taddei F, Klinkel S, Butenweg C (2014) Parametric investigation of the soil-structure interaction effects on the dynamic behavior of a wind turbine considering a layered soil. Wind Energy. doi:10.1002/we.1703
32. Warburton GB, Ayorinde EO (1980) Optimum absorber parameters for simple systems. Earthquake Engng Struct Dyn 8(3):197–217
33. Zhao X, Maißer P (2006) Seismic response analysis of wind turbine towers including soil-structure interaction. J Multi-body Dynam 220(1):53–61

Chapter 13
A Semi-active Control System for Wind Turbines

N. Caterino, C.T. Georgakis, F. Trinchillo and A. Occhiuzzi

Abstract A semi-active (SA) control system based on the use of smart magnetorheological (MR) dampers to control the structural response of a wind turbine is proposed herein. The innovative approach is based on the implementation and use of a variable-properties base restraint. This is able to modify in real time its mechanical properties according to the instantaneous decision of a given control logic, the latter addressed to control one or more structural response parameters. The smart base restraint is thought to be a combination of a smooth hinge, elastic springs, large-scale adjustable MR dampers, and a control algorithm that instantaneously commands the latter during the motion, making them to modulate the reactive force as needed to achieve the performance goals. The design and operation of such a system are shown with reference to a case study consisting of an almost 100 m tall wind turbine, realized in a 1/20 scale model at the Denmark Technical University (DTU). Shaking table tests have been performed under the action of two different types of wind loads and by using two purposely written control logics, highlighting the high effectiveness of the proposed SA control technique and encouraging to further investigate in such direction.

Keywords Semi-active control · Wind turbine · Magnetorheological damper · Smart material · Control algorithm

N. Caterino (✉) · F. Trinchillo · A. Occhiuzzi
University of Naples "Parthenope", Naples, Italy
e-mail: nicola.caterino@uniparthenope.it

F. Trinchillo
e-mail: francesco.trinchillo@uniparthenope.it

A. Occhiuzzi
e-mail: antonio.occhiuzzi@uniparthenope.it

C.T. Georgakis
Technical University of Denmark (DTU), Copenhagen, Denmark
e-mail: cg@byg.dtu.dk

13.1 Introduction

In the last years the need for optimization procedures to design higher and higher wind turbines, even offshore, in a cost-effective way and of control techniques to reduce the wind-induced structural demand has definitely grown. Most of the scientific literature on this topic is related to passive control strategies, often based on the use of tuned mass or tuned liquid dampers.

Herein, the possible use of a semi-active (SA) control technique is investigated, based on the use of magnetorheological (MR) dampers, also performing large-scale shaking table tests. Previous researches on SA control of wind turbines are not much based on numerical simulations.

Kirkegaard et al. [1] for the first time explored the possibility of using MR dampers to control a wind turbine, numerically evaluating their effectiveness when driven by a classical optimal clipped control algorithm. The proposed idea was pioneering and, also because of this, it results to be very interesting, even if difficult to be implemented in a real case. As a matter of a fact, the authors consider the installation of an MR device at the base of the tower, in vertical position, so as to be able to be solicited by relative vertical displacements induced by the top movement of the turbine to which the damper should be mechanically connected. Also an experimental test model has been built by the said authors, even if adopted for passive tests only (constant voltage fed to the MR damper at the maximum level—"passive-on" condition). The wind turbine model was a 3 m high steel frame with a 200 kg top mass. The MR damper was connected to the shaking table and to the top of the frame structure by a steel bar designed so as to avoid buckling. Comparing numerical (SA) and experimental (passive) results in terms of top displacement, appreciable improvements in the SA strategy are highlighted by the authors.

Karimi et al. [2] and Luo et al. [3–5] showed the effectiveness of SA control for floating wind turbines by using tuned liquid column dampers (TLCD). This kind of device is generally used as a passive damper, even if it may turn into an SA damper with the addition of a controllable valve. With a control logic based on an H_∞ feedback methodology, the authors proposed to adopt the orifice opening according to the structure response and loading conditions. Luo et al. also explored the possibility of using MR fluids within the TLCD, rather than a common viscous fluid, so leading to a "smart" TLCD [6, 7]. The numerical simulations reported in the above papers show that this kind of control strategy may lead to a strong reduction of the top displacement.

Arrigan et al. [8] considered SA tuned mass dampers (STMD) to control wind turbine blades in flapwise vibrations. Four STMDs were added to the wind turbine numerical model, one to each blade tip and one at the nacelle to control the response of each component. Simulations made by the authors showed a significant reduction in displacement response of the system for turbulent wind loading. A successful response reduction under a steady wind load was demonstrated.

Rodríguez et al. [9] explored the possibility to use passive or SA dampers in a toggle brace assembly integrated within the hollow column of a wind turbine tower. They evaluated the effectiveness of this control technique in terms of reduction of base bending moment for extreme and fatigue loads. Different configurations of such system have been compared by authors, each defined by a given number, position, and inclination of the devices in both the horizontal and vertical planes. The best option leads to a reduction in the moment demand at the base of the tower up to 20 % in extreme cases and around 10 % in fatigue.

The basic idea for the SA control technique proposed herein consists in using the smart MR devices so as to realize a time-variant base restraint, whose "stiffness" is in real time driven by a purposely written control logic. The latter instantaneously takes decision and calibrates MR dampers to reduce the bending stress at the base of the tower, secondarily to bound the top displacement within acceptable limits so as to avoid significant, detrimental second order effects.

This strategy has been experimentally assessed at the shaking table facility of the Denmark Technical University (DTU) in Copenaghen, where the present control concept was initially conceived. Two different base accelerograms were imposed for the tests, equivalent to an extreme short operating gust and a longer high velocity wind buffeting, respectively. Moreover, two distinct control algorithms have been designed and adopted for the tests, different in the way they approach the problem. The first is inspired to the eigenstructure selection technique [10, 11] and is addressed to significantly increase the modal damping ratios, and to make the fundamental mode similar to a rigid rotation of the tower around the base hinge. The second algorithm follows a more physical approach, being designed to bound the stress at the base and, as a secondary objective, the top displacement demand within given limits.

All the performed tests highlight the effectiveness of the proposed control technique in reducing the stress demand at the base, this at the cost, in the worst case, of a slight increase in top displacement.

13.2 Basic Idea of the Semi-active Control Strategy

The realization of a time-variant restraint at the base of the tower exploiting the potential of smart dampers is the basic idea herein proposed to reduce wind-induced structural demand to high-rise turbines. This is roughly described in Fig. 13.1, where the original wind turbine is modeled as a single degree of freedom dynamic system with top mass, stiffness, and inherent damping equal to m, k_T and c_T respectively, fully restrained at the base (Fig. 13.1a). The idea is replacing this perfectly rigid base restraint with a controllable one that, during the motion, can be instantaneously made more or less "stiff" depending on what is more beneficial in terms of reducing the structural demand. Figure 13.1b schematically describes a possible way to materialize this concept, by installing at the base of the tower a smooth hinge, a rotational spring (stiffness k_ϕ), and a rotational variable damper

Fig. 13.1 Basic idea of SA control of a wind turbine via MR dampers
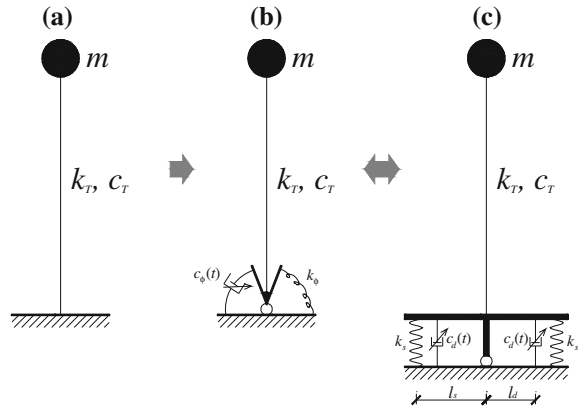
(damping constant c_ϕ, variable in time) externally driven in real time by a control algorithm. The same concept can be practically implemented by means of two vertical linear springs (k_s) installed at a given distance (l_s) from the hinge and two vertical variable dampers (c_d), each placed at the distance l_d from the hinge (Fig. 13.1c).

MR dampers are suggested to be adopted as variable devices within this setup. At macro scale, MR fluids behave as semi-solid bodies as far as the shear stress does not exceed a threshold, whose value depends on the intensity of the magnetic field the fluid is immersed in, the latter depending in turn on the current intensity in coils placed around the fluid. This behavior is associated to the nature of the fluid, a suspension of micron-sized magnetizable particles. Upon application of a magnetic field, particles align and form fibrous aggregates that generate orders-of-magnitude viscosity changes within characteristic times of milliseconds.

When the base damping is set to a low value, the tower is able to relax, hence to convert its potential energy into kinetic energy and to reduce the bending moment at the base. Thus the SA base system implies stress reduction, even at the cost of a possible increase of top displacement, which has to be bounded within certain limits to control the top displacements. The springs allow to reset the tower to the initial position at the end of a severe wind-induced excitation.

This idea has been physically realized and tested at the laboratory of the DTU (Copenaghen) by using prototype MR dampers provided by Maurer Söhne (Germany). The results gained from this campaign will be presented and discussed in the following sections.

13.3 Experimental Setup

A 3 MW wind turbine with horizontal power transmission axle has been assumed as reference structure for the experimental campaign performed at the DTU laboratory (Fig. 13.2). The tower is 102.4 m tall, made of steel Q345 (modulus of
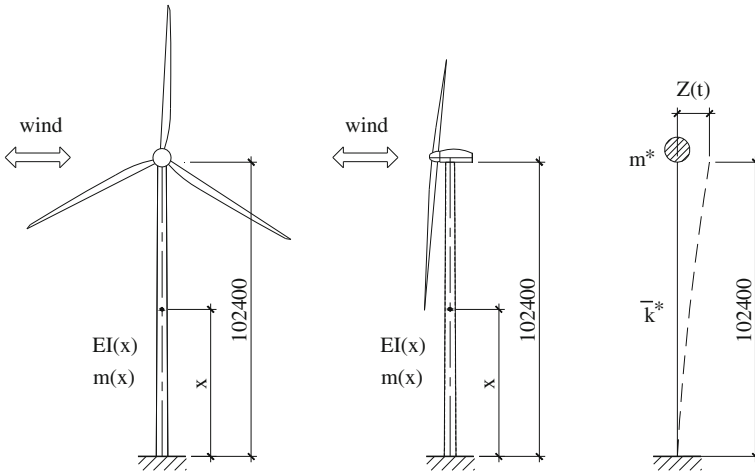
Fig. 13.2 Structural model of the reference wind turbine [12]. Dimensions in milimeters

elasticity 206,000 MPa, Poisson ratio 0.3, yielding stress 345 MPa), with a variable hollow circular cross section with external diameter variable from 2.30 m (top) to 4.15 m (bottom). The weight of the tower, including the flanges and internals, is 3,713 kN (body) and 1,210 kN (nacelle, including the rotor blades). Chen and Georgakis [12, 13] showed the equivalence, from a dynamic point of view, of this structure with a single degree of freedom (DOF) system made up of a tapered tubular cantilever beam with a concentrated mass at the top. In the same studies, the development of a 1/20-scale model of the prototype structure is presented. This test model is characterized by a 5.12 m high vertical tube with uniform cross section $\Phi 133/4$ (i.e., a hollow circular one with 133 mm of external diameter and 4 mm in thickness), chosen according to the principle of the equivalent flexural stiffness, with a lumped mass of 280 kg placed at the top (Fig. 13.3).

The base of the model is realized so as to be stiff enough, by means of two parallel, horizontal steel C profiles (UPN 240 cross section) whose top and bottom flanges are firmly bolted to stiff, horizontal steel plates. It is connected in the middle to the shaking table through a cylindrical steel hinge, with interposed a small, stiff steel frame. On both sides of the base, one cylindrical spring (89 kN/m stiff) and one MR damper (described in the next section) are installed.

The shaking table facility used for the test consists of a platform made of 20 mm thick aluminum plates 1.5×1.5 m in plan. The table can be moved in a single horizontal direction by a 100 kN hydraulic actuator MTS 244.22. Stiffness grid plates of 300×300 mm are welded to the top and bottom plates. Furthermore, in the areas where the forces are transmitted, additional stiffeners have been added.

Fig. 13.3 Experimental setup
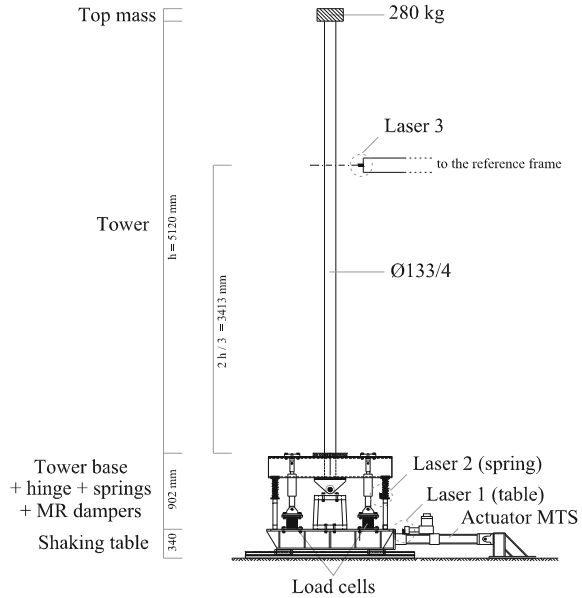
Figure 13.3 shows the overall experimental setup, whereas Fig. 13.4 includes a detail of the base to better understand how the smart base restraint has been realized. Such figures also report the type and position of all the transducers adopted, whereas further details are given in the following sections. Some photographs of the setup are given in Fig. 13.5.

13.3.1 Electronic Equipment and Transducers

The electronic equipment adopted for the experimental activity on the wind turbine model can be formally distinguished into two parts: conventional tools for structural laboratory tests and an extra-equipment properly required for SA control by means of two MR dampers.

The position of the transducers belonging to the first group is shown in Figs. 13.3 and 13.4. The horizontal displacements of the shaking table were measured through a laser transducer supported by a steel stick (WayCon laser, model LAS-T-500, range of measure 50–550 mm). The same kind of laser transducer was located at 2/3 of total height of the tower and fixed to an external wood stick to measure the absolute horizontal displacement of that section. The axial displacements of springs were measured by a third laser transducer attached on the steel plate where one of the 2 springs (the one closer to the actuator) is installed (WayCon laser, model LAS-T-250, range of measure 50–300 mm). Rotation of the base and axial displacements of MR dampers have been calculated
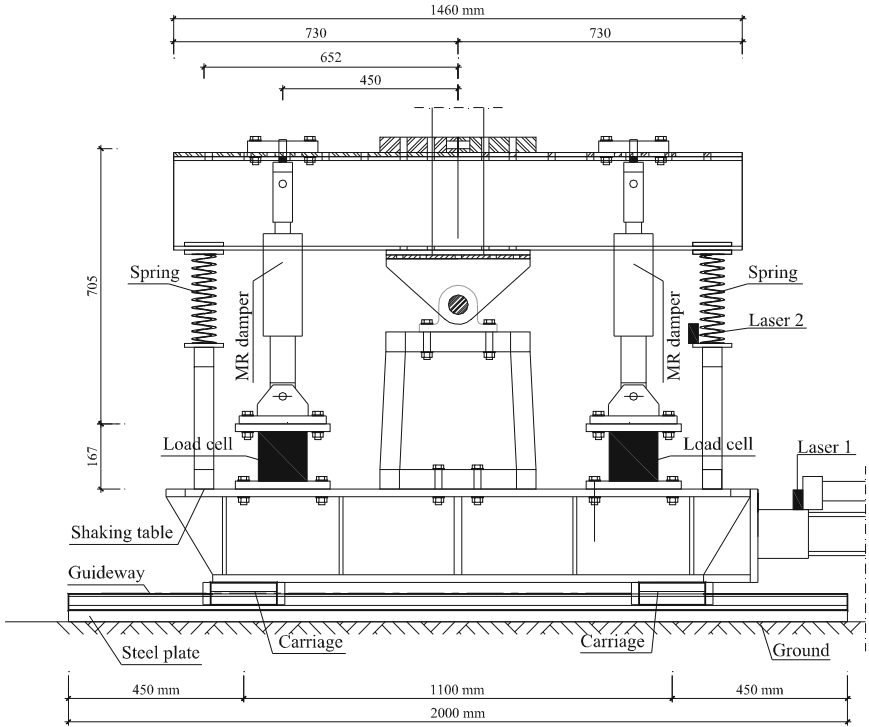
Fig. 13.4 Detail of the base of the mock-up structure

online, by considering the reciprocal position of cylindrical hinge, dissipators, and springs (Fig. 13.4). Two load cells mounted under each MR device allowed to measure the reacting forces (AMTI load cells, model MC5-5000, range ±22 kN). It is worth noting that base stress and top displacement have been calculated online from the above-mentioned available displacement measures, being the stress of steel well below the yielding value.

The additional electronic equipment used to drive the SA tests include (Fig. 13.6):

1. No. 2 power supplies type BOP (Bipolar Power Supply) provided by Kepco Inc. (New York, USA), model 50–4 M, maximum power output of 200 W, maximum input power of 450 W, power source-power sink capabilities in the range ±50 V (voltage) and ±4 A (current); commanded from a remote location (PC) through a voltage signal in the range 0–10 V, with alternative operations as voltage driver (control loop gain 5.0 V/V) or as current driver (control loop gain 0.4 A/V);

2. No. 1 embedded controller National Instruments PXI-8196 RT, high-performance platform for testing in real time;

Fig. 13.5 Photograph of the structural model installed at the DTU laboratory. Overall view (**a**), *lateral* (**b**) and *front* (**c**) view of the base
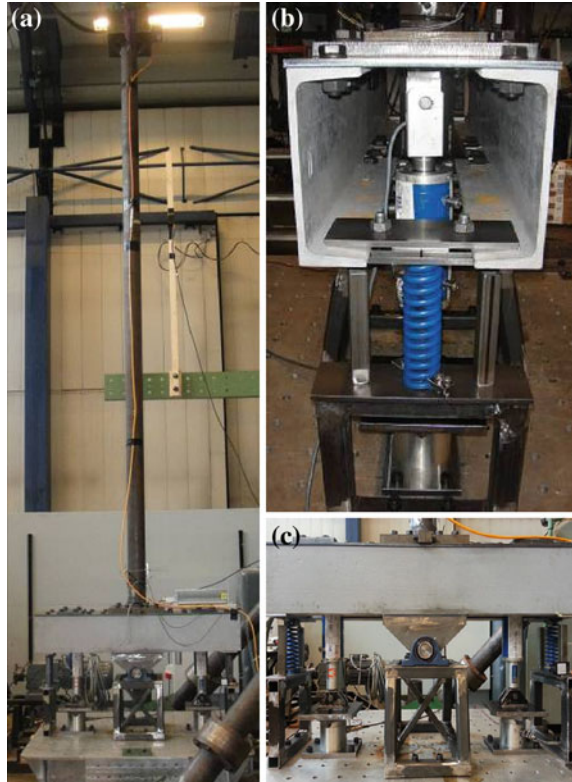
3. No. 2 data acquisition boards National Instruments PXI-6259, multi-function high-speed, optimized for high accuracies and speed of acquisition (up to 2,800 kHz), 8-channel analog inputs, 4 analog outputs (in the range ±10 V), 16 bits of resolution;

4. No. 1 digital multimeter National Instruments PXI-4065, 6 ½-digit for high speed measuring of voltage, current and resistance;

5. No. 2 connector blocks National Instruments BNC-2110;

6. No. 1 voltage attenuator module (10 to 1) National Instruments SCC-A10, dual channel, with voltage inputs up to ±60 V ("C" in Fig. 13.6);

7. No. 1 capacitance of 1.0 μF needed to stabilize the current loop ("A" in Fig. 13.6);

8. The software environment NI Labview Professional Development System ("B" in Fig. 13.6);

9. Real time operating system labview by NI for testing in real time;

10. No. 1 chassis national instruments able to host components 2, 3, 4 ("D" in Fig. 13.6).

No. 2 terminal
National Instruments
BNC-2110

No. 2 power supplies
BOP 50-4 M
from Kepco Inc.

Digital multimeter
National Instruments
PXI-4065

(b)

(c)   **(d)**

(a)

Embedded controller
National Instruments
PXI-8196 RT

No. 2 data acquisition
National Instruments
PXI-6259
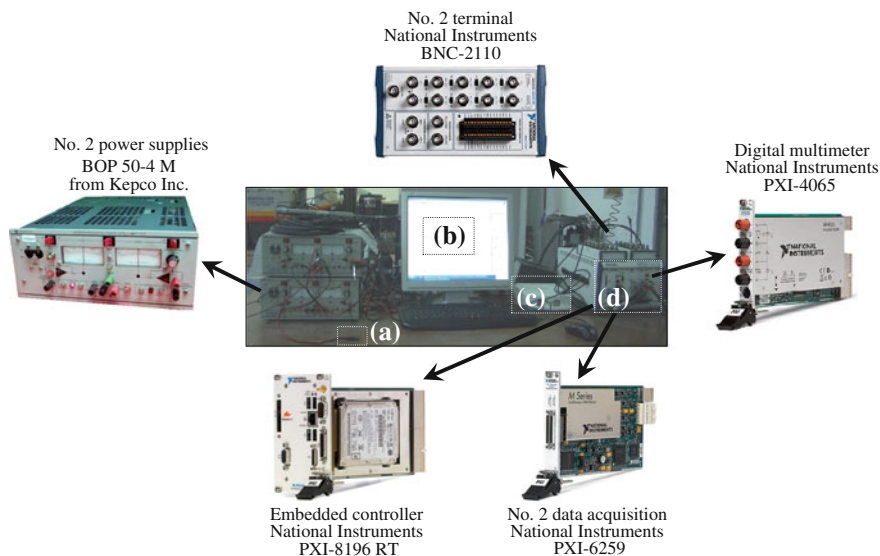
Fig. 13.6 Electronic equipment for acquisition and semi-active control

13.4 Magnetorheological Dampers

The devices adopted for the tests were two full-scale prototype SA MR dampers (Fig. 13.7) designed and manufactured by the German company Maurer Söhne. The overall dimensions of each device are 675 mm (length) × 100 mm (external diameter), with a mass of about 16 kg. A maximum force of about 30 kN can be developed along the longitudinal axis, whereas the presence of special spherical pin joints at both ends prevents the rise of bending, shear, and torsional moment in the piston rod. The dampers have a stroke of ±25 mm. The external diameters of the piston head and of the piston rod are 100 and 64 mm, respectively. A magnetic circuit composed of coils, in series with a global resistance of 3.34 Ω, can generate the magnetic field in the device. The current in the circuit can be provided in the range 0 ÷ 4 A.

The MR dampers were first experimentally tested by using a self-balanced testing apparatus (Fig. 13.8). Some general information is provided herein. Further details can be found in [14].

Figure 13.9 shows the results of four "passive" (constant value of current) tests done imposing the same harmonic displacement at the mobile end of the device (frequency 1.5 Hz, amplitude 20 mm) with four different current levels (0.0, 0.9, 1.8, and 2.7 A).

The force-displacement and force-velocity cycles clearly show how the damper's mechanical behavior strongly depends on the magnetic field inside the device and, in turn, on the current intensity inside the coils. In particular, the maximum

Fig. 13.7 One of the two prototype MR dampers
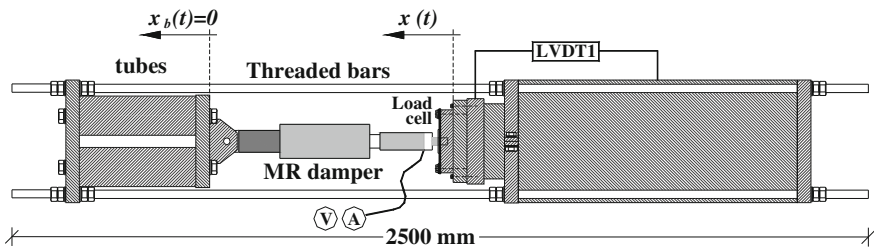
Fig. 13.8 Photograph and sketch of the experimental apparatus
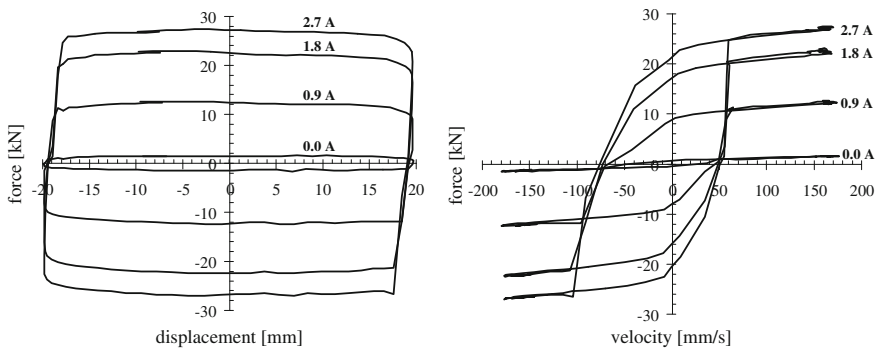
Fig. 13.9 Experimental response of one MR damper under 1.5 Hz, ±20 mm harmonic displacement
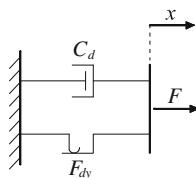
Fig. 13.10 Bingham model for MR dampers

measured force turned out to be approximately 2 kN when no current was given to the damper and to achieve the values 12, 22, and 27 kN when the feeding currents 0.9, 1.8, and 2.7 A were provided, respectively.

The force-displacement loops look substantially like a superposition of a viscous and friction-like behavior (Fig. 13.10), both depending on the magnitude of the current intensity [15]. This behavior, based on the properties of Bingham solids [16], can be analytically described as in Eq. 13.1 where $\dot{x}$ is the relative velocity between the damper's ends, C_d the viscous damping, F_{dy} the plastic threshold, both functions of the applied magnetic field and, in turn, of the intensity of current i:

$$F = C_d(i) \cdot \dot{x} + F_{dy}(i) \cdot \mathrm{sgn}(\dot{x}). \tag{13.1}$$

The relationships C_d (i) and F_{dy} (i) have been found by interpolating by a second order polynomial function the experimental data (Eqs. 13.2–13.3, where A, kN, s, m are the adopted units of measure) and are graphically described in Fig. 13.11.

$$C_d(i) = -1.870\,i^2 + 13.241\,i + 6.851 \tag{13.2}$$

$$F_{dy}(i) = -1.952\,i^2 + 13.962\,i + 0.181. \tag{13.3}$$

The curves in Fig. 13.11 show an asymptotic trend of the MR effect associated to magnetic saturation of the MR fluid.

A detailed report of the response time analysis of such prototype MR dampers based on the above-mentioned experimental data is also presented in [17]. The promptness turned out to be mainly related to the electric part of the control chain. "Power source—power sink" capabilities resulted to be crucial to make the device able to operate in real time. Furthermore, current-driven operations rather than voltage-driven resulted to be strongly recommended to dramatically shorten control lead times. In voltage-driven operations, the power supply provides a fixed voltage and the current slowly modifies until it reaches the desired value, corresponding to the ratio voltage/resistance. In current-driven operations, the power supply provides a fast changing voltage spike so as to quickly modify the current inside the damper, causing in turn a fast change in the mechanical behavior of the damper. If the current must be increased, the power supply provides for a short
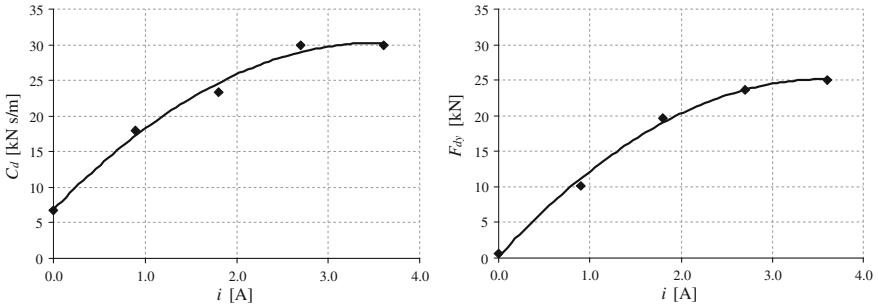
Fig. 13.11 Bingham model parameters for the prototype MR dampers

Fig. 13.12 Qualitative trends in current and voltage for two alternative approaches to control MR dampers (t^* is the instant of command)
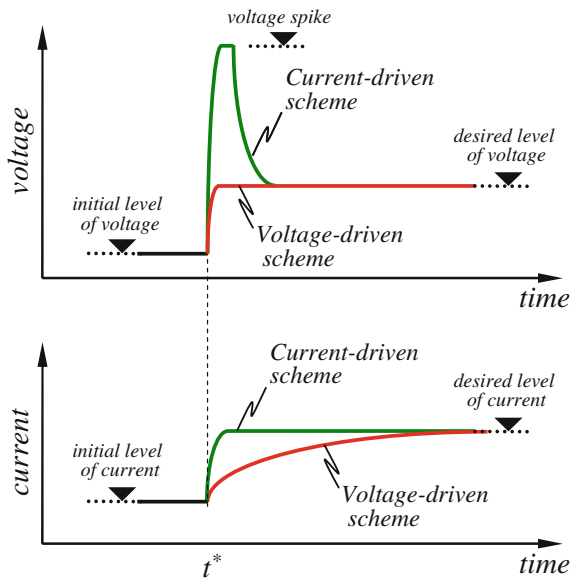
period a voltage spike and then sets the voltage to the reference value, whereas if the current must be decreased, a negative spike of voltage is issued.

Figure 13.12 qualitatively shows what happens to voltage and current into an MR damper when the two approaches are adopted, showing the delay with which the current (and the corresponding magnetic field) reaches the desired value when a voltage-based approach is adopted.

It is experimentally demonstrated that using current-based strategy for control and an appropriate and suitably tuned electric hardware, the response time of the above-mentioned prototype SA MR dampers can be comfortably bounded to 8–10 ms.

Recently, these smart devices has been successfully used also in a wide experimental campaign to SA control earthquake-induced vibrations of a 3D large scale steel structure installed on a shaking table facility at the University of Basilicata (Italy), allowing a comparison of four different control algorithms and resulting very effective in reducing structural response [18]. Herein, the high versatility of SA control strategies based on MR dampers is demonstrated.

13.5 Control Algorithms

The first controller adopted for the shaking table tests is based on the eigen-structure selection theory [10, 11]. It is a full-state feedback algorithm relying on real-time definition of a desired control force and on the ability of the SA reacting forces to mimic it during the motion. The second algorithm instead is designed to bound the stress at the base within acceptable, given limits, also controlling the top displacement to avoid the occurrence of significant second order effects.

A simplified, lumped-mass model of a wind turbine tower mounted on a rotating base is shown in Fig. 13.13. The base is linked to the ground through two elastic elements (springs), two SA MR dampers and a hinge, as described in Sect. 13.2. In the figure:

h	is the height of the tower;
m_1-m_r	are the lumped masses of the model;
k_1-k_r	are the stiffnesses associated to the various DOFs;
c_1-c_r	are the viscous damping coefficients associated to the various DOFs;
α	is the rotation of the base;
$\delta_0 = \alpha \times h$	is the corresponding rigid displacement of the top of the tower;
δ_1-δ_r	are the elastic displacements of the lumped masses;
k_s	is the stiffness of each base spring;
f_{d1}-f_{dm}	are m independent control forces available;
l_s	is the distance between each spring and the hinge;
l_d	is the distance between each SA MR damper and the hinge.

The equations of motion of the $n = r + 1$ DOFs system in the absence of any external disturbance are

$$\mathbf{M}\ddot{\boldsymbol{\delta}} + \mathbf{C}\dot{\boldsymbol{\delta}} + \mathbf{K}\boldsymbol{\delta} = -\mathbf{P}\mathbf{f}_d \qquad (13.4)$$

where $\mathbf{M}$, $\mathbf{C}$ and $\mathbf{K}$ are, respectively, the mass, damping, and stiffness matrices, $\mathbf{P}$ is the $n \times m$ allocation matrix of the control forces f_{di} collected in the control vector $\mathbf{f}_d$ and $\boldsymbol{\delta} = [\delta_0 \ \delta_1 \ \dots \ \delta_r]^T$ is the vector collecting the DOFs, whose components are scalar functions of time. However, the dependency from time will be explicitly written only when needed.

Fig. 13.13 Lumped-mass
structural model of a wind
turbine
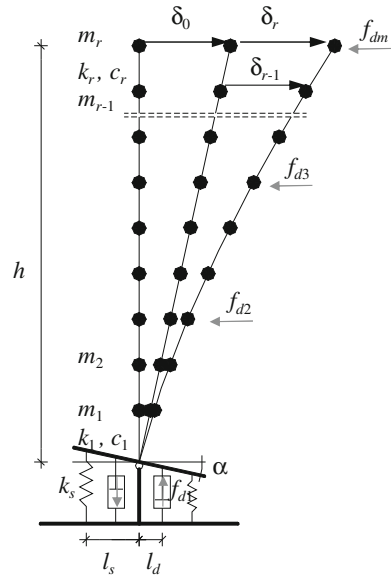
When the control forces are not present, in the typical hypothesis of neglecting damping, the eigenvector analysis of the system described by Eq. 13.4, namely the search for solutions of the equation

$$\omega^2 \mathbf{I} - \mathbf{M}^{-1}\mathbf{K} = 0 \quad (\text{dim } \mathbf{I} = n \times n) \tag{13.5}$$

where $\mathbf{I}$ is the identity matrix, yields real eigenvalues ω_i (angular frequencies), each associated to real eigenvectors $\boldsymbol{\varphi}_i$, that can be ordered in the columns of a matrix $\boldsymbol{\Phi}$:

$$\boldsymbol{\Phi} = \begin{bmatrix} \varphi_1 & \vdots & \varphi_2 & \vdots & ... & \vdots & \varphi_n \end{bmatrix} \tag{13.6}$$

The linear system of n time-invariant differential equations of the second order (Eq. 13.4) can be also written as a set of $2n$ linear time-invariant first order differential equations in the state-space representation:

$$\dot{\mathbf{z}} = \mathbf{A}\,\mathbf{z} + \mathbf{B}\,\mathbf{f}_d \tag{13.7}$$

where

$$
\begin{aligned}
\mathbf{A} &= \begin{bmatrix} \mathbf{0}_{n \times n} & \mathbf{I}_{n \times n} \\ -\mathbf{M}^{-1}\mathbf{K} & -\mathbf{M}^{-1}\mathbf{C} \end{bmatrix} \quad (\text{dim } \mathbf{A} = 2n \times 2n) \\
\mathbf{B} &= \begin{bmatrix} \mathbf{0}_{n \times 1} \\ -\mathbf{M}^{-1}\mathbf{P} \end{bmatrix} \quad (\text{dim } \mathbf{B} = 2n \times m)
\end{aligned}
\tag{13.8}
$$

and

$$\mathbf{z} = [\boldsymbol{\delta}\,\dot{\boldsymbol{\delta}}]^{\mathrm{T}} = \begin{bmatrix} \delta_0 & \ldots & \delta_r & \dot{\delta}_0 & \ldots & \dot{\delta}_r \end{bmatrix}^{\mathrm{T}} \tag{13.9}$$

is the system state. The $2n$ eigenvalues and eigenvectors of $\mathbf{A}$ fully describe the free motion of the system shown in Fig. 13.13 when uncontrolled ($f_{di} = 0$). In particular, for the structural system considered, the complex eigenvalues s_i come in conjugate pairs which correspond to angular frequencies ω_i and modal damping ratios ξ_i [19] as follows (j is the complex unity):

$$s_{i,ic} = -\zeta_i \omega_i \pm \mathrm{j}\,\omega_i \sqrt{1 - \xi_i^2} \tag{13.10}$$

or, conversely, as

$$\omega_i = |s_i|\ \xi_i = -\frac{\mathrm{Real}(s_i)}{|s_i|}. \tag{13.11}$$

Each modal frequency and damping ratio can be drawn through Eq. 13.11 from either the corresponding eigenvalue s_i or from its complex conjugate $s_{i,c}$. Analogously, the $2n$ eigenvectors of $\mathbf{A}$ come in complex conjugate pairs that can be collected in a $2 \times 2n$ matrix $\boldsymbol{\Psi}$:

$$\boldsymbol{\Psi} = \begin{bmatrix} \boldsymbol{\psi}_1 & \boldsymbol{\psi}_{1,c} & \ldots & \boldsymbol{\psi}_n & \boldsymbol{\psi}_{n,c} \\ s_1\boldsymbol{\psi}_1 & s_{1,c}\boldsymbol{\psi}_{1,c} & \ldots & s_n\boldsymbol{\psi}_n & s_{n,c}\boldsymbol{\psi}_{n,c} \end{bmatrix} \tag{13.12}$$

Each column of the matrix $\boldsymbol{\Psi}$ can be thought as made of 2 n-component vectors. The first n-component vector is actually the complex modal shape, the second part is the modal shape times the corresponding complex frequency. If damping can be neglected, the following equation holds:

$$\boldsymbol{\Phi} = \begin{bmatrix} \boldsymbol{\varphi}_1 & \boldsymbol{\varphi}_2 & \ldots & \boldsymbol{\varphi}_n \end{bmatrix} = \begin{bmatrix} \boldsymbol{\psi}_1 & \boldsymbol{\psi}_2 & \ldots & \boldsymbol{\psi}_n \end{bmatrix} = \boldsymbol{\Psi}* \tag{13.13}$$

otherwise $\boldsymbol{\psi}_i$ is the complex modal shape corresponding to the real, undamped counterpart $\boldsymbol{\varphi}_i$, but explicitly considering the damping. $\boldsymbol{\Psi}*$ here denotes the subset of $\boldsymbol{\Psi}$ directly comparable to $\boldsymbol{\Phi}$.

Let us assume that each control force f_{di}, at a given instant of time, has a specific value f_{ui}, function of the system's state through a gain matrix $\mathbf{G}$ as follows:

$$\mathbf{f}_d(t) = [f_{d1}(t) \quad \ldots \quad f_{dm}(t)]^{\mathrm{T}} = \mathbf{f}_u(t) = [f_{u1}(t) \quad \ldots \quad f_{um}(t)]^{\mathrm{T}} = -\mathbf{G} \cdot \mathbf{z}(t). \tag{13.14}$$

In this case, the free vibrations (Eq. 13.7) becomes:

$$\dot{\mathbf{z}} = \mathbf{A}\,\mathbf{z} + \mathbf{B}\,\mathbf{f}_d = \mathbf{A}\,\mathbf{z} + \mathbf{B}(-\mathbf{G}\mathbf{z}) = (\mathbf{A}-\mathbf{B}\mathbf{G}) = \mathbf{A}_{\mathrm{CL}}\,\mathbf{z}. \qquad (13.15)$$

Eigenvalues and eigenvectors of $\mathbf{A}_{\mathrm{CL}}$ (summarizing the properties of the closed loop controlled system) are different from those of $\mathbf{A}$ or, in other words, frequencies, damping ratios, and modal shapes of the controlled system are different from those of the uncontrolled one. Therefore, a question arises if modal parameters can be modified in a more favorable way. An answer to this question was probably first introduced by Moore [11] and then explored by many scholars, but the authors are unaware of any application to the particular case of SA controlled wind turbines. In the latter case, in order to reduce stresses in the supporting tower, it would be desirable to have a first modal shape of the controlled structure dominated by a highly damped rigid motion around the hinged base and higher modes with mass participation factors close to 0.

Let us assume that a matrix $\mathbf{G}$ does exist so that $s_{d,i}$ and $\boldsymbol{\psi}_{d,i}$ are the desired eigenvalue and eigenvector of the i-th mode of the closed loop (CL) system. When the CL system vibrates according to that mode, the system state varies proportionally to the displacements and velocities described by the corresponding eigenvector:

$$\mathbf{z}(t) = \boldsymbol{\psi}_{d,i} \cdot \mathrm{e}^{s_{d,i}\cdot t} \qquad (13.16)$$

and in this case the desired control forces $\mathbf{f}_{ui}$ can be expressed as:

$$\mathbf{f}_{ui}(t) = \mathbf{u}_i \cdot \mathrm{e}^{s_{d,i}\cdot t} = -\mathbf{G}\,\mathbf{z}(t) = -\mathbf{G}\,\boldsymbol{\psi}_{d,i} \cdot \mathrm{e}^{s_{d,i}\cdot t}. \qquad (13.17)$$

The product $\mathbf{A}_{\mathrm{CL}}.\boldsymbol{\psi}_{d,i}$ can be written as:

$$\mathbf{A}_{\mathrm{CL}}\,\boldsymbol{\psi}_{d,i} = (\mathbf{A} - \mathbf{B}\,\mathbf{G})\,\boldsymbol{\psi}_{d,i} = \mathbf{A}\,\boldsymbol{\psi}_{d,i} + \mathbf{B}\left(-\mathbf{G}\,\boldsymbol{\psi}_{d,i}\right) = \mathbf{A}\,\boldsymbol{\psi}_{d,i} + \mathbf{B}\,\mathbf{u}_i. \qquad (13.18)$$

Being $s_{d,i}$ and $\boldsymbol{\psi}_{d,i}$ an eigenvalue and the corresponding eigenvector of $\mathbf{A}_{\mathrm{CL}}$, the same product is also equal to:

$$\mathbf{A}_{\mathrm{CL}}\,\boldsymbol{\psi}_{d,i} = s_{d,i}\,\boldsymbol{\psi}_{d,i}. \qquad (13.19)$$

By combining Eqs. 13.18 and 13.19,

$$\mathbf{A}_{\mathrm{CL}}\,\boldsymbol{\psi}_{d,i} = \mathbf{A}\,\boldsymbol{\psi}_{d,i} + \mathbf{B}\,\mathbf{u}_i = s_{d,i}\,\boldsymbol{\psi}_{d,i} \qquad (13.20)$$

or

$$\mathbf{B}\,\mathbf{u}_i = \left(s_{d,i}\,\mathbf{I} - \mathbf{A}\right)\boldsymbol{\psi}_{d,i} \qquad (13.21)$$

and, finally,

$$\boldsymbol{\psi}_{d,i} = \left[\left(s_{d,i}\,\mathbf{I} - \mathbf{A} \right)^{-1}\mathbf{B} \right] \mathbf{u}_{\mathrm{i}} = \mathbf{H}_i\,\mathbf{u}_{\mathrm{i}} \ (\dim \mathbf{H}_i = 2n \times m). \tag{13.22}$$

Equation 13.22 shows the relationship among the desired eigenvalue $s_{d,i}$ and eigenvector $\boldsymbol{\psi}_{d,i}$, the matrix of the original, uncontrolled system $\mathbf{A}$ and the corresponding control forces $\mathbf{u}_i$, i.e., the control forces able to make the controlled system vibrate according to desired modal shape, frequency and damping ratio. Should the matrix $\mathbf{H}_i$ be invertible, calculation of the control forces $\mathbf{u}_i$ would be straightforward. However, it is generally not. An approximate approach to solve Eq. 13.22 for $\mathbf{u}_i$ is to consider the pseudo-inverse matrix $\mathbf{H}_i{}^{\wedge}$ of $\mathbf{H}_i$. In this case, $\mathbf{u}_i$ can be approximately evaluated as

$$\mathbf{u}_i = \mathbf{H}_i^{\wedge}\boldsymbol{\psi}_{d,i} = \left[\left(\mathbf{H}_i^{\mathrm{T}}\,\mathbf{H}_i \right)^{-1}\mathbf{H}_i^{\mathrm{T}} \right]\boldsymbol{\psi}_{d,i}. \tag{13.23}$$

However, by using the approximation expressed by Eq. 13.23, the actual eigenvector $\boldsymbol{\psi}_{\mathrm{CL},i}$ of the CL system will be similar, but not exactly equal to the desired one $\boldsymbol{\psi}_{d,i}$:

$$\boldsymbol{\psi}_{\mathrm{CL},i} = \mathbf{H}_i\,u_i \cong \boldsymbol{\psi}_{d,i}\,. \tag{13.24}$$

If the approximation of Eq. 13.23 is acceptable, by selecting the desired frequency and damping ratio (through $s_{d,i}$) and the shape (through $\boldsymbol{\psi}_{\mathrm{CL},i}$) of each mode of vibration, it is possible to calculate the corresponding values of the desired control forces $\mathbf{u}_i$ and the resulting CL eigenvector $\boldsymbol{\psi}_{\mathrm{CL},i}$, to be collected in the matrices $\mathbf{U}$ and $\boldsymbol{\Psi}_{\mathrm{CL}}$, respectively:

$$\begin{aligned} \mathbf{U} &= \begin{bmatrix} u_1 & u_2 & \ldots & u_{2n} \end{bmatrix} \quad (\dim \mathbf{U} = m \times 2n) \\ \boldsymbol{\Psi}_{\mathrm{CL}} &= \begin{bmatrix} \boldsymbol{\psi}_{\mathrm{CL},1} & \boldsymbol{\psi}_{\mathrm{CL},2} & \cdots & \boldsymbol{\psi}_{\mathrm{CL},2n} \end{bmatrix} \quad (\dim \boldsymbol{\Psi}_{\mathrm{CL}} = 2n \times 2n). \end{aligned} \tag{13.25}$$

Recalling Eq. 13.17, it is:

$$\mathbf{U} = -\mathbf{G}\,\boldsymbol{\Psi}_{CL} \tag{26}$$

and, therefore, the gain matrix can be found as

$$\mathbf{G} = -\,\mathbf{U} \cdot \boldsymbol{\Psi}_{\mathrm{CL}}^{-1}. \tag{13.27}$$

Once $\mathbf{G}$ is calculated through Eq. 13.27, the corresponding control forces $\mathbf{f}_u$ defined by Eq. 13.14 are able to approximately transform the original structure so that it has the desired modal properties:

- frequency and damping ratio of each selected mode;
- modal shapes.

It is worth to notice that the procedure described before works also if only a portion of a CL eigenvector is desired to have a given shape. In other words, the selection can be also referred to portions of some or all CL eigenvectors. Due to the approximate calculations introduced before, the less demanding is the eigenvector selection, the most accurate is the result, i.e., the closer are CL and desired eigenvectors.

Provided that more than one independent controller be available and that the positioning of such controllers yields a controllable system, for a feed-back controlled wind turbine it is thus possible to directly design the modal behavior, in terms of both modal frequencies and damping ratio, and modal shapes. When there is only one controller available, as in the case of the experimental activity described herein, it is possible to directly design modal frequencies and damping ratio only, and to indirectly control modal shapes.

13.5.1 Closed-Loop Eigenstructure Selection (CLES) Algorithm

A simplified structural model of the wind turbine mock up described in the previous sections is shown in Fig. 13.14. It is a 2 DOFs system whose equations of motion in the absence of any external disturbance are:

$$
\begin{bmatrix} m_T & m_T \\ 0 & m_\alpha/h \end{bmatrix} \begin{bmatrix} \ddot{\delta}_{el} \\ \ddot{\delta}_{rig} \end{bmatrix} + \begin{bmatrix} c_T & 0 \\ 0 & 0 \end{bmatrix} \begin{bmatrix} \dot{\delta}_{el} \\ \dot{\delta}_{rig} \end{bmatrix} + \begin{bmatrix} k_T & 0 \\ 0 & 2 \cdot k_s \cdot l_s^2/h \end{bmatrix} \begin{bmatrix} \delta_{el} \\ \delta_{rig} \end{bmatrix}
$$
$$
= - \begin{bmatrix} 0 \\ 2 \cdot l_d \end{bmatrix} \cdot f_d \tag{13.28}
$$

or

$$
\mathbf{M}\ddot{\delta} + \mathbf{C}\dot{\delta} + \mathbf{K}\delta = -\mathbf{p}f_d \tag{13.29}
$$

where:

$m_T = m_{top} + m_{tow}$	is the translational mass of the model;
$m_{top} = 280$ kg	is the translational mass at the top of the tower;
$m_{tow} = 15.4$ kg	is the 1st mode translational mass of the vertical structure;
$m_\alpha = 8,329$ kg m^2	is the rotational mass of the model;
$c_T = 32.4$ Ns/m	is the equivalent linear viscous damping of the tower;
$k_T = 13,855$ N/m	is the lateral stiffness of the tower;
$k_s = 89,000$ N/m	is the stiffness of each base spring;
$l_s = 0.65$ m	is distance between each spring and the hinge;
$l_d = 0.45$ m	is distance between each SA MR damper and the hinge;
$h = 5.26$ m	is the height of the tower;
f_d	is the force exerted by each SA MR damper;
α	is the rotation of the base;
$\delta_{rig} = \alpha \times h$	is the rigid portion of the top displacement;

Fig. 13.14 Structural model
of the tested mock-up
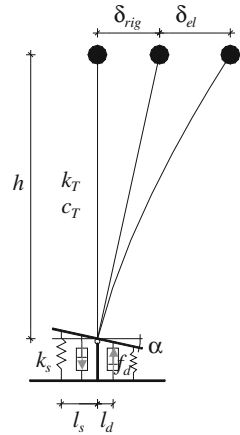
δ_{el} is the elastic part of the top displacement;

M, **C**, and **K**   are the mass, damping, and stiffness matrices;

p   is the vector describing the position of the dampers;

$\delta = [\delta_{el}\ \delta_{rig}]^{T}$ is the vector collecting the DOFs of the system.

Parameters c_T and k_T have been defined according to a preliminary identification campaign of the fixed base tower, which turned out to show a natural period of vibration of 0.92 s and a damping ratio equal to 0.8 % [12, 13]. Once the tower is mounted on the rotating support, the resulting 2 DOFs free ($f_d = 0$) system described by Eq. 13.28 has modal periods equal to:

$$1\text{st mode}: \quad T_1 = 2.09\,\text{s};$$
$$2\text{nd mode}: \quad T_2 = 0.92\,\text{s}.$$

The first mode is dominated by a rigid rotation around the base hinge, whereas the second replies the elastic motion of the tower alone on a fixed base, as shown in Eq. 13.30 where the undamped modal shapes are ordered as columns of the matrix $\mathbf{\Phi}$ and normalized, for clarity, so that one component of each eigenvector is set to 1:

$$\mathbf{\Phi} = \begin{bmatrix} 1.000 & 0.000 \\ 0.239 & 1.000 \end{bmatrix} \begin{pmatrix} \delta_{\text{rig}} \\ \delta_{\text{el}} \end{pmatrix}. \tag{13.30}$$

By considering the dampers in their "off" state, they are equivalent to linear viscous damper with a constant $c_d = 6{,}900$ Ns/m [17]. In this case, the force in each damper is equal to (the sign is already considered in the model of Fig. 13.14).

$$f_d = c_d \cdot l_d \cdot \dot{\delta}_{\text{rig}}/h \tag{13.31}$$

and Eq. 13.28 can be written as

$$\begin{bmatrix} m_T & m_T \\ 0 & m_\alpha/h \end{bmatrix} \begin{bmatrix} \ddot{\delta}_{el} \\ \ddot{\delta}_{rig} \end{bmatrix} + \begin{bmatrix} c_T & 0 \\ 0 & 2 \cdot c_d \cdot l_d^2/h \end{bmatrix} \begin{bmatrix} \dot{\delta}_{el} \\ \dot{\delta}_{rig} \end{bmatrix} + \begin{bmatrix} k_T & 0 \\ 0 & 2 \cdot k_s \cdot l_s^2/h \end{bmatrix} \begin{bmatrix} \delta_{el} \\ \delta_{rig} \end{bmatrix} = \begin{bmatrix} 0 \\ 0 \end{bmatrix}.$$

(13.32)

or

$$\mathbf{M} \ddot{\boldsymbol{\delta}} + \mathbf{C}_{off} \dot{\boldsymbol{\delta}} + \mathbf{K} \boldsymbol{\delta} = \mathbf{0} \tag{13.33}$$

being $\mathbf{C}_{off}$ the damping matrix when the SA MR dampers are switched off. This system can be equivalently described in the state space as

$$\dot{\mathbf{z}} = \mathbf{A}_{off} \, \mathbf{z} \tag{13.34}$$

where $\mathbf{z}$ is the state vector of the system and $\mathbf{A}_{off}$ is the matrix describing the dynamic behavior of the tested model when the dampers are switched off, defined as follows:

$$\mathbf{z} = \begin{bmatrix} \delta_{el} & \delta_{rig} & \dot{\delta}_{el} & \dot{\delta}_{rig} \end{bmatrix}^T; \quad \mathbf{A}_{off} = \begin{bmatrix} \mathbf{0}_{2\times2} & \mathbf{I}_{2\times2} \\ -\mathbf{M}^{-1}\mathbf{K} & -\mathbf{M}^{-1}\mathbf{C}_{off} \end{bmatrix} \tag{13.35}$$

The complex eigenvalues of $\mathbf{A}_{off}$ describe the periods T_i and the modal damping ratios ξ_i of the tested model. They are as follows:

$$\text{1st mode}: \quad T_1 = 2.09 \, \text{s} \quad \xi_1 = 5.6\,\%;$$
$$\text{2nd mode}: \quad T_2 = 0.92 \, \text{s} \quad \xi_2 = 0.8\,\%.$$

The first objective of the control algorithm is to achieve higher damping ratios without changing the periods of vibration. This objective can be reached through the classical pole placement procedure of System's Theory. If a "desired" force u for each damper is assumed, Eq. 13.29 can be written, in the state space, as

$$\dot{\mathbf{z}} = \mathbf{A}\,\mathbf{z} + \mathbf{b}\,u \tag{13.36}$$

where

$$\mathbf{A} = \begin{bmatrix} \mathbf{0}_{2\times2} & \mathbf{I}_{2\times2} \\ -\mathbf{M}^{-1}\mathbf{K} & -\mathbf{M}^{-1}\mathbf{C} \end{bmatrix} \quad \mathbf{b} = \begin{bmatrix} \mathbf{0}_{2\times1} \\ -\mathbf{M}^{-1}\mathbf{p} \end{bmatrix} \tag{13.37}$$

If the control force is proportional to the system's state through Eq. 13.14, it can be showed that the gain matrix $\mathbf{G}$ can be designed so as that the eigenvalues of the controlled system can be arbitrarily assigned or, in other words, the desired

values of damping ratios and natural periods can be achieved [10]. Therefore, the matrix $\mathbf{G}$ can be designed so as to achieve the first objective of maintaining the modal periods while increasing the modal damping ratios.

As said before, within the experimental setup herein focused, only one independent control force was available, provided by the 2 SA MR dampers. Should more independent control forces be available, the gain matrix $\mathbf{G}$ could be designed to arbitrarily modify the modal shapes of the controlled system, too. Actually, this is the second objective of the control strategy adopted, i.e., to modify the modal behavior of the tower so as to obtain a dominant, highly damped mode corresponding to a rigid rotation of the structure around the base hinge and a secondary mode combining a rigid rotation to an elastic deformation of the tower bounded by a damping ratio significantly higher than that of the tower alone (0.8 %). Due to the presence of only one independent controller, the procedure described before cannot be applied. However, also the pole placement technique modifies, through $\mathbf{G}$, the CL system matrix and, in turn, its complex eigenvectors (i.e., the modal shapes of the controlled tower). Therefore, when the desired control force u is designed through Eq. 13.14 so as to obtain the given values of periods of vibration and modal damping ratios for the CL system, also the modal shapes of the controlled system change compared to the original, uncontrolled one. Based on a trial and error iterative procedure, authors ended up with the following feedback control law:

$$u = -2 \cdot \begin{bmatrix} g_1 & g_2 & g_3 & g_4 \end{bmatrix} \cdot \mathbf{z} \tag{13.38}$$

where:

$g_1 = 597$ N/m; $g_2 = 0$; $g_3 = 408$ Ns/m; $g_4 = 1{,}154$ Ns/m.

In this case, the CL controlled tower shows the following periods and damping ratios:

$$\text{1st mode}: \quad T_1 = 2.09\,\text{s} \quad \xi_1 = 20\,\%;$$
$$\text{2nd mode}: \quad T_2 = 0.92\,\text{s} \quad \xi_2 = 5\,\%.$$

Correspondingly, the complex eigenvectors of the controlled towers, ordered as columns of the matrix $\mathbf{\Psi}^*$ and normalized as before, are:

$$\mathbf{\Psi}_* = \begin{bmatrix} |1.000| \angle 0° & |0.084| \angle 93° \\ |0.234| \angle -27° & |1.000| \angle 0° \end{bmatrix} \quad \begin{pmatrix} \delta_{\text{rig}} \\ \delta_{\text{el}} \end{pmatrix} \tag{13.39}$$

Equation 13.39 shows only a portion ($\mathbf{\Psi}^*$) of the eigenvector matrix $\mathbf{\Psi}$ of the controlled tower. Indeed, in the present case the eigenvectors come in complex conjugate pairs carrying, each pair, exactly the same piece of information. Furthermore, each eigenvector has four components, two related to displacements (shown in Eq. 13.39) and two relates to velocities (out of interest in the present case). Complex eigenvectors in Eq. 13.39 are described through their module and

phase. The first mode resulted to be dominated by a rigid rotation of the tower around the base with a reasonably high damping ratio, whereas the second mode is dominated by the elastic strain of the tower. For the latter, however, in the controlled system a rigid rotation is also involved, so that a damping ratio of about 5 % ($\gg$0.8 %) can be obtained due to the SA MR dampers.

If active devices had been involved, the force $u(t)$ should be imposed instant by instant to them in order to achieve the target performances of the structure. In the present case of SA control, instead, this force has to be intended as a desired control action, that is the one the MR dampers have to mimic in real time to lead to an effective control of the tower response. Therefore, the CLES algorithm has been set so as to modulate the current fed to the SA MR dampers with the aim to make the reacting force $f_d(t)$ of each damper as close as possible to the theoretical value $u(t)$. This kind of logic can thus be expressed as follows:

$$
\begin{aligned}
&\text{if} \quad f_d(t) \cdot u(t) < 0 &&&&\rightarrow\quad i(t) = 0 \\
&\text{if} \quad f_d(t) \cdot u(t) \geq 0 &&\text{and}\quad |f_d(t)| < |u(t)| &&\rightarrow\quad i(t) = i(t - dt) + [i_{max} - i(t - dt)/n] \\
&\text{if} \quad f_d(t) \cdot u(t) \geq 0 &&\text{and}\quad |f_d(t)| \geq |u(t)| &&\rightarrow\quad i(t) = i(t - dt) + [0 - i(t - dt)/n]
\end{aligned}
\tag{13.40}
$$

where $i(t$–$dt)$ is the current commanded to the dampers in the instant before the actual one (t), dt is the sampling time for control (1 ms), n is a dimensionless parameter (≥ 1) introduced to smoothen the variation of the command current between 0 and i_{max}.

13.5.2 Two Variables (2VAR) Algorithm

An alternative control algorithm has been formulated and adopted for the shaking table tests of the wind turbine model. It is based on a more physical and easier approach in respect to the above-mentioned CLES controller.

The basic idea consists in controlling the base stress and top displacement so as to "force" them to be within a given range. Reducing top displacement and base stress are two performance objectives in conflict to each other. Actually, the demand of base bending stress can be reduced by "relaxing" the base restraint (i.e., reducing the damping of the SA devices). However, as a direct consequence, the top displacement demand (related to both the rigid body motion—due to the base rotation—and the elastic deflection of the tower) will increase.

This controller has been developed aiming to achieve a trade-off between these two contradictory objectives. To do that, first of all, a limit value for both base stress and top displacement have been assumed (σ_{lim} and x_{lim} in the following, respectively). Then, by denoting with $\sigma(t)$, $x(t)$ and $\dot{x}(t)$, respectively, the maximum stress at the base, the top displacement, and the top velocity at the instant of

time t, the following logic has been assumed to take the decision about the optimal status ("on" or "off") to be set for the dampers in that instant:

$$\text{if } |\sigma(t)| < \sigma_{\lim} \quad \rightarrow i(t) = i_{\max} \tag{13.41}$$

$$\text{if } |\sigma(t)| \geq \sigma_{\lim} \text{ and } |x(t)| < x_{\lim} \quad \rightarrow i(t) = 0 \tag{13.42}$$

$$\text{if } |\sigma(t)| \geq \sigma_{\lim} \text{ and } |x(t)| \geq x_{\lim} \text{ and } x(t)\dot{X}(t) > 0 \rightarrow i(t) = i_{\max} \tag{13.43}$$

$$\text{if } |\sigma(t)| \geq \sigma_{\lim} \text{ and } |x(t)| \geq x_{\lim} \text{ and } x(t)\dot{X}(t) \leq 0 \rightarrow i(t) = 0. \tag{13.44}$$

In other words, the controller keeps "stiffer" the base restraint until the stress does not exceed the limit value (Eq. 13.41), whereas "relaxes" it (switching off the MR dampers) when this limit is passed and the displacement falls within the limits (Eq. 13.42). When both stress and displacement are beyond the respective threshold values, the controller switches on the dampers if the displacement is going in the direction of a further increase (so trying to invert or at least to damp this trend; Eq. 13.43), otherwise it switches off the MR devices to make sure they do not hinder the ongoing reduction of displacement (Eq. 13.44).

Figure 13.15 graphically describes this algorithm, in a schematic way, showing what is the decision of the controller (switch on or switch off) depending on the occurrence of each of the four above-mentioned possible combination about the state of base stress and top displacement.

It is worth noting that the practical use of such control algorithm require a preliminary calibration through properly setting the three involved parameters, i.e. $i_{\max}$, $\sigma_{\lim}$ and $x_{\lim}$.

13.6 Experimental Activity and Results

Two load cases were considered:

- an extreme operating gust (EOG), i.e., a sharp increase, then decrease in wind speed within a short period of time;
- a high velocity wind buffeting, i.e., a load case (called "parking", PRK) that typically concerns a wind turbine when "parked" (with a controlled shutdown) due to the high-velocity wind.

Chen and Georgakis [12, 13], for both load cases, have defined an equivalent base acceleration time history (Fig. 13.16), that is the base input that would give the same top mass response of the real, fixed base structure subjected to the wind action. This kind of analysis has been made using the wind turbine aeroelastic code HAWC2 (Horizontal Axis Wind turbine simulation Code, second generation), realized at the DTU (Denmark) for calculating wind turbine response in time

Fig. 13.15 The logic behind the 2VAR controller (numbers refer to Eqs. 13.41–13.44)
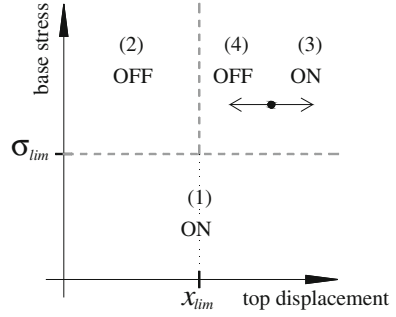
Fig. 13.16 Equivalent base accelerations corresponding to the two wind load cases: **a** Extreme operating gust (EOG), **b** Parking (PRK)
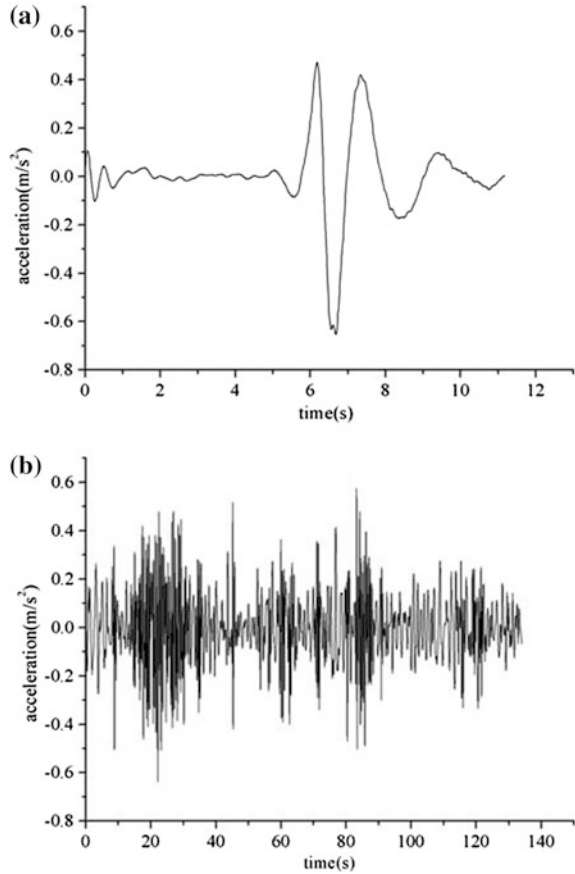
domain [20]. These accelerograms have been reproduced through the shaking table facility to perform all the dynamic tests discussed in the following.

The mock-up structure has been tested first in a fixed base (FB) condition. The FB configuration has been realized using the same setup of Fig. 13.4, simply

Table 13.1 Fixed base condition: peak response of the tower under both load cases

input	max|σ| [MPa]	max|x| [mm]
EOG	51	39
PRK	29	25

imposing the MR dampers to work as rigid links, feeding them with a constant current of 3 A during the overall duration of the tests. Actually the expected (then registered) maximum force applied to the dampers for the two FB tests were less than 5 kN, therefore much less than the threshold value for the "friction" force F_{dy} of the devices (about 27 kN for 3 A, according to Eq. 13.3). Table 13.1 summarizes the peak absolute value for displacement x (top of the tower relative to the base) and for base stress σ for both load cases.

The structural model has been tested first using the CLES control algorithm. The higher value of the dimensionless parameter n involved in the procedure, as previously said, gives smoother variations of command voltage in time. According to the results of three pre-tests, the values $n = 15$ for the EOG load case and $n = 1$ for PRK load case were selected.

Subsequently, various tests have been performed with the 2VAR control algorithm to evaluate and compare the effects, in terms of reduction of the structural response, of different couples of stress (σ_{lim}) and displacement (x_{lim}) limits chosen within the ranges [10, 40] MPa and [16, 46] mm respectively. The best combination of limit values resulted to be (σ_{lim}, x_{lim}) = (30 MPa, 46 mm) for the EOG load case, and (σ_{lim}, x_{lim}) = (12 MPa, 20 mm) for the PRK input.

For each of the above-mentioned tests the reduction of the base stress has been monitored as the first objective to be achieved. Moreover, the effectiveness in controlling top displacement has been evaluated, even if a moderate increase has been considered acceptable. In particular, peak top displacement less than 1.3 times the peak registered in the FB condition have been tolerated, not causing significant detrimental second order effects to the tower.

The main experimental results related to the four tests (two load cases, two controllers) are described in the next sections, first with reference to the EOG, then to the PRK load cases.

In the following, the command voltage has to be intended as a 0–10 V voltage signal in output from the controller (PC) and in input to the power supplies, the latter having, when adopted as current driver, a control loop gain 0.4 A/V. The maximum intensity of current inside the dampers for all the tests has been set equal to 1 A. Therefore, the maximum command signal is 2.5 V.

13.6.1 SA Control for the Extreme Operating Gust Load Case

An extreme operating gust (EOG) is a sharp increase and then decrease in wind speed that occurs over a short period of time while the turbine is operating. The equivalent base acceleration time history in Fig. 13.16 has been considered herein to assess the effectiveness of both SA control strategies, reproducing such input signal through the DTU shaking table, properly commanding the MTS actuator.

In the following, the results obtained with the CLES controller are described first, then those corresponding to the 2VAR logic.

13.6.1.1 CLES Controller: Response Reduction Under the EOG Load Case

The desired control force $u(t)$ as defined in Sect. 13.5.1 has been calculated in real time during the entire duration of the test. The CLES controller modulated the command signal so as to make the current vary between 0 and 1 A, aiming, at each instant of time, at making the MR reactive force as close to $u(t)$ as possible.

Figure 13.17 shows the results in terms of base stress, top displacement, command voltage, and forces, desired and actual force exerted by MR dampers, respectively. The time window 4–10 s has been plotted, i.e., that corresponding to the most significant part of the accelerogram imposed at the base. The first two diagrams—(a) and (b)—allow to compare the SA controlled response to that corresponding to the FB condition, under the same input base motion.

The actual control force of the MR dampers satisfactory tracked the desired one (Fig. 13.17d), thanks to the modulation of the command voltage according to the above-mentioned logic (Fig. 13.17c). This lead, as expected, to a strong reduction of base stress, trading off larger peak top displacement, however, within the tolerance assumed in respect to the one registered for the FB case. Table 13.2 helps synthesize such findings, in terms of peak values of base stress and of top displacement recorded for the whole duration of the test. The CLES controller, in respect to the FB case, reduced the peak base stress of 67 %, even at the cost of 28 % larger peak top displacement.

13.6.1.2 2VAR Controller: Response Reduction Under the EOG Load Case

The performance of the 2VAR controller with limit values of σ_{lim} and x_{lim} equal to 30 MPa and 46 mm, respectively, is described in the following. Figure 13.18 shows the results in terms of base stress, top displacements, and command voltage, allowing the comparison with the FB response under the same base input motion. The first two diagrams—(a) and (b)—are referred to the overall duration of the
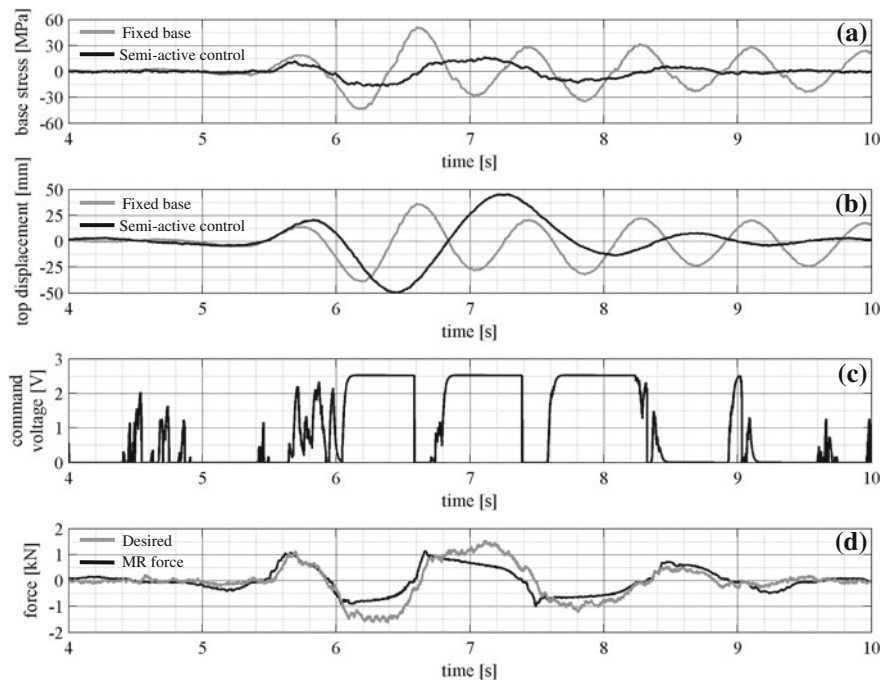
Fig. 13.17 EOG load case: SA control via the CLES controller and comparison with the FB case

Table 13.2 EOG input: peak response of the FB structure and of the SA case using the CLES controller

Case	max$|\sigma|$	max$|x|$
Fixed base	51 MPa	39 mm
Semi-active CLES	17 MPa	50 mm
FB → SA	−67 %	+28 %

Percentage variation from the first to the second condition

EOG accelerogram, whereas diagrams (c), (d), and (e) are focused on a 2 s time window (5.5–7.5 s), so highlighting the behavior of the uncontrolled and controlled tower during the strongest phase of the base excitation.

It can be observed that the top displacement always resulted to be within the limit of 46 mm, therefore only conditions in Eqs. 13.41 and 13.42 occurred. Figure 13.18c–e highlights the position of two instants of time (6.19 and 6.77 s) where the condition of Eq. 13.42 and of Eq. 13.41, respectively occurred, causing a switch-off and a switch-on of the current in the devices. Looking again at Fig. 13.18, the reduction of stress and displacement compared to FB case (except for the peak displacement) is quite evident. In particular, around the strong phase of the excitation, the control algorithm, also thanks the promptness of the control
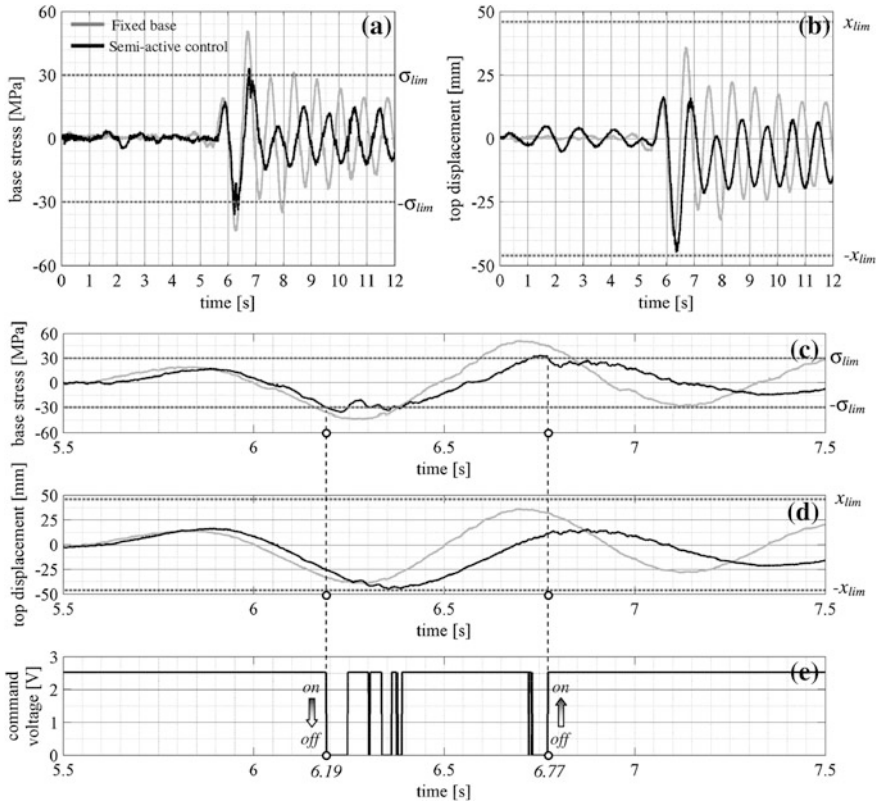
Fig. 13.18 EOG load case: SA control via the 2VAR controller and comparison of the response with the FB case

chain, perfectly worked in "pushing down" the peak values of stress demand, forcing it to stay within the fixed limits.

Table 13.3, as for the CLES controller examined above, shows the peak values of base stress and top displacement for the FB and the 2VAR controlled cases. It allows to conclude that the 2VAR control logic, in respect to the FB case, reduced the peak base stress of 29 %, even at the cost of a 15 % increase of the peak top displacement.

13.6.2 SA Control for the Parking Load Case

When a pitch-controlled wind turbine shuts down due to the high-velocity wind, the loss of power leads to a sudden pitch of the rotor blades, leading to a "sling-shot" effect, followed by a free-decay response. When parked, the wind turbine

Table 13.3 EOG input: peak response of the FB structure and of the SA case using the 2VAR controller

Case	max|σ|	max|x|
Fixed base	51 MPa	39 mm
Semi-active 2VAR	36 MPa	45 mm
FB → SA	−29 %	+15 %

Percentage variation from the first to the second condition

will be subjected to high velocity wind buffeting, which is herein referred to as "parking" (PRK) load case.

The equivalent base acceleration time history in Fig. 13.16 has been considered to assess the effectiveness of both SA control strategies, reproducing such input signal by the shaking table. In the following, the results obtained with the CLES controller first, then with the 2VAR control logic, are discussed. Since the long duration of the input (more than 2 min), a 10 s time window has been chosen to plot the response time-histories, not to lose their readability and to show in a clearer manner how the controllers worked.

For the PRK load case, the control activity resulted to be higher than in the EOG case. The control algorithms switched on or off the MR devices many more times, making them able to better dissipate the input energy. From this perspective, the higher acceleration demand (value and number of peaks) corresponding to the PRK load case justifies the better response reduction achieved by the same SA system if compared to the EOG input.

13.6.2.1 CLES Controller: Response Reduction Under the PRK Load Case

Figure 13.19 shows the results in terms of base stress, top displacements, command voltage, and forces, respectively desired and actually exerted by MR dampers, within the selected 10 s time window. Also in this case, the controller has been able to drive MR dampers to react similarly to the ideal device, i.e., the one that would exactly output the desired control force $u(t)$. With reference to the assumed sample time window, Fig. 13.19 clearly shows that the CLES controller lead to a strong reduction of the base stress, without significantly altering the response in terms of displacement. Confirming this finding, Table 13.4 shows peak values, over the entire input duration, of base stress and top displacement and their percentage variation in respect to the FB case. The peak base stress results to be reduced of 48 %, while the peak top displacement did not change appreciably.
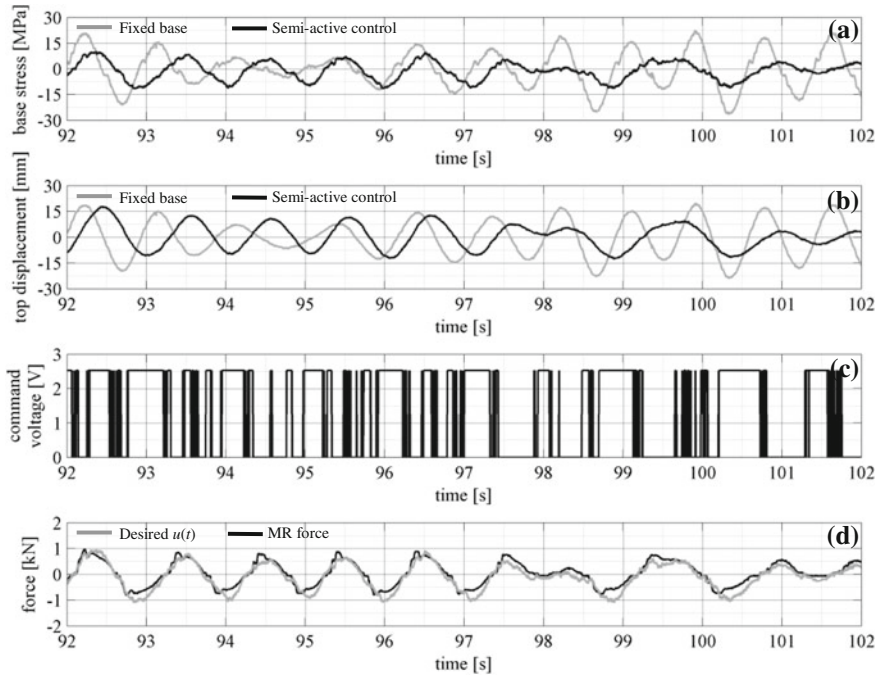
Fig. 13.19 PRK load case: SA control via the CLES controller and comparison of the response with the FB case

Table 13.4 PRK input: peak response of the FB structure and of the SA case using the CLES controller

Case	max|σ|	max|x|
Fixed base	29 MPa	25 mm
Semi-active CLES	15 MPa	25 mm
FB → SA	−48 %	0 %

Percentage variation from the first to the second condition

13.6.2.2 2VAR Controller: Response Reduction Under the PRK Load Case

The 2VAR controller for the PRK input has been set with $\sigma_{lim} = 12$ MPa and $x_{lim} = 20$ mm, as said above. Figure 13.20 shows the results in terms of base stress, top displacements, and command voltage, allowing the comparison with the FB response under the same base input motion, over the above 10 s time window.

The effectiveness of the SA control strategy based on the 2VAR logic clearly emerges comparing the plots of the response parameters with those referred to the FB case. As a matter of a fact, both base stress and top displacement in the SA test result to be forced by the controller to stay within the assigned limits.
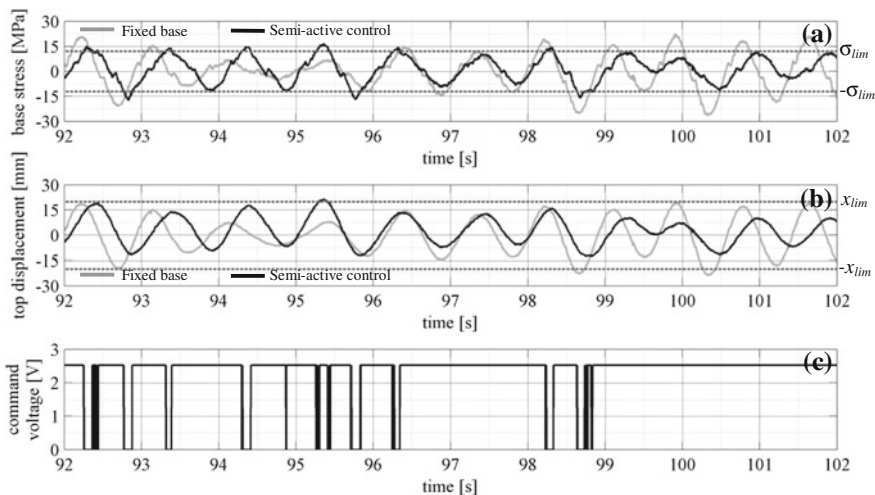
Fig. 13.20 PRK load case: SA control via the 2VAR controller and comparison of the response with the FB case

Table 13.5 PRK input: peak response of the FB structure and of the SA case using the 2VAR controller

Case	max$|\sigma|$	max$|x|$
Fixed base	29 MPa	25 mm
Semi-active 2VAR	20 MPa	23 mm
FB → SA	–31 %	–8 %

Percentage variation from the first to the second condition

As previously done with reference to the other application, the peak values for base stress and top displacement are assumed as synthetic indicators of the response for both FB and 2VAR controlled cases. Table 13.5 shows these values and the percentage variation from the FB to the SA case. It allows to conclude that the 2VAR control logic, for the PRK load case, lead to a significant reduction of the peak base stress (31 %), even if smaller than the one (48 %) obtained with the CLES controller. On the other hand, the 2VAR control logic has also been able to damp the top displacement, making the peak value 8 % smaller with respect to the FB case.

13.7 Conclusions

The theoretical base and the experimental activity about an SA control system for wind turbines based on MR devices has been described. The main findings of the research activity are as follows:

- Structural control of wind turbines based on SA MR dampers and on a base restraint rearrangement of the tower looks feasible;
- Significant reduction of stresses in the turbine tower can be reached trading off a minor increase of the top displacement. Due to the proposed control system, however, displacements of the tower are only partly related to strain;
- Obviously, control algorithms play a relevant role in the behavior of the controlled systems. However, in judging their performances the complexity and the overall reliability of the system (number and type of sensors, real-time computing effort needed) should be taken into account.

A further optimization of the response of a wind turbine can be envisioned by considering the possibility of fully reshaping the modal behavior. The theoretical base of such a strategy is also presented herein, based on the exploitation of more than one independent control force. The possibility of adopting multiple SA MR dampers in the structural control of wind turbines represents the next research step, currently in progress, of the research activity.

References

1. Kirkegaard PH, Nielsen SRK, Poulsen BL, Andersen J, Pedersen LH, Pedersen BJ (2002) Semiactive vibration control of wind turbine tower using an MR damper, structural dynamics: EURODYN 2002. Balkema Publishers A.A., Taylor and Francis, Netherlands, Rotterdam, pp 1575–1580
2. Karimi HR, Zapateiro M, Luo N (2010) Semiactive vibration control of offshore wind turbine towers with tuned liquid column dampers using h_∞ output feedback control. In: Proceedings of IEEE international conference on control applications, Yokohama, Japan
3. Luo N, Bottasso CL, Karimi HR, Zapateiro M (2011) Semiactive control for floating offshore wind turbines subject to aero-hydro dynamic loads. In: Proceedings of international conference on renewable energies and power quality—ICREPQ 2011, Las Palmas de Gran Canaria, Spain
4. Luo N (2011) Smart structural control strategies for the dynamic load mitigation in floating offshore wind turbines. In: Proceedings of international workshop on advanced smart materials and smart structures technology—ANCRiSST, Dalian, China
5. Luo N (2012) Analysis of offshore support structure dynamics and vibration control of floating wind turbines. USTC J 42(5):1–8
6. Luo N, Pacheco L, Vidal Y, Li H (2012) Smart structural control strategies for offshore wind power generation with floating wind turbines. In: Proceedings of international conference on renewable energies and power quality—ICREPQ 2012, Santiago de Compostela, Spain
7. Luo N, Pacheco L, Vidal Y, Zapateiro M (2012) Dynamic load mitigation for floating offshore wind turbines supported by structures with mooring lines. In: Proceedings of european conference on structural control—EACS, Genova, Italy
8. Arrigan J, Pakrashi V, Basu B, Nagarajaiah S (2011) Control of flapwise vibrations in wind turbine blades using semi-active tuned mass dampers. Struct Control Health Monit 18:840–851. doi:10.1002/stc.404
9. Rodríguez TA, Carcangiu CE, Amo I, Martin M, Fischer T, Kuhnle B, Scheu M (2011) Wind turbine tower load reduction using passive and semi-active dampers. In: Proceedings of the european wind energy conference—EWEC 2011, Brussels, Belgium
10. Luenberger DG (1979) Introduction to dynamic systems. John Wiley and Sons, New York

11. Moore BC (1976) On the flexibility offered by state feedback in multivariable systems beyond closed loop eigenvalue assignment. IEEE Trans Autom Control 21:689–692
12. Chen J, Georgakis CT (2013) Tuned rolling-ball dampers for vibration control in wind turbines. J Sound Vib 332:5271–5282. doi:10.1016/j.jsv.2013.05.019
13. Chen J, Georgakis CT (2013) Spherical tuned liquid damper for vibration control in wind turbines. J Vib Control, SAGE Pbs, (in press). doi:10.1177/1077546313495911
14. Caterino N, Spizzuoco M, Occhiuzzi A (2011) Understanding and modeling the physical behavior of magnetorheological dampers for seismic structural control. Smart Mater Struct 20:065013. doi:10.1088/0964-1726/20/6/065013
15. Occhiuzzi A, Spizzuoco M, Serino G (2003) Experimental analysis of magnetorheological dampers for structural control. Smart Mater Struct 12:703–711. doi:10.1088/0964-1726/12/5/306
16. Carlson JD, Jolly MR (2000) MR fluid, foam and elastomer devices. Mechatronics 10:555–569
17. Caterino N, Spizzuoco M, Occhiuzzi A (2013) Promptness and dissipative capacity of MR dampers: experimental investigations. Struct Control Health Monit 20(12):1424–1440. doi:10.1002/stc.1578
18. Caterino N, Spizzuoco M, Occhiuzzi A (2014) Shaking table testing of a steel frame structure equipped with semi-active MR dampers: comparison of control algorithms, Smart Struct Syst, Technopress (in press)
19. Occhiuzzi A (2009) Additional viscous dampers for civil structures: analysis of design methods based on modal damping ratios. Eng Struct 31(5):1093–1101
20. Larsen TJ, Hansen AM (2008) HAWC2 user manual. Risø National Laboratory, Technical University of Denmark, Roskilde, Denmark

Part V
Test-Bench for Research/Education

Chapter 14
Wind Farm Lab Test-Bench for Research/Education on Optimum Design and Cooperative Control of Wind Turbines

Mario García-Sanz, Harry Labrie and Julio Cesar Cavalcanti

Abstract This chapter presents a low-cost, flexible lab test-bench wind farm for advanced research and education on wind turbine and wind farm design and control. The mechanical, electrical, electronic and control system design of the wind turbines, along with the dynamic models, parameters and classical pitch and torque controllers are introduced in detail. Furthermore, the study presents a variety of experiments that (a) quantifies the effect of the number of blades in the aerodynamic efficiency, (b) estimates the generator efficiency, (c) validates the rotor-speed pitch control system, (d) proves the concept of maximum power point tracking for individual wind turbines, (e) estimates the aerodynamic C_p/λ characteristics, (f) calculates the power curve, and (g) studies the effect of wind farm topology configurations on the individual and global power efficiency. The experimental results prove that the dynamics of the test-bench corresponds well with full-scale wind turbines. This fact makes the test-bench wind farm appropriate for advanced research and education in wind energy systems.

M. García-Sanz (✉) · H. Labrie · J.C. Cavalcanti
Control and Energy Systems Center, Case Western Reserve University,
Cleveland, OH, USA
e-mail: mario@case.edu
URL: http://cesc.case.edu

H. Labrie
e-mail: hel4@case.edu

J.C. Cavalcanti
e-mail: jxc802@case.edu

411

14.1 Introduction

Wind turbines are complex systems with large flexible structures that work under very turbulent and unpredictable environmental conditions and for a variable electrical grid. When wind turbines are combined into large wind farms, additional turbine interaction problems, grid integration issues, and cooperative control matters add more complexity to the engineering design and control.

The efficiency and reliability of a wind farm strongly depend on the applied control strategies. Large nonlinear characteristics and high model uncertainty due to the interaction of the aerodynamics, mechanical, and electrical subsystems, both at the turbine level and the wind farm level are central difficulties in the design process. Stability problems, maximization of wind energy conversion issues, load reduction strategies, mechanical fatigue minimization problems, reliability matters, availability aspects, and costs per kWh reduction strategies demand advanced cooperative control systems to regulate variables such as pitch, torque, power, rotor speed, yaw orientation, temperatures, currents, voltages, and power factors of every wind turbine [1, 2].

Every new design and control idea in the wind energy field has to be tested and validated in a realistic scenario before moving forward to a final certification and commercial implementation. Frequently, this experimentation and validation is extremely expensive or even not possible. For all these reasons, this chapter presents a new low-cost and flexible test-bench wind farm for advanced research and education in optimum wind turbine/wind farm design and cooperative control.

14.2 System Description

Figure 14.1 shows a general view of the wind farm test-bench. It includes four variable-speed pitch-controlled wind turbines (1), a supervisory control and data acquisition (SCADA) system with a central control unit (2), a smart grid with batteries for energy storage, variable electrical loads, solar panels and switches for different grid topologies (3), and a group of fans to create different wind profiles and disturbances (4).

14.2.1 Wind Turbine Description

Figure 14.2 shows a general view of each wind turbine unit. It is a variable-speed pitch-controlled wind turbine composed of a multi-blade aerodynamic rotor (1) able to support a set of 2, 3, 4, 5 or 6 blades.

The drive-train has a mechanical gearbox with a brushless induction electrical generator (2) and a connection (11) to the grid system through the current/torque

Fig. 14.1 Wind farm general view: (*1*) wind turbines; (*2*) SCADA and central control system; (*3*) smart micro grid with batteries, electrical loads, switches and solar panels; (*4*) fan system

Fig. 14.2 Wind turbine general view: (*1*) 6-blade rotor; (*2*) generator; (*3*) micro-controller; (*4*) yaw motor; (*5*) pitch motor; (*6*) rotor speed encoder; (*7*) pitch angle sensor; (*8*) yaw angle sensor; (*9*) current sensor and current/torque actuator; (*10*) voltage sensor; (*11*) grid connection
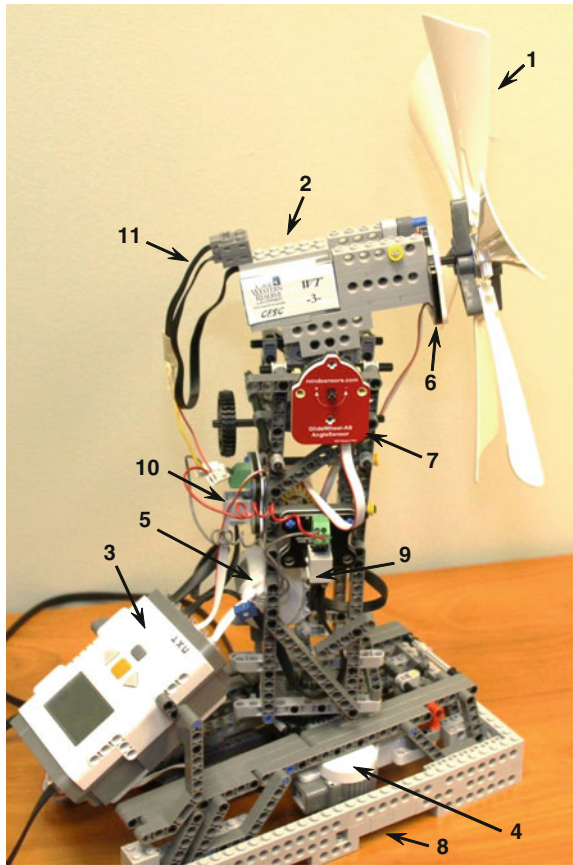
actuator (10). A set of micro-controllers (3) collect all the sensor information (6, 7, 8, 9, 10) and drives the pitch (5) and yaw (4) motors. The sensors collect in real-time data of rotor speed (6), pitch angle (7), yaw angle (8), and current (9) and voltage (10) at the output of the generator. In addition, with the above information, the system identifies in real-time the mechanical torque T_r applied to the shaft— see Eq. (14.43)—and the power P—see Eq. (14.1)—generated by the wind turbine.

The mechanical structure of the turbine, including the foundation, tower, blades and gearboxes for the pitch and yaw systems are built of LEGO blocks and wheels, giving highly modular characteristics to the prototypes. The real-time control system runs on LEGO microprocessors (3) and an external computer with Matlab—(2) in Fig. 14.1.

14.2.1.1 Aerodynamics: Rotor Blades

Figure 14.3 presents the four wind turbines of the wind farm, with three different rotor options (3, 4 and 6 rotor-blade) and a particular site configuration, while generating power into the electrical grid, and with the hierarchical control system: five NXT LEGO microprocessors for the distributed individual wind turbine control and the central computer under Matlab for the SCADA and central control system.

Each wind turbine uses a horizontal axis rotor that (1) can be configured to use two, three, four, five or six blades each, and (2) can be easily lengthened by adding an additional piece at the blades' root. The blades themselves have a drag model airfoil design, meaning the drag coefficient C_D of the blade is significantly larger than the lift coefficient C_L. In addition to a drag model airfoil, the blades each have additional texturing near the end of the blade to contribute to the effectiveness of the drag system. Figure 14.4 shows a 3-blade and a 6-blade rotor options.

Fig. 14.3 Wind farm control for optimum energy production with 3, 4 and 6 rotor-blade wind turbines
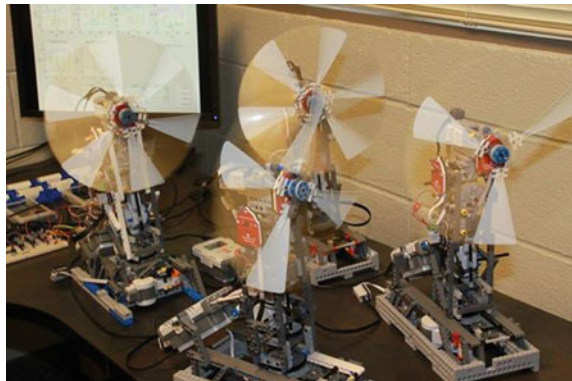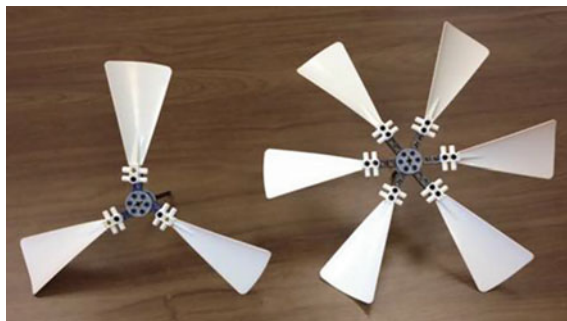
Fig. 14.4 Aerodynamics: 3-blade and 6-blade rotor options

14.2.1.2 Mechanics: Main Structures, Power Train, Tower, Nacelle, Gearboxes

The structure of the wind turbine is built around the pitch and yaw gearboxes. In order to change the angle of attack of the wind on the blades a pitch-controlled full sized wind turbine changes the pitch angle of the blades relative to the center of the rotor. This is infeasible on a small scale, so in order to implement control of the angle of attack in a comparable manner the actuators move the entire nacelle pitch angle relative to the horizontal axis. The effect on the rotor speed is very strong, as it is in a commercial wind turbine, so high precision is necessary, making a direct drive method (motor directly connected to the pitch shaft) ineffective. Thus a gearbox is implemented which gives the controller very high precision control of the pitch angle of the nacelle with minimal backlash (see Fig. 14.5). Then, the
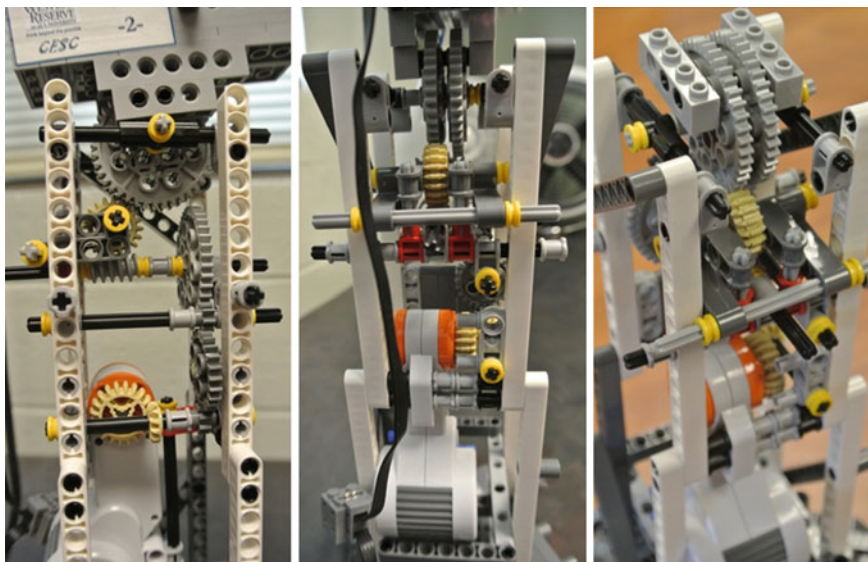
Fig. 14.5 Pitch system: motor, gearbox, mechanical configuration and tower

motor is connected to a series of gears which step up in size, decreasing the rate of rotation at each step. The largest of these moves a worm gear, giving a huge increase in the precision while simultaneously reducing backlash, with a total gearbox ratio of $r_{tg} = 1/140$. The worm moves two other gears, also stepping up in size, the larger of which is directly connected to the nacelle. In this way, the resulting pitch angle is the nacelle pitch angle relative to the horizontal axis perpendicular to the wind direction. It is represented as β in Fig. 14.12.

For the nacelle angle relative to the vertical axis, the yaw angle, we developed a second gearbox to move the entire tower relative to the base (see Fig. 14.6). This gearbox is much less complex; however, it does reduce error from the motor and increase precision. The base itself, aside from housing the motor and gearbox for the yaw control, is built to be relatively heavy to anchor the system better. It also allows for the NXT microcontroller to be attached. In this way, the resulting yaw angle is the tower angle relative to the vertical axis that passes through the center of the tower. It is represented as α in Fig. 14.12.

14.2.1.3 Electrical Components: Generator, Grid Connection

The wind turbines use a DC motor made by LEGO as a simple generator (the E-motor)—see Fig. 14.2, element (2) and Fig. 14.7a. It has a single rotor and a small gearbox with a 9.5:1 gearing ratio. It can either induce a voltage or be
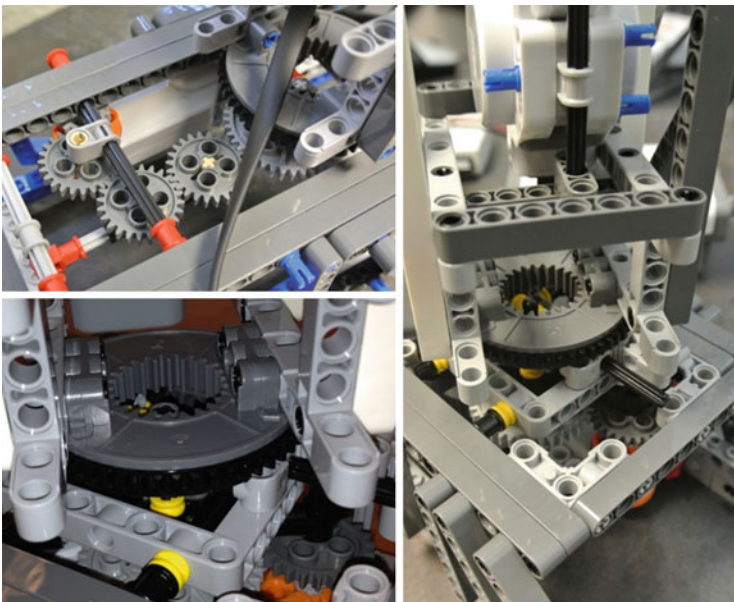
Fig. 14.6 Yaw system: motor, gearbox, mechanical configuration, tower and foundation

Fig. 14.7 a DC generator with gearbox (E-motor), **b** Actuator (NXT-motor), **c** Angle sensor (Glide-Wheel-AS), **d** CurrentMeter for NXT, **e** VoltMeter for NXT

induced to move by an applied voltage. The linear characteristics of the E-motor/generator are calculated based on [8], so that:

$$P_{\text{mec}} = T_r \, \Omega_r \; ; \quad P_{\text{elec}} = u_{\text{gen}} \, i_{\text{gen}} \; ; \quad P_{\text{elec}} = P_{\text{mec}} \, \eta_g \qquad (14.1)$$

$$T_g = K_T \, i_{\text{gen}}, \text{ where } K_T = 0.0609 \, \text{Nm/A} \qquad (14.2)$$

$$P_{\text{losses}} = P_{cu} + P_{\text{rotation}}; \; P_{\text{cu}} = i_{\text{gen}}^2 R_a, \; R_a = 21.95 \, \text{ohm}; \; P_{\text{rotation}} = 0.1508 \, \text{W} \tag{14.3}$$

being P_{mec} the mechanical power at the generator shaft (in watts), T_r the mechanical torque at the shaft (in Nm), Ω_r the rotor speed (in rad/s), P_{elec} the electrical power produced by the generator (in watts), u_{gen} the voltage at the output of the generator (in volts), i_{gen} the generator current (in A), η_g the generator efficiency, T_g the electrical torque (in Nm), and P_{losses} the generator losses (in watts) due to the Joule effect P_{cu} and friction P_{rotation}.

The generator is connected to the grid system through an actuator able to change the current i_{gen}—see Fig. 14.2, element (9)- and therefore the electrical generator torque T_g, which is opposite to the mechanical torque T_r in Fig. 14.12, Table 14.1 and Eqs. (14.24), (14.27), (14.43) and (14.44).

14.2.1.4 Sensors: Rotor Speed, Pitch and Yaw Angles, Voltage, Currents, Torque, Power, Wind

There are various electronics on each wind turbine, falling into two categories: actuators and sensors. There are three kinds of sensors on the wind turbine. On the nacelle there is a glide wheel angle sensor—see Fig. 14.2, number (6), Fig. 14.7c and Ref. [6], which is configured to record the rotor velocity. This sensor has a one degree resolution and very low resistance as it has almost exactly the same surface area as the generator, so it does not strongly affect the mechanics or aerodynamics

Table 14.1 Parameters for wind turbine model (see Fig. 14.12 and [2])

K_l low-speed shaft torsional stiffness coefficient (Nm/rad)	B_l low-speed shaft torsional damping coefficient (Nms/rad)
K_h high-speed shaft torsional stiffness coefficient (Nm/rad)	B_h high-speed shaft torsional damping coefficient (Nms/rad)
θ_l angular position of the gearbox low- speed part (rad)	θ_h angular position of the gearbox high-speed part (rad)
T_l torque applied to the gearbox by the low-speed shaft (Nm)	T_h torque applied to the gearbox by the high-speed shaft (Nm)
R_t gear ratio (-)	I_w equivalent moment of inertia of gearbox elements, at θ_l (kg m2)
v_1 upstream wind speed (m/s)	N number of blades (-)
m_t mass of the tower (kg)	m_n mass of the nacelle (kg)
m_h mass of the hub (kg)	m_b mass of each blade (kg)
r_b blade radius (m)	h tower height (m)
y_t axial displacement nacelle (m)	γ angular displacement blade (rad)
K_t tower stiffness coefficient (N/m)	B_t tower damping coefficient (Ns/m)
K_b blade stiffness coefficient (N/m)	B_b blade damping coefficient (Ns/m)
I_r moment of inertia of elements at Ω_r (rotor, blades, hub, shaft, etc.) (Kg m^2)	Ig moment of inertia of elements at Ω_g (generator, shaft, etc.) (Kg m^2)
θ_r rotor angular position (rad)	θ_g generator angular position (rad)
$\Omega_r = \dot{\theta}_r$ rotor angular speed (rad/s)	$\Omega_g = \dot{\theta}_g$ generator angular speed (rad/s)
T_r aerodynamic torque applied by the wind on the rotor (Nm)	Tg antagonistic electrical torque applied on the shaft (Nm)
F_T thrust force applied by the wind on the rotor (N)	

r_p distance from the center of the rotor to the center of pressure, or point where the equivalent lumped force F_T is applied. $r_p = (2/3)\ r_b$ (m)

of the system. For each angle (pitch and yaw), at the end of the actuator drive-train (end of the gearbox—see Figs. 14.5 and 14.6), there is an encoder. These encoders are the same as the glide wheel on the rotor (see Fig. 14.7c and [6]). They are configured to record the absolute angle of the nacelle and tower for the pitch and yaw angles, respectively—see Fig. 14.2, numbers (7) and (8).

For measuring the electrical properties of the wind turbine there is a current sensor (CurrentMeter for NXT) and a voltage sensor (VoltMeter for NXT) on each wind turbine—see Figs. 14.7d and e respectively, and Fig. 14.2, numbers (9) and (10). The current sensor has a resolution of 1 mA and can measure currents up to 12.5 A. The voltage sensor has a resolution of 1 mv and can measure voltages up to 26 v. These sensors are very reliable and the inherent offset errors are easily accounted for in software. Although they are not made by LEGO, they are built specifically to work with LEGO NXT Intelligent Brick firmware and are shaped to work the LEGO blocks [6]. Each sensor is directly connected to the NXT microcontroller.

14.2.1.5 Actuators: Pitch and Yaw Motors, Torque

The pitch and yaw actuators—see Fig. 14.2, numbers (5) and (4) respectively- are NXT motors (see Fig. 14.7b and [5]). They are DC motors and deliver a high torque thanks to its internal speed reduction gear train (gearing ratio = 1:48). Because of that, they turn slowly and efficiency is somewhat reduced. Although each one includes an internal rotation encoder to measure the position of the shaft with one degree resolution, we use glide wheel angle sensors at the end position of the actuator drive-train in order to have a direct measurement of the actual angles (see also Sect. 14.2.1.4).

The NXT motors consume a current of 60 mA in a no-load situation and up to 2 A in a stalled situation, with a maximum stalled torque of 50 N cm for a few seconds. The NXT motors are protected by a thermistor (Raychem RXE065 or Bourns MF-R065). That means that the high 2 A current and associated stalled torque can be sustained only for a few seconds. They have a non-standard phone plug type to connect to the NXT microprocessor. At the regular 9 v input the motors run at 170 revolutions per minute (rpm). For other inputs the motors follow the linear characteristics:

$$\Omega_{\text{motor}} = (170/9)\, u \tag{14.4}$$

$$\Omega_{\text{motor}} = -(170/50)\, T_{\text{motor}} + 170 \tag{14.5}$$

$$i_{\text{motor}} = \begin{cases} (00.94/30)\, T_{\text{motor}} + 0.06 & (\text{for } 0 \le T_{\text{motor}} \le 30\,\text{N.cm}) \\ (1/20)\, T_{\text{motor}} - 1/2 & (\text{for } T_{\text{motor}} > 30\,\text{N.cm}) \end{cases} \tag{14.6}$$

with Ω_{motor} the motor speed in rpm, u the voltage applied to the motor in volts, T_{motor} the motor torque in N. cm and i_{motor} the motor current in A [8].

14.2.1.6 WT Microprocessors: Real-Time Control for Rotor Speed, Pitch, Yaw, Torque, Power

The individual wind turbine control system is based on the intelligent NXT 2.0 LEGO® brick, which has a 32-bit microprocessor, a large matrix display, 4 input and 3 output ports, and Bluetooth and USB communication links. The system is interchangeable with the new EV3 Intelligent LEGO® Brick [5] or the Arduino microcontroller [9].

Each wind turbine has one NXT microcontroller attached to the foundation (see Fig. 14.2). It is connected to the pitch and yaw motors (output ports) and the rotor speed, pitch angle, voltage, and current sensors (input ports). An additional NXT microcontroller is connected to the four yaw angle sensors (input ports) of the four wind turbines of the wind farm.

In this way, the wind farm control system presents a hierarchical structure, with a central computer that runs under Matlab for the Supervisory Control and Data

Acquisition (SCADA) system, and the five LEGO microprocessors for the distributed wind turbine control units.

14.2.2 Wind Farm Description

The wind farm (see Fig. 14.1) is composed of (1) four variable-speed pitch-controlled wind turbines (2) a supervisory control and data acquisition (SCADA) system with a central control unit (3) a smart grid with batteries for energy storage, variable electrical loads, solar panels, and switches for different grid topologies, and (4) a group of fans to create different wind profiles and disturbances.

14.2.3 Supervisory Control and Data Acquisition (SCADA) System

The Supervisory Control and Data Acquisition (SCADA) system is the central computer-controlled system that monitors the wind farm (the four wind turbines and micro grid) and coordinates the distributed controllers of each wind turbine. It is based on Matlab [7] and runs on a personal computer. Figure 14.8 shows one of

	Turbine 1	Turbine 2	Turbine 3	Turbine 4
Voltage (V)	2.3090	1.6570	2.2890	2.0260
Current (mA)	18	23	5	26
Rotor Velocity (rpm)	254	167	233	211
Power (mW)	41.5620	38.1110	11.4450	52.6760
Torque(mNm)	1.5626	2.1792	0.4691	2.3840
Pitch Angle (degrees)	0	0	0	0
Yaw Angle (degrees)				
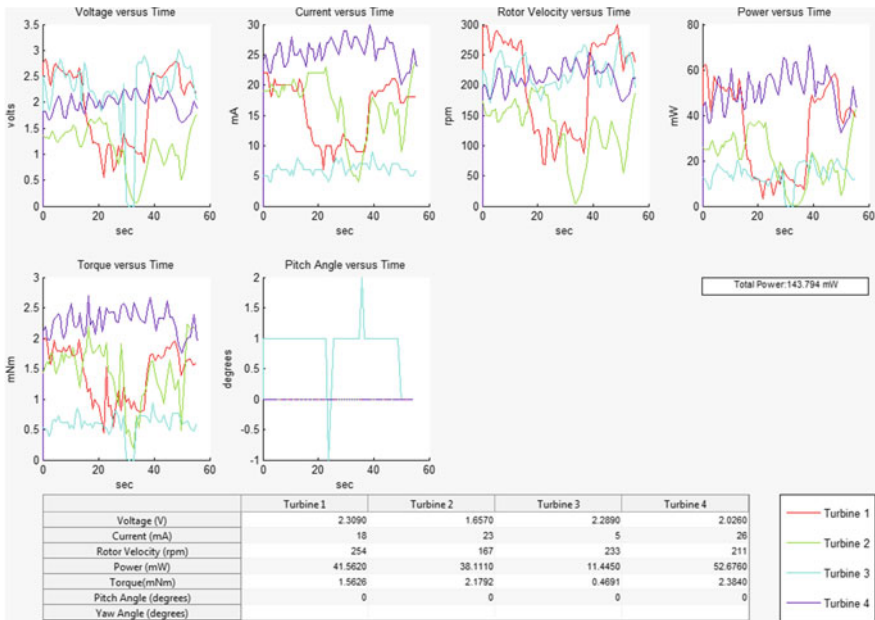
Fig. 14.8 Supervisory control and data acquisition (SCADA) system

the main windows of the SCADA system, with real-time data collected by the sensors of the four wind turbines: voltages, currents, rotor speeds, powers, torques, pitch angles and yaw angles.

14.2.4 Smart Micro Grid

An electrical smart micro grid with variable load is connected to the generators of the four wind turbines at the output of the farm. The micro grid is composed of a set of batteries for energy storage, variable electrical loads, solar panels as additional renewable generators and switches to create different grid topologies (see Fig. 14.9).

14.2.5 Wind Source Equipment

A group of three fans creates the wind profile, with variable speed, direction and frequency of variation (see Fig. 14.1). The two largest fans are used to generate the main wind flow and the smallest one to create wind disturbances and turbulences in speed and direction.
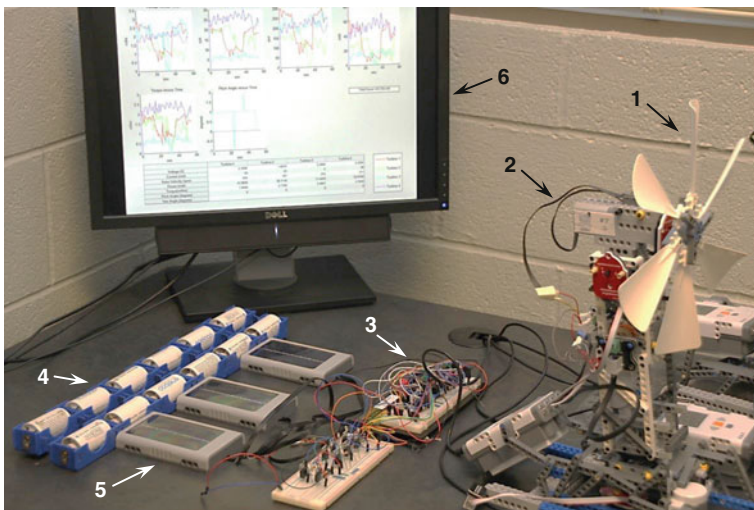
Fig. 14.9 Smart micro grid: (*1*) wind turbines; (*2*) grid connection; (*3*) switches and electrical loads; (*4*) batteries; (*5*) solar panels; (*6*) SCADA and central control system

14.3 Modeling of Wind Turbines

14.3.1 Power Curve of a Wind Turbine

A qualitative power curve of a variable-speed wind turbine is shown in Fig. 14.10. This graph presents the actual power P supplied by the wind turbine to the grid versus the undisturbed upstream wind speed v_1. Two main areas (below and above rated power P_r) and four regions (Regions 1 through 4) divide the graph.

Below rated power ($v_1 < V_r$) the wind turbine produces only a fraction of its rated power, and therefore, an optimization strategy to capture the maximum amount of energy at every wind speed needs to be performed. Above rated power ($V_r < v_1$) the wind speed has more power than the rated power, and a limitation control strategy to generate only the rated power is required. The four regions of the power curve present the following characteristics:

- *Region* 1. The objective in this region is to obtain the maximum efficiency. This is usually done by means of controlling the rotor speed Ω_r by changing the electrical torque T_g, to compensate the wind speed variations and keep the turbine at the maximum aerodynamic power coefficient $C_{p\max}$ (MPPT: *Maximum Power Point Tracking*). The power P supplied by the wind turbine to the grid follows the expression:

$$P = P_g \, \eta_c = \frac{1}{2} \, \rho \, A_r \, C_p \, v_1^3 \, \eta_g \, \eta_c = T_r \, \Omega_r \, \eta_g \, \eta_c = P_a \, \eta_g \, \eta_c \qquad (14.7)$$
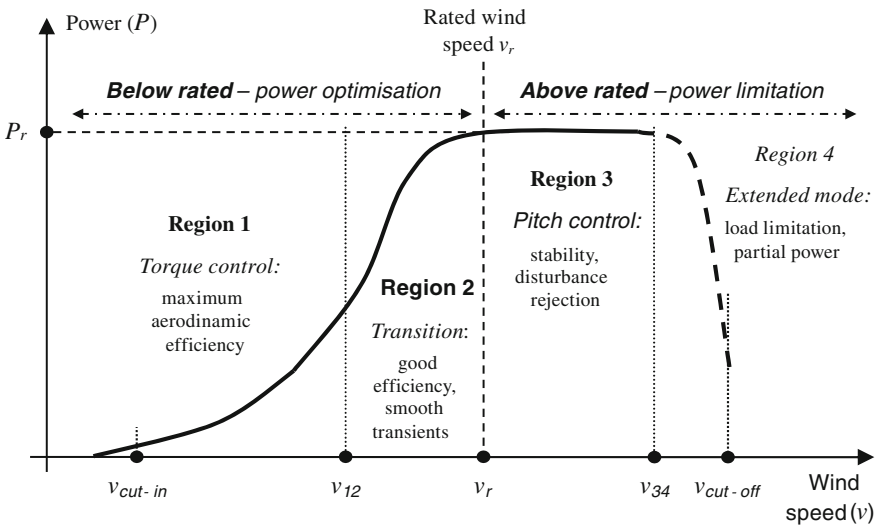

Fig. 14.10 Power curve of a variable-speed wind turbine (see [2])

where P_g is the power supplied by the electrical generator, η_c the efficiency from the output of the generator to the grid connection, ρ is the air density, $A_r = \pi\, r_b^2$ the rotor effective surface, r_b the rotor radius, C_p the aerodynamic power coefficient (see also Sect. 14.3.3), v_1 the undisturbed upstream wind speed, η_g the electrical generator efficiency, T_r the mechanical torque at the shaft due to the wind, Ω_r the rotor speed, P_a the power at the shaft given by the aerodynamics, and λ is the tip speed ratio,

$$\lambda = \Omega_r r_b / v_1 \tag{14.8}$$

- *Region* 2. It is the transition between a torque control with fixed pitch mode (Region 1) to a fixed torque with a variable pitch mode (Region 3).
- *Region* 3. The objective in this region is to limit and control the incoming power at rated power, regulate the rotor speed and minimize the mechanical loads. This is done by means of controlling the rotor speed Ω_r by changing the pitch angles β (*Pitch control*).
- *Region* 4. An extended mode in very high winds can be obtained by means of varying the pitch closed-loop performance. Through a rotor speed Ω_r limitation, the extreme loads can be reduced.

14.3.2 Power Generation According to the Number of Blades

It is well known that in the ideal scenario of an infinite number of blades and no losses the upper limit for the aerodynamic rotor power coefficient is the *Betz limit*: $C_{pmax} = 0.593$. For a real situation, considering a finite number of blades N, typical frictional losses, and rotating wakes in the out-coming airflow, the aerodynamic power coefficient C_p is always smaller than the *Betz limit*. Figure 14.11a presents some typical C_p curves versus the tip speed ratio λ and for different pitch angles β. A numerical approximation of the aerodynamic power coefficient C_p is given by the following equations (see [2], Chap. 12),

$$C_P(\lambda, \beta) = c_1 \left(\frac{c_2}{\lambda_i} - c_3\beta - c_4 \right) \exp(-c_5/\lambda_i)$$
$$\lambda_i = \left(\frac{1}{\lambda + c_6\beta} - \frac{c_7}{\beta^3 + 1} \right)^{-1} \tag{14.9}$$

where: $c_1 = 0.39$; $c_2 = 116$; $c_3 = 0.4$; $c_4 = 5$; $c_5 = 16.5$; $c_6 = 0.089$; $c_7 = 0.035$

The maximum value of these curves (maximum power coefficient C_{pmax}) depends on the number of blades N. An experimental expression that presents the

(a)

(b) C_p
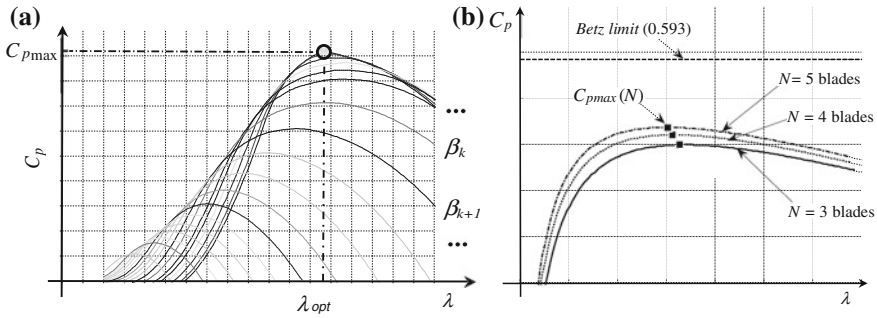
Fig. 14.11 **a** Typical aerodynamic power coefficient C_p as a function of λ and β. **b** Maximum power coefficient $C_{p\mathrm{max}}$ for different number of blades N at a given β [2]

effect of the number of blades N in the maximum rotor power coefficient $C_{p\mathrm{max}}$ for a classical wind turbine with $25 < C_L/C_D < \infty$ is shown in (14.10),

$$
C_{p\mathrm{max}} = 0.593\,\lambda_{\mathrm{opt}} \left[\lambda_{\mathrm{opt}} + \frac{1.32 + \left(\dfrac{\lambda_{\mathrm{opt}} - 8}{20}\right)^2}{N^{2/3}} \right]^{-1} - \frac{0.57\lambda_{\mathrm{opt}}^2}{\dfrac{C_L}{C_D}\left(1 + \dfrac{1}{2N}\right)} \tag{14.10}
$$

where N is the number of blades, C_L is the rotor lift coefficient and C_D is the rotor drag coefficient (see also [2], Chap. 12). Figure 14.11b shows some calculations of $C_{p\mathrm{max}}$ using this expression with $C_L/C_D = 76$ and for $N = 3, 4$ and 5

14.3.3 Dynamics of Rotor Speed Versus Torque, Pitch Angle and Wind Velocity Variation

Figure 14.12 shows a variable-speed pitch-controlled wind turbine with a mechanical (gearbox) drive-train. A shaft connects a large inertia rotor at one end (blades) with a gearbox, which is coupled to a generator at the other end. The wind applies an aerodynamic torque T_r to the rotor, which is connected to the low-speed shaft of the gearbox. At the other end of the drive-train, the generator, with a power converter, applies an antagonistic electrical torque T_g on the high-speed shaft of the gearbox. The rotor presents a moment of inertia I_r. The shaft has a torsional stiffness coefficient K_s and a viscous damping coefficient B_s. The generator shows a moment of inertia I_g. The rotor angle is θ_r, the rotor speed is $\Omega_r = d\theta_r/dt$, and the generator angle is θ_g. Also, ψ is the yaw angle error (nacelle-wind angle) and β is the pitch angle (blades).

The excitation current, I_x, is introduced in the rotor, and the active and reactive power, respectively P and Q, are supplied to the grid. f, U and ϕ are the frequency, voltage, and power factor at the grid connection point respectively.
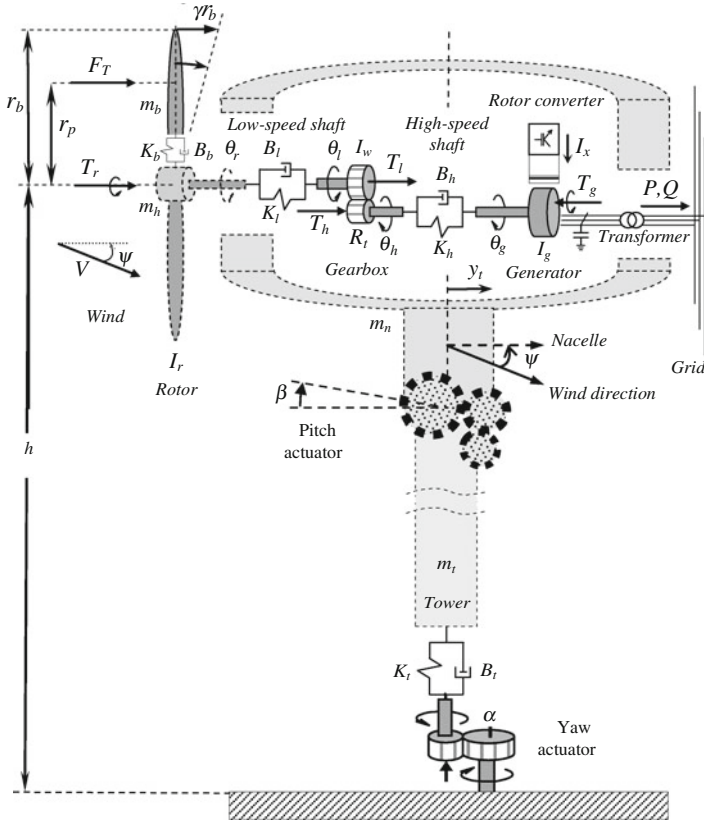
Fig. 14.12 A variable-speed pitch-controlled wind turbine (see [2])

The Euler−Lagrange method (energy-based approach) is applied to obtain general mechanical state space model of wind turbine. The main parameters of the wind turbine model are described in Table 14.1 (see [2] for more details).

The wind turbine dynamic equations of motion that describe the behavior of the system, under the influence of external forces (wind), and as a function of time, are developed as a set of mechanical differential equations. The equations of motion in Lagrangian mechanics are the Lagrange equations of the second kind, also known as the Euler−Lagrange equations. Note that E_k is used for kinetic energy and E_p for potential energy. D_n is the dissipation function to include non-conservative forces, Q_i the conservative generalized forces and q_i for the generalized coordinates. Defining L as the Lagrangian function $L = E_k - E_p$, the Euler−Lagrange equation is as follows:

$$\frac{\mathrm{d}}{\mathrm{d}t}\left(\frac{\partial L}{\partial \dot{q}_i}\right) - \frac{\partial L}{\partial q_i} + \frac{\partial D_n}{\partial \dot{q}_i} = Q_i \qquad (14.11)$$

The generalized coordinates q_i are (see also Fig. 14.12):

$$\boldsymbol{q} = [q_i] = [\, y_t \quad \gamma \quad \theta_r \quad \theta_g \quad \theta_l \,]^T \tag{14.12}$$

where y_t is the axial displacement of the nacelle, γ is the angular displacement of the blades out of the plane of rotation, θ_r is the rotor angular position, θ_g is the generator angular position and θ_l the gearbox low-speed shaft position.

The Energy and dissipation function equations, E_k, E_p, D_n are:

$$E_k = \frac{m_1}{2}\dot{y}_t^2 + \frac{m_2}{2}(r_b\dot{\gamma} + \dot{y}_t)^2 + \frac{I_r}{2}\dot{\theta}_r^2 + \frac{I_g}{2}\dot{\theta}_g^2 + \frac{I_w}{2}\dot{\theta}_l^2 \tag{14.13}$$

$$E_p = \frac{K_t}{2}y_t^2 + \frac{N}{2}K_b(r_b\gamma)^2 + \frac{K_l}{2}(\theta_r - \theta_l)^2 + \frac{K_h}{2}(R_t\theta_l - \theta_g)^2 \tag{14.14}$$

$$D_n = \frac{B_t}{2}\dot{y}_t^2 + \frac{N}{2}B_b(r_b\dot{\gamma})^2 + \frac{B_l}{2}(\dot{\theta}_r - \dot{\theta}_l)^2 + \frac{B_h}{2}(R_t\dot{\theta}_l - \dot{\theta}_g)^2 \tag{14.15}$$

Based on Eqs. (14.11) through (14.15), the state space description for the wind turbine is (see [2], Chap. 12, for details):

$$\dot{x} = Ax + Bu; \; y = Cx \tag{14.16}$$

$$A = \begin{bmatrix}
0 & 0 & 0 & 0 & 0 & 1 & 0 & 0 & 0 & 0 \\
0 & 0 & 0 & 0 & 0 & 0 & 1 & 0 & 0 & 0 \\
0 & 0 & 0 & 0 & 0 & 0 & 0 & 1 & 0 & 0 \\
0 & 0 & 0 & 0 & 0 & 0 & 0 & 0 & 1 & 0 \\
0 & 0 & 0 & 0 & 0 & 0 & 0 & 0 & 0 & 1 \\
-\dfrac{K_t}{m_1} & \dfrac{NK_br_b}{m_1} & 0 & 0 & 0 & -\dfrac{B_t}{m_1} & \dfrac{NB_br_b}{m_1} & 0 & 0 & 0 \\
\dfrac{K_t}{m_1r_b} & -\dfrac{(m_1+m_2)NK_b}{m_1m_2} & 0 & 0 & 0 & \dfrac{B_t}{m_1r_b} & -\dfrac{(m_1+m_2)NB_b}{m_1m_2} & 0 & 0 & 0 \\
0 & 0 & -\dfrac{K_l}{I_r} & 0 & \dfrac{K_l}{I_r} & 0 & 0 & -\dfrac{B_l}{I_r} & 0 & \dfrac{B_l}{I_r} \\
0 & 0 & 0 & -\dfrac{K_h}{I_g} & \dfrac{K_hR_t}{I_g} & 0 & 0 & 0 & -\dfrac{B_h}{I_g} & \dfrac{B_hR_t}{I_g} \\
0 & 0 & \dfrac{K_l}{I_w} & \dfrac{K_hR_t}{I_w} & -\dfrac{K_l+K_hR_t^2}{I_w} & 0 & 0 & \dfrac{B_l}{I_w} & \dfrac{B_hR_t}{I_w} & -\dfrac{B_l+B_hR_t^2}{I_w}
\end{bmatrix}$$

$$\tag{14.17}$$

$$B = \begin{bmatrix}
0 & 0 & 0 \\
0 & 0 & 0 \\
0 & 0 & 0 \\
0 & 0 & 0 \\
0 & 0 & 0 \\
\dfrac{1}{m_1}\left(1 - \dfrac{r_p}{r_b}\right) & 0 & 0 \\
\dfrac{1}{m_1r_b}\left(\dfrac{(m_1+m_2)r_p}{m_2r_b} - 1\right) & 0 & 0 \\
0 & \dfrac{1}{I_r} & 0 \\
0 & 0 & -\dfrac{1}{I_g} \\
0 & 0 & 0
\end{bmatrix} \tag{14.18}$$

$$C = \begin{bmatrix} 0 & 0 & 0 & 0 & 0 & 1 & 0 & 0 & 0 & 0 \\ 0 & 0 & 0 & 0 & 0 & 0 & 1 & 0 & 0 & 0 \\ 0 & 0 & 0 & 0 & 0 & 0 & 0 & 1 & 0 & 0 \\ 0 & 0 & 0 & 0 & 0 & 0 & 0 & 0 & 1 & 0 \\ 0 & 0 & 0 & 0 & 0 & 0 & 0 & 0 & 0 & 1 \end{bmatrix} \tag{14.19}$$

where:

$$\text{State variables}: \boldsymbol{x} = \begin{bmatrix} y_t & \gamma & \theta_r & \theta_g & \theta_l & \dot{y}_t & \dot{\gamma} & \dot{\theta}_r & \dot{\theta}_g & \dot{\theta}_l \end{bmatrix}^T \tag{14.20}$$

$$\text{Inputs}: \boldsymbol{u} = \begin{bmatrix} F_T & T_r & T_g \end{bmatrix}^T \tag{14.21}$$

$$\text{Outputs}: \boldsymbol{y} = \begin{bmatrix} \dot{y}_t & \dot{\gamma} & \dot{\theta}_r & \dot{\theta}_g & \dot{\theta}_l \end{bmatrix}^T \tag{14.22}$$

According to the rotor aerodynamics and the characteristics of C_p and C_T (see [2]), the inputs of Eqs. (14.16) and (14.21), F_T and T_r, depend on v_1, β and Ω_r in a nonlinear way. If the aerodynamic part of these equations is linearized around a working point $(v_{10}, \beta_0, \Omega_{r0})$, and the bias components are ignored, the inputs F_T and T_r can be described by a transfer matrix whose elements are just gains, so that,

$$\begin{bmatrix} F_T(s) \\ T_r(s) \end{bmatrix} = \begin{bmatrix} K_{F\Omega} & K_{FV} & K_{F\beta} \\ K_{T\Omega} & K_{TV} & K_{T\beta} \end{bmatrix} \begin{bmatrix} \Omega_r(s) \\ v_1(s) \\ \beta(s) \end{bmatrix} \tag{14.23}$$

where the gains are calculated by using the C_T and C_p curves. Now, the transfer matrix description $\boldsymbol{G}(s)$ of the wind turbine is calculated by using the transformation $\boldsymbol{G}(s) = \boldsymbol{C}(s\boldsymbol{I} - \boldsymbol{A})^{-1}\boldsymbol{B}$ for $\boldsymbol{y}(s) = \boldsymbol{G}(s)\boldsymbol{u}(s)$.

$$\begin{bmatrix} \dot{y}_t(s) \\ \dot{\gamma}(s) \\ \Omega_r(s) \\ \Omega_g(s) \\ \Omega_l(s) \end{bmatrix} = \boldsymbol{P}(s)\begin{bmatrix} \beta_d(s) \\ T_{gd}(s) \end{bmatrix} + \boldsymbol{D}(s)v_1(s) \tag{14.24}$$

where the plant matrix and the disturbance matrix are,

$$\boldsymbol{P}(s) = \begin{bmatrix} \mu_{11}(s)\frac{\mu_{32}(s)\left(K_{F\Omega}K_{T\beta} - K_{F\beta}K_{T\Omega}\right) + K_{F\beta}}{1 - \mu_{32}(s)K_{T\Omega}}A_\beta(s) & \mu_{11}(s)\frac{\mu_{33}(s)K_{F\Omega}}{1 - \mu_{32}(s)K_{T\Omega}}A_T(s) \\ \mu_{21}(s)\frac{\mu_{32}(s)\left(K_{F\Omega}K_{T\beta} - K_{F\beta}K_{T\Omega}\right) + K_{F\beta}}{1 - \mu_{32}(s)K_{T\Omega}}A_\beta(s) & \mu_{21}(s)\frac{\mu_{33}(s)K_{F\Omega}}{1 - \mu_{32}(s)K_{T\Omega}}A_T(s) \\ \mu_{32}(s)\frac{K_{T\beta}}{1 - \mu_{32}(s)K_{T\Omega}}A_\beta(s) & \mu_{33}(s)\frac{1}{1 - \mu_{32}(s)K_{T\Omega}}A_T(s) \\ \mu_{42}(s)\frac{K_{T\beta}}{1 - \mu_{32}(s)K_{T\Omega}}A_\beta(s) & \frac{\mu_{42}(s)\mu_{33}(s)K_{T\Omega} + \mu_{43}(s) - \mu_{43}(s)\mu_{32}(s)K_{T\Omega}}{1 - \mu_{32}(s)K_{T\Omega}}A_T(s) \\ \mu_{52}(s)\frac{K_{T\beta}}{1 - \mu_{32}(s)K_{T\Omega}}A_\beta(s) & \frac{\mu_{52}(s)\mu_{33}(s)K_{T\Omega} + \mu_{53}(s) - \mu_{53}(s)\mu_{32}(s)K_{T\Omega}}{1 - \mu_{32}(s)K_{T\Omega}}A_T(s) \end{bmatrix}$$

$$\tag{14.25}$$

$$\boldsymbol{D}(s) = \begin{bmatrix} \mu_{11}(s)\dfrac{\mu_{32}(s)\,(K_{F\Omega}K_{TV} - K_{FV}K_{T\Omega}) + K_{FV}}{1 - \mu_{32}(s)K_{T\Omega}} \\ \mu_{21}(s)\dfrac{\mu_{32}(s)\,(K_{F\Omega}K_{TV} - K_{FV}K_{T\Omega}) + K_{FV}}{1 - \mu_{32}(s)K_{T\Omega}} \\ \mu_{32}(s)\dfrac{K_{TV}}{1 - \mu_{32}(s)K_{T\Omega}} \\ \mu_{42}(s)\dfrac{K_{TV}}{1 - \mu_{32}(s)K_{T\Omega}} \\ \mu_{52}(s)\dfrac{K_{TV}}{1 - \mu_{32}(s)K_{T\Omega}} \end{bmatrix} \tag{14.26}$$

The rotational speed Ω_r of the wind turbine rotor is continuously modified (a) by the controllers and actuators, which changes the blade pitch angles β_d and the electrical torque T_{gd}; (b) by the wind speed v_1; and (c) through the dynamics of the rotor speed Ω_r itself (see Fig. 14.13).

The transfer functions of the rotor speed $\Omega_r(s)$ versus the demanded blade pitch angle $\beta_d(s)$, the demanded electrical torque $T_{\mathrm{gd}}(s)$, and the wind speed $v_1(s)$, are (see Fig. 14.13 and Ref. [2], Chap. 12, for details),

$$\Omega_r(s) = F_1(s)v_1(s) + F_2(s)\beta_d(s) + F_3(s)T_{\mathrm{gd}}(s) \tag{14.27}$$

where,

$$F_1(s) = \frac{K_{TV}\,n_{\mu 32}(s)}{d_{tf}(s)} = D_1(s) \tag{14.28}$$

$$F_2(s) = \frac{K_{T\beta}\,n_{\mu 32}(s)A_{\beta}(s)}{d_{tf}(s)} = P(s) \tag{14.29}$$

$$F_3(s) = \frac{n_{\mu 33}(s)A_T(s)}{d_{tf}(s)} = H(s) \tag{14.30}$$

and,

$$n_{\mu 32}(s) = I_g I_w s^4 + (B_h I_w + I_g B_l + I_g B_h R_t^2)\,s^3 + (B_h B_l + I_g K_l + I_g K_h R_t^2 \\ + K_h I_w)\,s^2 +_h B_l + B_h K_l)\,s + K_h K_l \tag{14.31}$$

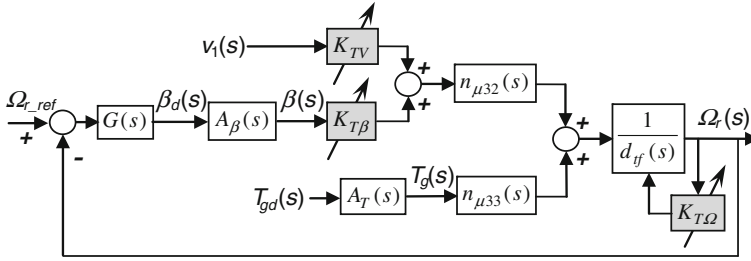$$n_{\mu 33}(s) = -B_h R_t B_l s^2 - R_t\,(K_h B_l + B_h K_l)\,s - K_h R_t K_l \tag{14.32}$$

Fig. 14.13 Block diagram for rotor speed control system [2]

$$
\begin{aligned}
d_{tf}(s) = {} & d_{\mu32}(s) - n_{\mu32}(s)K_{T\Omega} \\
= {} & I_r I_w I_g s^5 + [(I_r I_g B_l + B_h I_r I_w + I_r I_g B_h R_T^2 + B_l I_w I_g) - (I_g I_w)K_{T\Omega}]s^4 \dots \\
& + [(K_l I_w I_g + B_h I_r B_l + B_l I_g B_h r_t^2 + K_h I_r I_w + I_r I_g K_l + B_l B_h I_w + I_r I_g K_h R_t^2) \\
& - (B_h I_w + I_g B_l + I_g B_h R_t^2)K_{T\Omega}]s^3 \dots \\
& + [(B_l K_h I_w + K_l I_g B_h R_t^2 + K_h I_r B_l + B_h I_r K_l + K_l B_h I_w + I_g B_l K_h R_t^2) \\
& - (B_h B_l + I_g K_l + I_g K_h R_t^2 + K_h I_w)K_{T\Omega}]s^2 \dots \\
& + [(I_g K_l K_h R_t^2 + K_h I_r K_l + K_l K_h I_w) - (K_h B_l + B_h K_l)K_{T\Omega}]s \\
& - (K_h B_l + B_h K_l)K_{T\Omega}
\end{aligned}
$$

$$(14.33)$$

14.4 System Identification

Figure 14.14 shows the control system block diagram of the wind turbine. $G_p(s)$, $G_t(s)$, c_1 and c_2 are part of the control algorithm, which works in the metric system. $G_p(s)$ is the rotor speed pitch controller, $G_t(s)$ the torque controller, and c_1 and c_2 the coefficients needed to operate with the NXT motor and the Glide-Wheel sensor (see Sect. 14.2), which work in degrees and rpm respectively: $c_1 = 180/\pi$ deg/rad and $c_2 = \pi/30$ rad/s/rpm.

The blocks $F_1(s)$, $F_2(s)$ and $F_3(s)$ in Fig. 14.14 correspond to the Eqs. (14.28)–(14.30) developed in Sect. 14.3.3, all in the metric system. They represent respectively the transfer functions from the wind speed, pitch angle and electrical torque to the rotor speed. The following sections identify experimentally the parameters of the dominant dynamics of these transfer functions.

14.4.1 Rotor-Speed Versus Pitch-Angle Transfer Function $F_2(S)$

The dominant dynamics of the rotor-speed versus pitch-angle transfer function $\Omega_{rs}(s)/\beta(s) = P_1(s)$, and the transfer function of the pitch-angle versus actuator-input

Fig. 14.14 WT control system block diagram

$\beta(s)/\beta_{di}(s) = A_\beta(s)r_{tg}$ are identified experimentally by applying step inputs to the pitch motor of the wind turbines under different wind speeds. Figure 14.14 shows the input/output signals.

For the estimation of the first transfer function the wind speed is set as a periodic function $v_1 = v_{1m} + v_{1a}\ \sin(2\pi f\ t + \theta)$ m/s, with $v_{1a} = 0.125$ m/s, $f = 0.2$ Hz, and $\theta = 58°$, and under three scenarios of average wind speed: $v_{1m} = 3.68, 4.22,$ and 4.75 m/s. During the experiments the generator torque T_{gd} and the yaw angle $\alpha = 0$ are maintained constant. Then the pitch angle at the nacelle β is changed from 0 to 5° and the rotor speed Ω_{rs} is measured. For the second transfer function a second experiment studies the wind turbine with no wind ($v_1 = 0$) and constant torque T_{gd}, when the actuator input β_{di} is changed from 0 to 700° and the actual pitch angle at the nacelle β is measured.

Using the signals obtained in these experiments and applying classical system identification techniques, the structure, parameters, and uncertainty of both transfer functions are found as shown in Eqs. (14.34) and (14.35).

$$\frac{\Omega_{rs}(s)}{\beta(s)} = P_1(s) = \frac{k_1}{\left(\frac{s}{\omega_{n1}}\right)^2 + \frac{2\zeta_1 s}{\omega_{n1}} + 1} \tag{14.34}$$

$$\begin{aligned}\frac{\beta(s)}{\beta_{di}(s)} &= r_{tg}\,A_\beta(s) \\ &= r_{tg}\ \frac{1}{\left[\left(\frac{s}{\omega_{n2}}\right)^2 + \frac{2\zeta_2 s}{\omega_{n2}} + 1\right]^2}\ \text{represents the dynamics of the actuator}\end{aligned}$$

$$\tag{14.35}$$

The estimated parameters for Eqs. (14.34) and (14.35) for different wind speeds, and with Ω_{rs} in rpm and β and β_{di} in degrees, are:

- For $v_{1m} = 3.68$ m/s

$$k_1 = -4.1067, \ \omega_{n1} = 0.675 \ \text{rad/s}, \ \zeta_1 = 0.4815$$

- For $v_{1m} = 4.22$ m/s

$$k_1 = -5.4756, \ \omega_{n1} = 0.675 \ \text{rad/s}, \ \zeta_1 = 0.4815$$

- For $v_{1m} = 4.75$ m/s

$$k_1 = -5.4756, \ \omega_{n1} = 0.675 \ \text{rad/s}, \ \zeta_1 = 0.4815$$

- For all v_1

$$\omega_{n2} = 5 \ \text{rad/s}, \ \zeta_2 = 0.83, \ r_{tg} = 1/140$$

Now, the complete plant F_2(s) in Fig. 14.14 and expressions (14.27) and (14.29) is:

$$
\begin{aligned}
F_2(s) = P(s) = \frac{\Omega_r(s)}{\beta_d(s)} &= \ c_2 \, P_1(s) \ r_{tg} \, A_\beta(s) \, c_1 \\
&= c_2 \, \frac{K_{T\beta} \, n_{\mu32}(s)}{d_{tf}(s)} \ r_{tg} \, A_\beta(s) \ c_1 \ ; \ \frac{[\text{rad/sec}]}{[\text{rad}]}
\end{aligned}
\tag{14.36}
$$

Figures 14.15a–c present the first set of experiments for $v_{1m} = 3.68$, 4.22, and 4.75 m/s respectively, and with constant T_{gd}. They show (a) the experimental rotor speed Ω_{rs} in rpm, measured with the rotor speed Glide-Wheel sensor when the nacelle pitch angle β changes as a step input from 0 to 5°; and (b) the estimated rotor speed using Eq. (14.34) for the same pitch angle β.

Figure 14.15d presents the second set of experiments, with $v_1 = 0$ and a constant T_{gd}, showing (a) the experimental pitch angle β measured with the nacelle Glide-Wheel sensor when a 0 to 700° step is applied to the actuator input β_{di} and (b) the estimated nacelle pitch angle using Eq. (14.35) for the same actuator input β_{di}.

14.4.2 Rotor-Speed Versus Electrical-Torque Transfer Function F_3(S)

The dominant dynamics of the rotor-speed versus electrical-torque transfer function $\Omega_{rs}(s)/T_g(s)$ is identified experimentally by applying step inputs to the electrical torque of the wind turbines under different wind speeds and a constant pitch angle (see Figs. 14.14 and 14.24). The experimental rotor speed Ω_{rs} is measured with the rotor speed Glide-Wheel sensor (in rpm), and the applied electrical torque
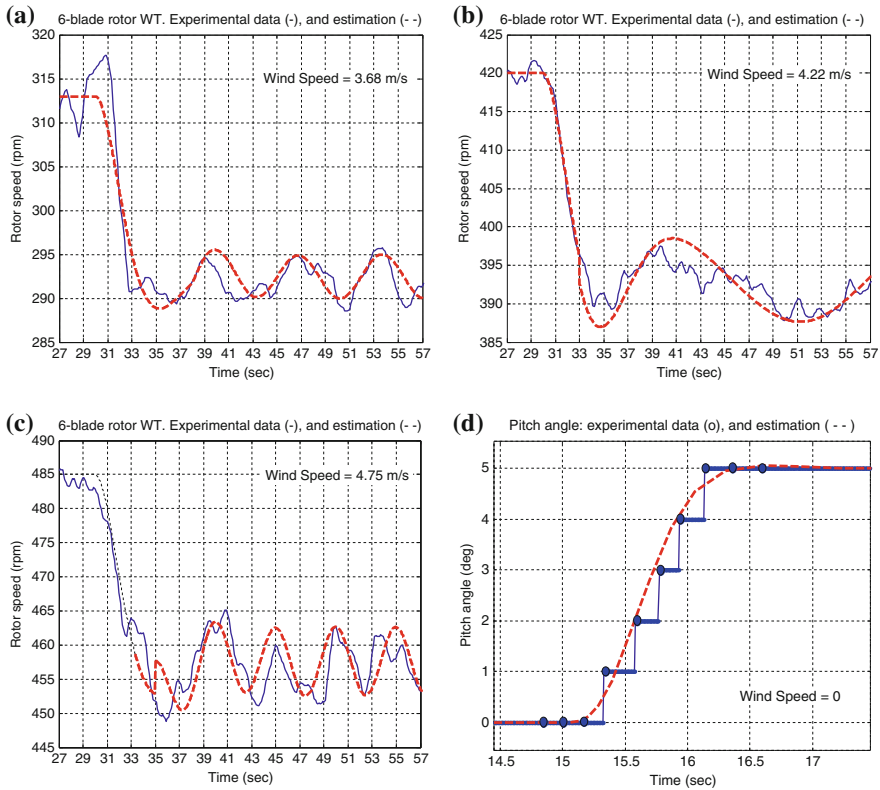
Fig. 14.15 System identification: (**a–c**) rotor-speed versus pitch-angle $P_1(s) = \Omega_{rs}(s)/\beta(s)$; and (**d**) pitch-angle versus the actuator input $A_\beta(s)r_{tg} = \beta(s)/\beta_{di}(s)$. Sensor signals (*solid lines*) and estimated signals using Eqs. (14.34) and (14.35) (*dashed lines*). Sampling rate is 2.5 Hz

T_g is measured using the current sensor (Sect. 14.2.1.4), and is given in Nm. Using the signals obtained in these experiments and applying classical system identification techniques, the structure, parameters and uncertainty of the transfer function is found as shown in Eq. (14.37a). Figure 14.24a shows the applied input T_g in mN.m and Fig. 14.24b the experimental rotor speed Ω_{rs} and the estimated rotor speed with the model in Eq. (14.37), both in rpm.

$$\frac{\Omega_{rs}(s)}{T_g(s)} = Q(s)\left(\frac{1}{c_2}\right) = \frac{k_{wt}}{\left(\frac{s}{\omega_{nwt}}\right)^2 + \frac{2\zeta_{wt}s}{\omega_{nwt}} + 1}\left(\frac{1}{c_2}\right) \tag{14.37a}$$

where: $k_{wt} = -7165$, $\omega_{nwt} = 10.1256$ rad/s, $\zeta_{wt} = 0.7$, and where Ω_{rs} is in rpm and T_g in Nm.

The complete plant $F_3(s)$ in Fig. 14.14 and expressions (14.27) and (14.30) are (metric system):

$$F_3(s) = H(s) == \frac{\Omega_r(s)}{T_{gd}(s)} = A_T(s)\,Q(s) = A_T(s)\,\frac{n_{\mu 33}(s)}{d_{tf}(s)} \; ; \; \frac{[\text{rad/s}]}{[\text{Nm}]} \qquad (14.37b)$$

14.4.3 Rotor Speed Versus Wind Speed Transfer Function $F_I(S)$

The gain of the rotor-speed versus wind-speed transfer function $\Omega_{rs}(s)/v_1(s)$ is identified experimentally by changing the wind speed to different values—see Fig. 14.15a–c for $v_{1m} = 3.68$, 4.22 and 4.75 m/s, $t < 30$ s−, $v_1 = v_{1m} + v_{1a}$ $\sin(2\pi f\, t + \theta)$, as shown in Eq. (14.38).

$$\frac{\Omega_{rs}(s)}{v_1(s)} = \frac{k_{wv}}{\tau_1 s + 1} \qquad (14.38a)$$

where: $k_{wv} = 160.87$; $\tau_1 = 1.35$ s, $v_{1a} = 0.125$ m/s, $f = 0.2$ Hz, $\theta = 58°$, Ω_{rs} in rpm and v_1 in m/s.

The plant $F_1(s)$ in Fig. 14.14 and expressions (14.27) and (14.28) are (metric system):

$$F_1(s) = D_1(s) = \frac{\Omega_r(s)}{v_1(s)} = \frac{k_{wv}}{\tau_1 s + 1} c_2; \; \frac{[\text{rad/s}]}{[\text{m/s}]} \qquad (14.38b)$$

14.5 Control System Design

14.5.1 Rotor Speed Control System

The Quantitative feedback theory (QFT)—see [2–4]—has demonstrated to be an excellent controller design methodology to deal with the compromises between several, often conflicting, performance specifications, model uncertainty, and practical implementation. Its transparent design process allows the designer to consider all these compromises simultaneously, and to find the controller that satisfies the set of requested performance specifications for every plant within the model uncertainty while using the minimum amount of feedback. In this section, we present the QFT design of the controller to regulate the rotor speed of the wind turbines with the pitch angle actuators.

14.5.1.1 Control Objectives and Configuration

The main objective of the pitch control system (see Fig. 14.10 in Region 3) is: (a) to regulate the rotor speed at the rated (nominal) value $\Omega_r = \Omega_{r\text{-ref}}$; (b) to reject the

wind disturbances (effect of v_1 variation); and (c) to avoid over-speed situations (with significant $\Delta\Omega_r$) that can be dangerous for the turbine.

Based on Figs. 14.13 and 14.14 and Eqs. (14.27)–(14.38), Fig. 14.16 shows a simplified block diagram for the rotor speed/pitch control system.

14.5.1.2 Modeling

The dynamics between the rotor-speed $\Omega_{rs}(t)$, given by the pitch angle sensor at the nacelle, and the controller signal $\beta_{di}(t)$ at the actuator input was calculated in Eqs. (14.34) and (14.35), and is summarized here for convenience—see Eq. (14.39).

$$\frac{\Omega_{rs}(s)\ [\text{rpm}]}{\beta_{di}(s)\ [°]} = P_1(s)\ r_{tg}\ A_\beta(s) = \frac{k_1}{\left(\frac{s}{\omega_{n1}}\right)^2 + \frac{2\zeta_1 s}{\omega_{n1}} + 1}\ r_{tg}\ \frac{1}{\left[\left(\frac{s}{\omega_{n2}}\right)^2 + \frac{2\zeta_3 s}{\omega_{n2}} + 1\right]^2} \tag{14.39}$$

with:

$k_1 \in [-5.4756,\ -4.6733] \pm 10\%,\ \omega_{n1} \in [0.675 \pm 10\%]$ rad/sec, $\zeta_1 \in [0.4815 \pm 10\%]$
$\omega_{n2} = 5$ rad/s, $\zeta_2 = 0.83$, $r_{tg} = 1/140$

where the rotor-speed $\Omega_r(s)$ is in *rpm* (the rotor sensor gives the information in rpm) and the demanded pitch angle β_{di} in *degrees* (the NXT motor needs degrees).

The QFT templates of this model—Eq. (14.39)—, including the parametric uncertainty, are calculated with the QFT Control Toolbox [2, 3] and are shown in Fig. 14.17.

14.5.1.3 Control Specifications

The performance specifications required for the rotor speed controllers include robust stability and robust disturbance rejection. They are defined in Eqs. (14.40) and (14.41).

Specification 1 (Robust Stability).

$$\left|\frac{\Omega_r(j\omega)}{\Omega_{r\_ref}(j\omega)}\right| = \left|\frac{P(j\omega)\,G(j\omega)}{1 + P(j\omega)\,G(j\omega)}\right| \leq \mu = 1.3\ ,\ \forall\omega \tag{14.40}$$

This stability specification, $\mu = 1.3$ in magnitude Eq. (14.40), is introduced in the QFT Control Toolbox [2, 3]. It implies a gain margin of 4.95 dB and a phase margin of 45.23°.
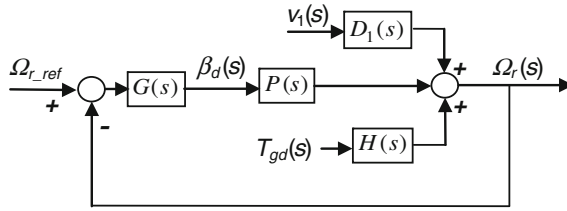
Fig. 14.16 Simplified block diagram for rotor speed control system [2]
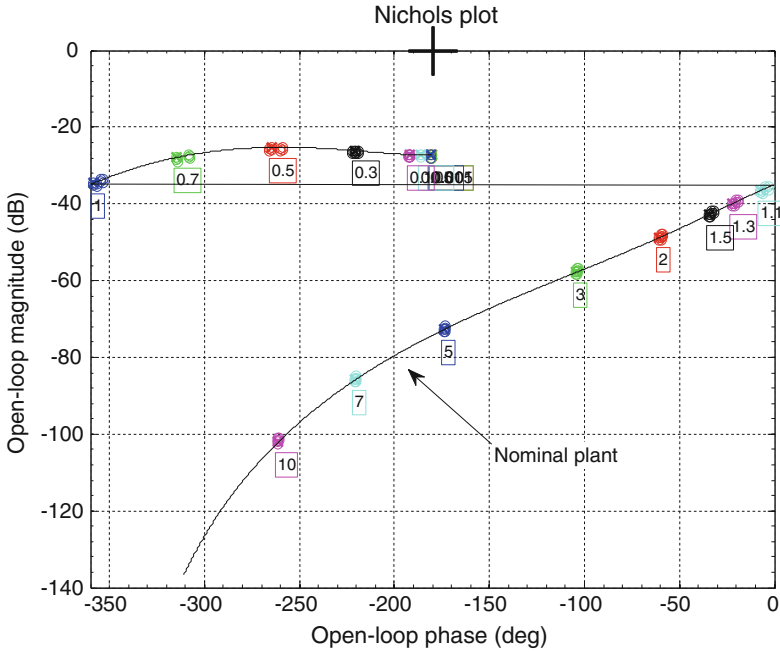

Fig. 14.17 QFT templates for $\Omega_{rs}(s)/\beta_{di}(s)$ and $\omega = [0.001\ 0.005\ 0.01\ 0.05\ 0.1\ 0.3\ 0.5\ 0.7\ 1\ 1.1\ 1.3\ 1.5\ 2\ 3\ 5\ 7\ 10]$ rad/s

Specification 2 (Robust Output Disturbance Rejection).

$$\left| \frac{\Omega_r(j\omega)}{d(j\omega)} \right| = \left| \frac{1}{1 + P(j\omega)\, G(j\omega)} \right| \leq \left| \frac{6j\omega}{6j\omega + 1} \right|, \text{ for } \omega$$
$$= [\,0.001 \quad 0.005 \quad 0.01 \quad 0.05 \quad 0.1\,]\ \text{rad/s} \tag{14.41}$$

The QFT bounds are calculated with the QFT Control Toolbox [2, 3] and are shown in Fig. 14.18, with the worst case scenario (intersection of bounds) for the stability and output disturbance rejection specifications and for $\Omega_{rs}(s)/\beta_{di}(s)$—Eq. (14.39)—at all the frequencies of interest.

14.5.1.4 Controller Design

A robust controller $G_p(s)$ for the system $\Omega_{rs}(s)/\beta_{di}(s)$—Eq. (14.39) and the above performance specifications—Eqs. (14.40) and (14.41)—is calculated by using the loop-shaping window of the QFT Control Toolbox [2, 3], as shown in Fig. 14.18. The controller $G_p(s)$ has a Proportional-Integral (PI) structure with a first order filter, as shown in Eq. (14.42). It meets all the performance specifications, which are the QFT bounds requirements at every frequency of interest, as is seen in Fig. 14.18.

$$G_p(s)\, c_2\, c_1 = \frac{\beta_{di}(s)}{e(s)} = \frac{-4.5\left(\frac{s}{2}+1\right)}{s\left(\frac{s}{4}+1\right)} \quad (\text{analog } ''s'' \text{ expression}) \qquad (14.42a)$$

$$G_p(z)\, c_2\, c_1 = \frac{\beta_{di}(z)}{e(z)} = \frac{-7.8722\,z^{-1} + 1.1389\,z^{-2}}{1 - 1.0025\,z^{-1} + 0.0025\,z^{-2}} \quad (\text{digital } ''z'' \text{ expression})$$
$$(14.42b)$$

The *controller algorithm* is:

- Rotor speed data received from the sensor (Glide-Wheel AS): $\Omega_{rs}(n)$ in rpm.
- Error calculation: $e(n) = \Omega_{rs\_ref}(n) - \Omega_{rs}(n)$, with $\Omega_{rs\_ref}(n)$ and $\Omega_{rs}(n)$ in rpm.
- Control law, based on Eqs. (14.42a) and (14.42b):

$$\beta_{di}(n) = 1.0025\,\beta_{di}(n-1) - 0.0025\,\beta_{di}(n-2) - 7.8722\,e(n-1) + 1.1389\,e(n-2)$$
$$(14.42c)$$

being $\beta_{di}(n)$ the demanded pitch angle at the input of the NxT motor in degrees, $e(n) = \Omega_{rs\_ref}(n) - \Omega_{rs}(n)$ the control error in rpm, and $T_{sampling} = 1.5$ s the sampling time (see also Fig. 14.14). An anti-wind-up function is also implemented in the algorithm to help the controller when the actuator is saturated at the upper or lower limits.

Equation (14.42a) shows the controller in continuous-time $G_p(s)c_2c_1$. Equation (14.42b) shows the controller in discrete-time $G_p(z)c_2c_1$ after a discretization with a zero-order hold approach and for a sampling time $T_{sampling} = 1.5$ s. And Eq. (14.42c) shows the control algorithm in terms of the actuator inputs $\beta_{di}(n-k)$ (in degrees) and the control errors $e(n-k)$ (in rpm), implemented in the microcontroller with a sampling time of 1.5 s.

14.5.2 Power/Torque Control System

Power maximization is typically achieved by optimizing in real-time the power coefficient C_p for each tip speed ratio $\lambda = \Omega_r r_b/v_1$—see Fig. 14.11a. As wind speed v_1 changes, the rotor speed Ω_r is automatically modified in order to keep the
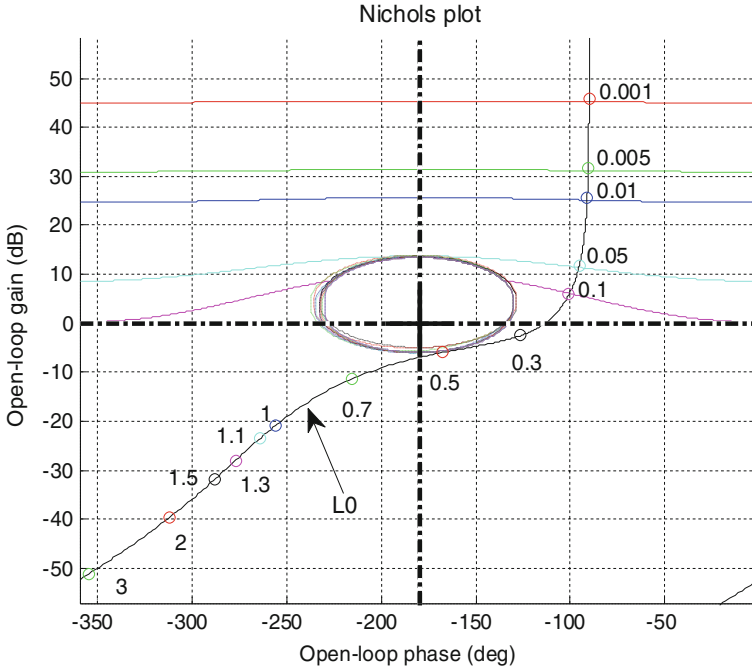
Fig. 14.18 QFT bounds and controller loop-shaping for $L_0(s) = P_0(s)G_p(s)c_2c_1 = [\Omega_{rs}(s)/\beta_{di}(s)]_0 G_p(s)c_2c_1$

machine at maximum C_p. This is usually performed by controlling the electrical torque T_g and pitch angle β.

The electrical torque T_g is manipulated in Regions 1 and 2 (below rated, Fig. 14.10) in order to get a maximum aerodynamic efficiency C_p. This strategy aims to keep optimal the relation between wind speed v_1 and rotor speed Ω_r as long as possible—see λ_{opt} in Fig. 14.11a. To do so, the rotor speed Ω_r is modified by changing the electrical torque T_g, opposite to the wind torque T_r, to follow the wind speed changes, and then keep $\lambda = \lambda_{opt}$.

From Eq. (14.7), the aerodynamic torque T_r on the rotor is,

$$T_r(t) = 0.5 \; \rho \; A \; C_p(t) \; v_1(t)^3 \Big/ \Omega_r(t) \tag{14.43}$$

Now, neglecting mechanical losses in the shaft, the resulting demanded electrical torque T_{gd} that maximizes the power capture at every wind speed is:

$$T_{gd}(t) = K_a \; \Omega_r(t)^2 \tag{14.44}$$

with,

$$K_a = 0.5 \, \rho \, A \, r_b^3 \, C_{pmax} \Big/ \lambda_{opt}^3 \tag{14.45}$$

and where C_{pmax} is the maximum power coefficient, obtained at λ_{opt}—see Fig. 14.11a.

Equation (14.44) shows a very simple and useful expression to set up the torque in Regions 1 and 2 (below rated, Fig. 14.10). The expression is based on the rotor speed sensor Ω_r and the C_p/λ curves provided by the blade manufacturer (Fig. 14.11). These curves usually give only a first approach for steady state and laminar flow conditions. For a more complete approach, some improvement can be done by slightly changing Eqs. (14.44) and (14.45), taking into account drive-train losses and some additional dynamic conditions. Due to the erosion and dirtiness of the blades and the variation of the air density at different weather conditions, the aerodynamic power coefficient C_p also becomes time variant. Then, for a more advanced approach, a reduction of the constant K_a, or the application of adaptive techniques to estimate it, will be appropriate to optimize the energy capture (*Maximum Power Point Tracking*, MPPT).

14.6 Research and Education Experiments

14.6.1 Effect of Number of Blades, Aerodynamic and Generator Efficiency

As we saw in Sect. 14.2.1.3, the generator torque T_g, and as a result the generator power P_g and efficiency η_g, varies with the rotor speed Ω_r according to Eqs. (14.1)–(14.3)—see also Fig. 14.20a. At the same time, the number of blades of the rotor affects the rotor speed and then the aerodynamic power coefficient C_p, as it was described in Sect. 14.3.2 and Eqs. (14.7) (14.8) and (14.10).

The rotor radius of each wind turbine is $r_b = 0.13$ m, and the rotor effective surface $A_r = \pi \, r_b^2 = 0.0531$ m^2. Knowing the normal air density $\rho = 1.225$ kg/m^3, and putting a wind turbine under the effect of an average wind speed of $v_1 = 4.24$ m/s, a constant pitch angle $\beta = 0$, a constant yaw angle $\alpha = 0$ and a constant demanded electrical torque T_{gd}, the results of the experiments for a rotor with 2,3,4, and 6 blades are shown in Table 14.2 and Fig. 14.19.

The last row shows the experimental results found for the aerodynamic power coefficient C_p for a rotor with 2, 3, 4 and 6 blades—see also Fig. 14.20b.

The results are consistent with the typical aerodynamic power coefficient in classical drag-machines. Additionally, the profile of the C_p/N curve found is similar to the experimental expression (14.10).

Table 14.2 Effect of number of blades on power generation and aerodynamic efficiency

Rotor	2-blades	3-blades	4-blades	6-blades
Ω_r (rpm)	86.32	412.35	494.22	502.44
P_g (mW)	9.89	158.08	216.24	214.97
η_g (per unit)	0.0545	0.4011	0.4595	0.4614
P_a (mW)	181	394	470	466
λ	0.28	1.32	1.59	1.61
C_p	0.073	0.159	0.190	0.188

where Ω_r the rotor speed, P_g is the power supplied by the electrical generator, η_g the electrical generator efficiency, P_a the power at the shaft given by the aerodynamics and C_p the aerodynamic power coefficient
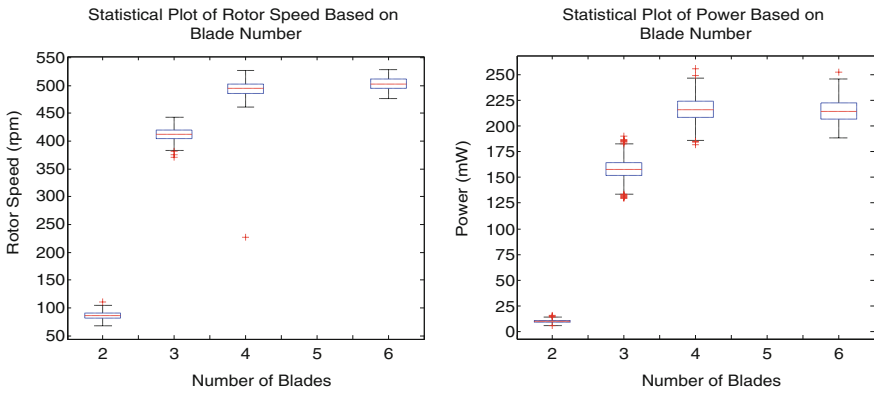
Fig. 14.19 Effect of the number of blades on the rotor speed Ω_r and on the generator power P_g
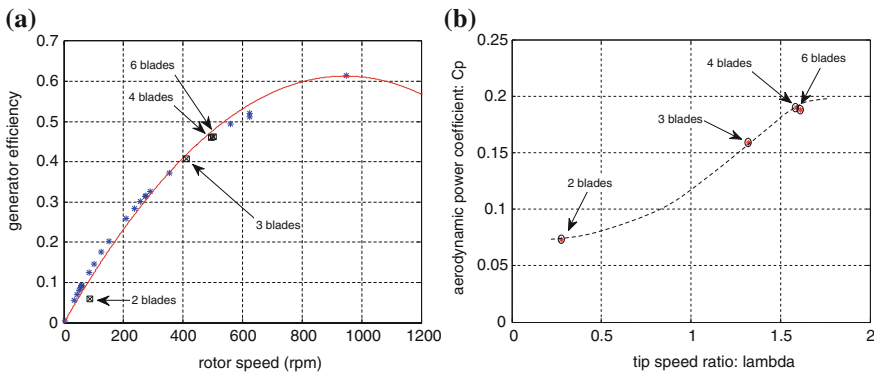
Fig. 14.20 **a** Efficiency η_g of the electrical generator: all the experimental cases presented in Sects. 14.4.1, 14.6.1, 14.6.2 and 14.6.3. The maximum generator efficiency is 0.6131 at 945 rpm. **b** Aerodynamic power coefficient versus tip speed ratio as a function of number of blades for $N = 2, 3, 4, 6$

The generator efficiency—Fig. 14.20a is modeled as a second order polynomial, as shown in Eq.(14.46), where the rotor speed Ω_r is in rpm and the generator efficiency η_g in per unit.

$$\eta_g = -6.8654 \times 10^{-7}(\Omega_r - 945)^2 + 0.6131 \qquad (14.46)$$

14.6.2 Rotor Speed Control with Pitch System

This section applies the control algorithm designed in Sect. 14.5.1—Eq. (14.42)-to regulate the rotor speed $\Omega_r(t)$ of the wind turbine with the pitch angle actuator $\beta_d(t)$ in Region 3 (above rated, Fig. 14.10). The main objective of the pitch control system is to regulate the rotor speed at the rated (nominal) value $\Omega_r = \Omega_{r\text{-ref}}$, rejecting the wind disturbances v_1, and avoiding over-speed situations that can be dangerous for the turbine.

Figures 14.14 and 14.16 show the control system configuration and Figs. 14.21, 14.22, 14.23 the results of this experiment. The wind speed is set as a periodic function $v_1 = v_{1m} + v_{1a} \sin(2\pi f\, t + \theta)$ m/s, with $v_{1a} = 0.125$ m/s, $f = 0.2$ Hz, $\theta = 58°$, and $v_{1m} = 3.66$ m/s at $0 \leq t < 25$ s and $t > 31$ s, and $v_{1m} = 4.3$ m/s at $25 \leq t \leq 31$ s—see Fig. 14.21a. The rotor speed control system is set at a set point rotor speed $\Omega_r = \Omega_{r\text{-ref}} = 320$ rpm.

Using the control algorithm calculated in Eq. (14.42), the wind turbine changes the controller output (the demanded pitch angle or motor input β_{di}) as shown in Fig. 14.21b, and then the nacelle pitch angle β, also shown in Fig. 14.21b, to keep the rotor speed Ω_r at the nominal value $\Omega_{r\text{-ref}} = 320$ rpm, as shown in Fig. 14.22a.
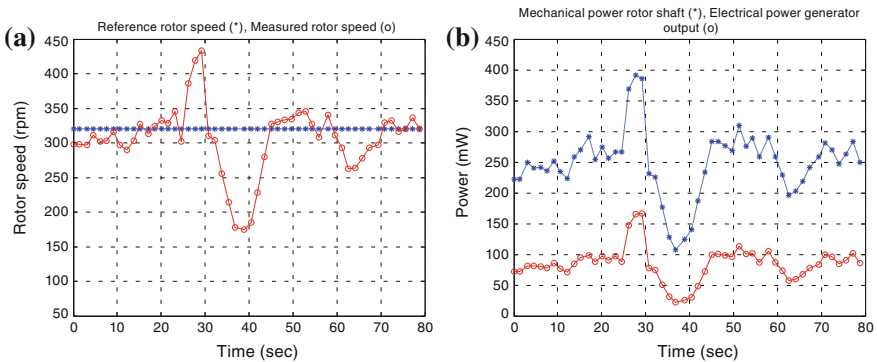
The experimental mechanical power at the rotor shaft P_a given by the wind speed v_1, and the electrical power at the generator output P_g are both shown in Fig. 14.22b. Finally Fig. 14.23 shows experimental results for (a) the wind speed v_1 and blade tip speed $\Omega_r r_b$; (b) the tip-speed ratio λ; (c) the aerodynamic power coefficient C_p; and (d) the C_p versus λ plot.

14.6.3 Maximum Power Point Tracking for Individual Wind Turbine

For Maximum Power Point Tracking (MPPT), Fig. 14.24 shows an experiment of a 6-blade wind turbine working with a constant pitch angle $\beta = 0$, a constant yaw angle $\alpha = 0$, and under a wind speed profile $v_1 = v_{1m} + v_{1a} \sin(2\pi f\, t + \theta)$, with $v_{1m} = 4.75$ m/s, $v_{1a} = 0.125$ m/s and $f = 0.2$ Hz, $\theta = 58°$. At time $t = 20$ s the antagonistic electrical torque T_{gd} (generator torque command) varies from 5.45 to 4.5 mNm—see Fig. 14.24a. As a result the rotor speed Ω_r speeds up from 560 rpm (58.64 rad/s) to 625 rpm (65.45 rad/s)—see Fig. 14.24c. This implies a change in
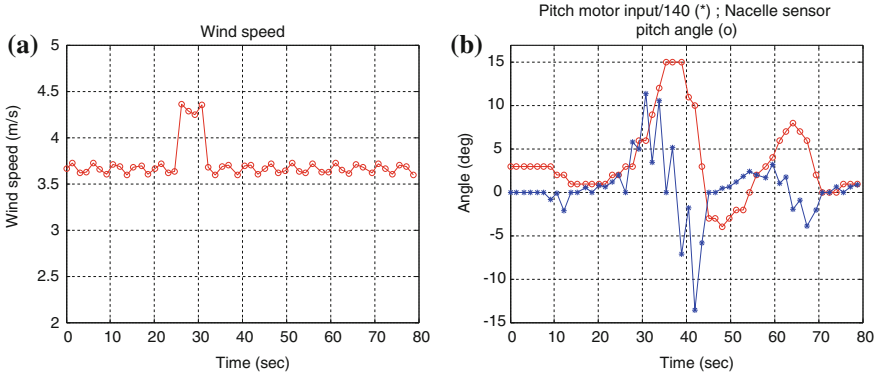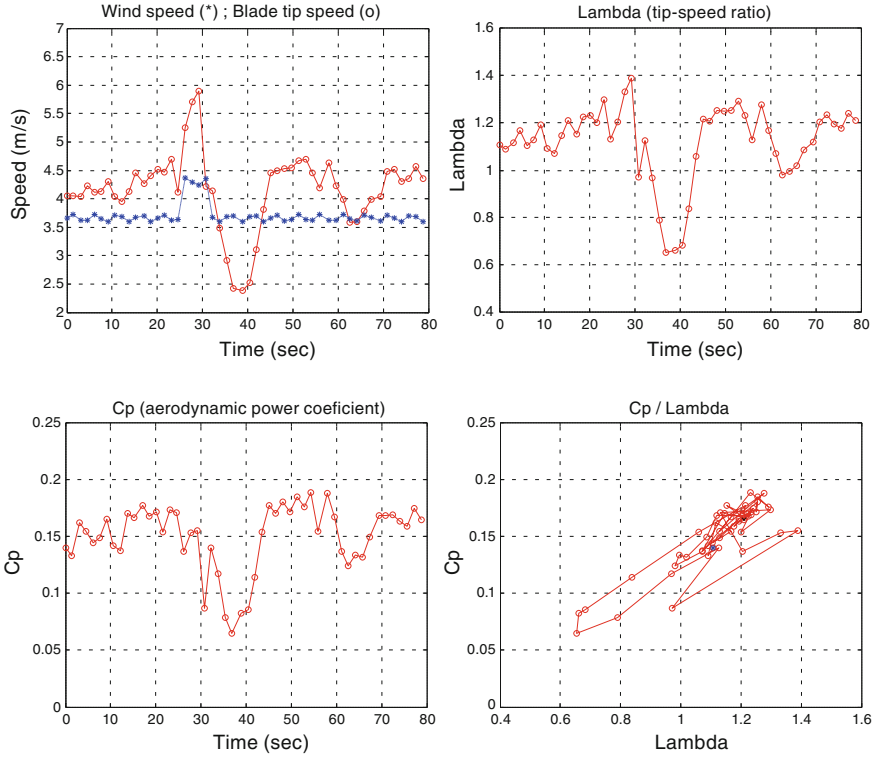
Fig. 14.21 Rotor speed control experiment: **a** wind speed v_1; **b** actuator input $\beta_{\mathrm{d}i}$ /140 and nacelle pitch angle sensor β


Fig. 14.22 Rotor speed control experiment: **a** reference rotor speed $\Omega_{r\text{-}ref}$ and measured rotor speed Ω_r; **b** mechanical power at rotor shaft P_a and electrical power at the generator output P_g

the tip speed (the rotor radius is $r_b = 0.13$ m) from 7.62 to 8.51 m/s—see Fig. 14.24b. As the average wind speed is $v_{1m} = 4.75$ m/s, the average tip speed ratio changes accordingly from $\lambda = 1.60$ to $\lambda = 1.79$—see Fig. 14.24d and therefore the aerodynamic power coefficient from $C_p = 0.179$ to $C_p = 0.156$—see Fig. 14.25.

These experimental results confirm the fact that the variation of the electrical torque T_{gd} in Regions 1 and 2 (below rated, Fig. 14.10) can be used to optimize the energy production of each wind turbine. Then, as seen in Sect. 14.5.2, a MPPT strategy can be used to maximize the energy production—see Eqs. (14.44) to (14.45).

Fig. 14.23 Rotor speed control experiment: **a** wind speed v_1 and blade tip speed $\Omega_r r_b$; **b** tip-speed ratio λ; **c** aerodynamic power coefficient C_p; **d** C_p versus λ
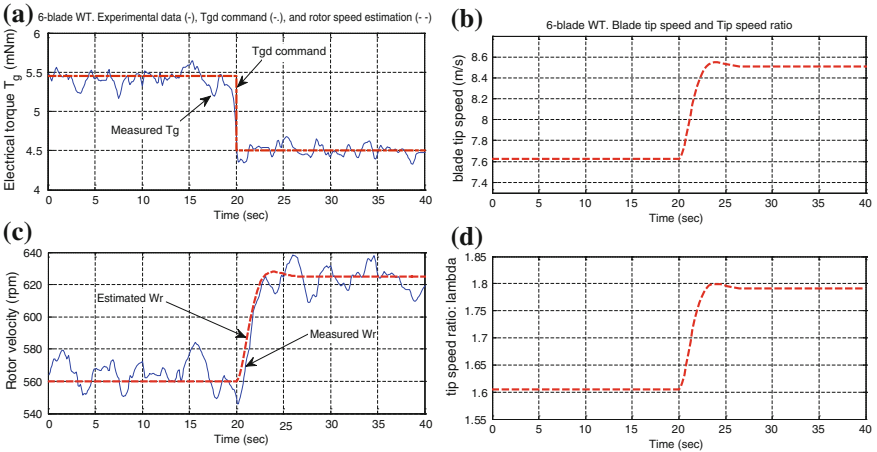
Fig. 14.24 Effect of electrical torque T_g on rotor speed Ω_r: **a** Experimental electrical torque T_g—in mNm; **b** Blade tip speed Ω_{rs} –in rpm; **c** Experimental and estimated rotor speed—in m/s; **d** Tip speed ratio λ

Fig. 14.25 Experimental
estimation of the C_p/λ
characteristic of the 6-blade
rotor wind turbine, $\beta = 0$
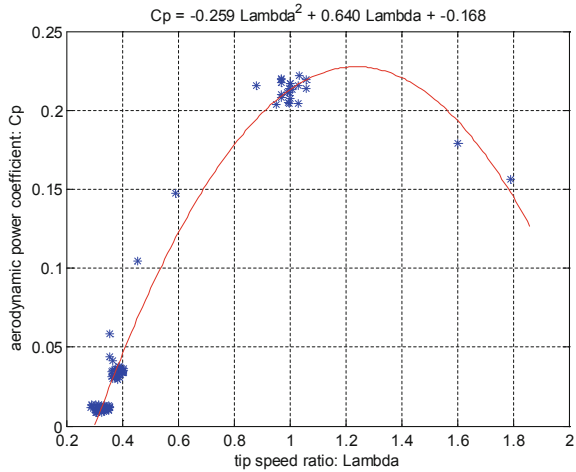
14.6.4 Estimation of the C_p/λ Characteristic of the 6-Blade Rotor Wind Turbine

This section estimates the C_p/λ characteristic of a 6-blade wind turbine. For a constant wind speed $v_{1m} = 3.65$ m/s, pitch angle $\beta = 0°$ and yaw angle $\alpha = 0°$, the demanded electrical torque T_{gd} of the generator is changed from a minimum to a maximum value ($R_{load} = 133$ to 0 ohm). As a result the rotor speed Ω_r and the generated power P_g of the wind turbine change. Knowing the generator efficiency η_g at different rotor speeds—Eq. (14.46) and Fig. 14.20a, and using Eq. (14.7) with the turbine's parameters ($r_b = 0.13$ m, $A_r = \pi \ r_b^2 = 0.0531$ m^2, $\rho = 1.225$ kg/m^3), the C_p/λ characteristic of the wind turbine is calculated according to Eq. (14.47), as shown in Fig. 14.25.

$$C_p = \frac{(P_g/\eta_g)}{0.5\,\rho\,A_r\,v_{1m}^3}; \quad \lambda = \frac{\Omega_r\,r_b}{v_{1m}} \tag{14.47}$$

The maximum aerodynamic power coefficient is $C_{pmax} = 0.227$ at an optimum tip-speed ratio $\lambda_{opt} = 1.224$. A second order polynomial approach of the experimental data is shown in Eq. (14.48).

$$C_p = -0.259\,\lambda^2 + 0.640\,\lambda - 0.168 \tag{14.48}$$

14.6.5 Power Curve for the 6-Blade Rotor Wind Turbine

After the estimation of the aerodynamic power coefficient at different tip-speed ratios for a 6-blade rotor wind turbine (C_p/λ characteristic, Sect. 14.6.4) and the estimation of the generator efficiency at different rotor speeds—see Eq. (14.46)

and Fig. 14.20a, this section presents the experimental power curves for the 6-blade rotor wind turbine.

The study applies the optimum MPPT control strategy presented in Eqs. (14.44) and (14.45), considering the generator losses—Eq. (14.46)- and with $K_a = 8.8453 \times 10^{-6}$. All the experiments maintain the pitch angle in Region 1 at $\beta = 0°$. Figure 14.26a shows the power curve (P_g vs. v_1) for Regions 1, 2, and 3 (see also Fig. 14.10) of three scenarios: using a 100, 90 and 80 % of the maximum power coefficient $C_{p\max}$. Figure 14.26b shows the rotor speed Ω_r of the wind turbine at the operating wind speeds v_1 for the three cases.

The rated (nominal) power for the 6-blade wind turbine is $P_{g\_rated} = 150$ m-Watts. For the 100 % $C_{p\max}$ case the rated power is achieved at a wind speed $v_{1\_rated} = 4.2$ m/s with a rated rotor speed $\Omega_{r\_rated} = 324$ rpm, the cut-in (wind turbine connection) is at $v_1 = 2$ m/s and $\Omega_r = 180$ rpm, the cut-off (wind turbine disconnection) is at $v_1 = 5.0$ m/s and $\Omega_r = 324$ rpm, Region 1 is between 2 m/s $\leq v_1 < 3.6$ m/s, Region 2 between 3.6 m/s $\leq v_1 < 4.2$ m/s, and Region 3 between 4.2 m/s $\leq v_1 < 5.0$ m/s.

For the 90 % case, the rated power is achieved at a wind speed $v_{1\_rated} = 4.2$ m/s with a rated rotor speed $\Omega_{r\_rated} = 333$ rpm, the cut-in is at $v_1 = 2$ m/s and $\Omega_r = 180$ rpm, the cut-off is at $v_1 = 5.0$ m/s and $\Omega_r = 333$ rpm, Region 1 is between 2 m/s $\leq v_1 < 3.7$ m/s, Region 2 between 3.7 m/s $\leq v_1 < 4.2$ m/s, and Region 3 between 4.2 m/s $\leq v_1 < 5.0$ m/s.

For the 80 % case, the rated power is achieved at a wind speed $v_{1\_rated} = 4.2$ m/s with a rated rotor speed $\Omega_{r\_rated} = 344$ rpm, the cut-in is at $v_1 = 2$ m/s and $\Omega_r = 180$ rpm, the cut-off is at $v_1 = 5.0$ m/s and $\Omega_r = 344$ rpm, Region 1 is between 2 m/s $\leq v_1 < 3.8$ m/s, Region 2 between 3.8 m/s $\leq v_1 < 4.2$ m/s, and Region 3 between 4.2 m/s $\leq v_1 < 5.0$ m/s.

14.6.6 Wind Farm Topology Configurations and Effect on Power Efficiency

Topology configuration is critical to the efficiency and effective power generation of a wind farm system. The aerodynamic effects of each wind turbine on the wind profile around them are profound. In commercial wind farms, wind turbines are most often placed far enough apart that their effects are negligible (typically about 9 rotor diameters apart in the predominant wind direction and 5 rotor diameters apart in the perpendicular direction).

However, with an appropriate advanced controller it may be possible to place individual wind turbines closer together and compensate for the effects on the wind profile to maximize energy production in a fixed area. In order to accomplish this, these effects must first be observed and modeled. This section shows the convenience of the test bench for this analysis.
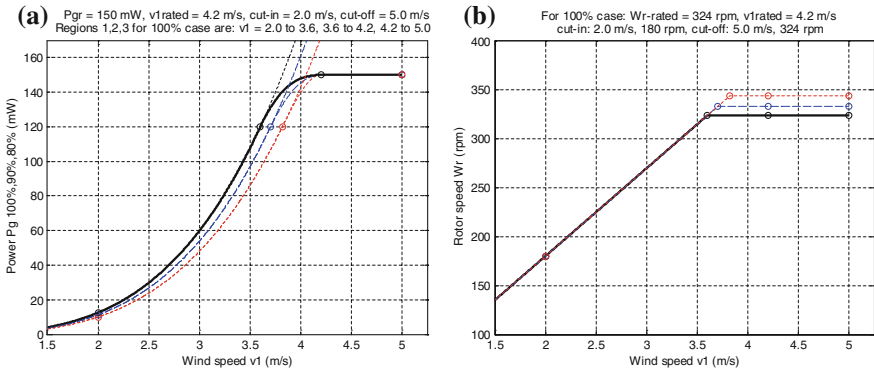
Fig. 14.26 Experimental characterization of a 6-blade rotor wind turbine for 100, 90 and 80 % C_{pmax}: **a** Power curves; **b** Rotor speed versus wind speed
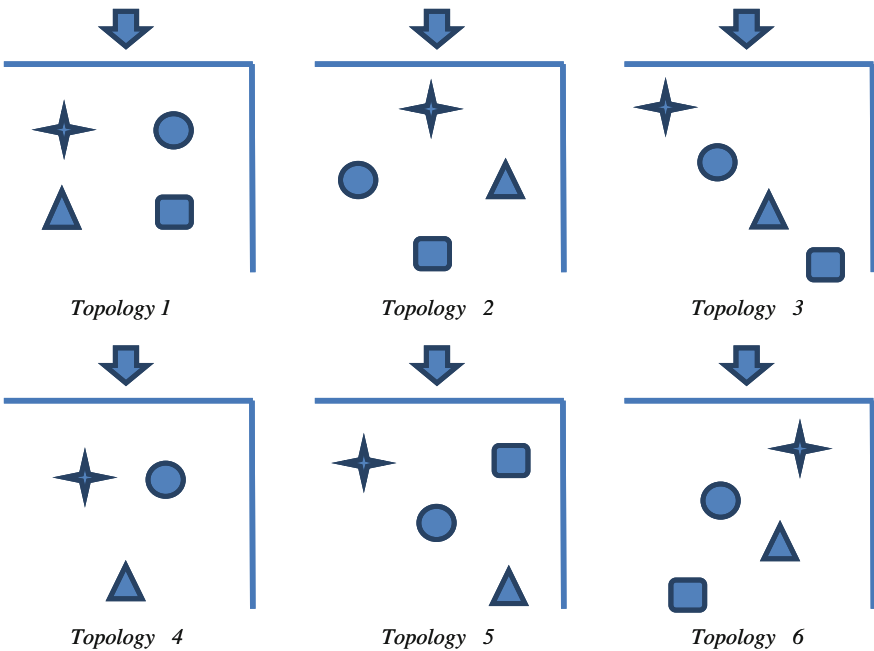
Fig. 14.27 Wind farm topology configurations for different global power efficiency, with T1 ✦, T2 ⬤, T3 ▲, T4 ▣

Figure 14.27 and Tables 14.3, 14.4, 14.5 shows the configuration of the wind farm for six different experiments. Each wind turbine has a 6-blade rotor, has no active controllers, a constant pitch angle $\beta = 0$, a constant yaw angle $\alpha = 0$, and a constant demanded torque T_{gd}. The geometric position of each wind turbine in the

Table 14.3 Wind farm configuration: positions (cm)

Topology	Wind turbines			
	T1	T2	T3	T4
1	(20.32,25.40)	(10.16, 25.40)	(10.16, 96.52)	(20.32, 96.52)
2	(40.64, 15.24)	(66.04, 55.88)	(15.24, 55.88)	(40.64, 96.52)
3	(55.88, 15.24)	(45.72, 35.56)	(35.56, 60.96)	(45.72, 81.28)
4	(55.88, 20.32)	(25.4, 20.32)	(40.64, 55.88)	–
5	(55.88, 15.24)	(45.72, 35.56)	(35.56, 60.96)	(20.32, 15.24)
6	(25.4, 20.32)	(45.72, 35.56)	(40.64, 60.96)	(55.88, 71.12)

wind farm is shown in Fig. 14.27 and Table 14.3. The rotor velocity and electrical power generation is measured for each configuration. Tables 14.4 and 14.5 show the experimental results.

The aerodynamic effects on the wind profile in some cases are strong enough to completely disrupt the airflow to some turbines (see zeroes in Table 14.5). The most efficient configuration is the second topology in which one turbine is placed at the front of the configuration, therefore receiving the strongest uninterrupted airflow. Interestingly, this is the most efficient, despite the fourth turbine being completely motionless.

Table 14.4 Wind farm configuration: rotor speed (rpm)

Topology	Wind turbines			
	T1	T2	T3	T4
1	207.89	126.34	44.31	52.26
2	947.68	101.25	56.73	0
3	236.50	60.99	84.17	3.08
4	275.04	353.55	59.43	0
5	272.48	256.22	34.81	151.59
6	289.08	623.25	0	59.62

Table 14.5 Wind farm configuration: generated power (mW)

Topology	Wind turbines				Total WF
	T1	T2	T3	T4	
1	81.84	49.74	17.44	20.57	169.61
2	373.10	39.86	22.34	0	435.30
3	93.11	24.01	33.14	1.21	151.48
4	108.28	139.19	23.40	0	270.87
5	107.28	100.87	13.71	59.68	281.53
6	113.81	245.37	0	23.47	382.66

14.7 Conclusions

This chapter presented a new low-cost, flexible test-bench wind farm for advanced research and education in optimum wind turbine and wind farm design, modeling, estimation, and multi-loop cooperative control. It is shown in detail the mechanical, electrical, electronic, and control system design of the wind turbines. The chapter also finds the dynamic models, estimates the parameters and model uncertainty, and designs some classical controllers. Moreover, the study presents a variety of experiments that (a) quantifies the effect of the number of blades in the aerodynamic efficiency, (b) estimates the generator efficiency, (c) validates the proposed rotor-speed pitch control system, (d) proves the concept of maximum power point tracking for individual wind turbines, (e) estimates the aerodynamic C_p/λ characteristics, (f) calculates the power curve, and (g) studies the effect of wind farm topology configurations on the individual and global power efficiency. The experimental results proved that the performance dynamics of the lab test-bench corresponds very well with full-scale wind turbines. This fact makes the system appropriate for advanced research and education in wind energy systems.

14.8 Future Work

The wind turbine design, dynamics modeling, estimation and system identification, turbine control system, wind farm hierarchical control, and experimentation are going to be implemented as laboratory classes for undergraduate and graduate engineering courses on renewable energy and automatic control at the University. The excellent experimental results achieved with the test-bench wind farm, with a performance dynamics that corresponds well with full-scale wind turbines, will allow the students to conduct realistic hands-on experiments and understand wind energy concepts in depth. Also, the high modularity and flexibility of the wind turbines and the wind farm will facilitate to develop, implement, and validate experimentally new research ideas of all kind.

References

1. Burton T, Jenkins N, Sharpe D, Bossanyi E (2011) Wind energy handbook, vol 2. John Wiley & Sons, New York
2. García-Sanz M, Houpis CH (2012) Wind energy systems: control engineering design. CRC Press, Taylor and Francis, Boca Raton

3. García-Sanz M, Mauch A, Philippe C (2014) The QFT control toolbox (QFTCT) for Matlab. CWRU, UPNA and ESA-ESTEC, Version 5.01. http://cesc.case.edu
4. Houpis CH, Rasmussen SJ, García-Sanz M (2006) Quantitative feedback theory: fundamentals and applications, 2nd edn. CRC Press, Taylor and Francis, Boca Raton
5. Lego mindstorms (2014). http://www.lego.com/en-us/mindstorms
6. Mindsensors. Sensors for Lego. http://mindsensors.com/
7. Matlab (2014). Mathworks. http://www.mathworks.com/products/matlab/
8. Lego motor characteristics. http://www.philohome.com/motors/motorcomp.htm
9. Arduino microcontroller. http://arduino.cc/

Chapter 15
Hardware in the Loop Wind Turbine Simulator for Control System Testing

Yolanda Vidal, Leonardo Acho, Ningsu Luo and Christian Tutiven

Abstract This chapter illustrates how to set up an inexpensive but effective Hardware-in-the-Loop (HIL) platform for the test of wind turbine (WT) controllers. The dynamics of the WT are simulated on the open-source National Renewable Energy Laboratory WT simulator called FAST (Fatigue, Aerodynamics, Structures, and Turbulence), which emulates all required input signals of the controller and reacts to the controller commands (almost) like an onshore real turbine of 5 MW. The dynamic torque control system runs on an open hardware Arduino microcontroller board, which is connected to the virtual WT via USB. In particular, the power generation control in the full load region for variable-speed variable-pitch wind turbines is considered through torque and pitch control. The HIL proposed platform is used to characterize the behavior of the WT in normal operation as well as in fault operation. In particular, a stuck/unstuck fault is modeled and the behavior of a proposed chattering torque controller is analyzed in comparison to a baseline torque controller.

Keywords Hardware-in-the-loop · FAST · Arduino · Control · Fault

Nomenclature

β_k Pitch control, $k = 1, 2, 3$

Y. Vidal (✉) · L. Acho · C. Tutiven
Departament de Matemàtica Aplicada III, Universitat Politècnica
de Catalunya-BarcelonaTECH, Barcelona, Spain
e-mail: yolanda.vidal@upc.edu

L. Acho
e-mail: leonardo.acho@upc.edu

C. Tutiven
e-mail: christian_tutiven@hotmail.com

N. Luo
Department of Electrical Engineering, Electronics and Automatic Control,
University of Girona, Girona, Spain
e-mail: ningsu.luo@udg.edu

τ_c	Generator torque control
ω_g	Generator speed
$\hat{\omega}_g$	Filtered generator speed
ω_{ng}	Rated generator speed
P_e	Electrical power
P_{ref}	Reference power
θ	Scheduling parameter
$\dot{x}$	Denotes dx/dt

15.1 Introduction

With wind turbines becoming larger and more flexible, the control system has become extremely important and so has a testing environment for the control system itself. A comprehensive assessment of WT controllers in the lab reduces risks of erroneous implementations in the field and significantly shortens commissioning times.

Following the lead of the auto industry, the WT industry has begun moving toward adoption of hardware-in-the-loop (HIL) simulation as a method for real-time testing of embedded control systems during the development phase without using prototypes. On the contrary of computer simulation, HIL simulation uses one or several actual components instead of their simulation model. The other parts of the process are simulated [7]. Such a methodology has been used in aeronautics for a long time [12]. Traction applications are nowadays more and more developed using HIL simulation before the final implementation [14, 17]. HIL tests are essential for fast and cost-effective commissioning of controllers in the field (or at sea in the case of offshore wind farms). A major benefit of doing these simulations is that it allows design engineers to optimize the control system during the development stage, which is going to have a big impact on reliability. Moreover, engineers can take exactly the same code that was used in the simulation and run it directly on the deployed target, saving time and effort in the design process. Finally, the controllers must be tested in extreme cases, such as faults on sensors an/or actuators of the WT. However, testing these cases experimentally can seriously damage the WT, thus a HIL approach is preferable.

To this end, a HIL test setup for WT controllers is developed in this chapter. The torque controller and the communication system can be integrated as hardware in a real-time simulator, which models the behavior of the WT. The HIL proposed platform is used to characterize the behavior of the WT in region 3 in normal operation as well as in fault operation. In particular, a stuck/unstuck fault is modeled and the behavior of a proposed chattering torque controller is analyzed in comparison to a baseline torque controller.

This chapter is divided into seven main sections. In Sect. 15.1, we introduce the scope of the chapter. Section 15.2 is devoted to the HIL setup, explaining in detail each part and how to setup the overall testbed. Section 15.3 introduces the 5 MW reference WT used in the simulations and Sect. 15.4 accounts for the wind modeling. The torque controllers compared in the simulations as well as the pitch controller are stated in Sect. 15.5. The obtained HIL results are discussed and analyzed in Sect. 15.6. Finally, Sect. 15.7 states the conclusions of this chapter.

15.2 HIL Test Setup

The overall testing platform consists of two major parts:

- A computer that runs the WT simulator (FAST).
- The turbine controller, programmed on an Arduino Mega microcontroller board [1], running the dynamic torque control system which is connected to the virtual WT via USB.

The HIL test platform is shown in Fig. 15.1. The next subsections present in detail each of these parts and how to setup the overall system.
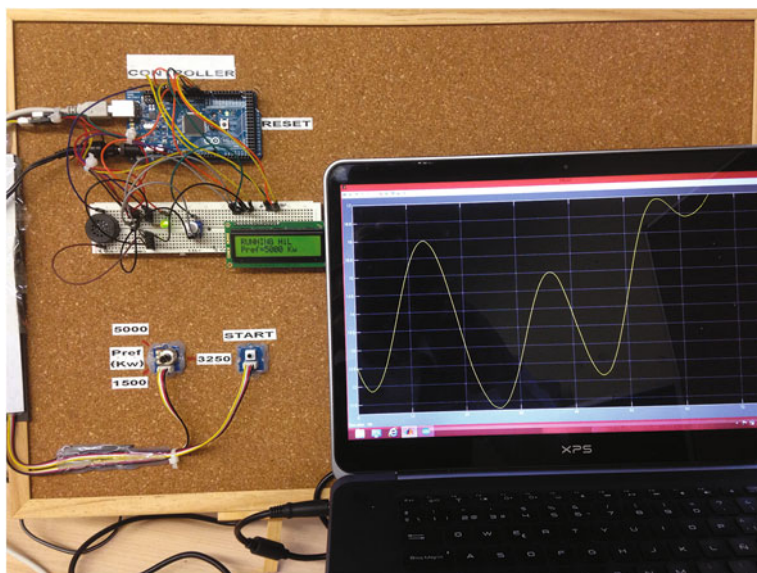
Fig. 15.1 Experimental setup for the HIL WT control test

15.2.1 FAST (Wind Turbine Simulator)

The NREL's National Wind Technology Center (NWTC) develops advanced computer-aided engineering (CAE) tools to support the wind industry with state-of-the-art design and analysis capabilities. The NWTC has developed many software tools that produce realistic models that simulate the behavior of a wind turbine in complex environments and model the effects of turbulent inflow, unsteady aerodynamic forces, structural dynamics, drivetrain response, control systems, and hydrodynamic loading for offshore applications. NREL has also developed preprocessors to build the models, post-processors to analyze the results, and utilities to run and manage the processing tasks.

The NWTC CAE tools have become the industry standard for analysis and development and are used by thousands of American and international wind turbine designers, manufacturers, consultants, certifiers, researchers, and educators. These tools are developed as free, publicly available, open-source, professional-grade products as a resource for the wind industry. The open-source approach facilitates the credibility and adaptability of the tool within the industry. The tools are modular, well documented, and are supported by NREL through workshops and an on-line forum (http://wind.nrel.gov/forum/wind/viewforum.php?f=4). They have been verified through model-to-model comparisons, validated with test measurements, and certified by Germanischer Lloyd. As a technical supervisory organization, Germanischer Lloyd services include the mitigation of risks and assurance of technical compliance for oil, gas, and industrial installations as well as wind energy parks.

The FAST code [8] is a comprehensive aeroelastic simulator capable of predicting the extreme and fatigue loads of two- and three-bladed HAWTs. This simulator was chosen for validation because, in 2005, it was evaluated by Germanischer Lloyd WindEnergie and found suitable for the calculation of onshore WT loads for design and certification [13]. An interface between FAST and Simulink was also developed with MATLAB$^{\circledR}$, enabling users to implement advanced turbine controls in Simulink$^{\circledR}$ convenient block diagram form. The FAST subroutines are linked with a Matlab standard gateway subroutine so the FAST motion equations (in an S-function) can be incorporated in a Simulink model. This introduces tremendous flexibility for WT control implementation during simulation. Generator torque, nacelle yaw, and pitch control modules can be designed in the Simulink environment and simulated while using the complete nonlinear aeroelastic WT equations of motion, which are available in FAST. The WT block contains the S-function block with the FAST motion equations and blocks that integrate the degree-of-freedom accelerations to obtain velocities and displacements. Thus, the equations of motion are formulated in the FAST S-function and solved using one of the Simulink solvers. FAST main features can be summarized as follows:

- Computes structural-dynamic and control-system responses as part of the aero-hydro-servo-elastic solution.
- Uses a combined 24-DOF modal and multi-body representation.

- Control system modeling through subroutines, DLLs, or Simulink with MATLAB.
- Nonlinear time-domain solution for loads analysis.
- Linearization procedure for controls and stability analysis.

We use FAST to simulate the WT and also the wind speed signal. FAST runs on a laptop with processor Intel Core i5-3230 M to 3.2 GHz and 8GB2 SDRAM DDR3 to 1600 MHz.

15.2.2 Arduino Microcontroller Board

In contrast to free or open-source software, which is already widely used, open hardware is quite new. One of the open-source hardware projects that quickly became popular is Arduino. It was created in 2005 at the Interaction Design Institute Ivrea (Italy) as a system that allowed students to develop interactive designs. Arduino (http://arduino.cc/en/) is an open-source physical computing platform based on a simple microcontroller board, and it offers a software development environment. The programming language is C/C++ and a number of libraries make standard applications like printing on an alphanumeric LCD or using serial communication simple. The board can be programmed using an USB-interface, and the program is stored in the internal EEPROM of the micro-controller. Arduino can be used to develop interactive objects, taking inputs from a variety of switches or sensors, and controlling a variety of lights, motors, and other physical outputs. Arduino can function autonomously without being connected to a computer, or alternatively programmed to respond mainly to commands sent from the computer via various software interfaces or to the data acquired from the input channels. An extensive documentation about the hard- and software can be found in Arduino's web site: http://arduino.cc.

In this work the Arduino Mega2560 microcontroller board has been used. It has 54 digital input/output pins, 16 analog inputs, 4 UARTs (hardware serial ports), a 16 MHz crystal oscillator, a USB connection, a power jack, an ICSP header, and a reset button. It contains everything needed to support the microcontroller; simply connecting it to a computer with a USB cable or powering it with a AC-to-DC adapter or battery to get started. Table 15.1 summarizes the Arduino Mega2560 characteristics.

We use Arduino as the controller hardware. We program the controller in C code (Arduino language) and download it to the Arduino board to run it in real-time. The following components were used:

- Start-button to start the controller.
- Buzzer to play tone when controller starts and stops.
- Potentiometer (10 kH) to prescribe the reference power to the WT.
- LCD-Display where the commanded reference power is displayed.

A diagram representation of the HIL setup is shown in Fig. 15.2.

Table 15.1 Summary of Arduino Mega2560 characteristics

Arduino Mega2560	
Microcontroller	ATmega2560
Operating voltage	5 V
Input voltage (recommended)	7–12 V
Input voltage (limits)	6–20 V
Digital I/O pins	54 (of which 15 provide PWM output)
Analog input pins	16
DC current per I/O pin	40 mA
DC current for 3.3 V pin	50 mA
Flash memory	256 KB of which 8 KB used by bootloader
SRAM	8 KB
EEPROM	4 KB
Clock speed	16 MHz
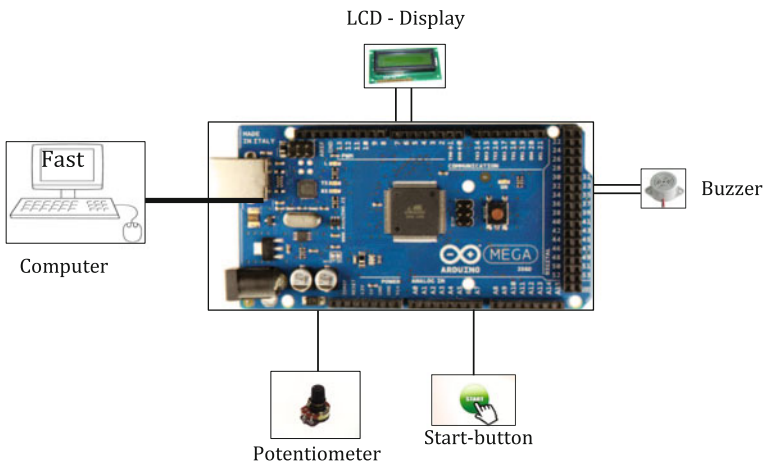
Fig. 15.2 Block diagram of the HIL experimental setup

15.2.3 Setup

The HIL allows control system hardware (Arduino) to be connected directly to FAST simulations. The Arduino receives inputs from the potentiometer (reference power, P_{ref}) and the WT simulator (generator speed, ω_g) and outputs the torque controller command to the WT simulator. The wind inflow for the simulation is also given by FAST. A gain scheduled Proportional-Integral (PI) pitch control is programmed in the WT simulator. Thus, only the torque controller is programmed in Arduino.

The steps to set up the HIL experiment are:

- Program, in Arduino language, the torque controller, (Euler numerical integration has been used) and download it to the hardware.
- Reconfigure the Simulink FAST WT simulator in order to communicate with the hardware inputs and outputs.
- Hardware interface via Universal Serial Bus (USB) port.
- Sampling period of 0.3 s due to single channel communication management via USB.
- The Matlab Real-Time Sync block allows to synchronize the Simulink model with the real-time clock. Simulink is run in normal mode.
- To run in real-time we use a fixed-step solver with appropriate step size.

The Arduino and Matlab scripts as well as the Simulink diagram are given in the Appendix.

15.3 Onshore Reference Wind Turbine

The experimental setup is carried out by means of the onshore version of the 5 MW reference wind turbine described in [9]. The parameters of the turbine are summarized in Table 15.2. This book chapter deals with the full load region of operation, that is where the wind speed is above its rated value. The proposed torque and pitch controllers main task is that the electric power follows the rated power of 5 MW.

15.4 Wind Modeling

In fluid dynamics, turbulence is a flow regime characterized by chaotic property changes. This includes low momentum diffusion, high momentum convection, and rapid variation of pressure and velocity in space and time. In the simulations in this book chapter, new wind data sets are generated with TurbSim [10], a stochastic, full-field, turbulent-wind simulator developed by NREL. TurbSim generates a rectangular grid which holds the wind data. In the input text file, that TurbSim uses as an input, we define:

- Grid settings and position matched with the rotor diameter, and the center of the grid positioned at hub height. This represents a grid size of 130×130 m^2 centered at 19.55 m.
- The Kaimal turbulence model is selected.
- The turbulence intensity is set to 10 %.
- Normal wind type is chosen with a logarithmic profile.
- Reference height is set to 90.25 m. This is the height where the mean wind speed is simulated.
- Mean (total) wind speed is set to 18.2 m/s.

Table 15.2 Wind turbine characteristics

Reference wind turbine	
Rated power	5 MW
Number of blades	3
Rotor/hub diameter	126, 3 m
Hub height	90 m
Cut-in, rated, cut-out wind speed	3, 11.4, 25 m/s
Rated generator speed (ω_{ng})	1173.7 rpm
Gearbox ratio	97

Fig. 15.3 Sample wind speed
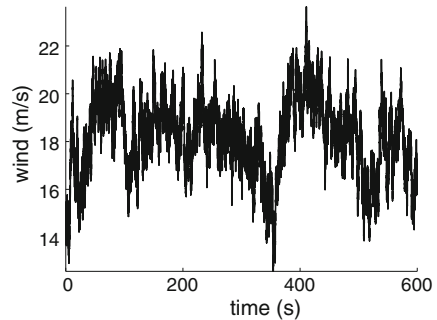
- The roughness factor is set to 0.01 m which corresponds to a terrain type of open country without significant buildings and vegetation.

It can be seen from Fig. 15.3 that the wind speed covers the full load region (also called region 3). In particular, note that from 350 to 400 s its value ranges from the minimum 12.91 m/s up to the maximum of 22.57 m/s.

15.5 Control Strategy

In this section a baseline torque controller and a proposed chattering torque controller are introduced. As the generator may not be able to supply the desired electro-mechanic torque depending on the operating conditions, both torque controllers are saturated to a maximum of 47402.91 Nm and a maximum generator torque rate saturation of 15000 Nm/s, see [9].

15.5.1 Baseline Torque Controller

The torque control and the pitch control, both, will use the generator speed measurement as input. As proposed by [9] to mitigate high-frequency excitation of

the control systems, we filtered the generator speed measurement for both the torque and pitch controllers using a recursive, single-pole low-pass filter with exponential smoothing.

The 5 MW reference wind turbine given by FAST contains a torque controller. In Region 3, this controller maintains constant the generator power, thus the generator torque is inversely proportional to the filtered generator speed, or,

$$\tau_c = \frac{P_{\text{ref}}}{\hat{\omega}_g}, \tag{15.1}$$

where P_{ref} is the reference power and $\hat{\omega}_g$ is the filtered generator speed. This controller will be referred as the baseline torque controller.

15.5.2 Chattering Torque Control

In this subsection a chattering torque controller is proposed [15].

The electrical power-tracking error is defined as

$$e = P_{\text{e}} - P_{\text{ref}}, \tag{15.2}$$

where P_{e} is the electrical power and P_{ref} is the reference power. We impose a first-order dynamic to this error,

$$\dot{e} = -ae - K_{\alpha}\text{sgn}(e) \quad a, K_{\alpha} > 0, \tag{15.3}$$

and consider that the electrical power is described as [2, 3, 5, 11]

$$P_{\text{e}} = \tau_c \omega_g, \tag{15.4}$$

where τ_c is the torque control and ω_g is the generator speed. By substitution of Eqs. (15.2) and (15.4) into (15.3), and assuming that P_{ref} is a constant function, we obtain

$$\dot{\tau}_c \omega_g + \tau_c \dot{\omega}_g = -a(\tau_c \omega_g - P_{\text{ref}}) - K_{\alpha}\text{sgn}(P_{\text{e}} - P_{\text{ref}}),$$

which, can also be written as

$$\dot{\tau}_c = \frac{-1}{\omega_g}\left[\tau_c(a\omega_g + \dot{\omega}_g) - aP_{\text{ref}} + K_{\alpha}\text{sgn}(P_{\text{e}} - P_{\text{ref}})\right]. \tag{15.5}$$

Theorem 1 The proposed controller 5 ensures finite time stability [4]. Moreover, the settling time can be chosen by properly defining the values of the parameters a and K_{α}.

Proof We now present the Lyapunov function

$$V = \frac{1}{2}e^2. \tag{15.6}$$

Then, based on Eq. (15.3), the time derivative along the trajectory of the system yields

$$\dot{V} = e\dot{e} = e(-ae - K_\alpha \text{sgn}(e)) = -ae^2 - K_\alpha|e| < 0. \tag{15.7}$$

Thus, V is globally positive definite and radially unbounded, while the time derivative of the Lyapunov-candidate-function is globally negative definite; so the equilibrium is proven to be globally asymptotically stable. Moreover, finite time stability can be proven. Equation (15.7) can be written as

$$\dot{V} \leq -K_\alpha|e| = -K_\alpha\sqrt{2}\sqrt{V}.$$

Thus, $\dot{V} + K_\alpha\sqrt{2}\sqrt{V}$ is negative semidefinite and Theorem 1 in [4] can be applied to conclude that the origin is a finite time stable equilibrium. Furthermore, from [4], the settling time function t_s is described as

$$t_s \leq \frac{1}{K_\alpha\sqrt{2}}(V)^{1/2},$$

and using Eq. (15.6) leads to

$$t_s \leq \frac{e}{K_\alpha}.$$

□

The proposed simple nonlinear torque control, see Eq. (15.5), does not require information from the turbine total external damping or the turbine total inertia. This control only requires the generator speed and electrical power of the WT. Thus, our proposed controller requires few WT parameters and it does not need to filter the generator speed measurement.

15.5.3 Pitch Control

To assist the torque controller with regulating the wind turbine electric power output, while avoiding significant loads and maintaining the rotor speed within acceptable limits, a collective pitch controller is added to the rotor speed tracking error. The pitch angle controller is a gain scheduling PI-controller with the generator speed as input and the pitch servo set-point as output. That is,

$$\beta_k = K_p(\theta)(\omega_g - \omega_{\text{ng}}) + K_i(\theta) \int_0^t (\omega_g - \omega_{\text{ng}})\mathrm{d}t, \quad K_p > 0, \ K_i > 0, k = 1, 2, 3,$$

where ω_g is the generator speed, ω_{ng} is the nominal generator speed (at which the rated electrical power of the wind turbine is obtained) and the scheduling parameter θ is taken to be the previous measured collective blade pitch angle. As the three pitch angles are measured, β_k, the collective pitch angle is obtained by averaging the measurements of all pitch angles. The scheduled gains are calculated following [9]. Finally, a pitch limit saturation to a maximum of 45° and a pitch rate saturation of 8°/s is implemented, see [9].

Recall that when using the baseline torque controller the filtered generator speed measurement is used for both the torque and pitch controllers. However, when using the chattering controller no filters are needed neither in the torque control nor in the pitch control.

Note that the pitch control is not simulated as HIL. Only the torque control is implemented in the Arduino hardware.

15.6 HIL Results

For the proposed controller in Eq. (15.5), the values $a = 1$ and $K_\alpha = 1.5 \times 10^5$ have been used in the simulations. This controller depends on $\dot{\omega}_g$, thus we computed a first order approximation of $\dot{\omega}_g$ in the Arduino board.

15.6.1 Healthy

The simulation results for the healthy case show that for both controllers:

- The electrical power follows the reference independently of the wind fluctuations, as shown in Fig. 15.4 (left).
- The torque action achieves reasonable values, as shown in Fig. 15.4 (right).
- The blade pitch angle is always within the authorized variation domain, as shown in Fig. 15.5 (left).
- The generator speed is near its nominal value of (1173.7 rpm) due to the pitch control action, as shown in Fig. 15.5 (right).

15.6.2 Faulty

Blade pitch system faults have the highest failure rate in WT. In this chapter a fault related to the third pitch actuator has been studied. In the studied fault the gain scheduled PI collective pitch control is performed by using the average of the
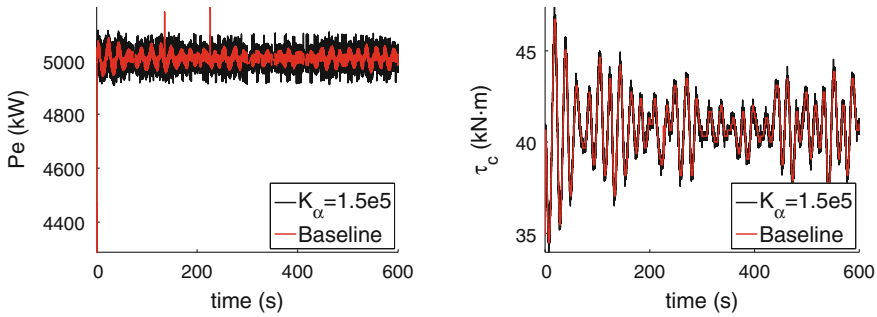
Fig. 15.4 Power output (*left*) and torque control (*right*)
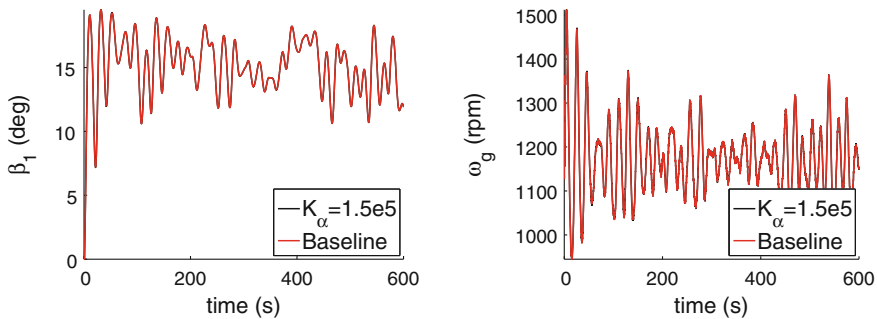

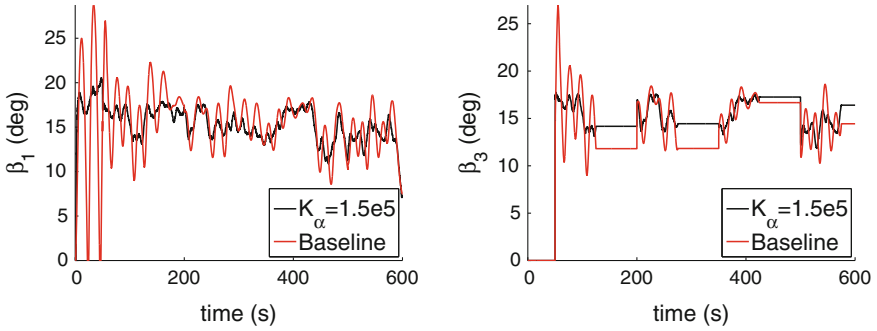**Fig. 15.5** Pitch angle (*left*) and generator speed (*right*)

measurement of all pitch angles. In particular, the actuator is stuck to 0 degrees at the beginning of the computation then after 50 s it gets unstuck and then each period of 75 s we switch between being stuck/unstuck. We modeled this fault using the following ordinary differential equation:

$$\dot{\beta}_3 = p(-\beta_3 + \beta_1)$$

where p is a pulse generator of amplitude 10, period 150 s, pulse width (% of period) 50, and a phase delay of 50 s. When p equals 0 the third actuator is stuck and when p equals 10 then β_3 follows again the pitch control, β_1. Initially, the third actuator is stuck to 0°. The simulation results for the faulty case show that:

- The first blade pitch angle is always within the authorized variation domain, as shown in Fig. 15.6 (left), but with higher oscillations for the baseline controller. Thus, our proposed controller induces less vibrations in the structure as the range of movement of the pitch angle is smaller.
- The third blade switches between being stuck/unstuck as can be seen in Fig. 15.6 (right).
- The transient response of the electrical power has a larger oscillation for the baseline controller, as shown in Fig. 15.7 (left).
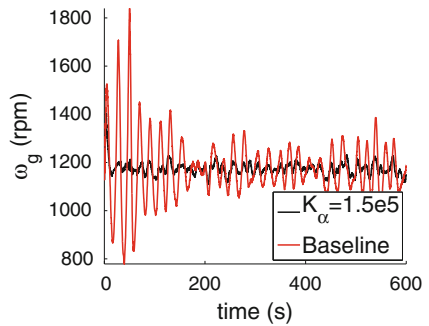
Fig. 15.6 First (healthy) pitch angle (*left*) and third (faulty) pitch angle (*right*) for the faulty case
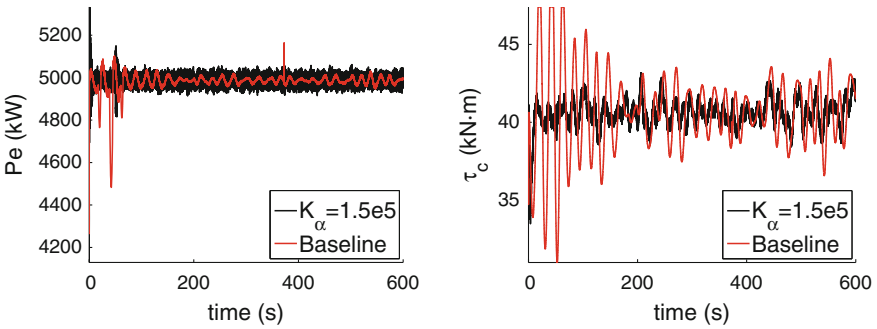
Fig. 15.7 Power output (*left*) and torque control (*right*) for the faulty case

Fig. 15.8 Generator speed for the faulty case

- The torque action for the baseline controller achieves the saturation limit (47.40 kN·m) whereas the proposed chattering controller does not, as shown in Fig. 15.7 (right). When achieving the saturation limit vibrations and limit cycles can appear, see [16].
- The generator speed for the baseline controller has larger oscillations, as shown in Fig. 15.8.

15.7 Conclusions

This chapter presented an inexpensive but effective HIL platform. By using open-source solutions both in respect to hardware (Arduino) and software (FAST) the capabilities to modify the proposed HIL platform are greatly broadened and allow novel ways of interaction between the developers and end users [6]. Active user communities exist around Arduino (http://arduino.cc/playground) and FAST (http://wind.nrel.gov/forum/wind/viewforum.php?f=4).

In conclusion, the HIL proposed platform was found to be suitable for control system testing. It can be used to characterize the behavior of wind turbines in normal operation as well as in fault operation. The low-cost and ease of use makes it attractive in educational and research environments with limited budgets, and in particular for researchers, students, and universities with limited resources.

Appendix

Arduino script of the proposed controller:

```
#include<LiquidCrystal.h>
LiquidCrystal lcd(12,11,5,4,3,2);

int sign(double x){return (x>0)-(x<0);}
int pinsw=10;
int pinled=9;

void setup(){
  pinMode(pinsw,INPUT);
  pinMode(pinled,OUTPUT);
  Serial.begin(9600);delay(250);
  lcd.begin(16,2);
}

byte A;
float u=36600,n1=0,Pref=5000000,lect,lect_ant,un;
int s=1,sw=1;

void loop(){
    lcd.clear();
    lcd.setCursor(0,0); lcd.print("PRESS START");
    if(digitalRead(pinsw)==HIGH){//Press start button
      digitalWrite(pinled,HIGH);      //Switch on LED
      tone(13,440,500); // Start up music
      lcd.setCursor(0,0);
```

```
      lcd.clear(); lcd.print("RUNNING HiL");
      lcd.setCursor(0,1);
      lcd.print("Pref=");
      lcd.setCursor(5,1);
      lcd.print(Pref);
      lcd.setCursor(9,1);
      lcd.print(" Kw     ");

      lect=-1;lect_ant=-1;
      for(long i=0; i<200000L;i++){
        while(Serial.available()>0){//ARDUINO reads wg
            A=Serial.read();
            if(A==45){ //minus sign
              s=-1;A=Serial.read();
            }
            if(A==43){//plus sign
            A=Serial.read();
            }
            n1=n1*10+(A-48);lect=s*n1;//ASCII to DEC
        }
        n1=0;s=1;

        if (lect>0){
          //TORQUE CONTROL, lect=Wg, u=Torque
          lect=0.105*lect; //read wg (rpm to rad/s)
          if (lect_ant==-1){
            lect_ant=lect;
          }
          //Euler numerical integration step size 0.3s
          un=u+0.3*(-u-u*((lect-lect_ant)/0.3)/lect+
          Pref/lect-150000*sign(u*lect-Pref)/lect);
          Serial.println(long(u));
          u=un;
          lect_ant=lect;
        }
        delay(150);
        delay(150);
        delay(150);
        delay(150);
      }
      tone(13,440,500);delay(1000);tone(13,440,500);
  }
 digitalWrite(pinled,LOW);
 delay(150);
}
```

Matlab script to run in real-time the HiL (FAST and Arduino):

```
clear all; close all;clc;
Simsetup;
global leer; leer=-1;
delete(instrfind({'Port'},{'COM3'}));
puerto_serial=serial('COM3');
puerto_serial.BaudRate=9600;
fopen(puerto_serial);
disp('Please start Arduino and then press a key');
pause;
disp('Starting FAST Simulation');
open_system('NREL5MW_SMC');
%Initial value of tau_c
set_param('NREL5MW_SMC/tau','Gain',num2str(26600));
% Starts Simulink
set_param('NREL5MW_SMC','SimulationCommand','Start');
h=add_exec_event_listener('NREL5MW_SMC/omega_g',...
'PostOutputs',@read_data);
while leer<0
    pause(0.1);
end
for i=1:48000
%Matlab sends to Arduino the value of wg
        fwrite(puerto_serial,num2str(round(leer)));
        pause(0.3);
        lect_usb=fscanf(puerto_serial,'%d');
        set_param('NREL5MW_SMC/tau','Gain',...
         num2str(lect_usb));
end
fclose(puerto_serial);
set_param('NREL5MW_SMC','SimulationCommand','Stop');
beep;
delete(puerto_serial);
```

Matlab function:

```
function leer=read_data(block,evenData);
global leer;
rt=get_param('NREL5MW_SMC/omega_g','RuntimeObject');
t=block.CurrentTime;
leer=block.InputPort(1).Data;
```
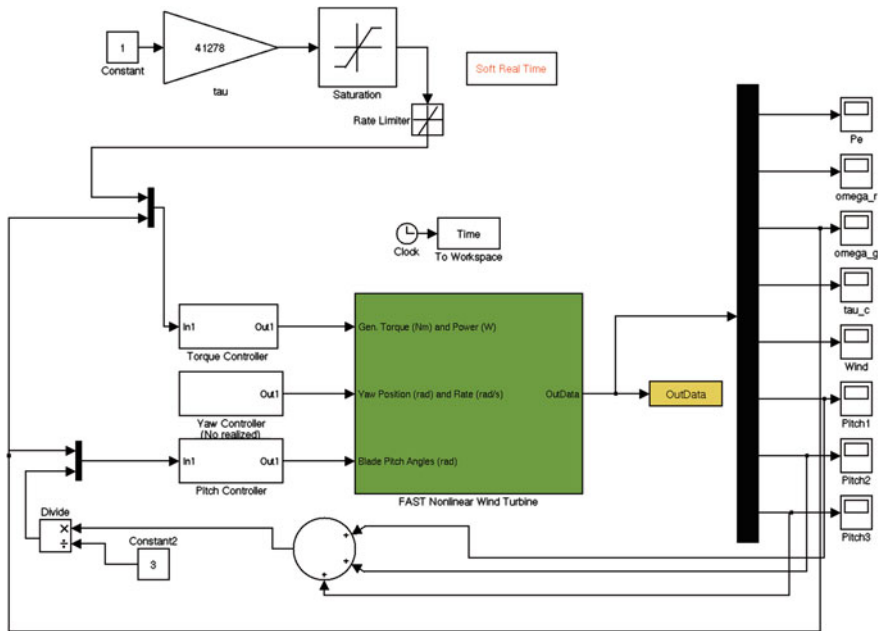
The Simulink diagram is given in Fig. 15.9.

Fig. 15.9 Simulink diagram

References

1. Arduino (2014) url: http://arduino.cc
2. Beltran B, Ahmed-Ali T, El Hachemi Benbouzid M (2008) Sliding mode power control of variable-speed wind energy conversion systems. IEEE Trans Energy Convers 23(2):551–558. Doi: 10.1109/TEC.2007.914163
3. Beltran B, Ahmed-Ali T, Benbouzid M (2009) High-order sliding-mode control of variable-speed wind turbines. IEEE Trans Ind Electron 56(9):3314–3321. doi:10.1109/TIE.2008.2006949
4. Bhat S, Bernstein D (1997) Finite-time stability of homogeneous systems. In: American control conference, 1997. Proceedings of the 1997, vol 4, pp 2513–2514. Doi: 10.1109/ACC.1997.609245
5. Boukhezzar B, Lupu L, Siguerdidjane H, Hand M (2007) Multivariable control strategy for variable speed, variable pitch wind turbines. Renewable Energy 32(8):1273–1287. doi: 10.1016/j.renene.2006.06.010, url: http://www.sciencedirect.com/science/article/pii/S0960148106001261
6. De Paoli S, Storni C (2011) Produsage in hybrid networks: sociotechnical skills in the case of Arduino. New Rev Hypermedia Multimedia 17(1):31–52

7. Hanselmann H (1996) Hardware-in-the-loop simulation testing and its integration into a cacsd toolset. In: Computer-aided control system design, 1996., proceedings of the 1996 IEEE international symposium on, IEEE, pp 152–156

8. Jonkman J (2013) NWTC computer-aided engineering tools (FAST). url: http://wind.nrel.gov/designcodes/simulators/fast/

9. Jonkman JM, Butterfield S, Musial W, Scott G (2009) Definition of a 5-MW reference wind turbine for offshore system development. Technical report, National Renewable Energy Laboratory, Golden, Colorado, nREL/TP-500-38060

10. Kelley N, Jonkman B (2013) NWTC computer-aided engineering tools (Turbsim). url: http://wind.nrel.gov/designcodes/preprocessors/turbsim/

11. Khezami N, Braiek NB, Guillaud X (2010) Wind turbine power tracking using an improved multimodel quadratic approach. ISA Trans 49(3):326–334. Doi: 10.1016/j.isatra.2010.03.008, url: http://www.sciencedirect.com/science/article/pii/S0019057810000273

12. Maclay D (1997) Simulation gets into the loop. IEEE Rev 43(3):109–112

13. Manjock A (2005) Evaluation Report: Design codes FAST and ADAMS for load calculations of onshore wind turbines, Germanischer Lloyd WindEnergie, Report no. 72042

14. Terwiesch P, Keller T, Scheiben E (1999) Rail vehicle control system integration testing using digital hardware-in-the-loop simulation. IEEE Trans Control Syst Technol 7(3):352–362

15. Vidal Y, Acho L, Luo N, Zapateiro M, Pozo F (2012) Power control design for variable-speed wind turbines. Energies 5(8):3033–3050. doi:10.3390/en5083033

16. Vincent TL, Grantham WJ (1999) Nonlinear and optimal control systems. John Wiley & Sons, Inc., New York

17. Zhang Q, Reid J, Wu D et al (2000) Hardware-in-the-loop simulator of an off-road vehicle electrohydraulic steering system. Trans ASAE 43(6):1323–1330